ISSN 1949-8470 (online)

World Journal of *Radiology*

World J Radiol 2018 January 28; 10(1): 1-8

Published by Baishideng Publishing Group Inc

WJR World Journal of Radiology

Contents

Monthly Volume 10 Number 1 January 28, 2018

ORIGINAL ARTICLE

Prospective Study

CORRECTION

World Journal of Radiology
Volume 10 Number 1 January 28, 2018

Contents

NAME OF JOURNAL
World Journal of Radiology

ISSN
ISSN 1949-8470 (online)

LAUNCH DATE
January 31, 2009

FREQUENCY
Monthly

EDITORIAL OFFICE
Xiu-Xia Song, Director
World Journal of Radiology
Baishideng Publishing Group Inc
7901 Stoneridge Drive, Suite 501, Pleasanton, CA 94588, USA
Telephone: +1-925-2238242
Fax: +1-925-2238243
E-mail: editorialoffice@wjgnet.com
Help Desk: http://www.f6publishing.com/helpdesk
http://www.wjgnet.com

PUBLISHER
Baishideng Publishing Group Inc
7901 Stoneridge Drive, Suite 501,
Pleasanton, CA 94588, USA
Telephone: +1-925-2238242
Fax: +1-925-2238243
E-mail: bpgoffice@wjgnet.com
Help Desk: http://www.f6publishing.com/helpdesk
http://www.wjgnet.com

PUBLICATION DATE
January 28, 2018

INSTRUCTIONS TO AUTHORS
http://www.wjgnet.com/bpg/gerinfo/204

ONLINE SUBMISSION
http://www.f6publishing.com

World Journal of Radiology

Submit a Manuscript: http://www.f6publishing.com

World J Radiol 2018 January 28; 10(1): 1-6

DOI: 10.4329/wjr.v10.i1.1

ISSN 1949-8470 (online)

ORIGINAL ARTICLE

Prospective Study

Computed tomography as primary postoperative follow-up after laparoscopic Roux-en-Y gastric bypass

Tarik Delko, Diana Mattiello, Thomas Koestler, Urs Zingg, Silke Potthast

Tarik Delko, Department of Surgery, University Hospital Basel, Basel 4031, Switzerland

Diana Mattiello, Thomas Koestler, Urs Zingg, Department of Surgery, Limmattal Hospital, Schlieren 8952, Switzerland

Silke Potthast, Department of Radiology, Limmattal Hospital, Schlieren 8952, Switzerland

ORCID number: Tarik Delko (0000-0003-4868-6665); Diana Mattiello (0000-0003-4724-0717); Thomas Koestler (0000-0002-1581-423X); Urs Zingg (0000-0001-9751-4064); Silke Potthast (0000-0002-4756-4634).

Author contributions: Delko T, Mattiello D, Koestler T, Zingg U and Potthast S each contributed to designing the study, performing the research and writing the paper.

Institutional review board statement: Institutional Review Board approval was obtained (KEK-ZH-Nr: 2013-0390; Zurich, Switzerland).

Informed consent statement: Written informed consent was obtained from all individuals who participated in the study.

Conflict-of-interest statement: All authors of this manuscript declare no conflicts of interest (financial and non-financial) with any companies, whose products or services may be related to the subject matter of the article.

Data sharing statement: No additional data are available.

Manuscript source: Invited manuscript

Correspondence to: Silke Potthast, MD, Chief Doctor, Department of Radiology, Limmattal Hospital, Urdorferstr 100, Schlieren 8952, Switzerland. silke.potthast@spital-limmattal.ch
Telephone: +41-44-7368170
Fax: +41-44-7332189

Received: November 1, 2017
Peer-review started: November 2, 2017
First decision: November 30, 2017
Revised: December 3, 2017
Accepted: January 25, 2018
Article in press: January 25, 2018
Published online: January 28, 2018

Abstract

AIM

To evaluate upper abdominal computed tomography (CT) scan as primary follow-up after laparoscopic Roux-en-Y gastric bypass (LRYGB).

METHODS

This prospective study was approved by the Ethical Committee of the State of Zurich, and informed consent was obtained from all patients. Sixty-one patients who underwent LRYGB received upper abdominal CT on postoperative day 1, with the following scan parameters: 0.6 mm collimation, 1.2 mm pitch, CareKV with reference 120 mAs and 120 kV, and 0.5 s rotation time. Diluted water-soluble radiographic contrast-medium (50 mL) was administered to achieve gastric pouch distension without movement of the patient. 3D images were evaluated to assess postoperative complications and the radiation dose received was analysed.

RESULTS

From the 70 patients initially enrolled in the study, 9 were excluded from analysis upon the intraoperative decision to perform a sleeve gastrectomy and not a LRYGB. In all of the 61 patients who were included in the analysis, CT

was feasible and there were no instances of aspiration or vomiting. In 7 patients, two upper abdominal scans were necessary as the pouch was not distended by contrast medium in the first acquisition. Radiologically, no leak and no relevant stenosis were found on the first postoperative day. These early postoperative CT findings were consistent with the findings at clinical follow-up 6 wk postoperatively, with no leaks, stenosis or obstructions being diagnosed. The average total dose length product in CT was 536.6 mGycm resulting in an average effective dose of 7.8 mSv. The most common surgical complication, superficial surgical site infections (n = 4), always occurred at the upper left trocar site, where the circular stapler had been introduced.

CONCLUSION

Early LRYGB postoperative multislice spiral CT scan is feasible, with low morbidity, and provides more accurate anatomical information than standard upper gastrointestinal contrast study.

Key words: Laparoscopic proximal Roux-en-Y gastric bypass; Abdominal computed tomography; Stenosis; Upper gastrointestinal study; Anastomotic leak

Core tip: In most bariatric centres, a routine upper gastrointestinal (UGI) study is performed in the early postoperative period. Yet, the real value of a standard postoperative radiological exam after laparoscopic Roux-en-Y gastric bypass is debatable. From the available data, an UGI is not necessary as a standard postoperative exam and, similarly, a routine computed tomography (CT) scan might not be indicated. For patients who experience unexpectedly difficult surgery or abnormal postoperative clinical course, CT is the diagnostic tool of choice, especially considering that a number of patients with pathological findings in UGI contrast studies will additionally undergo CT scan.

Delko T, Mattiello D, Koestler T, Zingg U, Potthast S. Computed tomography as primary postoperative follow-up after laparoscopic Roux-en-Y gastric bypass. *World J Radiol* 2018; 10(1): 1-6 Available from: URL: http://www.wjgnet.com/1949-8470/full/v10/i1/1.htm DOI: http://dx.doi.org/10.4329/wjr.v10.i1.1

INTRODUCTION

Morbid obesity has become a major worldwide health problem, with increasing prevalence[1-3]. The most effective treatment to reduce weight in obese patients is bariatric surgery. Consequently, the number of bariatric procedures has increased dramatically over the last decade[4]. The laparoscopic Roux-en-Y gastric bypass (LRYGB) is the most common bariatric procedure worldwide. Early morbidity and mortality of LRYGB is generally very low[5]. In a majority of bariatric centres, postoperative upper gastrointestinal (UGI) contrast studies are performed routinely in order to evaluate complications that may arise in the early postoperative period, such as anastomotic leaks or strictures[6,7]. The usefulness of UGI examination is debatable, considering its radiation dose and the diagnostic information obtained[6,8-10].

UGI examinations are insufficient to accurately assess certain postoperative surgical problems, such as hematoma or fluid collections, and have only limited sensitivity (*i.e.*, 25% for correctly diagnosing a leak)[11]. Furthermore, in case of UGI indicating an early postoperative complication, a multislice computed tomography (CT) will be additionally performed to better delineate the pathologic features[12,13] and to provide guidance for possible interventional procedures such as aspiration or drainage of fluid collections. Several studies have suggested the usefulness of CT to investigate postoperative complications after LRYGB; however, data on routinely performed CT after bariatric surgery are scarce[13-15]. Hence, the prospective study described herein was conducted to assess the feasibility and usefulness of CT scan as a primary early postoperative radiological measure in patients who underwent LRYGB.

MATERIALS AND METHODS

Informed consent was obtained from all patients. This prospective study was performed at Limmattal Hospital and approved by the Ethical Committee of Zurich, Switzerland. All patients were preoperatively assessed according to the guidelines of the Swiss Study Group for Morbid Obesity. A total of 70 patients undergoing LRYGB were enrolled during the 10-mo study period (July 2014 to May 2015). Surgery was performed by two surgeons, each having individual experience of over 500 LRYGB procedures.

LRYGB procedure

A laparoscopic six-port technique with prior creation of the pneumoperitoneum by Veress needle was used. The greater omentum was split and the ligament of Treitz identified. The length of the biliopancreatic limb was measured to 50 cm and the jejunum divided using an Echelon Flex™ Powered Endopath® Stapler (60 mm, white; Ethicon, Somerville, NJ, United States). Next, the proximal stomach was divided using the Echelon Flex™ Powered Endopath® Stapler (60 mm, blue; Ethicon). The first cartridge was fired perpendicular to the lesser curvature and one to two additional cartridges parallel to the lesser curvature up to the angle of His, lateral to the Besley's fat pad.

Once the small pouch was created, an end-to-side, ante-colic and ante-gastric gastro-jejunal anastomosis was created using a Premium Plus CEEA™ 25 mm circular stapler (Covidien, Dublin, Republic of Ireland). Then, the jejuno-jejunal anastomosis was created 150

Table 1 Patient demographic and clinical data

Feature	Data, *n* (%)
Patients	61
Age, yr	40.3 (19-62)
BMI, kg/m^2	41 (35-48.1)
Female	50 (82)
Male	11 (18)
ASA Ⅰ	0 (0)
ASA Ⅱ	30 (49.1)
ASA Ⅲ	31 (50.9)
ASA Ⅳ	0 (0)

ASA: American Society of Anesthesiologists; BMI: Body mass index.

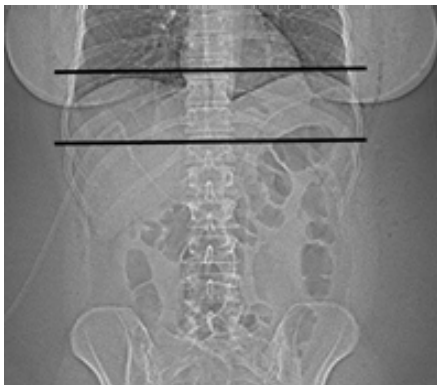

Figure 1 Scout view with depicted scan length.

cm distal to the gastro-jejunal anastomosis by using the Echelon Flex™ Powered Endopath® Stapler (60 mm, white; Ethicon), with closure of the stapler entry defect using absorbable PDS® (polydioxanone) 3-0 suture (Ethicon). All mesenteric defects were closed systematically with non-absorbable interrupted Prolene® 3-0 sutures (Ethicon).

CT technique

CT scanning was performed on the first morning postoperatively. All patients were kept as nil per os until the upper abdomen CT had been performed. A clinical scanner equipped with modern dose reduction software was used (Somatom Definition 64; Siemens Healthineers, Erlangen, Germany), with the following scan parameters: collimation, 0.6 mm; pitch, 1.2 mm; CareKV with reference 120 mAs and reference 120 kV; rotation time, 0.5 s. The scan was acquired in supine position and a scout scan was acquired. Diluted water-soluble radiographic contrast-medium (50 mL) (Telebrix Gastro®, Guerbet, France) was given in a spout cup to achieve gastric pouch distension without movement of the patient.

The scan was performed in cranio-caudal direction, starting at the level of the distal oesophagus and stopping just distal to the pouch (Figure 1). The average total dose length product was registered and radiation dose was calculated. Image data was transferred to a 3D workstation and 3D images were created for evaluation of leaks and stenosis. The procedure was performed in all patients by the same senior radiologist with more than 15 years of experience in body radiology. If no significant stenosis or leak was diagnosed, a liquid diet was started.

Basic demographic, pre-, peri- and postoperative data was collected prospectively and entered into a database (Excel®, Office, Microsoft). Postoperative morbidity was separated into surgical and non-surgical categories. Surgical morbidity included anastomotic leak, deep surgical site infection (*i.e.,* intra-abdominal), superficial surgical site infection, re-laparoscopy and re-laparotomy. Non-surgical morbidity included pulmonary or cardiac complications as well as renal failure. Special attention was given to CT-related morbidity, such as aspiration of contrast fluid, and the presence of leakage, slow transit or stenosis in the postoperative CT scan.

RESULTS

A total of 70 patients were enrolled in the study. Nine of those were excluded upon intraoperative decision to perform a sleeve gastrectomy and not a LRYGB; the main reason for procedure switch was suspected tension at the gastro-jejunostomy due to short and fatty mesentery. Among the 61 included patients, 50 were female and 11 were male, with a mean age of 40.3 years. The basic demographic and clinical data are presented in Table 1.

All patients tolerated early CT well and no vomiting occurred. 3D analysis of imaging was feasible in all patients and the proximal anastomosis was depicted very well (Figure 2). In 7 patients, two upper abdominal scans were necessary as the pouch was not distended by contrast medium in the first acquisition. The average total dose length product in CT was 536.6 mGycm and 7.8 mSv, respectively. Radiologically, no cases of leak or relevant stenosis were found on the first postoperative day. These early postoperative CT findings were consistent with the clinical follow-up at 6 wk postoperatively, for which no leaks, stenosis or obstructions were diagnosed. The morbidity data are presented in Table 2.

Non-surgical morbidity was very low. CT diagnosed atelectases in 85.3% of the patients and pleural effusions in 41% of the patients. In these patients, physiotherapy, which is part of the standard postoperative protocol, was intensified and fluid volume treatment was optimized, but no interventional treatment was required. In 1 patient with pneumonia, an antibiotic therapy was started. Moderate to severe diffuse hepatic steatosis was seen in 11 patients. One patient showed a kidney stone on the left side with no clinical symptoms.

The most common surgical complication, superficial surgical site infections (n = 4), occurred exclusively at the upper left trocar site, where the circular stapler had been introduced. No intra-abdominal re-operation due to complications was necessary. No radiological drain placement was needed within 6 wk postoperatively.

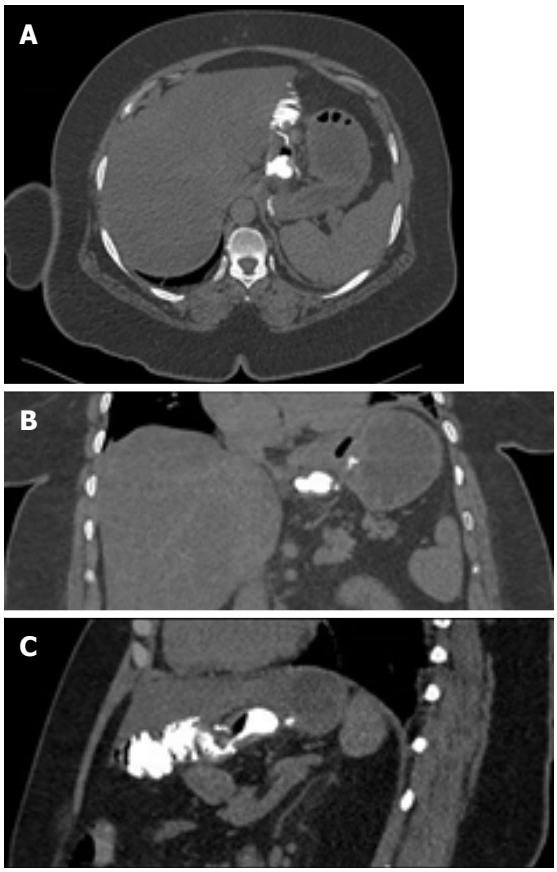

Figure 2 Proximal anastomosis with oral contrast-filled pouch. A: Axial; B: Coronal; C: Sagittal.

DISCUSSION

The present study of a large prospective cohort of patients who underwent LRYGB shows that CT scan performed on the first postoperative day is feasible and safe, and has high diagnostic accuracy. The CT was able to diagnose pulmonary changes that had been missed using UGI.

The usefulness of postoperative imaging after LRYGB, especially UGI studies, is under debate. Several studies have questioned the use of routine imaging, in particular UGI, in the early postoperative phase due to lack of sensitivity, high cost and the substantial radiation exposure to patients[5-7]. Most bariatric surgeons consider UGI useful to assess the gastric pouch and gastro-jejunostomy for anastomotic leaks or strictures in the early postoperative phase[12]. However, evaluation of a possible leak at the level of the biliopancreatic anastomosis is not possible with a routine UGI[16]. The positive predictive value and the sensitivity of diagnosing a leak by UGI were 31% and 25%, respectively, and the procedure has limited or no value in finding extra-luminal problems, such as hematoma, and is of no use for evaluating the biliopancreatic limb.

The effectiveness of UGI contrast studies has been evaluated in a number of research studies[8-10,17,18]. Brockmeyer *et al*[6] reported a 100% specificity for detection of a stenosis in a total of 319 patients. However, no leaks were detected on day 1 or 2 after surgery; although, 10 leaks occurred during further follow-up (all diagnosed by CT). Therefore, these authors stopped performing routine UGI on postoperative day 1 after a bariatric surgery.

Table 2 Morbidity according to surgical and non-surgical complications

Surgical		Non-surgical, *n* (%)	
Anastomotic leak	0	Atelectasis	52 (85.3)
Superficial hematoma	1 (1.6)	Pleural effusion	25 (41.0)
Superficial surgical site infection	4 (6.6)	Pneumonia	1 (1.6)
Re-laparoscopy	0	Cardiac complications	1 (1.6)
Intraluminal bleeding	1 (1.6)	Renal failure	0
		Steatosis hepatitis	7 (11.5)
		Kidney stone	1 (1.6)

Dallal *et al*[17] found that using clinical indicators of a leak or bleeding was sufficient for diagnosis, and no additional data from drains or an UGI study were necessary. The reported anastomotic leakage rate following LRYGB varies from 0.1%-5.6%, depending on the definition of a leak and the volume of the reporting surgical unit[19]. Leaks are the most significant factor for postoperative mortality in those patients[19,20]. Diagnosis usually takes place within the first 10 days after surgery[21]. A large prospective study[22] with 3018 patients diagnosed anastomotic leaks in 2.1% at a median of 3 d after LRYGB.

The earlier an anastomotic leak diagnosis is made, the better a patient's prospects. This is mainly because early detection allows for an early therapeutic intervention, such as re-operation, surgical drainage or the application of stents. Delayed diagnosis of a leak leads to peritonitis and subsequently to a significantly higher mortality. In contrast to Dallal *et al*[17], we believe that radiological examination is an important adjunct since the clinical evaluation of these morbidly obese patients is difficult. The only clinical symptoms may be tachycardia and abdominal discomfort. In most bariatric centres, an UGI swallow study is performed on the first postoperative day[21] to assess for anastomotic stenosis or slow contrast transit, as well as to exclude an early postoperative leak primarily to allow the start of liquid intake. Therefore, it was decided to perform a CT scan on the first postoperative scan.

In UGI contrast studies, extra-luminal contrast extending into the upper left abdomen is regarded as highly suspicious with respect to a potential leak at the gastro-jejunostomy. Major leaks can be identified in up to 100% of patients by using UGI, but minor leaks are often missed. The latter are preferably diagnosed on CT scans[12,23-25]. Sometimes, the only sign of extra-luminal contrast in UGI studies is an opacification of the surgical drain that was placed nearby. But, some surgeons tend to omit a drain, and the opportunity of detecting this discrete sign is lost[26]. If no complication is detected by radiological means, oral intake is started. If UGI contrast studies are suspicious of a leak, stenosis or any other obstruction, usually, a CT scan is performed[12].

An anastomotic leak can show various manifestations on CT, including gas or fluid collections adjacent to the pouch, a tract of enteric contrast extending through the anastomotic defect, staple line dehiscence or diffuse peritoneal fluid[14]. Assessment of the jejuno-jejunostomy is easily feasible by CT.

Anastomotic stenosis or obstruction can be due to oedema, hematoma, ischemia or a blood clot at the circular stapled anastomosis[16]. These phenomena are more common at the gastro-jejunostomy (3%-9%) compared to the jejuno-jejunostomy (0.8%-2%)[16]. UGI contrast studies allow finding of an obstructed flow of contrast. But, in order to identify the underlying cause, again, a CT is usually performed. Although CT does not allow dynamic imaging, abnormal pouch distension and a contrast-filled oesophagus are indicators of an obstruction at the proximal anastomosis. CT can differentiate between any transient cause of obstruction, such as hematoma or oedema within the bowel wall, and a more permanent cause, such as kinking. Whereas the former will usually resolve within a few days and mandates only a slower increase of the oral diet, the latter will lead to further invasive procedures, such as endoscopy or re-operation. Furthermore, in case of suspected bleeding, a CT scan with an arterial phase can be performed to exclude surgical bleeding that needs to be addressed by re-operation.

Concerning the radiation dose, the individual dose received was 7.8 mSv for a limited CT scan in the obese patients of the present study. UGI radiation doses of 4 mSv per exam are known from the literature[9]. However, this is a very high radiation dose considering its limited use of diagnosing relevant pathologies. In contrast, CT scans, despite having a higher radiation dose, provide detailed depiction of the proximal and distal anastomosis and of any complication within the soft-tissue and lung base. CT scans also provide guidance for any possible interventional procedures. In addition, bariatric surgery patients may receive radiation doses from further postoperative radiological exams that could potentially increase their lifetime risk of cancer[9]. All these factors need to be considered when implementing postoperative protocols.

Our present study showed that CT is feasible and safe, and that a number of extra-gastrointestinal pathologies were detectable by this imaging modality. However, the real value as a standard postoperative radiological exam after LRYGB is debatable. From the available data, an UGI is not necessary as a standard postoperative exam, and similarly, a routine CT might not be indicated. However, if a patient undergoes unexpectedly difficult surgery or displays an abnormal postoperative clinical course, CT is the diagnostic tool of choice and the indication should be given liberally, especially when one considers the fact that a number of patients with pathological findings in UGI contrast studies will additionally undergo a CT scan.

The main limitation of this study is the fact that no surgical complications, such as leaks or obstructions, occurred in our study population. Therefore, no statement can be made on the sensitivity or specificity of CT regarding these pathologies on the first postoperative day. However, in our opinion, this technique is superior to a UGI study, since distinctive features such as fluid collection or free air surrounding the anastomosis, which are evidence for more serious complications, can be seen on CT images. Such has been demonstrated by Yu *et al*[14] in a retrospective study. While the risk-to-benefit ratio may be justified, strategies to minimize radiation dose should be emphasized and the appropriate technique in radiology should be selected judiciously.

In conclusion, early postoperative CT scan is feasible and safe. It has advantages over a standard UGI study as it provides more accurate information of the early postoperative anatomy after LRYGB and detects extra-gastrointestinal pathologies.

ARTICLE HIGHLIGHTS

Research background

The laparoscopic Roux-en-Y gastric bypass (LRYGB) is the most common bariatric procedure worldwide. In a majority of bariatric centres, postoperative upper gastrointestinal (UGI) contrast studies are performed routinely in order to evaluate for complications. The usefulness of UGI examinations is debatable considering its related radiation dose and the obtained diagnostic information.

Research motivation

Several studies have suggested the usefulness of computed tomography (CT) to investigate postoperative complications after LRYGB, but data on routinely performed CT after bariatric surgery are scarce. UGI contrast studies are insufficient to accurately assess certain postoperative surgical problems, such as hematoma or fluid collections, and have only limited sensitivity for correctly diagnosing a leak, whereas CT can clearly diagnose these complications.

Research objectives

The prospective study was conducted to assess the feasibility and usefulness of CT scan as a primary early postoperative radiological measure in patients who underwent LRYGB.

Research methods

Sixty-one patients who underwent LRYGB received upper abdominal CT on postoperative day 1. Diluted water-soluble radiographic contrast-medium (50 mL) was administered to achieve gastric pouch distension without movement of the patient. 3D images were evaluated to assess postoperative complications and the radiation dose received was analysed.

Research results

In 61 patients who were included in the analysis, CT was feasible and there were no instances of aspiration or vomiting. In 7 patients, two upper abdominal scans were necessary as the pouch was not distended by contrast medium in the first acquisition. Radiologically, no leak and no relevant stenosis were found on the first postoperative day. These early postoperative CT findings were consistent with the findings at clinical follow-up 6 wk postoperatively, with no leaks, stenosis or obstructions being diagnosed. The average total dose length product in CT was 536.6 mGycm resulting in an average effective dose of 7.8 mSv.

Research conclusions

Early LRYGB postoperative CT scan is feasible, with low morbidity, and provides more accurate anatomical information than standard upper gastrointestinal contrast study.

Research perspectives

The main limitation of this study is the fact that no surgical complications,

such as leaks or obstructions, occurred in our study population. Therefore, no statement can be made on the sensitivity or specificity of CT regarding these pathologies on the first postoperative day. From this point of view large trials are necessary to enable a statement on the sensitivity and specificity of CT in this patient cohort.

REFERENCES

1 **Ogden CL**, Carroll MD, Curtin LR, McDowell MA, Tabak CJ, Flegal KM. Prevalence of overweight and obesity in the United States, 1999-2004. *JAMA* 2006; **295**: 1549-1555 [PMID: 16595758 DOI: 10.1001/jama.295.13.1549]

2 **Fisher BL**, Schauer P. Medical and surgical options in the treatment of severe obesity. *Am J Surg* 2002; **184**: 9S-16S [PMID: 12527344 DOI: 10.1016/S0002-9610(02)01173-X]

3 **Allison DB**, Fontaine KR, Manson JE, Stevens J, VanItallie TB. Annual deaths attributable to obesity in the United States. *JAMA* 1999; **282**: 1530-1538 [PMID: 10546692 DOI: 10.1001/jama.282.16.1530]

4 **Blachar A**, Federle MP, Pealer KM, Ikramuddin S, Schauer PR. Gastrointestinal complications of laparoscopic Roux-en-Y gastric bypass surgery: clinical and imaging findings. *Radiology* 2002; **223**: 625-632 [PMID: 12034927 DOI: 10.1148/radiol.2233011323]

5 **Doraiswamy A**, Rasmussen JJ, Pierce J, Fuller W, Ali MR. The utility of routine postoperative upper GI series following laparoscopic gastric bypass. *Surg Endosc* 2007; **21**: 2159-2162 [PMID: 17514398 DOI: 10.1007/s00464-007-9314-9]

6 **Brockmeyer JR**, Simon TE, Jacob RK, Husain F, Choi Y. Upper gastrointestinal swallow study following bariatric surgery: institutional review and review of the literature. *Obes Surg* 2012; **22**: 1039-1043 [PMID: 22527600 DOI: 10.1007/s11695-012-0658-4]

7 **Singh R**, Fisher BL. Sensitivity and specificity of postoperative upper GI series following gastric bypass. *Obes Surg* 2003; **13**: 73-75 [PMID: 12630617 DOI: 10.1381/096089203321136629]

8 **Blanchet MC**, Mesmann C, Yanes M, Lepage S, Marion D, Gelas P, Gouillat C. 3D gastric computed tomography as a new imaging in patients with failure or complication after bariatric surgery. *Obes Surg* 2010; **20**: 1727-1733 [PMID: 20730506 DOI: 10.1007/s11695-010-0256-2]

9 **Oei TN**, Shyn PB, Govindarajulu U, Flint R. Diagnostic medical radiation dose in patients after laparoscopic bariatric surgery. *Obes Surg* 2010; **20**: 569-573 [PMID: 19779760 DOI: 10.1007/s11695-009-9966-8]

10 **Mittermair R**, Sucher R, Perathoner A, Wykypiel H. Routine upper gastrointestinal swallow studies after laparoscopic sleeve gastrectomy are unnecessary. *Am J Surg* 2014; **207**: 897-901 [PMID: 24119721 DOI: 10.1016/j.amjsurg.2013.06.015]

11 **Rawlins L**, Penn R, Schirmer B, Hallowell P. Accuracy of routine postoperative swallow study in predicting leak or obstruction after gastric bypass. *Surg Obes Relat Dis* 2015; **11**: 1-4 [PMID: 25553886 DOI: 10.1016/j.soard.2014.07.019]

12 **Blachar A**, Federle MP, Pealer KM, Abu Abeid S, Graif M. Radiographic manifestations of normal postoperative anatomy and gastrointestinal complications of bariatric surgery, with emphasis on CT imaging findings. *Semin Ultrasound CT MR* 2004; **25**: 239-251 [PMID: 15272548 DOI: 10.1053/j.sult.2004.03.005]

13 **Alva S**, Eisenberg D, Duffy A, Roberts K, Israel G, Bell R. Virtual three-dimensional computed tomography assessment of the gastric pouch following laparoscopic Roux-Y gastric bypass. *Obes Surg* 2008; **18**: 364-366 [PMID: 18274830 DOI: 10.1007/s11695-008-9438-6]

14 **Yu J**, Turner MA, Cho SR, Fulcher AS, DeMaria EJ, Kellum JM, Sugerman HJ. Normal anatomy and complications after gastric bypass surgery: helical CT findings. *Radiology* 2004; **231**: 753-760 [PMID: 15163816 DOI: 10.1148/radiol.2313030546]

15 **Karcz WK**, Kuesters S, Marjanovic G, Suesslin D, Kotter E, Thomusch O, Hopt UT, Felmerer G, Langer M, Baumann T. 3D-MSCT gastric pouch volumetry in bariatric surgery-preliminary clinical results. *Obes Surg* 2009; **19**: 508-516 [PMID: 19104904 DOI: 10.1007/s11695-008-9776-4]

16 **Lehnert B**, Moshiri M, Osman S, Khandelwal S, Elojeimy S, Bhargava P, Katz DS. Imaging of complications of common bariatric surgical procedures. *Radiol Clin North Am* 2014; **52**: 1071-1086 [PMID: 25173659 DOI: 10.1016/j.rcl.2014.05.009]

17 **Dallal RM**, Bailey L, Nahmias N. Back to basics--clinical diagnosis in bariatric surgery. Routine drains and upper GI series are unnecessary. *Surg Endosc* 2007; **21**: 2268-2271 [PMID: 17483995 DOI: 10.1007/s00464-007-9368-8]

18 **Carter JT**, Tafreshian S, Campos GM, Tiwari U, Herbella F, Cello JP, Patti MG, Rogers SJ, Posselt AM. Routine upper GI series after gastric bypass does not reliably identify anastomotic leaks or predict stricture formation. *Surg Endosc* 2007; **21**: 2172-2177 [PMID: 17483998 DOI: 10.1007/s00464-007-9326-5]

19 **Fernandez AZ Jr**, DeMaria EJ, Tichansky DS, Kellum JM, Wolfe LG, Meador J, Sugerman HJ. Experience with over 3,000 open and laparoscopic bariatric procedures: multivariate analysis of factors related to leak and resultant mortality. *Surg Endosc* 2004; **18**: 193-197 [PMID: 14691697 DOI: 10.1007/s00464-003-8926-y]

20 **Schauer PR**, Ikramuddin S, Gourash W, Ramanathan R, Luketich J. Outcomes after laparoscopic Roux-en-Y gastric bypass for morbid obesity. *Ann Surg* 2000; **232**: 515-529 [PMID: 10998650 DOI: 10.1097/00000658-200010000-00007]

21 **Carucci LR**, Turner MA. Radiologic evaluation following Roux-en-Y gastric bypass surgery for morbid obesity. *Eur J Radiol* 2005; **53**: 353-365 [PMID: 15741009 DOI: 10.1016/j.ejrad.2004.12.010]

22 **Gonzalez R**, Sarr MG, Smith CD, Baghai M, Kendrick M, Szomstein S, Rosenthal R, Murr MM. Diagnosis and contemporary management of anastomotic leaks after gastric bypass for obesity. *J Am Coll Surg* 2007; **204**: 47-55 [PMID: 17189112 DOI: 10.1016/j.jamcollsurg.2006.09.023]

23 **Marshall JS**, Srivastava A, Gupta SK, Rossi TR, DeBord JR. Roux-en-Y gastric bypass leak complications. *Arch Surg* 2003; **138**: 520-523; discussion 523-524 [PMID: 12742956 DOI: 10.1001/archsurg.138.5.520]

24 **Podnos YD**, Jimenez JC, Wilson SE, Stevens CM, Nguyen NT. Complications after laparoscopic gastric bypass: a review of 3464 cases. *Arch Surg* 2003; **138**: 957-961 [PMID: 12963651 DOI: 10.1001/archsurg.138.9.957]

25 **Hamilton EC**, Sims TL, Hamilton TT, Mullican MA, Jones DB, Provost DA. Clinical predictors of leak after laparoscopic Roux-en-Y gastric bypass for morbid obesity. *Surg Endosc* 2003; **17**: 679-684 [PMID: 12618940 DOI: 10.1007/s00464-002-8819-5]

26 **Carucci LR**, Turner MA, Conklin RC, DeMaria EJ, Kellum JM, Sugerman HJ. Roux-en-Y gastric bypass surgery for morbid obesity: evaluation of postoperative extraluminal leaks with upper gastrointestinal series. *Radiology* 2006; **238**: 119-127 [PMID: 16373763 DOI: 10.1148/radiol.2381041557]

P- Reviewer: Gao BL, Mastoraki A **S- Editor**: Cui LJ **L- Editor**: A
E- Editor: Li RF

World Journal of Radiology

Submit a Manuscript: http://www.f6publishing.com

World J Radiol 2018 January 28; 10(1): 7-8

DOI: 10.4329/wjr.v10.i1.7

ISSN 1949-8470 (online)

CORRECTION

Correction to "Asymmetrically hypointense veins on T2*w imaging and susceptibility-weighted imaging in ischemic stroke" [*World J Radiol* 2013; 5(4): 156-165]

Ulf Jensen-Kondering, Ruwen Böhm

Ulf Jensen-Kondering, Institute of Neuroradiology, University of Schleswig-Holstein, Campus Kiel, Kiel 24105, Germany

Ruwen Böhm, Institute of Experimental and Clinical Pharmacology, University of Schleswig-Holstein, Campus Kiel, Kiel 24105, Germany

ORCID number: Ulf Jensen-Kondering (0000-0002-0860-4410).

Author contributions: Jensen-Kondering U and Böhm R contributed to this correction.

Conflict-of-interest statement: No potential conflicts of interest relevant to this article were reported.

Manuscript source: Unsolicited manuscript

Correspondence to: Dr. Ulf Jensen-Kondering, MD, Attending Doctor, Institute of Neuroradiology, University of Schleswig-Holstein, Campus Kiel, Haus 41, Arnold-Heller-Str. 3, Kiel 24105, Germany. ulfrjensen@web.de
Telephone: +49-431-5974806
Fax: +49-431-5974913

Received: December 7, 2017
First decision: December 11, 2017
Revised: December 25, 2017
Accepted: January 25, 2018
Article in press: January 25, 2018

Published online: January 28, 2018

Jensen-Kondering U, Böhm R. Correction to "Asymmetrically hypointense veins on T2*w imaging and susceptibility-weighted imaging in ischemic stroke" [*World J Radiol* 2013; 5(4): 156-165]. *World J Radiol* 2018; 10(1): 7-8 Available from: URL: http://www.wjgnet.com/1949-8470/full/v10/i1/7.htm DOI: http://dx.doi.org/10.4329/wjr.v10.i1.7

CORRECTION

Correction to: Jensen-Kondering U, Böhm R. Asymmetrically hypointense veins on T2*w imaging and susceptibility-weighted imaging in ischemic stroke. *World J Radiol* 2013; 5(4): 156-165 PMID: 23671751 DOI: 10.4329/wjr.v5.i4.156[1].

Results

Third paragraph: (1) (n = 17441 patients) should read (n = 441 patients) instead; (2) (n = 4111 patients) should read (n = 111 patients) instead.

Fourth paragraph: (1) (> 6 h, n = 15579 patients) should read (> 6 h, n = 579 patients) instead; (2) (⩽ 6 h = 11337 patients) should read (⩽ 6 h = 337 patients) instead; (3) (170 patients) should read (180 patients) instead.

Table 3

Conventional MRI, column 2: 11 (242) should read 11 (81) instead.

Discussion

Figure 1A: χ^{DHb} 0.4-0.5 should read χ^{DHb} normal instead.

Figure 1B: χ^{DHb} 0.7-1 should read χ^{DHb} elevated instead.

REFERENCES

1 **Jensen-Kondering U**, Böhm R. Asymmetrically hypointense veins on T2*w imaging and susceptibility-weighted imaging in ischemic stroke. *World J Radiol* 2013; **5**: 156-165 [PMID: 23671751 DOI: 10.4329/wjr.v5.i4.156]

S- Editor: Cui LJ **L- Editor**: A **E- Editor**: Li RF

Published by **Baishideng Publishing Group Inc**
7901 Stoneridge Drive, Suite 501, Pleasanton, CA 94588, USA
Telephone: +1-925-223-8242
Fax: +1-925-223-8243
E-mail: bpgoffice@wjgnet.com
Help Desk: http://www.f6publishing.com/helpdesk
http://www.wjgnet.com

ISSN 1949-8470 (online)

World Journal of *Radiology*

World J Radiol 2018 February 28; 10(2): 9-23

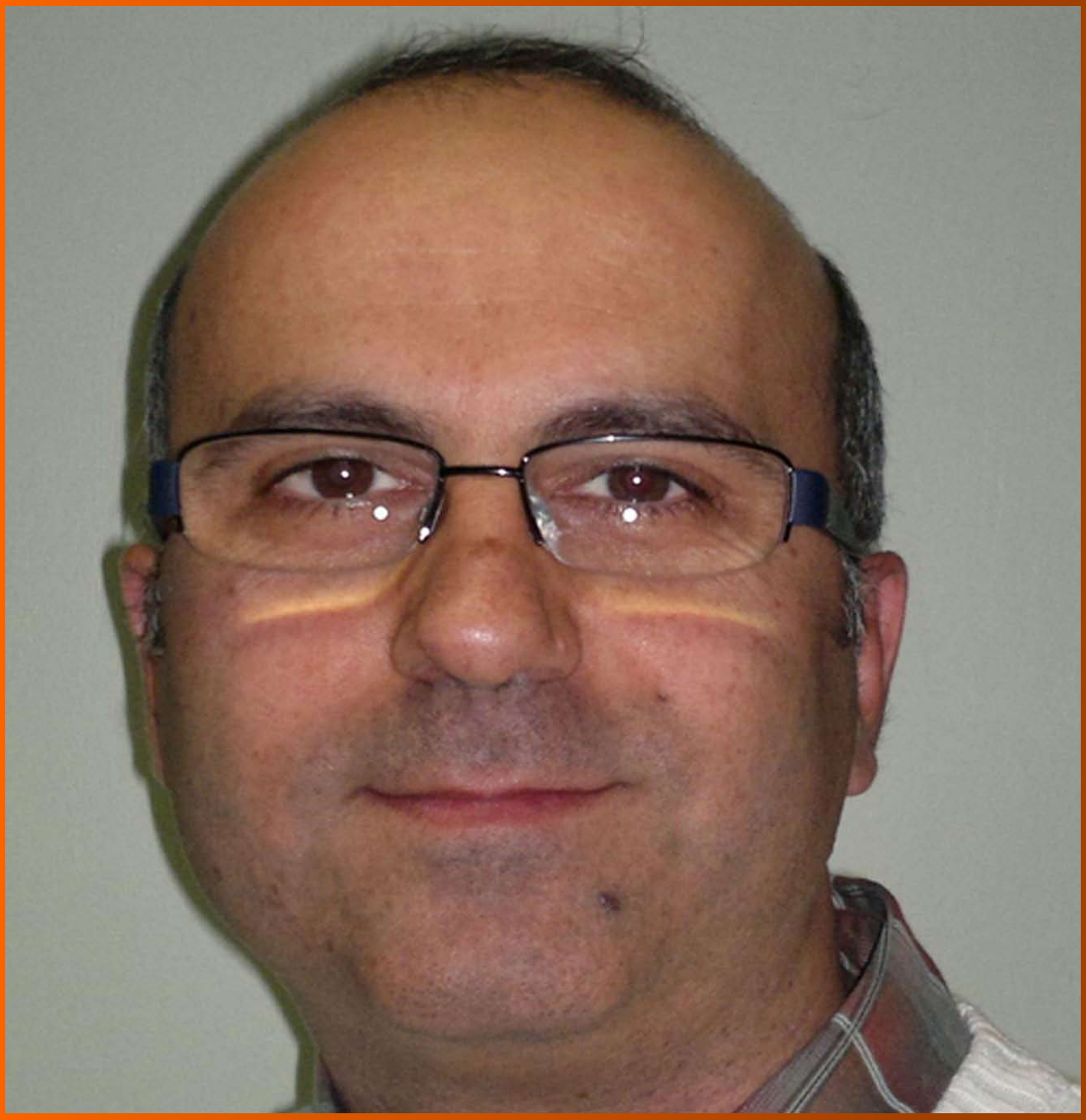

Published by Baishideng Publishing Group Inc

WJR World Journal of Radiology

Contents

Monthly Volume 10 Number 2 February 28, 2018

MINIREVIEWS

World Journal of Radiology
Volume 10 Number 2 February 28, 2018

Contents

NAME OF JOURNAL
World Journal of Radiology

ISSN
ISSN 1949-8470 (online)

LAUNCH DATE
January 31, 2009

FREQUENCY
Monthly

EDITORIAL OFFICE
Xiu-Xia Song, Director
World Journal of Radiology
Baishideng Publishing Group Inc
7901 Stoneridge Drive, Suite 501, Pleasanton, CA 94588, USA
Telephone: +1-925-2238242
Fax: +1-925-2238243
E-mail: editorialoffice@wjgnet.com
Help Desk: http://www.f6publishing.com/helpdesk
http://www.wjgnet.com

PUBLISHER
Baishideng Publishing Group Inc
7901 Stoneridge Drive, Suite 501,
Pleasanton, CA 94588, USA
Telephone: +1-925-2238242
Fax: +1-925-2238243
E-mail: bpgoffice@wjgnet.com
Help Desk: http://www.f6publishing.com/helpdesk
http://www.wjgnet.com

PUBLICATION DATE
February 28, 2018

INSTRUCTIONS TO AUTHORS
http://www.wjgnet.com/bpg/gerinfo/204

ONLINE SUBMISSION
http://www.f6publishing.com

World Journal of Radiology

Submit a Manuscript: http://www.f6publishing.com

World J Radiol 2018 February 28; 10(2): 9-23

DOI: 10.4329/wjr.v10.i2.9

ISSN 1949-8470 (online)

MINIREVIEWS

Magnetic resonance imaging ancillary features used in Liver Imaging Reporting and Data System: An illustrative review

David Campos-Correia, João Cruz, António P Matos, Filipa Figueiredo, Miguel Ramalho

David Campos-Correia, Department of Radiology, Centro Hospitalar de Lisboa Ocidental, Lisbon 1349-019, Portugal

João Cruz, António P Matos, Filipa Figueiredo, Miguel Ramalho, Department of Radiology, Hospital Garcia de Orta, Almada 2805-267, Portugal

ORCID number: David Campos-Correia (0000-0001-5513-7897); João Cruz (0000-0003-1386-736X); António P Matos (0000-0002-8118-1696); Filipa Figueiredo (0000-0001-6276-2949); Miguel Ramalho (0000-0003-2522-1670).

Author contributions: All authors have contributed equally to this work in form of literature review, manuscript writing, editing, figure collection, annotation and captioning.

Conflict-of-interest statement: There is no conflict of interest associated with any of the senior author or other co-authors contributed their efforts in this manuscript.

Manuscript source: Invited manuscript

Correspondence to: Miguel Ramalho, MD, Assistant Professor, Department of Radiology, Hospital Garcia de Orta, EPE, Av. Torrado da Silva, Almada 2805-267, Portugal. miguel-ramalho@netcabo.pt
Telephone: +351-212-940294
Fax: +351-212-957004

Received: January 1, 2018
Peer-review started: January 2, 2018
First decision: January 15, 2018
Revised: January 24, 2018
Accepted: February 25, 2018
Article in press: February 25, 2018

Published online: February 28, 2018

Abstract

Hepatocellular carcinoma (HCC) usually develops in the setting of chronic liver disease. In the adequate clinical context, both multiphasic contrast-enhanced CT and magnetic resonance imaging are non-invasive modalities that allow accurate diagnosis and staging of HCC, although the latter demonstrates greater sensitivity and specificity. Imaging criteria for HCC diagnosis rely on hemodynamic features such as hyperenhancement in the arterial phase and washout in the portal or equilibrium phase. However, imaging performance drops considerably for small (< 20 mm) nodules because their tendency to exhibit atypical enhancement patterns. In order to improve accuracy in the diagnosis and staging of HCC, particularly in cases of atypical nodules, ancillary features, *i.e.*, imaging characteristics that modify the likelihood of HCC, have been described and incorporated into clinical reports, especially in Liver Imaging Reporting and Data System. In this paper, ancillary imaging features will be reviewed and illustrated.

Key words: Hepatocellular carcinoma; Ancillary features; Magnetic resonance imaging; Liver Imaging Reporting and Data System; Cirrhosis; Liver

Core tip: Hepatocellular carcinoma (HCC) usually develops in the setting of chronic liver disease. Imaging criteria for HCC diagnosis rely on hemodynamic features, however, imaging diagnostic performance drops considerably for small (< 20 mm) nodules because of their tendency to exhibit atypical enhancement patterns. In order to improve accuracy in these non-typical lesions, the use of ancillary features

has been incorporated into clinical reports, especially in Liver Imaging Reporting and Data System. In this paper, ancillary imaging features will be reviewed and illustrated.

Campos-Correia D, Cruz J, Matos AP, Figueiredo F, Ramalho M. Magnetic resonance imaging ancillary features used in Liver Imaging Reporting and Data System: An illustrative review. *World J Radiol* 2018; 10(2): 9-23 Available from: URL: http://www.wjgnet.com/1949-8470/full/v10/i2/9.htm DOI: http://dx.doi.org/10.4329/wjr.v10.i2.9

INTRODUCTION

Hepatocellular carcinoma (HCC) is the most common primary malignancy of the liver and the fifth most common neoplasm in the world. It ranks third among reasons for cancer-related mortality[1,2].

HCC develops in a cirrhotic background in the setting of chronic hepatic inflammation. Approximately 80% of HCC cases are associated with chronic hepatitis B virus (HBV) or hepatitis C virus (HCV) infections[1,3].

Early stage recognition of HCC make these patients eligible for potentially curative therapies, including surgical resection, liver transplantation or thermoablative treatments[4,5], with 5-year survival rates ranging between 50%-70%[6]. Conversely, advanced HCCs confer a very poor prognosis.

Gadolinium-enhanced MRI has been shown to represent the mainstay of noninvasive evaluation of the cirrhotic liver, with higher sensitivity than CT for the detection of HCC (77%-100% and 68%-91% respectively)[7-8], independent of lesion size.

MR imaging also provides high soft-tissue contrast, improving both lesion detection and characterization. Multiparametric data can be obtained through T1-weighed (T1-WI) and T2-weighted (T2-WI) sequences, functional sequences [diffusion-weighted imaging (DWI)], and contrast uptake. The increasingly frequent integration of hepatobiliary contrast agents in MR imaging protocols is emerging as the foremost method in the diagnosis and staging of HCC.

Imaging criteria for the diagnosis of HCC are based on the hemodynamic features of the nodule (arterial hyperenhancement and venous/delayed washout)[9]. Thus, precise timing of the arterial phase is crucial for optimal HCC detection. Subtle arterial enhancement may be detected using post-processed subtraction arterial images, which are especially useful for nodules with intrinsic high T1 signal intensity[8]. Imaging plays an important role in the differentiation of HCC from nonmalignant cirrhosis-associated nodules, (*e.g.*, regenerative nodules, low-grade dysplastic nodules, high-grade dysplastic nodules) and non-hepatocellular malignancies that may occur in the cirrhotic liver, mainly intrahepatic cholangiocarcinoma (ICC), which account for up to 5% of cancers in cirrhotic patients[7].

Recent recommendations by the American Association for the Study of Liver Diseases (AASLD) state that, among patients at risk, the non-invasive diagnosis of HCC can be confidently made if a nodule larger than 10 mm shows the typical hemodynamic features of HCC on either CT or MRI[10]. The current diagnostic approach has been structured in clinical practice guidelines and includes biopsy of suspicious hepatic lesions that do not meet typical HCC imaging criteria[7]. Nevertheless, biopsy comprises specific drawbacks including high interobserver variability among pathologists when interpreting small hepatic nodules in cirrhotic livers, and possible risks and complications such as needle track seeding and hemorrhage[5].

Organizations such as the AASLD, the European Association for the Study of the Liver (EASL) or the Organ Procurement and Transplantation Network (OPTN), have defined rigid and highly specific criteria for the diagnosis of HCC, which are credited to a shift in tumor blood supply from primarily portal venous to primarily arterial branches, recruited during neoangiogenesis. As a result, hyperenhancement relative to the background liver parenchyma is observed in the arterial phase[11], and as blood typically passes through HCCs into the venous outflow more rapidly than normal hepatic parenchyma, a characteristic "washout" appearance (tumor hypoenhancement in comparison to the liver parenchyma in the portal venous or delayed phase) may also be detected[7,11,12] (Figure 1). The combination of arterial hyperenhancement followed by washout in the portal venous/delayed phase has a sensitivity ranging between 64%-89%, specificity of 96% and positive predictive value of 93% for the diagnosis of HCC among patients at risk[12].

The capsule appearance is another important feature considered by some guidelines and attributed to compressed parenchyma, fibrosis, dilated sinusoids/blood vessels around the mass, or a combination of the above characteristics, which are observed in advanced HCCs (Figure 1). A peripheral rim of smooth and progressive enhancement with hyperenhancement in the portal venous or delayed phase can be seen. In at-risk patients, the capsule appearance holds a high positive predictive value for HCC, with specificity reportedly ranging between 83%-96%. However, sensitivity is only moderate, ranging between 43%-55%[13,14]. The capsule appearance should not be mistaken for peripheral enhancement of ICC and fibrous tissue surrounding cirrhotic nodules. Even in the absence of a typical washout appearance, the combination of arterial phase hyperenhancement and capsule appearance strongly suggests the diagnosis of HCC[7,15] (Figure 2). Zhang *et al*[16] showed that CT against MR produced false-negative findings of pseudo-capsule by 42.9%, with subsequent underestimation of LI-RADS scores by 16.9% for LR-3, 37.3% for LR-4, and 8.5% for LR-5. Corwin *et al*[17] compared CT and MR in grading LI-RADS and reported that 42% of the findings were upgraded on MRI when compared with CT. Nearly one-third of the upgrades

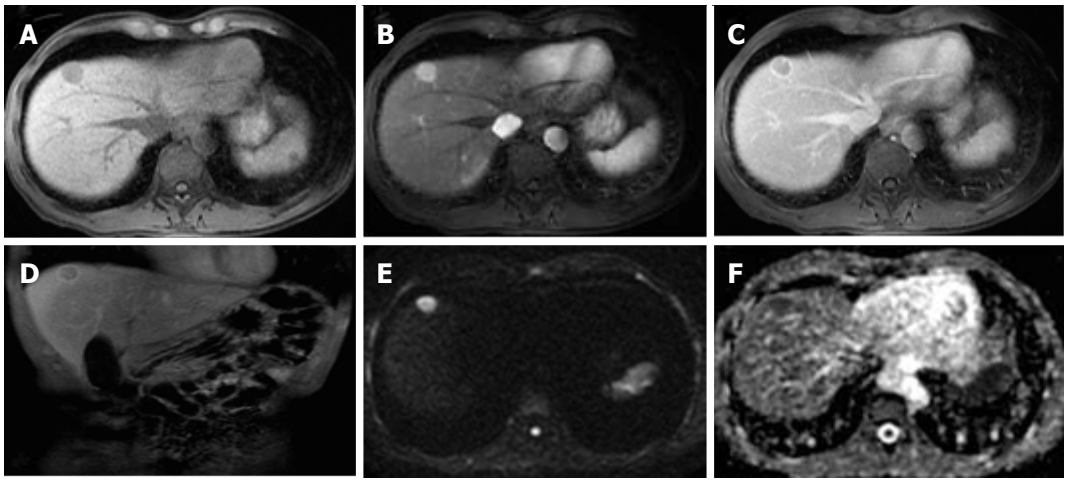

Figure 1 Classical hepatocellular carcinoma, in a patient with hepatitis B infection. Pre-contrast (A) and post-contrast fat-suppressed 3D-GRE T1-weighted images during the late hepatic arterial (B) and delayed phases (C, D), respectively, diffusion weighted image (DWI) (B = 600); (E) and ADC map (F). A nodular lesion is depicted in the right liver lobe with mildly low T1 signal intensity (arrow, A) that shows hyperenhancement in the late arterial phase (B) and washout and pseudocapsule enhancement in the delayed phases (C, D). Note the bright signal intensity on the B was 600 of the DWI sequence (E) and low signal on the ADC map (F) consistent with restriction to diffusion. These are typical hepatocellular carcinoma (HCC) findings in a patient at risk for HCC.

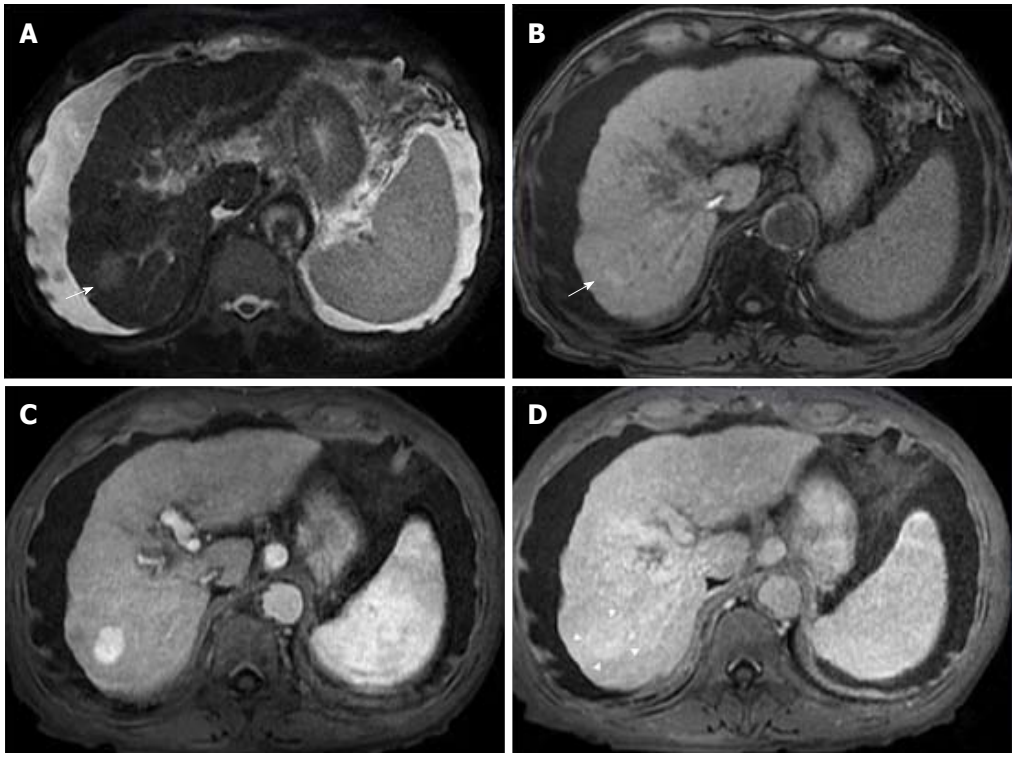

Figure 2 Late capsular enhancement/capsule appearance. Fat-suppressed T2-weighted image (A), and pre- (B) and post-contrast fat-suppressed 3D-GRE T1-weighted images during the late hepatic arterial (C) and delayed phases (D). There is a 3 cm nodule in the right hepatic lobe, which demonstrates mildly high T2 signal intensity (arrow, A) and near iso T1 signal intensity on precontrast T1-weighted images (arrow, B). Arterial hyperenhancement is seen (C) and in the delayed phase, the nodule becomes isointense compared to the background liver, without definite washout (D). A thin peripheral rim of smooth hyperenhancement is seen in the delayed phase (D). Note that despite the lack of delayed washout the presence of late capsule enhancement allows a confident diagnosis of hepatocellular carcinoma.

were to categories 4, 5, or 5 V. This was mainly due to the detection of arterial hyperenhancement or a delayed enhancing capsule not previously recognized on CT[17].

The American College of Radiology (ACR) developed LI-RADS with the purpose of improving standardization in the performance and interpretation of CT and MRI for the diagnosis of HCC among high-risk patients[15]. In addition to major imaging features (wash-in, washout and peripheral capsule) LI-RADS, contrary to other classification systems, uses ancillary imaging features to adjust the LI-RADS category. Ancillary imaging features result due to a combination of radiologists' experience and the necessity to complement a diagnosis in cases where typical dynamic characteristics are lacking.

Table 1 Hepatocellular carcinoma non-specific features suggesting malignancy

Feature	Critical details
Mild to moderate T2 hyperintensity	Well-differentiated HCCs and small moderately differentiated HCCs can be iso or hypointense in T2-WI
	Metastasis and ICC can show mild to moderate T2 hyperintensity
Restricted diffusion	Cirrhotic parenchyma may show restricted diffusion (due to abundance of fibrotic tissue)
	Various HCCs, especially those < 20 mm, tend not to show diffusion restriction
Lesional fat sparing	Applicable in the setting of fatty liver infiltration
	Must be differentiated from hepatic fat sparing areas
Lesional iron sparing	Applicable in the setting of iron-overloaded liver
	May also be observed in other malignancies such as ICC and non-malignant processes such as confluent fibrosis
Diameter increase less than threshold growth	Defined by a diameter increase of a lesion by a minimum of 5 mm, ⩾ 50% over ⩽ 6 mo or ⩾ 100% over > 6 mo
Corona (peri-lesional) enhancement	May also be found in other hypervascular lesions, such as metastasis
	Usually not present in early stage HCCs

HCC: Hepatocellular carcinoma.

Table 2 Hepatocellular carcinoma specific features suggesting malignancy

Feature	Critical details
Intra-lesional fat	Characteristic of early HCC;
	Exception: Steatohepatitic variant of HCC, which may exhibit marked intralesional fat even if they represent progressed cancer
Nodule-in-nodule architecture	"Subnodule" corresponding to the HCC typically shows enhancement characteristics similar to other HCCs;
	"Parent" nodule is typically hyperintense on T1-WI, hypointense on T2-WI and hypo- or isoenhancing on the arterial phase (atypical of HCC)
Mosaic architecture	Extremely unusual in other tumors;
	Uncommon in small HCCs;
	May be helpful for the diagnosis of large hypovascular HCCs
Blood products	Associated with HCC expansion;
	Previous biopsy should be discarded

HCC: Hepatocellular carcinoma.

Although they modify the likelihood of HCC, in isolation, they do not allow for the reliable categorization of observations. Ancillary features have been described and included in the LI-RADS v2014 classification system[15]. Some of these features are specific to MRI, and those that are common to both CT and MRI are generally more easily identifiable on MRI. Ancillary features can be divided into those that favor the diagnosis of benignity and those that favor malignancy, the latter being further subdivided into non-specific and specific to HCC[7,15]. The different LI-RADS categories: LR-1 (definitely benign), LR-2 (probably benign), LR-3 (indeterminate probability of HCC), LR-4 (probably HCC), and LR-5 (definitely HCC)[15] are based on the combination of major and/or ancillary imaging features favoring benignity or malignancy. As a rule, ancillary features may be used at the radiologist's discretion for improved detection, increased confidence, or category adjustment. For category adjustment, one or more ancillary features favoring malignancy may upgrade category up to LR-4, but cannot be used to upgrade a lesion to a LR-5 category[5,15].

LI-RADS, like any other imaging-based diagnostic systems, do possess limitations and problems that need to be addressed. Nevertheless, LI-RADS is being continually refined and updated in response to advances in research and technology. At its current level of development, LI-RADS are mainly used to separate the diagnosis of HCC (LR-5) and non-HCC nodules (LR-1 and 2). Another very important application is reserved for LR-4 and LR-3 categories, specifically to adapt patient management, including adopting a more aggressive approach or undergoing elective biopsy among patients with ancillary findings that favor HCC or malignancy.

In this article, we will review and illustrate each of the different ancillary MRI findings of malignancy by subdividing them into: (1) Non-specific features suggesting malignancy, *i.e.*, those that may be frequently found among other malignancies (Table 1); and (2) HCC-specific features suggesting malignancy, which are mostly found in HCCs (Table 2).

NON-SPECIFIC FEATURES SUGGESTING MALIGNANCY

Mild to moderate T2 hyperintensity

Mild or moderate T2 hyperintensity comparing to the liver is highly suggestive of malignancy (Figure 2)[15]. Cirrhotic and dysplastic nodules are characteristically iso or hypointense on T2-WI, and only very rarely appear mild/moderately hyperintense. This feature can be useful for the differentiation between a dysplastic nodule and a small HCC, especially when the latter presents as a hypervascular nodule without washout (Figure 3). HCCs tend to show minimal to mildly increased signal intensity on T2-WI, with specificity and

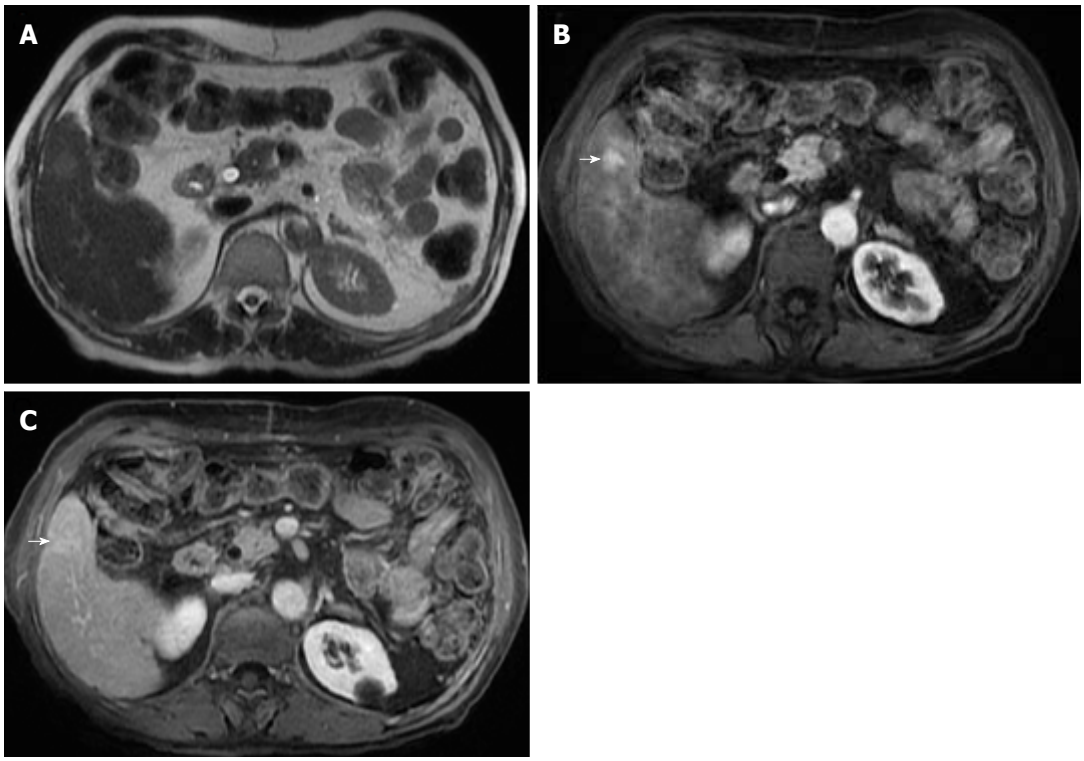

Figure 3 Small hepatocellular carcinoma without washout. T2-weighted image (A), and post-contrast fat-suppressed 3D-GRE T1-weighted images during the late hepatic arterial (B) and delayed phase (C). A small nodule with mild signal increase on T2 weighed image is seen in the right liver lobe (A). It shows intense increased arterial hyperenhancement (arrow, B) and fading in subsequent phases without a clear washout in the delayed phase (C).

a positive predictive value ranging between 73%-100% and 72%-100% respectively[14,18,19]. The addition of T2-WI hyperintensity to the AASLD criteria improved the detection rate of HCC, especially in nodules < 20 mm, by increasing sensitivity from 67.6% to 79%[20,21]. Sofue *et al*[22] evaluated the imaging features in MRI associated with the upgrade to a LI-RADS 5 category and verified that the risk factors in the 56 LR-4 observations, which were upgraded to LR-5, included mild to moderate T2 hyperintensity ($P < 0.001$) and growth ($P < 0.001$). Hyperintensity on T2-WI and DWI could also be useful in differentiating hypovascular HCCs from dysplastic nodules, which are perceived as hypointense nodules in the hepatobiliary phase[23].

Mild T2 hyperintensity may also have prognostic value, being found in 77% of HCCs larger than 30 mm[7]. However, many well-differentiated HCCs and some small, moderately differentiated HCCs can be iso or hypointense in T2-WI, and both metastasis and intrahepatic cholangiocarcinomas (ICC) can show mild T2 hyperintensity[7].

Restricted diffusion

DWI has been increasingly used as a cancer-imaging tool in clinical practice. DWI measures the random motion of water molecules inside a voxel of tissue. DWI hyperintensity (relative to liver parenchyma) is expected within an HCC due to its highly cellular tissue (see Figure 1)[3,24]. In contrast, benign nodules usually present a similar microstructure to their surrounding tissues, and therefore free water movement is preserved. As such, DWI may be useful in detecting HCC amongst benign nodules and arterially enhancing pseudolesions, predicting histological grade, and assessing response to treatment, since treatment-induced necrotic and inflammatory tissue result in a loss of cellular density and an increase in membrane permeability with subsequent diminished restriction to diffusion[24].

Some studies compared the HCC diagnostic sensitivity and specificity of DWI and contrast-enhanced sequences, reporting lower sensitivity of DWI for lesions < 20 mm and similar results for lesions > 20 mm[25,26]. However, all reports seemed to agree that DWI, as a diagnostic criterion for HCC, improved the sensitivity of conventional MRI, and the greatest benefit lied in the combined use of both (pooled sensitivity and specificity: 93% and 84% combined, respectively)[27] (Figure 4). However, cirrhotic parenchyma may itself show restricted diffusion, presumably owing to the abundance of fibrotic tissue, which results in reduced HCC conspicuity in DWI[18].

The limitation of this feature is its sensitivity, since many HCCs, especially those smaller than 20 mm, do not tend to show restricted diffusion.

Lesional fat sparing

In patients at risk of HCC with fatty liver infiltration, if a suspicious lesion has a lower fractional fat content than that of the background liver, then it is an ancillary

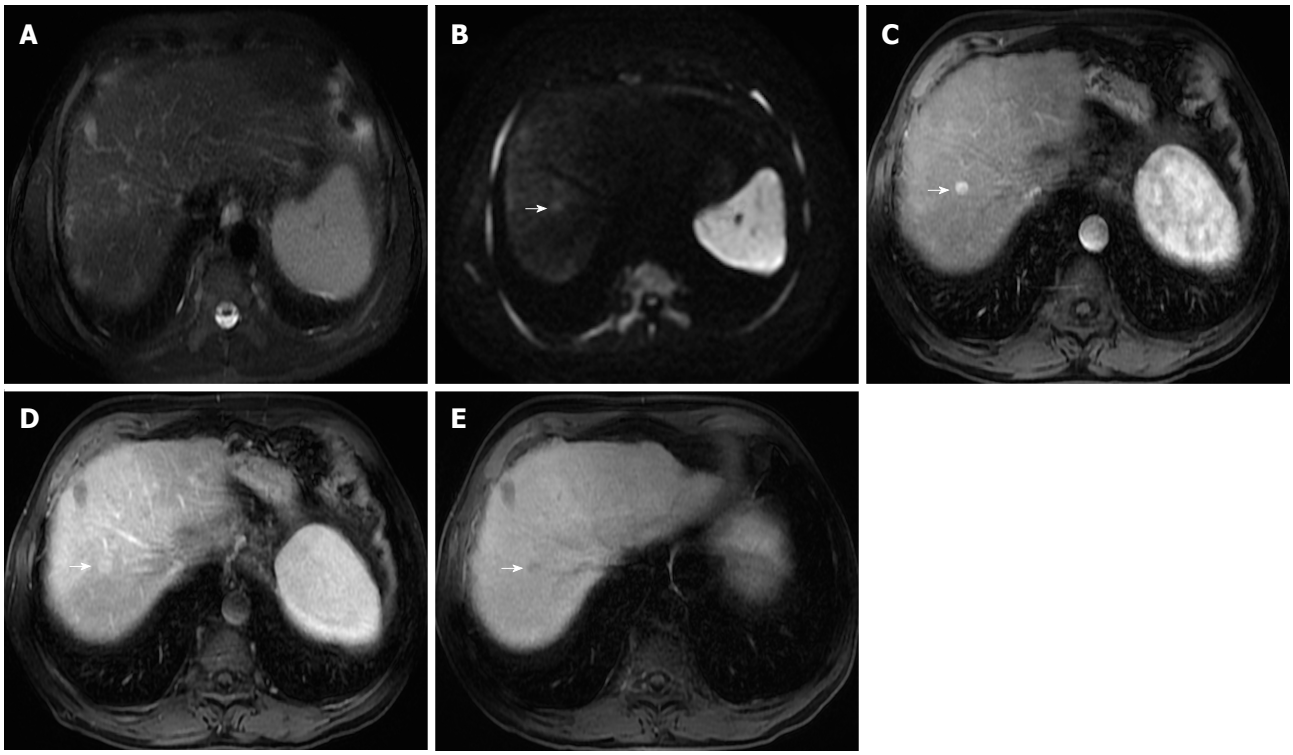

Figure 4 Small hepatocellular carcinoma. Fat-suppressed T2-weighted image (A), diffusion-weighted image (DWI; B = 600) (B), and hepatobiliary contrast enhanced (gadobenate dimeglumine) fat-suppressed 3D-GRE T1-weighted images in the late hepatic arterial (C), delayed (D), and hepatobiliary phases (E). A small nodule in the right hepatic lobe is seen, showing near isointense signal on T2- weighted image (A) and mild high signal intensity on DWI (arrow, B). An increased arterial enhancement is seen (arrow, C), fading out in the delayed phase (D) and decreased uptake on the hepatobiliary phase (arrow, E). These findings are suspicious for malignancy. This nodule was ablated and histologically proven HCC.

feature favoring HCC (Figure 5). However, this only applies in the presence of fatty liver infiltration, and must be differentiated from hepatic fat sparing areas by way of confirmation of the different enhancement pattern from that of background liver, which is better performed using subtraction technique[3,12,15].

Lesional iron sparing

As with lesional fat sparing, the absence of iron deposition in a suspicious lesion within an iron-overloaded liver parenchyma is highly suggestive of premalignancy or malignancy, since high-grade dysplastic nodules and HCC cells lose the ability to concentrate iron (Figure 6). This feature applies only to solid masses appearing in iron-overloaded livers that unequivocally have a lower fractional iron content than background liver. Liver iron deposition can be shown as signal loss on the second echo of a dual-echo sequence or as abnormal hypointensity on T2 or T2*-weighted images[8,10,15]. MRI is more sensitive and specific in detecting lesional iron sparing than CT[7]. A limitation of this feature is that it is only relevant to solid nodules found in iron-overloaded livers and not specific to HCC, as it may also be observed in other malignancies, such as ICC, and non-malignant processes such as confluent fibrosis[7].

Hepatocyte-specific/ hepatobiliary contrast agents

Hepatobiliary contrast agents (HSA) have been increasingly recognized as an important tool for HCC diagnosis. Hepatocyte-specific MR contrast agents initially distribute in the extracellular fluid compartment, allowing for multiphasic dynamic post-contrast imaging, which is comparable to extracellular agents. They are subsequently taken up by functioning hepatocytes and excreted in bile, allowing for a late hepatobiliary phase (HBP) acquisition[3,28,29]. Due to the action of cellular membrane transporters named Organic Anionic Transporting Polypeptides (OATP) and Multidrug Resistance-associated Proteins (MRPs), only normal functioning hepatocytes take up HSA and excrete them into the biliary tree. In hepatobiliary phase images, both the liver and the bile ducts appear markedly enhanced. Blood vessels, as well as all non-hepatocellular lesions and lesions with impaired hepatocytes appear hypointense[28].

Two HSAs are currently available: Gadoxetic acid disodium (Eovist®/Primovist®; Bayer Healthcare) and gadobenate dimeglumine (MultiHance®; Bracco Diagnostics). Gadoxetic acid is highly liver-specific with approximately 50% of the injected dose taken up by functioning hepatocytes and excreted in bile, allowing for delayed uptake imaging within 20 min from the time of injection, compared to the uptake of 3%-5% for gadobenate dimeglumine, which allows for delayed uptake imaging within 2-3 h[3,28]. Gadoxetic acid is currently widely used due to the rapid

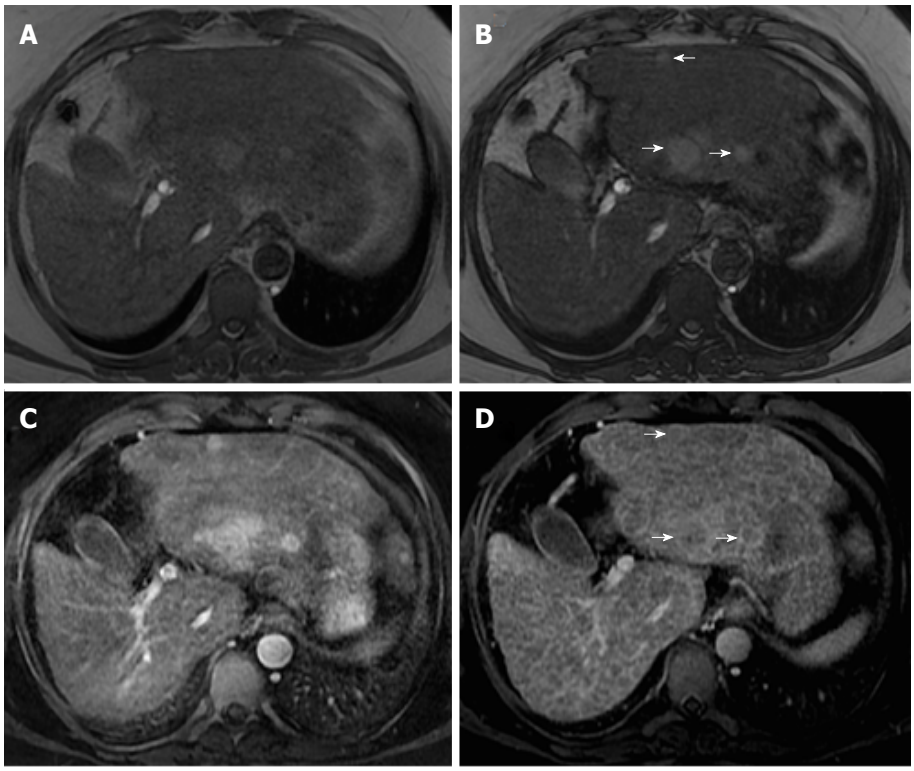

Figure 5 Lesional fat-sparing, in a case of multifocal hepatocellular carcinoma in a cirrhotic liver. Dual echo in- (A) and out-of-phase (B) 2D-GRE T1 weighted images, post-contrast fat-suppressed 3D-GRE T1-weighted images during the late hepatic arterial (C) and delayed phase (D). In a patient with cirrhosis and fatty infiltration, perceived as loss of signal intensity in the out-of-phase images (B) in comparison with the in-phase images (A), three lesions with lower fractional fat content than the background liver are seen with higher signal intensity (arrows, B). These lesions show arterial hyperenhancement (C) and washout and late capsule enhancement in the delayed phase (arrows, D), consistent with HCCs.

acquisition of HBP images (10-20 min after contrast injection) and more intense HBP enhancement[29]. The aforementioned differences in biliary elimination of gadoxetic acid compared to other contrast agents affect lesion appearance, and consequently image interpretation. Despite the advantages of lesion detection and characterization, it may also generate new pitfalls in imaging interpretation, which are related to the less favorable behavior as an extracellular agent, and the "pseudowashout" phenomenon observed in benign lesions. Generally, washout is synonymous with malignant lesions, particularly certain hypervascular metastases and HCC, but when gadoxetic acid is used, the "pseudowashout" phenomenon may, in lesser-experienced hands, lead to misinterpretation of benign lesions as malignant. This agent does not provide a conventional delayed vascular phase, instead it provides a transitional phase that overlaps the portal venous and the hepatobiliary phase (transition from extracellular-dominant to intracellular-dominant enhancement), leading to intense hepatic parenchymal enhancement in late dynamic postcontrast phases. Therefore, hypo-intensity relative to the liver in the transitional phase may reflect hyperenhancement of the liver rather than lesion washout[8,28].

As OATP expression decreases during hepato-carcinogenesis, iso signal intensity (SI) to high SI on HBP images is generally suggestive of benign lesions (RNs or low-grade DNs), whilst low SI on HBP images is a strong predictor of premalignancy or malignancy (high-grade DNs or HCCs)[7,19,29]. When it comes to HBP images, most HCCs, including many early-stage HCCs, usually express low SI in strongly enhanced normal hepatic parenchyma due to the absence of functioning hepatocytes or decreased expression of OATP. One important benefit of the hepatobiliary phase is that it helps to distinguish arterially enhancing pseudolesions (such as arterio-portal shunts) from HCC, and identify early HCCs that are frequently isoenhancing in the vascular phases, and cannot therefore be reliably detected with the help of extracellular agents[7]. Nevertheless, approximately 10%-12% of HCCs show high SI on HBP images. These usually represent well-differentiated HCCs that may retain enough hepatocellular and OATP expression to allow the uptake of hepatobiliary-specific agents[7,19,29].

Advanced cirrhosis may also limit the detection of early HCC when using gadoxetic acid-enhanced MRI due to compromised uptake of hepatobiliary-specific agents by damaged hepatocytes, resulting in a decreased distinction between the background liver parenchyma and the lesion (Figure 7)[16].

The combination of routine dynamic and hepatobiliary imaging has been reported to be both sensitive and specific to HCC, with two recent meta-analyses describing a pooled sensitivity of 91% and specificity of

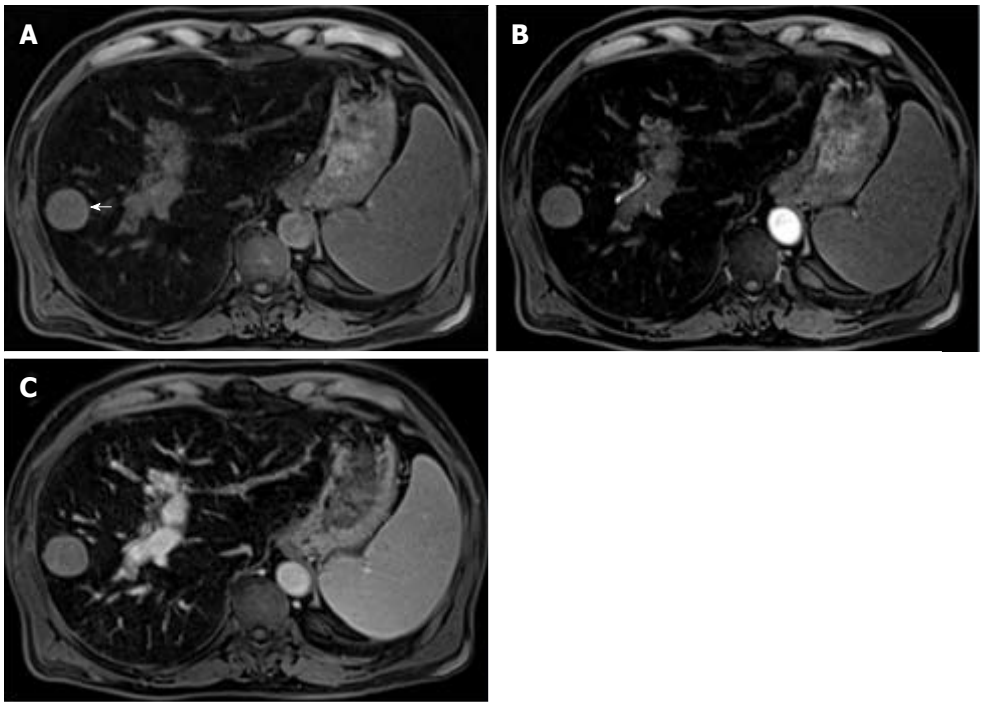

Figure 6 Lesional iron sparing. Pre-contrast (A) and post-contrast fat-suppressed 3D-GRE T1-weighted images during the late hepatic arterial (B) and delayed (C) phases. An iron-overloaded cirrhotic liver shows marked signal loss on T1-weighted images. A non-siderotic nodule is seen in the right liver lobe (arrow, A). Dynamic evaluation is limited and does not allow a confident diagnosis of hepatocellular carcinoma (HCC). This nodule underwent biopsy and HCC was confirmed.

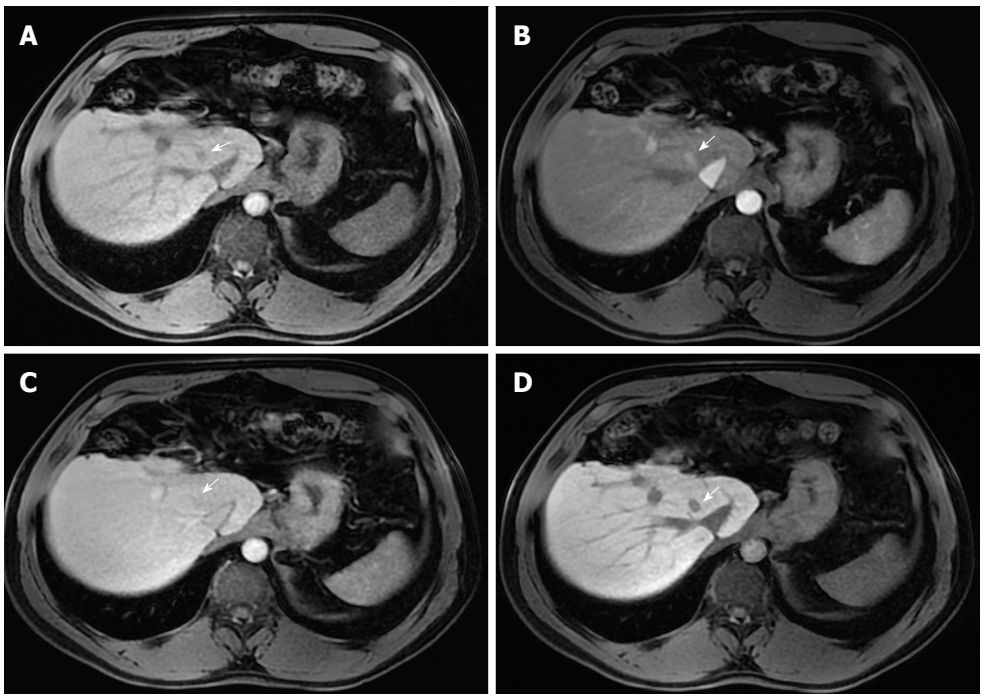

Figure 7 Small hepatocellular carcinoma in a patient with chronic liver disease and a previous left hepatectomy. Pre- (A) and post-contrast (gadoxetate disodium) fat-suppressed 3D-GRE T1-weighted images in the arterial (B), delayed (C) and hepatobiliary phases (D). A small HCC is shown in segment VIII displaying mild low T1 signal intensity (arrow, A), arterial hyper-enhancement (arrow, B) and no appreciable washout on the delayed phase (arrow, C). Low signal intensity is noted on the hepatobiliary phase (arrow, D). This example proves the benefit of hepatobiliary contrast agents in further characterization of liver nodules in the setting of chronic liver disease.

93%[27,30].

Peri-tumoral hypointensity seen on gadoxetic acid-enhanced hepatobiliary phase images was also seen in a retrospective study to be a specific, although insensitive, marker for microvascular invasion; the authors attributed this phenomenon to altered expression of OATP or MRP2 receptors in the hepatic parenchyma caused by hemodynamic changes associated with tumor

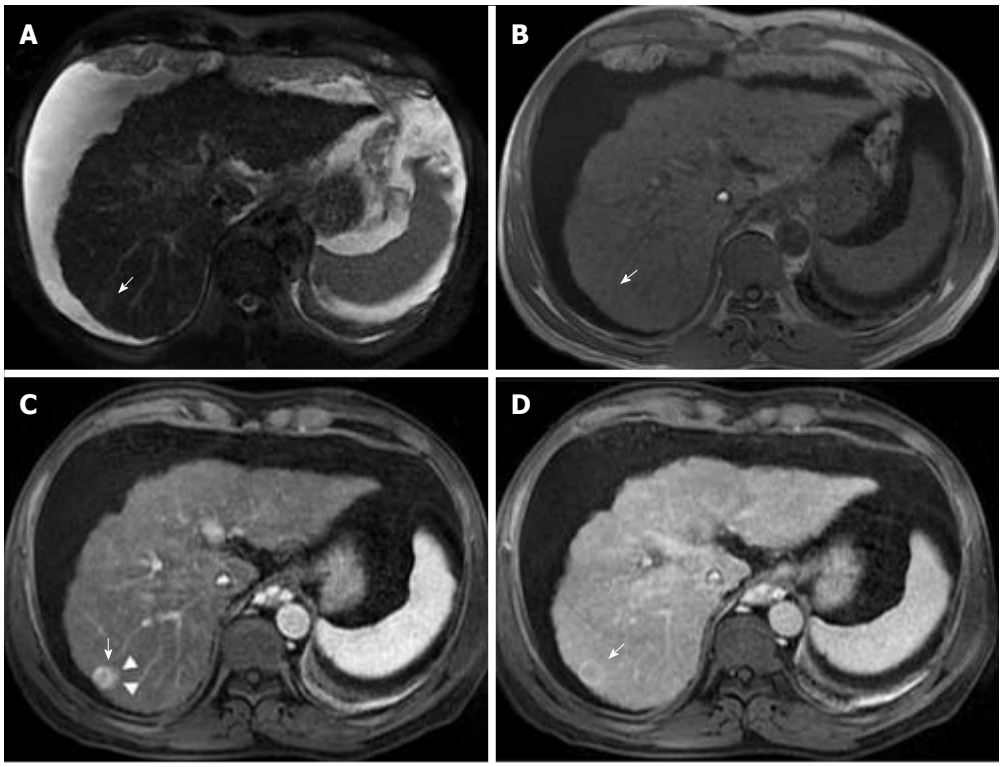

Figure 8 Corona enhancement. T2-weighted image (A), unenhanced in-phase T1-weighted GRE images (B), and post-contrast fat-suppressed 3D-GRE T1-weighted images during the late hepatic arterial (C) and delayed phases (D). A small nodule in the right hepatic lobe with near isointense T2 signal (A) and iso to hypointense T1 signal (B) shows heterogeneous arterial ring-like enhancement in the arterial phase. Enhancement of the peri-lesional parenchyma is recognized (arrow, C). This transient enhancement is known as corona enhancement and suggests a more aggressive course. Washout is seen on delayed phase images (D).

obstruction of minute portal veins[31].

Therefore, gadoxetic acid-enhanced MRI has a higher sensitivity with regard to the diagnosis of HCC, (especially for lesions ⩽ 20 mm), improves the characterization of arterially enhancing lesions that do not exhibit definite washout on subsequent imaging, helps differentiate arterially enhancing pseudolesions from HCC (Figures 4 and 7), and aids in the detection of lesions that are isointense to the background hepatic parenchyma on all other sequences, but has a high risk of transforming into hypervascular HCCs[3,10].

Diameter increase less than threshold growth

HCCs frequently pose diagnostic dilemmas due to differences in technique between the two subsequent examinations and measurement inequalities, hence rendering an increase in diameter, which is often difficult to ascertain.

Using the LI-RADS guidelines, the threshold growth is defined by a diameter increase of a lesion by a minimum of 5 mm, of ⩾ 50% over ⩽ 6 mo, or ⩾ 100% over > 6 mo[15]. A new lesion measuring ⩾ 10 mm also represents threshold growth, regardless of the time interval. These are major features of HCC. An increase in diameter less than the threshold growth is an ancillary feature that favors HCC. However, LI-RADS do not stipulate a minimum increase in diameter for its use as an ancillary feature. A note should be made that when measuring lesion diameter, the largest dimension should be used, *i.e.*, outer edge to outer edge- and it should be measured in the sequence, phase, and imaging plane in which the margins are most sharply defined, and in which there is no (or less) anatomic distortion (preferably not in the arterial phase, due to the possible presence of peri-lesional enhancement).

Corona (peri-lesional) enhancement

Corona enhancement is defined as a zone (or rim) of peri-lesional enhancing parenchyma seen in hypervascular and progressed HCC in the late arterial or early portal venous phase, which fades to isoenhancement in the subsequent phases (Figure 8)[15]. It represents the rapid drainage of contrast material from the arterially hyperenhancing lesion to the peri-tumoral parenchyma, carried by the tumor draining vessels, just a few seconds after the tumor itself begins to enhance[7,15].

This feature is not specific to HCC, since it may also be found in other hypervascular lesions, such as metastasis. However, its presence may be useful in distinguishing between small HCCs and vascular pseudolesions (*e.g.*, arterio-portal shunts).

Corona enhancement may also have some prognostic value as it is not usually present in early stage HCCs, which have hepatic vein drainage, but in less differentiated lesions. In addition, some studies have suggested that large, irregular or distorted corona enhancement predicts microvascular invasion[32,33]. Metastatic satellite nodules and local recurrences after

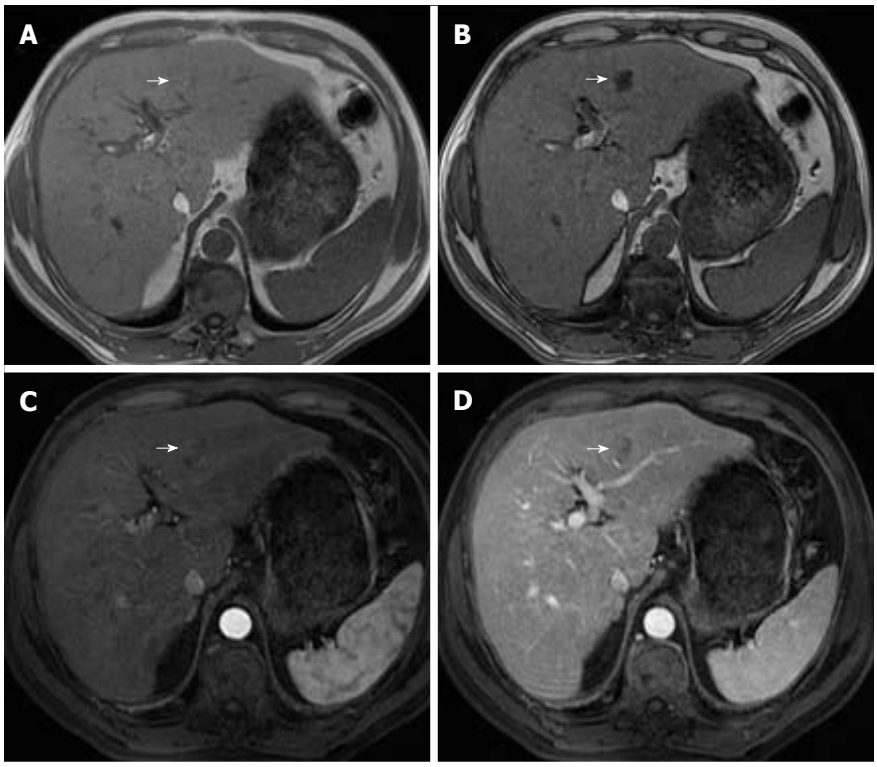

Figure 9 Intra-lesional fat in early hepatocellular carcinoma. Dual echo in-phase (A) and out-of-phase (B) GRE T1 weighted images, and post-contrast fat-suppressed 3D-GRE T1-weighted images during late hepatic arterial (C) and delayed phase (D). A nodule is seen in the left hepatic lobe, which demonstrates intrinsic mild increased T1 signal on the in-phase images (arrow, A) and loss of signal on the out-of-phase images (arrow, B). This nodule shows heterogeneous mildly arterial hyperenhancement (arrow, C) and no washout is appreciable (arrow, D).

resection or ablation also frequently develop corona-like enhancement areas[34].

In lesions with diffuse arterial phase hyperenhancement, corona enhancement and capsule appearance may overlap in imaging. If rim enhancement occurs in the arterial phase or portal venous phase and subsequently fades in later phases, it is suggestive of corona enhancement. If rim enhancement increases in portal venous phase and delayed phase, it suggests capsule appearance[15].

HCC-SPECIFIC FEATURES SUGGESTING MALIGNANCY

Intralesional fat

Intra-lesional fat indicates the presence of fat in higher concentration within a lesion than background liver tissue. Fatty metaplasia is frequently histologically observed in early HCCs, and its detection in imaging favors this diagnosis (Figure 9). It has, however, limited sensitivity, ranging from 12%-37% in reported series[14,35]. Furthermore, its specificity is only moderate, ranging from 68%-91%[14,35], so it cannot be used to establish the diagnosis of HCC, since high-grade and occasionally low-grade dysplastic nodules also show intralesional fat[10,12]. Nevertheless, in a high-risk patient, the identification of intralesional fat in a suspicious nodule raises concerns about malignancy or premalignancy and should prompt, at least, a closer follow-up[10,12,15].

The evaluation of intralesional microscopic and macroscopic fat can be achieved using T1 weighted "in and out of phase" chemical shift imaging and fat-suppressed images respectively (Figure 10). Whether the lesion has a higher fractional fat content than the liver or its enhancement is different from that of background liver parenchyma must be confirmed by the presence of hepatic steatosis[10,12,15].

As it is characteristic of early but not progressed HCC, intralesional fat may also have prognostic value. It generally denotes a longer time for progression and a lesser risk of developing metastases than non–fat-containing HCCs[12].

The steatohepatitic variant of HCC, a newly described variant, however, is an exception. Strongly associated with underlying steatohepatitis and metabolic syndrome, steatohepatitic HCCs may exhibit marked intralesional fat even if they represent progressed cancers with an advanced tumoral grade[12,36].

Remarkably, in a cirrhotic liver, the presence of intralesional fat in a single nodule is characteristic of early HCC, especially if larger than 15 mm (Figure 9). On the other hand, it is an unspecific finding, since low and high-grade dysplastic nodules may also contain fat. In addition, the presence of numerous fat-containing nodules measuring < 10 mm is suggestive of a benign nature[37] (Figure 11).

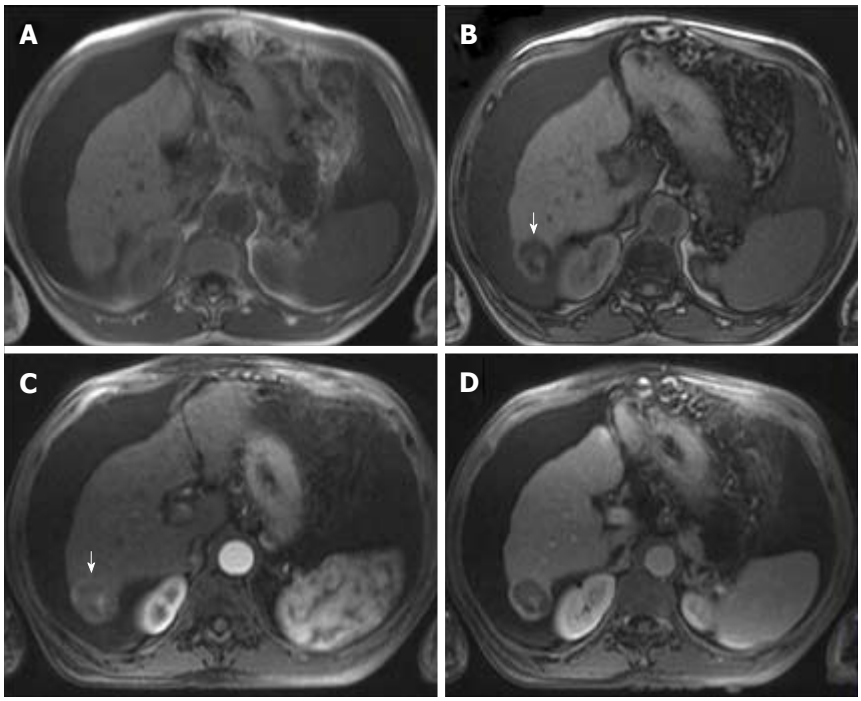

Figure 10 Fatty hepatocellular carcinoma. Dual echo in-phase (A) and out-of-phase (B) GRE T1 weighted images and post-contrast fat-suppressed 3D-GRE T1-weighted images during late hepatic arterial (C) and delayed phase (D). A right hepatic lobe nodule shows loss of signal intensity on the out-of-phase (arrow, B) in comparison with the in-phase (A) images. This nodule shows heterogeneous arterial hyperenhancement (arrow, C) and a clear washout is appreciable (D) in keeping with fatty hepatocellular carcinoma.

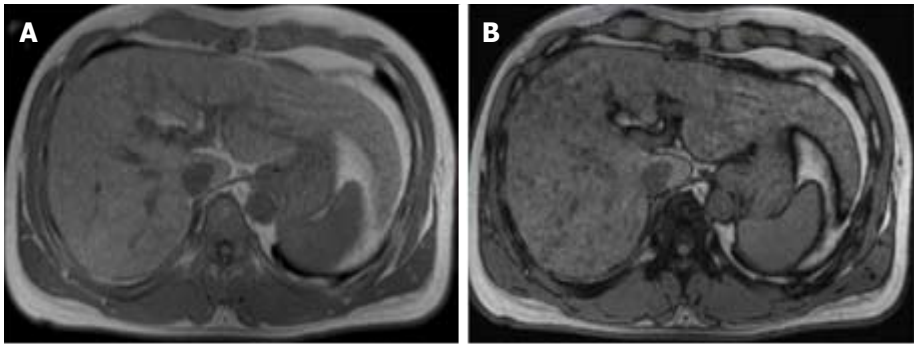

Figure 11 Fat-containing regenerative nodules. Dual echo in-phase (A) and out-of-phase (B) GRE T1 weighted images. The presence of numerous fat-containing nodules measuring less than 10 mm is highly indicative of benign nature.

Nodule-in-nodule architecture

This finding represents the development of a progressed HCC within a dysplastic nodule (Figure 12). The "subnodule" corresponding to the HCC typically exhibits enhancement characteristics similar to other HCCs. The surrounding "parent" nodule, corresponding to more well-differentiated tissue, is typically hyperintense in T1-WI, hypointense in T2-WI and arterial phase hypo- or isoenhancing, which is atypical of HCC.

Fat or iron deposition can also occur in the parent nodule, and less frequently in the subnodule, reflecting the inability of neoplastic hepatocytes to concentrate iron and fat[12,15]. To our knowledge, its sensitivity to HCC diagnosis has not yet been defined, but it constitutes an uncommon finding in CT or MRI, and its value is therefore unclear.

Mosaic architecture

Mosaic architecture refers to the presence of randomly distributed internal nodules, or compartments, differing in enhancement, intensity, shape and size and often separated by fibrous septations[12,15]. Among high-risk patients, most lesions with mosaic architecture represent HCCs; this feature being more characteristic of large HCCs. Although heterogeneity is a common characteristic of many liver lesions, mosaic architecture is extremely unusual in other tumors[7].

Care must be taken, however, to differentiate mosaic architecture from intralesional necrosis, which manifests as hyperintensity on T2-WI[38]. In addition, the incremental value of this feature relating to HCC diagnosis may be modest because it is uncommon in small HCCs. Some authors have studied the accuracy of

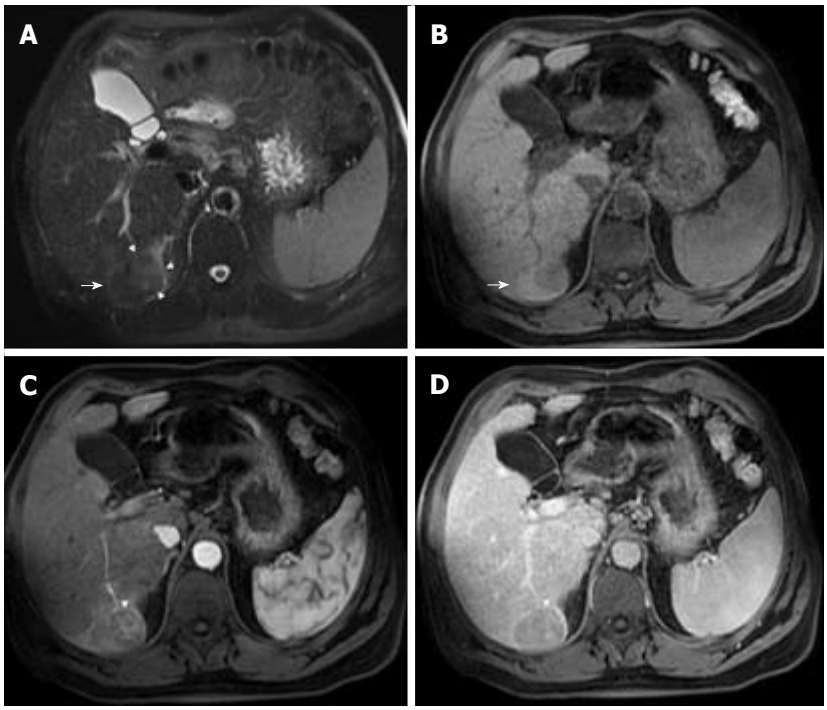

Figure 12 Nodule-in-nodule architecture. Fat-suppressed T2-weighted image (A), pre- (B) and post-contrast fat-suppressed 3D-GRE T1-weighted images during the late hepatic arterial (C) and delayed phases (D). A small nodule within a larger nodule is seen in the right liver lobe (arrow A, B) showing distinct mild high signal intensity on the T2-weighted image (arrowheads, A), heterogeneous arterial hyperenhancement (arrowhead, C) and subtle washout (arrowhead, D). This imaging appearance is highly suggestive of a progressed hepatocellular carcinoma within a dysplastic nodule.

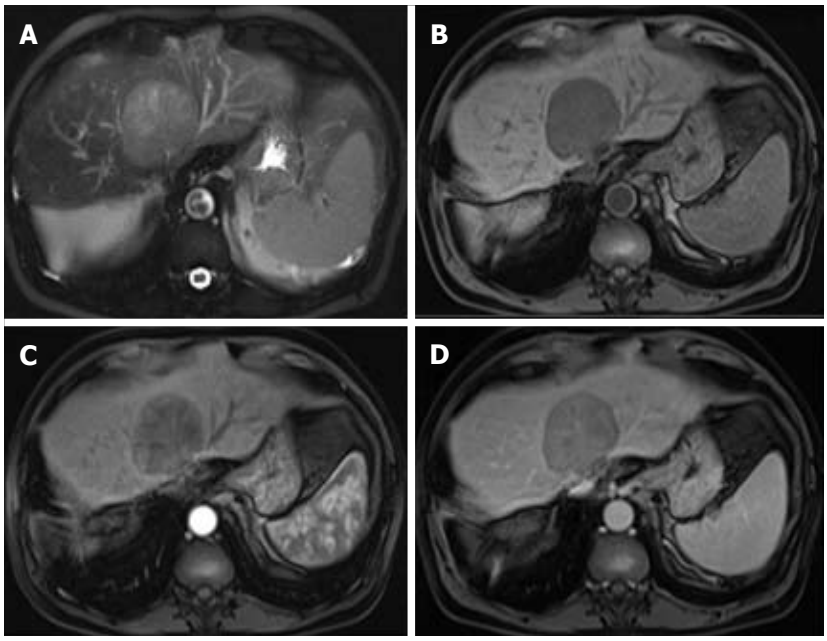

Figure 13 Mosaic architecture. Fat-suppressed T2-weighted image (A), pre (B) and post-contrast fat-suppressed 3D-GRE T1-weighted images during the late hepatic arterial (C) and delayed (D) phases. A large mass showing randomly distributed internal compartments with different signal intensities on the T2 weighed image (A) and variable enhancement patterns on the late arterial (C) and delayed phases (D). This is an extremely unusual feature in non- hepatocellular carcinoma (HCC) tumors. In large, arterial hyperenhancement might be more difficult to recognize and as in this case and the presence of mosaic architecture aids in the diagnosis of HCC.

this finding and have reported a sensitivity of up to 63% (in studies with limited population), and more recently of up to 31% using conventional MR sequences[39,40,41]. Nonetheless, this feature may be helpful for the diagnosis of large hypovascular HCCs in which arterial hyperenhancement is often more difficult to appreciate (Figure 13) and is also being recognized for its prognostic value[38].

Blood products

The presence of intralesional or peri-lesional hemorrhage in the absence of previous biopsy, intervention or trauma is also an ancillary feature favoring HCC, as

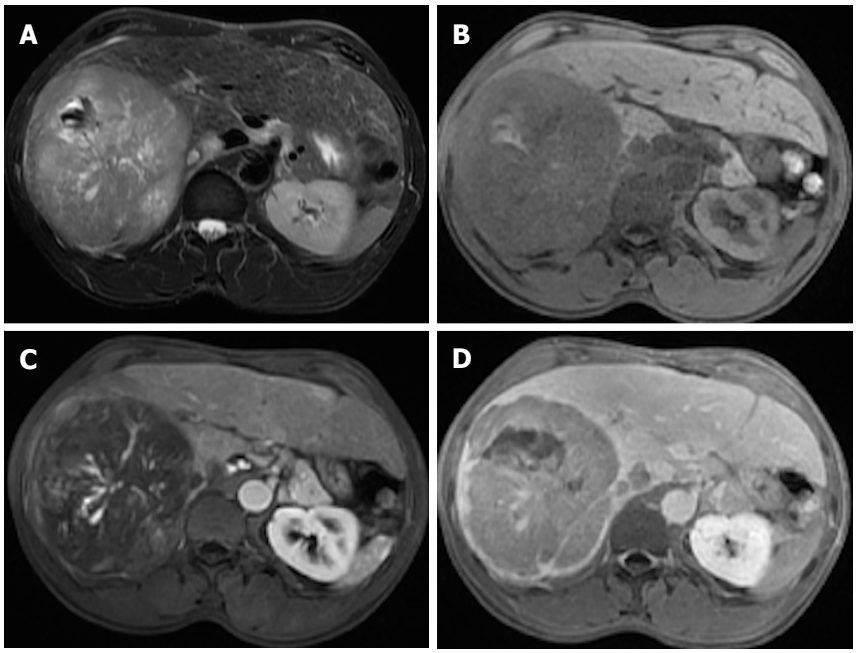

Figure 14 Blood products in a large hepatocellular carcinoma. Fat-suppressed T2-weighted image (A), pre- (B) and post-contrast fat-suppressed 3D-GRE T1-weighted images during the late hepatic arterial (C) and delayed (D) phases. Intralesional areas of high T1 signal intensity images (B) and predominantly low T2 signal intensity (A) can be seen. Thick intralesional arteries are appreciated during the arterial phase (C) and delayed washout and capsular enhancement is also demonstrated (D) in keeping with partly hemorrhagic HCC.

it is associated with HCC expansion[41]. In MRI, blood products usually manifest as areas with predominantly high signal intensity on T1-WI and heterogeneous, and predominantly low signal intensity on T2-WI. Due to T2* shortening, there may be signal loss on the second echo of a dual-echo gradient-echo sequence[15] (Figure 14). Chen *et al*[40] reported a sensitivity of 64% for intralesional hemorrhage in HCC diagnosis.

CONCLUSION

Gadolinium-enhanced MR imaging has become the non-invasive method of choice for HCC diagnosis among patients at risk. Arterial wash-in and portal or delayed-phase washout allows for a precise diagnosis, discarding the need for histologic confirmation. However, the diagnosis may be challenging in the absence of typical dynamic features. This is even more important when early diagnosis is critical in the management of HCC patients. In this setting, ancillary imaging features may provide additional information, which can be used for further lesional characterization, and hence increase diagnostic sensitivity. These include non-specific features suggesting malignancy (mild-moderate T2 hyperintensity, restricted diffusion, lesional fat sparing, lesional iron sparing, a diameter increase less than threshold growth and corona enhancement) and HCC-specific features suggesting malignancy (intra-lesional fat, nodule-in-nodule architecture, mosaic architecture and the presence of blood products). Recognition of these features is extremely important for practicing radiologists.

REFERENCES

1 **El-Serag HB**. Epidemiology of viral hepatitis and hepatocellular carcinoma. *Gastroenterology* 2012; **142**: 1264-1273.e1 [PMID: 22537432 DOI: 1053/j.gastro.2011.12.061]
2 **Llovet JM**, Fuster J, Bruix J; Barcelona-Clínic Liver Cancer Group. The Barcelona approach: diagnosis, staging, and treatment of hepatocellular carcinoma. *Liver Transpl* 2004; **10**: S115-S120 [PMID: 14762851 DOI: 10.1002/lt.20034]
3 **Ramalho M**, Matos AP, AlObaidy M, Velloni F, Altun E, Semelka RC. Magnetic resonance imaging of the cirrhotic liver: diagnosis of hepatocellular carcinoma and evaluation of response to treatment - Part 1. *Radiol Bras* 2017; **50**: 38-47 [PMID: 28298731 DOI: 10.1590/0100-3984.2015.0132]
4 **Llovet JM**, Burroughs A, Bruix J. Hepatocellular carcinoma. *Lancet* 2003; **362**: 1907-1917 [PMID: 14667750 DOI: 10.1016/S0140-6736(03)14964-1]
5 **Mitchell DG**, Bruix J, Sherman M, Sirlin CB. LI-RADS (Liver Imaging Reporting and Data System): summary, discussion, and consensus of the LI-RADS Management Working Group and future directions. *Hepatology* 2015; **61**: 1056-1065 [PMID: 25041904 DOI: 10.1002/hep.27304]
6 **Bruix J**, Llovet JM. Major achievements in hepatocellular carcinoma. *Lancet* 2009; **373**: 614-616 [PMID: 19231618 DOI: 10.1016/S0140-6736(09)60381-0]
7 **Choi JY**, Lee JM, Sirlin CB. CT and MR imaging diagnosis and staging of hepatocellular carcinoma: part II. Extracellular agents, hepatobiliary agents, and ancillary imaging features. *Radiology* 2014; **273**: 30-50 [PMID: 25247563 DOI: 10.1148/radiol.14132362]
8 **Watanabe A**, Ramalho M, AlObaidy M, Kim HJ, Velloni FG, Semelka RC. Magnetic resonance imaging of the cirrhotic liver: An update. *World J Hepatol* 2015; **7**: 468-487 [PMID: 25848471 DOI: 10.4254/wjh.v7.i3.468]
9 **Bruix J**, Sherman M; Practice Guidelines Committee, American Association for the Study of Liver Diseases. Management of hepatocellular carcinoma. *Hepatology* 2005; **42**: 1208-1236 [PMID: 16250051 DOI: 10.1002/hep.20933]

10 **Bruix J**, Sherman M; American Association for the Study of Liver Diseases. Management of hepatocellular carcinoma: an update. *Hepatology* 2011; **53**: 1020-1022 [PMID: 21374666 DOI: 10.1002/hep.24199]

11 **Hayashi M**, Matsui O, Ueda K, Kawamori Y, Gabata T, Kadoya M. Progression to hypervascular hepatocellular carcinoma: correlation with intranodular blood supply evaluated with CT during intraarterial injection of contrast material. *Radiology* 2002; **225**: 143-149 [PMID: 12354998 DOI: 10.1148/radiol.2251011298]

12 **Niendorf E**, Spilseth B, Wang X, Taylor A. Contrast Enhanced MRI in the Diagnosis of HCC. *Diagnostics* (Basel) 2015; **5**: 383-398 [PMID: 26854161 DOI: 10.3390/diagnostics5030383]

13 **Khan AS**, Hussain HK, Johnson TD, Weadock WJ, Pelletier SJ, Marrero JA. Value of delayed hypointensity and delayed enhancing rim in magnetic resonance imaging diagnosis of small hepatocellular carcinoma in the cirrhotic liver. *J Magn Reson Imaging* 2010; **32**: 360-366 [PMID: 20677263 DOI: 10.1002/jmri.22271]

14 **Rimola J**, Forner A, Tremosini S, Reig M, Vilana R, Bianchi L, Rodríguez-Lope C, Solé M, Ayuso C, Bruix J. Non-invasive diagnosis of hepatocellular carcinoma ≤ 2 cm in cirrhosis. Diagnostic accuracy assessing fat, capsule and signal intensity at dynamic MRI. *J Hepatol* 2012; **56**: 1317-1323 [PMID: 22314420 DOI: 10.1016/j.jhep.2012.01.004]

15 **An C**, Rakhmonova G, Choi JY, Kim MJ. Liver imaging reporting and data system (LI-RADS) version 2014: understanding and application of the diagnostic algorithm. *Clin Mol Hepatol* 2016; **22**: 296-307 [PMID: 27304548 DOI: 10.3350/cmh.2016.0028]

16 **Zhang YD**, Zhu FP, Xu X, Wang Q, Wu CJ, Liu XS, Shi HB. Liver Imaging Reporting and Data System:: Substantial Discordance Between CT and MR for Imaging Classification of Hepatic Nodules. *Acad Radiol* 2016; **23**: 344-352 [PMID: 26777590 DOI: 10.1016/j.acra.2015.11.002]

17 **Corwin MT**, Fananapazir G, Jin M, Lamba R, Bashir MR. Differences in Liver Imaging and Reporting Data System Categorization Between MRI and CT. *AJR Am J Roentgenol* 2016; **206**: 307-312 [PMID: 26797357 DOI: 10.2214/AJR.15.14788]

18 **Rhee H**, Kim MJ, Park YN, Choi JS, Kim KS. Gadoxetic acid-enhanced MRI findings of early hepatocellular carcinoma as defined by new histologic criteria. *J Magn Reson Imaging* 2012; **35**: 393-398 [PMID: 21990116 DOI: 10.1002/jmri.22828]

19 **Piana G**, Trinquart L, Meskine N, Barrau V, Beers BV, Vilgrain V. New MR imaging criteria with a diffusion-weighted sequence for the diagnosis of hepatocellular carcinoma in chronic liver diseases. *J Hepatol* 2011; **55**: 126-132 [PMID: 21145857 DOI: 10.1016/j.jhep.2010.10.023]

20 **Ouedraogo W**, Tran-Van Nhieu J, Baranes L, Lin SJ, Decaens T, Laurent A, Djabbari M, Pigneur F, Duvoux C, Kobeiter H, Deux JF, Rahmouni A, Luciani A. Evaluation of noninvasive diagnostic criteria for hepatocellular carcinoma on pretransplant MRI (2010): correlation between MR imaging features and histological features on liver specimen. *J Radiol* 2011; **92**: 688-700 [PMID: 21819911]

21 **Golfieri R**, Grazioli L, Orlando E, Dormi A, Lucidi V, Corcioni B, Dettori E, Romanini L, Renzulli M. Which is the best MRI marker of malignancy for atypical cirrhotic nodules: hypointensity in hepatobiliary phase alone or combined with other features? Classification after Gd-EOB-DTPA administration. *J Magn Reson Imaging* 2012; **36**: 648-657 [PMID: 22592930 DOI: 10.1002/jmri.23685]

22 **Sofue K**, Burke LMB, Nilmini V, Alagiyawanna M, Muir AJ, Choudhury KR, Jaffe TA, Semelka RC, Bashir MR. Liver imaging reporting and data system category 4 observations in MRI: Risk factors predicting upgrade to category 5. *J Magn Reson Imaging* 2017; **46**: 783-792 [PMID: 28083902 DOI: 10.1002/jmri.25627]

23 **Hwang J**, Kim YK, Jeong WK, Choi D, Rhim H, Lee WJ. Nonhypervascular Hypointense Nodules at Gadoxetic Acid-enhanced MR Imaging in Chronic Liver Disease: Diffusion-weighted Imaging for Characterization. *Radiology* 2015; **276**: 137-146 [PMID: 25734551 DOI: 10.1371/journal.pone.0174594]

24 **Lim KS**. Diffusion-weighted MRI of hepatocellular carcinoma in cirrhosis. *Clin Radiol* 2014; **69**: 1-10 [PMID: 24034549 DOI: 10.1016/j.crad.2013.07.022]

25 **Quaia E**, De Paoli L, Pizzolato R, Angileri R, Pantano E, Degrassi F, Ukmar M, Cova MA. Predictors of dysplastic nodule diagnosis in patients with liver cirrhosis on unenhanced and gadobenate dimeglumine-enhanced MRI with dynamic and hepatobiliary phase. *AJR Am J Roentgenol* 2013; **200**: 553-562 [PMID: 23436844 DOI: 10.2214/AJR.12.8818]

26 **Wu LM**, Xu JR, Lu Q, Hua J, Chen J, Hu J. A pooled analysis of diffusion-weighted imaging in the diagnosis of hepatocellular carcinoma in chronic liver diseases. *J Gastroenterol Hepatol* 2013; **28**: 227-234 [PMID: 23190006 DOI: 10.1111/jgh.12054]

27 **Liu X**, Zou L, Liu F, Zhou Y, Song B. Gadoxetic acid disodium-enhanced magnetic resonance imaging for the detection of hepatocellular carcinoma: a meta-analysis. *PLoS One* 2013; **8**: e70896 [PMID: 23967130]

28 **Matos AP**, Velloni F, Ramalho M, AlObaidy M, Rajapaksha A, Semelka RC. Focal liver lesions: Practical magnetic resonance imaging approach. *World J Hepatol* 2015; **7**: 1987-2008 [PMID: 26261689 DOI: 10.4254/wjh.v7.i16.1987]

29 **Park YS**, Lee CH, Kim JW, Shin S, Park CM. Differentiation of hepatocellular carcinoma from its various mimickers in liver magnetic resonance imaging: What are the tips when using hepatocyte-specific agents? *World J Gastroenterol* 2016; **22**: 284-299 [PMID: 26755877 DOI: 10.3748/wjg.v22.i1.284]

30 **Wu LM**, Xu JR, Gu HY, Hua J, Chen J, Zhu J, Zhang W, Hu J. Is liver-specific gadoxetic acid-enhanced magnetic resonance imaging a reliable tool for detection of hepatocellular carcinoma in patients with chronic liver disease? *Dig Dis Sci* 2013; **58**: 3313-3325 [PMID: 23884757 DOI: 10.1007/s10620-013-2790-y]

31 **Kim KA**, Kim MJ, Jeon HM, Kim KS, Choi JS, Ahn SH, Cha SJ, Chung YE. Prediction of microvascular invasion of hepatocellular carcinoma: usefulness of peritumoral hypointensity seen on gadoxetate disodium-enhanced hepatobiliary phase images. *J Magn Reson Imaging* 2012; **35**: 629-634 [PMID: 22069244 DOI: 10.1002/jmri.22876]

32 **Nishie A**, Yoshimitsu K, Asayama Y, Irie H, Tajima T, Hirakawa M, Ishigami K, Nakayama T, Kakihara D, Nishihara Y, Taketomi A, Honda H. Radiologic detectability of minute portal venous invasion in hepatocellular carcinoma. *AJR Am J Roentgenol* 2008; **190**: 81-87 [PMID: 18094297 DOI: 10.2214/AJR.07.2810]

33 **Chou CT**, Chen RC, Lee CW, Ko CJ, Wu HK, Chen YL. Prediction of microvascular invasion of hepatocellular carcinoma by pre-operative CT imaging. *Br J Radiol* 2012; **85**: 778-783 [PMID: 21828149 DOI: 10.1259/bjr/65897774]

34 **Sakon M**, Nagano H, Nakamori S, Dono K, Umeshita K, Murakami T, Nakamura H, Monden M. Intrahepatic recurrences of hepatocellular carcinoma after hepatectomy: analysis based on tumor hemodynamics. *Arch Surg* 2002; **137**: 94-99 [PMID: 11772225]

35 **Kim TK**, Lee KH, Jang HJ, Haider MA, Jacks LM, Menezes RJ, Park SH, Yazdi L, Sherman M, Khalili K. Analysis of gadobenate dimeglumine-enhanced MR findings for characterizing small (1-2-cm) hepatic nodules in patients at high risk for hepatocellular carcinoma. *Radiology* 2011; **259**: 730-738 [PMID: 21364083 DOI: 10.1148/radiol.11101549]

36 **Salomao M**, Remotti H, Vaughan R, Siegel AB, Lefkowitch JH, Moreira RK. The steatohepatitic variant of hepatocellular carcinoma and its association with underlying steatohepatitis. *Hum Pathol* 2012; **43**: 737-746 [PMID: 22018903 DOI: 10.1016/j.humpath.2011.07.005]

37 **Yu JS**, Chung JJ, Kim JH, Kim KW. Fat-containing nodules in the cirrhotic liver: chemical shift MRI features and clinical implications. *AJR Am J Roentgenol* 2007; **188**: 1009-1016 [PMID: 17377037 DOI: 10.2214/AJR.06.0756]

38 **Li M**, Xin Y, Fu S, Liu Z, Li Y, Hu B, Chen S, Liang C, Lu L. Corona Enhancement and Mosaic Architecture for Prognosis and Selection Between of Liver Resection Versus Transcatheter Arterial Chemoembolization in Single Hepatocellular Carcinomas >5cm Without Extrahepatic Metastases: An Imaging-Based Retrospective

Study. *Medicine* (Baltimore) 2016; **95**: e2458 [PMID: 26765441 DOI: 10.1097/MD.0000000000002458]

39 **Honda H**, Onitsuka H, Murakami J, Kaneko K, Murayama S, Adachi E, Kanematsu T, Sugimachi K, Masuda K. Characteristic findings of hepatocellular carcinoma: an evaluation with comparative study of US, CT, and MRI. *Gastrointest Radiol* 1992; **17**: 245-249 [PMID: 1319366]

40 **Stevens WR**, Gulino SP, Batts KP, Stephens DH, Johnson CD. Mosaic pattern of hepatocellular carcinoma: histologic basis for a characteristic CT appearance. *J Comput Assist Tomogr* 1996; **20**: 337-342 [PMID: 8626886]

41 **Chen W**, DelProposto Z, Liu W, Kassir M, Wang Z, Zhao J, Xie B, Wen Y, Wang J, Hu J. Susceptibility-weighted imaging for the noncontrast evaluation of hepatocellular carcinoma: a prospective study with histopathologic correlation. *PLoS One* 2014; **9**: e98303 [PMID: 24879409 DOI: 10.1371/journal.pone.0098303]

P- Reviewer: Bramhall S, Guan YS, Qin JM **S- Editor**: Cui LJ
L- Editor: A **E- Editor**: Li RF

Published by **Baishideng Publishing Group Inc**
7901 Stoneridge Drive, Suite 501, Pleasanton, CA 94588, USA
Telephone: +1-925-223-8242
Fax: +1-925-223-8243
E-mail: bpgoffice@wjgnet.com
Help Desk: http://www.f6publishing.com/helpdesk
http://www.wjgnet.com

ISSN 1949-8470 (online)

World Journal of *Radiology*

World J Radiol 2018 March 28; 10(3): 24-29

Published by Baishideng Publishing Group Inc

WJR World Journal of Radiology

Contents

Monthly Volume 10 Number 3 March 28, 2018

ORIGINAL ARTICLE

Basic Study

World Journal of Radiology
Volume 10 Number 3 March 28, 2018

Contents

NAME OF JOURNAL
World Journal of Radiology

ISSN
ISSN 1949-8470 (online)

LAUNCH DATE
January 31, 2009

FREQUENCY
Monthly

EDITORIAL OFFICE
Xiu-Xia Song, Director
World Journal of Radiology
Baishideng Publishing Group Inc
7901 Stoneridge Drive, Suite 501, Pleasanton, CA 94588, USA
Telephone: +1-925-2238242
Fax: +1-925-2238243
E-mail: editorialoffice@wjgnet.com
Help Desk: http://www.f6publishing.com/helpdesk
http://www.wjgnet.com

PUBLISHER
Baishideng Publishing Group Inc
7901 Stoneridge Drive, Suite 501,
Pleasanton, CA 94588, USA
Telephone: +1-925-2238242
Fax: +1-925-2238243
E-mail: bpgoffice@wjgnet.com
Help Desk: http://www.f6publishing.com/helpdesk
http://www.wjgnet.com

PUBLICATION DATE
March 28, 2018

INSTRUCTIONS TO AUTHORS
http://www.wjgnet.com/bpg/gerinfo/204

ONLINE SUBMISSION
http://www.f6publishing.com

World Journal of Radiology

Submit a Manuscript: http://www.f6publishing.com

World J Radiol 2018 March 28; 10(3): 24-29

DOI: 10.4329/wjr.v10.i3.24

ISSN 1949-8470 (online)

ORIGINAL ARTICLE

Basic Study

Effect of varying computed tomography acquisition and reconstruction parameters on semi-automated clot volume quantification

Audrey E Kaufman, Alison N Pruzan, Ching Hsu, Sarayu Ramachandran, Adam Jacobi, Zahi A Fayad, Venkatesh Mani

Audrey E Kaufman, Alison N Pruzan, Sarayu Ramachandran, Adam Jacobi, Zahi A Fayad, Venkatesh Mani, Department of Radiology, Icahn School of Medicine at Mount Sinai, New York, NY 10029, United States

Audrey E Kaufman, Alison N Pruzan, Sarayu Ramachandran, Zahi A Fayad, Venkatesh Mani, Translational and Molecular Imaging Institute, Icahn School of Medicine at Mount Sinai, Hess Center for Science and Medicine, New York, NY 10029, United States

Ching Hsu, Daiichi Sankyo Inc., Basking Ridge, NJ 07920, United States

ORCID number: Audrey E Kaufman (0000-0002-9221-9004); Alison N Pruzan (0000-0002-3054-6341); Ching Hsu (0000-0003-0616-2468); Sarayu Ramachandran (0000-0002-9917-5876); Adam Jacobi (0000-0002-9057-9129); Zahi A Fayad (0000-0002-3439-7347); Venkatesh Mani (0000-0002-0432-2918).

Author contributions: All authors designed the experiment; Kaufman AE, Pruzan AN, Ramachandran S and Mani V performed the experiment; Kaufman AE performed the image analysis; Pruzan AN and Hsu C performed statistical analysis; Kaufman AE and Mani V wrote the draft of the manuscript; all authors critically reviewed the manuscript.

Institutional review board statement: As this is an *in-vitro* study, institutional review board approval was not required.

Conflict-of-interest statement: Hsu C is an employee of Daiichi Sankyo Inc; all other authors have no conflicts to disclose.

Manuscript source: Invited manuscript

Correspondence to: Venkatesh Mani, PhD, Associate Professor, Director, Department of Radiology, Icahn School of Medicine at Mount Sinai, 1470 Madison Avenue, New York, NY 10029, United States. venkatesh.mani@mountsinai.org
Telephone: +1-212-824844
Fax: +1-240-3688096

Received: February 9, 2018
Peer-review started: February 10, 2018
First decision: March 12, 2018
Revised: March 14, 2018
Accepted: March 19, 2018
Article in press: March 20, 2018
Published online: March 28, 2018

Abstract

AIM

To examine effects of computed tomography (CT) image acquisition/reconstruction parameters on clot volume quantification *in vitro* for research method validation purposes.

METHODS

This study was performed in conformance with HIPAA and IRB Regulations (March 2015-November 2016). A ten blood clot phantom was designed and scanned on a dual-energy CT scanner (SOMATOM Force, Siemens Healthcare GmbH, Erlangen, Germany) with varying pitch, iterative reconstruction, energy level and slice

thickness. A range of clot and tube sizes were used in an attempt to replicate *in vivo* emboli found within central and segmental branches of the pulmonary arteries in patients with pulmonary emboli. Clot volume was the measured parameter and was analyzed by a single image analyst using a semi-automated region growing algorithm implemented in the FDA-approved Siemens *syngo*.via image analysis platform. Mixed model analysis was performed on the data.

RESULTS

On the acquisition side, the continuous factor of energy showed no statistically significant effect on absolute clot volume quantification (P = 0.9898). On the other hand, when considering the fixed factor of pitch, there were statistically significant differences in clot volume quantification (P < 0.0001). On the reconstruction side, with the continuous factor of reconstruction slice thickness no statistically significant effect on absolute clot volume quantification was demonstrated (P = 0.4500). Also on the reconstruction side, with the fixed factor of using iterative reconstructions there was also no statistically significant effect on absolute clot volume quantification (P = 0.3011). In addition, there was excellent R^2 correlation between the scale-measured mass of the clots both with respect to the CT measured volumes and with respect to volumes measure by the water displacement method.

CONCLUSION

Aside from varying pitch, changing CT acquisition parameters and using iterative reconstructions had no significant impact on clot volume quantification with a semi-automated region growing algorithm.

Key words: Computed tomography angiography; Radiographic phantom; Computer-assisted image analysis; Pulmonary embolism; Thrombolytic therapy

Core tip: This *in vitro* study showed that with the exception of pitch, varying the computed tomography pulmonary angiography image acquisition parameters and using iterative reconstructions had no significant impact on clot volume quantification when using a semi-automated region growing algorithm. This finding is applicable to validating core lab analysis in multicenter clinical trials with imaging endpoints, where a wide range of acquisition and reconstruction parameters are used.

Kaufman AE, Pruzan AN, Hsu C, Ramachandran S, Jacobi A, Fayad ZA, Mani V. Effect of varying computed tomography acquisition and reconstruction parameters on semi-automated clot volume quantification. *World J Radiol* 2018; 10(3): 24-29 Available from: URL: http://www.wjgnet.com/1949-8470/full/v10/i3/24.htm DOI: http://dx.doi.org/10.4329/wjr.v10.i3.24

INTRODUCTION

Pulmonary embolism (PE) occurs in greater than one third of patients with deep venous thrombosis, and together the two disease states are termed venous thromboembolism[1]. In the United States, venous thromboembolism occurs with an average annual incidence of greater than 275000 among white people of predominantly European ancestry and African Americans combined[2]. With its high mortality rate, PE represents the most significant sequela of deep venous thrombosis[3,4].

In clinical practice, computed tomography (CT) Pulmonary Angiography (CTPA) is commonly performed as it has been shown to help with risk stratification of PE[5-7] . Clot burden is not used as a diagnostic or prognostic tool in clinical practice. However, quantification of clot burden is used in research to assess the efficacy, potency and optimal duration of pharmaceuticals such as thrombolytics[8].

In vivo quantification of clot burden can be performed using CTPA and segmenting the non-enhanced thrombus using semi-automated region growing algorithms[9]. The effects of various imaging parameters both on the CT acquisition side (energy, pitch) as well as reconstruction side (slice thickness, iterative reconstruction) on the quantification of pulmonary embolism measurements have not been studied extensively. Thus, the purpose of this study is to examine the effects of varying CT image acquisition and reconstruction parameters on the quantification of clot volumes *in vitro* with the goal of solidifying this method as a means of measuring *in vivo* thrombus volume in PE. This study has not been performed for clinical diagnostic or primary therapeutic purposes, but rather the sole intention of this study is for research purposes where clot burden and its change over time are utilized as endpoints in clinical drug trials. There is value in determining this because in multicenter clinical trials involving imaging endpoints there can be great variability in methods of acquisition and reconstruction. The overall objective is to confirm viability of this method in multicenter clinical pharmaceutical trials where site-to-site variability in parameters is common.

MATERIALS AND METHODS

Ten clots of varying sizes were created in test tubes by allowing venous blood to coagulate by exposure to air. The purpose of making ten clots was to replicate various sized emboli found *in vivo*. Each clot was weighed on a laboratory precision scale and assessed for volume using the water displacement method and graduated cylinders. The clots were imaged in Falcon tubes and test tubes of varying diameters filled with a diluted solution of Isovue 370 (1:25 volume in saline to simulate typical Hounsfield units of blood in pulmonary arteries after injection of iodinated contrast

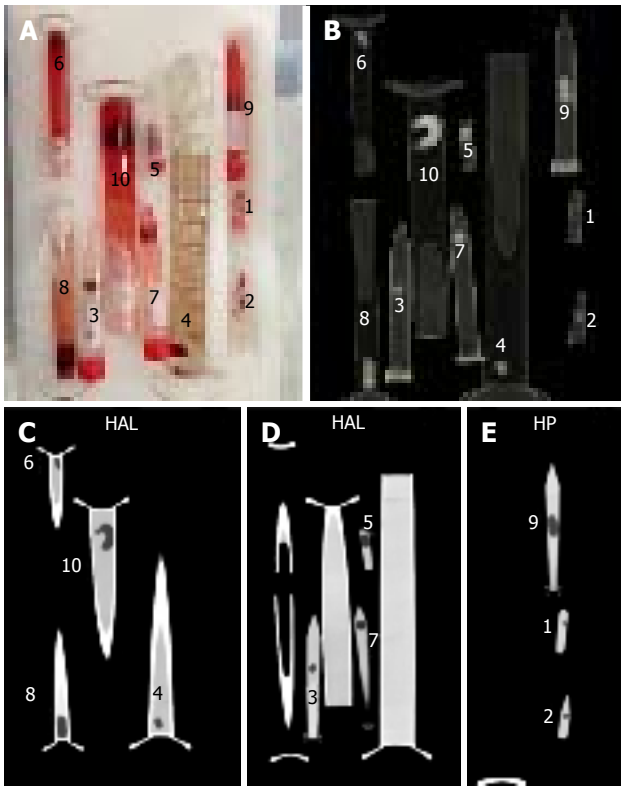

Figure 1 Photograph of 10 blood clot phantom (A); Volume rendered 3D reconstructed CT image of 10 blood clot phantom (B); Coronal CT images of ten blood clot phantom showing in (C) clots numbered 4, 6, 8 and 10, in (D) clots numbered 3, 5, and 7 and in (E) clots numbered 1, 2 and 9.

in a CTPA scan). All 10 clots in the tubes were scanned simultaneously on a Siemens Force dual energy CT scanner (SOMATOM Force, Siemens Healthcare GmbH, Erlangen, Germany) using various image acquisition and reconstruction parameters. Figure 1 shows an image of the clots in the tubes and corresponding sample CT and Table 1 demonstrates details of the acquisition and reconstruction parameters.

Analyst 1 (AEK, a board certified diagnostic radiologist with six years clinical experience) identified the 10 individual clots within their respective tubes within each of the 120 acquisitions. The clot volume was the measured parameter. Each clot was analyzed using a semi-automated region growing algorithm implemented in the FDA approved Siemens *syngo.via* image analysis platform. This region growing algorithm is similar to what has been used in previous studies for quantification of PE clot volume[9] and is also based on the methods shown in the following papers[10-12]. A total of 1200 volume measurements were made. The results of the volume water displacement method (with an average of 5 measurements per clot) were used as the gold standard comparison with the CT volume data.

A mixed model statistical method was used to analyze the *in vitro* data. The discrete factors were pitch (0.6, 0.9, 1.2) and the Siemens Advanced Modeled Iterative Reconstruction known as ADMIRE (Yes/No).

Table 1 Clot scan parameters

Energy (kVp)	Pitch	Slice thickness (mm)	Recon kernel	ADMIRE
80	0.6	0.6	Bv36	On
90	0.9	1		Off
100	1.2	1.5		
110		2		
120				

kVp: Peak kilovoltage; Bv: Body vascular; ADMIRE: Siemens Advanced Modeled Iterative Reconstruction.

The energy level in kVp (80, 90, 100, 110, 120) and slice thickness in millimeters (0.6, 1, 1.5, 2) were set as continuous factors. The volume of the clots themselves was set as a random factor.

Analysis of the *in vitro* study was performed using SAS/STAT software, Version 9 of the SAS System for Windows. ©2013, SAS Institute Inc. SAS and all other SAS Institute Inc. product or service names are registered trademarks or trademarks of SAS Institute Inc., Cary, NC, United States. All plots were drawn using GraphPad Prism 7 for Mac, GraphPad Software, San Diego California, United States, www.graphpad.com.

RESULTS

Analysis of Clot 10 is shown as an example in Figure 2 which illustrates the effects of the varying acquisition and reconstruction parameters on quantification of clot volume. In each graph displayed, the y-axis shows the difference between the measured volume and the gold standard volume for Clot 10. The x-axis shows the effect of varying the following: (1) Energy/pitch; (2) energy/slice thickness; (3) slice thickness/pitch; (4) energy/ADMIRE; (5) pitch/ADMIRE; and (6) slice thickness/ADMIRE respectively. The complete analysis of all ten clots is available in supplementary figures 1-6.

Overall statistical analysis of the raw clot volume data revealed no statistical significance among the levels for the fixed factor of ADMIRE (P = 0.3011) nor for the continuous factors of energy (P = 0.9898) and slice thickness (P = 0.4500). There was, however, statistical significance found among the levels for the fixed factor of pitch (P < 0.0001).

The correlation between the independent measurements of the mass of the clots in grams *vs* the mean CT acquired volumes in cubic centimeters appears in Figure 3 with an excellent R^2 correlation value of 0.9956. Additionally, the correlation between the independent measurements of the mass of the clots in grams *vs* the volume by physical measurements in cubic centimeters (average of 5 measurements) appears in Figure 4 with an excellent R^2 correlation value of 0.9987.

DISCUSSION

In this *in vitro* study, we assessed the effect of a variety of image acquisition and reconstruction parameters

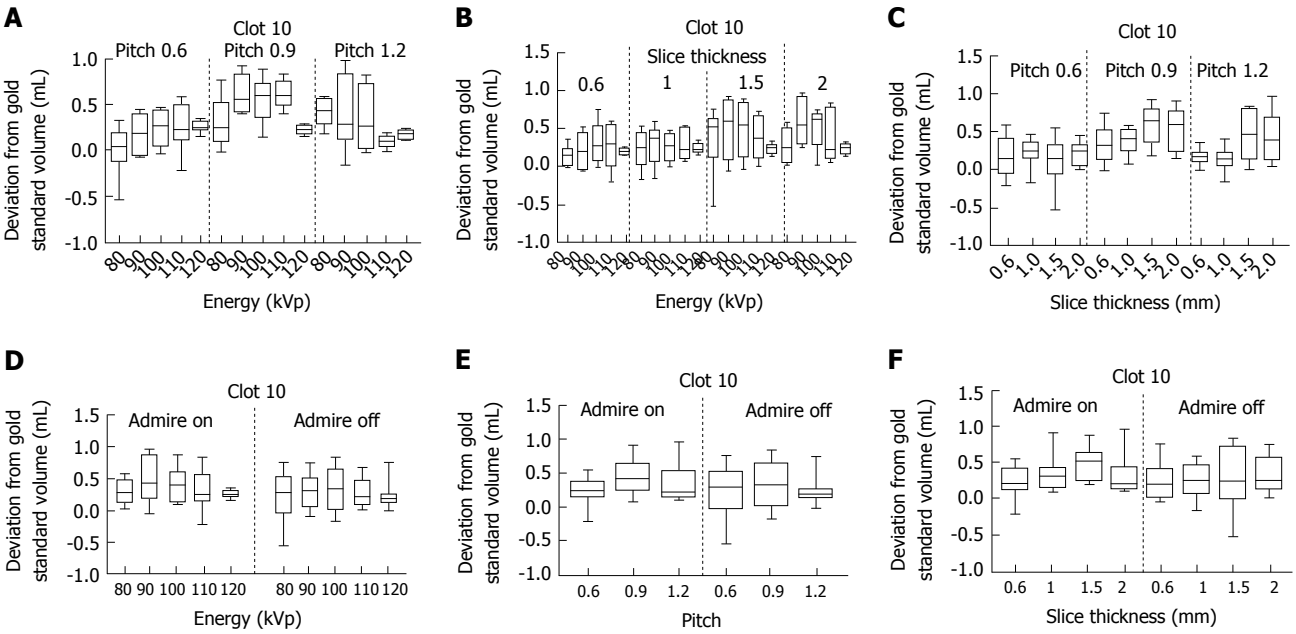

Figure 2 Box plots showing the difference between the segmented volume and the mean measured (gold standard) volume for Clot 10 as it relates to the following acquisition and reconstruction parameters. A: Energy and pitch; B: Energy and slice thickness; C: Slice thickness and pitch; D: Energy and Siemens Advanced Modeled Iterative Reconstruction (ADMIRE); E: Pitch and ADMIRE; F: Slice thickness and ADMIRE.

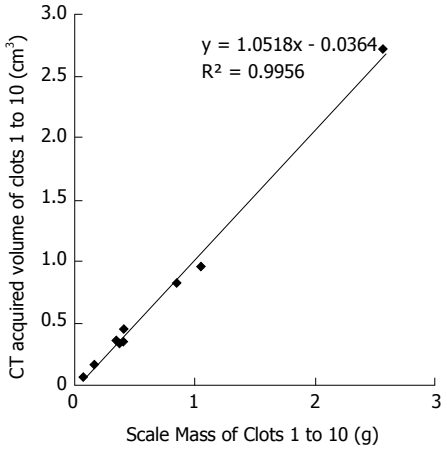

Figure 3 Correlation between scale measured mass *vs* computed tomography acquired volume of 10 clots with an excellent R^2 correlation value of 0.9956.

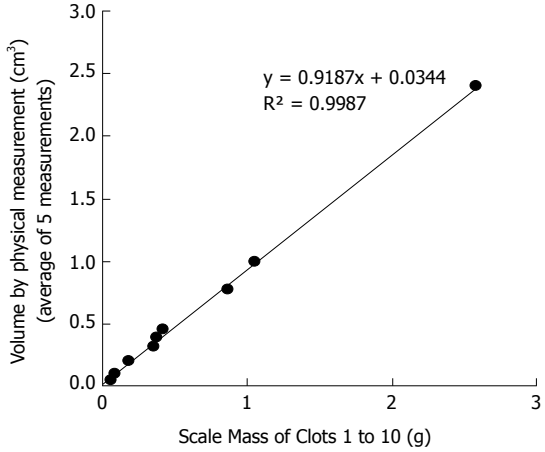

Figure 4 Correlation between scale measured mass *vs* volume by physical measurement (cm^3) (average of 5 measurements) of 10 clots with an excellent R^2 correlation value of 0.9987.

on volumetric measurements using a phantom of ten separate blood clots. We used a range of clot and tube sizes in an attempt to replicate *in vivo* emboli found within central and segmental branches of the pulmonary arteries. The results of our *in vitro* phantom study showed that varying the parameters of slice thickness, energy and ADMIRE caused no statistically significant differences in measured volumes for all clots in the raw data analysis. However, varying the pitch demonstrated statistical significance, specifically that volumes provided higher estimates for pitch = 0.9 compared to pitch = 0.6 or 1.2. Although this may relate to limitations in the accuracy of our gold standard, it is recommended to give protocol guidance to sites to insure accuracy and repeatability in embolus volume measurements.

Radiation dose (tube current-time product in milliampere seconds) is also inversely related to the pitch. This may indicate that changing the tube current and/or using dose modulation may also have an effect on the quantification of thrombus volume. This effect was however not explicitly tested and is one of the limitations of our study[12]. With a thorough search of PubMed (using key words pulmonary; emboli; PE; impact; energy; kV; CT; volume; quantification; measurement; reconstruction; density; iterative; angio; effect; Hounsfield; scan) looking at the impact of scan and reconstruction settings as they relate to pulmonary emboli, there was one study of note performed by Ogden *et al*[13] which showed that varying the strength of iterative reconstruction causes very little measurable

effect on density measurement values for varying concentrations of iodine regardless of beam energy. This is applicable to the present study as the semi-automated region growing algorithm in Siemens *syngo*. via image analysis platform creates volumetric masks using region growing based on density measurement values.

Aside from the pitch setting, the *in vitro* study showed no significant impact on clot volume quantification. This result indicates that measurement of clot volumes using semi-automated analysis may be robust across a range of image acquisition and reconstruction parameters that may typically be used at various imaging centers in a multicenter study with adequate control for pitch.

Our study showed reasonable correlation of actual clot weights *vs* volumes measured using CT derived values with $R^2 = 0.9956$ (Figure 3) and independently using the gold standard with $R^2 = 0.9987$ (Figure 4). It should be noted however that the displacement method for measuring clot volumes *in vitro* is challenging and subject to errors of measurement. Additionally, we compared the individual clot volumes with the mean of the total CT acquired clot volumes for each clot in supplementary figures 7-12. In this scenario, none of the imaging parameters including pitch showed any significant effect on volumetric quantification further strengthening the possibility that the results for pitch being a factor in volume quantification could be due to inaccurate gold standard clot volume measurements.

Limitations of the study included the failure to use a "human thorax" phantom, which would have introduced a varying degree of scatter radiation that would have possibly affected the images and thus measurement accuracy. An additional limitation involves some degree of imprecision of the water displacement volume analysis of the 10 clots. Also, although we applied multiple variables including energy, pitch and reconstruction methods and used a range of clot sizes, other variables were not included such as additional reconstruction methods.

In conclusion, the *in vitro* data showed that with the exception of pitch, varying the CTPA image acquisition parameters and using iterative reconstructions had no significant impact on clot volume quantification.

ARTICLE HIGHLIGHTS

Research background

Pulmonary embolism is a common and serious medical problem often evaluated using computed tomography (CT) pulmonary angiography. In the clinical setting the disease course is not followed by embolic volume measurements; however in clinical pharmaceutical trials, measuring embolic load is useful to assess for drug efficacy, potency and optimal duration of treatment. Volume measurements can be made using semi-automated region-growing techniques and the goal of this study was to assess the accuracy of these measurements.

Research motivation

Our Core Research Imaging Lab group specializes in cardiovascular disease. Frequently we analyze data coming from multiple outside radiology centers where imaging protocols often vary from one site to another. To assess the validity of region growing volume measurements in CT pulmonary angiography, we devised this study to assess for significant differences in results with changes in acquisition and reconstruction of images that often occur in multicenter studies such as the ones in which we participate.

Research objectives

The overall goal was to validate the imaging assessment methods used in multicenter clinical trials evaluating treatment options for pulmonary embolism using CT angiography.

Research methods

In this study ten blood clots were made and each clot was weighed on a laboratory precision scale and assessed for volume (the gold standard) using the water displacement method in graduated cylinders. Volume measurements were made on CT images of the blood clots in test tubes. The CT images were obtained with varying acquisition and reconstruction parameters and the clots were placed in diluted contrast material to simulate pulmonary emboli as they would appear in a CT angiogram. A single image analyst made the measurements using a semi-automated region growing algorithm using FDA-approved Siemens *syngo.via* image analysis platform. A mixed model statistical analysis was performed on the data.

Research results

Overall the study showed that varying the image acquisition parameters and using iterative reconstructions had no significant impact on clot volume measurements with, however, the exception of pitch.

Research conclusions

The new findings of this study are that varying the image acquisition parameters and reconstructions did not have a significant impact on clot volume measurements, with the exception of pitch. In terms of pitch, pitch = 0.9 yielded higher volume measurements than with pitch = 0.6 or 1.2. This could be due to limitations in the accuracy of our gold standard, yet it is recommended to give pitch protocol guidance to sites for accuracy and repeatability in volume measurements. The present study confirms and validates research methods currently in use. The study found that using data acquired in the multicenter setting is viable for volume assessment of pulmonary emboli in pharmaceuticals research and thus, has an important impact on the development of therapies for this common and severe medical problem.

Research perspectives

Our findings indicate that care must be taken when evaluating data from multiple centers while evaluating thrombus volume in pulmonary embolism and appropriate corrections made for differences in acquisition and reconstruction across the multiple sites. Future research can evaluate more imaging parameters such as tube current used for its role on pulmonary embolism thrombus volume quantification.

REFERENCES

1 **Giordano NJ**, Jansson PS, Young MN, Hagan KA, Kabrhel C. Epidemiology, Pathophysiology, Stratification, and Natural History of Pulmonary Embolism. *Tech Vasc Interv Radiol* 2017; **20**: 135-140 [PMID: 29029707 DOI: 10.1053/j.tvir.2017.07.002]

2 **Heit JA**. Venous thromboembolism: disease burden, outcomes and risk factors. *J Thromb Haemost* 2005; **3**: 1611-1617 [PMID: 16102026 DOI: 10.1111/j.1538-7836.2005.01415.x]

3 **Laporte S**, Mismetti P, Décousus H, Uresandi F, Otero R, Lobo JL, Monreal M; RIETE Investigators. Clinical predictors for fatal pulmonary embolism in 15,520 patients with venous thromboembolism: findings from the Registro Informatizado de la Enfermedad TromboEmbolica venosa (RIETE) Registry. *Circulation* 2008; **117**: 1711-1716 [PMID: 18347212 DOI: 10.1161/CIRCULATIONAHA.107.726232]

4 **Heit JA**, Silverstein MD, Mohr DN, Petterson TM, O'Fallon WM, Melton LJ 3rd. Predictors of survival after deep vein thrombosis

and pulmonary embolism: a population-based, cohort study. *Arch Intern Med* 1999; **159**: 445-453 [PMID: 10074952 DOI: 10.1001/archinte.159.5.445]

5 **Hariharan P**, Dudzinski DM, Rosovsky R, Haddad F, MacMahon P, Parry B, Chang Y, Kabrhel C. Relation Among Clot Burden, Right-Sided Heart Strain, and Adverse Events After Acute Pulmonary Embolism. *Am J Cardiol* 2016; **118**: 1568-1573 [PMID: 27742425 DOI: 10.1016/j.amjcard.2016.08.025]

6 **Meinel FG**, Nance JW Jr, Schoepf UJ, Hoffmann VS, Thierfelder KM, Costello P, Goldhaber SZ, Bamberg F. Predictive Value of Computed Tomography in Acute Pulmonary Embolism: Systematic Review and Meta-analysis. *Am J Med* 2015; **128**: 747-59.e2 [PMID: 25680885 DOI: 10.1016/j.amjmed.2015.01.023]

7 **Vedovati MC**, Becattini C, Agnelli G, Kamphuisen PW, Masotti L, Pruszczyk P, Casazza F, Salvi A, Grifoni S, Carugati A, Konstantinides S, Schreuder M, Golebiowski M, Duranti M. Multidetector CT scan for acute pulmonary embolism: embolic burden and clinical outcome. *Chest* 2012; **142**: 1417-1424 [PMID: 22628491 DOI: 10.1378/chest.11-2739]

8 **Aghayev A**, Furlan A, Patil A, Gumus S, Jeon KN, Park B, Bae KT. The rate of resolution of clot burden measured by pulmonary CT angiography in patients with acute pulmonary embolism. *AJR Am J Roentgenol* 2013; **200**: 791-797 [PMID: 23521450 DOI: 10.2214/AJR.12.8624]

9 **Furlan A**, Patil A, Park B, Chang CC, Roberts MS, Bae KT. Accuracy and reproducibility of blood clot burden quantification with pulmonary CT angiography. *AJR Am J Roentgenol* 2011; **196**: 516-523 [PMID: 21343492 DOI: 10.2214/AJR.10.4603]

10 **Belongie S**, Carson C, Greenspan H, Malik J. Color- and texture-based image segmentation using EM and its application to content-based image retrieval. In: Sixth International Conference on Computer Vision; 1998: 675-682 [DOI: 10.1109/ICCV.1998.710692]

11 **Boser BE**, Guyon IM, Vapnik VN. A training algorithm for optimal margin classifiers. In: Proceedings of the fifth annual workshop on Computational learning theory- COLT '92; 1992 July 27-29; Pittsburgh, Pennsylvania, United States. New York: ACM Press; 1992: 144-152 [DOI: 10.1145/130385.130401]

12 **Primak AN**, McCollough CH, Bruesewitz MR, Zhang J, Fletcher JG. Relationship between noise, dose, and pitch in cardiac multi-detector row CT. *Radiographics* 2006; **26**: 1785-1794 [PMID: 17102050 DOI: 10.1148/rg.266065063]

13 **Ogden K,** Greene-Donnelly K, Vallabhaneni D, Scalzetti E. The Effect of Iterative Reconstruction and CT Tube Voltage on Hounsfield Unit Values of Iodinated Contrast. *Med Phys* 2016; **43**: 3658-3658 [DOI: 10.1118/1.4957017]

P- Reviewer: Said AM **S- Editor**: Cui LJ **L- Editor**: A
E- Editor: Li D

Published by **Baishideng Publishing Group Inc**
7901 Stoneridge Drive, Suite 501, Pleasanton, CA 94588, USA
Telephone: +1-925-223-8242
Fax: +1-925-223-8243
E-mail: bpgoffice@wjgnet.com
Help Desk: http://www.f6publishing.com/helpdesk
http://www.wjgnet.com

ISSN 1949-8470 (online)

World Journal of *Radiology*

World J Radiol 2018 April 28; 10(4): 30-45

Published by Baishideng Publishing Group Inc

WJR World Journal of Radiology

Contents

Monthly Volume 10 Number 4 April 28, 2018

REVIEW

World Journal of Radiology
Volume 10 Number 4 April 28, 2018

Contents

NAME OF JOURNAL
World Journal of Radiology

ISSN
ISSN 1949-8470 (online)

LAUNCH DATE
January 31, 2009

FREQUENCY
Monthly

EDITORIAL OFFICE
Jin-Lei Wang, Director
World Journal of Radiology
Baishideng Publishing Group Inc
7901 Stoneridge Drive, Suite 501, Pleasanton, CA 94588, USA
Telephone: +1-925-2238242
Fax: +1-925-2238243
E-mail: editorialoffice@wjgnet.com
Help Desk: http://www.f6publishing.com/helpdesk
http://www.wjgnet.com

PUBLISHER
Baishideng Publishing Group Inc
7901 Stoneridge Drive, Suite 501,
Pleasanton, CA 94588, USA
Telephone: +1-925-2238242
Fax: +1-925-2238243
E-mail: bpgoffice@wjgnet.com
Help Desk: http://www.f6publishing.com/helpdesk
http://www.wjgnet.com

PUBLICATION DATE
April 28, 2018

INSTRUCTIONS TO AUTHORS
http://www.wjgnet.com/bpg/gerinfo/204

ONLINE SUBMISSION
http://www.f6publishing.com

World Journal of Radiology

Submit a Manuscript: http://www.f6publishing.com

World J Radiol 2018 April 28; 10(4): 30-45

DOI: 10.4329/wjr.v10.i4.30

ISSN 1949-8470 (online)

REVIEW

Susceptibility weighted imaging: Clinical applications and future directions

Ahmet Mesrur Halefoglu, David Mark Yousem

Ahmet Mesrur Halefoglu, Department of Radiology, Sisli Hamidiye Etfal Training and Research Hospital, University of Health Sciences, Istanbul 34371, Turkey

David Mark Yousem, Division of Neuroradiology, Department of Radiology, Johns Hopkins Medical Institution, Baltimore, MI 21287, United States

ORCID number: Ahmet Mesrur Halefoglu (0000-0002-2054-3550); David Mark Yousem (0000-0002-1222-6643).

Author contributions: All authors equally contributed to this paper with conception and design of the study, literature review and analysis, drafting, critical revision and editing, and final approval of the final version.

Conflict-of-interest statement: No potential conflicts of interest.

Manuscript source: Unsolicited manuscript

Correspondence to: Ahmet Mesrur Halefoglu, MD, Professor, Department of Radiology, Sisli Hamidiye Etfal Training and Research Hospital, University of Health Sciences, Birlik sok, Parksaray ap, No: 17/4, Istanbul 34371, Turkey. halefoglu@hotmail.com
Telephone: +90-212-3735000
Fax: +90-212-2415015

Received: March 17, 2018
Peer-review started: March 17, 2018
First decision: April 4, 2018
Revised: April 8, 2018
Accepted: April 20, 2018
Article in press: April 20, 2018
Published online: April 28, 2018

Abstract

Susceptibility weighted imaging (SWI) is a recently developed magnetic resonance imaging (MRI) technique that is increasingly being used to narrow the differential diagnosis of many neurologic disorders. It exploits the magnetic susceptibility differences of various compounds including deoxygenated blood, blood products, iron and calcium, thus enabling a new source of contrast in MR. In this review, we illustrate its basic clinical applications in neuroimaging. SWI is based on a fully velocity-compensated, high-resolution, three dimensional gradient-echo sequence using magnitude and phase images either separately or in combination with each other, in order to characterize brain tissue. SWI is particularly useful in the setting of trauma and acute neurologic presentations suggestive of stroke, but can also characterize occult low-flow vascular malformations, cerebral microbleeds, intracranial calcifications, neurodegenerative diseases and brain tumors. Furthermore, advanced MRI post-processing technique with quantitative susceptibility mapping, enables detailed anatomical differentiation based on quantification of brain iron from SWI raw data.

Key words: Quantitative susceptibility mapping; Brain; Ischemia; Magnetic resonance imaging; Susceptibility weighted imaging

Core tip: Susceptibility weighted imaging has a variety of applications in neuroradiology practice and should be included in routine protocols. It can detect micro- and macrohemorhages and delineate cerebral microvasculature and can also reveal low-flow vascular malformations. It has been proven as a complementary, valuable imaging sequence in the management of stroke patients. It provides differentiation of calcium from hemorrhage in the brain. It plays an important role in the evaluation of traumatic brain injury patients and aids in the characterization and grading of cerebral tumors.

Quantitative susceptibility mapping can be applied on many neurodegenerative disorders by assessing brain iron content.

Halefoglu AM, Yousem DM. Susceptibility weighted imaging: Clinical applications and future directions. *World J Radiol* 2018; 10(4): 30-45 Available from: URL: http://www.wjgnet.com/1949-8470/full/v10/i4/30.htm DOI: http://dx.doi.org/10.4329/wjr.v10.i4.30

INTRODUCTION

Susceptibility weighted imaging (SWI) is an magnetic resonance imaging (MRI) technique that exploits the magnetic susceptibility differences of various compounds, such as blood, iron, and diamagnetic calcium, thus enabling new sources of MR contrast[1-3].

SWI has been shown to provide clinically useful complementary information to conventional spin-echo MRI sequences. Additionally, through post-processed quantitative susceptibility mapping (QSM) SWI sequences allow data driven research to evaluate compounds that alter the magnetic field of the brain, a strategy most useful in neurodegenerative disorders. In this review, we highlight many clinical applications of SWI in the evaluation and differential diagnosis of diverse central nervous system (CNS) pathologic conditions. We close with an assessment of the future of SWI and QSM.

PRINCIPLES AND TECHNICAL ASPECTS OF SWI

Local magnetic field heterogeneity leading to T2 shortening may be induced by paramagnetic, diamagnetic and ferromagnetic substances and results in signal loss on T2* weighted gradient-echo (GE) sequences (proton relaxation enhancement). The susceptibility effect is most visible in non-refocused GE techniques using long echo times (TE), short flip angles, and high field strengths. Although SWI relies on GE sequences, it has enhanced susceptibility sensitivity compared with conventional T2* weighted GE sequences because it is based on a high-resolution, long TE, flow-compensated, 3D GE imaging technique containing filtered phase information in each voxel[4]. In SWI, the magnitude and phase MR data are brought together and a phase mask is created. Multiplying these with the original magnitude images result in a final magnitude SWI dataset. Both magnitude and phase information are essential for proper tissue characterization, and are brought together to create an SWI image[5]. Finally, these images are further processed with a minimum intensity projection algorithm (minIP) to obtain 3-10 mm thick high signal to noise minIP slabs. These minIP images thereby reveal the continuity of tortuous veins across the slices while attenuating the signal coming from the brain tissue[4]. On magnitude images, the longer TE of the SWI sequence (*e.g.*, 40 ms at 1.5 tesla) compared with conventional GE sequences (TE 25 ms) allows for more phase dispersion and T2 shortening of the protons in the local inhomogenous magnetic field. Thus SWI highlights small changes in susceptibility across a voxel as signal intensity loss. A low flip angle can keep the CSF brighter than the surrounding parenchyma. Consequently, the magnitude image highlights areas with short T2* and leads to lower signal in major veins due to the presence of deoxyhemoglobin[6]. SWI sequence parameters for 1.5 and 3 Tesla Siemens (Erlangen, Germany) and Philips (the Netherlands) magnets are shown in Tables 1-4.

Paramagnetic materials have at least one unpaired electron in the system, but diamagnetic materials have all their electrons paired. Diamagnetic materials are repelled by a magnetic field; an applied magnetic field creates an induced magnetic field in them in the opposite direction, causing a repulsive force. In contrast, paramagnetic and ferromagnetic materials are attracted by a magnetic field. Oxyhemoglobin is diamagnetic in nature, whereas deoxyhemoglobin is paramagnetic. The paramagnetic deoxyhemoglobin serves as an intrinsic contrast agent on SWI sequences, and is low in signal. This causes magnetic field inhomogeneity due to two effects: A reduction of T2* and a phase difference between the vessel and its surrounding tissue. This property also forms the basic principle for blood oxygen level dependent functional and venographic imaging.

Paramagnetic substances display positive phase shift in left-handed MR systems such as the Avanto system of Siemens magnets (Erlangen, Germany). Hence, the phase images are particularly useful for differentiating between paramagnetic susceptibility effects of blood products such as deoxygenated hemoglobin, intracellular methemoglobin, hemosiderin and ferritin (positive shift) and diamagnetic effects of calcium (negative or no shift)[7,8]. Unfortunately, ferrocalcinosis may lead to confusing signal intensity patterns as even basal ganglia "calcification" is often a mixture of paramagnetic iron and diamagnetic calcium. Yamada *et al*[8] demonstrated that all basal ganglia calcifications show a paramagnetic susceptibility effect, whereas other calcifications located outside the basal ganglia (such as choroid plexus or dural calcifications) exhibit exclusively a diamagnetic susceptibility effect. Iron accumulation in brain not only occurs in aging but is also encountered in diverse neurodegenerative diseases.

SWI sequences have some intrinsic disadvantages. Undesirable magnetic susceptibility sources that cause artifacts occuring at air-tissue interfaces such as the areas adjacent to the temporal bone and sinuses limit investigation of these regions. Also the blooming artifact, a useful sign for detecting sources of field inhomogeneity, may sometimes lead to extreme tissue signal cancellation and loss of anatomical borders[4].

Table 1 Susceptibility weighted imaging sequence parameters for 1.5 T Siemens Magnetom Avanto syngo magnet

Slab group 1	
Slabs	1
Dist. factor	20%
Position	L0.0 A16.0 H37.8
Orientation	T > C-6.9
Phase enc. dir.	R >> L
Rotation	90.00 deg
Phase oversampling	0%
Slibe oversampling	23.10%
Slices per slab	104
FoV read	230 mm
FoV phase	75%
Slice thickness	1.50 mm
TR	28 ms
TE	20.00 ms
Averages	1
Concatenations	1
Filter	Prescan normalize
Matrix size	256 × 256
TA	4.44
PAT	2
Voxel size	1.0 mm × 0.9 mm × 1.5 mm
Flip angle	15 deg
Dimension	3D
Bandwidth	120 Hz/Px
Slice resolution	100%
Coil elements	HE1-4

Table 2 Susceptibility weighted imaging sequence parameters for 3 T Siemens Magnetom TrioTim syngo magnet

Slab group 1	
Slabs	1
Dist. factor	20%
Position	L0.0 A16.0 H37.8
Orientation	T > C-6.9
Phase enc. dir.	R >> L
Rotation	90.00 deg
Phase oversampling	0%
Slibe oversampling	23.10%
Slices per slab	104
FoV read	230 mm
FoV phase	75%
Slice thickness	1.50 mm
TR	28 ms
TE	20.00 ms
Averages	1
Concatenations	1
Filter	Prescan normalize
Matrix size	256 × 256
TA	4.44
PAT	2
Voxel size	1.0 mm × 0.9 mm × 1.5 mm
Flip angle	15 deg
Dimension	3D
Bandwidth	120 Hz/Px
Slice resolution	100%
Coil elements	HEA; HEP; NE1, 2

CLINICAL APPLICATIONS

Cerebral amyloid angiopathy

Cerebral amyloid angiopathy (CAA) is a small vessel disease characterized by amyloid β protein deposition within the cerebral arterioles leading to fibrinoid necrosis and vessel fragility. CAA causes microhemorrhages in and around the arteriole vessel wall extending into the parenchyma[9]. CAA is a major cause of primary lobar intracranial hemorrhage and cerebral microhemorrhages in the elderly[10]. CT and routine MRI techniques are usually not able to detect cerebral microbleeds; however, SWI with its unique sensitivity to susceptibility effects, clearly demonstrates lobar and microhemorrhages predominantly in the frontal and parietal cortical and subcortical regions (Figure 1). In contrast, microhemorrhages resulting from hypertensive or atherosclerotic microangiopathy have a predilection of deep gray matter or the infratentorial location (Figure 2). CAA is also manifested by white matter hyperintensities on MRI sequences which may be accompanied clinically by cognitive impairment[11]. Detection of two or more lobar hemorrhages of any duration, high signal intensity changes in the white matter and multiple cerebral microbleeds at the corticomedullary junction are highly suspicious for CAA (10) (Figure 1). Linn *et al*[12] have highlighted the presence of hemosiderosis on the pial surface of the brain, likely from the leakage of blood products from repetitive superficial hemorrhages in as much as 35% of CAA cases.

Hypertensive cerebral angiopathy

Hypertensive cerebral angiopathy may also be characterized by multiple silent cerebral microhemorrhages. Unlike CAA, cerebral microhemorrhages associated with chronic systemic hypertension are more commonly found in the thalamus, basal ganglia, cerebellum and pons[10] (Figure 2). These hypertensive cerebral microhemorrhages are a risk factor for development of a subsequent intracerebral macrohematomas/lobar hemorrhages[13]. The number of cerebral microhemorrhages corresponds also with blood pressure levels. Such micro-and macrohemorrhages are exquisitely well-demonstrated by SWI particularly with acute deoxyhemoglobin or chronic hemosiderin.

TRAUMATIC BRAIN INJURIES

Diffuse axonal injury (DAI) is a type of traumatic brain injury, in which torsional forces generated by rapid acceleration or deceleration of the head cause shearing of axons. Areas most vulnerable to shear injury include the cerebral gray-white matter junction, splenium of the corpus callosum, basal ganglia and dorsolateral brainstem[10]. The extent of the axonal injury has been shown to correlate with a poor prognosis, as do parenchymal hemorrhages[14]. Recent studies have shown that SWI is more sensitive than CT or GE sequences in terms of detecting suspected hemorrhagic DAI[15]. Most DAI patients have small punctate hemorrhages located in the deep subcortical white matter[16] (Figure 3). Tong *et al*[17,18] and Babikian *et al*[19] demonstrated that SWI is 3-6 times more sensitive than T2* GE sequences in terms of detecting the number, size, volume and distribution of hemorrhagic lesions seen in DAI cases.

Table 3 Susceptibility weighted imaging sequence parameters for 1.5 T Philips Achieva magnet

FoV read	230 mm
Slice thickness	5 mm
Gap	0
TR	35 ms
TE	50 ms
Matrix size	256 x 512
TA	5.15
Flip angle	15 deg
Coil elements	8 channel SENSE head coil

Table 4 Susceptibility weighted imaging sequence parameters for 3 T Philips Achieva magnet

FoV read	230 mm
Slice thickness	5 mm
Gap	0
TR	23 ms
TE	20 ms
Matrix size	218 × 127
TA	4.08
Flip angle	10 deg
Coil elements	8 channel SENSE head coil

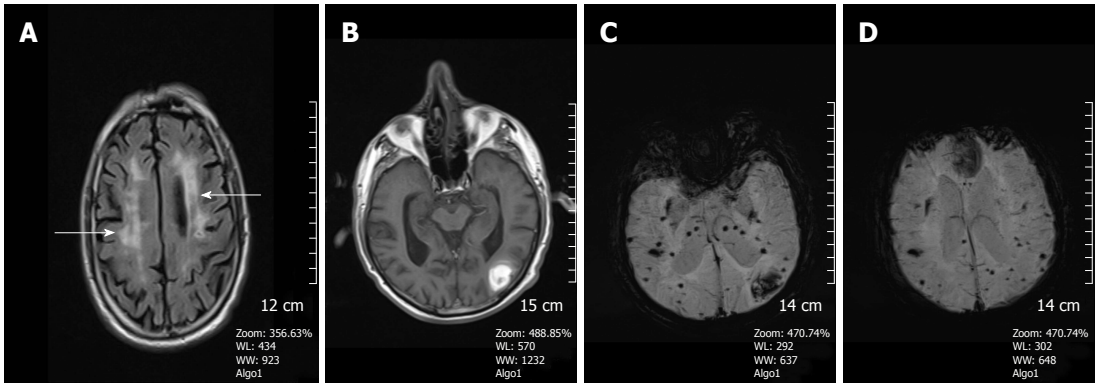

Figure 1 A 68-year-old man with cerebral amyloid angiopathy. A: Axial FLAIR image demonstrates periventricular confluent hyperintense regions; B: Axial T 1 weighted SE image shows high signal intensity subacute hemorrhage in the left occipital lobe; C and D: On SWI minIP images, hemorrhage is depicted as a hypointense signal intensity lesion and, in addition to the left occipital lobar hemorrhage, one can see multiple microhemorrhagic lesions in the cortical and subcortical white matter from cerebral amyloid angiopathy. SWI: Susceptibility weighted imaging; minIP: Minimum intensity projection algorithm; SE: Spin echo.

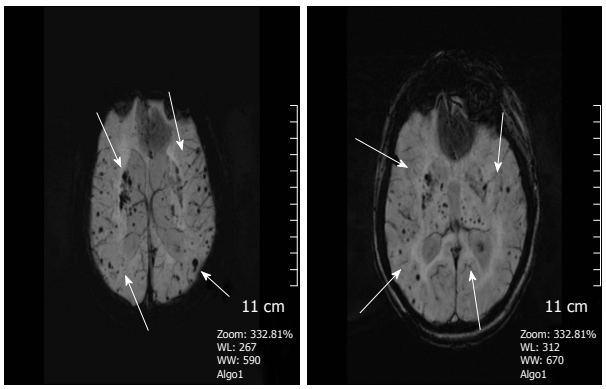

Figure 2 A 45-year-old woman with long standing chronic hypertension. SWI minIP images depicts numerous microhemorrhages in the deep basal ganglia, thalami, and subcortical white matter regions, typical of hypertensive microangiopathy. SWI: Susceptibility weighted imaging.

Because of this, the previously held concept of "non-hemorrhagic shearing injury" has largely been debunked. Those formerly "bland lesions" of DAI are now shown to have microbleeds on SWI. Brain stem involvement in DAI patients is also a very important predictor that determines the long-term outcome[20]. Mittal *et al*[16] demonstrated that SWI was more helpful in detecting traumatic lesions occuring in the brainstem than any other MRI sequence, and revealed intraventricular and subarachnoid hemorrhage, invisible on CT. Long term hemosiderosis from recurrent traumatic bleeds (which may occur in non-accidental trauma) is also best detected on SWI. Epidural and subdural hematomas can also be demonstrated well on SWI sequences as long as air-bone interfaces do not lead to masking artifacts.

CNS VASCULAR MALFORMATIONS

True arteriovascular malformations (AVMs) usually are present at birth and can become large with time. These AVMs are characterized by their high-flow and therefore can usually be detected by conventional MRI/MR angiography techniques. In contrast, low-flow vascular malformations including cerebral cavernous malformations (CCMs), developmental venous anomalies (DVAs) and CaTe (capillary telengiectasias) may be inapparent on fast spin echo (FSE) MRI/MR angiography techniques because they mainly contain slow-flow small vessels. Although T2* weighted GE imaging is capable of detecting small venous structures and hemosiderin deposition in cavernomas and CaTes, the incorporation of the magnitude and phase information in SWI provides improved sensitivity for identifying low-flow vascular malformations that are undetectable on GE sequences[21,22]. Lee *et al*[21] showed that SWI is the ideal imaging sequence for screening patients who have a high clinical suspicion of low-flow vascular malformations. These lesions may be responsible for cryptogenic

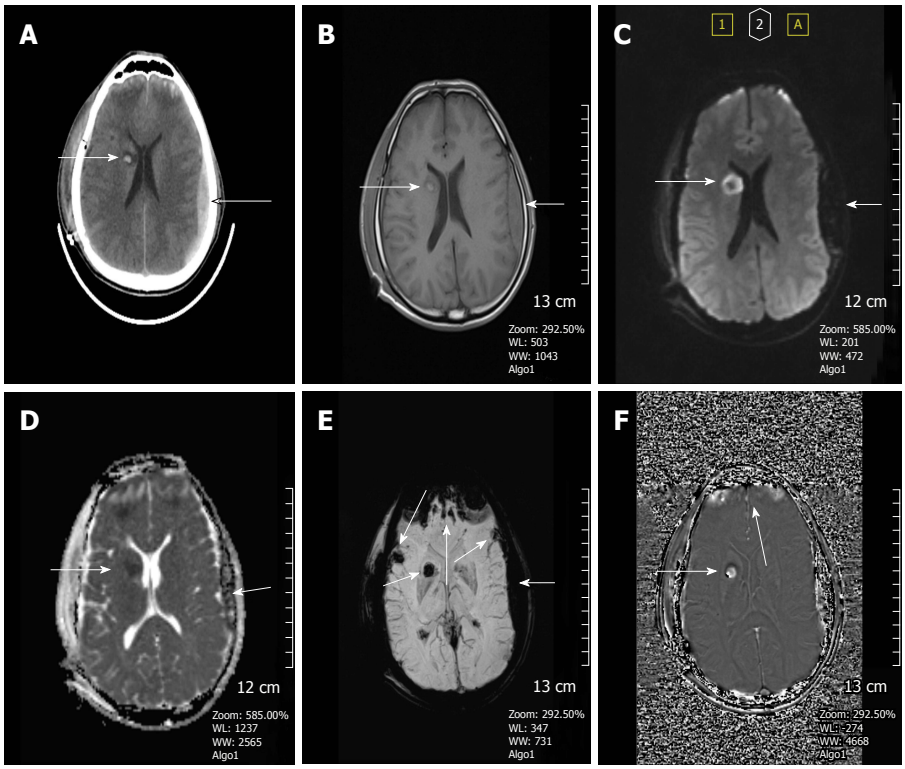

Figure 3 A 37-year-old man who had an accident was in coma after traumatic brain injury. A: On the non-contrast CT image, bilateral frontal subcortical and right basal ganglia hyperdense hemorrhagic foci with surrounding hypodense edema are seen consistent with diffuse axonal injury. Also left parieto-temporal subdural hemorrhage is present. Post-op changes are present on the right with a tiny frontal subdural hematoma; B: SE T1W image, can only reveal hyperintense right basal ganglia hemorrhagic lesion with surrounding hypointense edema and left subdural hemorrhage, but can not demonstrate the other parenchymal lesions; C: Diffusion weighted image (DWI) reveals hyperintense caudate lesions; D: Apparent diffusion coefficients (ADC) map demonstrates restricted diffusion within the lesions; E: SWI minIP image, clearly depicts multiple frontal cortical and subcortical and also right basal ganglion microhemorrhages better than those of CT and T1W MR image. The bilateral subdural hematomas are nearly as dark as the cortical bone; F: Phase contrast SWI image, hemorrhagic lesions show a bright/positive shift effect on phase image, due to paramagnetic susceptibility effect. SWI: Susceptibility weighted imaging; minIP: Minimum intensity projection algorithm; SE: Spin echo.

epilepsy, recurrent subarachnoid hemorrhage and/or hemosiderosis, and hemorrhagic injury to cranial nerves. Because the incidence of hemorrhage from occult cerebrovascular malformations is contingent on whether they have ever bled, using SWI to detect previous bleeding helps prognosticate on future risk[23].

CCMs are composed of abnormally enlarged capillary cavities surrounded by a single layer of endothelium without intervening with brain parenchyma and comprise 10%-20% of all cerebrovascular malformations[24]. The MRI findings of CCMs are variable, depending on the presence of calcification and hemorrhage within the lesions, but they typically show a mixed signal intensity, usually recognized as "popcorn-like" with a central reticulated core surrounded by a peripheral rim of hemosiderin[15] (Figure 4). Since recurrent microhemorhages occur in the CCM lesions, they may contain deoxyhemoglobin acutely or hemosiderin chronicly, both dark on SWI[25,26] (Figure 5). Symptomatic, growing and recurrently hemorrhagic CCMs are considered for surgical resection.

DVAs are the most common type of cerebral vascular malformations (⩽ 60%) and are often discovered incidentally during routine MRI examinations[27]. A DVA consists of radially arranged venous structures converging to a centrally located venous trunk, which drains normal brain parenchyma[28]. They are mainly asymptomatic lesions, do not often bleed, and neurosurgical intervention is largely contraindicated due to the risk of venous infarction[29]. However, they have a high association with other vascular malformations, especially CCMs. SWI better shows the collector (head of Medusa) and deep medullary veins (snake hair of Medusa) than T1W contrast enhanced images by virtue of the low intensity of the dark veins on miniIP images (Figure 6).

CaTes are asymptomatic small vascular malformations typically ranging from several milimeters to 2 cm in size, primarly found in the pons. They may occur sporadically or may be seen with syndromes like hereditary hemorrhagic telangiectasia or after radiation therapy[30]. They are characterized by faint contrast enhancement on T1W images and therefore can be easily missed. On SWI, they can be readily identified as hypointense lesions, from deoxyhemoglobin or hemosiderin deposited in this low-flow vascular malformation (Figure 7).

Sturge-Weber syndrome (SWS) is a neurocutaneous disorder, typically seen in children and characterized by a cutaneous angioma, glaucoma and leptomeningial venous angiomatosis[31]. The imaging findings consist of unilateral cerebral atrophy, cortical "tram-track" calcifications, impaired cortical venous outflow and abnormal deep

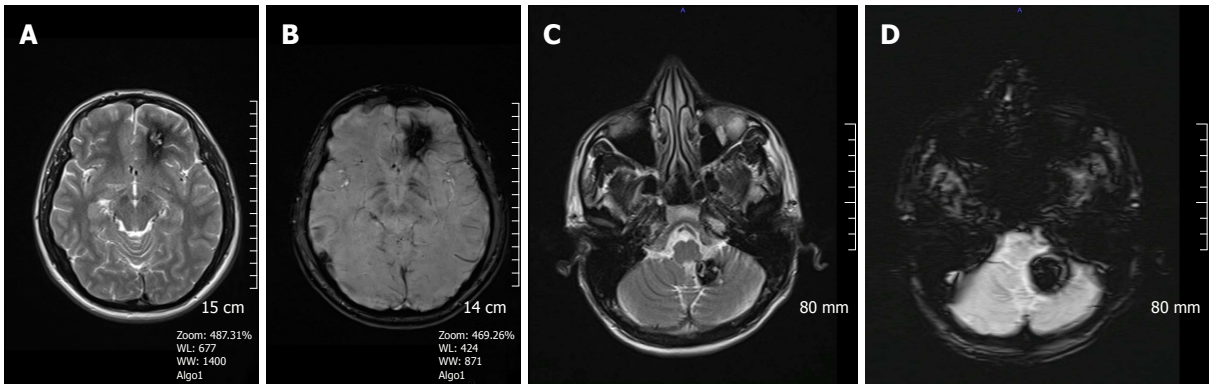

Figure 4 A 21-year-old man with left frontal cavernous malformation. A: On the axial FSE T2W image, a left frontal cavernous malformation is seen with typical pop-corn appearance, surrounded by a thick hemosiderin rim; B: SWI shows prominent blooming artĺfact due to paramagnetic effect. Another patient is a 39-year-old man with left cerebellar tonsil cavernous malformation; C: Axial FSE T2W image, clearly depicts the cavernous malformation consisting of a high signal intensity core and a peripheric low signal intensity hemosiderin; D: On SWI, the lesion is more conspicuous. Note how the brighter central areas on the T2WI are obscured by the susceptibility artifact. SWI: Susceptibility weighted imaging; FSE: Fast spin echo.

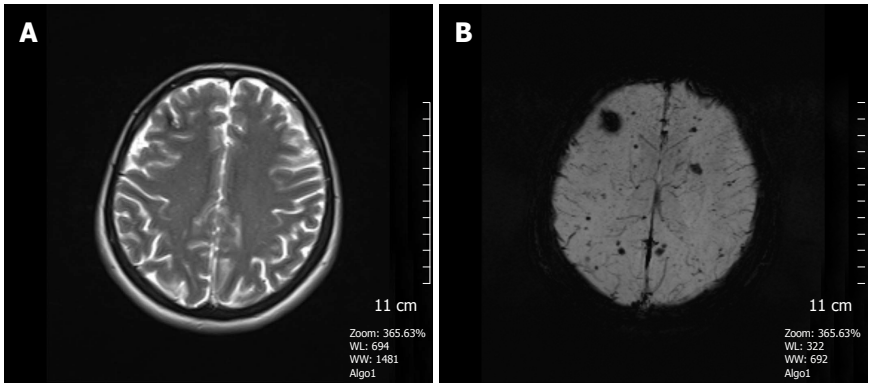

Figure 5 A 41-year-old woman who had a history of familial cavernous malformation underwent magnetic resonance imaging screening. A: Axial FSE T2W image, a right frontal subcortical small cavernous malformation is seen on this image; B: SWI minIP image, numerous tiny cavernous malformations throughout the brain parenchyma is detected. FSE T2W image is unable to show these lesions. The patient was considered to have familial cerebral cavernous malformation. SWI: Susceptibility weighted imaging; FSE: Fast spin echo.

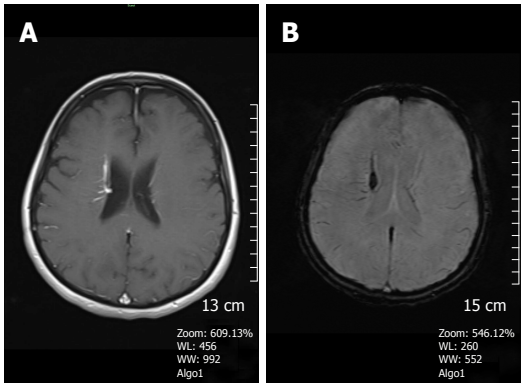

Figure 6 A 62-year-old woman complaining of long-term headache attacks. A: Axial post-contrast T1W image shows contrast- enhanced dilated medullary veins which seem to converge into a dilated transcortical collector vein in the right periventricular region consistent with developmental venous anomaly; B: Axial SWI minIP image, has an excellent agreement with former image, revealing classical caput medusa appearance. SWI: Susceptibility weighted imaging; minIP: Minimum intensity projection algorithm.

venous collaterals. SWI has been found to be superior to post gadolinium-enhanced T1WI in characterizing calcification, abnormal periventricular and transmedullary veins, cortical gyriform hypointensities and gray-white matter abnormalities (Figure 8)[22], but enhanced T1W images depict the leptomeningial angiomatosis and enlarged choroid plexus more clearly.

Cerebral venous sinus thrombosis and venous infarction

Patients with cerebral venous sinus thrombosis (CVST) may present with headaches or non-specific signs due to increased intracranial pressure (ICP). Remaining undiagnosed, it can become deadly if it progresses to malignant increased ICP[32]. An acute CVST shows deoxyhemoglobin in the involved veins, seen as prominent hypointense signal intensity areas with "blooming" artifact on SWI (Figure 9). SWI may demonstrate engorgement of the venous system as an early sign of CVST and can also show the associated parenchymal hemorrhage which occurs in 73% of venous infarctions[33].

ARTERIAL STROKE

Acute cerebral infarct with or without hemorrhage occurs due to thromboembolism or atherosclerotic stenosis of a vessel. Vascular occlusion causes a susceptibility change

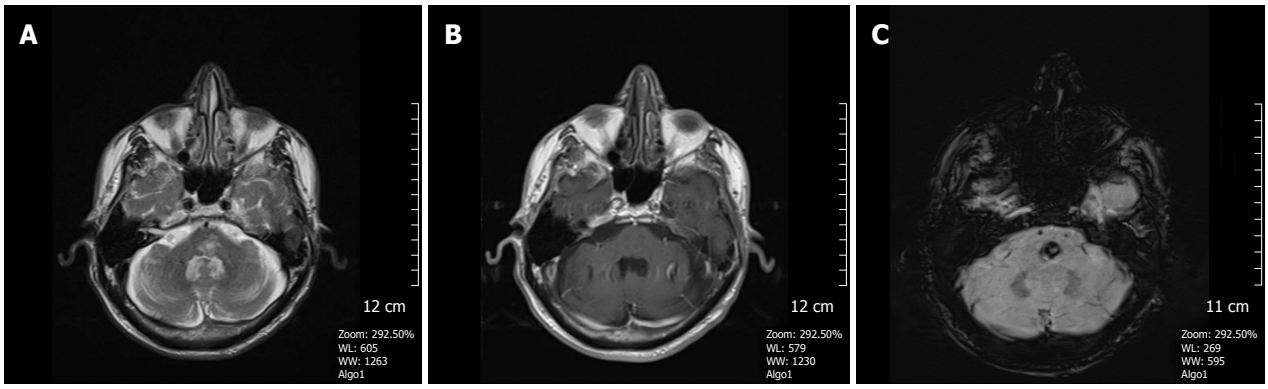

Figure 7 A 65-year-old man with incidentally discovered capillary telangiectasia in the pons. A: Axial FSE T2W image shows a hyperintense lesion located in the central pons; B: Axial contrast-enhanced T1W image reveals very little contrast enhancement in the lesion; C: SWI image demonstrates a markedly hypointense lesion in the pons indicating a capillary telangiectasia based on its location and size. SWI: Susceptibility weighted imaging; FSE: Fast spin echo.

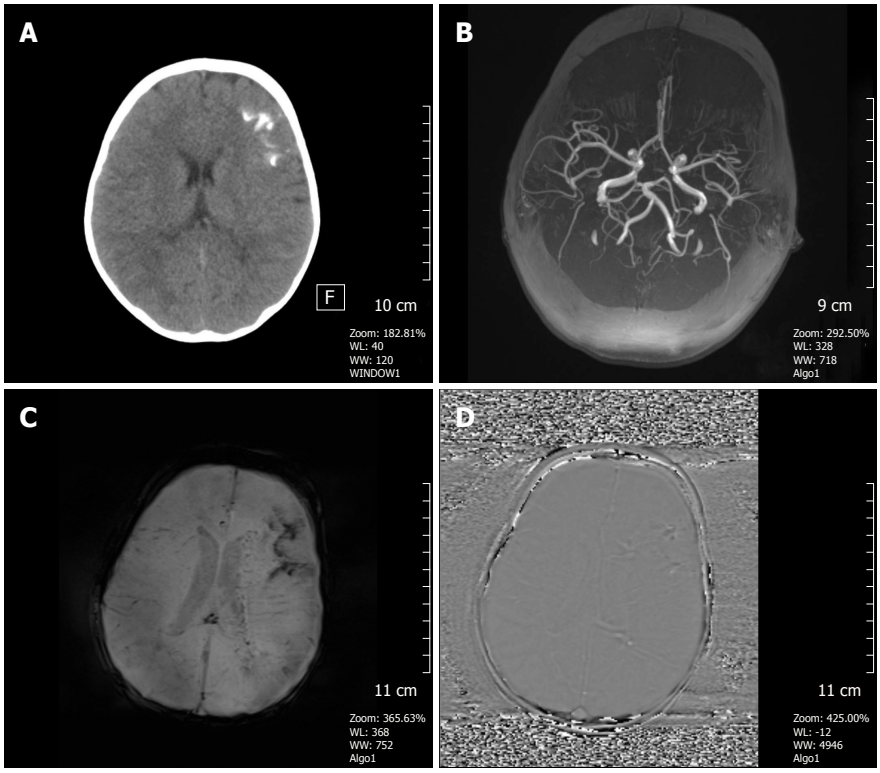

Figure 8 A 3-year-old girl with Sturge-Weber syndrome. A: Non-contrast CT image shows hyperdense tram-track calcifications along the left frontal gyri; B: Axial MIP TOF MRA shows a normal cranial angiogram; C: Axial SWI minIP image, hypointense gyral calcification is clearly depicted, also deep abnormal transmedullary veins are visible; D: SWI phase image confirms these calcifications as low signal intensitiy areas. SWI: Susceptibility weighted imaging; minIP: Minimum intensity projection algorithm.

by decreasing the arterial flow, and increases pooling of deoxygenated blood, thus leading to a high concentration of deoxyhemoglobin[34]. In the setting of acute stroke, such conversion to deoxhyhemoglobin can occur as early as 2 h after the onset of symptoms.

In the setting of stroke, SWI assists in identifying: (1) Hemorrhages within the infarct region, thus enabling the differentiation of a hemorrhagic from a bland ischemic stroke. Many studies have also proven that SWI is more sensitive in revealing hemorrhage within the acute infarct regions than CT and 2D GE T2* weighted sequences[35,36]. SWI can also detect acute subarachnoid hemorrhage and is very sensitive to subacute and chronic subarachnoid hemorrhages, sometimes missed by CT and FLAIR[3] (Figure 10); (2) Prominent hypointense draining veins within areas of impaired perfusion (Figure 11). The visualization of these prominent veins allows for the identification of diffusion-perfusion mismatch representing penumbral brain tissue in a different fashion than current perfusion weighted imaging techniques[16]. The oxygen extraction fraction (OEF) which reflects the ratio of deoxyhemoglobin to

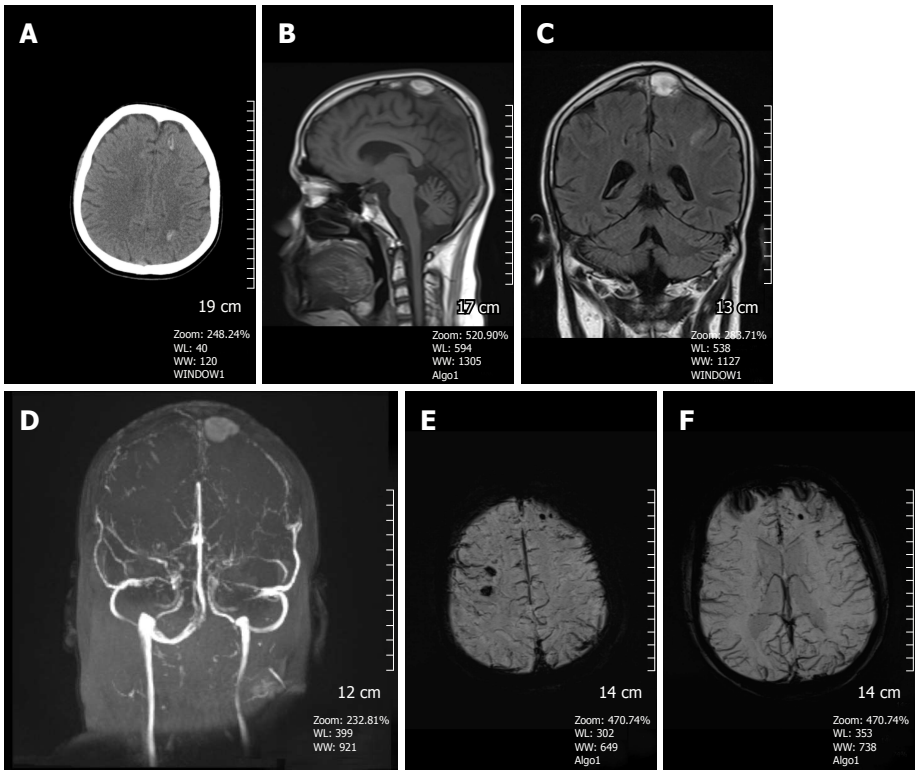

Figure 9 A 16-year-old man presented with superior sagittal sinus thrombosis. A: Non-contrast CT image shows hyperdense hemorrhagic foci in the left frontal and left parietal lobe at the convexity level (arrows); B: On the sagittal T1W image, a hyperintense thrombus is detected in the superior sagittal sinus; C: Coronal FSE T2W image, thrombus again shows hyperintense signal intensity; D: Time of flight non-contrast MR venography, absence of normal venous flow and accompanying thrombus are clearly depicted; E and F: SWI minIP images demonstrates hypointense microhemorrhages in the brain parenchyma with diffuse dilated venous structures indicating venous engorgement due to venous hypertension. SWI: Susceptibility weighted imaging; minIP: Minimum intensity projection algorithm.

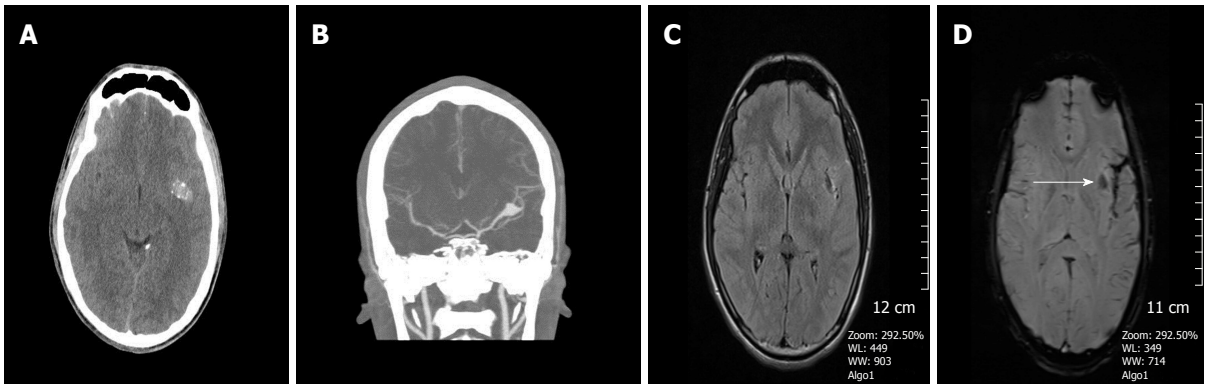

Figure 10 An 18-year-old man presenting with drastic headache and dizziness. A: Non-contrast CT image reveals a partially calcified hyperdense lesion suspicious for left MCA aneurysm versus cavernoma; B: CT angiography demonstrates a left MCA M 1 distal segment aneurysm; C: FLAIR image, left sylvian fissure seems unremarkable with no hemorrhage seen; D: SWI magnitude image shows hypointense acute subarachnoid hemorrhage along the left sylvian fissure. Subinsular low intensity is at edge of aneurysm (arrow). SWI: Susceptibility weighted imaging.

oxyhemoglobin in the capillaries and veins, is significantly increased in the penumbra following occlusion of the artery. This high OEF in cortical veins is presumably responsible for the increased conspicuity in the infarct region[30,36]; (3) Acute intra-arterial thrombus: The susceptibility vessel sign (SVS) is defined as the presence of hypointensity from scute deoxyhemoglobin thrombus within the intracranial arteries in which the diameter of the hypointense vessel exceeds the contralateral vessel diameter[37,38] (Figures 12 and 13). Lingegowda *et al*[39] found an 82% sensitivity and 100% specificity for the SVS in the determination of all acute major intracranial occlusions. They also showed that SVS is more sensitive and specific than the hyperdense artery sign on CT[40,41] and the hyperintense vessel sign on FLAIR images for intracranial artery occlusions. Huang *et al*[42] found that patients with negative prominent veins and positive susceptibility vessel sign exhibited poor outcomes; and (4) Hemorrhagic transformation of acute ischemic infarction: Approximately 20%-40% of patients bleed

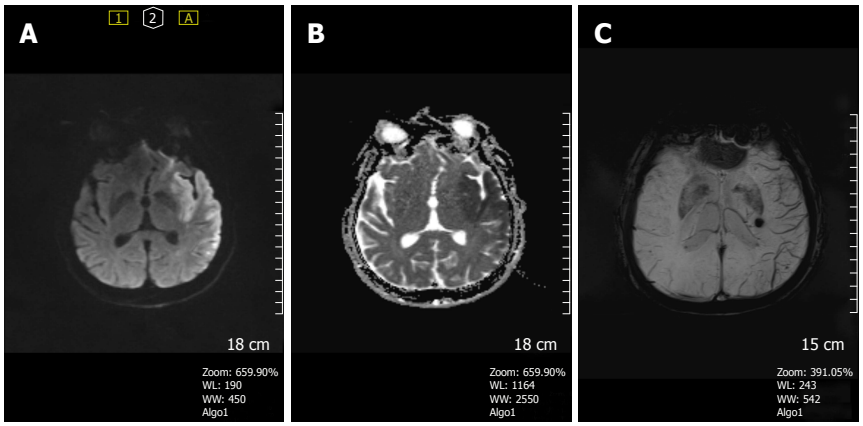

Figure 11 A 38-year-old man complaining of right side weakness. A: DWI shows hyperintense lesion in the left temporo-insular region; B: ADC map reveals restricted diffusion in the corresponding area indicating a left MCA acute infarct; C: SWI minIP image, prominent cortical veins are seen within the left MCA territory reflecting relatively increased deoxyhemoglobin concentration in the ischemic region. Incidental cavernoma in left thalamus is seen. SWI: Susceptibility weighted imaging; minIP: Minimum intensity projection algorithm; DWI: Diffusion weighted image; ADC: Apparent diffusion coefficients.

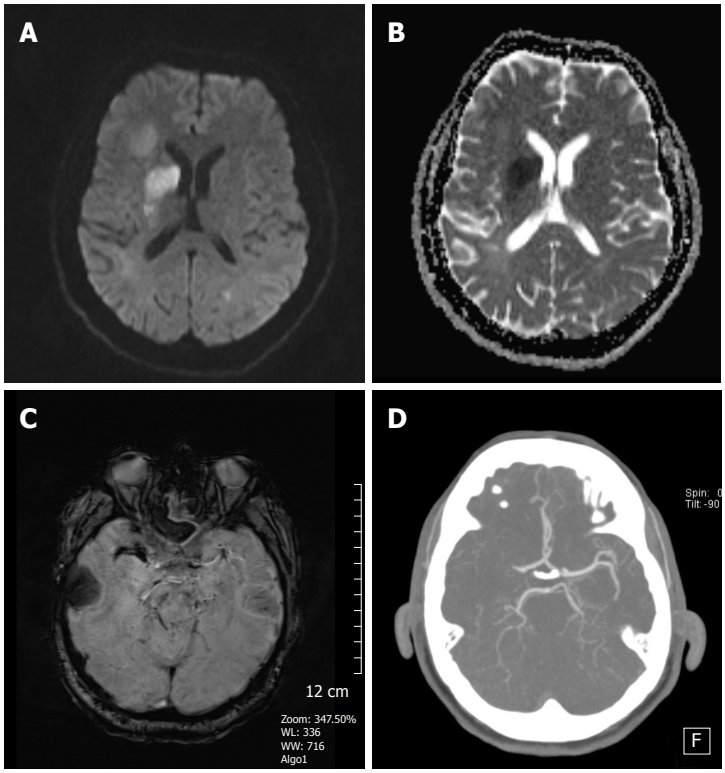

Figure 12 A 68-year-old woman with right lenticulostriate acute infarct. A: DWI reveals high signal intensity lesion in the right caudate nucleus head and lentiform nucleus region; B: ADC map shows restricted diffusion consistent with an acute infarct; C: Non-contrast CT image, hyperdense artery sign is seen along the right MCA artery; D: SWI magnitude image shows susceptibility vessel sign in the same region corresponding to the CT image indicating an acute thrombus. SWI: Susceptibility weighted imaging; DWI: Diffusion weighted image; ADC: Apparent diffusion coefficients; MCA: Middle cerebral artery.

within the first week after a stroke[43] (Figure 14). Old microhemorrhages in a stroke patient may presage the vulnerability of the vascular system[44]. In patients with a small number of microhemorrhages (< 5), thrombolytic therapy can be applied safely, whereas patients with large numbers of microhemorrhages (> 5) have a great risk for potential hemorrhagic transformation from thrombolytic therapy[45-49]. Huang *et al*[42] showed that microhemorrhages were significantly associated with later hemorrhagic transformation. SWI is able to detect microhemorrhages within the infarct region more accurately than T2* weighted GE sequences.

NEURODEGENERATIVE DISEASES

It is widely accepted that iron deposition in the brain increases with normal aging, particularly in the basal ganglia region primarily in the form of ferritin and ferrocalcinosis (Figure 15). Increased iron levels in the CNS are encountered in a variety of neurodegenerative

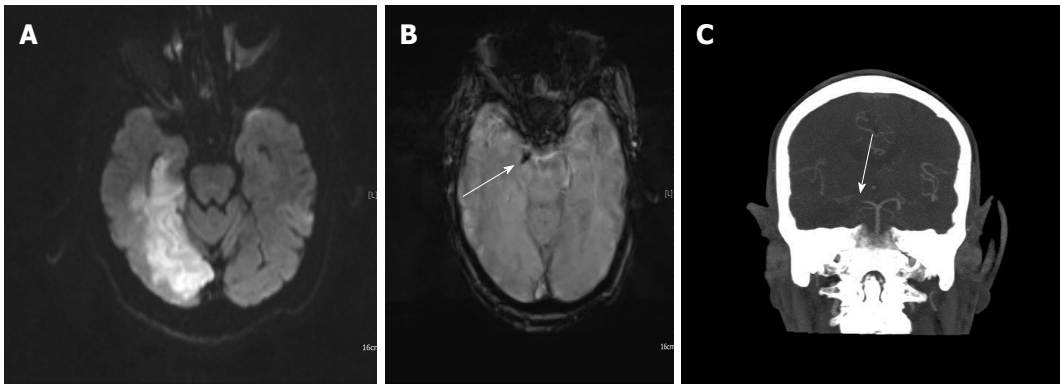

Figure 13 An 87-year-old woman with right posterior cerebral artery infarct. A: DWI shows right temporo-occipital PCA territory infarct; B: SWI magnitude image shows right PCA P1 segment susceptibility sign; C: Coronal CT MIP angiography image confirms right proximal PCA occlusion. SWI: Susceptibility weighted imaging; PCA: Posterior cerebral artery; DWI: Diffusion weighted image.

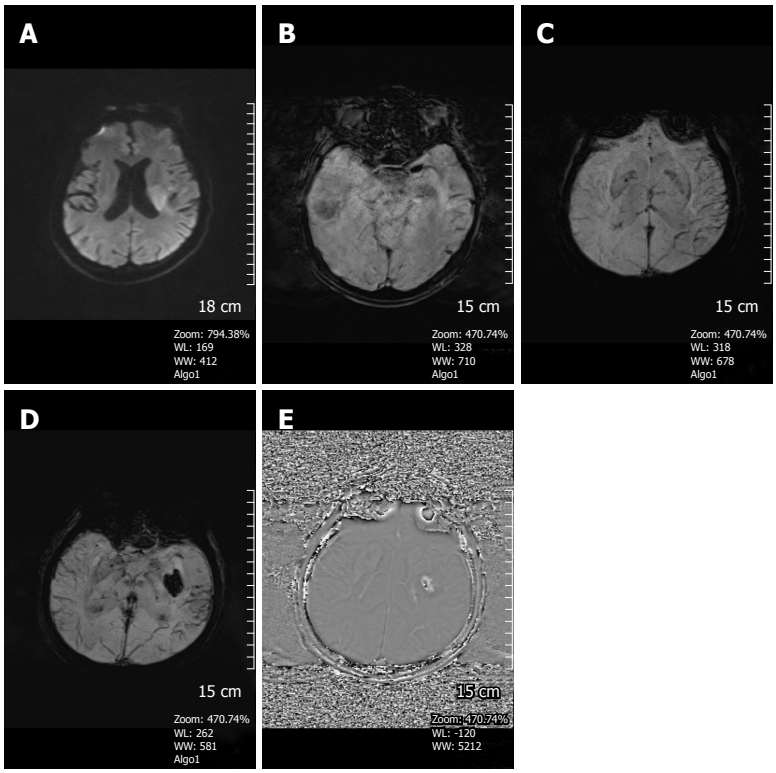

Figure 14 A 50-year-old man patient with acute left middle cerebral artery infarct. A: DWI, showing a left periventricular hyperintense lesion; B: SWI magnitude image detects left MCA susceptibility vessel sign; C: SWI minIP image reveals prominent hypointense veins in the infarct region; D: Three days later, new SWI minIP image shows hemorrhage in the infarct area indicating development of hemorrhagic transformation. There continues to be perminent venous visualization in the left temporal lobe; E: SWI phase image confirms the hemorrhage leading to a positive shift effect. SWI: Susceptibility weighted imaging; PCA: Posterior cerebral artery; DWI: Diffusion weighted image; minIP: Minimum intensity projection algorithm; MCA: Middle cerebral artery.

diseases, superimposed on the normal senescent iron increase[50,51] in the globus pallidum, substantia nigra, red nucleus, subthalamic nucleus and dentate nucleus. Increased iron deposition is found in Parkinson's disease, Huntington's disease, Alzheimer's disease, Multiple sclerosis (MS), Amyotrophic lateral sclerosis, Hallervorden-Spatz syndrome, Wilson's Disease (copper) and Pantothenate kinase-associated neurodegeneration (PKAN)[52] (Table 5). In neurodegenerative diseases, the ability to measure the amount of ferritin in the brain may help predict prognosis, disease progression and treatment outcomes.

SWI shows differences in stable and progressive MCI[57]. Fourteen percent of controls, 33% of patients with stable MCI and 54% of those with progressive MCI had microhemorrhages. Furthermore, the iron content in the right pallidum and right substantia nigra was greater in progressive MCI than stable MCI.

Barnaure *et al*[58] studied 328 cognitively normal control subjects and 71 patients with MCI using SWI on a 3T magnet to investigate the presence and distribution of cerebral microbleeds. They found no difference be-

Table 5 Increased iron levels in the central nervous system

Entity	Increased iron location	Ref.
Parkinson's disease	SN, pars compacta, brainstem	[53]
Alzheimer's disease	Hippocampus, GP	[54]
PKAN	GP, SN sparing DN	[55]
Infantile neuroaxonal dystrophy	GP, SN, DN	[55]
Neuroferritinopathy	GP, P, DN with cavitation	[55]
Aceruloplasminemia	BG, thalami with no cavitation	[55]
Huntington's disease	CN, P	[56]
Progressive MCI versus stable MCI	Right GP, SN	[57]
Multiple sclerosis	CN, P and thalamic pulvinar	[60]

CN: Caudate nucleus; GP: Globus Pallidus; P: Putamen; BG: Basal Ganglia; SN: Substantia Nigra; DN: Dentate nucleus; PKAN: Pantothenate kinase-associated neurodegeneration.

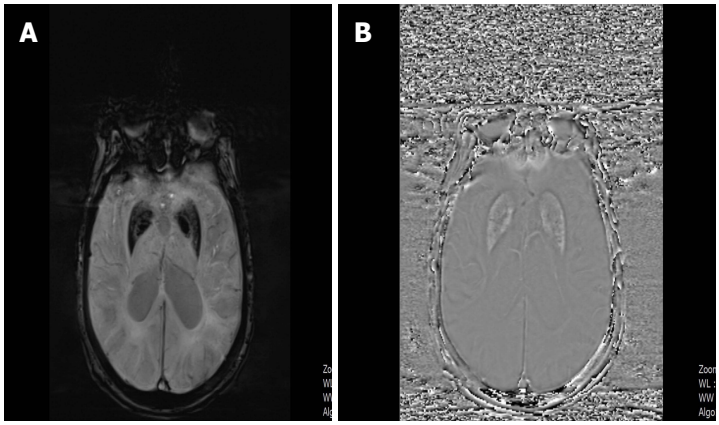

Figure 15 A 79-year-old woman with Alzhemier's disease. A: SWI minIP image shows hypointense signal intensity in the globus pallidus and putamen indicating increased iron deposition; B: SWI phase image reveals hyperintense signal in the basal ganglia due to the positive shift effect of paramagnetic iron. SWI: Susceptibility weighted imaging; minIP: Minimum intensity projection algorithm.

tween the two groups in terms of cerebral microbleed prevalence, distribution and severity. The patients' cognitive decline over an 18 mo period did not correlate with microbleeds. They concluded that microbleeds do not predict cognitive decline in advanced age.

MS affects both brain and spinal cord and is typically imaged with FLAIR and contrast-enhanced T1W images. The sensitivity of MRI in depicting MS lesions in the brain is demonstrated to be high, but its specificity remains low. SWI helps by revealing the perivenular distribution of the demyelinating lesions by showing the MS plaque surrounding the small veins[59]. This has been used to distinguish MS from SAPHO (synovitis, acne, pustulosis, hyperostosis and osteitis) syndrome white matter lesions.

Rudko *et al*[61] have shown that the levels of iron deposition in patients with MS correlates better with disability than MS plaque volume. They have also shown increased iron content in patients with clinically isolated syndrome (CIS).

BRAIN TUMORS

SWI can help in the grading of cerebral tumors because it provides identification of both hemorrhagic and calcified foci inside the tumors and also allows assessment of the detailed internal angioarchitecture of the tumors. High grade tumors like glioblastomas usually contain a hemorrhagic component (Figure 16)[3,62-64].

Sehgal *et al*[65] demonstrated that in the majority of cases, SWI was equivalent to T1W contrast-enhanced images in the grading of gliomas. The criteria used for this comparison were tumor visibility, boundaries, edema, vessels, blood products, internal architecture and image quality. Mittal *et al*[16] have showed that high rCBV values on PWI and high choline-creatine ratios on MR spectroscopy found in tumors exhibit a good correlation with evidence of blood products demonstrated within the tumor using SWI.

In assessing brain tumors, calcification is considered as a very important indicator. Calcification is diamagnetic, whereas hemorrhage is paramagnetic, therefore resulting in opposite signal intensities on SWI phase images[66]. For the determination of calcification in brain tumors such as oligodendrogliomas, Zulfigar *et al*[67] found that adding SWI sequences led to a statistically significant improvement in the sensitivity for the detection of intratumoral calcification by 53% (from 33% to 86%) but no change in specificity.

SWI can also be used to distinguish vestibular schwannomas from cerebellopontine angle meningiomas.

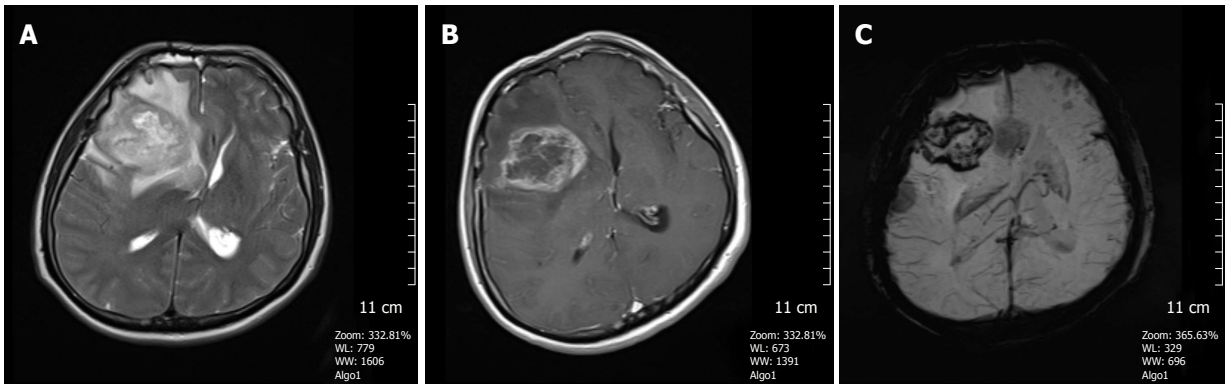

Figure 16 A 48-year-old man with a history of glioblastoma multiforme. A: FSE T2W image, a heterogenous high signal intensity right frontal lobe mass and surrounding hyperintense infiltrative edema is seen. Tumor is compressing the right lateral ventricule and leading to right to left shift; B: Axial SE T1W contrast- enhanced image, tumor shows heterogenous contrast enhancement; C: SWI minIP image reveals microhemorrhages in the periphery of the tumor indicating a high grade neoplasm. SWI: Susceptibility weighted imaging; minIP: Minimum intensity projection algorithm; FSE: Fast spin echo.

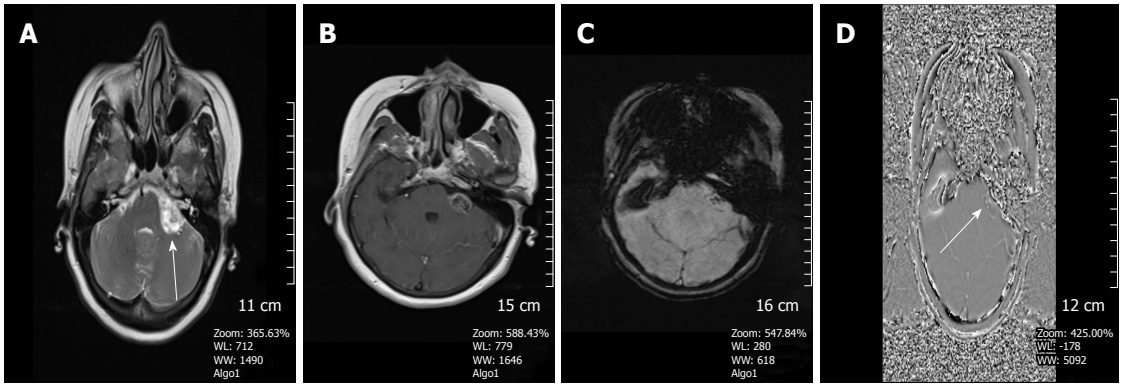

Figure 17 A 55-year-old woman complaining of left-sided tinnitus. A: Axial FSE T2W image, a heterogenous high signal intensity mass in the left cerebellopontine angle cistern is present; B: On the axial SE T1W contrast- enhanced image, heterogenous contrast enhancement is seen; C: SWI magnitude image reveals punctate hypointense foci within the mass indicating a probable acoustic schwannoma; D: SWI phase image confirms bright microhemorrhages causing a paramagnetic effect. SWI: Susceptibility weighted imaging; FSE: Fast spin echo.

Microhemorrhages occur with schwannomas, not found in the meningiomas[68] (Figure 17).

The dual rim sign (hyperintense inner, hypiointense outer) from the respiratorty burst of bacteria converting hemoglobin to methemoglobin has been shown to differentiate abscesses (present) from glioblastoma (absent) in the face of a ring enhancing mass[69].

QSM

QSM is a recently developed sophisticated postprocessing technique and numerically solves the inverse source-effect problem to quantify local tissue magnetic susceptibility from the major magnetic field distribution, reflected in the phase images of SWI[70]. The mapping of iron can play a crucial role in the setting of many important neurologic disorders. In early Parkinson's disease (PD), iron elevation in the specific brain regions including the substantia nigra is a pathognomonic feature of the disease and this can be measured by QSM[71]. He *et al*[72] evaluated 44 early PD patients; susceptibility values within the substantia nigra and red nucleus contralateral to the most affected limb were elevated compared to a healthy control group. Bilateral substantia nigra magnetic susceptibility showed a positive correlation with disease duration[72].

Acosta-Cabronero *et al*[73] examined 66 patients with idiopathic PD and found increased R2* and susceptibility values in the substantia nigra, red nucleus, thalamus and globus pallidus. QSM additionally correlated with disease severity in these patients.

Moon *et al*[74] investigated the presence and pattern of brain iron accumulation in vascular dementia (VaD) and Alzheimer's disease (AD) patients by means of QSM. Both in VaD and AD patients significantly higher susceptibility values were found in the caudate nucleus and putamen compared to control subjects. Age and cognitive disease severity of both patient groups were not correlated with increased iron accumulation in their basal ganglia (Figure 18).

Dominguez *et al*[75] measured iron accumulation in the basal ganglia in both premanifest and symptomatic Huntington's disease (HD) patients with QSM. Both groups of patients demonstrated substantially elevated iron content in the caudate nucleus, globus pallidus and putamen compared to normal control subjects. In-

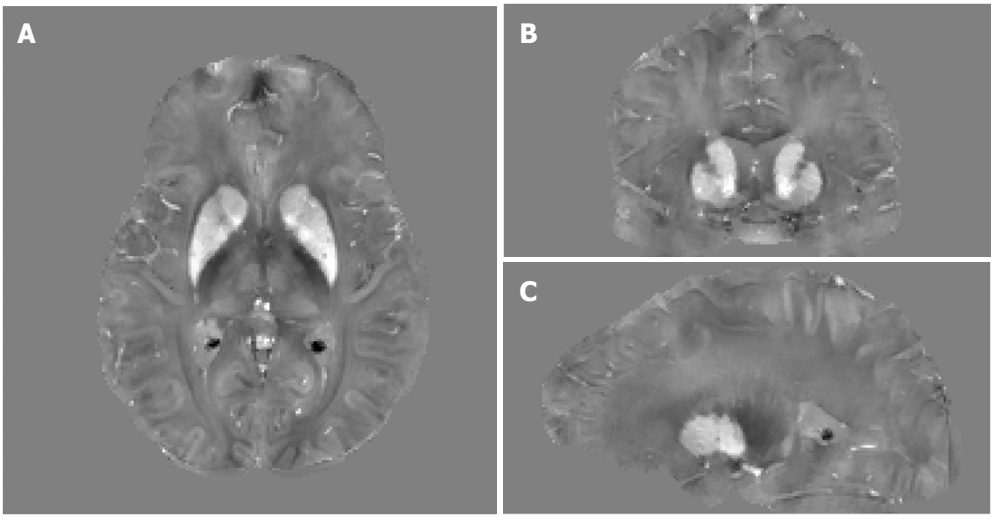

Figure 18 Example orthogonal views of quantitative susceptibility mapping images of a 41-year-old female premanifest HD patient showing the basal ganglia where increased tissue magnetic susceptibility can be observed in iron-rich gray matter structures such as the caudate nuclei and putamen. Extra iron overload in the striatum in these patients as compared to age-matched controls is believed to be associated with HD pathophysiology. Gray scale is in [-0.2, 0.2] ppm.

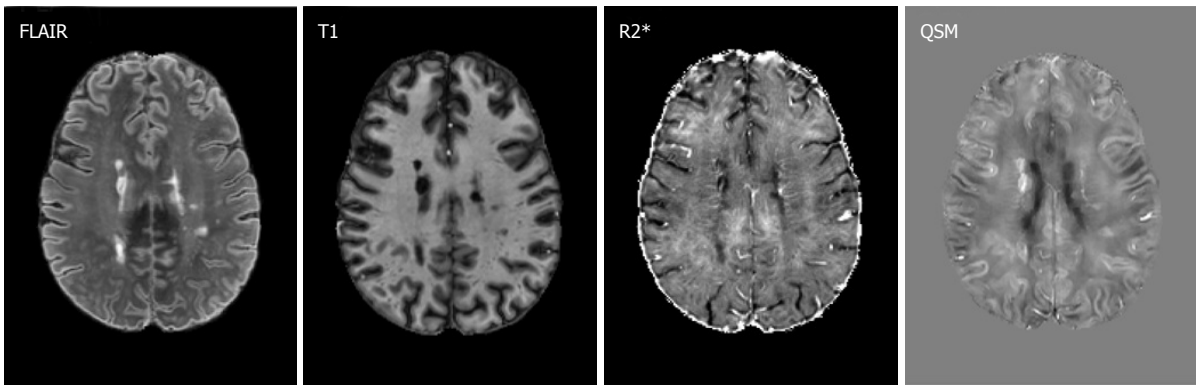

Figure 19 Example quantitative susceptibility mapping image of a 55-year-old female relapsing-remitting MS patient, shows hyperintense susceptibility MS lesions, and the corresponding FLAIR, T1 and R2* images. Multiple contrast analysis using R2* and QSM may be helpful identifying different pathological changes in MS lesions. Gray scale is [-0.12, 0.12] ppm in QSM image and [0, 80] Hz in R2* image. MS data was acquired using similar 7T protocol as the HD study. QSM: Quantitative susceptibility mapping.

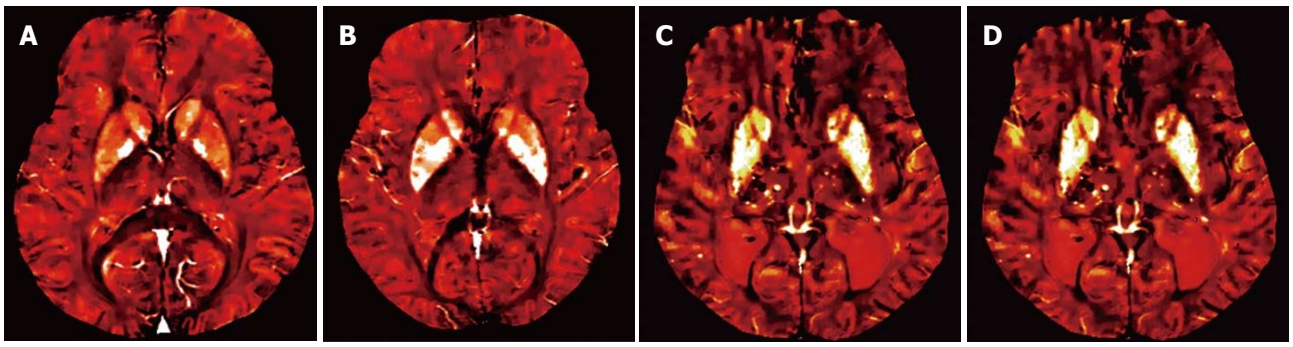

Figure 20 Increased iron accumulation of caudate and putamen is noted in patients with Alzheimer's disease and vascular dementia as compared with normal subjects.

creased iron levels showed significant correlation with disease severity (Figure 19). QSM is also capable of quantifying elevated iron levels in the motor cortex of amyotrophic lateral sclerosis patients. Furthermore, in Wilson's disease, iron accumulation and quantification can be demonstrated by QSM[71]. Iron chelation therapy in PD can be monitored by QSM[71]. Walsh *et al*[76] have shown that the deficits of patients with MS more strongly correlate with QSM values of brain iron content than the MS plaque volume (Figure 20).

CONCLUSION

SWI is a very useful imaging tool with a variety of ap-

plications in neuroradiology practice and should be included in routine protocols. As demonstrated, it is very helpful in detecting micro-and macro-hemorhages and delineating cerebral microvasculature and low-flow vascular malformations. It is regarded as a complementary, valuable imaging sequence in the management of stroke patients. It facilitates differentiation of calcium from hemorrhage in the brain. It is helpful in the evaluation of traumatic brain injury patients and aids in the characterization and grading of cerebral tumors. QSM can shed light on many neurodegenerative disorders in a more rigorous statistical way by assessing brain iron content. Further investigations are needed for expanding the roles of SWI and QSM in neuroradiology clinical and research arenas.

ACKNOWLEDGMENTS

Our thanks to Xu Li, PhD, from Johns Hopkins Medical Institution, Radiology and Radiological Sciences, Baltimore, Maryland, United States, for his support in providing the QSM part figures (18 and 19) of our article. We are also grateful to the Korean Journal of Radiology for their permission of Figure 20.

REFERENCES

1 **Reichenbach JR**, Venkatesan R, Schillinger DJ, Kido DK, Haacke EM. Small vessels in the human brain: MR venography with deoxyhemoglobin as an intrinsic contrast agent. *Radiology* 1997; **204**: 272-277 [PMID: 9205259 DOI: 10.1148/radiology.204.1.9205259]
2 **Reichenbach JR**, Haacke EM. High-resolution BOLD venographic imaging: a window into brain function. *NMR Biomed* 2001; **14**: 453-467 [PMID: 11746938 DOI: 10.1002/nbm.722]
3 **Thomas B**, Somasundaram S, Thamburaj K, Kesavadas C, Gupta AK, Bodhey NK, Kapilamoorthy TR. Clinical applications of susceptibility weighted MR imaging of the brain - a pictorial review. *Neuroradiology* 2008; **50**: 105-116 [PMID: 17929005 DOI: 10.1007/s00234-007-0316-z]
4 **Gasparotti R**, Pinelli L, Liserre R. New MR sequences in daily practice: susceptibility weighted imaging. A pictorial essay. *Insights Imaging* 2011; **2**: 335-347 [PMID: 22347957 DOI: 10.1007/s13244-011-0086-3]
5 **Haacke EM**, Xu Y, Cheng YC, Reichenbach JR. Susceptibility weighted imaging (SWI). *Magn Reson Med* 2004; **52**: 612-618 [PMID: 15334582 DOI: 10.1002/mrm.20198]
6 **Haacke EM**, Mittal S, Wu Z, Neelavalli J, Cheng YC. Susceptibility-weighted imaging: technical aspects and clinical applications, part 1. *AJNR Am J Neuroradiol* 2009; **30**: 19-30 [PMID: 19039041 DOI: 10.3174/ajnr.A1400]
7 **Rauscher A**, Sedlacik J, Barth M, Mentzel HJ, Reichenbach JR. Magnetic susceptibility-weighted MR phase imaging of the human brain. *AJNR Am J Neuroradiol* 2005; **26**: 736-742 [PMID: 15814914]
8 **Yamada N**, Imakita S, Sakuma T, Takamiya M. Intracranial calcification on gradient-echo phase image: depiction of diamagnetic susceptibility. *Radiology* 1996; **198**: 171-178 [PMID: 8539373 DOI: 10.1148/radiology.198.1.8539373]
9 **Greenberg SM**, Eng JA, Ning M, Smith EE, Rosand J. Hemorrhage burden predicts recurrent intracerebral hemorrhage after lobar hemorrhage. *Stroke* 2004; **35**: 1415-1420 [PMID: 15073385 DOI: 10.1161/01.STR.0000126807.69758.0e]
10 **Blitstein MK**, Tung GA. MRI of cerebral microhemorrhages. *AJR Am J Roentgenol* 2007; **189**: 720-725 [PMID: 17715122 DOI: 10.2214/AJR.07.2249]
11 **Smith EE**, Gurol ME, Eng JA, Engel CR, Nguyen TN, Rosand J, Greenberg SM. White matter lesions, cognition, and recurrent hemorrhage in lobar intracerebral hemorrhage. *Neurology* 2004; **63**: 1606-1612 [PMID: 15534243 DOI: 10.1212/01.WNL.0000142966.22886.20]
12 **Linn J**, Halpin A, Demaerel P, Ruhland J, Giese AD, Dichgans M, van Buchem MA, Bruckmann H, Greenberg SM. Prevalence of superficial siderosis in patients with cerebral amyloid angiopathy. *Neurology* 2010; **74**: 1346-1350 [PMID: 20421578 DOI: 10.1212/WNL.0b013e3181dad605]
13 **Tsushima Y**, Tanizaki Y, Aoki J, Endo K. MR detection of microhemorrhages in neurologically healthy adults. *Neuroradiology* 2002; **44**: 31-36 [PMID: 11942497 DOI: 10.1007/s002340100649]
14 **Medana IM**, Esiri MM. Axonal damage: a key predictor of outcome in human CNS diseases. *Brain* 2003; **126**: 515-530 [PMID: 12566274 DOI: 10.1093/brain/awg061]
15 **Schaefer PW**, Huisman TA, Sorensen AG, Gonzalez RG, Schwamm LH. Diffusion-weighted MR imaging in closed head injury: high correlation with initial glasgow coma scale score and score on modified Rankin scale at discharge. *Radiology* 2004; **233**: 58-66 [PMID: 15304663 DOI: 10.1148/radiol.2323031173]
16 **Mittal S**, Wu Z, Neelavalli J, Haacke EM. Susceptibility-weighted imaging: technical aspects and clinical applications, part 2. *AJNR Am J Neuroradiol* 2009; **30**: 232-252 [PMID: 19131406 DOI: 10.3174/ajnr.A1461]
17 **Tong KA**, Ashwal S, Holshouser BA, Shutter LA, Herigault G, Haacke EM, Kido DK. Hemorrhagic shearing lesions in children and adolescents with posttraumatic diffuse axonal injury: improved detection and initial results. *Radiology* 2003; **227**: 332-339 [PMID: 12732694 DOI: 10.1148/radiol.2272020176]
18 **Tong KA**, Ashwal S, Holshouser BA, Nickerson JP, Wall CJ, Shutter LA, Osterdock RJ, Haacke EM, Kido D. Diffuse axonal injury in children: clinical correlation with hemorrhagic lesions. *Ann Neurol* 2004; **56**: 36-50 [PMID: 15236400 DOI: 10.1002/ana.20123]
19 **Babikian T**, Freier MC, Tong KA, Nickerson JP, Wall CJ, Holshouser BA, Burley T, Riggs ML, Ashwal S. Susceptibility weighted imaging: neuropsychologic outcome and pediatric head injury. *Pediatr Neurol* 2005; **33**: 184-194 [PMID: 16139733 DOI: 10.1016/j.pediatrneurol.2005.03.015]
20 **Mannion RJ**, Cross J, Bradley P, Coles JP, Chatfield D, Carpenter A, Pickard JD, Menon DK, Hutchinson PJ. Mechanism-based MRI classification of traumatic brainstem injury and its relationship to outcome. *J Neurotrauma* 2007; **24**: 128-135 [PMID: 17263676 DOI: 10.1089/neu.2006.0127]
21 **Lee BC**, Vo KD, Kido DK, Mukherjee P, Reichenbach J, Lin W, Yoon MS, Haacke M. MR high-resolution blood oxygenation level-dependent venography of occult (low-flow) vascular lesions. *AJNR Am J Neuroradiol* 1999; **20**: 1239-1242 [PMID: 10472978]
22 **Barnes SR**, Haacke EM. Susceptibility-weighted imaging: clinical angiographic applications. *Magn Reson Imaging Clin N Am* 2009; **17**: 47-61 [PMID: 19364599 DOI: 10.1016/j.mric.2008.12.002]
23 **Yousem DM**, Flamm ES, Grossman RI. Comparison of MR imaging with clinical history in the identification of hemorrhage in patients with cerebral arteriovenous malformations. *AJNR Am J Neuroradiol* 1989; **10**: 1151-1154 [PMID: 2512776]
24 **Lehnhardt FG**, von Smekal U, Rückriem B, Stenzel W, Neveling M, Heiss WD, Jacobs AH. Value of gradient-echo magnetic resonance imaging in the diagnosis of familial cerebral cavernous malformation. *Arch Neurol* 2005; **62**: 653-658 [PMID: 15824268 DOI: 10.1001/archneur.62.4.653]
25 **Cooper AD**, Campeau NG, Meissner I. Susceptibility-weighted imaging in familial cerebral cavernous malformations. *Neurology* 2008; **71**: 382 [PMID: 18663188 DOI: 10.1212/01.wnl.0000319659.86629.c8]
26 **Abla A**, Wait SD, Uschold T, Lekovic GP, Spetzler RF. Developmental venous anomaly, cavernous malformation, and capillary telangiectasia: spectrum of a single disease. *Acta Neurochir* (Wien)

2008; **150**: 487-489; discussion 489 [PMID: 18351283 DOI: 10.1007/s00701-008-1570-5]
27 **Abe T**, Singer RJ, Marks MP, Norbash AM, Crowley RS, Steinberg GK. Coexistence of occult vascular malformations and developmental venous anomalies in the central nervous system: MR evaluation. *AJNR Am J Neuroradiol* 1998; **19**: 51-57 [PMID: 9432157]
28 **Töpper R**, Jürgens E, Reul J, Thron A. Clinical significance of intracranial developmental venous anomalies. *J Neurol Neurosurg Psychiatry* 1999; **67**: 234-238 [PMID: 10407000 DOI: 10.1136/jnnp.67.2.234]
29 **Tong KA**, Ashwal S, Obenaus A, Nickerson JP, Kido D, Haacke EM. Susceptibility-weighted MR imaging: a review of clinical applications in children. *AJNR Am J Neuroradiol* 2008; **29**: 9-17 [PMID: 17925363 DOI: 10.3174/ajnr.A0786]
30 **Comi AM**. Update on Sturge-Weber syndrome: diagnosis, treatment, quantitative measures, and controversies. *Lymphat Res Biol* 2007; **5**: 257-264 [PMID: 18370916 DOI: 10.1089/lrb.2007.1016]
31 **Hinman JM**, Provenzale JM. Hypointense thrombus on T2-weighted MR imaging: a potential pitfall in the diagnosis of dural sinus thrombosis. *Eur J Radiol* 2002; **41**: 147-152 [PMID: 11809544 DOI: 10.1016/S0720-048X(01)00365-5]
32 **Mammen EF**. Pathogenesis of venous thrombosis. *Chest* 1992; **102**: 640S-644S [PMID: 1451539 DOI: 10.1378/chest.102.6_Supplement.640S]
33 **Khandelwal N**, Agarwal A, Kochhar R, Bapuraj JR, Singh P, Prabhakar S, Suri S. Comparison of CT venography with MR venography in cerebral sinovenous thrombosis. *AJR Am J Roentgenol* 2006; **187**: 1637-1643 [PMID: 17114562 DOI: 10.2214/AJR.05.1249]
34 **Viallon M**, Altrichter S, Pereira VM, Nguyen D, Sekoranja L, Federspiel A, Kulcsar Z, Sztajzel R, Ouared R, Bonvin C, Pfeuffer J, Lövblad KO. Combined use of pulsed arterial spin-labeling and susceptibility-weighted imaging in stroke at 3T. *Eur Neurol* 2010; **64**: 286-296 [PMID: 20980761 DOI: 10.1159/000321162]
35 **Hermier M**, Nighoghossian N. Contribution of susceptibility-weighted imaging to acute stroke assessment. *Stroke* 2004; **35**: 1989-1994 [PMID: 15192245 DOI: 10.1161/01.STR.0000133341.74387.96]
36 **Cheng AL**, Batool S, McCreary CR, Lauzon ML, Frayne R, Goyal M, Smith EE. Susceptibility-weighted imaging is more reliable than T2*-weighted gradient-recalled echo MRI for detecting microbleeds. *Stroke* 2013; **44**: 2782-2786 [PMID: 23920014 DOI: 10.1161/STROKEAHA.113.002267]
37 **Flacke S**, Urbach H, Keller E, Träber F, Hartmann A, Textor J, Gieseke J, Block W, Folkers PJ, Schild HH. Middle cerebral artery (MCA) susceptibility sign at susceptibility-based perfusion MR imaging: clinical importance and comparison with hyperdense MCA sign at CT. *Radiology* 2000; **215**: 476-482 [PMID: 10796928 DOI: 10.1148/radiology.215.2.r00ma09476]
38 **Rovira A**, Orellana P, Alvarez-Sabín J, Arenillas JF, Aymerich X, Grivé E, Molina C, Rovira-Gols A. Hyperacute ischemic stroke: middle cerebral artery susceptibility sign at echo-planar gradient-echo MR imaging. *Radiology* 2004; **232**: 466-473 [PMID: 15215546 DOI: 10.1148/radiol.2322030273]
39 **Lingegowda D**, Thomas B, Vaghela V, Hingwala DR, Kesavadas C, Sylaja PN. 'Susceptibility sign' on susceptibility-weighted imaging in acute ischemic stroke. *Neurol India* 2012; **60**: 160-164 [PMID: 22626696 DOI: 10.4103/0028-3886.96389]
40 **Kesavadas C**, Santhosh K, Thomas B. Susceptibility weighted imaging in cerebral hypoperfusion-can we predict increased oxygen extraction fraction? *Neuroradiology* 2010; **52**: 1047-1054 [PMID: 20567811 DOI: 10.1007/s00234-010-0733-2]
41 **Assouline E**, Benziane K, Reizine D, Guichard JP, Pico F, Merland JJ, Bousser MG, Chabriat H. Intra-arterial thrombus visualized on T2* gradient echo imaging in acute ischemic stroke. *Cerebrovasc Dis* 2005; **20**: 6-11 [PMID: 15925876 DOI: 10.1159/000086120]
42 **Huang P**, Chen CH, Lin WC, Lin RT, Khor GT, Liu CK. Clinical applications of susceptibility weighted imaging in patients with major stroke. *J Neurol* 2012; **259**: 1426-1432 [PMID: 22186853 DOI: 10.1007/s00415-011-6369-2]
43 **Kidwell CS**, Saver JL, Villablanca JP, Duckwiler G, Fredieu A, Gough K, Leary MC, Starkman S, Gobin YP, Jahan R, Vespa P, Liebeskind DS, Alger JR, Vinuela F. Magnetic resonance imaging detection of microbleeds before thrombolysis: an emerging application. *Stroke* 2002; **33**: 95-98 [PMID: 11779895 DOI: 10.1161/hs0102.101792]
44 **Chalela JA**, Kang DW, Warach S. Multiple cerebral microbleeds: MRI marker of a diffuse hemorrhage-prone state. *J Neuroimaging* 2004; **14**: 54-57 [PMID: 14748209 DOI: 10.1177/1051228403258673]
45 **Kesavadas C**, Thomas B, Pendharakar H, Sylaja PN. Susceptibility weighted imaging: does it give information similar to perfusion weighted imaging in acute stroke? *J Neurol* 2011; **258**: 932-934 [PMID: 21116823 DOI: 10.1007/s00415-010-5843-6]
46 **Chalela JA**, Kidwell CS, Nentwich LM, Luby M, Butman JA, Demchuk AM, Hill MD, Patronas N, Latour L, Warach S. Magnetic resonance imaging and computed tomography in emergency assessment of patients with suspected acute stroke: a prospective comparison. *Lancet* 2007; **369**: 293-298 [PMID: 17258669 DOI: 10.1016/S0140-6736(07)60151-2]
47 **Wycliffe ND**, Choe J, Holshouser B, Oyoyo UE, Haacke EM, Kido DK. Reliability in detection of hemorrhage in acute stroke by a new three-dimensional gradient recalled echo susceptibility-weighted imaging technique compared to computed tomography: a retrospective study. *J Magn Reson Imaging* 2004; **20**: 372-377 [PMID: 15332242 DOI: 10.1002/jmri.20130]
48 **von Kummer R**. MRI: the new gold standard for detecting brain hemorrhage? *Stroke* 2002; **33**: 1748-1749 [PMID: 12105345 DOI: 10.1161/01.STR.0000019882.06696.D6]
49 **Wintermark M**, Sanelli PC, Albers GW, Bello JA, Derdeyn CP, Hetts SW, Johnson MH, Kidwell CS, Lev MH, Liebeskind DS, Rowley HA, Schaefer PW, Sunshine JL, Zaharchuk G, Meltzer CC; American Society of Neuroradiology; American College of Radiology; Society of NeuroInterventional Surgery. Imaging recommendations for acute stroke and transient ischemic attack patients: a joint statement by the American Society of Neuroradiology, the American College of Radiology and the Society of NeuroInterventional Surgery. *J Am Coll Radiol* 2013; **10**: 828-832 [PMID: 23948676 DOI: 10.1016/j.jacr.2013.06.019]
50 **Haacke EM**, Cheng NY, House MJ, Liu Q, Neelavalli J, Ogg RJ, Khan A, Ayaz M, Kirsch W, Obenaus A. Imaging iron stores in the brain using magnetic resonance imaging. *Magn Reson Imaging* 2005; **23**: 1-25 [PMID: 15733784 DOI: 10.1016/j.mri.2004.10.001]
51 **Harder SL**, Hopp KM, Ward H, Neglio H, Gitlin J, Kido D. Mineralization of the deep gray matter with age: a retrospective review with susceptibility-weighted MR imaging. *AJNR Am J Neuroradiol* 2008; **29**: 176-183 [PMID: 17989376 DOI: 10.3174/ajnr.A0770]
52 **Hecht MJ**, Fellner C, Schmid A, Neundörfer B, Fellner FA. Cortical T2 signal shortening in amyotrophic lateral sclerosis is not due to iron deposits. *Neuroradiology* 2005; **47**: 805-808 [PMID: 16175348 DOI: 10.1007/s00234-005-1421-5]
53 **Martin WR**, Wieler M, Gee M. Midbrain iron content in early Parkinson disease: a potential biomarker of disease status. *Neurology* 2008; **70**: 1411-1417 [PMID: 18172063 DOI: 10.1212/01.wnl.0000286384.31050.b5]
54 **Schenck JF**, Zimmerman EA, Li Z, Adak S, Saha A, Tandon R, Fish KM, Belden C, Gillen RW, Barba A, Henderson DL, Neil W, O'Keefe T. High-field magnetic resonance imaging of brain iron in Alzheimer disease. *Top Magn Reson Imaging* 2006; **17**: 41-50 [PMID: 17179896 DOI: 10.1097/01.rmr.0000245455.59912.40]
55 **McNeill A**, Birchall D, Hayflick SJ, Gregory A, Schenk JF, Zimmerman EA, Shang H, Miyajima H, Chinnery PF. T2* and FSE MRI distinguishes four subtypes of neurodegeneration with brain iron accumulation. *Neurology* 2008; **70**: 1614-1619 [PMID: 18443312 DOI: 10.1212/01.wnl.0000310985.40011.d6]
56 **van Bergen JM**, Hua J, Unschuld PG, Lim IA, Jones CK, Margolis RL, Ross CA, van Zijl PC, Li X. Quantitative Susceptibility Mapping Suggests Altered Brain Iron in Premanifest Huntington

Disease. *AJNR Am J Neuroradiol* 2016; **37**: 789-796 [PMID: 26680466 DOI: 10.3174/ajnr.A4617]
57 **Haller S**, Bartsch A, Nguyen D, Rodriguez C, Emch J, Gold G, Lovblad KO, Giannakopoulos P. Cerebral microhemorrhage and iron deposition in mild cognitive impairment: susceptibility-weighted MR imaging assessment. *Radiology* 2010; **257**: 764-773 [PMID: 20923870 DOI: 10.1148/radiol.10100612]
58 **Barnaure I**, Montandon ML, Rodriguez C, Herrmann F, Lövblad KO, Giannakopoulos P, Haller S. Clinicoradiologic Correlations of Cerebral Microbleeds in Advanced Age. *AJNR Am J Neuroradiol* 2017; **38**: 39-45 [PMID: 27686485 DOI: 10.3174/ajnr.A4956]
59 **Tan IL**, van Schijndel RA, Pouwels PJ, van Walderveen MA, Reichenbach JR, Manoliu RA, Barkhof F. MR venography of multiple sclerosis. *AJNR Am J Neuroradiol* 2000; **21**: 1039-1042 [PMID: 10871010]
60 **Haacke EM**, Ayaz M, Khan A, Manova ES, Krishnamurthy B, Gollapalli L, Ciulla C, Kim I, Petersen F, Kirsch W. Establishing a baseline phase behavior in magnetic resonance imaging to determine normal vs. abnormal iron content in the brain. *J Magn Reson Imaging* 2007; **26**: 256-264 [PMID: 17654738 DOI: 10.1002/jmri.22987]
61 **Rudko DA**, Solovey I, Gati JS, Kremenchutzky M, Menon RS. Multiple sclerosis: improved identification of disease-relevant changes in gray and white matter by using susceptibility-based MR imaging. *Radiology* 2014; **272**: 851-864 [PMID: 24828000 DOI: 10.1148/radiol.14132475]
62 **Rauscher A**, Sedlacik J, Fitzek C, Walter B, Hochstetter A, Kalff R, Kaiser WA, Reichenbach JR. High resolution susceptibility weighted MR-imaging of brain tumors during the application of a gaseous agent. *Rofo* 2005; **177**: 1065-1069 [PMID: 16021537 DOI: 10.1055/s-2005-858428]
63 **Sehgal V**, Delproposto Z, Haacke EM, Tong KA, Wycliffe N, Kido DK, Xu Y, Neelavalli J, Haddar D, Reichenbach JR. Clinical applications of neuroimaging with susceptibility-weighted imaging. *J Magn Reson Imaging* 2005; **22**: 439-450 [PMID: 16163700 DOI: 10.1002/jmri.20404]
64 **Hammond KE**, Lupo JM, Xu D, Metcalf M, Kelley DA, Pelletier D, Chang SM, Mukherjee P, Vigneron DB, Nelson SJ. Development of a robust method for generating 7.0 T multichannel phase images of the brain with application to normal volunteers and patients with neurological diseases. *Neuroimage* 2008; **39**: 1682-1692 [PMID: 18096412 DOI: 10.1016/j.neuroimage.2007.10.037]
65 **Sehgal V**, Delproposto Z, Haddar D, Haacke EM, Sloan AE, Zamorano LJ, Barger G, Hu J, Xu Y, Prabhakaran KP, Elangovan IR, Neelavalli J, Reichenbach JR. Susceptibility-weighted imaging to visualize blood products and improve tumor contrast in the study of brain masses. *J Magn Reson Imaging* 2006; **24**: 41-51 [PMID: 16755540 DOI: 10.1002/jmri.20598]
66 **Wu Z**, Mittal S, Kish K, Yu Y, Hu J, Haacke EM. Identification of calcification with MRI using susceptibility-weighted imaging: a case study. *J Magn Reson Imaging* 2009; **29**: 177-182 [PMID: 19097156 DOI: 10.1002/jmri.21617]
67 **Zulfiqar M**, Dumrongpisutikul N, Intrapiromkul J, Yousem DM. Detection of intratumoral calcification in oligodendrogliomas by susceptibility-weighted MR imaging. *AJNR Am J Neuroradiol* 2012; **33**: 858-864 [PMID: 22268093 DOI: 10.3174/ajnr.A2862]
68 **Thamburaj K**, Radhakrishnan VV, Thomas B, Nair S, Menon G. Intratumoral microhemorrhages on T2*-weighted gradient-echo imaging helps differentiate vestibular schwannoma from meningioma. *AJNR Am J Neuroradiol* 2008; **29**: 552-557 [PMID: 18079187 DOI: 10.3174/ajnr.A0887]
69 **Toh CH**, Wei KC, Chang CN, Hsu PW, Wong HF, Ng SH, Castillo M, Lin CP. Differentiation of pyogenic brain abscesses from necrotic glioblastomas with use of susceptibility-weighted imaging. *AJNR Am J Neuroradiol* 2012; **33**: 1534-1538 [PMID: 22422181 DOI: 10.3174/ajnr.A2986]
70 **Reichenbach JR**, Schweser F, Serres B, Deistung A. Quantitative Susceptibility Mapping: Concepts and Applications. *Clin Neuroradiol* 2015; **25** Suppl 2: 225-230 [PMID: 26198880 DOI: 10.1007/s00062-015-0432-9]
71 **Eskreis-Winkler S**, Zhang Y, Zhang J, Liu Z, Dimov A, Gupta A, Wang Y. The clinical utility of QSM: disease diagnosis, medical management, and surgical planning. *NMR Biomed* 2017; **30**: [PMID: 27906525 DOI: 10.1002/nbm.3668]
72 **He N**, Ling H, Ding B, Huang J, Zhang Y, Zhang Z, Liu C, Chen K, Yan F. Region-specific disturbed iron distribution in early idiopathic Parkinson's disease measured by quantitative susceptibility mapping. *Hum Brain Mapp* 2015; **36**: 4407-4420 [PMID: 26249218 DOI: 10.1002/hbm.22928]
73 **Acosta-Cabronero J**, Williams GB, Cardenas-Blanco A, Arnold RJ, Lupson V, Nestor PJ. In vivo quantitative susceptibility mapping (QSM) in Alzheimer's disease. *PLoS One* 2013; **8**: e81093 [PMID: 24278382 DOI: 10.1371/journal.pone.0081093]
74 **Moon Y**, Han SH, Moon WJ. Patterns of Brain Iron Accumulation in Vascular Dementia and Alzheimer's Dementia Using Quantitative Susceptibility Mapping Imaging. *J Alzheimers Dis* 2016; **51**: 737-745 [PMID: 26890777 DOI: 10.3233/JAD-151037]
75 **Domínguez JF**, Ng AC, Poudel G, Stout JC, Churchyard A, Chua P, Egan GF, Georgiou-Karistianis N. Iron accumulation in the basal ganglia in Huntington's disease: cross-sectional data from the IMAGE-HD study. *J Neurol Neurosurg Psychiatry* 2016; **87**: 545-549 [PMID: 25952334 DOI: 10.1136/jnnp-2014-310183]
76 **Walsh AJ**, Blevins G, Lebel RM, Seres P, Emery DJ, Wilman AH. Longitudinal MR imaging of iron in multiple sclerosis: an imaging marker of disease. *Radiology* 2014; **270**: 186-196 [PMID: 23925273 DOI: 10.1148/radiol.13130474]

P- Reviewer: Sergi CM, Schoenhagen P, Ueda H **S- Editor**: Ji FF
L- Editor: A **E- Editor**: Tan WW

Published by **Baishideng Publishing Group Inc**
7901 Stoneridge Drive, Suite 501, Pleasanton, CA 94588, USA
Telephone: +1-925-223-8242
Fax: +1-925-223-8243
E-mail: bpgoffice@wjgnet.com
Help Desk: http://www.f6publishing.com/helpdesk
http://www.wjgnet.com

ISSN 1949-8470 (online)

World Journal of *Radiology*

World J Radiol 2018 May 28; 10(5): 46-51

Published by Baishideng Publishing Group Inc

WJR World Journal of Radiology

Contents

Monthly Volume 10 Number 5 May 28, 2018

CASE REPORT

Contents

World Journal of Radiology
Volume 10 Number 5 May 28, 2018

ABOUT COVER

Editorial Board Member of *World Journal of Radiology*, Milan Vosmik, MD, PhD, Chief Doctor, Department of Oncology and Radiotherapy, University Hospital Hradec Kralove, Hradec Kralove 500 05, Czech Republic

AIM AND SCOPE

World Journal of Radiology (*World J Radiol*, *WJR*, online ISSN 1949-8470, DOI: 10.4329) is a peer-reviewed open access academic journal that aims to guide clinical practice and improve diagnostic and therapeutic skills of clinicians.

WJR covers topics concerning diagnostic radiology, radiation oncology, radiologic physics, neuroradiology, nuclear radiology, pediatric radiology, vascular/interventional radiology, medical imaging achieved by various modalities and related methods analysis. The current columns of *WJR* include editorial, frontier, diagnostic advances, therapeutics advances, field of vision, mini-reviews, review, topic highlight, medical ethics, original articles, case report, clinical case conference (clinicopathological conference), and autobiography.

We encourage authors to submit their manuscripts to *WJR*. We will give priority to manuscripts that are supported by major national and international foundations and those that are of great basic and clinical significance.

INDEXING/ABSTRACTING

World Journal of Radiology is now indexed in PubMed, PubMed Central, and Emerging Sources Citation Index (Web of Science).

NAME OF JOURNAL
World Journal of Radiology

ISSN
ISSN 1949-8470 (online)

LAUNCH DATE
January 31, 2009

FREQUENCY
Monthly

EDITORIAL OFFICE
Jin-Lei Wang, Director
World Journal of Radiology
Baishideng Publishing Group Inc
7901 Stoneridge Drive, Suite 501, Pleasanton, CA 94588, USA
Telephone: +1-925-2238242
Fax: +1-925-2238243
E-mail: editorialoffice@wjgnet.com
Help Desk: http://www.f6publishing.com/helpdesk
http://www.wjgnet.com

PUBLISHER
Baishideng Publishing Group Inc
7901 Stoneridge Drive, Suite 501,
Pleasanton, CA 94588, USA
Telephone: +1-925-2238242
Fax: +1-925-2238243
E-mail: bpgoffice@wjgnet.com
Help Desk: http://www.f6publishing.com/helpdesk
http://www.wjgnet.com

PUBLICATION DATE
May 28, 2018

INSTRUCTIONS TO AUTHORS
http://www.wjgnet.com/bpg/gerinfo/204

ONLINE SUBMISSION
http://www.f6publishing.com

World Journal of Radiology

Submit a Manuscript: http://www.f6publishing.com

World J Radiol 2018 May 28; 10(5): 46-51

DOI: 10.4329/wjr.v10.i5.46

ISSN 1949-8470 (online)

CASE REPORT

Traumatic peroneal split lesion with retinaculum avulsion: Diagnosis and post-operative multymodality imaging

Aldo Fischetti, Jeries P Zawaideh, Davide Orlandi, Stefano Belfiore, Enzo SIlvestri

Aldo Fischetti, Jeries P Zawaideh, Department of Health Sciences (DISSAL), Radiology Section, University of Genoa, Genoa 16100, Italy

Davide Orlandi, Enzo SIlvestri, Radiology Department, Ospedale Evangelico Internazionale, Genova 16122, Italy

Stefano Belfiore, Orthopedic and Trauma Department, Ospedale Evangelico Internazionale, Genova 16122, Italy

ORCID number: Aldo Fischetti (0000-0002-9415-4179); Jeries P Zawaideh (000-0002-1304-7495); Davide Orlandi (0000-0001-5569-3359); Stefano Belfiore (000-0002-4707-0335); Enzo SIlvestri (0000-0002-1566-9722).

Author contributions: Fischetti A, Zawaideh JP and Orlandi D designed the report; Orlandi D performed the ultrasound examination and reported the MRI scan; Belfiore S performed the orthopedic surgery; all the authors revised the literature, wrote and reviewed the manuscript.

Informed consent statement: The patient was informed and provided written consent for the study.

Conflict-of-interest statement: All the authors report no conflict of interest.

Manuscript source: Invited manuscript

Correspondence to: Davide Orlandi, MD, PhD, Radiology Department, Ospedale Evangelico Internazionale, Corso Solferino 1A, Genova 16122,
Italy. my.davideorlandi@gmail.com
Telephone: +39-333-7880696

Received: February 13, 2018
Peer-review started: February 13, 2018
First decision: April 11, 2018
Revised: April 23, 2018
Accepted: May 23, 2018
Article in press: May 23, 2018
Published online: May 28, 2018

Abstract

Tears of peroneus brevis tendon represent a cause of underdiagnosed lateral ankle pain and instability. The typical clinical presentation is retro-malleolar pain, in some cases associated with palpable swelling around the fibular malleolus, pain during activities and difficulty in walking. We present a case of peroneus brevis split lesion with superior peroneal retinaculum avulsion in a young athlete who referred to the emergency ward of our hospital for left ankle pain after an inversion injury. An early diagnosis allowed treating the injury and promptly resuming sport activity, after rehabilitation training. Surgical reconstruction key-points and post-surgical follow-up were also discussed. A late diagnosis would have caused a symptomatology worsening and an increased recovery time.

Key words: Multimodality imaging; Tendon injuries; Orthopedic surgery; Sport medicine; Ankle instability

Core tip: The article is based on the findings observed in a patient who was followed in our institution for a split lesion of the peroneus brevis after an inversion ankle sprain. Split lesion of peroneus brevis is usually under diagnosed, therefore we want to highlight the importance of ancillary sign, as detachment of an osseous fragment seen on the X-ray, since an early diagnosis can allow the patient to reduce recovery ti-

me. In the manuscript, we also provide post-operative ultrasound imaging which can be helpful during follow-up for monitoring the patient and to help him to restart sport practices.

Fischetti A, Zawaideh JP, Orlandi D, Belfiore S, SIlvestri E. Traumatic peroneal split lesion with retinaculum avulsion: Diagnosis and post-operative multymodality imaging. *World J Radiol* 2018; 10(5): 46-51 Available from: URL: http://www.wjgnet.com/1949-8470/full/v10/i5/46.htm DOI: http://dx.doi.org/10.4329/wjr.v10.i5.46

INTRODUCTION

The peroneus longus (PL) and brevis (PB) arise from the posterolateral surface of the fibula and the fascia of their homonymous muscle. Peroneal tendons share a common synovial sheath and pass posteriorly to the fibular malleolus, inside the retro-malleolar groove: At this level, they are stabilized by the superior peroneal retinaculum (SPR). Usually, the peroneus brevis tendon locates antero-medially to the peroneus longus. On the lateral surface of the calcaneus the tendons run superficial to the calcaneofibular ligament (CFL) and lateral to the talo-calcanear ligaments[1].

Distal to the CFL the tendons run superior (PB) and inferior (PL) to the peroneal trochlea on the lateral calcaneal wall, kept in place by the inferior peroneal retinaculum (IPR). The PB inserts on the base of the fifth metatarsal bone while the PL have a wide insertion on the lateral aspect of the base of the first metatarsal bone and the lateral side of the medial cuneiform. Both tendons are plantar flexors of the ankle and everters of the subtalar and mid-tarsal joints. Tears of peroneus brevis tendon are a frequent cause of underdiagnosed lateral ankle pain and instability. Several studies confirm that these lesions are more common than previously believed[2]. They represent frequently an overlooked clinical condition[3]. The typical clinical presentation is retro-malleolar pain, in some cases associated with palpable swelling around the fibular malleolus, pain during activities and difficulty in walking.

Patients usually do not remember a specific episode of trauma, however, in case of misdiagnosed peroneal lesion, they often mention chronic lateral ankle instability symptoms, which went on even for years[2]. We report a case of a young athlete with a traumatic SPR avulsion and associated PB split lesion, to highlight the crucial role of associated conditions such as a flat retro-malleolar groove in the development of such an injury also including imaging findings, clinical characteristics, and treatment options in order to reduce risk of recurrence or any further instability.

CASE REPORT

A 27 years old man presented at the emergency department with pain at the left ankle after an inversion injury; the lateral aspect of the ankle was swollen with only minor subcutaneous hematoma on the fibular malleolus. The patient reported no history of recent trauma. Plain films of the ankle were done to evaluate the bone status: The exam excluded fracture of the ankle, but revealed the detachment of an osseous fragment from the lateral aspect of the fibular malleolus (Figure 1). We suspected a traumatic lesion of the SPR and the lateral tendon compartment of the ankle. An ultrasound (US) examination was immediately performed by the on-call radiologist with a portable system (My Lab Alpha, Esaote Biomedica, Italy, equipped with a 3-13 Mhz linear probe), to evaluate the possible involvement of the lateral compartment ligaments and tendons of the ankle, usually damaged after an inversion ankle injury.

US examination demonstrated a diffuse swelling at the posterolateral aspect of the fibular malleolus with complete tear of the SPR and consequent instability of the PB (Figure 2A), which tended to the anterior subluxation at dynamic tests (flexion, extension and eversion of the foot). Moreover, US examination shows also a split lesion of the PB, which on axial US scan appears divided in two hemi-tendons at the level of deflection point on the fibular malleolus, with PL lying in the middle and separating them. The longitudinal tear of the PB had a distal extension of around 2 cm without involvement of the distal insertion on the base of the fifth metatarsal bone. Only minor anterior talofibular ligament (aTFL) sprain and no significant involvement of CFL or tibiofibular syndesmosis were found. The patient evaluation was completed with a magnetic resonance imaging (MRI) exam, performed after one week from the injury, in prevision of surgery (Figure 2B). Sequences T1-w, T2-w and with Short Tau Inversion Recovery in the three planes of the space were used. MRI examination confirmed the PB split lesion extended more distally than that showed by US examination (around 4 cm). No involvement of the distal PB insertion was found.

MRI also detects the avulsion of the fibular insertion of the SPR and a shallow retro-malleolar groove with associated anterior luxation of the peroneus brevis tendon. Furthermore, MRI showed a minor bone bruise of the distal tibial epiphysis and tibio-talar joint effusion. The anterior talo-fibular ligament was thickened but undamaged. The deltoid ligament presented fibro-scarring alterations, by previous trauma.No significant alterations affected the other tendons of the ankle. Surgery started with a curve incision of the posterolateral aspect of the ankle that revealed diffuse swelling of the SPR that was completely detached from its anterior insertion (Figure 3A). A wide longitudinal tear of the PB was also confirmed, with anterior luxation of the medial hemi-tendon, which represent about the 70% of the total PB.

Incision of the IPR was performed in order to expose the whole extension of the longitudinal tear, then, after curettage of the damaged edges of the peroneus brevis tendon, a lateral side-to-side suture of PB was done. IPR was also sutured (Figure 3B). Subsequent moderate

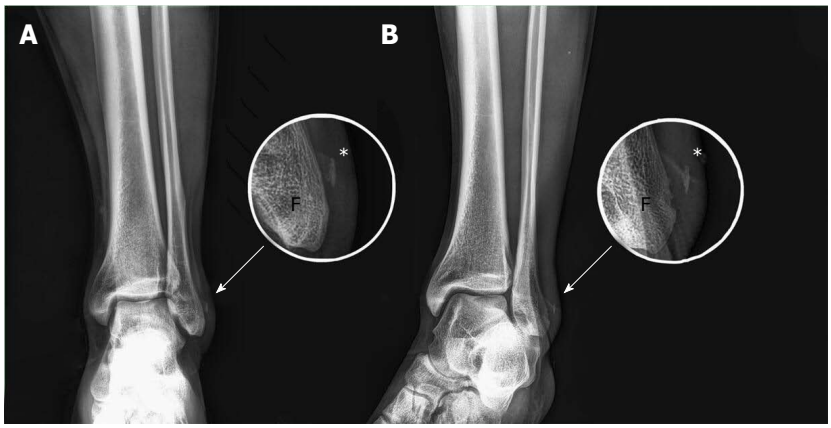

Figure 1 X-ray: AP and oblique view, no fractures of the peroneal malleolus are shown. On the magnification a detachment of a small bony foil (periosteum) is appreciable (*). A: AP; B: Oblique view. F: Fibula.

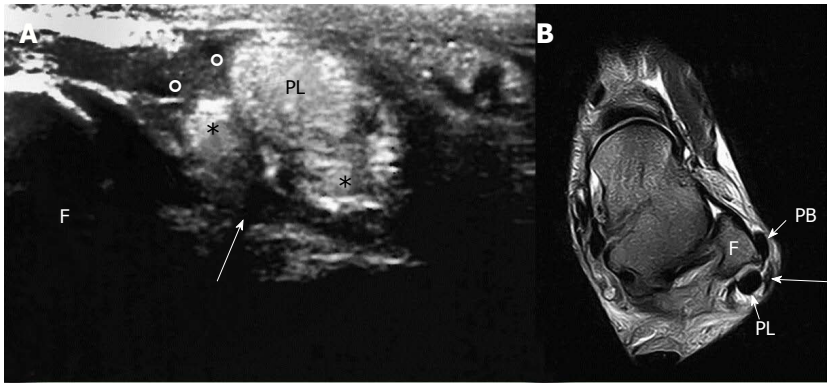

Figure 2 Ultrasound and magnetic resonance imaging evaluation of the injured ankle. A: US examination of the injured ankle: Avulsed retinaculum (°); two hemi-tendons due to split lesion of peroneus brevis (*); CFL (arrow). B: MRI T2w axial sequence: MRI shows PB anterior subluxation. The avulsion of the retinaculum (arrow) can be observed. US: Ultrasound; MRI: Magnetic resonance imaging; PB: Peroneus brevis; PL: Peroneus longus.

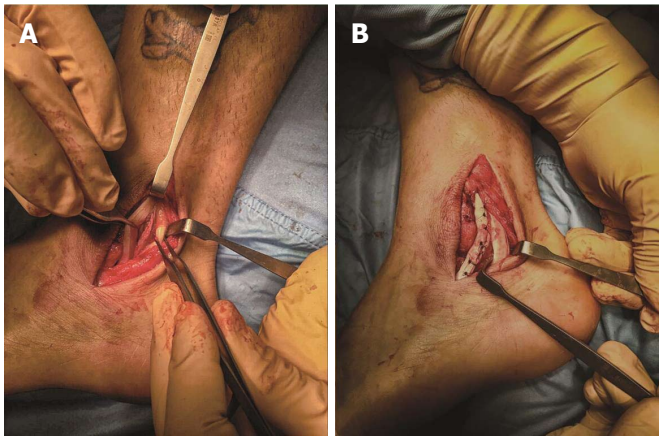

Figure 3 The surgical procedure. A: Surgical view: The peroneus longus (PL) resides more posteriorly, while is well visible the peroneus brevis (PB) is torn in two hemi-tendons the anterior part is about the 70% of the total peroneus brevis tendon; B: At the end of operation the two PB hemi-tendons are sutured together; posteriorly PL can be appreciated.

milling of the retro-malleolar groove in order to restore physiological concavity and SPR reinsertion with a trans-osseous wiring was performed, using interrupted sutures are passed through the fibula and SPR in a horizontal fashion. The lowest 2 or 3 sutures were passed transosseously through the posterolateral aspect of the fibula and then through the posterior aspect of the SPR to wrap it over the peroneal tendons and minimize any chance for recurrent peroneal subluxation. A 0.054 K-wire was used for the repair holes through

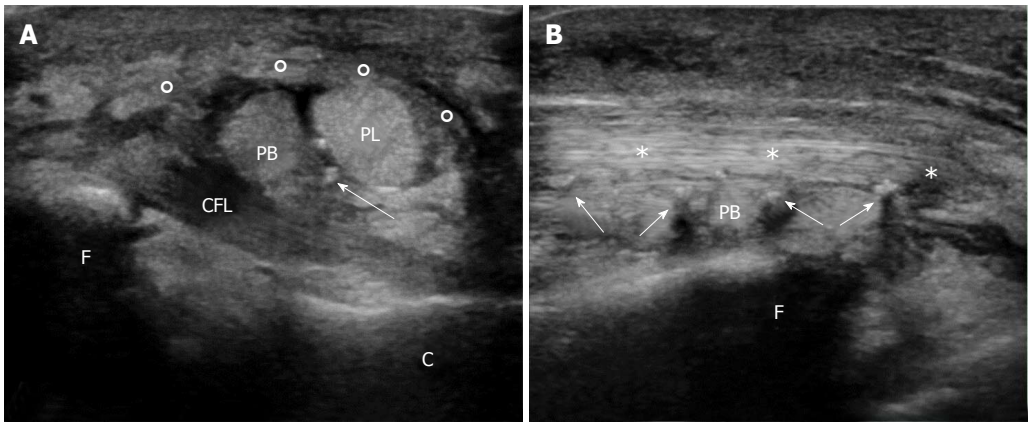

Figure 4 Post-surgical ultrasound examination of the injured ankle. A: Axial US scan: the restored retinaculum (o) covers the two peroneus tendon, peroneus longus (PL) superiorly, and peroneus brevis (PB) inferiorly. Note the inhomogeneity of the lower part of the PB due to surgery. Suture stitches can be seen as hyperechoic spots (white arrows); fibula (F); calcaneus (C); calcaneofibular ligament (CFL); B: Longitudinal US scan. US: Ultrasound.

which No. 1.0 Vicryl suture (Polisorb, Covidien, Dublin, Ireland) can be passed[4]. The postoperative course was uneventful, the patient recovered promptly and was discharged on the same day. After surgery, a plaster cast was used for 2-6 wk; after 6-8 wk, the rehabilitation training was initiated. After approximately 12 wk, the patient could resume the sport activity.

The patient was followed up with clinical and ultrasound examination after four weeks. The patient referred increased stability of the ankle, and no significant discomfort. Ultrasound evaluation, performed with a high-end US apparel (Samsung RS80 Prestige, Samsung Medical, South Korea; equipped with 8-15 Mhz linear probe) revealed a mild residual swelling at the level of the reconstructed SPR, which appear continuous, with correct localization of the peroneal tendons in the retro-malleolar groove, PB tendon was also continuous and showed several hyperechoic spots on its course due to the suture wires (Figure 4). US scan during dynamic maneuvers demonstrated an excellent peroneal tendons stability at the level of the restored retro-malleolar groove[5]. The clinical follow-up examination performed after 6 mo from surgery confirmed the stability of PB; the treatment allowed the patient to restart sport practices after the rehabilitation program. The patient referred no symptoms during sport activity and an optimal performance during the sport events.

DISCUSSION

PB resides in a vulnerable position, between the retro-malleolar groove and the peroneus longus tendon: during the dorsiflexion of the foot, it is compressed by the peroneus longus against the fibular malleolus. Moreover, the vascular supply to the tendon is reduced inside the fibular groove; finally the anatomic variants afore mentioned compromise the competence of SPR, reducing the stability of the peroneus brevis tendon[6]. When a tear occurs, the peroneus longus tendon migrates forward into the peroneus brevis, determining a split lesion. The association with SPR injury causes the dislocation of the tendon out of the fibular groove. There are many anatomic variants that predispose to PB disease: (1) Morphology of the retro-malleolar groove: In the 82% of the population it has a concave aspect; flat or convex aspects predispose to lateral dislocation and PB longitudinal tears. This condition could lead to peroneal instability and spontaneous dislocation, however, like in the presented case and in more than 60% of patient no symptoms or abnormalities could be detected at clinical evaluation[7]; (2) Peroneus Quartus Muscle: The most common accessory muscle of the ankle (12%-22% of the population), accessory muscle, that arises from the distal third of the lateral fibula, to insert on calcaneus or cuboid, passing posterior to peroneal tendons. It is usually asymptomatic, but it may produce impingement inside of the retro-malleolar groove and predispose to peroneus brevis tendon dislocation and tears; and (3) Low-lying PB muscle belly: Is an abnormally distal extension of the PB muscle at the level of the retro-malleolar groove and predispose to peroneal tendon diseases and SPR injuries.

PB split lesions are visible on US investigation and are lesions of continuity that affected the long axis of the tendon[8]. The exams should be performed with static and dynamic imaging (flexion, extension and eversion), along short and long axis, with the patient in supine decubitus and the ankle internally rotated[9]. Split lesion causes the formation of two hemi-tendons, usually different in size, that surround the peroneus longus tendon. Frequently, fluid distension of the synovial peroneal tendon sheath with increased vascularity at power Doppler are associated[8].

The diagnosis of peroneus brevis split lesion is typically formulated in the basis of clinical examination and US, but MRI is useful to evaluate the suffering of the subchondral bone and the extension of the tendon lesion, possible predisposing factors and helpful for planning the appropriate treatment[3,6]. MRI exam should be performed in the three planes axial, coronal

and sagittal, with patient in supine decubitus and the ankle in neutral position[9]. Our protocol includes T1-w sequences in coronal and sagittal planes, T2-w sequences with and without fat suppression in the three planes and a PD sequence in coronal plane for their high contrast characteristic. On axial MRI images, the damaged PB assumes a characteristic "C shaped" or "chevron shaped"[5] configuration, that envelops the peroneus longus tendon, migrated anteriorly. The central portion of the tendon becomes very thinned and, in some case, it may be not well visualized.The longitudinal tear can be visualized also in the other planes, coronal and sagittal. The rupture of the SPR is associated with the dislocation of the tendon, laterally to the fibular malleolus. In our case, the rupture of the SPR, and, consequently, the peroneal tendon involvement, was suspected at the radiograph, suggesting a timely diagnosis and an early treatment.

Treatment of peroneus brevis tendon tears is initially conservative, with rest, ice, compression, and elevation (RICE), anti-inflammatory can also be prescribed to reduce inflammation and pain therapy and orthotics[6]. Refractory case, with associated lateral ankle pain and instability, or anatomic variants and SPR lesions need to undergo to surgical intervention, such as debridement, re-suturing and attachment of the tendon. If lateral ankle instability is present, the tendon lesion should be repaired at the same time of the ligament stabilization[2]. The longitudinal lesion is repaired with a side-to-side suture, combined with the reconstruction of SPR and the excision of the degenerative tissue. The results of the surgical treatment are satisfactory in most patients[2], usually with a restored level of activity and without any further instability. Also different surgical techniques were proposed for peroneal tear and instability (*e.g.*, bone block procedures, tissue transfer procedures, and rerouting procedures), however, the advantages of the proposed approach include better cosmesis, less soft tissue dissection, no wound retraction needed, detection of coexisting pathology, less postoperative pain, less peritendinous fibrosis, and less subjective tightness at peroneal tendons[10,11]. This case suggests that timely integrated imaging could be helpful not only in order to diagnose peroneal injuries but also to detect associated conditions that could be extremely relevant for surgical planning. This is extremely important in the management of the athletes, which have to rapidly resume sports activities after an accident. Split lesion of PB is usually underdiagnosed: In this case, radiograph findings were immediately suspected for a lateral compartment lesion, confirmed by second level exams. The early diagnosis allowed the patient to reduce recovery time and promptly restart sport practices. Moreover, ultrasound imaging, thanks to its dynamic capabilities, can be an effective practical option for evaluating lateral ankle instability, especially in cases of partial SPR tears and slight peroneal tendon subluxation.

ARTICLE HIGHLIGHTS

ARTICLE HIGHLIGHTS

Case characteristics

Left ankle pain after an inversion injury, muscle functional impairment.

Clinical diagnosis

Swollen left ankle.

Differential diagnosis

Differential diagnosis includes fibular malleolus fracture.

Laboratory diagnosis

Unremarkable laboratory examination.

Imaging diagnosis

A radiography of the ankle excluded bone fracture but revealed the detachment of an osseous fragment; ultrasound demonstrated a diffuse swelling at the posterolateral aspect of the fibular malleolus and a split lesion of the peroneus (PB); MRI scan confirmed the PB split lesion and detects the avulsion of the fibular insertion of the superior peroneal retinaculum (SPR) and a shallow retro-malleolar groove with associated anterior luxation of the peroneus brevis tendon.

Treatment

RICE treatment consists of rest, ice, compression, and elevation, anti-inflammatory can also be prescribed to reduce inflammation. Surgical treatment involves a side-to-side suture, combined with the reconstruction of SPR and the excision of the degenerative tissue.

Experiences and lessons

This case suggests that integrated imaging is helpful for injury diagnosis and surgical planning. Unclear images, such as small bone detachment at plain films can be precious hints for the detection of underlying tendon pathology.

REFERENCES

1 **Sconfienza LM**, Orlandi D, Lacelli F, Serafini G, SIlvestri E. Dynamic high-resolution US of ankle and midfoot ligaments: normal anatomic structure and imaging technique. *Radiographics* 2015; **35**: 164-178 [PMID: 25590396 DOI: 10.1148/rg.351130139]

2 **Karlsson J**, Wiger P. Longitudinal Split of the Peroneus Brevis Tendon and Lateral Ankle Instability: Treatment of Concomitant Lesions. *J Athl Train* 2002; **37**: 463-466 [PMID: 12937568]

3 **Dombek MF**, Lamm BM, Saltrick K, Mendicino RW, Catanzariti AR. Peroneal tendon tears: a retrospective review. *J Foot Ankle Surg* 2003; **42**: 250-258 [PMID: 14566716 DOI: 10.1016/S1067-2516(03)00314-4]

4 **van Dijk PAD**, Vopat BG, Guss D, Younger A, DiGiovanni CW. Retromalleolar Groove Deepening in Recurrent Peroneal Tendon Dislocation: Technique Tip. *Orthop J Sports Med* 2017; **5**: 2325967117706673 [PMID: 28540318 DOI: 10.1177/2325967117706673]

5 **Neustadter J**, Raikin SM, Nazarian LN. Dynamic sonographic evaluation of peroneal tendon subluxation. *AJR Am J Roentgenol* 2004; **183**: 985-988 [PMID: 15385290 DOI: 10.2214/ajr.183.4.1830985]

6 **Major NM**, Helms CA, Fritz RC, Speer KP. The MR imaging appearance of longitudinal split tears of the peroneus brevis tendon. *Foot Ankle Int* 2000; **21**: 514-519 [PMID: 10884113 DOI: 10.1177/107110070002100612]

7 **Molini L**, Bianchi S. US in peroneal tendon tear. *J Ultrasound* 2014; **17**: 125-134 [PMID: 24883136 DOI: 10.1007/s40477-014-0072-y]

8 **Park HJ**, Cha SD, Kim HS, Chung ST, Park NH, Yoo JH, Park JH, Kim JH, Lee TW, Lee CH, Oh SM. Reliability of MRI findings

of peroneal tendinopathy in patients with lateral chronic ankle instability. *Clin Orthop Surg* 2010; **2**: 237-243 [PMID: 21119941 DOI: 10.4055/cios.2010.2.4.237]

9 **Wang XT**, Rosenberg ZS, Mechlin MB, Schweitzer ME. Normal variants and diseases of the peroneal tendons and superior peroneal retinaculum: MR imaging features. *Radiographics* 2005; **25**: 587-602 [PMID: 15888611 DOI: 10.1148/rg.253045123]

10 **Taljanovic MS**, Alcala JN, Gimber LH, Rieke JD, Chilvers MM, Latt LD. High-resolution US and MR imaging of peroneal tendon injuries. *Radiographics* 2015; **35**: 179-199 [PMID: 25590397 DOI: 10.1148/rg.351130062]

11 **Hau WWS**, Lui TH, Ngai WK. Endoscopic Superior Peroneal Retinaculum Reconstruction. *Arthrosc Tech* 2017; **7**: e45-e51 [PMID: 29552468 DOI: 10.1016/j.eats.2017.08.050]

P- Reviewer: Ma DL, Robertson GA **S- Editor**: Ji FF **L- Editor**: A
E- Editor: Tan WW

Published by **Baishideng Publishing Group Inc**
7901 Stoneridge Drive, Suite 501, Pleasanton, CA 94588, USA
Telephone: +1-925-223-8242
Fax: +1-925-223-8243
E-mail: bpgoffice@wjgnet.com
Help Desk: http://www.f6publishing.com/helpdesk
http://www.wjgnet.com

ISSN 1949-8470 (online)

World Journal of *Radiology*

World J Radiol 2018 June 28; 10(6): 52-64

Published by Baishideng Publishing Group Inc

WJR World Journal of Radiology

Contents

Monthly Volume 10 Number 6 June 28, 2018

REVIEW

Contents

World Journal of Radiology
Volume 10 Number 6 June 28, 2018

ABOUT COVER

Editorial Board Member of *World Journal of Radiology*, Carlo N De Cecco, MD, PhD, Assistant Professor, Department of Radiology and Radiological Sciences, Medical University of South Carolina, Charleston, SC 29401, United States

AIM AND SCOPE

World Journal of Radiology (*World J Radiol*, *WJR*, online ISSN 1949-8470, DOI: 10.4329) is a peer-reviewed open access academic journal that aims to guide clinical practice and improve diagnostic and therapeutic skills of clinicians.

WJR covers topics concerning diagnostic radiology, radiation oncology, radiologic physics, neuroradiology, nuclear radiology, pediatric radiology, vascular/interventional radiology, medical imaging achieved by various modalities and related methods analysis. The current columns of *WJR* include editorial, frontier, diagnostic advances, therapeutics advances, field of vision, mini-reviews, review, topic highlight, medical ethics, original articles, case report, clinical case conference (clinicopathological conference), and autobiography.

We encourage authors to submit their manuscripts to *WJR*. We will give priority to manuscripts that are supported by major national and international foundations and those that are of great basic and clinical significance.

INDEXING/ABSTRACTING

World Journal of Radiology is now indexed in PubMed, PubMed Central, and Emerging Sources Citation Index (Web of Science).

NAME OF JOURNAL
World Journal of Radiology

ISSN
ISSN 1949-8470 (online)

LAUNCH DATE
January 31, 2009

FREQUENCY
Monthly

EDITORIAL OFFICE
Jin-Lei Wang, Director
World Journal of Radiology
Baishideng Publishing Group Inc
7901 Stoneridge Drive, Suite 501, Pleasanton, CA 94588, USA
Telephone: +1-925-2238242
Fax: +1-925-2238243
E-mail: editorialoffice@wjgnet.com
Help Desk: http://www.f6publishing.com/helpdesk
http://www.wjgnet.com

PUBLISHER
Baishideng Publishing Group Inc
7901 Stoneridge Drive, Suite 501,
Pleasanton, CA 94588, USA
Telephone: +1-925-2238242
Fax: +1-925-2238243
E-mail: bpgoffice@wjgnet.com
Help Desk: http://www.f6publishing.com/helpdesk
http://www.wjgnet.com

PUBLICATION DATE
June 28, 2018

INSTRUCTIONS TO AUTHORS
http://www.wjgnet.com/bpg/gerinfo/204

ONLINE SUBMISSION
http://www.f6publishing.com

World Journal of Radiology

Submit a Manuscript: http://www.f6publishing.com

World J Radiol 2018 June 28; 10(6): 52-64

DOI: 10.4329/wjr.v10.i6.52

ISSN 1949-8470 (online)

REVIEW

Magnetic resonance angiography for the primary diagnosis of pulmonary embolism: A review from the international workshop for pulmonary functional imaging

Nanae Tsuchiya, Edwin JR van Beek, Yoshiharu Ohno, Hiroto Hatabu, Hans-Ulrich Kauczor, Andrew Swift, Jens Vogel-Claussen, Jürgen Biederer, James Wild, Mark O Wielpütz, Mark L Schiebler

Nanae Tsuchiya, Department of Radiology, Graduate School of Medical Science, University of the Ryukyus, Okinawa 903-0215, Japan

Nanae Tsuchiya, Mark L Schiebler, Department of Radiology, University of Wisconsin-Madison, Madison, WI 53792, United States

Edwin JR van Beek, Edinburgh Imaging, Queen's Medical Research Institute, University of Edinburgh, Edinburgh EH16 4TJ, United Kingdom

Yoshiharu Ohno, Division of Functional and Diagnostic Imaging Research, Department of Radiology, Kobe University Graduate School of Medicine, Kobe 650-0017, Japan

Hiroto Hatabu, Department of Radiology, Brigham and Women's Hospital, Boston, MA 02115, United States

Hans-Ulrich Kauczor, Mark O Wielpütz, Department of Diagnostic and Interventional Radiology, University Hospital of Heidelberg, Heidelberg 69120, Germany

Andrew Swift, Department of Radiology, Royal Hallamshire Hospital, University of Sheffield, Sheffield S10 2JF, United Kingdom

Jens Vogel-Claussen, Department of Radiology, Carl-Neuberg Strasse 1, Hannover-Gr-Buchholz 30625, Germany

Jürgen Biederer, Radiology Darmstadt, Gross-Gerau County Hospital, Gross-Gerau 64521, Germany

James Wild, Department of Infection, Immunity and Cardiovascular Disease, University of Sheffield, Sheffield S10 2JF, United Kingdom

ORCID number: Nanae Tsuchiya (0000-0003-2556-8287); Edwin JR van Beek (0000-0002-2777-5071); Yoshiharu Ohno (0000-0002-4431-1084); Hiroto Hatabu (0000-0002-6259-0814); Hans-Ulrich Kauczor (0000-0001-7224-4758); Andrew Swift (0000-0001-9048-0121); Jens Vogel-Claussen (0000-0001-5595-6948); Jürgen Biederer (0000-0002-4262-6285); James Wild (0000-0002-7246-8660); Mark O Wielpütz (0000-0001-6962-037X); Mark L Schiebler (0000-0002-9120-5428).

Author contributions: Tsuchiya N contributed to design of the study, literature review and analysis, drafting and critical revision and editing, and final approval of the final version; van Beek EJR, Hatabu H and Kauczor HU contributed to conception and design of the study, drafting and critical revision and editing, and final approval of the final version; Ohno Y, Vogel-Claussen J, Wild J and Schiebler ML contributed to conception and design of the study, literature review and analysis, drafting and critical revision and editing, and final approval of the final version; Swift A and Wielpütz MO contributed to literature review and analysis, drafting and critical revision and editing, and final approval of the final version; Biederer J contributed to conception of study, literature review and analysis, drafting and critical revision and editing, and final approval of the final version.

Conflict-of-interest statement: There are no conflicts of interest related to this work. No financial support.

Manuscript source: Invited manuscript

Correspondence to: Mark L Schiebler, MD, Professor, Department of Radiology, University of Wisconsin-Madison, 600 Highland Avenue, Madison, WI 53792, United States. mschiebler@uwhealth.org
Telephone: +1-608-2657250

Fax: +1-608-2631229

Received: January 27, 2018
Peer-review started: January 30, 2018
First decision: March 19, 2018
Revised: April 25, 2018
Accepted: May 30, 2018
Article in press: May 30, 2018
Published online: June 28, 2018

Abstract

Pulmonary contrast enhanced magnetic resonance angiography (CE-MRA) is useful for the primary diagnosis of pulmonary embolism (PE). Many sites have chosen not to use CE-MRA as a first line of diagnostic tool for PE because of the speed and higher efficacy of computerized tomographic angiography (CTA). In this review, we discuss the strengths and weaknesses of CE-MRA and the appropriate imaging scenarios for the primary diagnosis of PE derived from our unique multi-institutional experience in this area. The optimal patient for this test has a low to intermediate suspicion for PE based on clinical decision rules. Patients in extremis are not candidates for this test. Younger women (< 35 years of age) and patients with iodinated contrast allergies are best served by using this modality We discuss the history of the use of this test, recent technical innovations, artifacts, direct and indirect findings for PE, ancillary findings, and the effectiveness (patient outcomes) of CE-MRA for the exclusion of PE. Current outcomes data shows that CE-MRA and NM V/Q scans are effective alternative tests to CTA for the primary diagnosis of PE.

Key words: Female; Lung; Neoplasms; Hypersensitivity; Pulmonary embolism; Magnetic resonance angiography; Radiation induced; Outcome assessment (health care); Artifacts; Computerized tomography angiography

Core tip: Pulmonary contrast enhanced magnetic resonance angiography (CE-MRA) is an effective alternative test for the primary diagnosis of pulmonary embolism (PE). In outcomes studies the negative predictive value of CE-MRA at 6 mo was 99%, which is similar to the negative predictive value of multidetector computerized tomographic angiography. The optimal patient selection is for younger female patients with a low to intermediate risk of PE or those with iodinated contrast allergies.

Tsuchiya N, van Beek EJR, Ohno Y, Hatabu H, Kauczor HU, Swift A, Vogel-Claussen J, Biederer J, Wild J, Wielpütz MO, Schiebler ML. Magnetic resonance angiography for the primary diagnosis of pulmonary embolism: A review from the international workshop for pulmonary functional imaging. *World J Radiol* 2018; 10(6): 52-64 Available from: URL: http://www.wjgnet.com/1949-8470/full/v10/i6/52.htm DOI: http://dx.doi.org/10.4329/wjr.v10.i6.52

INTRODUCTION

Acute pulmonary embolism (PE) affects 0.1% of the population annually and is associated with significant morbidity and mortality[1,2]. Common symptoms of PE are acute chest pain and dyspnea. When the patients have symptoms suspected PE, the first step is use of a clinical decision rules (CDR) such as the Wells' score, the Pulmonary Embolism Rule-out Criteria (PERC), the Revised Geneva score, the Simplified Revised Geneva score and a D-dimer test[3-5].

CTA of the chest is the current gold standard for the diagnosis of PE. In the recently published American College of Radiology (ACR) Appropriateness Criteria[6] for "Acute chest pain-suspected PE of intermediate probability with a negative D-dimer or low pretest probability", pulmonary magnetic resonance angiography (CE-MRA) is listed as 2 out of 10 for appropriateness (where 10/10 is the highest value for appropriateness), while multi-detector computed tomographic angiography (CTA) chest is listed at 5 out of 10 and a chest X-ray (CXR) is rated a 9 out 10. For "acute chest pain-suspected PE of intermediate probability with a positive D-dimer or high pretest probability", the ACR appropriateness criteria rate CE-MRA as 6 out of 10, CTA chest is rated at 9 out of 10 and a CXR is rated at 9 out 10. It is important to remember that the use of D-dimer for inpatients is limited due to their many comorbities. Further imaging workup is unnecessary for the patients with a negative D-dimer and a low clinical risk profile to exclude PE because the negative predictive value (NPV) does not change with the addition of an imaging test[3,4].

EARLY WORK

The use of pulmonary MRA is playing an increasingly important role for the primary diagnosis of PE and other causes of acute chest pain[2,7]. Early studies in this area began in 1993 and demonstrated the efficacy for the non-contrast MRA for depiction of PE. However, there were limitations that hampered routine clinical use. In one of the early prospective studies (18 patients) of the efficacy of non-contrast enhanced MRA for the diagnosis of PE found the sensitivity of two-dimensional time-of-flight pulmonary breath-hold MRA for detection of acute PE was 85% and was much lower for chronic emboli at 42%[8]. This group also showed that the size of the emboli was important for CE-MRA detection (PE larger than 1 cm were found with more than 75% confidence)[8]. In another prospective study (20 patients) from 1993, two-dimensional time-of-flight MRA had a sensitivity of 92%-100% and specificity of 62% for the diagnosis of PE[9]. A major limitation of these studies was their low sensitivity and specificity for chronic emboli, which were smaller and located eccentrically within

the pulmonary arteries (web-like). These limitations were due to low resolution, the artifacts from slow blood flow, and respiratory-motion artifacts (30-s breath-hold).

Since the 2000's, several studies have evaluated the performance of traditional contrast CE-MRA methods, namely breathhold, non-time resolved, 3D Cartesian encoded and T1-weighted spoiled gradient echo acquisitions. These studies[10-17] were often performed without parallel imaging and did not employ time-resolved (*e.g.*, 4 dimensional) k-space sampling which delineates the arterial and venous phases of the bolus passage thereby separating the pulmonary arteries from the pulmonary veins. In addition, 3D time-resolved CE-perfusion was not performed in conjunction with the routine CE-MRA in these works[10-17]. In comparison with the historic reference standard digital subtraction angiography (DSA), CE-MRA yielded a sensitivity and specificity for the detection of PE between 75% and 100% and 95% and 100%, respectively; with good interobserver agreement (k values of 0.57-0.83)[10-17].

In contrast to traditional CE-MRA, a study using time-resolved CE-MRA directly compared diagnostic performance with DSA, CTA and/or nuclear medicine ventilation/perfusion imaging, and showed better diagnostic performance than could be attained with DSA, CTA and/or nuclear medicine studies[14]. They showed a sensitivity and specificity of time-resolved CE-MRA of 83% and 97% on a per-vascular zone basis and 92% and 94% on a per-patient basis. In addition, the efficacy of time-resolved CE-MRA was higher than ventilation and perfusion scintigraphy (V/Q scan) on a per-patient basis. This study also showed that in comparison with CTA and VQ scans, time-resolved CE-MRA demonstrated equal to or higher sensitivity [92% *vs* 83% (CTA) and 67% (VQ scan)] and specificity [94% *vs* 94% (CTA) and 78% (VQ scan)] for the detection of PE[14].

Although time-resolved CE-MRA is useful for diagnosis of PE, dynamic first-pass CE-perfusion magnetic resonance imaging (MRI) is also helpful for disease severity assessment and outcome prediction in PE patients[17]. In this study, the acute pulmonary thromboembolism (APTE) index, which was defined as the ratio between the volume of perfusion defects and the total lung volume determined by means of dynamic first-pass CE-perfusion MRI, showed accuracy for the prediction of patient outcome similar to that of the right ventricular/left ventricular (RV/LV) diameter ratio[17]. In addition, the specificity and accuracy of the RV/LV diameter ratio and the APTE index determined by means of dynamic first-pass CE-perfusion MRI were significantly higher than those of APTE indexes obtained from embolic burdens and observed on CTACTA and time-resolved CE-MRA, although logistic regression analysis demonstrated that each index was a significant predictor[17]. Although quantitatively analyzable software was not commercially available, this study showed the potential utility of quantitatively assessed dynamic first-pass CE-perfusion MRI for patients with PE. Therefore, not only clinical researchers but also clinicians continue to urge companies in the field to provide appropriate MR systems, bolus injection protocols, MR sequences and software for clinical settings using this technique for suspected PE patients. Furthermore, there has been some work showing an advantage of MRI pulmonary perfusion assessment for patients suspected PE[17,18].

TEST EFFICACY

Prospective Investigation of Pulmonary Embolism Diagnosis Ⅲ (PIOPED Ⅲ) was a multicenter study designed to assess the efficacy of CE-MRA (without/with MR venography) for diagnosing PE and venous thromboembolism (VTE)[16]. They found that CE-MRA was technically inadequate in 25% of their studies and that CE-MRA had a sensitivity of 78%, and a specificity of 99%[16]. The two major reasons for this high rate of technical inadequacy were a strict definition for complete visualization of the subsegmental pulmonary arteries and the fact that some centers were just not as good as others in producing high quality studies[19]. They also found that using a combination of MRA and MR venography had a sensitivity of 92% and a specificity of 96%[16]. Their results showed limited efficacy of CE-MRA for the diagnosis of PE. Based on their findings, the authors recommended that CE-MRA should only be considered at those centers that had a sufficient technical expertise and in those patients for where standard tests were contraindicated[16].

The limitations of PIOPED Ⅲ included a slightly lower resolution CE-MRA and a lack of consistent technical quality amongst the multiple centers[16]. This study mentioned that CE-MRA could detect PE in a main or lobar pulmonary artery with a sensitivity of 79%. They also showed a sensitivity of 50% for segmental PE and 0% for detecting subsegmental PE (SSPE)[16]. In PIOPED Ⅲ, the proportion of technically inadequate examinations varied between centers and ranged from 11% up to 51%[16]. The reason why CE-MRA was technically inadequate was poor arterial opacification (67%), motion artifact (36%), wrap-around artifact (4%), and parallel imaging artifact (2%)[16]. Further retrospective analysis was by the PIOPED Ⅲ investigators to identify the factors of the CE-MRA examination that were associated with poor technical quality; they found that the two most important elements influencing MRA interpretability were vascular opacification and motion artifact[20].

TREATMENT FOR SUBSEGMENTAL PE REMAINS A CONUNDRUM

The significance of detecting subsegmental PE (SSPE) has been an ongoing debate for more than a decade[21]. An isolated SSPE could be a symptom of a thrombotic state, and may require treatment[22]. Recently Mehta

et al[23] have shown that withholding anticoagulation in patients with a single SSPE and negative bilateral lower extremity venous duplex ultrasound exams was a safe and effective strategy. However, systematic reviews demonstrated that no randomized controlled trial evidence exists to allow for a safe conclusion as to whether or not withholding anticoagulant therapy in isolated SSPE is safe[24,25]. Therefore, the detection of SSPE will remain an important issue. All interested parties should know that isolated SSPE are a problem for any diagnostic test, including the old gold (now bronze) reference method pulmonary angiography[26] and the new gold standard CTA[27]. Nevertheless, long-term follow-up studies after normal pulmonary angiography[28], normal perfusion scintigraphy[29] and normal CTA[30] have shown a low risk for recurrent disease after a single SSPE.

MITIGATION OF MEDICAL RADIATION

The reasons to continue to work on improving non-contrast and CE-MRA for diagnosing PE is the mitigation of medical radiation[31-34]. Ionizing radiation administered for medical imaging is of increasing clinical concern[3,35,36] and is a risk factor for the development of primary breast cancer[37,38]. The increased risk of breast cancer is associated with more imaging follow-up, higher cumulative radiation doses and exposure at a younger age[38]. CE-MRA is the only non-ionizing imaging modality with data supporting for the primary diagnosis of PE[39]. This modality is particularly useful for the follow up of previously diagnosed PE in younger individuals and the pediatric population to determine the efficacy of anticoagulation therapy, or the presence of new PE, as there is no incremental medical radiation. This strength of CE-MRA (no ionizing radiation) in younger patients helps to mitigate its lower efficacy for the detection of SSPE.

TEST EFFECTIVENESS

At University of Wisconsin-Madison over 2000 pulmonary CE-MRA examinations for the primary diagnosis of PE have been performed over the last ten years (2007-2017). The routine MRI protocol at UW-Madison is shown in Tables 1 and 2. We retrospectively reviewed the first 675 patients who underwent CE-MRA for the primary diagnosis of PE to determine the six-month adverse event rate following the use of CE-MRA[39]. For all these patients, the same 13-17 s breath hold contrast enhanced CE-MRA method was used, and the details of the MRA imaging protocol has been previously described[2]. We excluded 56 of 675 (8.3%) patients for the following reasons: on anti-coagulation, pre-existing IVC filter, or atrial fibrillation. Two of 675 (0.3%) were incomplete electronic medical record (EMR). Eventually, we included 617 (91.4%) patients to assess the effectiveness of CE-MRA[39]. Of the included cases, 500 (81%) were negative for PE, 17 (2.8%) were equivocal, 46 (7.5%) were positive for PE (Figure 1)[39]. The proportion of technically limited CE-MRA exams, as determined by the word "limited" in the final report, was 8.8%. This result is far lower than the 25% technical failure rate reported in the PIOPED Ⅲ[16]. This improvement in technical success likely reflects the maturation of CE-MRA methodology since the time of the PIOPED Ⅲ scans nearly a decade ago (2006-2008). In addition, this improvement may be related to the fact that lack of visualization of the subsegmental pulmonary arteries was not a criterion for determining the presence of a limited examination. Only three of 500 (0.6%) patients with a negative CE-MRA exam experienced a VTE within 6 mo of their exam. Thus, using just the rate of VTE, the NPV of CE-MRA was 99.4% in a data set that reflects the real world experience of this test[39]. This value is similar to the reported NPV for CTA (98.8%)[40]. At our single site, we have found that CE-MRA to be a safe and effective alternative to CTA for the primary diagnosis of PE.

PATIENT SELECTION

For accurate diagnosis, it is important to understand its appropriate use in the patient population. CE-MRA for the primary diagnosis of PE is most effective when used in patients with the following criteria: (1) a low to intermediate pretest probability for venous thromboembolic disease; (2) patients with iodinated contrast allergies; (3) female subjects less than 35 years of age that are potentially at slightly higher risk from medical radiation; and (4) for patients with renal insufficiency (eGFR < 30) the use of ferumoxytol as an MRA contrast agent may be considered. The contraindications for CE-MRA are as follows: (1) MRI incompatible implants[41]; (2) claustrophobia; (3) critically ill patients with a high pretest probability for PE; (4) inability to hold their breath for > 13 s; and (5) patients with gadolinium and ferumoxytol contrast allergies[42,43]. Please be aware of the fact that MRI is not safe for suspected PE patients that are unstable. This is because cardiopulmonary resuscitation can only be performed after the patient is out of the magnet room.

OVERVIEW OF TECHNICAL METHODS FOR CE-MRA IN ACUTE PE

Imaging the lungs with CE-MRA is inherently challenging as the method of blood pool enhancement is predominantly a T1 weighted contrast that is also constrained by a heavily T2* weighted background signal of the air within the lungs (0.5 ms and 2 ms T2*; at 1.5T and 3T respectively)[44]. As such, delineation of the smaller vessels is difficult and this is made more challenging by the changes in susceptibility of the vessels with contrast passage due to the T2* blooming effect. This effect can be mitigated by employing the following: (1) short echo time gradient echo sequenc-

Table 1 Pulmonary contrast-enhanced magnetic resonance angiograph imaging protocol at UW-Madison after Nagle *et al*[76]

Three-plane SSFSE localizers
Pre-contrast T1 weighted 3D SGRE
Pulmonary arterial phase T1-weighted 3D SGRE
Immediate post-contrast T1-weighted 3D SGRE
Low flip angle post-contrast T1-weighted 3D SGRE
T1-weighted 2D axial or 3D SGRE with fat saturation

SGRE: Spoiled gradient recalled echo; MRA: Magnetic resonance angiograph; SSFSE: Single-shot fast spin-echo.

Table 2 Pulmonary contrast-enhanced magnetic resonance angiograph pulse sequence parameters after Schiebler *et al*[2]

Parameter	Value
FOV	18-45 (to fit the patient) cm
Slice acquisition plane	Sagittal
Resolution[1]	SI 0.7 × RL 0.7 × AP 1.0 mm3
TR/TE	2.9 ms/1.0 ms
Parallel imaging factor	3.6
Flip angle	28° (15°for 2nd post-contrast "low flip angle" scan)
Bandwidth	± 88 kHz/pixel
Time for Breath hold	15-21 s

[1]Interpolated resolution in all three planes. TR: Time to repetition; TE: Time to echo; FOV: Field of view.

es[45], for better resolution of the underlying lung and vessel morphology; (2) scans at expiration; and (3) parallel imaging[46]. Due to the above reasons, CE-MRA is primarily performed at 1.5T. However, using methods like ultra-short echo time radial sampling[47] CE-MRA is also feasible at 3T. Incorporation of modest image acceleration factors using receiver array coils with auto calibrated parallel imaging and centric k-space encoding also helps in best capturing peak pulmonary arterial enhancement during bolus passage[2,48].

NON-CONTRAST PULMONARY MRA

Multiple approaches are available for non-contrast imaging of the pulmonary arteries, pulmonary veins and perfusion of the lung parenchyma (Figure 2). The general protocol recommendations for imaging acute PE includes fast MRI imaging sequences to increase sensitivity and specificity[15,49]. First, a steady state GRE sequence acquired in two or three planes during free breathing, may serve for early detection of large central emboli within the first five minutes of the examination - with a sensitivity of 90% and a specificity approaching 100% (Figure 3)[15,50,51]. Central embolism detected at this time can be directly referred to the intensive care unit for treatment, this is as efficient as diagnosis using CTA[49]. In many cases, such as in pregnancy when the administration of Gadolinium based contrast agents (GABA's) is critical, using a non-contrast enhanced MRA can provide a reliable exclusion of a massive central PE. The further contrast-enhanced steps of the recommended examination protocol would contribute to confirm this result and increase sensitivity and specificity (Figure 3)[2,49]. The diagnostic accuracy of a non-contrast enhanced examination could be improved by additional non-contrast enhanced perfusion imaging, based either on arterial spin labeling or on Fourier decomposition (Figure 2). Both have been shown to be sensitive for lung perfusion deficits related to acute PE, but are still on an experimental level[52].

The high contrast to noise of the blood pool with a steady state free precession sequence means that it can serve as a non-contrast enhanced MR angiogram[53] when performed in 3D breathhold. Recent developments with 3D UTE SSFP and zero echo time sequences[54] also hold promise, however the lack of arterial and venous separation poses diagnostic limitations on this method when compared to state of the art CE MRA. Fourier decomposition (FD) MRI uses a continuously acquired two-dimensional steady-state free-precession (SSFP) or fast low angle shot (FLASH) acquisitions[55,56]. Since lung signal changes with inspiration depth (highest signal with lowest pulmonary air content in expiration) and cardiac motion (lowest signal with maximum blood flow in systole), both result in periodic changes of lung parenchymal signal that can be separated by means of Fourier decomposition[57]. Perfusion and ventilation-weighted images are generated from the high frequency oscillations related to the effects of pulsatile blood flow and the low-frequency lung signal oscillation related to respiration without contrast[55,58]. Further promising new developments of this technique using self-gated non-contrast-enhanced functional lung imaging (SENCEFUL) or phase-resolved functional lung (PREFUL) MRI have reported[59,60]. Principally, this technique has the potential to replace V/Q scans and has been already been validated against single-photon emission computed tomography (SPECT) perfusion and ventilation imaging[61], and against hyperpolarized 3He and perfusion MRI[62,63]. In a single center study, perfusion weighted FD MRI showed encouraging results for the diagnosis of PE in the non-acute clinical setting[64]. Arterial spin labeling (ASL) uses the intrinsic contrast of magnetized, inflowing blood into the imaging plane or volume without the need of contrast material injection[52,65]. In scientific applications, ASL has been used to study of the effects of inhaled oxygen concentration and physical exercise on ventilation-perfusion heterogeneity of the lungs in healthy human subjects[66-68]. However, although being principally suitable for the detection of lung perfusion deficits related to acute PE, neither arterial spin labeling nor Fourier decomposition MRI have been clinically implemented for the assessment of acute PE, mainly because of the lower robustness against artifacts, lower spatial resolution and inferior signal to noise compared to contrast enhanced dynamic perfusion imaging[52]. Therefore, currently only steady-state GRE sequences are used when a non-contrast enhanced MRI of the pulmonary vessels is required.

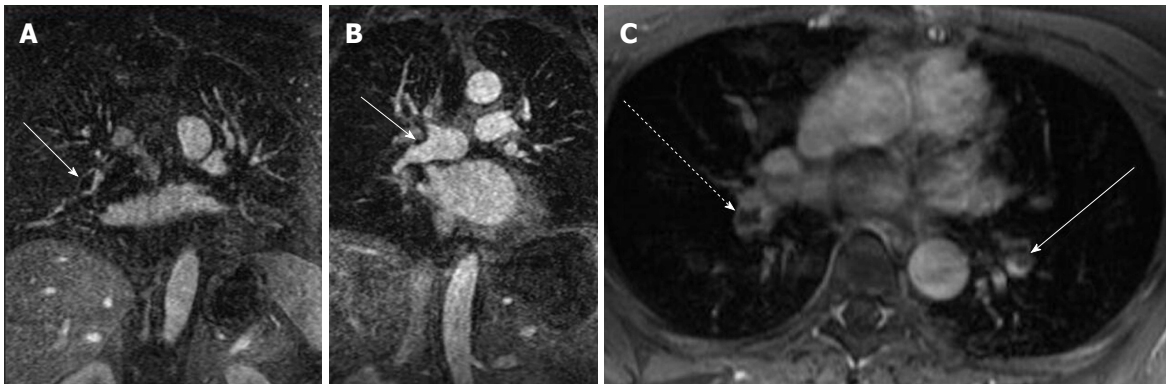

Figure 1 Direct findings of pulmonary embolism. A: CE-MRA shows a filling defect in the interlobar artery (white arrow) consistent with the expected appearance of a pulmonary embolus (arrow); B: CE-MRA showing an eccentrically located pulmonary embolus that spans the truncus anterior and interlobar artery (arrow); C: Post gadolinium fat saturated breath hold axial spoiled gradient echo image showing bilateral filling defects in the lower lobe pulmonary arteries (interlobar PE-dashed arrow, left lower lobe pulmonary artery-arrow). CE-MRA: Contrast enhanced magnetic resonance angiograph; PE: Pulmonary embolism.

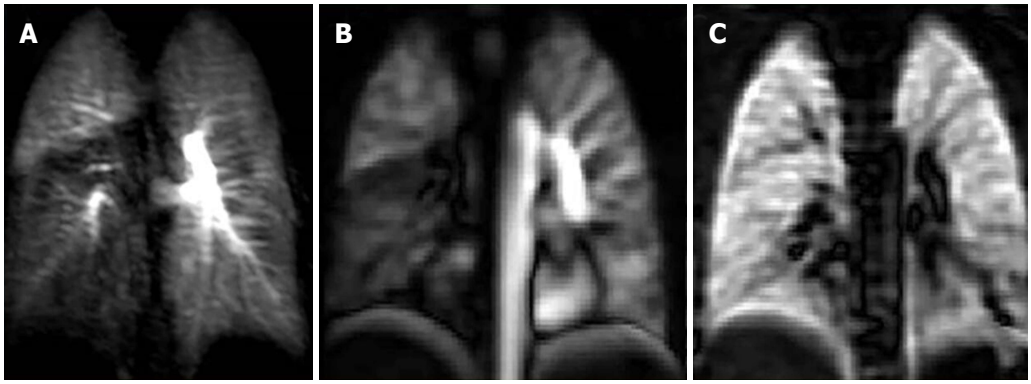

Figure 2 Case of pulmonary embolism to the right lower lobe. A: Coronal dynamic contrast MRI shows notable right lower lobe hypo-perfusion in a 25-year-old female with known acute pulmonary embolism one month ago; B: Corresponding (non-contrast) Fourier decomposition (FD) perfusion; C: Ventilation-weighted FD MR images also depict right lower lobe hypo-perfusion and normal ventilation (VQ mismatch). MRI: Magnetic resonance imaging.

SAFETY OF GADOLINIUM BASED CONTRAST AGENTS

Currently GBCA's are used for CE-MRA, even in those patients with borderline renal function[69]. A recent meta-analysis has shown that higher iconicity, protein binding and macrocyclic structures of GBCA's are associated with an increased number of acute allergic reactions[42].

Recently work has shown gadolinium deposition in the brains, skin and bones of patients with normal renal function[70-72]. This can occur when linear or macrocyclic chelates GBCAs are used[73]. The association between the tissue deposition of gadolinium from GBCAs and any short or long-term clinical importance remains to be determined[74]. Due to concerns over brain Gadolinium deposition, macrocyclic agents such gadoterate meglumine and gadobutol are preferred[75].

We currently recommend injection of 0.1 mmol/kg of GBCA diluted to a total volume of 30 mL with saline injected at 1.5 mL/s at end-expiration[2,76]. The total length of time for the bolus administration of contrast material is important. Diluting the contrast with normal saline up to a volume of 30 mL allows administration of the entire length of the acquisition and thus helps to limit Maki artifacts (Figure 3). This artifact occurs when the scan acquisition starts before the bolus arrives, the effect is an edge-enhanced image and this can simulate PE[77].

RENAL FAILURE

An option for patients with renal failure or GBCA allergy is the off-label use of Ferumoxytol as a MRA contrast agent[78]. Ferumoxytol is an intravenously administered ultrasmall superparamagnetic iron oxide agent for treatment of anemia in adult patients. The standard intravenous dose is 3.0 mg/kg. There is a Food and Drug Administration "black box" warning against the rapid bolus administration of this agent, as it has been associated with hypotension and death. The rate of anaphylaxis is low at 0.02% to 1.3%[43]. Its T1 and T2 shortening effects, long blood-pool residence time and clearance through the reticuloendothelial system makes this a versatile MRI contrast agent[43,79]. Moreover, Ferumoxytol avoids any risk of Nephrogenic Systemic Fibrosis for patients with renal failure.

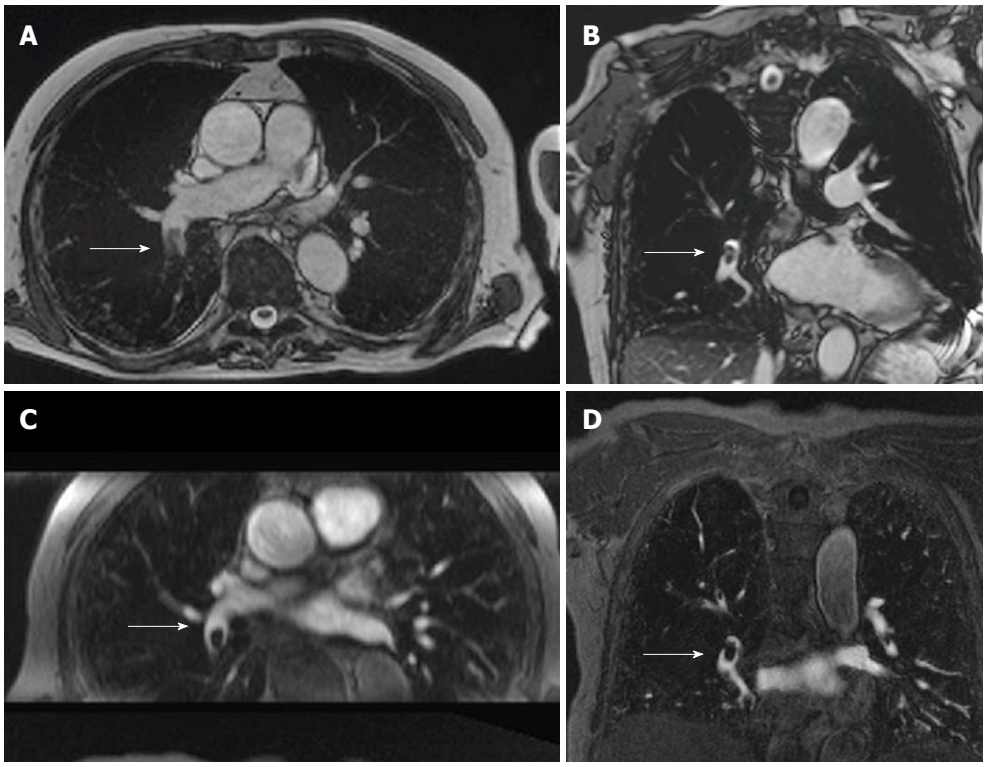

Figure 3 Non-contrast pulmonary magnetic resonance angiograph of an 82-year-old male with a history of san acute onset of dyspnea. A: Transverse non-contrast enhanced steady state GRE; B: Coronal oblique non-contrast enhanced steady-state GRE images of a fresh embolus in the right lower lobe artery; C: For comparison the transverse reformation; D: The original coronal images from the contrast-enhanced MRA (images courtesy of Heussel CP and Wielpuetz M, Thoraxklinik, Heidelberg, Germany). GRE: Gradient recalled echo; MRA: Magnetic resonance angiograph.

PREGNANCY

PE is one of the causes of death in the pregnancy[80,81]. The diagnosis of PE in these patients is challenging because of the necessity of keeping medical radiation exposure to a minimum. The American Thoracic Society and the Society of Thoracic Radiology have reached consensus in this clinical scenario[82]. They recommend ventilation-perfusion (V/Q) scintigraphy as a first line test to detect PE in pregnant patients with normal chest radiographs, with CTA reserved for those mothers with abnormal chest radiographs or indeterminate V/Q scans[82]. This remains an active area of research[83]. Non-contrast MRA using bright blood pulse sequences (bSSFP) and unenhanced Fourier decomposition lung perfusion are other options in this scenario that is non-ionizing and without contrast for the mother and fetus (Figure 2)[72,84]. Unfortunately, CE-MRA using GBCAs is limited because these agents cross the placenta to the fetus and there are reports of rheumatological, inflammatory, and infiltrative skin conditions in those exposed neonates[85]. Fortunately, there is another option for CE-MRA in this situation; the United States Food and Drug Administration has approved Ferumoxytol for use in pregnancy as a treatment for anemia, and we have used it (off-label) for CE-MRA in pregnant patients[86]. A recent Cochrane review assessed the value CTA, lung scintigraphy or MRA in pregnant patients with suspected PE[87]. No MRI examinations met the inclusion criteria for the study. The authors concluded that both CTA and lung scintigraphy are appropriate for exclusion of PE in pregnancy, however it was unclear which test had the higher accuracy. They emphasized the need for direct comparisons and the need to include MRI in prospective trials in this clinical scenario[87].

ARTIFACTS

Truncation artifact (Gibbs" ringing) is showed as a distinct central signal intensity drop within the pulmonary vasculature in pulmonary contrast-enhanced MRA[88]. Gibbs' ringing may be misdiagnosed as PE (Figure 4), particularly by inexperienced MRA readers. The differentiation between Gibbs' ringing and emboli is important. The signal intensity of this artifact is typically 50% or higher than the enhanced surrounding vessel lumen[88]. Errors approximation in the Fourier transformation from k-space to image space causes this artifact (Figure 3). Routine Cartesian reconstructions of k-space into image space performs better when used for estimating gradual transitions in tissue signal intensity, not sharp ones[88]. There are cases where a Gibbs' artifact is not distinguishable from a small central non-occlusive PE[88]. In those cases, a confirmatory CTA exam is required for an accurate diagnosis. The Maki artifact[77] can also simulate a PE. This error in image interpretation is avoidable by using multiple contrast phases and extending the bolus so that contrast is al-

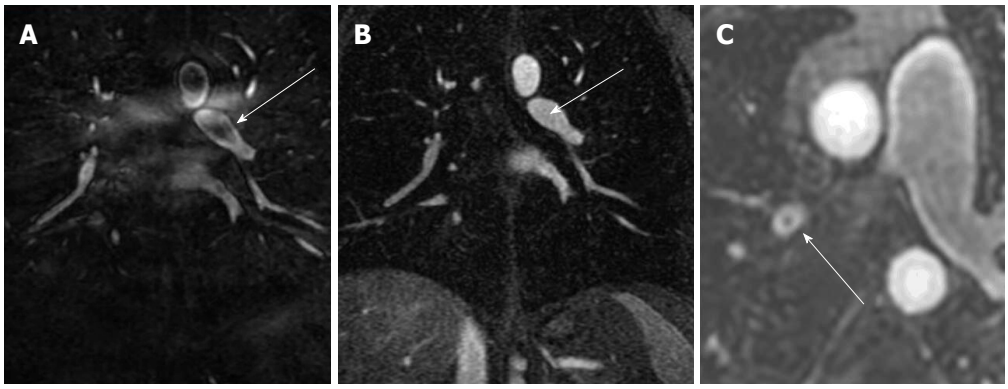

Figure 4 Artifacts: The Maki artifact. A: Acquisition of the central aspect of k-space was before the bolus of contrast agent filled the pulmonary artery causing a pseudo-clot within the left lower lobe pulmonary artery (arrow); B: Later phase acquisition from the same patient shows normal contrast enhancement of the Left lower lobe pulmonary artery (arrow); C: Gibbs'' ringing artifact can simulate a central filling defect. Typically, the signal of emboli will be less than 50% of the signal intensity of the lumen.

ways flowing into the pulmonary arteries during the first acquisition (Figure 3)[76].

ANCILLARY FINDINGS

The ancillary findings observed on CE-MRA exams in those patients without PE are similar to those of CTA (Figure 5)[89,90]. The field of view is larger and the soft tissue contrast is better on CE-MRA exams than CTA. In a recent study, the incidence of actionable findings (requiring follow up) from CE-MRA exams was 17% (pleural effusion, pneumonia, malignancy, ascending aortic aneurysm, aortic dissection, pericardial effusion, heart failure, septic emboli, lung abscess, trauma, and sarcoidosis). While the incidence of incidental findings (those findings not requiring follow up) was 36% (mild dependent atelectasis, small pleural effusion, normal vascular variant, simple cysts in liver or kidney and post-surgical changes)[89].

DIRECT AND INDIRECT FINDINGS OF PE

Just like multidetector computed tomographic angiography MDCT, PE are detected as a lumenal filling defect in the pulmonary arteries on CE-MRA (Figure 1). Other direct findings include that arterial cutoff sign, double bronchus sign, and high T1 signal intensity clots. The indirect findings include atelectasis, pleural effusion, high signal adjacent draining pulmonary vein, the "W-B-W" (white-black-white) sign, perfusion defects, enhancing visceral pleural surfaces, and an enlarged pulmonary trunk. Other findings indicative of right heart strain and elevated central venous pressure can help to estimate the degree of right heart dysfunction with larger clot burden[7,91].

FREE BREATHING PE-MRA

In the PIOPED Ⅲ study, the sensitivity of PE detected by MRA in subsegmental artery was 0%[16]. The emboli in subsegmental vessels on MRA are difficult to distinguish from lung parenchyma or a nearby bronchus as this is a "black-on-black" perceptual event. Bannas *et al*[47] showed that free-breathing 3D radial ultra-short time to echo (UTE) imaging[45] can detect PE in subsegmental vessels. The reason for this is the high SNR of lung parenchyma in the UTE image. Their method used a free-breathing 3D radial UTE technique, which is quite advantageous in the setting of dyspnea, a common presenting symptom of PE.

OVERDIAGNOSIS OF PE USING MDCT

MDCT is the gold standard for the primary diagnosis of PE[6]. The SSPE, which are not detected with V/Q scintigraphy or earlier generation single detector CT, are now routinely diagnosed with MDCT[92]. Le Gal *et al*[92] in a review found that that MDCT found twice as many SSPE as the single detector CT scans. Sheh *et al*[93] First introduced the concept of "overdiagnosis" of PE due to the change from V/Q scintigraphy to MDCT and an increased diagnosis of a much less fatal spectrum of PE. In contrast to the idea that SSPE is benign, other authors have shown that the presence of SSPE remains important for the likelihood of future venous thromboembolism (VTE)[94-96]. Current clinical practice guidelines suggest that anticoagulation therapy of these SSPE should be tailored to the individual patient's risks and benefits[96]. The American College of Chest Physicians 2016 guidelines now recommend withholding anticoagulation for SSPE in those patients with a low risk for recurrent thrombus and no concurrent deep vein thrombosis[97].

WEAKNESSES OF MRA

There are limitations for the use of MRA for the primary diagnosis of PE. First, this modality should not be used for unstable patients. Second, patients with allergies to gadolinium based contrast material should only be imaged if there is no access to MDCT or Ventilation Perfusion scanning, and only then after premedication

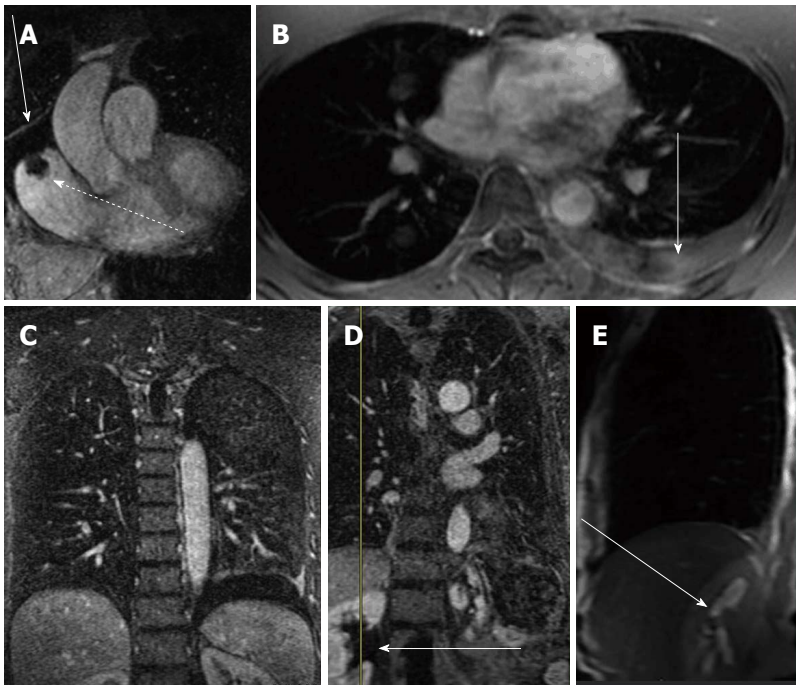

Figure 5 Ancillary findings on contrast enhanced magnetic resonance angiograph exams. A: Contrast enhanced MRA shows a right atrial thrombus from a long standing indwelling central venous catheter (dashed arrow) and a pericardial effusion (straight arrow); B: Post contrast breath hold fat saturated gradient echo showing a left pleural effusion (arrow); C: CE-MRA coronal image showing the same left pleural effusion (arrow); D: CE-MRA showing right renal pelvis hydronephrosis (arrow); E: Fast spin echo scout sagittal image through the right renal pelvis showing the high signal intensity of the hydronephrosis (arrow). CE-MRA: Contrast enhanced magnetic resonance angiograph.

with steroids for 24 h and Benadryl. Third, small children or adults who are unable to hold their breath, or hold still, for the 13-20 s MRA are poor candidates for this exam. Fourth, readers experienced with the interpretation of MRA for PE are needed to ensure that the correct diagnosis is reached in these exams. Fifth, up to date MRI hardware (high performance gradients and multicoils) and software (rapid k-space sampling and accelerated image acquisition) are needed to allow for the acquisition of 3D MRA exams with nearly isotropic voxels. There is noise associated with the rapid switching of the gradient coils that may bother some patients if there is not adequate hearing protection.

The costs of this test will vary depending on each country's healthcare plan. In our experience, the cost of this procedure is similar to MSCT for PE. There can be access challenges for the emergent use of CE-MRI for PE from the Emergency Department. With effort, we have found that the time from order to final interpretation of these exams can be around one hour[76]. Experienced sites will not have difficulty starting a CE-MRA program for the primary diagnosis of PE, however we recognize that there are many medical centers that do not have access to these instruments and lack adequately trained medical/technical staff for the performance of these exams. In this low to intermediate risk patient population, there are many patients that do not need imaging; this is why the careful application of CDR's is needed to screen all patients prior to ordering an exam for PE.

PERFORMANCE GAP: CE-MRA EFFECTIVENESS > EFFICACY

The most recent effectiveness data from UW-Madison showed a negative predictive value of 99% (95%CI: 97%-100%) in 500 patients[39]. The reader can easily surmise that this effectiveness value (NPV-99%) is quite different than the efficacy value (sensitivity -77%) reported in PIOPED Ⅲ[16]. How do we reconcile this difference? Perhaps this relative "over-performance" of CE-MRA, using outcomes data as a surrogate for effectiveness, *vs* the lower efficacy can be explained by the following possibilities: (1) Better technical CE-MRA exams than were available for PIOPED Ⅲ; (2) Readers experienced with the artifacts of this exam; and (3) Small PE in younger and healthy patients, that may be missed on CE-MRA or NM V/Q scanning are not important for survival or subsequent VTE. One reason for this may be that these isolated SSPE's may indeed be "scrubbed" from the pulmonary arterial vasculature by the patient's endogenous thrombolytic activity. Another possible reason is that there is a great deal of cardiopulmonary reserve and that sacrifice of a few subsegmental pulmonary arteries is not significant in the normal population. Please note that the situation of repeated SSPE may lead to chronic thromboembolic pulmonary hypertension[98].

Recently Cronin and Dwamena[99] have used the PIOPED Ⅱ data to calculate likelihood ratios (LR) for PE in this cohort based on the pretest probability from

CDR (*e.g.*, Wells' score, Geneva score and Pisa score). The use of LR is important in this age of outcomes driven research as these reflect the clinical utility of any given testing method. The numerator of the positive LR (+LR) is the sensitivity of the test for that disease. The denominator is 1-specificity of the test for that disease[99]. Their analysis showed that the use of CE-MRA for the diagnosis of PE had a higher LR+ than CTA[99].

LR+ = Sensitivity/(1-specificity)

CONCLUSION

Currently computed tomographic angiography is the study of choice for the diagnosis of PE. We have reviewed our experience using pulmonary CE-MRA as a first line diagnostic test for patients suspected of having PE. We have found equivalent six-month outcomes to computed tomographic angiography when using this test. We recommend using strict patient selection criteria for improving the likelihood for the technical success of this test. First, a low to intermediate pretest probability for venous thromboembolic disease by the formalized is used of CDR (Wells' criteria, PERC or the Geneva score); Second, patients with iodinated contrast allergies can benefit from using this test; Third, female subjects less than 35 years of age to mitigate medical radiation exposure to the breast; Fourth, employing ferumoxytol as the MRA contrast agent in renal failure patients; Finally, yet importantly, ensuring that the patient is stable and can hold their breath for the 13-17 s CE-MRA. There is no overdiagnosis of PE when CE-MRA or NM V/Q scanning is used. In other words, these "less sensitive" tests may suffice for the primary diagnosis of PE. We are supportive of funding for randomized clinical trials to evaluate whether or not the clinical outcomes significantly vary between CTA and CE-MRA for the primary diagnosis of PE, as this remains an unmet need.

ACKNOWLEDGEMENTS

The authors wish to acknowledge the research support of the Department of Radiology, UW-Madison and GE Healthcare.

REFERENCES

1 **Siegel R**, Naishadham D, Jemal A. Cancer statistics, 2012. *CA Cancer J Clin* 2012; **62**: 10-29 [PMID: 22237781 DOI: 10.3322/caac.20138]

2 **Schiebler ML**, Nagle SK, François CJ, Repplinger MD, Hamedani AG, Vigen KK, Yarlagadda R, Grist TM, Reeder SB. Effectiveness of MR angiography for the primary diagnosis of acute pulmonary embolism: clinical outcomes at 3 months and 1 year. *J Magn Reson Imaging* 2013; **38**: 914-925 [PMID: 23553735 DOI: 10.1002/jmri.24057]

3 **Levin D**, Seo JB, Kiely DG, Hatabu H, Gefter W, van Beek EJ, Schiebler ML; 2013 International Workshop for Pulmonary Functional Imaging (IWPFI). Triage for suspected acute Pulmonary Embolism: Think before opening Pandora's Box. *Eur J Radiol* 2015; **84**: 1202-1211 [PMID: 25864020 DOI: 10.1016/j.ejrad.2015.03.023]

4 **Harringa JB**, Bracken RL, Nagle SK, Schiebler ML, Pulia MS, Svenson JE, Repplinger MD. Negative D-dimer testing excludes pulmonary embolism in non-high risk patients in the emergency department. *Emerg Radiol* 2017; **24**: 273-280 [PMID: 28116533 DOI: 10.1007/s10140-017-1478-6]

5 **Sikkens JJ**, Beekman DG, Thijs A, Bossuyt PM, Smulders YM. How Much Overtesting Is Needed to Safely Exclude a Diagnosis? A Different Perspective on Triage Testing Using Bayes' Theorem. *PLoS One* 2016; **11**: e0150891 [PMID: 26939066 DOI: 10.1371/journal.pone.0150891]

6 **Expert Panels on Cardiac and Thoracic Imaging**. Kirsch J, Brown RKJ, Henry TS, Javidan-Nejad C, Jokerst C, Julsrud PR, Kanne JP, Kramer CM, Leipsic JA, Panchal KK, Ravenel JG, Shah AB, Mohammed TL, Woodard PK, Abbara S. ACR Appropriateness Criteria® Acute Chest Pain-Suspected Pulmonary Embolism. *J Am Coll Radiol* 2017; **14**: S2-S12 [PMID: 28473076 DOI: 10.1016/j.jacr.2017.02.027]

7 **François CJ**, Hartung MP, Reeder SB, Nagle SK, Schiebler ML. MRI for acute chest pain: current state of the art. *J Magn Reson Imaging* 2013; **37**: 1290-1300 [PMID: 23589367 DOI: 10.1002/jmri.24173]

8 **Schiebler ML**, Holland GA, Hatabu H, Listerud J, Foo T, Palevsky H, Edmunds H, Gefter WB. Suspected pulmonary embolism: prospective evaluation with pulmonary MR angiography. *Radiology* 1993; **189**: 125-131 [PMID: 8372181 DOI: 10.1148/radiology.189.1.8372181]

9 **Grist TM**, Sostman HD, MacFall JR, Foo TK, Spritzer CE, Witty L, Newman GE, Debatin JF, Tapson V, Saltzman HA. Pulmonary angiography with MR imaging: preliminary clinical experience. *Radiology* 1993; **189**: 523-530 [PMID: 8210385 DOI: 10.1148/radiology.189.2.8210385]

10 **Meaney JF**, Weg JG, Chenevert TL, Stafford-Johnson D, Hamilton BH, Prince MR. Diagnosis of pulmonary embolism with magnetic resonance angiography. *N Engl J Med* 1997; **336**: 1422-1427 [PMID: 9145679 DOI: 10.1056/NEJM199705153362004]

11 **Gupta A**, Frazer CK, Ferguson JM, Kumar AB, Davis SJ, Fallon MJ, Morris IT, Drury PJ, Cala LA. Acute pulmonary embolism: diagnosis with MR angiography. *Radiology* 1999; **210**: 353-359 [PMID: 10207414 DOI: 10.1148/radiology.210.2.r99fe53353]

12 **Oudkerk M**, van Beek EJ, Wielopolski P, van Ooijen PM, Brouwers-Kuyper EM, Bongaerts AH, Berghout A. Comparison of contrast-enhanced magnetic resonance angiography and conventional pulmonary angiography for the diagnosis of pulmonary embolism: a prospective study. *Lancet* 2002; **359**: 1643-1647 [PMID: 12020524 DOI: 10.1016/S0140-6736(02)08596-3]

13 **Ohno Y**, Kawamitsu H, Higashino T, Takenaka D, Watanabe H, van Cauteren M, Fujii M, Hatabu H, Sugimura K. Time-resolved contrast-enhanced pulmonary MR angiography using sensitivity encoding (SENSE). *J Magn Reson Imaging* 2003; **17**: 330-336 [PMID: 12594723 DOI: 10.1002/jmri.10261]

14 **Ohno Y**, Higashino T, Takenaka D, Sugimoto K, Yoshikawa T, Kawai H, Fujii M, Hatabu H, Sugimura K. MR angiography with sensitivity encoding (SENSE) for suspected pulmonary embolism: comparison with MDCT and ventilation-perfusion scintigraphy. *AJR Am J Roentgenol* 2004; **183**: 91-98 [PMID: 15208117 DOI: 10.2214/ajr.183.1.1830091]

15 **Kluge A**, Luboldt W, Bachmann G. Acute pulmonary embolism to the subsegmental level: diagnostic accuracy of three MRI techniques compared with 16-MDCT. *AJR Am J Roentgenol* 2006; **187**: W7-14 [PMID: 16794142 DOI: 10.2214/AJR.04.1814]

16 **Stein PD**, Chenevert TL, Fowler SE, Goodman LR, Gottschalk A, Hales CA, Hull RD, Jablonski KA, Leeper KV Jr, Naidich DP, Sak DJ, Sostman HD, Tapson VF, Weg JG, Woodard PK; PIOPED III (Prospective Investigation of Pulmonary Embolism Diagnosis III) Investigators. Gadolinium-enhanced magnetic resonance angiography for pulmonary embolism: a multicenter prospective study (PIOPED III). *Ann Intern Med* 2010; **152**: 434-443, W142-W143 [PMID: 20368649 DOI: 10.7326/0003-4819-152-7-201004060-00008]

17 **Ohno Y**, Koyama H, Matsumoto K, Onishi Y, Nogami M, Take-

naka D, Yoshikawa T, Matsumoto S, Sugimura K. Dynamic MR perfusion imaging: capability for quantitative assessment of disease extent and prediction of outcome for patients with acute pulmonary thromboembolism. *J Magn Reson Imaging* 2010; **31**: 1081-1090 [PMID: 20432342 DOI: 10.1002/jmri.22146]

18 **Kalb B**, Sharma P, Tigges S, Ray GL, Kitajima HD, Costello JR, Chen Z, Martin DR. MR imaging of pulmonary embolism: diagnostic accuracy of contrast-enhanced 3D MR pulmonary angiography, contrast-enhanced low-flip angle 3D GRE, and nonenhanced free-induction FISP sequences. *Radiology* 2012; **263**: 271-278 [PMID: 22438448 DOI: 10.1148/radiol.12110224]

19 **Sostman HD**, Jablonski KA, Woodard PK, Stein PD, Naidich DP, Chenevert TL, Weg JG, Hales CA, Hull RD, Goodman LR, Tapson VF. Factors in the technical quality of gadolinium enhanced magnetic resonance angiography for pulmonary embolism in PIOPED III. *Int J Cardiovasc Imaging* 2012; **28**: 303-312 [PMID: 21347594 DOI: 10.1007/s10554-011-9820-7]

20 **Woodard PK**, Chenevert TL, Sostman HD, Jablonski KA, Stein PD, Goodman LR, Londy FJ, Narra V, Hales CA, Hull RD, Tapson VF, Weg JG. Signal quality of single dose gadobenate dimeglumine pulmonary MRA examinations exceeds quality of MRA performed with double dose gadopentetate dimeglumine. *Int J Cardiovasc Imaging* 2012; **28**: 295-301 [PMID: 21337023 DOI: 10.1007/s10554-011-9821-6]

21 **Goodman LR**. Small pulmonary emboli: what do we know? *Radiology* 2005; **234**: 654-658 [PMID: 15734923 DOI: 10.1148/radiol.2343041326]

22 **Yoo HH**, Queluz TH, El Dib R. Anticoagulant treatment for subsegmental pulmonary embolism. *Cochrane Database Syst Rev* 2016; **(1)**: CD010222 [PMID: 26756331 DOI: 10.1002/14651858.CD010222.pub3]

23 **Mehta D**, Barnett M, Zhou L, Woulfe T, Rolfe-Vyson V, Rowland V, Simpson D, Merriman E. Management and outcomes of single subsegmental pulmonary embolus: a retrospective audit at North Shore Hospital, New Zealand. *Intern Med J* 2014; **44**: 872-876 [PMID: 24942202 DOI: 10.1111/imj.12507]

24 **Carrier M**, Righini M, Wells PS, Perrier A, Anderson DR, Rodger MA, Pleasance S, Le Gal G. Subsegmental pulmonary embolism diagnosed by computed tomography: incidence and clinical implications. A systematic review and meta-analysis of the management outcome studies. *J Thromb Haemost* 2010; **8**: 1716-1722 [PMID: 20546118 DOI: 10.1111/j.1538-7836.2010.03938.x]

25 **Yoo HH**, Queluz TH, El Dib R. Anticoagulant treatment for subsegmental pulmonary embolism. *Cochrane Database Syst Rev* 2014; **(4)**: CD010222 [PMID: 24771493 DOI: 10.1002/14651858.CD010222.pub2]

26 **van Beek EJ**, Bakker AJ, Reekers JA. Pulmonary embolism: interobserver agreement in the interpretation of conventional angiographic and DSA images in patients with nondiagnostic lung scan results. *Radiology* 1996; **198**: 721-724 [PMID: 8628860 DOI: 10.1148/radiology.198.3.8628860]

27 **Anderson DR**, Kahn SR, Rodger MA, Kovacs MJ, Morris T, Hirsch A, Lang E, Stiell I, Kovacs G, Dreyer J, Dennie C, Cartier Y, Barnes D, Burton E, Pleasance S, Skedgel C, O'Rouke K, Wells PS. Computed tomographic pulmonary angiography vs ventilation-perfusion lung scanning in patients with suspected pulmonary embolism: a randomized controlled trial. *JAMA* 2007; **298**: 2743-2753 [PMID: 18165667 DOI: 10.1001/jama.298.23.2743]

28 **van Beek EJ**, Brouwerst EM, Song B, Stein PD, Oudkerk M. Clinical validity of a normal pulmonary angiogram in patients with suspected pulmonary embolism-a critical review. *Clin Radiol* 2001; **56**: 838-842 [PMID: 11895301 DOI: 10.1053/crad.2001.0778]

29 **van Beek EJ**, Kuyer PM, Schenk BE, Brandjes DP, ten Cate JW, Büller HR. A normal perfusion lung scan in patients with clinically suspected pulmonary embolism. Frequency and clinical validity. *Chest* 1995; **108**: 170-173 [PMID: 7606954 DOI: 10.1378/chest.108.1.170]

30 **van der Hulle T**, van Es N, den Exter PL, van Es J, Mos ICM, Douma RA, Kruip MJHA, Hovens MMC, Ten Wolde M, Nijkeuter M, Ten Cate H, Kamphuisen PW, Büller HR, Huisman MV, Klok FA. Is a normal computed tomography pulmonary angiography safe to rule out acute pulmonary embolism in patients with a likely clinical probability? A patient-level meta-analysis. *Thromb Haemost* 2017; **117**: 1622-1629 [PMID: 28569924 DOI: 10.1160/TH17-02-0076]

31 **Brenner DJ**. What we know and what we don't know about cancer risks associated with radiation doses from radiological imaging. *Br J Radiol* 2014; **87**: 20130629 [PMID: 24198200 DOI: 10.1259/bjr.20130629]

32 **Shuryak I**, Brenner DJ. Mechanistic analysis of the contributions of DNA and protein damage to radiation-induced cell death. *Radiat Res* 2012; **178**: 17-24 [PMID: 22663149 DOI: 10.1667/RR2877.1]

33 **Brenner DJ**. Radiation and chest CT scans: are there problems? What should we do? *Chest* 2012; **142**: 549-550 [PMID: 22948569 DOI: 10.1378/chest.12-0490]

34 **Brenner DJ**. We can do better than effective dose for estimating or comparing low-dose radiation risks. *Ann ICRP* 2012; **41**: 124-128 [PMID: 23089011 DOI: 10.1016/j.icrp.2012.07.001]

35 **Journy NMY**, Dreuil S, Boddaert N, Chateil JF, Defez D, Ducoule-Pointe H, Garcier JM, Guersen J, Habib Geryes B, Jahnen A, Lee C, Payen-de-la-Garanderie J, Pracros JP, Sirinelli D, Thierry-Chef I, Bernier MO. Individual radiation exposure from computed tomography: a survey of paediatric practice in French university hospitals, 2010-2013. *Eur Radiol* 2018; **28**: 630-641 [PMID: 28836026 DOI: 10.1007/s00330-017-5001-y]

36 **Journy NM**, Lee C, Harbron RW, McHugh K, Pearce MS, Berrington de González A. Projected cancer risks potentially related to past, current, and future practices in paediatric CT in the United Kingdom, 1990-2020. *Br J Cancer* 2017; **116**: 109-116 [PMID: 27824812 DOI: 10.1038/bjc.2016.351]

37 **Pijpe A**, Andrieu N, Easton DF, Kesminiene A, Cardis E, Noguès C, Gauthier-Villars M, Lasset C, Fricker JP, Peock S, Frost D, Evans DG, Eeles RA, Paterson J, Manders P, van Asperen CJ, Ausems MG, Meijers-Heijboer H, Thierry-Chef I, Hauptmann M, Goldgar D, Rookus MA, van Leeuwen FE; GENEPSO; EMBRACE; HEBON. Exposure to diagnostic radiation and risk of breast cancer among carriers of BRCA1/2 mutations: retrospective cohort study (GENE-RAD-RISK). *BMJ* 2012; **345**: e5660 [PMID: 22956590 DOI: 10.1136/bmj.e5660]

38 **Drooger JC**, Hooning MJ, Seynaeve CM, Baaijens MH, Obdeijn IM, Sleijfer S, Jager A. Diagnostic and therapeutic ionizing radiation and the risk of a first and second primary breast cancer, with special attention for BRCA1 and BRCA2 mutation carriers: a critical review of the literature. *Cancer Treat Rev* 2015; **41**: 187-196 [PMID: 25533736 DOI: 10.1016/j.ctrv.2014.12.002]

39 **Schiebler M**, Francois C, Repplinger M, Hamedani A, Lindholm C, Vigen K, Munoz del Rio A, Grist T, Reeder S, Nagle S. Effectiveness of Pulmonary Contrast Enhanced Magnetic Resonance Angiography for the primary workup of pulmonary embolism. ISMRM 24th Annual Meeting and Exhibition; 2016 May 7-13; Singapore; Oral abstract presentation, No. 1074

40 **Mos IC**, Klok FA, Kroft LJ, DE Roos A, Dekkers OM, Huisman MV. Safety of ruling out acute pulmonary embolism by normal computed tomography pulmonary angiography in patients with an indication for computed tomography: systematic review and meta-analysis. *J Thromb Haemost* 2009; **7**: 1491-1498 [PMID: 19552684 DOI: 10.1111/j.1538-7836.2009.03518.x]

41 **Shellock FG**. Magnetic resonance safety update 2002: implants and devices. *J Magn Reson Imaging* 2002; **16**: 485-496 [PMID: 12412025 DOI: 10.1002/jmri.10196]

42 **Behzadi AH**, Zhao Y, Farooq Z, Prince MR. Immediate Allergic Reactions to Gadolinium-based Contrast Agents: A Systematic Review and Meta-Analysis. *Radiology* 2018; **286**: 731 [PMID: 29356629 DOI: 10.1148/radiol.2017174037]

43 **Vasanawala SS**, Nguyen KL, Hope MD, Bridges MD, Hope TA, Reeder SB, Bashir MR. Safety and technique of ferumoxytol administration for MRI. *Magn Reson Med* 2016; **75**: 2107-2111 [PMID: 26890830 DOI: 10.1002/mrm.26151]

44 **Alsop DC**, Hatabu H, Bonnet M, Listerud J, Gefter W. Multislice, breathhold imaging of the lung with submillisecond echo

times. *Magn Reson Med* 1995; **33**: 678-682 [PMID: 7596272 DOI: 10.1002/mrm.1910330513]
45 **Johnson KM**, Fain SB, Schiebler ML, Nagle S. Optimized 3D ultrashort echo time pulmonary MRI. *Magn Reson Med* 2013; **70**: 1241-1250 [PMID: 23213020 DOI: 10.1002/mrm.24570]
46 **Griswold MA**, Blaimer M, Breuer F, Heidemann RM, Mueller M, Jakob PM. Parallel magnetic resonance imaging using the GRAPPA operator formalism. *Magn Reson Med* 2005; **54**: 1553-1556 [PMID: 16254956 DOI: 10.1002/mrm.20722]
47 **Bannas P**, Bell LC, Johnson KM, Schiebler ML, François CJ, Motosugi U, Consigny D, Reeder SB, Nagle SK. Pulmonary Embolism Detection with Three-dimensional Ultrashort Echo Time MR Imaging: Experimental Study in Canines. *Radiology* 2016; **278**: 413-421 [PMID: 26422185 DOI: 10.1148/radiol.2015150606]
48 **Brau AC**, Beatty PJ, Skare S, Bammer R. Comparison of reconstruction accuracy and efficiency among autocalibrating data-driven parallel imaging methods. *Magn Reson Med* 2008; **59**: 382-395 [PMID: 18228603 DOI: 10.1002/mrm.21481]
49 **Biederer J**, Beer M, Hirsch W, Wild J, Fabel M, Puderbach M, Van Beek EJ. MRI of the lung (2/3). Why … when … how? *Insights Imaging* 2012; **3**: 355-371 [PMID: 22695944 DOI: 10.1007/s13244-011-0146-8]
50 **Kluge A**, Gerriets T, Stolz E, Dill T, Mueller KD, Mueller C, Bachmann G. Pulmonary perfusion in acute pulmonary embolism: agreement of MRI and SPECT for lobar, segmental and subsegmental perfusion defects. *Acta Radiol* 2006; **47**: 933-940 [PMID: 17077044 DOI: 10.1080/02841850600885377]
51 **Kluge A**, Gerriets T, Müller C, Ekinci O, Neumann T, Dill T, Bachmann G. [Thoracic real-time MRI: experience from 2200 examinations in acute and ill-defined thoracic diseases]. *Rofo* 2005; **177**: 1513-1521 [PMID: 16302132 DOI: 10.1055/s-2005-858688]
52 **Biederer J**, Heussel CP, Puderbach M, Wielpuetz MO. Functional magnetic resonance imaging of the lung. *Semin Respir Crit Care Med* 2014; **35**: 74-82 [PMID: 24481761 DOI: 10.1055/s-0033-1363453]
53 **Edelman RR**, Silvers RI, Thakrar KH, Metzl MD, Nazari J, Giri S, Koktzoglou I. Nonenhanced MR angiography of the pulmonary arteries using single-shot radial quiescent-interval slice-selective (QISS): a technical feasibility study. *J Cardiovasc Magn Reson* 2017; **19**: 48 [PMID: 28662717 DOI: 10.1186/s12968-017-0365-3]
54 **Gibiino F**, Sacolick L, Menini A, Landini L, Wiesinger F. Free-breathing, zero-TE MR lung imaging. *MAGMA* 2015; **28**: 207-215 [PMID: 25200814 DOI: 10.1007/s10334-014-0459-y]
55 **Bauman G**, Puderbach M, Deimling M, Jellus V, Chefd'hotel C, Dinkel J, Hintze C, Kauczor HU, Schad LR. Non-contrast-enhanced perfusion and ventilation assessment of the human lung by means of fourier decomposition in proton MRI. *Magn Reson Med* 2009; **62**: 656-664 [PMID: 19585597 DOI: 10.1002/mrm.22031]
56 **Voskrebenzev A**, Gutberlet M, Becker L, Wacker F, Vogel-Claussen J. Reproducibility of fractional ventilation derived by Fourier decomposition after adjusting for tidal volume with and without an MRI compatible spirometer. *Magn Reson Med* 2016; **76**: 1542-1550 [PMID: 26745750 DOI: 10.1002/mrm.26047]
57 **Suga K**, Ogasawara N, Okada M, Tsukuda T, Matsunaga N, Miyazaki M. Lung perfusion impairments in pulmonary embolic and airway obstruction with noncontrast MR imaging. *J Appl Physiol* (1985) 2002; **92**: 2439-2451 [PMID: 12015358 DOI: 10.1152/japplphysiol.00900.2001]
58 **Bauman G**, Johnson KM, Bell LC, Velikina JV, Samsonov AA, Nagle SK, Fain SB. Three-dimensional pulmonary perfusion MRI with radial ultrashort echo time and spatial-temporal constrained reconstruction. *Magn Reson Med* 2015; **73**: 555-564 [PMID: 24604452 DOI: 10.1002/mrm.25158]
59 **Fischer A**, Weick S, Ritter CO, Beer M, Wirth C, Hebestreit H, Jakob PM, Hahn D, Bley T, Köstler H. SElf-gated Non-Contrast-Enhanced FUnctional Lung imaging (SENCEFUL) using a quasi-random fast low-angle shot (FLASH) sequence and proton MRI. *NMR Biomed* 2014; **27**: 907-917 [PMID: 24820869 DOI: 10.1002/nbm.3134]
60 **Voskrebenzev A**, Gutberlet M, Klimeš F, Kaireit TF, Schönfeld C, Rotärmel A, Wacker F, Vogel-Claussen J. Feasibility of quantitative regional ventilation and perfusion mapping with phase-resolved functional lung (PREFUL) MRI in healthy volunteers and COPD, CTEPH, and CF patients. *Magn Reson Med* 2018; **79**: 2306-2314 [PMID: 28856715 DOI: 10.1002/mrm.26893]
61 **Bauman G**, Lützen U, Ullrich M, Gaass T, Dinkel J, Elke G, Meybohm P, Frerichs I, Hoffmann B, Borggrefe J, Knuth HC, Schupp J, Prüm H, Eichinger M, Puderbach M, Biederer J, Hintze C. Pulmonary functional imaging: qualitative comparison of Fourier decomposition MR imaging with SPECT/CT in porcine lung. *Radiology* 2011; **260**: 551-559 [PMID: 21586678 DOI: 10.1148/radiol.11102313]
62 **Bauman G**, Scholz A, Rivoire J, Terekhov M, Friedrich J, de Oliveira A, Semmler W, Schreiber LM, Puderbach M. Lung ventilation- and perfusion-weighted Fourier decomposition magnetic resonance imaging: in vivo validation with hyperpolarized 3He and dynamic contrast-enhanced MRI. *Magn Reson Med* 2013; **69**: 229-237 [PMID: 22392633 DOI: 10.1002/mrm.24236]
63 **Bauman G**, Bieri O. Matrix pencil decomposition of time-resolved proton MRI for robust and improved assessment of pulmonary ventilation and perfusion. *Magn Reson Med* 2017; **77**: 336-342 [PMID: 26757102 DOI: 10.1002/mrm.26096]
64 **Schönfeld C**, Cebotari S, Voskrebenzev A, Gutberlet M, Hinrichs J, Renne J, Hoeper MM, Olsson KM, Welte T, Wacker F, Vogel-Claussen J. Performance of perfusion-weighted Fourier decomposition MRI for detection of chronic pulmonary emboli. *J Magn Reson Imaging* 2015; **42**: 72-79 [PMID: 25227559 DOI: 10.1002/jmri.24764]
65 **Keilholz SD**, Mai VM, Berr SS, Fujiwara N, Hagspiel KD. Comparison of first-pass Gd-DOTA and FAIRER MR perfusion imaging in a rabbit model of pulmonary embolism. *J Magn Reson Imaging* 2002; **16**: 168-171 [PMID: 12203764 DOI: 10.1002/jmri.10138]
66 **Arai TJ**, Henderson AC, Dubowitz DJ, Levin DL, Friedman PJ, Buxton RB, Prisk GK, Hopkins SR. Hypoxic pulmonary vasoconstriction does not contribute to pulmonary blood flow heterogeneity in normoxia in normal supine humans. *J Appl Physiol* (1985) 2009; **106**: 1057-1064 [PMID: 19057006 DOI: 10.1152/japplphysiol.90759.2008]
67 **Burnham KJ**, Arai TJ, Dubowitz DJ, Henderson AC, Holverda S, Buxton RB, Prisk GK, Hopkins SR. Pulmonary perfusion heterogeneity is increased by sustained, heavy exercise in humans. *J Appl Physiol* (1985) 2009; **107**: 1559-1568 [PMID: 19745192 DOI: 10.1152/japplphysiol.00491.2009]
68 **Mai VM**, Knight-Scott J, Berr SS. Improved visualization of the human lung in 1H MRI using multiple inversion recovery for simultaneous suppression of signal contributions from fat and muscle. *Magn Reson Med* 1999; **41**: 866-870 [PMID: 10332866 DOI: 10.1002/(SICI)1522-2594(199905)41:5<866::AID-MRM2>3.0.CO;2-D]
69 **Soulez G**, Bloomgarden DC, Rofsky NM, Smith MP, Abujudeh HH, Morgan DE, Lichtenstein RJ, Schiebler ML, Wippold FJ 2nd, Russo C, Kuhn MJ, Mennitt KW, Maki JH, Stolpen A, Liou J, Semelka RC, Kirchin MA, Shen N, Pirovano G, Spinazzi A. Prospective Cohort Study of Nephrogenic Systemic Fibrosis in Patients With Stage 3-5 Chronic Kidney Disease Undergoing MRI With Injected Gadobenate Dimeglumine or Gadoteridol. *AJR Am J Roentgenol* 2015; **205**: 469-478 [PMID: 26295633 DOI: 10.2214/AJR.14.14268]
70 **Prybylski JP**, Semelka RC, Jay M. The stability of gadolinium-based contrast agents in human serum: A reanalysis of literature data and association with clinical outcomes. *Magn Reson Imaging* 2017; **38**: 145-151 [PMID: 28089499 DOI: 10.1016/j.mri.2017.01.006]
71 **Huckle JE**, Altun E, Jay M, Semelka RC. Gadolinium Deposition in Humans: When Did We Learn That Gadolinium Was Deposited In Vivo? *Invest Radiol* 2016; **51**: 236-240 [PMID: 26588463 DOI: 10.1097/RLI.0000000000000228]
72 **Herédia V**, Altun E, Ramalho M, de Campos R, Azevedo R, Pamuklar E, Semelka RC. MRI of pregnant patients for suspected pulmonary embolism: steady-state free precession vs postgadolinium 3D-GRE. *Acta Med Port* 2012; **25**: 359-367 [PMID:

23534587]
73 **Kanda T**, Osawa M, Oba H, Toyoda K, Kotoku J, Haruyama T, Takeshita K, Furui S. High Signal Intensity in Dentate Nucleus on Unenhanced T1-weighted MR Images: Association with Linear versus Macrocyclic Gadolinium Chelate Administration. *Radiology* 2015; **275**: 803-809 [PMID: 25633504 DOI: 10.1148/radiol.14140364]
74 **Gulani V**, Calamante F, Shellock FG, Kanal E, Reeder SB; International Society for Magnetic Resonance in Medicine. Gadolinium deposition in the brain: summary of evidence and recommendations. *Lancet Neurol* 2017; **16**: 564-570 [PMID: 28653648 DOI: 10.1016/S1474-4422(17)30158-8]
75 **Aime S**, Caravan P. Biodistribution of gadolinium-based contrast agents, including gadolinium deposition. *J Magn Reson Imaging* 2009; **30**: 1259-1267 [PMID: 19938038 DOI: 10.1002/jmri.21969]
76 **Nagle SK**, Schiebler ML, Repplinger MD, François CJ, Vigen KK, Yarlagadda R, Grist TM, Reeder SB. Contrast enhanced pulmonary magnetic resonance angiography for pulmonary embolism: Building a successful program. *Eur J Radiol* 2016; **85**: 553-563 [PMID: 26860667 DOI: 10.1016/j.ejrad.2015.12.018]
77 **Maki JH**, Prince MR, Londy FJ, Chenevert TL. The effects of time varying intravascular signal intensity and k-space acquisition order on three-dimensional MR angiography image quality. *J Magn Reson Imaging* 1996; **6**: 642-651 [PMID: 8835958 DOI: 10.1002/jmri.1880060413]
78 **Finn JP**, Nguyen KL, Hu P. Ferumoxytol vs. Gadolinium agents for contrast-enhanced MRI: Thoughts on evolving indications, risks, and benefits. *J Magn Reson Imaging* 2017; **46**: 919-923 [PMID: 28160356 DOI: 10.1002/jmri.25580]
79 **Ripley B**, Wilson GJ, Lalwani N, Briller N, Neligan PC, Maki JH. Initial Clinical Experience with Dual-Agent Relaxation Contrast for Isolated Lymphatic Channel Mapping. *Radiology* 2018; **286**: 705-714 [PMID: 28934015 DOI: 10.1148/radiol.2017170241]
80 **Skeith L**, Rodger MA. Pulmonary Complications of Pregnancy: Venous Thromboembolism. *Semin Respir Crit Care Med* 2017; **38**: 135-147 [PMID: 28561245 DOI: 10.1055/s-0037-1602241]
81 **Tromeur C**, van der Pol LM, Klok FA, Couturaud F, Huisman MV. Pitfalls in the diagnostic management of pulmonary embolism in pregnancy. *Thromb Res* 2017; **151** Suppl 1: S86-S91 [PMID: 28262243 DOI: 10.1016/S0049-3848(17)30075-0]
82 **Leung AN**, Bull TM, Jaeschke R, Lockwood CJ, Boiselle PM, Hurwitz LM, James AH, McCullough LB, Menda Y, Paidas MJ, Royal HD, Tapson VF, Winer-Muram HT, Chervenak FA, Cody DD, McNitt-Gray MF, Stave CD, Tuttle BD; ATS/STR Committee on Pulmonary Embolism in Pregnancy. American Thoracic Society documents: an official American Thoracic Society/Society of Thoracic Radiology Clinical Practice Guideline--Evaluation of Suspected Pulmonary Embolism in Pregnancy. *Radiology* 2012; **262**: 635-646 [PMID: 22282185 DOI: 10.1148/radiol.11114045]
83 **Wan T**, Skeith L, Karovitch A, Rodger M, Le Gal G. Guidance for the diagnosis of pulmonary embolism during pregnancy: Consensus and controversies. *Thromb Res* 2017; **157**: 23-28 [PMID: 28686913 DOI: 10.1016/j.thromres.2017.06.025]
84 **Sommer G**, Bauman G, Koenigkam-Santos M, Draenkow C, Heussel CP, Kauczor HU, Schlemmer HP, Puderbach M. Non-contrast-enhanced preoperative assessment of lung perfusion in patients with non-small-cell lung cancer using Fourier decomposition magnetic resonance imaging. *Eur J Radiol* 2013; **82**: e879-e887 [PMID: 24041434 DOI: 10.1016/j.ejrad.2013.06.030]
85 **Ray JG**, Vermeulen MJ, Bharatha A, Montanera WJ, Park AL. Association Between MRI Exposure During Pregnancy and Fetal and Childhood Outcomes. *JAMA* 2016; **316**: 952-961 [PMID: 27599330 DOI: 10.1001/jama.2016.12126]
86 **Johns CS**, Schiebler ML, Swift AJ. Commentary on: Survey of UK imaging practice for the investigation of pulmonary embolism in pregnancy. *Clin Radiol* 2017; **72**: 702-703 [PMID: 28545683 DOI: 10.1016/j.crad.2017.04.018]
87 **van Mens TE**, Scheres LJ, de Jong PG, Leeflang MM, Nijkeuter M, Middeldorp S. Imaging for the exclusion of pulmonary embolism in pregnancy. *Cochrane Database Syst Rev* 2017; **1**: CD011053 [PMID: 28124411 DOI: 10.1002/14651858.CD011053.pub2]
88 **Bannas P**, Schiebler ML, Motosugi U, François CJ, Reeder SB, Nagle SK. Pulmonary MRA: differentiation of pulmonary embolism from truncation artefact. *Eur Radiol* 2014; **24**: 1942-1949 [PMID: 24863886 DOI: 10.1007/s00330-014-3219-5]
89 **Schiebler ML**, Ahuja J, Repplinger MD, François CJ, Vigen KK, Grist TM, Hamedani AG, Reeder SB, Nagle SK. Incidence of actionable findings on contrast enhanced magnetic resonance angiography ordered for pulmonary embolism evaluation. *Eur J Radiol* 2016; **85**: 1383-1389 [PMID: 27423676 DOI: 10.1016/j.ejrad.2016.05.008]
90 **Richman PB**, Courtney DM, Friese J, Matthews J, Field A, Petri R, Kline JA. Prevalence and significance of nonthromboembolic findings on chest computed tomography angiography performed to rule out pulmonary embolism: a multicenter study of 1,025 emergency department patients. *Acad Emerg Med* 2004; **11**: 642-647 [PMID: 15175202 DOI: 10.1197/j.aem.2003.12.021]
91 **Benson DG**, Schiebler ML, Nagle SK, François CJ. Magnetic Resonance Imaging for the Evaluation of Pulmonary Embolism. *Top Magn Reson Imaging* 2017; **26**: 145-151 [PMID: 28777163 DOI: 10.1097/RMR.0000000000000133]
92 **Le Gal G**, Righini M, Parent F, van Strijen M, Couturaud F. Diagnosis and management of subsegmental pulmonary embolism. *J Thromb Haemost* 2006; **4**: 724-731 [PMID: 16634736 DOI: 10.1111/j.1538-7836.2006.01819.x]
93 **Sheh SH**, Bellin E, Freeman KD, Haramati LB. Pulmonary embolism diagnosis and mortality with pulmonary CT angiography versus ventilation-perfusion scintigraphy: evidence of overdiagnosis with CT? *AJR Am J Roentgenol* 2012; **198**: 1340-1345 [PMID: 22623546 DOI: 10.2214/AJR.11.6426]
94 **Gómez-Sánchez MA**. What is the clinical significance of isolated subsegmental pulmonary embolism? *Rev Port Pneumol* 2014; **20**: 179-180 [PMID: 24931345 DOI: 10.1016/j.rppneu.2014.05.001]
95 **den Exter PL**, van Es J, Klok FA, Kroft LJ, Kruip MJ, Kamphuisen PW, Büller HR, Huisman MV. Risk profile and clinical outcome of symptomatic subsegmental acute pulmonary embolism. *Blood* 2013; **122**: 1144-1149; quiz 1329 [PMID: 23736701 DOI: 10.1182/blood-2013-04-497545]
96 **Carrier M**, Klok FA. Symptomatic subsegmental pulmonary embolism: to treat or not to treat? *Hematology Am Soc Hematol Educ Program* 2017; **2017**: 237-241 [PMID: 29222261 DOI: 10.1182/asheducation-2017.1.237]
97 **Kearon C**, Akl EA, Ornelas J, Blaivas A, Jimenez D, Bounameaux H, Huisman M, King CS, Morris TA, Sood N, Stevens SM, Vintch JRE, Wells P, Woller SC, Moores L. Antithrombotic Therapy for VTE Disease: CHEST Guideline and Expert Panel Report. *Chest* 2016; **149**: 315-352 [PMID: 26867832 DOI: 10.1016/j.chest.2015.11.026]
98 **Ende-Verhaar YM**, Cannegieter SC, Vonk Noordegraaf A, Delcroix M, Pruszczyk P, Mairuhu AT, Huisman MV, Klok FA. Incidence of chronic thromboembolic pulmonary hypertension after acute pulmonary embolism: a contemporary view of the published literature. *Eur Respir J* 2017; **49**: [PMID: 28232411 DOI: 10.1183/13993003.01792-2016]
99 **Cronin P**, Dwamena BA. A Clinically Meaningful Interpretation of the Prospective Investigation of Pulmonary Embolism Diagnosis (PIOPED) II and III Data. *Acad Radiol* 2018; **25**: 561-572 [PMID: 29337091 DOI: 10.1016/j.acra.2017.11.014]

P- Reviewer: Aday AW, Qi X **S- Editor**: Ji FF **L- Editor**: A
E- Editor: Tan WW

Published by **Baishideng Publishing Group Inc**
7901 Stoneridge Drive, Suite 501, Pleasanton, CA 94588, USA
Telephone: +1-925-223-8242
Fax: +1-925-223-8243
E-mail: bpgoffice@wjgnet.com
Help Desk: http://www.f6publishing.com/helpdesk
http://www.wjgnet.com

ISSN 1949-8470 (online)

World Journal of *Radiology*

World J Radiol 2018 July 28; 10(7): 65-82

Published by Baishideng Publishing Group Inc

WJR World Journal of Radiology

Contents

Monthly Volume 10 Number 7 July 28, 2018

ABOUT COVER

Editorial Board Member of *World Journal of Radiology*, Vlastimil Valek, MD, PhD, Professor, Department of Radiology, University Hospital Brno, Brno 62800, Czech Republic

AIM AND SCOPE

World Journal of Radiology (*World J Radiol*, *WJR*, online ISSN 1949-8470, DOI: 10.4329) is a peer-reviewed open access academic journal that aims to guide clinical practice and improve diagnostic and therapeutic skills of clinicians.

WJR covers topics concerning diagnostic radiology, radiation oncology, radiologic physics, neuroradiology, nuclear radiology, pediatric radiology, vascular/interventional radiology, medical imaging achieved by various modalities and related methods analysis. The current columns of *WJR* include editorial, frontier, diagnostic advances, therapeutics advances, field of vision, mini-reviews, review, topic highlight, medical ethics, original articles, case report, clinical case conference (clinicopathological conference), and autobiography.

We encourage authors to submit their manuscripts to *WJR*. We will give priority to manuscripts that are supported by major national and international foundations and those that are of great basic and clinical significance.

INDEXING/ABSTRACTING

World Journal of Radiology is now indexed in PubMed, PubMed Central, and Emerging Sources Citation Index (Web of Science).

NAME OF JOURNAL
World Journal of Radiology

ISSN
ISSN 1949-8470 (online)

LAUNCH DATE
January 31, 2009

FREQUENCY
Monthly

EDITORIAL OFFICE
Jin-Lei Wang, Director
World Journal of Radiology
Baishideng Publishing Group Inc
7901 Stoneridge Drive, Suite 501, Pleasanton, CA 94588, USA
Telephone: +1-925-2238242
Fax: +1-925-2238243
E-mail: editorialoffice@wjgnet.com
Help Desk: http://www.f6publishing.com/helpdesk
http://www.wjgnet.com

PUBLISHER
Baishideng Publishing Group Inc
7901 Stoneridge Drive, Suite 501,
Pleasanton, CA 94588, USA
Telephone: +1-925-2238242
Fax: +1-925-2238243
E-mail: bpgoffice@wjgnet.com
Help Desk: http://www.f6publishing.com/helpdesk
http://www.wjgnet.com

PUBLICATION DATE
July 28, 2018

INSTRUCTIONS TO AUTHORS
http://www.wjgnet.com/bpg/gerinfo/204

ONLINE SUBMISSION
http://www.f6publishing.com

World Journal of Radiology

Submit a Manuscript: http://www.f6publishing.com

World J Radiol 2018 July 28; 10(7): 65-77

DOI: 10.4329/wjr.v10.i.65

ISSN 1949-8470 (online)

ORIGINAL ARTICLE

Retrospective Study

Evaluation of pineal cysts with magnetic resonance imaging

Erkan Gokce, Murat Beyhan

Erkan Gokce, Department of Radiology, Gaziosmanpaşa University, School of Medicine, Tokat 60100, Turkey

Murat Beyhan, Department of Radiology, Tokat State Hospital, Tokat 60100, Turkey

ORCID number: Erkan Gokce (0000-0002-1809-2172); Murat Beyhan (0000-0002-8630-4632).

Author contributions: Gokce E and Beyhan M collected and analyzed the data equally; Gokce E designed, supervised and some statistical analysis the study; Gokce E and Beyhan M had taken part in literature research and manuscript preparation and had read and approved the final version.

Institutional review board statement: This study was reviewed and approved by the Ethics Committee of the Gaziosmanpaşa University School of Medicine (No: 18-KAEK-015).

Informed consent statement: Patients were not required to give informed consent to the study because figures used picture archiving and communication system were studied retrospectively. This study does not contain identifiable information of the participants.

Conflict-of-interest statement: The authors have no conflicts of interest to declare.

Data sharing statement: No additional data are available.

Manuscript source: Invited manuscript

Correspondence to: Erkan Gokce, MD, Associate Professor, Department of Radiology, Gaziosmanpaşa University, School of Medicine, Kaleardı Quarter, Muhittin Fisunoglu Street, Tokat 60100, Turkey. erkangokce@mynet.com

Telephone: +90-542-3798986
Fax: +90-362-2309105

Received: March 12, 2018
Peer-review started: March 13, 2018
First decision: April 23, 2018
Revised: April 29, 2018
Accepted: May 23, 2018
Article in press: May 23, 2018
Published online: July 28, 2018

Abstract

AIM

To evaluate radiological imaging findings of patients who had been found to have pineal cyst (PC) in brain magnetic resonance imaging (MRI).

METHODS

A total of 9546 patients who had brain MRI examination in March 2010-January 2018 period were studied. Fifty-six patients (44 female and 12 male) found to have PC were evaluated. Eighteen of the patients had had follow-up examinations of 2-94 mo (mean 30.50 ± 28.83). PC dimensions and volume, radiological imaging features (signal intensities, contours, internal septation-loculation and contrast-enhancement features) and natural history in cases who had been followed-up were evaluated by two radiologists.

RESULTS

Of 9546 patients, 5555 were female (58.2%) and 3991 male (41.8%). Age range was 1-99 (mean 43.18 ± 20.94). PC frequency was calculated to be 0.58%. Forty-four of the 56 patients (78.57%) with PC were female and 12 male (21.43%), and their age range was 5-61 (mean 31.26 ± 12.73). Thirty-five of the PCs were typical (62.50%) and 21 (37.50%) were atypical. No significant difference was found between initial and final imaging sizes of PCs which were monitored by follow-up examinations ($P > 0.05$).

CONCLUSION
PCs are cysts which do not show clear size and natural changes and are more frequently observed in females and in adult ages. Most of them are isointense with cerebrospinal fluid on T1 and T2A weighted images, hyperintense compared to cerebrospinal fluid on fluid-attenuated inversion recovery; sequence and smoothly contoured. Their typical forms have peripheral rim and multilocular ones may have septal contrast-enhancement.

Key words: Magnetic resonance imaging; Pineal cyst; Pineal region

Core tip: In this retrospective study, brain magnetic resonance images of 9546 patients were studied to detect incidence, size, contour, septation and contrast-enhancement features of pineal cysts (PCs). In addition, size and natural changes in follow-up examinations were also investigated. Classification of PCs based on routine magnetic resonance imaging examinations could change when examination was performed using high resolution sequences due to detection of septations within them. The present study revealed that no significant size or natural change was observed in follow-up examinations of PCs.

Gokce E, Beyhan M. Evaluation of pineal cysts with magnetic resonance imaging. *World J Radiol* 2018; 10(7): 65-77 Available from: URL: http://www.wjgnet.com/1949-8470/full/v10/i7/65.htm DOI: http://dx.doi.org/10.4329/wjr.v10.i7.65

INTRODUCTION

Pineal cysts (PC) are frequently asymptomatic, small sized, unilocular, benign pineal lesions which do not show size change[1]. They are generally made of three layers: fibrocollagen layer at the outside, pineal parenchymal layer which may have calcium deposits at the middle and hypocellular glial tissue layer which may have hemosiderin inside[1,2]. PCs may develop as secondary to focal degeneration of pineal gland or distension of pineal diverticulum remnant[3]. Increasing resolution and more frequent use of cranial imaging techniques along with use of contrast agent have led to an increase in incidental diagnosis of PCs[1]. Unilocular, smooth edged, round or ovoid shaped cysts which have homogenous interior signal feature and rim-shaped contrast-enhancement with less than 2 mm wall thickness on MRI are referred as typical PC[4,5]. Although there is an excess amount of reports in literature about typical PC stating that they are indeed incidental findings of radiological imaging and that they are stable over time, more complex and atypical pineal cystic lesions constitute a problem for radiologists[4-7]. In addition, it has been reported that pineal neoplasia could have imaging features similar to those of PC[5,8]. Some studies mentioned some cystic lesions in pineal region with complex imaging features, which are probably normal variants[5,9,10]. In the present study, radiological imaging findings of PCs determined in patients who had undergone brain magnetic resonance imaging (MRI) due to various reasons in a past eight-year period were evaluated.

MATERIALS AND METHODS

After the approval of local ethic committee (No. 18-KA-EK-015), 9546 patients who had brain MRI examinations in March 2010-January 2018 period in Radiology Department of Gaziosmanpaşa University Medical School were studied retrospectively. A total of 11695 consecutive brain MRI examinations were scanned. Scans were reviewed by experienced neuroradiologists (Gokce E and Beyhan M) to confirm radiologic diagnoses of PC. Patients with solid or semisolid masses in pineal gland location or other cystic lesions (arachnoid cyst, *etc*.) developing from neighboring structures and patients with operation history were excluded. There were no exclusion criteria related to pineal cyst size. Fifty-six patients (44 female and 12 male) with PCs were evaluated. Among the reasons for MRI requests were headache, cerebrovascular disease, epilepsy, vertigo, hand tremors and encephalitis. MRI examinations were carried out using an 8-channel 1.5 T MRI machine (GE Signa Excite HD; GE Healthcare, Milwaukee, WI, United States, 2005) until 2017, and a 16-channel 1.5 T MRI machine (GE Signa Explorer SV 25; GE Healthcare, Milwaukee, WI, United States, 2016) after 2017. MRI examination parameters before and after 2017 are given in Tables 1 and 2. Eighteen patients had 2-94 mo (mean 30.50 ± 28.83) of follow-ups. Contrast-enhanced MRI was performed in 21 of 56 patients.

Size and volume, radiological imaging features (signal intensities, contours, internal septation-loculation and contrast-enhancement properties) and size and natural changes of PCs (in patients who had follow-ups) were evaluated by two radiologists. PC dimensions were measured from outer wall to outer wall in sagittal, axial and coronal planes. Unilocular, smooth edged, ovoid PCs with homogenous interior structure and less than 2 mm wall thickness were considered typical PC (Figures 1-3), while multilocular PCs with walls thicker than 2 mm, septation or lobulated contours were considered atypical (Figures 4-10). In patients who had had follow-up examinations, size and natural differences were compared in initial and follow-up examinations.

Statistical analysis

Descriptive statistics were expressed as mean ± SD. Data regarding categorical variables were given as n (%). Categorical variables were compared using χ^2 tests. Independent-samples t-test and Mann-Whitney *U*

Table 1 Magnetic resonance imaging examination parameters before 2017

Parameter	T1 (SPGR)	T2 (SE)	FLAIR	DWI	Ax SPGR + C	Sag T1 SE + C	Ax T1 FS + C
TR (repetition time) (ms)	6.36	5700	8002	8000	6.36	440	620
TE (echo time) (ms)	2.23	134	80.9	104	2.23	12	20
Field of view (mm)	260	250	220	250	260	250	250
Slice thickness (mm)	4	5	5.5	5	4	5.5	5.5
Slice gap (mm)	2	6.5	6.5	6.5	2	6.5	7
NEX (No. of excitations)	1	1.5	1	2	1	1	1
TI (time inversion) ms	450		2000		450		
Machine	1.5 T GE Signa Excite HD (8 channel head coil)						

SPGR: Spoiled gradient recalled acquisition in steady state; SE: Spin echo; FLAIR: Fluid-attenuated inversion recovery; DWI: Diffusion weighted imaging; Ax: Axial plane; Sag: Sagittal plane; + C: Contrast-enhanced; FS: Fat saturation.

Table 2 Magnetic resonance imaging examination parameters after 2017

Parameter	T1 (BRAVO)	T2 (SE)	FLAIR FS	DWI	T1 (BRAVO) +C	Cor T1 (SE) + C	Ax T1 FS + C
TR (repetition time) (ms)	9.25	6282	10000	6992	9.25	3509	2744
TE (echo time) (ms)	3.58	124	91.7	84.4	3.58	17.8	17.5
Field of view (mm)	256	220	240	270	256	240	256
Slice thickness (mm)	1	5.5	5.5	5	1	5.5	5.5
Slice gap (mm)	0	7	7	5.5	0	7	7
NEX (No. of excitations)	1	2	1	2	1	1	1
TI (time inversion) (ms)	420		2688		420	1146	922
Machine	1.5 T GE Signa Explorer SV 25 (16 channel neurovascular-head coil)						

BRAVO: Brain volume imaging; SE: Spin echo; FLAIR: Fluid-attenuated inversion recovery; FS: Fat saturation; DWI: Diffusion weighted imaging; + C: Contrast-enhanced; Cor: Coronal plane; Ax: Axial plane.

Table 3 Demographic and clinical characteristics of patients with pineal cyst

Demographic and clinical characteristics	*n* (%)
No. of patients	56
Pineal cyst prevalence	0.58%
Median age (mean ± SD, range) (yr)	31.26 ± 12.73 (5–61)
Sex	
Female	44 (78.57)
Male	12 (21.43)
MRI request reasons	
Headache	42 (75)
Epilepsy	7 (12.50)
Cerebrovascular disease	4 (7.14)
Vertigo	1 (1.78)
Encephalitis	1 (1.78)
Hand tremor	1 (1.78)

MRI: Magnetic resonance imaging.

test were used to compare the means of two groups. The results of PC dimension measurements were compared using paired-samples *t*-test. A *P*-value of < 0.05 was considered significant. Statistical analyses were performed using the Statistical Package for Social Sciences 18.0 software (IBM Corp.; Armonk, NY, United States).

RESULTS

Studied brain MRI examinations belonged to 5555 women (58.2%) and 3991 men (41.8%), and the age range was 1-99 (mean 43.18 ± 20.94). Fifty-six patients were found to have had PC. Forty-four of them (78.57%) were female and 12 were men (21.43%). Calculated frequency of PC was 0.58%. Age range of patients with PC was 5-61 (mean: 31.26 ± 12.73). When the groups with and without PC were compared, a significant difference was found between the two groups for average age ($P < 0.001$). The difference between the genders for frequency of PC incidence was also significant ($P = 0.002$). The most common reason for MRI examination request was headache (42 patients). Demographic and clinical characteristics of patients with PC are given in Table 3.

One PC was slightly hyperintense on T2 weighed series compared to cerebrospinal fluid (CSF), but others were isointense (Figures 1-3). On T1 weighted series, three PCs were slightly hyperintense compared to CSF and other PCs were isointense. On fluid-attenuated inversion recovery (FLAIR) series, on the other hand, only six PCs were isointense with CSF, and others were hyperintense (Figure 2). No diffusion limitation was observed on diffusion MRI series in any PC (Figure 4). Contrast-enhancement was detected in PCs of all 21 patients who had undergone contrast-enhanced MRI examination. Vast majority of PC (71.42%) showed peripheral rim-like contrast-enhancement (Figure 1). However, peripheral rim-like contrast-enhancement and septal contrast-enhancement or partial rim style enhancement were less frequent (14.28% and 9.52%, respectively) (Figures 5, 7 and 10). One PC (4.76%)

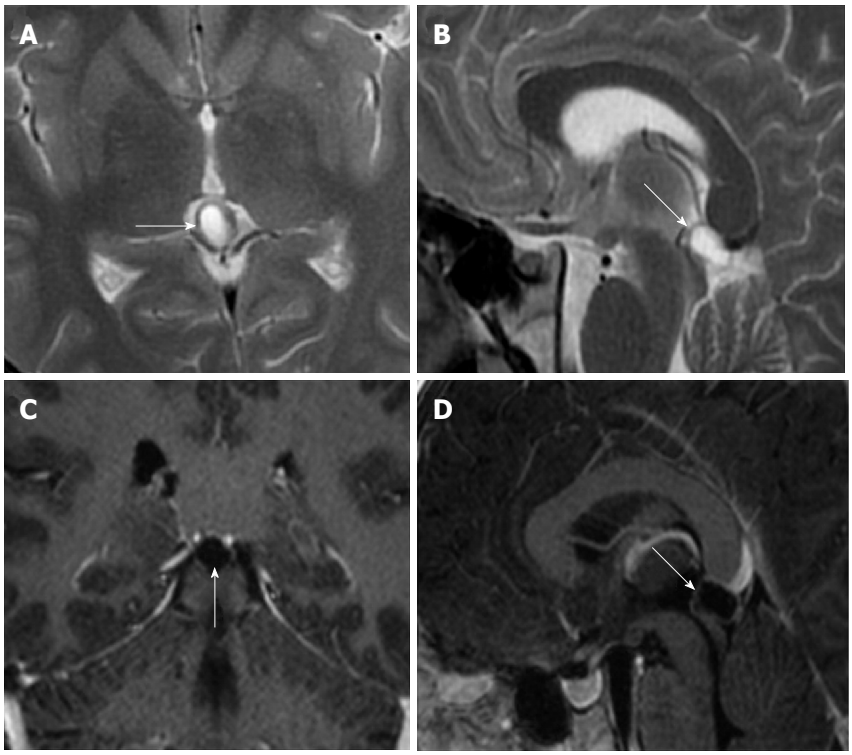

Figure 1 Eighteen years old male patient with typical pineal cyst (patient No. 43). A: Axial plane T2 weighted magnetic resonance imaging (MRI); B: Sagittal plane T2 weighted MRI; C: Axial plane T1 weighted contrast-enhanced MRI; D: Sagittal plane contrast-enhanced MRI. Typical pineal cyst is shown in the pineal region with unilocular homogeneous internal structure (arrows, A, B, C and D); Peripheral rim-like contrast-enhancement is shown (arrow, C and D).

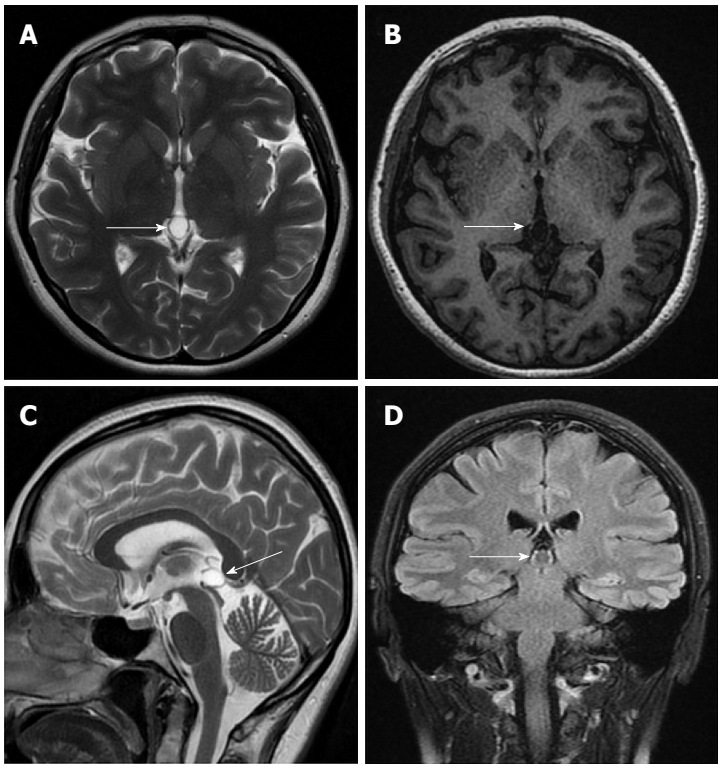

Figure 2 Thirty-three years old female patient with typical pineal cyst (patient No. 42). A: Axial plane T2 weighted magnetic resonance imaging (MRI); B: T1 weighted MRI; C: Sagittal plane T2 weighted MRI; D: Coronal plane FLAIR MRI. Typical pineal cysts are shown in the pineal region with unilocular homogeneous internal structure (white arrows, A, B, C and D); Isointense cyst with CSF (A, B and C); The slightly hyperintense pineal cyst compared to CSF is shown on FLAIR sequence (D). CSF: Cerebrospinal fluid; FLAIR: Fluid-attenuated inversion recovery.

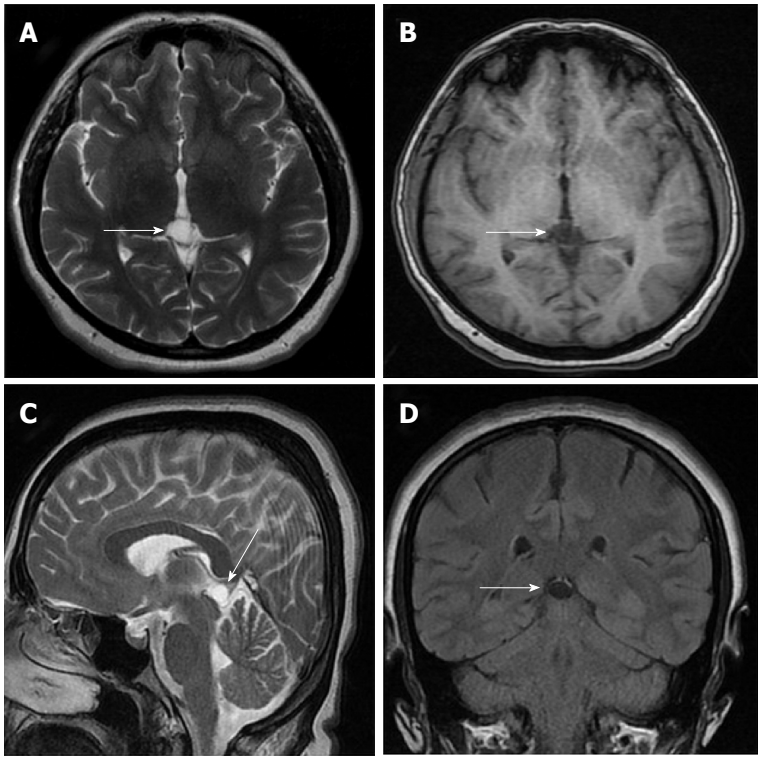

Figure 3 Thirty-five years old female patient with typical pineal cyst (patient No. 34). A: Axial plane T2 weighted magnetic resonance imaging (MRI); B: T1 weighted MRI; C: Sagittal plane T2 weighted MRI; D: Coronal plane FLAIR MRI. Typical pineal cyst is shown in the pineal region with unilocular homogeneous internal structure (white arrows, A, B, C and D); The isointense pineal cyst compared to CSF is shown in the pineal region (A, B, C and D). CSF: Cerebrospinal fluid; FLAIR: Fluid-attenuated inversion recovery.

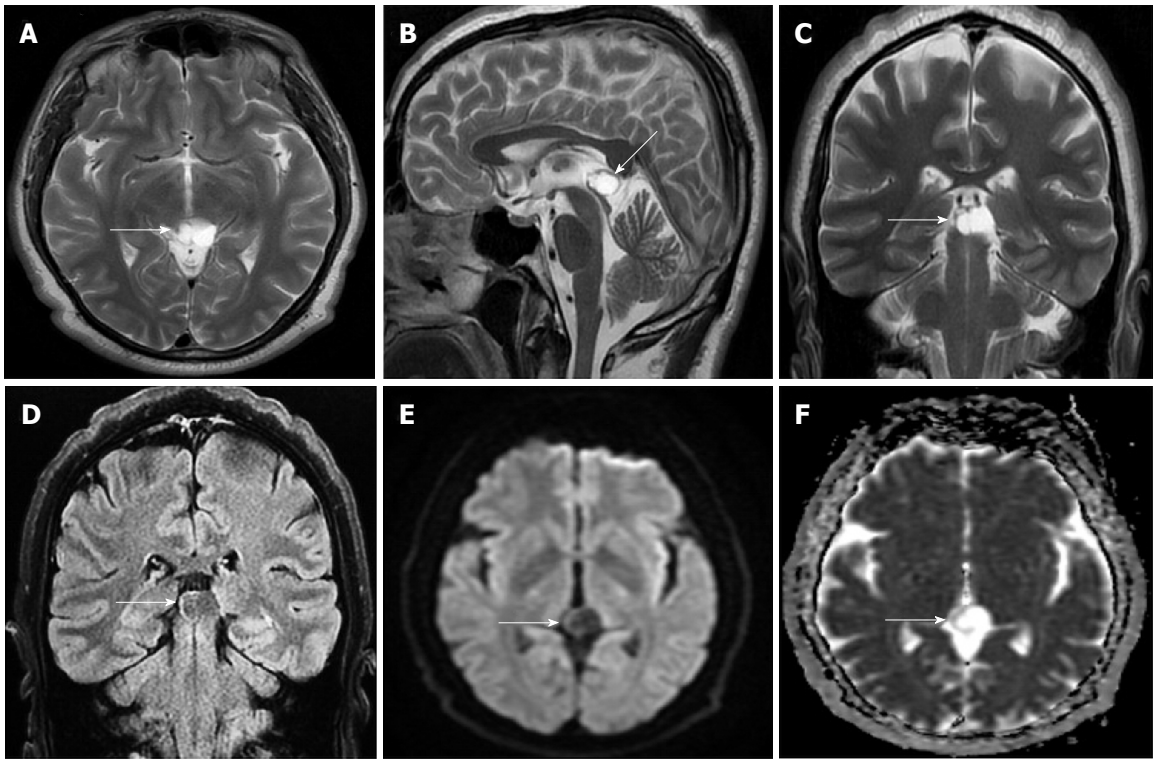

Figure 4 Fifty years old male patient with atypical pineal cyst (patient No. 40). Axial plane (A) sagittal plane magnetic resonance imaging (MRI) (B) coronal plane T2 weighted (C) and coronal plane FLAIR magnetic resonance imaging (D) axial plane diffusion weighted imaging (E) axial plane apparent diffusion coefficient map (F). A, B, C, D, E and F: Bilocular, lobule contoured atypical pineal cyst is shown in pineal area (white arrows); D: The slightly hyperintense pineal cyst compared to CSF is shown on FLAIR sequence; E and F: No diffusion restriction. CSF: Cerebrospinal fluid; FLAIR: Fluid-attenuated inversion recovery.

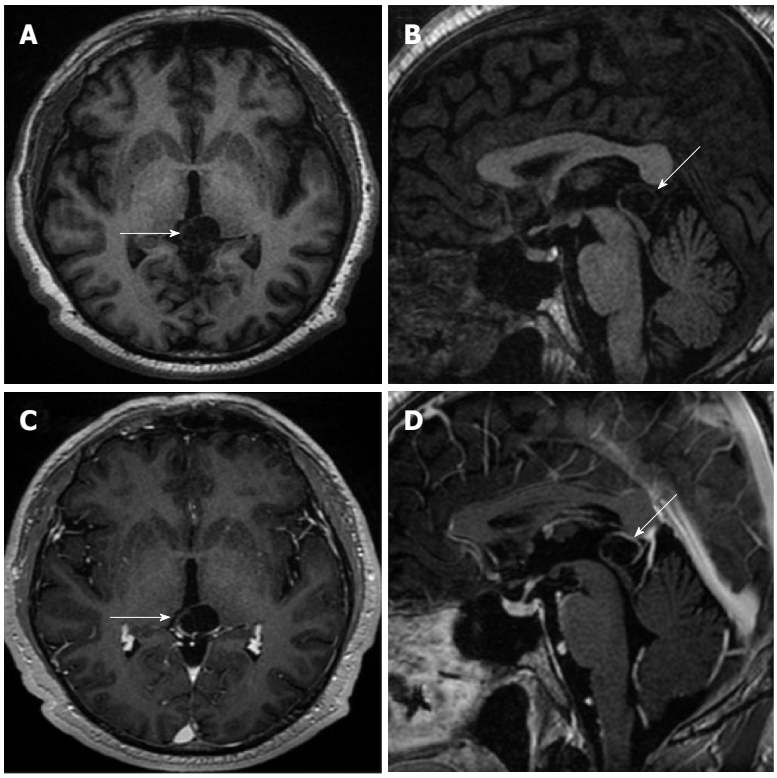

Figure 5 Fifty years old male patient with atypical pineal cyst (patient No. 40). Axial plane (A) sagittal plane T1 weighted (B) axial plane (C) sagittal plane contrast-enhanced magnetic resonance imaging (D). A, B, C and D: Bilocular, lobule contoured atypical pineal cyst is shown in pineal area (white arrows); C and D: Partial rim-like enhancement is shown (white arrows).

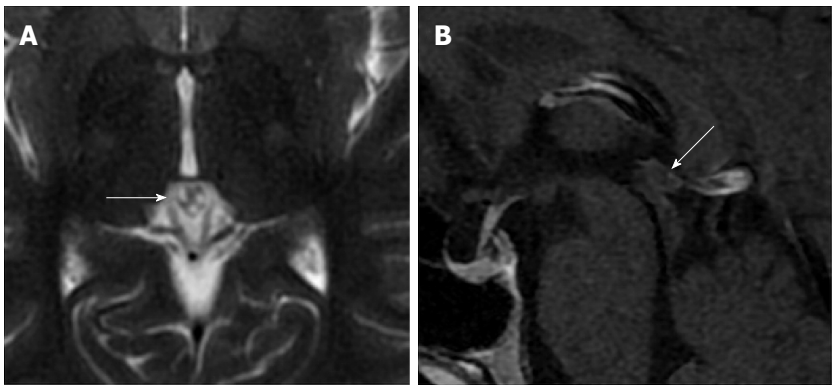

Figure 6 Thirty-six years old female patient with atypical pineal cyst (patient No. 2). Axial plane T2 weighted (A) sagittal plane (B) contrast-enhanced magnetic resonance imaging. A and B: Atypical pineal cysts are shown in the pineal region; A: Trilocular cyst (white arrow); B: Peripheral rim-like enhancement is shown (white arrow).

had intense heterogeneous contrast-enhancement, and complicated PC-pineocytoma differentiation could not be done radiologically (Figure 8). Most of the PCs were concluded to be typical (62.50%), while a smaller proportion was atypical (37.50%). Eighteen of the atypical PCs (32.4%) had two or more septation-loculation, and 11 (19.64%) had peripheral lobulation. Septation-loculation was observed in 9 (81.81%) of lobule-contoured PCs (Figure 9). MRI features of PCs are given in Table 4. Minimum and maximum PC diameters varied from 5.0 to 19.7 mm. Average PC sizes were 11.18 ± 3.03 mm in anteroposterior (AP), 10.41 ± 2.72 mm in mediolateral (ML) and 8.63 ± 2.47 mm in craniocaudal (CC) directions. Average PC volume was 0.62 ± 0.54 cm^3. A total of 18 PCs had follow-up examinations, and 10 of them were typical and 8 atypical. Natural change was not observed in any PCs with follow-ups. Amount of average dimension changes in PCs with follow-ups were (-0.08 ± 0.53) mm, (-0.22 ± 0.87) mm, and (0.16 ± 0.56) mm in AP, ML and CC dimensions, respectively. Thus, AP, ML and CC dimensions decreased in 6, 8 and 5 PCs, and increased in 5, 5 and 7 PCs, respectively. No significant difference was found between initial and final imaging sizes of

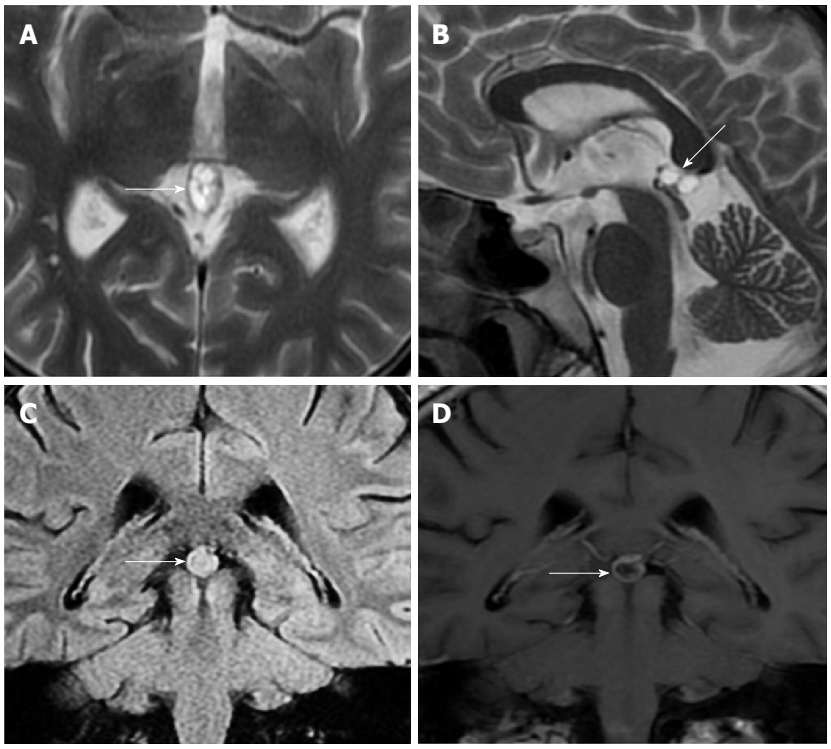

Figure 7 Thirty-three years old male patient with atypical pineal cyst (patient No. 41). Axial plane (A) sagittal plane T2 weighted (B) coronal plane FLAIR (C) coronal plane (D) contrast-enhanced magnetic resonance imaging. A and B: Atypical multilocular pineal cysts are shown in the pineal region (white arrows); C: The hyperintense pineal cyst compared to CSF is shown in the pineal region (white arrows); D: Peripheral rim-like and septal enhancement is shown (white arrows). CSF: Cerebrospinal fluid; FLAIR: Fluid-attenuated inversion recovery.

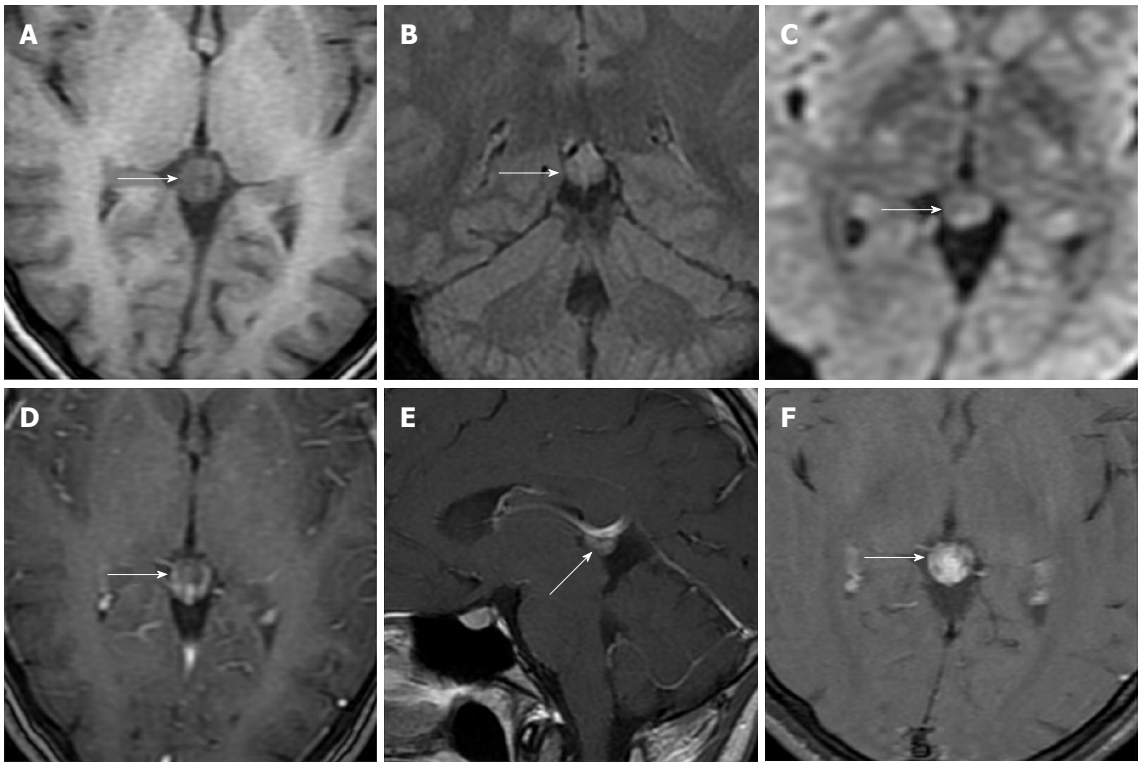

Figure 8 Twenty-two years old female patient with atypical pineal cyst (patient No. 50). Axial plane T1 weighted (A) coronal plane FLAIR (B) axial plane diffusion weighted (C) consecutive contrast-enhanced magnetic resonance imaging (D, E and F). A, B, C, D, E and F: Atypical pineal cyst or pineocytoma is not distinguished radiologically (white arrows); C: No diffusion restriction; D, E and F: Increasing gradually heterogeneous enhancement is shown in pineal region (white arrows). FLAIR: Fluid-attenuated inversion recovery.

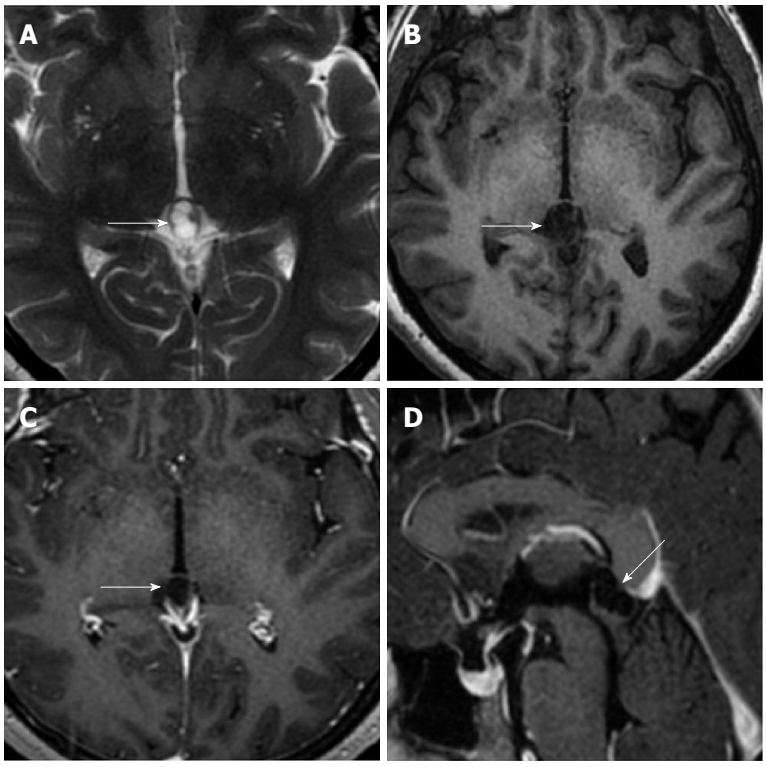

Figure 9 Thirty-three years old female patient with atypical pineal cyst (patient No. 53). Axial plane (A) T2 weighted (B) T1 weighted (C) contrast-enhanced (D) sagittal plane contrast-enhanced magnetic resonance imaging. A, B, C and D: Multilocular, lobule contoured, atypical pineal cyst is observed in pineal area (white arrows); C and D: Peripheral rim-like enhancement is shown (white arrows).

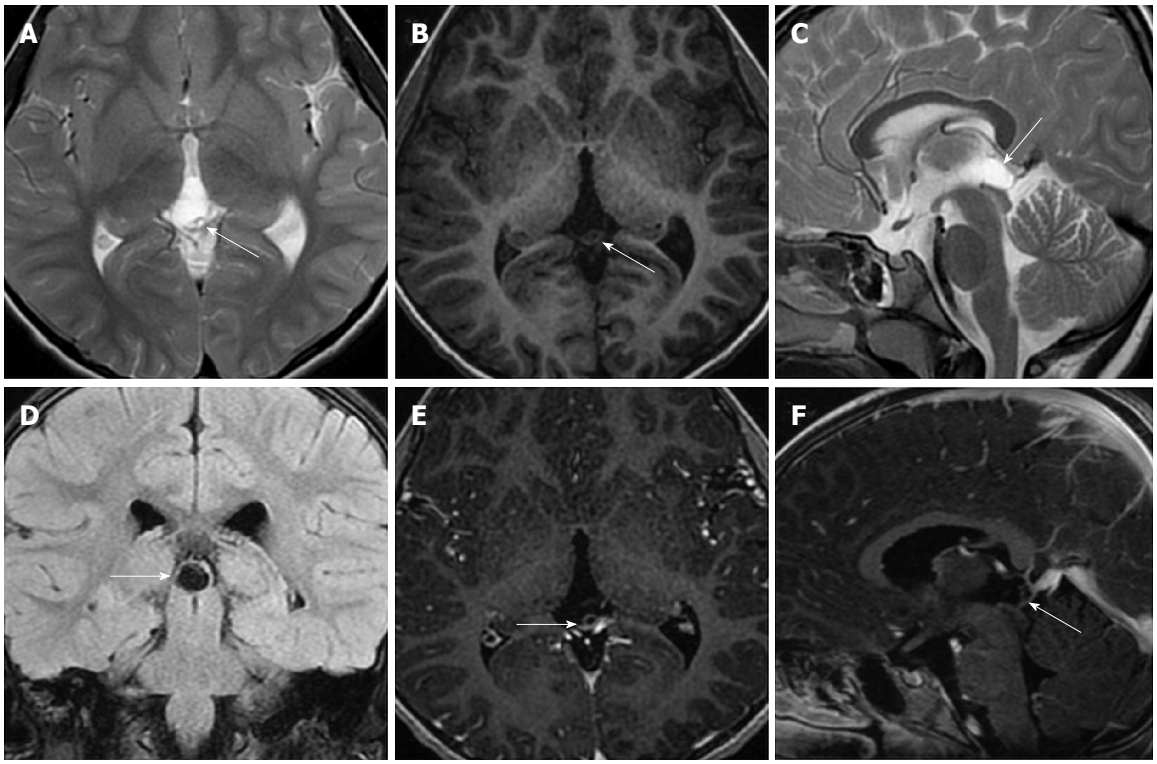

Figure 10 Five years old female patient with atypical pineal cyst (patient No. 44). Axial plane (A) T2 weighted (B) T1 weighted (C) sagittal plane T2 weighted (D) coronal plane FLAIR (E) axial plane (F) sagittal plane contrast-enhanced magnetic resonance imaging. A, B, C, D, E and F: Multilocular, lobule contoured, atypical pineal cyst is observed in pineal area (white arrows); D: The isointense pineal cyst compared to CSF is shown on FLAIR sequence; E and F: Peripheral rim-like and septal (white arrows) enhancement is shown. CSF: Cerebrospinal fluid; FLAIR: Fluid-attenuated inversion recovery.

Table 4 Magnetic resonance imaging features of pineal cysts

MRI features of pineal cysts	*n* (%)
Cyst type	
Typical	35 (62.50)
Atypical	21 (37.50)
Two or more septation-loculation	18 (32.14)
Contour lobularity	11 (19.64)
Cyst contrast-enhancement	21
Peripheral rim enhancement	15 (71.42)
Peripheral rim and septal enhancement	3 (14.28)
Partial rim enhancement	2 (9.52)
Dense heterogeneous enhancement	1 (4.76)
Cyst intensity relative to CSF on T2 weighted images	
Isointense	55 (98.21)
Hyperintense	1 (1.79)
Cyst intensity relative to CSF on T1 weighted images	
Isointense	53 (94.64)
Hyperintense	3 (5.36)
Cyst intensity relative to CSF on FLAIR images	
Isointense	6 (10.71)
Hyperintense	50 (89.29)
Diffusion restriction	0

MRI: Magnetic resonance imaging; CSF: Cerebrospinal fluid; FLAIR: Fluid-attenuated inversion recovery.

PCs which were monitored by follow-up examinations ($P > 0.05$). Initial dimensions and volumes of PCs and observed changes during the follow-up period are given in Table 5.

DISCUSSION

PC are observed in 0.6-10.8% of all random or consecutive brain MRI studies[5,11-14] and in 23% of healthy volunteers[15]. Al-Holou *et al*[16] found an incidence rate of 1.9% in an MRI study on a child population comprising 10821 children under 18 years of age. Lacroix-Boudhrioua *et al*[13] found a PC incidence rate of 11% in a high-resolution MRI study on a child patient group without a neurological indication. Considerable differences in reported PC incidence in MRI literature could be due to technical parameters or methodology (slice thickness, sequence type, strength of the magnetic field, size threshold of cysts included, *etc.*) as well as due to population differences (age, gender and race)[17]. In cadaver autopsies, pineal cyst incidence of up to 40% have been reported[5,18]. Higher incidence in autopsy series could be explained by the fact that small sized cysts of 2-5 mm can be detected only in cadaveric studies[13]. In the present study, only six of the 1327 patients (0.4%) who were 17 years of age and under were found to have PC. Frequency of PC in all ages combined was 0.58%, which was lower than the incidence rates reported in literature. Lower incidence rate in the present study could be due to population difference.

Al-Holou *et al*[12] found a prevalence of 2.0% in an adult population in the range of 19-30 years of age. Sawamura *et al*[19] reported a decrease in PC incidence after the age of 40. Al-Holou *et al*[12], on the other hand, mentioned that PC prevalence peaked at late childhood period and then started to decrease in adult age range. Most studies in literature reported lower PC incidence rates in infants and in old ages (older adults)[4,6,12,16,20-22]. In the present study, no PC was observed in infantile period, and the incidence of PC tended to increase towards the end of the second decade and peaked at the fourth decade. A slight decrease in prevalence was observed at the fifth decade, but the decrease in older ages was more pronounced.

There are many studies in literature reporting higher incidence of PCs in women[12,14,16,19]. Studying a population of children and young adults, Al-Holou *et al*[16] mentioned PC frequency of 2.4% in women and 1.5% in men. In a retrospective study by Al-Holou *et al*[12] carried out on 48417 patients who had brain MRI, frequency of pineal cyst was reported to be 1.1% in women and 0.8% in men. Similarly, Sawamura *et al*[19] found PC incidence rates of 1.6% for women and 0.96% for men. In the present study, on the other hand, relatively lower incidence rates of PC were observed, women having higher incidence rates (0.8%) than men (0.3%) similar to literature.

Most PCs are small sized[1,2]. Barboriak *et al*[4] reported that average PC diameter was 11.2 mm and volume was 1.42 cm^3. They also reported that 47% of PCs had 10 mm or smaller maximum linear dimension. Nevins *et al*[14] evaluated 281 PC, and found that median size of PCs at diagnosis was 10 mm. Al-Holou *et al*[12] found that starting dimensions of PCs were 9.7 ± 3.8 mm in sagittal anteroposterior, 6.8 ± 2.9 mm in sagittal craniocaudal and 7.0 ± 2.8 mm in axial width dimensions, and that 50% of PCs had less than 10 mm of maximum size. The authors also mentioned that sizes of PC in women and men were not significantly different, and volume of PCs was not significantly associated with age. Average PC dimension in the present study was 10.07 ± 2.93 mm in all planes (AP, ML and CC dimensions). Maximum dimension was less than 10 mm in 37.5% of PCs ($n = 21$), which was somewhat lower than what was reported in literature. This may be due to different measurement techniques used to determine PC dimensions. PC volumes in the present study were not significantly associated with gender or age of the patients ($P = 0.74$ and $P = 0.81$, respectively).

PCs typically have a benign prognosis, but some studies reported rare size changes of PCs over time[4,12,23]. Tamaki *et al*[7] and Golzarian *et al*[6] reported that size of PCs did not change in follow-up examinations. Al-Holou *et al*[12] found that only 2.6% of PCs which were monitored for periods varying from 6 mo to 3 years had an average maximum diameter increase of 3.5 mm, while size decreased in 15% and remained stable in 82% of them. In 32 patients monitored for periods ranging from six months to nine years, Barboriak *et al*[4] observed that maximal size did not change in 75.0% of PCs, 2-4 mm size decreases were observed in 9.37%, and 2-3 mm size increases were observed in 6.25% of

Table 5 IInitial dimensions and volumes and subsequent changes of pineal cysts

Pineal cyst dimensions and volume	Value (range)
Minimal-maximal linear dimension	5.0-19.70 mm
All plane mean dimension (AP, ML, CC)	10.07 ± 2.93 mm
Cyst volume (mean ± SD, range)	0.62 ± 0.54 (0.11-3.35) cm^3
Cyst dimension (mean ± SD, range) (mm)	
Anteroposterior (AP)	11.18 ± 3.03 (6.50-19.00)
Mediolateral (ML)	10.41 ± 2.72 (5.80-19.70)
Craniocaudal (CC)	8.63 ± 2.47 (5.0-18.30)
Changes in dimensions during follow-up period (mean ± SD, range) (mm)	
Anteroposterior (AP)	-0.08 ± 0.53 (-1.60-0.7)
Mediolateral (ML)	-0.22 ± 0.87 (-3-0.8)
Craniocaudal (CC)	0.16 ± 0.56 (-0.70-1.40)

the PCs. On the other hand, they also found that two cysts resolved completely, and a new cyst developed and grew to 12 mm. Nevins *et al*[14] reported that only 11 of the 181 PC that they followed for periods varying from 1 to 68 mo had dimensional changes. Seven of them had a 2 mm median diameter increase and the other four had 2.5 mm median diameter decrease[14]. Of the 18 PCs which were monitored by follow-up examinations in the present study, three (16.66%) had no size change, while five (27.77%) had size increases in all dimensions, four (22.22%) had size decreases and six (33.33%) had both increase and decreases in at least one dimension. Average increase in maximum diameter was 0.64 ± 0.37 mm (range: 0.1-1.4 mm), and average decrease in maximum diameter was 0.62 ± 0.45 mm (range: 0.1-1.6 mm). Size changes in PCs were much lower than those in literature. Barboriak *et al*[4] reported that no significant difference was observed for average volumes and maximum linear dimensions of PCs in initial and final MRI screenings. In parallel with Barboriak *et al*[4], changes between initial and final sizes of PCs were not statistically significant in the present study ($P > 0.05$). Barboriak *et al*[4] mentioned that MRI monitoring of incidentally determined asymptomatic cysts are not practical and suggested that cysts with atypical imaging features should be monitored. Nevins *et al*[14] recommended a single follow-up MRI scan with gadolinium at 12 mo after diagnosis and discharge if the pineal cyst has not increased in size. It has been indicated that follow-up imaging and even tissue sampling could be necessary for a lesion which does not meet MRI criteria of a typical pineal cyst or which manifests itself with clinical symptoms[10]. Nevertheless, many benign PC were reported to have irregular nodular enhancement on MR images[9]. Fleege *et al*[9] reported that 14 of 19 pineal lesions confirmed through histological examinations had been preoperatively concluded to be pineal neoplasms. The authors noted that PC had the appearance of complex cysts and cysts with fluid levels, calcification, hemorrhage, and enhancement[9]. Similarly, Fain *et al*[24] found abnormal rim enhancement on intracranial imaging in 50% of benign cysts confirmed by histological examination. It has been proposed that this abnormal peripheral rim enhancement could be associated with surrounding venous structures or displaced pineal gland[1,6,16]. Therefore, it was concluded that presence of a solid contrast-enhancement component in PC should be considered as a worrying appearance[5].

Radiological appearance of PCs changes by imaging modalities and parameters used. PCs are smooth-edged ovoid lesions which could generally be better visualized on sagittal plane in MRI. There are different reports in literature about signal properties of PCs obtained by different sequence parameters[6,19,21,25]. Osborn[26] indicated that almost all PCs appeared isointense or slightly intense with CSF on T2 weighted MR images, but on T1 weighted images, 50%-60% of them appeared slightly hyperintense compared to CSF, about 40% appeared isointense and 1%-2% with intracystic hemorrhage, on the other hand, appeared hyperintense. The author also reported that signal of most PCs was not completely suppressed on FLAIR images and appeared moderately hyperintense compared to brain parenchyma. Nevertheless, signal properties of PCs were found to vary depending upon its content, presence of hemorrhage and calcification[26]. More than 60%-90% of PCs were shown to have contrast-enhancement on contrast-enhanced series[1,2,26]. On diffusion MRI content of cyst typically does not have diffusion limitation[27]. Almost all PCs in the present study (98.21%) were isointense with CSF, and only one (1.79%) was slightly hyperintense on T2 weighted images. On T1 weighed series, 94.64% were isointense with CSF and only 5.36% was slightly hyperintense. On FLAIR series, 89.29% were hyperintense with CSF and 10.71% were isointense. Contrast-enhancement was observed in PCs of all patients who had contrast-enhanced examination. Barboriak *et al*[4] reported that only one cyst showed signal change on proton density weighted sequence during follow-up examinations. In the present study, no change was observed in MRI signal feature of any cyst in any sequence.

PCs were reported to have unilocular appearance in literature dealing with routine brain MRI studies[4,25]. Al-Holou *et al*[12], on the other hand, found that 11% of PCs had multicystic appearance or had atypical features due to abnormal contrasting. Jinkins *et al*[25]

mentioned that most PCs were unilocular but PCs in two patients had septation. Using FIESTA (fast imaging employing steady-state acquisition) sequence, Pastel *et al*[28] detected that six of the 10 PCs (60%) had internal septation or multiloculation. In their high-resolution MRI studies, Lacroix-Boudhrioua *et al*[13] found that 74% of PCs had septation. In addition, pathological studies reported multiple septations as common findings in PCs[12,18]. This fact means that majority of PC septations could not be detected in routine MRI series. In the present study, septation was observed in 18 PCs (32.14%). Three PCs which had been described as typical based on MRI exams before our MRI machine was upgraded (before 2017) were classified atypical in follow-up MRI exams carried out in 2017 and later due to observed internal septations. It was concluded that especially BRAVO sequence (high resolution three-dimensional T1-weighted gradient images) of isotropic 1 mm^3, both contrast-enhanced and without contrast-enhanced, improved the detection of internal septations. Studies in literature mentioned that growth and changing patterns of septated cysts are not significantly different from those of unilocular ones[5,12,28]. Similar to the studies in literature, no significant difference was observed between growth patterns of atypical and typical PCs ($P > 0.05$).

PCs are localized in pineal gland and may partly or completely occupy it. A typical pineal cyst shows a contrasting wall feature in a thin peripheral rim style of less than 2 millimeter[4]. Since there is no blood-brain barrier around pineal gland, contrast-enhancement is observed in cyst walls[11]. In the center of cyst, contrast-enhancement is not normally observed in images taken right after contrast matter administering. Nevertheless, in images taken 60-90 min later, cyst may have contrast-enhancement in a uniform and solid appearance[1]. In atypical PCs, findings such as internal septation or loculation, irregular nodular contrast-enhancement, edge lobulation and hemorrhage can be observed[1,4,11,16]. However, these atypical findings are not necessarily related to malignity or cyst enlargement[1]. In fact, high resolution MRI studies showed that internal septations and loculations can be detected in great majority of PCs[13,28]. Follow-up examinations in many studies, including the present one, showed that atypical PCs are not different from the typical ones in terms of size and natural change[4,12]. This finding suggests that internal septation-loculations or lobulations are in fact inherent in PCs and that typical-atypical classification based on these criteria should be reconsidered. Nevertheless, despite the advances in high resolution MRI, there are not definite radiological methods to distinguish benign PC from pineal region malignancies containing cystic components such as pineocytomas, pineoblastomas, germinomas or mature teratomas[29]. In addition, similar to pineal area tumors such as pineoblastomas, teratomas or pilocytic astrocytoma which look like large cysts, benign PCs which lead to intracystic hemorrhage and hydrocephaly and have a complicated appearance may mimic malignant tumors[9,30]. Since malignancy possibility is higher in PCs which grow and have high contrast-enhancement and hemorrhage, more frequent follow-ups or neurosurgical intervention may be necessary with these PCs[29].

PC could enlarge in time due to both intracystic fluid increase and hemorrhage and become symptomatic. Because of their mass effect on midbrain next to them, PCs could lead to Parinaud syndrome (paralysis of upward gaze, retraction in eyelid and abnormal pupil reactions)[31,32]. Sudden death events have been reported because of intra-cystic hemorrhage, also called pineal apoplexy, and acute hydrocephaly[33,34]. PCs with diameters smaller than 10 mm typically do not exert compression on adjacent structures such as cerebral aqueduct, vein of Galen, and the quadrigeminal plate, and they are frequently asymptomatic[1,20]. However, PCs with diameters larger than 15 mm could make local mass effect on adjacent structures and lead to neurological symptoms as a result of hydrocephaly due to compression of cerebral aqueduct[1]. Although there were seven PCs with maximum diameter of more than 15 mm in the present study, gross local mass effect or cerebral aqueduct compression was not observed in any patient. Patients may have a large scale of symptoms due to PC, headache being the most common. Other frequently observed symptoms in PC patients are seizures, dizziness, blurred vision, hemiparesis and vomiting[29]. Previously, headache in these patients were thought to be due to increased intracranial pressure. However, recent studies indicated a hormonal imbalance indicating melatonin as culprit[29,35]. In addition, a recent study reported that MR biomarkers (tectum-splenium-cyst ratio and thalamic and periventricular edema) could be associated with central venous hypertension and severity of symptoms in non-hydrocephalic, symptomatic PC patients[36]. Although PCs did not lead to clear compression findings in the present study, the most common symptom experienced by the patients was headache (75%).

Asymptomatic cysts could be accompanied by tectal deformities of different intensities[4]. Although higher deformity levels are observed in larger cysts as expected, Barboriak *et al*[4] reported that they could not obtain any finding indicating that cysts with higher level of deformities could further enlarge in follow-up examinations. Some studies reported hydrocephaly in patients with PCs larger than 20 mm[37]. On the other hand, Barboriak *et al*[4] found that only a moderate enlargement in ventricle was observed in two patients with PCs of that size. No patients had cysts with maximum diameter of more than 20 mm diameter, and hydrocephaly due to the mass effect of PC was not observed in any patient in the present study.

Because of the uncertainties about the natural history of PC, especially about asymptomatic ones, there is no consensus in the literature about what is the most appropriate treatment approach for PC[29].

Management options for asymptomatic cysts vary from total ignoring even without any follow-ups to surgical intervention. Surgical intervention is commonly refrained in asymptomatic patients[29]. Some clinicians suggest yearly follow-ups using clinical examination and imaging, but others do not recommend routine imaging for known PC[12,29]. Similarly, while some studies highly recommended routine clinical examinations and imaging in children[16,23,29,31], others considered PCs as common incidental findings and suggested no follow-ups or contrast-enhanced examinations for children without any neurological indications[13]. In symptomatic patients, especially in ones with hydrocephaly, surgical interventions such as shunt placement, cyst excision, endoscopic or stereotactic aspiration, and endoscopic third ventriculostomy could be preferred[29,38]. In their review paper, Májovský *et al*[39] reported positive feedbacks for elimination of symptoms after PC surgery in most symptomatic patients and even in patients with non-specific symptoms. Although the authors considered microsurgical resection of PCs, using supracerebellar-infratentorial approach, as a viable option for symptomatic patients, they noted that this suggestion was based on limited number of reports[39].

The present study has some limitations. First, relatively fewer PC were evaluated retrospectively in the present study. Second, only 21 of the patients (37.5%) had contrast-enhanced examination. Third, the number of cases with follow-ups was few and follow-up periods were not standard for patients who had them. Fourth, none of the patients had histopathological examinations. Finally, quite small size increase or decrease was observed in a small number of PC. Although we are confident that the change in size is accurate, there is a slight possibility that some of the changes may reflect measurement error.

In conclusion, PCs are cysts which do not have marked dimensional and natural changes. Their frequency is higher in women and adults, and their sizes are not associated with gender or age. Great majority of them are isointense with CSF on T1 and T2A series. On FLAIR sequence, they are hyperintense compared to CSF, and they may be smoothly contoured, unilocular or multilocular. Typical ones may have contrast-enhancement in peripheral rim style, while multilocular ones may have septal contrast-enhancement.

ARTICLE HIGHLIGHTS

Research background

Pineal cysts (PC) are cysts which are frequently detected incidentally in brain magnetic resonance imaging (MRI). No clear consensus has been reached yet over the classification and follow-up procedures in routine clinical practice. PCs were classified based on MRI findings in the present study. Unilocular, smooth edged, ovoid PCs with homogenous interior structure and less than 2 mm wall thickness were considered typical PC, while multilocular PCs with walls thicker than 2 mm, septation or contour lobulation were considered atypical. In addition, size and natural changes in follow-up examinations were also investigated.

Research motivation

Lack of a consensus over radiological classification and follow-up of PC, and their radiological findings that resemble other lesions of pineal area create difficulties. Presentation of radiological studies dealing with PCs in different population including follow-up images taken at different series could help to resolve this uncertainty.

Research objectives

In the present study, PCs detected using brain MRI examinations in our population were classified based on radiological imaging features. In addition, whether PCs had significant size or nature changes were also evaluated.

Research methods

A total of 9546 patients who had brain MRI examination in March 2010-January 2018 period were studied retrospectively for the presence of PCs. Sizes in three dimensions, volumes, contours, signal intensities, internal septation or loculation features and contrasting patterns of PCs were evaluated. Size and natural changes of PCs were investigated in patients during follow-up examinations with durations varying from 2 to 96 mo. Associations between PC frequency and gender, between PC volumes and gender and age, and amount of changes between initial and final sizes of PCs were statistically analyzed.

Research results

Fifty-six patients (44 female and 12 male) were found to have had PC. Age range of patients with PC was 5-61 (mean: 31.26 ± 12.73). Frequency of PC was 0.58%. PC incidence rates were significantly different in men and women. In terms of classification, 62.50% of the PCs were typical and 37.50% were atypical. Average PC sizes were 11.18 ± 3.03 mm in AP, 10.41 ± 2.72 mm in ML and 8.63 ± 2.47 mm in CC directions. Natural change was not observed in any PC with follow-ups. Average dimension changes in PCs with follow-ups were (-0.08 ± 0.53) mm, (-0.22 ± 0.87) mm, and (0.16 ± 0.56) mm in AP, ML and CC dimension, respectively. No significant difference was found between initial and final sizes of PCs which were monitored by follow-up examinations.

Research conclusions

It was revealed in the present study that classification of PCs concluded to be unilocular (*i.e.*, typical) based on routine MRI sequences could change to atypical when high resolution sequences indicated internal septations. No significant size or natural change was observed in follow-up examinations of PCs. Therefore, it could be suggested that asymptomatic PCs which do not show any size or natural changes during one- or two-year follow-ups should be removed from routine follow-up.

Research perspectives

The present study showed that PCs are cysts frequently observed as incidental lesions in brain MRI series, that they have an average diameter of 10 mm and that they have signal features similar to CSF in T1 and T2 weighed series while giving higher signal intensities than CSF in FLAIR sequence. In addition, it was revealed that typical or atypical classification of PCs could change based on resolution of sequence used in identification of PCs. Elimination of frequent follow-ups of asymptomatic PCs could lower cost and labor burden on health care system.

REFERENCES

1 **Choy W**, Kim W, Spasic M, Voth B, Yew A, Yang I. Pineal cyst: a review of clinical and radiological features. *Neurosurg Clin N Am* 2011; **22**: 341-351, vii [PMID: 21801982 DOI: 10.1016/j.nec.2011.06.001]

2 **Osborn AG**, Preece MT. Intracranial cysts: radiologic-pathologic correlation and imaging approach. *Radiology* 2006; **239**: 650-664 [PMID: 16714456 DOI: 10.1148/radiol.2393050823]

3 **Kahilogullari G**, Massimi L, Di Rocco C. Pineal cysts in children: case-based update. *Childs Nerv Syst* 2013; **29**: 753-760 [PMID: 23283557 DOI: 10.1007/s00381-012-2011-6]

4 **Barboriak DP**, Lee L, Provenzale JM. Serial MR imaging of pineal cysts: implications for natural history and follow-up. *AJR Am J Roentgenol* 2001; **176**: 737-743 [PMID: 11222216 DOI: 10.2214/ajr.176.3.1760737]

5 **Cauley KA**, Linnell GJ, Braff SP, Filippi CG. Serial follow-up MRI of indeterminate cystic lesions of the pineal region: experience at a

rural tertiary care referral center. *AJR Am J Roentgenol* 2009; **193**: 533-537 [PMID: 19620453 DOI: 10.2214/AJR.08.1906]
6 **Golzarian J**, Balériaux D, Bank WO, Matos C, Flament-Durand J. Pineal cyst: normal or pathological? *Neuroradiology* 1993; **35**: 251-253 [PMID: 8492885 DOI: 10.1007/BF00602604]
7 **Tamaki N**, Shirataki K, Lin TK, Masumura M, Katayama S, Matsumoto S. Cysts of the pineal gland. A new clinical entity to be distinguished from tumors of the pineal region. *Childs Nerv Syst* 1989; **5**: 172-176 [PMID: 2758432 DOI: 10.1007/BF00272122]
8 **Hayashida Y**, Hirai T, Korogi Y, Kochi M, Maruyama N, Yamura M, Yamashita Y. Pineal cystic germinoma with syncytiotrophoblastic giant cells mimicking MR imaging findings of a pineal cyst. *AJNR Am J Neuroradiol* 2004; **25**: 1538-1540 [PMID: 15502133]
9 **Fleege MA**, Miller GM, Fletcher GP, Fain JS, Scheithauer BW. Benign glial cysts of the pineal gland: unusual imaging characteristics with histologic correlation. *AJNR Am J Neuroradiol* 1994; **15**: 161-166 [PMID: 8141049]
10 **Fakhran S**, Escott EJ. Pineocytoma mimicking a pineal cyst on imaging: true diagnostic dilemma or a case of incomplete imaging? *AJNR Am J Neuroradiol* 2008; **29**: 159-163 [PMID: 17925371 DOI: 10.3174/ajnr.A0750]
11 **Mamourian AC**, Towfighi J. Pineal cysts: MR imaging. *AJNR Am J Neuroradiol* 1986; **7**: 1081-1086 [PMID: 3098073]
12 **Al-Holou WN**, Terman SW, Kilburg C, Garton HJ, Muraszko KM, Chandler WF, Ibrahim M, Maher CO. Prevalence and natural history of pineal cysts in adults. *J Neurosurg* 2011; **115**: 1106-1114 [PMID: 21780858 DOI: 10.3171/2011.6.JNS11506]
13 **Lacroix-Boudhrioua V**, Linglart A, Ancel PY, Falip C, Bougnères PF, Adamsbaum C. Pineal cysts in children. *Insights Imaging* 2011; **2**: 671-678 [PMID: 22347985 DOI: 10.1007/s13244-011-0117-0]
14 **Nevins EJ**, Das K, Bhojak M, Pinto RS, Hoque MN, Jenkinson MD, Chavredakis E. Incidental Pineal Cysts: Is Surveillance Necessary? *World Neurosurg* 2016; **90**: 96-102 [PMID: 26944882 DOI: 10.1016/j.wneu.2016.02.092]
15 **Pu Y**, Mahankali S, Hou J, Li J, Lancaster JL, Gao JH, Appelbaum DE, Fox PT. High prevalence of pineal cysts in healthy adults demonstrated by high-resolution, noncontrast brain MR imaging. *AJNR Am J Neuroradiol* 2007; **28**: 1706-1709 [PMID: 17885233 DOI: 10.3174/ajnr.A0656]
16 **Al-Holou WN**, Garton HJ, Muraszko KM, Ibrahim M, Maher CO. Prevalence of pineal cysts in children and young adults. Clinical article. *J Neurosurg Pediatr* 2009; **4**: 230-236 [PMID: 19772406 DOI: 10.3171/2009.4.PEDS0951]
17 **Jussila MP**, Olsén P, Salokorpi N, Suo-Palosaari M. Follow-up of pineal cysts in children: is it necessary? *Neuroradiology* 2017; **59**: 1265-1273 [PMID: 28942520 DOI: 10.1007/s00234-017-1926-8]
18 **Hasegawa A**, Ohtsubo K, Mori W. Pineal gland in old age; quantitative and qualitative morphological study of 168 human autopsy cases. *Brain Res* 1987; **409**: 343-349 [PMID: 3580881 DOI: 10.1016/0006-8993(87)90720-7]
19 **Sawamura Y**, Ikeda J, Ozawa M, Minoshima Y, Saito H, Abe H. Magnetic resonance images reveal a high incidence of asymptomatic pineal cysts in young women. *Neurosurgery* 1995; **37**: 11-15; discussion 15-16 [PMID: 8587669 DOI: 10.1227/00006123-199507000-00002]
20 **Sener RN**. The pineal gland: a comparative MR imaging study in children and adults with respect to normal anatomical variations and pineal cysts. *Pediatr Radiol* 1995; **25**: 245-248 [PMID: 7567225 DOI: 10.1007/BF02011087]
21 **Lee DH**, Norman D, Newton TH. MR imaging of pineal cysts. *J Comput Assist Tomogr* 1987; **11**: 586-590 [PMID: 3597879 DOI: 10.1097/00004728-198707000-00005]
22 **Lum GB**, Williams JP, Machen BC, Akkaraju V. Benign cystic pineal lesions by magnetic resonance imaging. *J Comput Tomogr* 1987; **11**: 228-235 [PMID: 3608546 DOI: 10.1016/0149-936X(87)90087-7]
23 **Mandera M**, Marcol W, Bierzyńska-Macyszyn G, Kluczewska E. Pineal cysts in childhood. *Childs Nerv Syst* 2003; **19**: 750-755 [PMID: 12920545 DOI: 10.1007/s00381-003-0813-2]
24 **Fain JS**, Tomlinson FH, Scheithauer BW, Parisi JE, Fletcher GP, Kelly PJ, Miller GM. Symptomatic glial cysts of the pineal gland. *J Neurosurg* 1994; **80**: 454-460 [PMID: 8113858 DOI: 10.3171/jns.1994.80.3.0454]
25 **Jinkins JR**, Xiong L, Reiter RJ. The midline pineal "eye": MR and CT characteristics of the pineal gland with and without benign cyst formation. *J Pineal Res* 1995; **19**: 64-71 [PMID: 8609598 DOI: 10.1111/j.1600-079X.1995.tb00172.x]
26 **Osborn AG**. Osborn's Brain: Imaging, Pathology, and Anatomy. 1st ed. Canada: Amirsys, 2013: 788-791
27 **Fang AS**, Meyers SP. Magnetic resonance imaging of pineal region tumours. *Insights Imaging* 2013; **4**: 369-382 [PMID: 23640020 DOI: 10.1007/s13244-013-0248-6]
28 **Pastel DA**, Mamourian AC, Duhaime AC. Internal structure in pineal cysts on high-resolution magnetic resonance imaging: not a sign of malignancy. *J Neurosurg Pediatr* 2009; **4**: 81-84 [PMID: 19569915 DOI: 10.3171/2008.5.17681]
29 **Starke RM**, Cappuzzo JM, Erickson NJ, Sherman JH. Pineal cysts and other pineal region malignancies: determining factors predictive of hydrocephalus and malignancy. *J Neurosurg* 2017; **127**: 249-254 [PMID: 27767399 DOI: 10.3171/2016.8.JNS16220]
30 **Sarikaya-Seiwert S**, Turowski B, Hänggi D, Janssen G, Steiger HJ, Stummer W. Symptomatic intracystic hemorrhage in pineal cysts. Report of 3 cases. *J Neurosurg Pediatr* 2009; **4**: 130-136 [PMID: 19645546 DOI: 10.3171/2009.4.PEDS08309]
31 **Wisoff JH**, Epstein F. Surgical management of symptomatic pineal cysts. *J Neurosurg* 1992; **77**: 896-900 [PMID: 1432132 DOI: 10.3171/jns.1992.77.6.0896]
32 **Ramji S**, Touska P, Rich P, MacKinnon AD. Normal neuroanatomical variants that may be misinterpreted as disease entities. *Clin Radiol* 2017; **72**: 810-825 [PMID: 28747250 DOI: 10.1016/j.crad.2017.06.118]
33 **Milroy CM**, Smith CL. Sudden death due to a glial cyst of the pineal gland. *J Clin Pathol* 1996; **49**: 267-269 [PMID: 8675746 DOI: 10.1136/jcp.49.3.267]
34 **Richardson JK**, Hirsch CS. Sudden, unexpected death due to "pineal apoplexy". *Am J Forensic Med Pathol* 1986; **7**: 64-68 [PMID: 3728423 DOI: 10.1097/00000433-198603000-00014]
35 **Peres MF**. Melatonin, the pineal gland and their implications for headache disorders. *Cephalalgia* 2005; **25**: 403-411 [PMID: 15910564 DOI: 10.1111/j.1468-2982.2005.00889.x]
36 **Eide PK**, Pripp AH, Ringstad GA. Magnetic resonance imaging biomarkers indicate a central venous hypertension syndrome in patients with symptomatic pineal cysts. *J Neurol Sci* 2016; **363**: 207-216 [PMID: 27000252 DOI: 10.1016/j.jns.2016.02.038]
37 **Fetell MR**, Bruce JN, Burke AM, Cross DT, Torres RA, Powers JM, Stein BM. Non-neoplastic pineal cysts. *Neurology* 1991; **41**: 1034-1040 [PMID: 2067630 DOI: 10.1212/WNL.41.7.1034]
38 **Berhouma M**, Ni H, Delabar V, Tahhan N, Memou Salem S, Mottolese C, Vallee B. Update on the management of pineal cysts: Case series and a review of the literature. *Neurochirurgie* 2015; **61**: 201-207 [PMID: 24907165 DOI: 10.1016/j.neuchi.2013.08.010]
39 **Májovský M**, Netuka D, Beneš V. Is surgery for pineal cysts safe and effective? Short review. *Neurosurg Rev* 2018; **41**: 119-124 [PMID: 28702847 DOI: 10.1007/s10143-017-0876-2]

P- Reviewer: Kumar J, Xiao E **S- Editor**: Ji FF
L- Editor: A **E- Editor**: Tan WW

World Journal of Radiology

Submit a Manuscript: http://www.f6publishing.com

World J Radiol 2018 July 28; 10(7): 78-82

DOI: 10.4329/wjr.v10.i7.78

ISSN 1949-8470 (online)

CASE REPORT

Obesity and pericallosal lipoma in X-linked emery-dreifuss muscular dystrophy: A case report - Does Emerin play a role in adipocyte differentiation?

Fabio Spanu, Luca Saba

Fabio Spanu, Luca Saba, Department of Radiology, Azienda Ospedaliero Universitaria, Cagliari 09045, Italy

ORCID number: Fabio Spanu (0000-0003-3765-3905); Luca Saba (0000-0003-2870-3771).

Author contributions: Spanu F designed and wrote the report and collected the patient's clinical data; Saba L provided the radiologic data, checked the case and reviewed the paper.

Conflict-of-interest statement: All authors have no conflicts of interest to report.

CARE Checklist (2013) statement: Guidelines of the CARE Checklist (2013) have been adopted while writing this manuscript.

Manuscript source: Unsolicited manuscript

Correspondence to: Fabio Spanu, MD, Surgeon, Department of Radiology, Azienda Ospedaliero Universitaria, Polo di Monserrato s.s. 554 Monserrato, Cagliari 09045, Italy. docfabio.spanu@gmail.com
Telephone: +39-705-1096242
Fax: +39-705-6092299

Received: April 25, 2018
Peer-review started: April 25, 2018
First decision: June 6, 2018
Revised: June 11, 2018
Accepted: June 27, 2018
Article in press: June 28, 2018
Published online: July 28, 2018

Abstract

Emery dreifuss muscular dystrophy (EDMD) is a rare genetic syndrome consisting of tendon retractions, progressive muscle atrophy and cardiac involvement. We report a case of an obese patient affected by the familial X-linked form in which a pericallosal lipoma was found during investigation for a suspected acute vasculopathy. To date, EDMD has never been associated with cerebral lipomas and the X-linked form was never considered to be involved in lipodystrophic syndromes or non-muscular conditions. Our case confirms the variable expressivity of the disease and suggests a possible role of Emerin in the intranuclear regulation of signals for adipocyte cell differentiation.

Key words: Familiar emery dreifuss muscular dystrophy; Emerin; Adipocyte differentiation; Pericallosal lipoma; Emery-dreifuss-distrophy

Core tip: To date, emery dreifuss muscular dystrophy has never been associated with cerebral lipomas, and the X-linked form was never considered to be involved in extra-muscular syndromes. We presented a case of a patient affected by the X-linked form with a particular adipose tissue distribution and a cerebral and spinal lipoma, thus suggesting a possible role of Emerin in the intranuclear regulation of signals for cell differentiation, or in lipidic intracellular dysmetabolism when absent.

Spanu F, Saba L. Obesity and pericallosal lipoma in X-linked emery-dreifuss muscular dystrophy: A case report - Does Emerin play a role in adipocyte differentiation? *World J Radiol* 2018; 10(7): 78-82 Available from: URL: http://www.wjgnet.com/1949-8470/full/v10/i7/78.htm DOI: http://dx.doi.org/10.4329/wjr.v10.i7.78

INTRODUCTION

Emery dreifuss muscular dystrophy (EDMD) is a rare genetic syndrome described for the first time in 1966 after studying families with slowly progressive muscular dystrophy compared to the Duchenne-type[1]. It belongs to the group of nuclear envelopathies, defects in proteins that make up the nuclear envelope. However, even when included among the subgroup of laminopathies, not all the pathogenic variants in EDMD show defects in lamins. Specifically, in the X-linked EDMD variant, the protein Emerin, normally ubiquitously expressed on the nuclear membrane, is absent in 95% of individuals[2]. This form has a similar clinical picture compared to the autosomal dominant variant (involving Lamin A/C)[3], although not exactly the same, and is characterized by joint contractures (usually the first sign), slow and progressive muscle weakness (appearing first in AD variants), and cardiac involvement with arrhythmias and dilated cardiomyopathies[4]. Most of emerinopathies are null variants, but the phenotype may show intra-familial variability. Nevertheless, in contrast to mutations in the *Lamin A/C* gene, XL-EDMDs are not associated with Dunnigan-type familial partial lipodystrophy nor with cerebral involvement, including the occurrence of intracranial lipomas[5].

CASE REPORT

A 27-year-old man with Emery-Dreifuss muscular dystrophy presented at E.D. three hours after the onset of objective vertigo, followed by painful left arm weakness. He was from a family with four brothers affected by the X-linked form of the disease, due to the 130 C > T (Q44X) non-sense mutation in the exon 2 of the *EMD* gene. He was obese, with a particular accumulation of facial and neck adipose tissue. He was pharmacologically treated with ramipril, bisoprolol and apixaban for cardiac rhythm disorders, monitored with a loop recorder reveal. His medical history revealed several episodes of aberrant intraventricular conduction followed by SVPT, with isolated episodes of bradycardia and atrial ectopic beats. Echocardiograms had shown bi-atrial and LV enlargement. Muscular involvement was moderate, with deterioration of medial head of gastrocnemius, semimembranosus and, although mildly, lateral head of gastrocnemius, vasti, adductor magnus and long head of biceps femoris. No clear deformities or contractures were evident, in contrast to the patient's two affected younger brothers and an affected first-grade cousin.

The clinical exam at the E.D. showed a left arm downward drift associated with local joint pain. The patient was alert, oriented and cooperative, and the thoracic and abdominal clinical evaluation showed normal findings. Suspecting an acute vasculopathy, he underwent an urgent head NCCT that revealed the presence of a left-sided hypodense peri-callosal curvilinear lesion (Figure 1). No clear cerebral ischemic signs were observed. Further CT Angiography showed the perilesional course of pericallosal arteries below the rostrum and the genu of the corpus callosum, where both were pushed to the right side of the lesion and upward, resulting (above the lesion) in a correspondence between the body and splenium of the corpus callosum (Figure 2). The left artery narrowed progressively when compared to the contralateral. Furthermore, the exam ruled out vascular obstructions. The scan at thoracic level revealed a lesion with similar density and characteristics at the T1-T2 level, posterior to the cord and occupying the extradural space (Figure 3) with apparent dural impression. Then, the patient was admitted at the ward and was subjected to an MRI the next day, which did not show diffusivity alterations, thus definitely excluding areas of ischemia. Along the pericallosal region from rostrum to splenium, the lesion described in the CT appeared hyperintense at T1-W and long TR sequences, and hypointense at fat suppression sequences, without contrast enhancement and with clearly defined limits (Figure 4). These findings confirmed the initial hypothesis of a complete, left-sided, curvilinear pericallosal lipoma. Callosal aplasia was not observed. The day after, the patient's pain was subsiding with painkillers, while his weakened arm had completely recovered, allowing him to be discharged to his home.

DISCUSSION

EDMD is a rare genetic disease with an estimated prevalence of 0.13:100000-0.2:100000 overall[6], and of 1:100000 inhabitants for the XL-EDMD variant[7]. We reported a case of XL-EDMD in a family of five members affected, and a sister carrier of the same mutation c.130 C < T (pQ44X), in exon 2 of the *EMD* or *STA* genes. This mutation inserts a stop at codon 44, causing early translation termination of Emerin, resulting in C-terminal truncation and *in vivo* destabilization with complete loss[8].

Emerin is a type 2 integral membrane protein of 29-kDa, a resident of the inner nuclear membrane (INM) that is closely linked to lamin proteins, components of the nuclear lamina. It has been observed that in cells lacking a functional A-type lamin gene, as is observed in AD-EDMD, Emerin is largely mislocalized to the peripheral endoplasmic reticulum (ER). It has been postulated that the nuclear lamina plays a crucial role in limiting the segregation of INM proteins to the outer nuclear membrane and peripheral ER[9]. The tissue-specificity associated with laminopathies may be explained by a dysfunction in specific processes which take place in the ER, like cholesterol and fatty acid synthesis, due to the accumulation of proteins that are no longer contained within the nuclear envelope. This would result in aberrant adipocyte development and lipodystrophic diseases, as can be observed in Dunnigan-type familial partial lipodystrophy associated with mutations in the lamin *A/C* gene, characterized by selective loss of subcutaneous fat from the limbs and trunk, and its accumulation in

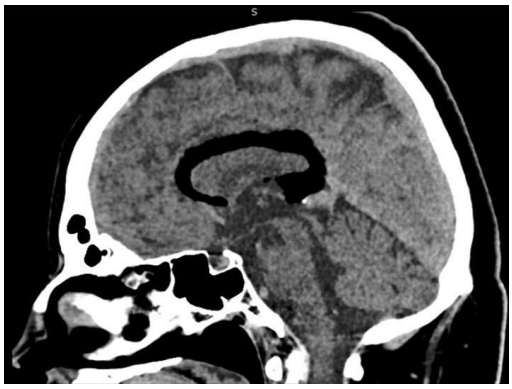

Figure 1 Paramedian left non-contrast computer tomography scan. This scan shows a curvilinear fat density lesion above the corpus callosum.

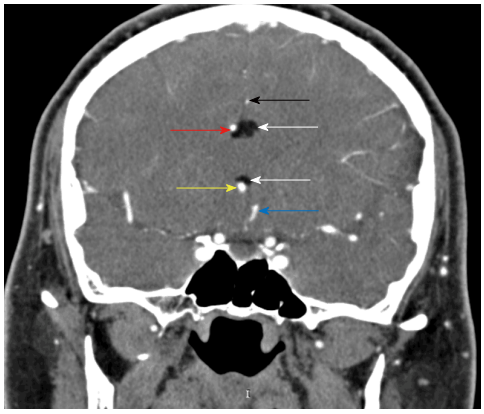

Figure 2 Coronal DSA. Shows the lipoma (white arrows), the right rostral A2 (yellow arrow), the right pericallosal artery (red arrow), the left rostral A2 (blue arrow), and the left pericallosal artery (black arrow).

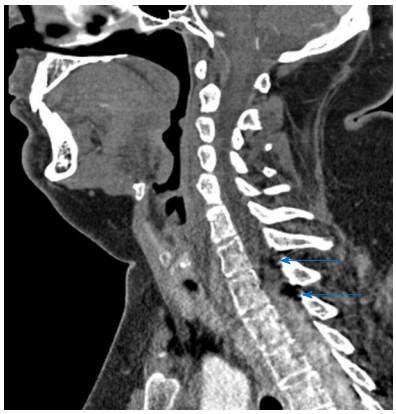

Figure 3 Sagittal CT angiography. Shows two hypodense images compatible with lipomas within the extradural compartment, dorsal to the cord at the T1-T2 level.

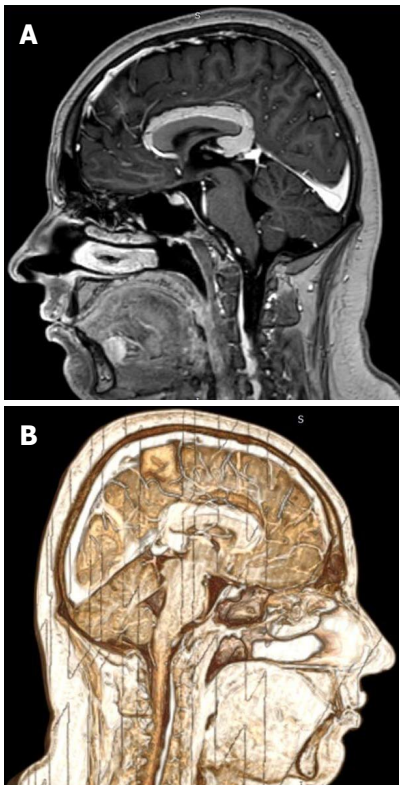

Figure 4 T1-W 3D TFE + MDC magnetic resonance imaging. A: Showing the relationships between vasculature, corpus callosum, lipoma and adjacent brain tissues; B: Showing the pericallosal lesion, compatible with a complete curvilinear lipoma without callosal aplasia.

the face and neck[10]. Similarly, muscles and myocardium may suffer from an impaired Ca^{2+} release in the sarcoplasmic reticulum during contraction.

An alternative hypothesis suggests that the accumulation of nuclear envelope proteins in the ER could promote alterations in intracellular signaling pathways with effects on gene expression and cell survival[11]. Different from laminopathies, Emerin in XL-EDMD is truncated at the C-terminus and is not detectable in the nuclear membrane. Thus, even if it is supposed to result in a more soluble form *in vitro*[12], the pathogenetic theory of accumulation seems less consistent.

Our patient showed a particular obese habitus, with accumulation of adipose tissue in the neck and facial districts with disproportionally leaner limbs. Evaluating the clinical course and the exams performed, the pericallosal and the spinal lipoma may be considered incidental findings, whereas the patient's symptoms could be related to an initial painful contracture that subsided after painkillers. Pericallosal are rare, fat-containing lesions, generally asymptomatic and accounting approximately for 0.1%-0.5% of all intracranial lesions[13]. Curvilinear and tubulonodular types have been described. Tubulonodular lipomas are considered more frequently associated with corpus callosum malformations[14], even if the series of Yilmaz *et al*[15] showed a stronger association with curvilinear lipomas. Our case is aligned with the classical association, which does not show clear morphological alterations in the corpus callosum. This may be important, since lipomas are considered as congenital malformations, and more often occur with cortical and callosal dysplasias and vascular malformations[16]. Nevertheless, Zettner and Netsky[17] pointed out that callosal dysgenesis are not the cause of lipomas, believing rather that the two conditions derive from two

distinct pathological processes, namely a meningeal maldifferentiation for lipomas and dysraphism for callosal abnormalities[17,18].

Finally, it is now clear that LEM domain proteins (such as LAP2B and Emerin) can interact with transcriptional regulators, playing a non-structural role in gene regulation. *In vitro* models speculate that Emerin binds A and B-type lamins as well as retinoblastoma (RB) proteins, which regulates the entry into S-phase and terminal differentiation, and at least four transcription factors, including germ-cell-less (GCL), BCL2-associated transcription factor (BTF) and barrier-to-autointegration factor (BAF)[19]. After binding Emerin, GCL acts on DP3-E2F by repressing its dependent gene expression, while BTF acts as a cell-death-promoting transcription repressor after binding a DNA-specific partner. BAF can bind directly to both Lamin A and Emerin, blocking GCL binding to Emerin, or can directly repress CRX-dependent genes *in vivo* after binding to double-stranded DNA. In muscle cells, Emerin binds several actin-binding proteins, including a nuclear isoform of Spectrin. This reinforces the lamina network by providing a further link between actin and protein 4.1, which is implicated in nuclei reconstruction after mitosis[19].

To date, EDMD has never been associated with cerebral lipomas, and the X-linked form was never considered to be involved in lipodystrophic syndromes or non-muscular conditions. Our case confirms the variable expressivity of the disease, and adds the suggestion of a possible role of Emerin in the intranuclear regulation of signals for adipocyte cell differentiation or lipidic intracellular metabolism in particular cell groups that are subject to specific and variable stimuli throughout a lifetime.

ARTICLE HIGHLIGHTS

Case characteristics

Spontaneous left arm weakness, objective vertigo, obesity.

Clinical diagnosis

Left arm downward drift associated with local joint pain.

Differential diagnosis

Acute vasculopathy; neuropathies; joint affections.

Laboratory diagnosis

Unremarkable laboratory examination.

Imaging diagnosis

A head NCCT revealed the presence of a left-sided hypodense peri-callosal curvilinear lesion; a CT Angiography ruled out vascular obstructions, while the thoracic scan showed two posterior extradural hypodense lesions at T1-T2. The MRI did not show diffusivity alterations: the curvilinear peri-callosal lesion appeared hyperintense in T1-W and hypointense at fat suppression sequences, without contrast enhancement, thus confirming the lipoma.

Treatment

Rest and painkillers.

Term explanation

Envelopathies: defects of proteins making up the nuclear envelope.

Experiences and lessons

A particular obesity pattern associated with cerebral-spinal lipomas may be related to the same gene defect in patients affected by the Emery-Dreifuss muscular dystrophy X-linked variant. In our case, lipomas may be considered incidental findings, whereas the patient's symptoms could be related to an initial painful contracture, which is a typical hallmark of the disease.

REFERENCES

1 **Emery AE**, Dreifuss FE. Unusual type of benign x-linked muscular dystrophy. *J Neurol Neurosurg Psychiatry* 1966; **29**: 338-342 [PMID: 5969090 DOI: 10.1136/jnnp.29.4.338]

2 **Yates JR**, Wehnert M. The Emery-Dreifuss Muscular Dystrophy Mutation Database. *Neuromuscul Disord* 1999; **9**: 199 [PMID: 10382916]

3 **Vytopil M**, Benedetti S, Ricci E, Galluzzi G, Dello Russo A, Merlini L, Boriani G, Gallina M, Morandi L, Politano L, Moggio M, Chiveri L, Hausmanova-Petrusewicz I, Ricotti R, Vohanka S, Toman J, Toniolo D. Mutation analysis of the lamin A/C gene (LMNA) among patients with different cardiomuscular phenotypes. *J Med Genet* 2003; **40**: e132 [PMID: 14684700 DOI: 10.1136/jmg.40.12.e132]

4 **Pasotti M**, Klersy C, Pilotto A, Marziliano N, Rapezzi C, Serio A, Mannarino S, Gambarin F, Favalli V, Grasso M, Agozzino M, Campana C, Gavazzi A, Febo O, Marini M, Landolina M, Mortara A, Piccolo G, Viganò M, Tavazzi L, Arbustini E. Long-term outcome and risk stratification in dilated cardiolaminopathies. *J Am Coll Cardiol* 2008; **52**: 1250-1260 [PMID: 18926329 DOI: 10.1016/j.jacc.2008.06.044]

5 **Shackleton S**, Lloyd DJ, Jackson SN, Evans R, Niermeijer MF, Singh BM, Schmidt H, Brabant G, Kumar S, Durrington PN, Gregory S, O'Rahilly S, Trembath RC. LMNA, encoding lamin A/C, is mutated in partial lipodystrophy. *Nat Genet* 2000; **24**: 153-156 [PMID: 10655060 DOI: 10.1038/72807]

6 **Norwood FL**, Harling C, Chinnery PF, Eagle M, Bushby K, Straub V. Prevalence of genetic muscle disease in Northern England: in-depth analysis of a muscle clinic population. *Brain* 2009; **132**: 3175-3186 [PMID: 19767415 DOI: 10.1093/brain/awp236]

7 **Bonne G**, Leturcq F, Ben Yaou R. Emery-Dreifuss Muscular Dystrophy. In: Adam MP, Ardinger HH, Pagon RA, Wallace SE, Bean LJH, Stephens K, Amemiya A, editors. SourceGeneReviews® [Internet]. Seattle (WA): University of Washington, Seattle; 1993-2018. 2004 Sep 29 [updated 2015 Nov 25]. [PMID: 20301609]

8 **Sullivan T**, Escalante-Alcalde D, Bhatt H, Anver M, Bhat N, Nagashima K, Stewart CL, Burke B. Loss of A-type lamin expression compromises nuclear envelope integrity leading to muscular dystrophy. *J Cell Biol* 1999; **147**: 913-920 [PMID: 10579712 DOI: 10.1083/jcb.147.5.913]

9 **Burke B**, Mounkes LC, Stewart CL. The nuclear envelope in muscular dystrophy and cardiovascular diseases. *Traffic* 2001; **2**: 675-683 [PMID: 11576443 DOI: 10.1034/j.1600-0854.2001.21001.x]

10 **Garg A**, Peshock RM, Fleckenstein JL. Adipose tissue distribution pattern in patients with familial partial lipodystrophy (Dunnigan variety). *J Clin Endocrinol Metab* 1999; **84**: 170-174 [PMID: 9920078 DOI: 10.1210/jcem.84.1.5383]

11 **Manilal S**, Recan D, Sewry CA, Hoeltzenbein M, Llense S, Leturcq F, Deburgrave N, Barbot J, Man N, Muntoni F, Wehnert M, Kaplan J, Morris GE. Mutations in Emery-Dreifuss muscular dystrophy and their effects on emerin protein expression. *Hum Mol Genet* 1998; **7**: 855-864 [PMID: 9536090 DOI: 10.1093/hmg/7.5.855]

12 **Pahl HL**, Baeuerle PA. The ER-overload response: activation of NF-kappa B. *Trends Biochem Sci* 1997; **22**: 63-67 [PMID: 9048485 DOI: 10.1016/S0968-0004(96)10073-6]

13 **Seidl Z**, Vaneckova M, Vitak T. Intracranial lipomas: a retros-

pective study. *Neuroradiol J* 2007; **20**: 30-36 [PMID: 24299585 DOI: 10.1177/197140090702000104]
14 **Yildiz H**, Hakyemez B, Koroglu M, Yesildag A, Baykal B. Intracranial lipomas: importance of localization. *Neuroradiology* 2006; **48**: 1-7 [PMID: 16237548 DOI: 10.1007/s00234-005-0001-z]
15 **Yilmaz MB**, Genc A, Egemen E, Yilmaz S, Tekiner A. Pericallosal Lipomas: A Series of 10 Cases with Clinical and Radiological Features. *Turk Neurosurg* 2016; **26**: 364-368 [PMID: 27161462 DOI: 10.5137/1019-5149.JTN.13008-14.0]
16 **Jiménez Caballero PE**. Interhemispheric lipoma associated with agenesis of the corpus callosum. *Neurologia* 2012; **27**: 515-517 [PMID: 21890243 DOI: 10.1016/j.nrl.2011.07.008]
17 **Zettner A**, Netsky MG. Lipoma of the corpus callosum. *J Neuropathol Exp Neurol* 1960; **19**: 305-319 [PMID: 13847327 DOI: 10.1097/00005072-196004000-00010]
18 **Wallace D**. Lipoma of the corpus callosum. *J Neurol Neurosurg Psychiatry* 1976; **39**: 1179-1185 [PMID: 1011028 DOI: 10.1136/jnnp.39.12.1179]
19 **Cohen M**, Lee KK, Wilson KL, Gruenbaum Y. Transcriptional repression, apoptosis, human disease and the functional evolution of the nuclear lamina. *Trends Biochem Sci* 2001; **26**: 41-47 [PMID: 11165516 DOI: 10.1016/S0968-0004(00)01727-8]

P- Reviewer: Bazeed MF, De Cecco CN, Mahajan A, Ulaşoğlu C
S- Editor: Ma YJ **L- Editor**: Filipodia **E- Editor**: Tan WW

Published by **Baishideng Publishing Group Inc**
7901 Stoneridge Drive, Suite 501, Pleasanton, CA 94588, USA
Telephone: +1-925-223-8242
Fax: +1-925-223-8243
E-mail: bpgoffice@wjgnet.com
Help Desk: http://www.f6publishing.com/helpdesk
http://www.wjgnet.com

ISSN 1949-8470 (online)

World Journal of *Radiology*

World J Radiol 2018 September 28; 10(9): 91-115

Published by Baishideng Publishing Group Inc

WJR World Journal of Radiology

Contents

Monthly Volume 10 Number 9 September 28, 2018

MINIREVIEWS

ORIGINAL ARTICLE

Basic Study

Retrospective Study

World Journal of Radiology
Volume 10 Number 9 September 28, 2018

Contents

NAME OF JOURNAL
World Journal of Radiology

ISSN
ISSN 1949-8470 (online)

LAUNCH DATE
January 31, 2009

FREQUENCY
Monthly

EDITORIAL OFFICE
Jin-Lei Wang, Director
World Journal of Radiology
Baishideng Publishing Group Inc
7901 Stoneridge Drive, Suite 501, Pleasanton, CA 94588, USA
Telephone: +1-925-2238242
Fax: +1-925-2238243
E-mail: editorialoffice@wjgnet.com
Help Desk: http://www.f6publishing.com/helpdesk
http://www.wjgnet.com

PUBLISHER
Baishideng Publishing Group Inc
7901 Stoneridge Drive, Suite 501,
Pleasanton, CA 94588, USA
Telephone: +1-925-2238242
Fax: +1-925-2238243
E-mail: bpgoffice@wjgnet.com
Help Desk: http://www.f6publishing.com/helpdesk
http://www.wjgnet.com

PUBLICATION DATE
September 28, 2018

World Journal of Radiology

Submit a Manuscript: http://www.f6publishing.com

World J Radiol 2018 September 28; 10(9): 91-99

DOI: 10.4329/wjr.v10.i9.91

ISSN 1949-8470 (online)

MINIREVIEWS

Role of imaging methods in diagnosis and treatment of Morton's neuroma

Fernando Ruiz Santiago, Pablo Tomás Muñoz, Patel Pryest, Alberto Martinez Martínez, Nicolás Prados Olleta

Fernando Ruiz Santiago, Pablo Tomás Muñoz, Alberto Martinez Martínez, Radiology Department, Hospital of Neuro-Traumatology (Virgen de las Nieves), Granada 18014, Spain

Patel Pryest, Radiology Department, North Tyneside General Hospital, North Shields NE29 8NH, United Kingdom

Nicolás Prados Olleta, Orthopaedic Department, Hospital of Neuro-Traumatology (Virgen de las Nieves), Granada 18014, Spain

ORCID number: Fernando Ruiz Santiago (0000-0002-6843-0803); Pablo Tomás Muñoz (0000-0002-6405-0811); Patel Pryest (0000-0001-6969-5793); Alberto Martinez Martínez (0000-0002-8069-9549); Nicolás Prados Olleta (0000-0003-0224-4570).

Author contributions: All authors contributed to the conception and design of the study, data acquisition, and manuscript preparation and review.

Conflict-of-interest statement: All authors declare no real or potential conflicts of interest related to this study or its publication.

Manuscript source: Invited manuscript

Correspondence to: Fernando Ruiz Santiago, PhD, Adjunct Professor, Chief Doctor, Radiology Department, Hospital of Neuro-Traumatology (Virgen de las Nieves), Carretera de Jaen SN, Granada 18014, Spain. ferusan12@gmail.com
Telephone: +34-62-7633829

Received: April 26, 2018
Peer-review started: April 26, 2018
First decision: June 14, 2018
Revised: July 21, 2018
Accepted: August 4, 2018
Article in press: August 5, 2018
Published online: September 28, 2018

Abstract

Among the many causes of forefoot pain, Morton's neuroma (MN) is often suspected, particularly in women, due to its high incidence. However, there remain controversies about its relationship with symptomatology and which diagnostic and treatment choices to choose. This article mainly focuses on the role of the various imaging methods and their abilities to support an accurate diagnosis of MN, ruling out other causes of forefoot pain, and as a way of providing targeted imaging-guided therapy for patients with MN.

Key words: Morton's neuroma; Diagnosis; Infiltrative; Imaging; Therapy

Core tip: Nowadays, ultrasound and magnetic resonance imaging provide accurate diagnosis of Morton's neuroma (MN) and are invaluable tools for ruling out other causes of forefoot pain. This extended review is intended to show the potential of imaging methods for diagnosis as well as treatment of MN.

Santiago FR, Muñoz PT, Pryest P, Martínez AM, Olleta NP. Role of imaging methods in diagnosis and treatment of Morton's neuroma. *World J Radiol* 2018; 10(9): 91-99 Available from: URL: http://www.wjgnet.com/1949-8470/full/v10/i9/91.htm DOI: http://dx.doi.org/10.4329/wjr.v10.i9.91

INTRODUCTION

Morton's neuroma (MN) is considered a nerve entrapment neuropathy, causing symptoms relating to impingement of the common plantar digital and proper plantar digital nerves, such as burning, tingling or numbness. It is a common problem but mainly affects middle-aged women, occurring more than 5 times more frequently in women than in men[1].

It is considered that MN occurs secondary to mechanical stress on the nerves, leading to proliferation of fibrosis in and around the affected nerve[2]. It has been reported to be more frequent in the 3rd web space (in 68% of cases), followed by the 2nd web space (in 32% of cases). The presence of a neuroma in the 1st and 4th web spaces is extremely rare[3]. Two main anatomical reasons have been postulated to explain this distribution; firstly, the 3rd metatarsal nerve is theoretically thicker because it is usually formed by the confluence of medial and lateral plantar nerves[4]; and, secondly, the larger shearing forces that occur at the 3rd web space due to the relatively greater mobility of the 4th metatarsal relative to the 3rd metatarsal[1].

Other authors have found a similar proportion of MN in the 2nd and 3rd web spaces[5,6] and this could be explained by the fact that the 2nd and 3rd intermetatarsal spaces are the narrowest of the foot[7]. The occurrence of multiple neuromas in the same foot has also been reported, but is considered rare by some authors[8]; although, in other case series, it has been found in between 28% and 65% of cases[5,6,9].

CLINICAL PRESENTATION

Not all patients with MN show clinical symptoms. The prevalence of asymptomatic MN has been reported as 33%-54% when using ultrasound (US) or magnetic resonance imaging (MRI) for diagnosis[9,10]. Nevertheless, when forefoot pain secondary to MN is present, it is elicited under pressure of the web space. The thumb index finger squeeze test has been reported to be the most sensitive screening method for clinical diagnosis of MN, having accuracy of around 96% (Figure 1). In this maneuver, the intermetatarsal space is squeezed between the tips of the index finger (dorsal) and thumb (plantar). The Mulder's click is reproduced by firm medial to lateral compression of the metatarsal heads, when one hand is clasping the forefoot. A palpable and/or audible click is perceived, though it is mainly present for larger neuromas; its accuracy is around 62%[5].

IMAGING OF MN

Pathognomonic diagnostic clinical tests for MN do not exist, and many of the clinical tests provide false positive results in feet with alternative pathologies[11]. Therefore, imaging may be required to confirm the diagnosis of MN and exclude other causes of forefoot pain, such as metatarsophalangeal joint arthritis or intermetatarsal bursitis. The available evidence suggests that US is more accurate than MRI for diagnosis of MN. Analysis of pooled sensitivity showed similarity between US (90%) and MRI (93%), both being relatively high; yet, MRI (68%) showed a relatively lower specificity than US (88%) in the detection of MN[12]. Diameter of the normal plantar digital nerve is around 1 mm at the level of the intermetatarsal heads[13] and can be identified on high-resolution sonography and MRI (Figure 2).

Figure 1 Thumb index finger squeeze test.

In US, MN is detected as a well-defined, round or ovoid mass in the short axis view and as an elongated/fusiform mass in the long axis view; it is hypoechoic relative to the adjacent tissues and located between the metatarsal heads along the plantar aspect of the intermetatarsal spaces[14] (Figure 3). Squeezing of the lateral aspect of the forefoot helps to extrude the intermetatarsal contents toward the plantar aspect of the forefoot, leading to a better delineation of the MN. This displacement may coincide with a palpable and/or audible click, known as the sonographic Mulder sign[15]. The extruding content may be formed by the MN and/or the bursa. It is theorized that the click will only happen when there is a MN because a thickened bursa is much more pliable than a neuroma[16]. As both entities may coexist, we can complete the US scan with another maneuver that will help in differentiating between MN and bursal tissue. The intermetatarsal space is compressed dorsally by the fingers whilst the probe is scanning along the plantar aspect of the web space in the long axis view. A MN will have a fusiform elongated shape and be displaceable, but it will not be as compressible as the intermetatarsal bursa. The bursa, located along the dorsal aspect of the intermetatarsal nerve, will show a more rounded or oval shape and will be compressible to a greater extent that the neural tissue (Figure 4).

US may also detect other causes of forefoot pain, such as joint pathology (osteoarthritis or synovitis), soft tissue abnormalities (bursitis or inflammation-related change) and even bone lesions (stress fracture, bone erosion or cyst). Soft tissue masses different from MN can also be characterized, differentiating solid from cystic content, as well as the presence of neovascularity. Any intermetatarsal mass longer than 20 mm should

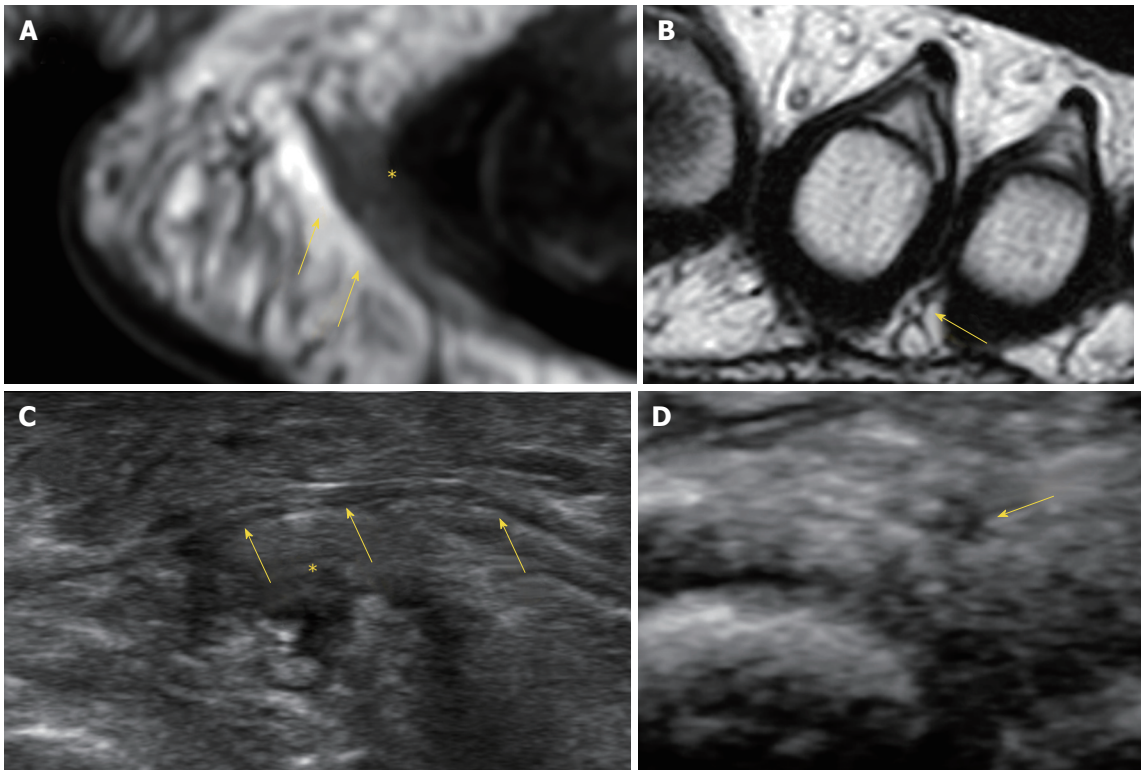

Figure 2 Imaging of the normal digital nerves. A, B: Long and short axis views of normal digital nerves (arrows) in magnetic resonance imaging (A) and ultrasound (US) (B); C, D: Long (C) and short (D) axis views of normal digital nerves (arrows) in US. In all images, arrows indicate normal digital nerve and asterisks (*) indicate bursa.

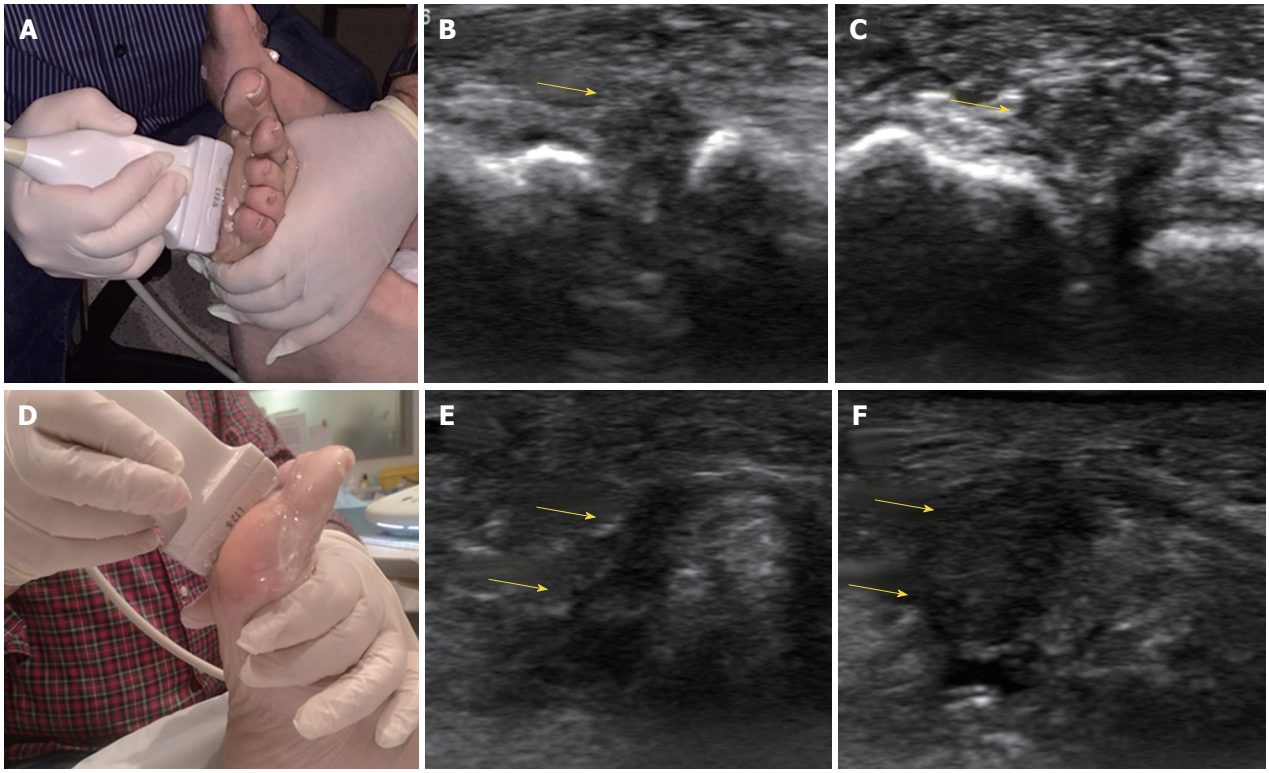

Figure 3 Ultrasound imaging of Morton's neuroma. A: Clasping of the forefoot in the short axis view; B, C: Short axis views of the intermetatarsal space before (B) and after (C) squeezing the forefoot; D: Clasping of the forefoot in the long axis view; E, F: Long axis views of the intermetatarsal space before (E) and after (F) squeezing the forefoot. In all images, arrows indicate Morton's neuroma.

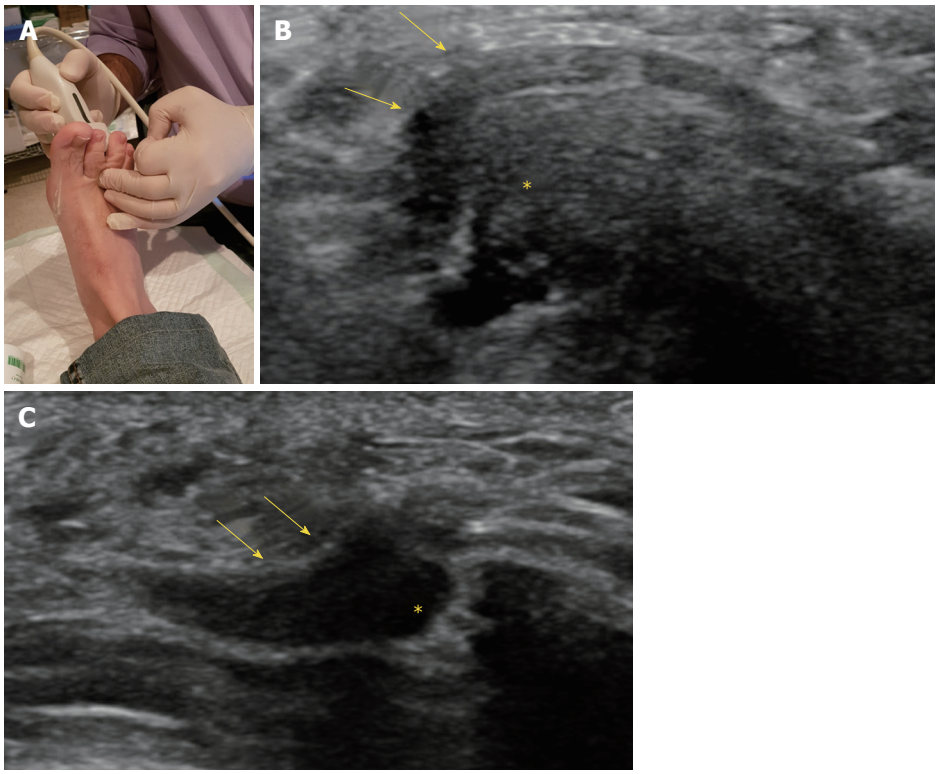

Figure 4 Displacement of Morton's neuroma. A: Pressure on the dorsal aspect of the web space; B, C: Long axis views of the neuroma and bursa before (B) and after (C) pressure of the dorsal aspect of the intermetatarsal space. In all images, arrows indicate Morton's neuroma and asterisks (*) indicate bursa.

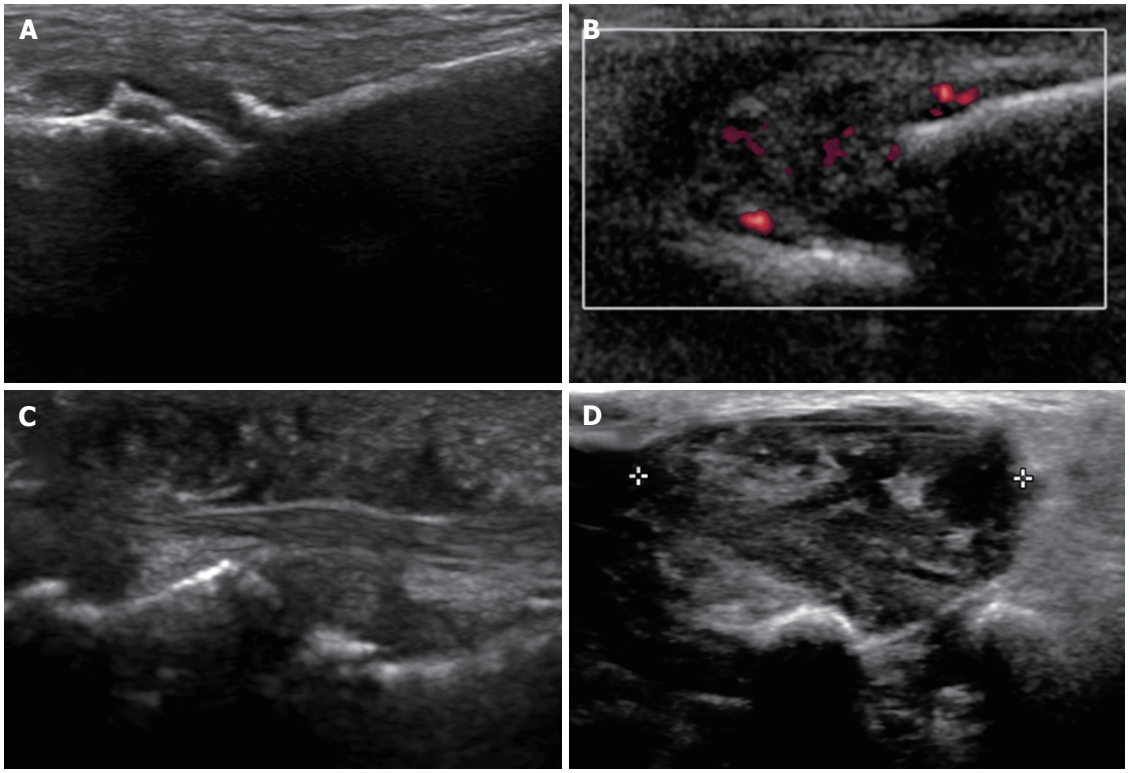

Figure 5 Causes of forefoot pain. A: Osteoarthritis; B: Rheumatoid arthritis with metatarsophalangeal joint subluxation; C: Psoriasis with soft tissue swelling; D: Giant cell tumor of the tendon sheath.

raise suspicion that it is not a neuroma[17]. If appropriate diagnosis is not achieved with imaging features alone, biopsy under US guidance may help to obtain an accurate diagnosis (Figure 5).

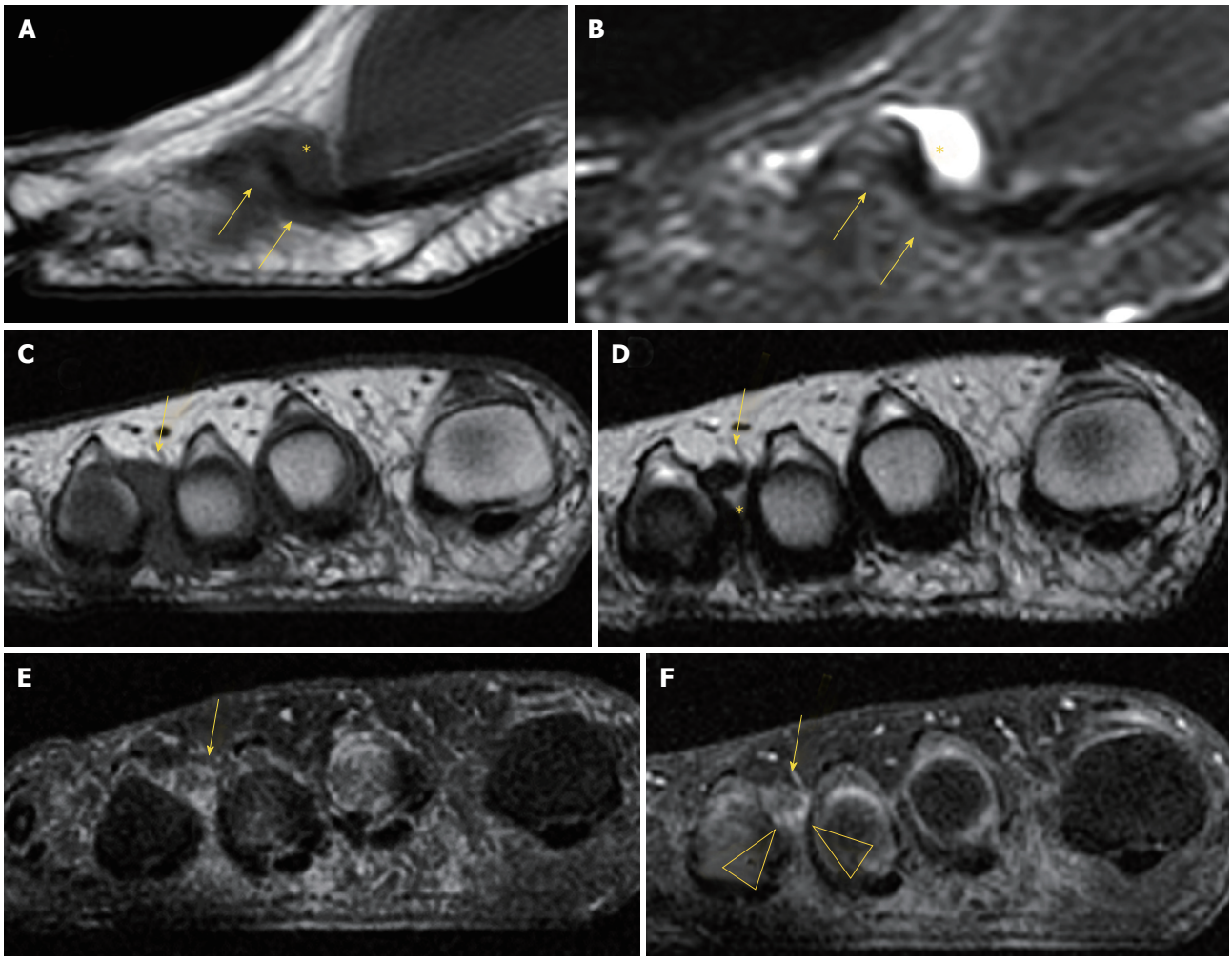

Figure 6 Magnetic resonance imaging of Morton's neuroma. A, B: Sagittal T1 (A) and short tau inversion recovery (B) of Morton's neuroma and bursa; C, D: Coronal T1 (C) and T2 (D) of Morton's neuroma and bursa. Coronal T1 fat before (A) and after gadolinium administration (B), showing enhancement of the bursal tissue surrounding the neuroma (arrowhead). In all images, arrows indicate Morton's neuroma and asterisks (*) indicate bursa.

On MRI, MN is usually seen as a well-demarcated ovoid or dumbbell-shaped intermetatarsal mass. This mass shows intermediate to low signal intensity on both T1-weighted images (T1WI) and T2WI[18]. By contrast, bursal tissue appears hypo- or isointense on T1WI and hyperintense on T2WI, allowing for differentiation between bursal and neural tissues. There is no typical enhancement pattern of MN after intravenous administration of gadolinium contrast medium, with varying degrees of enhancement reported in the literature[19]; in our experience, however, the enhancement of most MN is low to zero. When present, this is usually due to the enhancement of the bursal tissue surrounding the neuroma. In the appropriate clinical setting, administration of gadolinium contrast medium is not required for a reliable diagnosis of MN (Figure 6).

MRI may also detect other causes of forefoot pain, including abnormalities of the bone (edema, fracture, erosion and cyst) and soft tissues (such as bursitis, synovitis, muscle edema and atrophy, and plantar plate tears) (Figure 7).

MN TREATMENT

The treatment for MN should initially be conservative, including shoe modification, use of insoles and administration of antiinflammatory drugs. Percutaneous therapies may be the second step, and eventually surgery, if previous measures fail[2]. Success of conservative management approaches that include use of insoles and shoe modification has been reported to be around 48%[20].

The percutaneous treatments mainly include injections of local anesthetics with or without steroids, or of alcohol. Percutaneous injection may be performed blindly or under US guidance (Figure 8). Studies of US-guided injections have shown that anesthetics with corticosteroids produce an effect (at 3 mo follow-up) that is superior to anesthetic injections alone[21]. Previous nonrandomized cohort studies have also shown

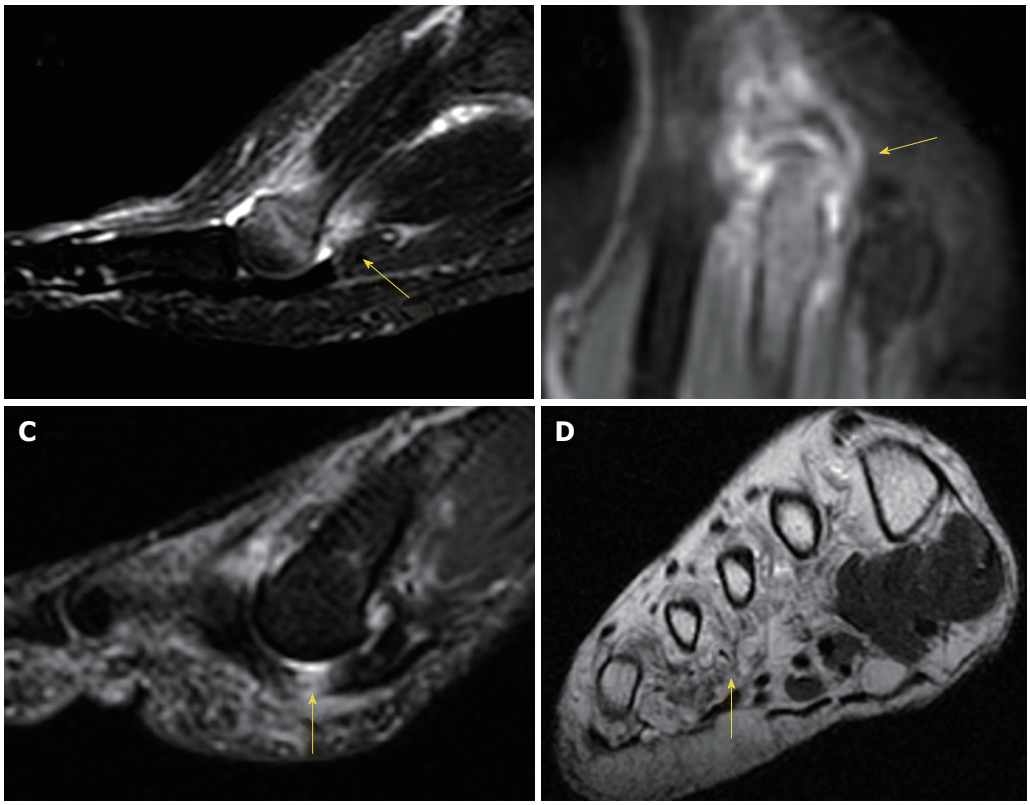

Figure 7 Magnetic resonance imaging in forefoot pain. A: Stress fracture of the 2nd metatarsal; B: Synovitis in rheumatoid arthritis; C: Plantar plate tear (arrow); D: Muscle atrophy in diabetes (arrow).

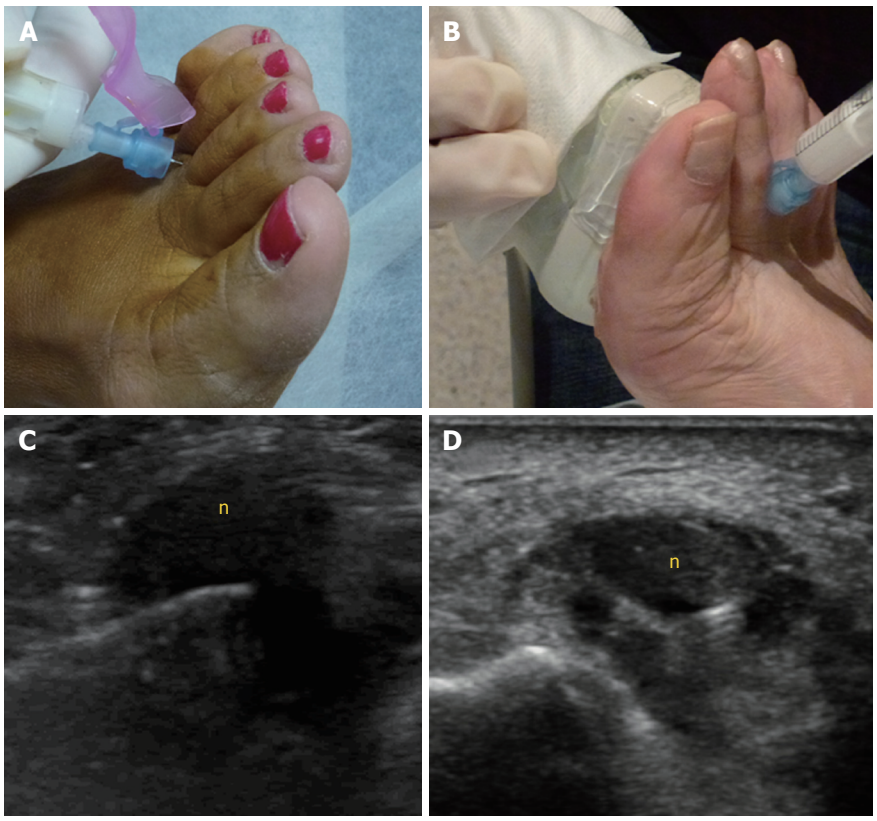

Figure 8 Morton's neuroma injections. A, B: Blind (A) and ultrasound (US)-guided (B) injections; C, D: Long (C) and short (D) axis views of an US-guided injection into a Morton's neuroma (denoted by "n").

a degree of improvement of about 45% for both blind and single US-guided injections[22], and of around 75% to 80% for blind multiple injections[23]. We only found one study comparing the blind technique, based on anatomical landmarks, to the echo-guided technique. In that study, no significant differences were found between the injection methods, but the sample size (only 36 cases) constitutes a substantial limitation that might have prevented the study from reaching a statistically significant difference[24].

Previous studies comparing modification of the forefoot loading area with injection of steroids have demonstrated greater pain improvement (at 6 mo follow-up) experienced by the steroid-treated group, but this difference disappeared at 1 year of follow-up[25].

The influence of neuroma size on treatment response to injections has also been debated. One study showed that neuromas less than 5 mm had a better response at 6 mo than those greater than 5 mm; at 12 mo, however, the response to injections was no longer significantly different for the two size groups[26]. A recent retrospective case series study found a cut-off value of 6.3 mm, above which larger MN s failed to respond, as well as to corticosteroid injections[27]. Overall, most of the reported data in the literature do not support any influence of neuroma size on the outcome[23,24,28].

Corticosteroids may cause dermal/subcutaneous tissue atrophy, hypopigmentation and fat necrosis, with reported incidence of 1%-5%[21,29] (Figure 9). Particulate steroids have greater dermal and subcutaneous tissue atrophy. Triamcinolone, in particular, has greater risk for inducing dermal changes than methylprednisolone, due to its increased crystal size[29].

Other drugs used in MN treatment include alcohol, botulinum toxin and hyaluronic acid. Alcohol injection has a reported success range between 69%-84%, with a complication rate of 3%[30,31]. The most specific complication of this procedure has been plantar pain, presumed due to an inflammatory reaction secondary to perilesional leakage of the alcohol[30]. Case series using botulinum toxin[32] and hyaluronic acid[33] have shown clinical benefits of 70.6% and 84% respectively. Nevertheless, more studies are needed before considering these injections an alternative to the more traditional treatments.

Percutaneous radiofrequency ablation[34] has also been used in patients unresponsive to conservative therapies. The reported success with radiofrequency ranges from 68% to 100%, probably influenced by technical factors such as variability in the number of ablation cycles and in patient's inclusion criteria[34,35]. A case series using cryoablation showed that 77.7% of patients were completely satisfied following treatment, but this result needs to be confirmed by further prospective studies in order to be considered a valid alternative to radiofrequency ablation[36]. The global rate

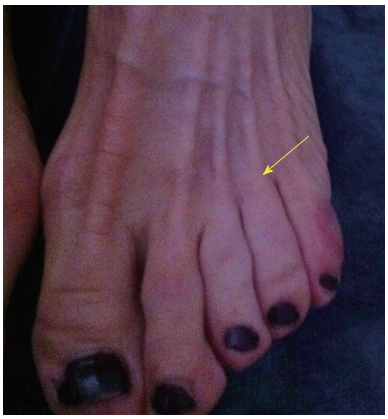

Figure 9 Skin discoloration after steroid injection.

of complications with radiofrequency ablation is about 5%, including hematoma and persistent pain, followed by temporary nerve irritation and infection, as well as pain and numbness at the injection site[31].

Surgical treatment is indicated after failure of conservative or percutaneous therapies. It consists of lesion excision (neurectomy) or intermetatarsal ligament resection (neurolysis) (Figure 10). Neurectomy may be performed either *via* a dorsal or plantar approach, according to surgeon preferences; no statistical differences in success rate have been reported. Surgical excision success ranges from 50% to 88%[31,37,38], with a complication rate of 25% for neurectomy and 7% for neurolysis, which would include infection, hematoma, hammertoe formation, hypertrophic or keloid scar formation, complex regional pain syndrome, and persistent postoperative pain, numbness and stiffness of the metatarsophalangeal joints. Recurrent painful neuromas after surgery have been described in 4% of cases and are less responsive to further surgical intervention; conservative measures would then have to be used prior to the consideration of further surgery[31,39].

A minimally invasive technique may be used for decompressing the nerve by division of the deep intermetatarsal ligament, either endoscopically or percutaneously. The reported success rate for decompression (sectioning of the deep transverse intermetatarsal ligament with/without osteotomy of the metatarsal heads) is around 94%, with a complication rate of 6%[31].

In summary, controversies still exist in the appropriate management of MN, including for the diagnosis and treatment algorithms. Although the clinical diagnosis of MN has a high accuracy, the coexistence of MN with many another causes of forefoot pain increases the importance of imaging techniques in achieving an accurate diagnosis, mainly when initial conservative measures fail to obtain any clinical improvement. Surgery should be considered when imaging findings support the clinical diagnosis of MN and when conservative measures

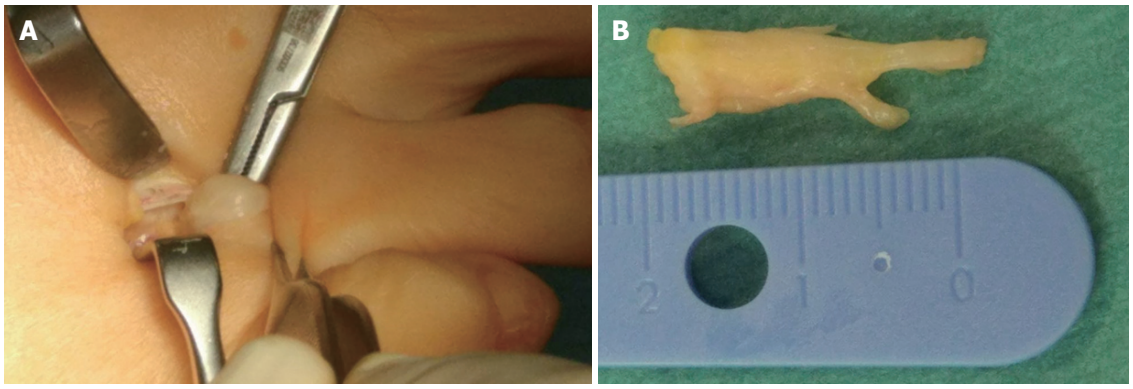

Figure 10 Surgical treatment of Morton's neuroma. A: Dorsal approach to Morton's neuroma; B: Surgical specimen.

including percutaneous treatment fail to improve the patient's symptoms.

REFERENCES

1 **Peters PG**, Adams SB Jr, Schon LC. Interdigital neuralgia. *Foot Ankle Clin* 2011; **16**: 305-315 [PMID: 21600450 DOI: 10.1016/j.fcl.2011.01.010]
2 **Jain S**, Mannan K. The diagnosis and management of Morton's neuroma: a literature review. *Foot Ankle Spec* 2013; **6**: 307-317 [PMID: 23811947 DOI: 10.1177/1938640013493464]
3 **Kasparek M**, Schneider W. Surgical treatment of Morton's neuroma: clinical results after open excision. *Int Orthop* 2013; **37**: 1857-1861 [PMID: 23851648 DOI: 10.1007/s00264-013-2002-6]
4 **Jones JR**, Klenerman L. A study of the communicating branch between the medial and lateral plantar nerves. *Foot Ankle* 1984; **4**: 313-315 [PMID: 6735288 DOI: 10.1177/107110078400400608]
5 **Mahadevan D**, Venkatesan M, Bhatt R, Bhatia M. Diagnostic Accuracy of Clinical Tests for Morton's Neuroma Compared With Ultrasonography. *J Foot Ankle Surg* 2015; **54**: 549-553 [PMID: 25432459 DOI: 10.1053/j.jfas.2014.09.021]
6 **Valero J**, Gallart J, González D, Deus J, Lahoz M. Multiple interdigital neuromas: a retrospective study of 279 feet with 462 neuromas. *J Foot Ankle Surg* 2015; **54**: 320-322 [PMID: 25128316 DOI: 10.1053/j.jfas.2014.05.011]
7 **Levitsky KA**, Alman BA, Jevsevar DS, Morehead J. Digital nerves of the foot: anatomic variations and implications regarding the pathogenesis of interdigital neuroma. *Foot Ankle* 1993; **14**: 208-214 [PMID: 8359767 DOI: 10.1177/107110079301400406]
8 **Thompson FM**, Deland JT. Occurrence of two interdigital neuromas in one foot. *Foot Ankle* 1993; **14**: 15-17 [PMID: 8425725 DOI: 10.1177/107110079301400103]
9 **Symeonidis PD**, Iselin LD, Simmons N, Fowler S, Dracopoulos G, Stavrou P. Prevalence of interdigital nerve enlargements in an asymptomatic population. *Foot Ankle Int* 2012; **33**: 543-547 [PMID: 22835390 DOI: 10.3113/FAI.2012.0543]
10 **Bencardino J**, Rosenberg ZS, Beltran J, Liu X, Marty-Delfaut E. Morton's neuroma: is it always symptomatic? *AJR Am J Roentgenol* 2000; **175**: 649-653 [PMID: 10954445 DOI: 10.2214/ajr.175.3.1750649]
11 **Owens R**, Gougoulias N, Guthrie H, Sakellariou A. Morton's neuroma: clinical testing and imaging in 76 feet, compared to a control group. *Foot Ankle Surg* 2011; **17**: 197-200 [PMID: 21783084 DOI: 10.1016/j.fas.2010.07.002]
12 **Xu Z**, Duan X, Yu X, Wang H, Dong X, Xiang Z. The accuracy of ultrasonography and magnetic resonance imaging for the diagnosis of Morton's neuroma: a systematic review. *Clin Radiol* 2015; **70**: 351-358 [PMID: 25466436 DOI: 10.1016/j.crad.2014.10.017]
13 **Nissen KI**. Plantar digital neuritis; Morton's metatarsalgia. *J Bone Joint Surg Br* 1948; **30B**: 84-94 [PMID: 18864949 DOI: 10.1302/0301-620X.30B1.84]
14 **Bignotti B**, Signori A, Sormani MP, Molfetta L, Martinoli C, Tagliafico A. Ultrasound versus magnetic resonance imaging for Morton neuroma: systematic review and meta-analysis. *Eur Radiol* 2015; **25**: 2254-2262 [PMID: 25809742 DOI: 10.1007/s00330-015-3633-3]
15 **Torriani M**, Kattapuram SV. Technical innovation. Dynamic sonography of the forefoot: The sonographic Mulder sign. *AJR Am J Roentgenol* 2003; **180**: 1121-1123 [PMID: 12646466 DOI: 10.2214/ajr.180.4.1801121]
16 **Simmons DN**. Imaging of the Painful Forefoot. *Techniques in Foot Ankle Surgery* 2008; **7**: 238-249 [DOI: 10.1097/BTF.0b013e31818f3505]
17 **Quinn TJ**, Jacobson JA, Craig JG, van Holsbeeck MT. Sonography of Morton's neuromas. *AJR Am J Roentgenol* 2000; **174**: 1723-1728 [PMID: 10845513 DOI: 10.2214/ajr.174.6.1741723]
18 **Weishaupt D**, Treiber K, Kundert HP, Zollinger H, Vienne P, Hodler J, Willmann JK, Marincek B, Zanetti M. Morton neuroma: MR imaging in prone, supine, and upright weight-bearing body positions. *Radiology* 2003; **226**: 849-856 [PMID: 12601213 DOI: 10.1148/radiol.2263011925]
19 **Van Hul E**, Vanhoenacker F, Van Dyck P, De Schepper A, Parizel PM. Pseudotumoural soft tissue lesions of the foot and ankle: a pictorial review. *Insights Imaging* 2011; **2**: 439-452 [PMID: 22347966 DOI: 10.1007/s13244-011-0087-2]
20 **Kilmartin TE**, Wallace WA. Effect of pronation and supination orthosis on Morton's neuroma and lower extremity function. *Foot Ankle Int* 1994; **15**: 256-262 [PMID: 7951964 DOI: 10.1177/107110079401500505]
21 **Thomson CE**, Beggs I, Martin DJ, McMillan D, Edwards RT, Russell D, Yeo ST, Russell IT, Gibson JN. Methylprednisolone injections for the treatment of Morton neuroma: a patient-blinded randomized trial. *J Bone Joint Surg Am* 2013; **95**: 790-798, S1 [PMID: 23636185 DOI: 10.2106/JBJS.I.01780]
22 **Hassouna H**, Singh D, Taylor H, Johnson S. Ultrasound guided steroid injection in the treatment of interdigital neuralgia. *Acta Orthop Belg* 2007; **73**: 224-229 [PMID: 17515235]
23 **Greenfield J**, Rea J Jr, Ilfeld FW. Morton's interdigital neuroma. Indications for treatment by local injections versus surgery. *Clin Orthop Relat Res* 1984; 142-144 [PMID: 6200264]
24 **Mahadevan D**, Attwal M, Bhatt R, Bhatia M. Corticosteroid injection for Morton's neuroma with or without ultrasound guidance: a randomised controlled trial. *Bone Joint J* 2016; **98-B**: 498-503 [PMID: 27037432 DOI: 10.1302/0301-620X.98B4.36880]
25 **Saygi B**, Yildirim Y, Saygi EK, Kara H, Esemenli T. Morton neuroma: comparative results of two conservative methods. *Foot Ankle Int* 2005; **26**: 556-559 [PMID: 16045848 DOI: 10.1177/107110070502600711]
26 **Makki D**, Haddad BZ, Mahmood Z, Shahid MS, Pathak S, Garnham I. Efficacy of corticosteroid injection versus size of plantar interdigital neuroma. *Foot Ankle Int* 2012; **33**: 722-726 [PMID: 22995258 DOI: 10.3113/FAI.2012.0722]
27 **Park YH**, Lee JW, Choi GW, Kim HJ. Risk factors and the

associated cutoff values for failure of corticosteroid injection in treatment of Morton's neuroma. *Int Orthop* 2018; **42**: 323-329 [PMID: 29230531 DOI: 10.1007/s00264-017-3707-8]

28 **Markovic M**, Crichton K, Read JW, Lam P, Slater HK. Effectiveness of ultrasound-guided corticosteroid injection in the treatment of Morton's neuroma. *Foot Ankle Int* 2008; **29**: 483-487 [PMID: 18510900 DOI: 10.3113/FAI.2008.0483]

29 **van Vendeloo SN**, Ettema HB. Skin depigmentation along lymph vessels of the lower leg following local corticosteroid injection for interdigital neuroma. *Foot Ankle Surg* 2016; **22**: 139-141 [PMID: 27301735 DOI: 10.1016/j.fas.2016.01.002]

30 **Hughes RJ**, Ali K, Jones H, Kendall S, Connell DA. Treatment of Morton's neuroma with alcohol injection under sonographic guidance: follow-up of 101 cases. *AJR Am J Roentgenol* 2007; **188**: 1535-1539 [PMID: 17515373 DOI: 10.2214/AJR.06.1463]

31 **Valisena S**, Petri GJ, Ferrero A. Treatment of Morton's neuroma: A systematic review. *Foot Ankle Surg* 2017; **pii**: S1268-7731(17)30065-6 [PMID: 29409240 DOI: 10.1016/j.fas.2017.03.010]

32 **Climent JM**, Mondéjar-Gómez F, Rodríguez-Ruiz C, Díaz-Llopis I, Gómez-Gallego D, Martín-Medina P. Treatment of Morton neuroma with botulinum toxin A: a pilot study. *Clin Drug Investig* 2013; **33**: 497-503 [PMID: 23740337 DOI: 10.1007/s40261-013-0090-0]

33 **Lee K**, Hwang IY, Ryu CH, Lee JW, Kang SW. Ultrasound-Guided Hyaluronic Acid Injection for the Management of Morton's Neuroma. *Foot Ankle Int* 2018; **39**: 201-204 [PMID: 29153007 DOI: 10.1177/1071100717739578]

34 **Masala S**, Cuzzolino A, Morini M, Raguso M, Fiori R. Ultrasound-Guided Percutaneous Radiofrequency for the Treatment of Morton's Neuroma. *Cardiovasc Intervent Radiol* 2018; **41**: 137-144 [PMID: 28956110 DOI: 10.1007/s00270-017-1786-y]

35 **Finney W**, Wiener SN, Catanzariti F. Treatment of Morton's neuroma using percutaneous electrocoagulation. *J Am Podiatr Med Assoc* 1989; **79**: 615-618 [PMID: 2625669 DOI: 10.7547/87507315-79-12-615]

36 **Cazzato RL**, Garnon J, Ramamurthy N, Tsoumakidou G, Caudrelier J, Thenint MA, Rao P, Koch G, Gangi A. Percutaneous MR-Guided Cryoablation of Morton's Neuroma: Rationale and Technical Details After the First 20 Patients. *Cardiovasc Intervent Radiol* 2016; **39**: 1491-1498 [PMID: 27189181 DOI: 10.1007/s00270-016-1365-7]

37 **Mann RA**, Reynolds JC. Interdigital neuroma--a critical clinical analysis. *Foot Ankle* 1983; **3**: 238-243 [PMID: 6832668 DOI: 10.1177/107110078300300411]

38 **Richardson DR**, Dean EM. The recurrent Morton neuroma: what now? *Foot Ankle Clin* 2014; **19**: 437-449 [PMID: 25129354 DOI: 10.1016/j.fcl.2014.06.006]

39 **Johnson JE**, Johnson KA, Unni KK. Persistent pain after excision of an interdigital neuroma. Results of reoperation. *J Bone Joint Surg Am* 1988; **70**: 651-657 [PMID: 3392057 DOI: 10.2106/00004623-198870050-00003]

P- Reviewer: Bazeed MF, Cerwenka H, Razek AAKA
S- Editor: Ji FF **L- Editor**: A **E- Editor**: Song H

World Journal of Radiology

Submit a Manuscript: http://www.f6publishing.com

World J Radiol 2018 September 28; 10(9): 100-107

DOI: 10.4329/wjr.v10.i9.100

ISSN 1949-8470 (online)

ORIGINAL ARTICLE

Basic Study

Optimized cardiac magnetic resonance imaging inversion recovery sequence for metal artifact reduction and accurate myocardial scar assessment in patients with cardiac implantable electronic devices

El-Sayed H Ibrahim, Mason Runge, Jadranka Stojanovska, Prachi Agarwal, Maryam Ghadimi-Mahani, Anil Attili, Thomas Chenevert, Chiel den Harder, Frank Bogun

El-Sayed H Ibrahim, Department of Radiology, Medical College of Wisconsin, Milwaukee, WI 53226, United States

Mason Runge, Jadranka Stojanovska, Prachi Agarwal, Maryam Ghadimi-Mahani, Anil Attili, Thomas Chenevert, Frank Bogun, Department of Radiology, University of Michigan, Ann Arbor, MI 48109, United States

Chiel den Harder, Department of Medical Physics, Leiden University Medical Center, Leiden 2333ZA, The Netherlands

ORCID numbers: El-Sayed H Ibrahim (0000-0003-4292-4669); Mason Runge (0000-0003-4321-8424); Jadranka Stojanovska (0000-0003-2742-6274); Prachi Agarwal (0000-0001-9157-703X); Maryam Ghadimi-Mahani (0000-0001-6451-2257); Anil Attili (0000-0003-4753-6892); Thomas Chenevert (0000-0003-1476-4274); Chiel den Harder (0000-0001-7430-6190); Frank Bogun (0000-0002-0391-7282).

Author contributions: Ibrahim EH and Stojanovska J designed research; Ibrahim EH, Stojanovska J, Agarwal P, Ghadimi-Mahani M and Attili A performed research; Ibrahim EH, Stojanovska J and Bogun F analyzed data; Runge M, Chenevert T, den Harder C and Bogun F contributed with analytic tools; Ibrahim E wrote the paper.

Institutional review board statement: The study is approved by the University of Michigan Institutional Review Board.

Informed consent statement: All study participants provided informed written consent prior to study enrollment.

Conflict-of-interest statement: The authors do not have conflicts of interest to declare.

Manuscript source: Unsolicited manuscript

Correspondence to: El-Sayed H Ibrahim, PhD, Associate Professor, Department of Radiology, Medical College of Wisconsin, 8701 Watertown Plank Rd, Milwaukee, WI 53226, United States. eibrahim@mcw.edu
Telephone: +1-414-9554663
Fax: +1-414-9556314

Received: April 26, 2018
Peer-review started: April 26, 2018
First decision: May 22, 2018
Revised: July 12, 2018
Accepted: July 14, 2018
Article in press: July 16, 2018
Published online: September 28, 2018

Abstract

Late gadolinium enhancement (LGE) cardiovascular magnetic resonance (CMR) is the gold standard for imaging myocardial viability. An important application of LGE CMR is the assessment of the location and extent of the myocardial scar in patients with ventricular tachycardia (VT), which allows for more accurate identification of the ablation targets. However, a large percentage of patients with VT have cardiac implantable electronic devices (CIEDs), which is a relative contraindication for cardiac magnetic resonance imaging due to safety and

image artifact concerns. Previous studies showed that these patients can be safely scanned on 1.5 T scanners provided that an adequate imaging protocol is adopted. Nevertheless, imaging patients with a CIED result in metal artifacts due to the strong frequency off-resonance effects near the device; therefore, the spins in the surrounding myocardium are not completely inverted, and thus give rise to hyperintensity artifacts. These artifacts obscure the myocardial scar tissue and limit the ability to study the correlation between the myocardial scar structure and the electro-anatomical map during catheter ablation. In this study, we developed a modified inversion recovery technique to alleviate the CIED-induced metal artifacts and improve the diagnostic image quality of LGE images in patients with CIEDs without increasing scan time or requiring additional hardware. The developed technique was tested in phantom experiments and *in vivo* scans, which showed its capability for suppressing the hyperintensity artifacts without compromising myocardium nulling in the resulting LGE images.

Key words: Magnetic resonance imaging; Heart; Late gadolinium enhancement; Viability imaging; Inversion recovery; Cardiac implantable electronic devices

Core tip: Late gadolinium-enhancement magnetic resonance imaging is the gold standard for imaging myocardial viability, especially for assessing location and extent of myocardial scar in patients with ventricular-tachycardia, which allows for more identification of the ablation targets. However, large percentages of these patients have cardiac-implantable electronic devices, which results in hyperintensity artifacts that obscure the myocardial scar. In this study, we developed a modified technique to alleviate the metal-induced image artifacts without increasing scan time or requiring additional hardware. The developed technique was tested in phantom and *in-vivo* scans, which showed its capability for suppressing the hyperintensity artifacts and improving diagnostic image quality.

Ibrahim EH, Runge M, Stojanovska J, Agarwal P, Ghadimi-Mahani M, Attili A, Chenevert T, den Harder C, Bogun F. Optimized cardiac magnetic resonance imaging inversion recovery sequence for metal artifact reduction and accurate myocardial scar assessment in patients with cardiac implantable electronic devices. *World J Radiol* 2018; 10(9): 100-107 Available from: URL: http://www.wjgnet.com/1949-8470/full/v10/i9/100.htm DOI: http://dx.doi.org/10.4329/wjr.v10.i9.100

INTRODUCTION

Late gadolinium enhancement (LGE) cardiovascular magnetic resonance (CMR) is the gold standard for imaging myocardial viability, scars, and focal fibrosis[1-5]. LGE CMR is based on an inversion recovery (IR) sequence to null myocardial signal and improve the visibility of contrast enhanced tissue[6-10]. An important application of LGE CMR is the assessment of the location and extent of the myocardial scar in patients with ventricular tachycardia (VT), which allows for more accurate identification of the arrhythmogenic substrate and ablation targets[11-13]. However, up to 75% of patients with VT who may benefit from LGE CMR have cardiac implantable electronic devices (CIEDs)[14], which is a relative contraindication for CMR due to safety and image artifact concerns[15,16]. The risks of imaging patients with CIEDs include tissue heating, generation of mechanical forces, and alteration of device function. Nevertheless, studies have shown that these patients can be safely scanned on 1.5 T scanners provided that a protocol with adequate programming of the CIED and monitoring of the patient during the CMR is performed[17,18].

The CIED-induced artifacts are mainly caused by the metallic composition of the device, which results in strong frequency off-resonances near the device, including around cardiac anatomical locations, such as the left ventricular apex, the lateral wall, and the outflow tract. It has been shown that a cardiac pulse generator that is 5-10 cm away from the heart results in a 2-6 kHz resonance frequency offset in the myocardium[19]. Because the frequency band of the inversion radiofrequency (RF) pulse commonly used in LGE MRI is limited, the spins in the affected myocardium regions are not completely inverted, and thus give rise to hyperintensity artifacts[20]. These artifacts obscure the myocardial scar tissue and limit the ability to study the correlation between the myocardial scar structure provided by the LGE image and the electro-anatomical map generated during catheter ablation.

A number of metal artifact reduction techniques have been previously reported, *e.g.*, multi-acquisition variable-resonance image combination (MAVRIC)[21,22] and slice encoding for metal artifact compensation (SEMAC)[23,24], which greatly reduce the metal artifacts. Nevertheless, these techniques require extended scan time because either the image acquisition is repeated several times (in different spectral bands) or additional phase-encoding is applied, which makes them impractical for cardiac imaging of patients with CIEDs.

In this study, we developed a modified IR technique to alleviate the CIED-induced metal artifacts and improve the diagnostic image quality of LGE images in patients with CIEDs without increasing scan time or requiring additional hardware.

MATERIALS AND METHODS

The IR pulse sequence was modified to include an adiabatic wideband IR RF pulse with adjustable frequency offset and bandwidth (BW), which allows for optimal myocardial signal nulling even in the presence of off-resonance effects from the CIEDs.

To mitigate the effect of the B1+ variation in CMR, which could be as high as 25% at 1.5 T and even higher at 3 T, adiabatic inversion pulses are often used to reduce the sensitivity to B1+ inhomogeneity[25]. In this study, we used hyperbolic secant (HS) adiabatic pulses, which provide excellent homogeneous and flat inversion profile across their BW[26].

The HS pulse is composed of the following amplitude and frequency modulation functions:

$A(t) = A_0 \text{ sech } (\alpha t)$ (1)

$\Delta\omega(t) = -c\alpha\tanh(\alpha t)$ (2)

where A_0 is the peak B1 amplitude, c is a phase parameter (dimensionless), and α is a frequency modulation parameter (in units of rad/s). The BW of the HS pulse can be obtained from the product of the amplitude modulation and phase modulation parameters: $c\alpha$. By modifying either or both of these parameters, the BW of the HS pulse can be altered.

A phantom experiment was conducted on a 1.5 T Achieva scanner (Philips, Best, Netherlands), where a CIED was placed one-inch away from a water-filled bottle doped with 0.15 mmol/kg of gadolinium (Gd) contrast material. A Look-Locker inversion time scout sequence[3] was used to identify the appropriate inversion time that nulls the MRI signal (TI = 250 ms), and cross-sectional images of the bottle were acquired using conventional and wideband IR (BW = 3000 Hz) sequences. The imaging parameters of the IR sequence were: repetition time (TR) = 6.7 ms, echo time (TE) = 3.2 ms, resolution = 1.4 × 2.2 mm^2, slice thickness = 8 mm, and specific absorption rate (SAR) limit = 2 W/kg.

The study was approved by our institutional review board (IRB) and written informed consent was obtained from all participants. Twelve patients (10 males, age = 60 ± 18 y.o.) with structural heart disease and a history of ventricular tachycardia (VT) and previously implanted CIEDs [7 patients with a biventricular implantable cardioverter defibrillator (ICD), 4 patients with a dual chamber ICD, and 1 patient with a single chamber ICD; manufacturer: Boston Scientific (n = 5), Medtronic (n = 5), and St Jude (n = 2)], who were referred for a pre-ablation CMR, were enrolled in this study.

The patients were imaged on the same scanner used in the phantom experiment using cine short-axis and long-axis images (steady-state free precession sequence, TR = 4.2 ms, TE = 1.8 ms, resolution = 1.4 × 1.4 mm^2, slice thickness = 8 mm) and the conventional and optimized wideband IR sequences for assessment of myocardial scar prior to an ablation procedure to treat VT. The patients received an intravenous injection of 0.15 mmol/kg of gadolinium contrast material (MultiHance, Bracco, Milan, Italy) approximately 15 min before LGE imaging.

The imaging parameters of the LGE sequences were similar to those used in the phantom scan, while the frequency BW and frequency shift parameters of the wideband LGE sequence were optimized for each patient to improve myocardial nulling while minimizing metal artifacts. Frequency bandwidth and frequency offset adjustments were in the ranges of 2000–4000 Hz and -1500–1500 Hz, respectively. The frequency bands that resulted in an artifact-free image were chosen and used for the rest of the LGE scan for each patient. The SAR of the IR sequences was limited to less than 2 W/kg to ensure imaging safety.

The protocol followed at our institution for CMR imaging of CIED patients has been described previously[27]; in brief it consists of: (1) Demonstration of an imaging necessity in the absence of an alternative imaging modality; (2) absence of device-related contraindications, including epicardial ICD defibrillation patches, and the elapsed time from lead implantation < 6 wk; (3) presence of a provider with CIED management expertise who programs the device to the appropriate settings for the MRI; and (4) re-interrogation and reprogramming of the device after completion of the scan, as well as at 1 wk and 3 mo post imaging.

The patients' vital signs were monitored during the scan by means of an electrocardiogram (ECG), pulse oximetry, and blood pressure measurement by an advanced cardiac life support-certified nurse practitioner, who was present during the entire scan.

All clinical images were reviewed by a fellowship-trained cardiovascular imaging physician with more than 10 years of experience, where the presence and location of artifact-containing segments were reported for each patient. A cardiac segment was considered to be affected by hyperintensity artifact if more than half of the segment was obscured by the artifact.

Contrast-to-noise ratio (CNR) between the blood-pool and myocardium was calculated as the difference between the mean signal intensity in the two regions divided by standard deviation of the background noise in a mid-ventricular slice of the heart. A statistical t-test was used to measure the CNR difference significance between the conventional and modified IR techniques.

RESULTS

Phantom experiment

The conventional IR sequence resulted in a hyperintensity artifact as shown in Figure 1. After using the wideband IR sequence with 3000-Hz bandwidth, the hyperintensity artifact was suppressed.

In vivo scans

All patients were at sinus rhythm during the CMR scan, and were successfully imaged without any adverse events, where the device parameters remained the same immediately, 1 wk, and 3 mo after the scans.

When the conventional IR sequence was utilized, all twelve studied subjects showed varying degrees of hyperintensity artifacts depending on the implanted CIED and its location, including artifacts in the anterior (10 subjects), anteroseptal (3 subjects), anterolateral (4 subjects), and inferior (2 subjects) walls of the left

Table 1 Distribution of left ventricle scar tissues in the studied subjects after using the wideband inversion recovery sequence

Level	Basal					Mid-ventricular						Apical				Apex Cap
Segment	Ant-Lat	Ant-Sept	Inf	Inf-Lat	Inf-Sept	Ant	Ant-Lat	Ant-Sept	Inf	Inf-Lat	Inf-Sept	Ant	Lat	Inf	Sept	
Subjects	1	2	4	4	3	2	1	3	4	2	5	2	4	3	4	2

Ant: Anterior; Inf: Inferior; Lat: Lateral; Sept: Septal.

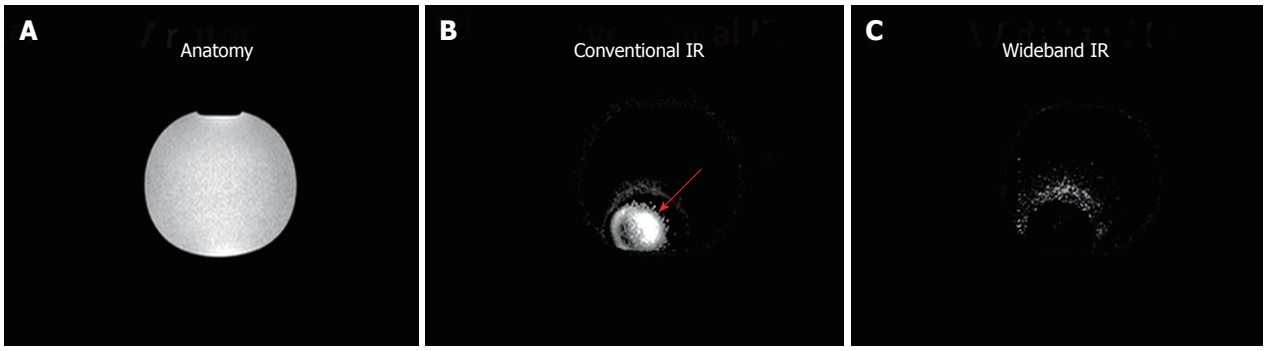

Figure 1 Phantom experiment. A: Anatomical image showing cross-section of a water-filled bottle doped with 0.15 mmol/kg of gadolinium (Gd) contrast material. An implantable cardiac defibrillator was placed one inch away from the imaged location; B: The same slice in (A) imaged using the conventional inversion recovery (IR) sequence targeted to null the signal of the doped water in the bottle. The image shows a hyperintensity artifact due to off-resonance signal (arrow); C: The same slice in (B) imaged using the wideband IR sequence, where the hyperintensity artifact was suppressed.

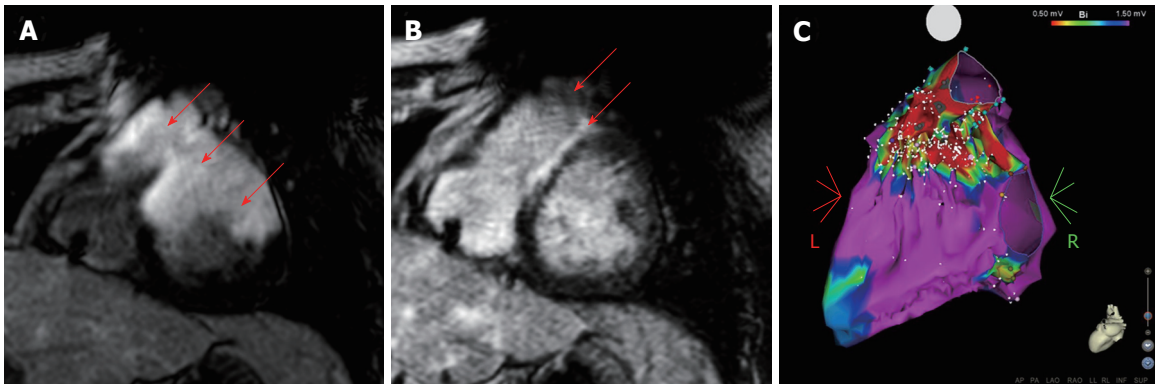

Figure 2 Effect of the improved inversion recovery sequence on removing late gadolinium enhancement hyperintensity artifacts and validation with an electroanatommic map. A: Conventional late gadolinium enhancement image showing metal hyperintensity artifact (arrows) from the implantable cardioverter defibrillator; B: The same image in (A) acquired with the improved late gadolinium enhancement sequence, which eliminated the artifact and revealed underlying scars (arrows); C: An electroanatommic map of the septal aspect of the right ventricle including the outflow tract. The map is a bipolar voltage map showing low voltage (< 1.5 mV) in the right ventricular outflow tract. The low voltage area (red color) corresponds nicely with the delayed enhancement localized in the septal aspect of the right ventricular outflow tract shown in (B).

ventricle (LV; especially at the apical and mid-ventricular levels), and in the inferior wall of the right ventricle (RV; 2 subjects).

The wideband IR sequence removed the hyperintensity artifacts, and did not introduce additional image artifacts when compared to the conventional IR sequence. This improved image quality allowed for anatomical details to be seen and scar assessment could be confidently performed, as shown in Figure 2.

After the hyperintensity artifacts, which mimicked or obscured the scar tissue, were removed with the wideband IR sequence, eight of the twelve patients showed varying degrees of LGE hyperenhancement in the LV and in the RV (inferior wall; 1 subject), while four patients did not show any signs of LGE hyperenhancement. Table 1 shows the distribution of the LV cardiac segments that showed hyperenhancement artifacts after using the wideband IR sequence.

Increasing the IR frequency BW resulted in improved artifact reduction, although this came at the cost of incomplete myocardial nulling, *i.e.*, reduced blood-to-myocardium CNR, as shown in Figure 3 (where the blood-myocardium CNR was 20.8, 13.2, 17.1, and 20.1 for conventional IR, and wideband IR with 6000 Hz, 4000 Hz, and 2000 Hz BW, respectively). Therefore, the BW was set to the minimum value that eliminated the artifact for each patient. Similarly, the frequency shift of the IR pulse affected the artifact appearance, as shown in Figure 4;

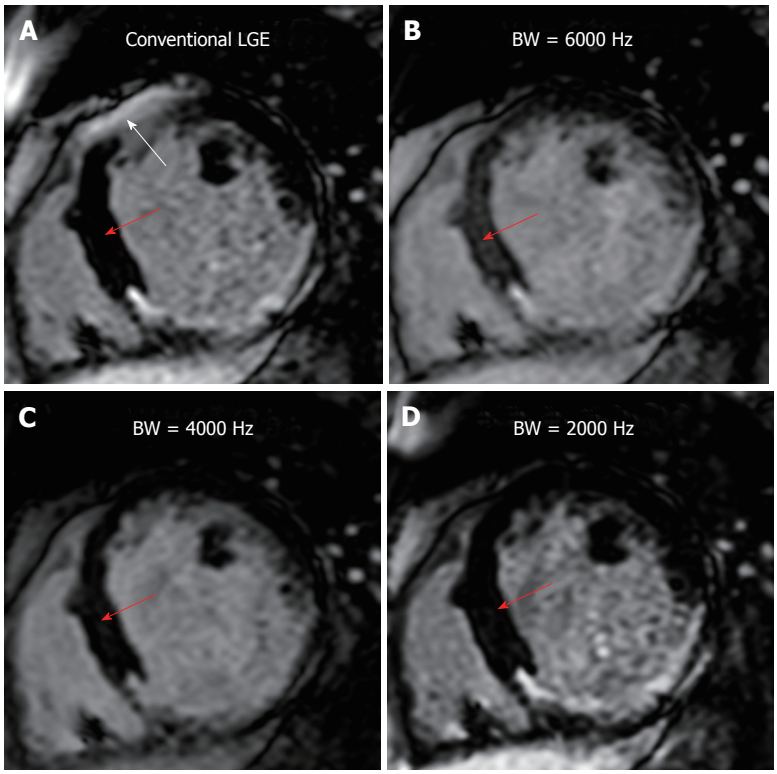

Figure 3 Effect of the inversion recovery bandwidth on myocardial nulling. A: Conventional late gadolinium enhancement showing a metal hyperintensity artifact (white arrow) mimicking an anterior scar, despite perfect myocardium nulling elsewhere (red arrow); B-D: Using wideband inversion recovery (IR) with different bandwidth (BW). Note that reducing the BW results in improved myocardial nulling (red arrows: the blood-myocardium contrast-to-noise ratio was 20.8, 13.2, 17.1, and 20.1 for conventional IR, and wideband IR with 6000 Hz, 4000 Hz, and 2000 Hz BW, respectively); however, too small BW (< 2000 Hz in this case) results in reappearance of the hyperintensity artifact, similar to that shown in (A).

therefore, proper setting of the frequency shift allows for removing the hyperintensity artifact without the need to increase the frequency BW; thus resulting in optimal myocardium nulling. Based on the studied cases, the optimal BW was in the range of 2000-3000 Hz and the optimal frequency shift was up to 1000 Hz.

In the studied patients, the blood-myocardium CNR was 23.5+/-11 for the wideband IR sequence, which was not significantly different (P = 0.03) from the CNR for conventional IR sequence (25.5+/-13). In the implemented CIED patient scans, the average SAR was 0.20 W/kg for both conventional and wideband IR scans, which is well below the 2 W/kg SAR limit.

DISCUSSION

The developed wideband IR sequence minimizes the CIED-generated hyperintensity artifacts through simple adjustment of the IR pulse's BW and offset frequency without increasing scan time or requiring additional hardware, which allows for accurate identification of arrhythmogenic substrate and improved ablation target localization in VT patients, as illustrated by the results of the phantom and *in vivo* scans.

The implemented wideband adiabatic IR scan could be performed within the same scan-time and produced similar SAR compared to the conventional IR scan, which is well below the 2 W/kg limit. Compared to previous efforts to reduce hyperintensity artifacts[19], the developed method provides the flexibility to adjust the IR pulse BW and frequency offset for optimal artifact suppression and myocardial nulling at the same time.

It should be noted that although the wideband IR sequence removed the hyperintensity artifacts, it did not correct for geometric distortions or signal voids caused by off-resonance, which were typically resolved using localized shimming. Otherwise, a spin-echo or an ultrashort echo time (UTE) sequence[26] could be used to correct for strong intra-voxel dephasing signal voids, although this is more of a problem in musculoskeletal applications due to metal implants. It should be noted that while such techniques minimize the metal artifacts effect on surrounding tissues, the place of the CIED will still show signal void or geometric artifacts, which become worse at higher field strengths. However, for safety purposes, imaging patients with CIEDs is typically limited to 1.5 T scanners; therefore, accentuated metal artifacts at higher field strengths is not a concern in this group of patients.

Finally, compared to 3D LGE sequences, extended signal voids and ripple artifacts did not occur in 2D LGE imaging because of the much thinner slice thickness in 2D imaging compared to the large slab thickness in 3D imaging; therefore, through-plane distortion in 2D LGE

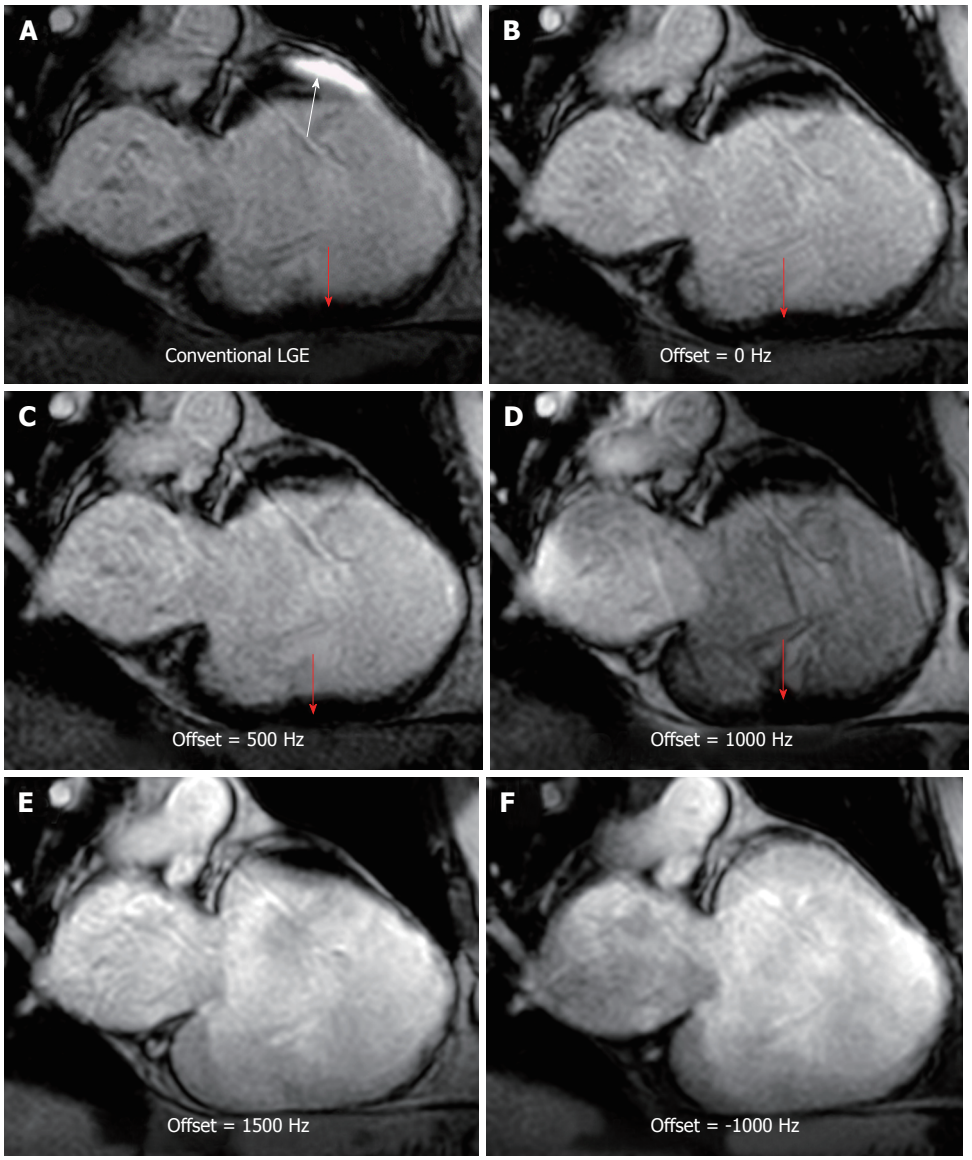

Figure 4 Effects of the inversion recovery frequency offset on myocardial nulling. A: Conventional late gadolinium enhancement (LGE) showing a metal hyperintensity artifact (white arrow), despite perfect myocardium nulling elsewhere (red arrow); B-F: LGE with wideband inversion recovery (IR). All cases have bandwidth (BW) = 2000 Hz, but different frequency offsets. Note the optimal myocardial nulling in all cases (red arrows in B-D) due to using the small IR BW. However, a too large frequency offset (E and F) results in reappearance of the hyperintensity artifacts that affect most of the myocardial tissues.

is typically negligible, as previously reported[20,28].

One limitation of our study is the small number of studied subjects. However, the intent of this study was to illustrate the feasibility of the developed technique and show its importance for revealing myocardial scar in patients with CIEDs, where the presence of hyperintensity artifacts resulted in images with non-diagnostic image quality. Future work includes testing the developed technique on a large number of VT patients with inter- and intra-observer variability analysis using an image quality scoring system.

In conclusion, we presented a modified wideband IR technique that alleviates the CIED-generated metal artifacts and improves the diagnostic image quality of the LGE images to reveal scar myocardial tissue in patients with CIEDs without increasing scan time or requiring additional hardware.

ARTICLE HIGHLIGHTS

Research background

Late gadolinium enhancement magnetic resonance imaging is typically used for myocardial viability imaging. An important application of the late gadolinium enhancement (LGE) technique is the assessment of myocardial scar in patients with ventricular tachycardia (VT) before the ablation procedure.

Research motivation

LGE imaging is challenging in patients with cardiac implantable electronic devices (CIEDs) due to device-generated metal hyperintensity artifacts, which compromise the effect of the IR pulse and obscure the region of interest.

Research objectives

To develop a modified inversion recovery (IR) technique that eliminates the LGE

hyperintensity artifacts and improves diagnostic image quality.

Research methods

The modified pulse sequence developed in this study includes a wideband IR RF pulse with adjustable frequency offset and bandwidth, which allows for optimal myocardial signal nulling even in the presence of CIEDs. A phantom experiment was performed and twelve *in vivo* scans were conducted on patients with CIEDs. The imaging parameters were optimized to improve myocardial nulling and minimize metal artifacts.

Research results

The developed wideband IR sequence significantly minimized the hyperintensity artifacts, such that scar assessment could be confidently performed. Increasing the IR frequency BW results in better artifact reduction, although this improvement is achieved at the cost of incomplete myocardial nulling.

Research conclusions

The developed wideband IR technique minimizes the CIED-generated hyperintensity artifacts without increasing scan time, and allows for accurate identification of ablation targets in VT patients. The RF pulse BW should be set to the minimum value that eliminates the artifact. Further, proper setting of the frequency offset could allow for removing the artifact without the need to increase the frequency BW. Based on the studied cases, optimal BW is in the range of 2000-3000 Hz with optimal frequency shift up to 1000 Hz.

Research perspectives

The developed optimized IR technique allows MRI to play a larger role in treatment planning in VT patients with CIEDs. Future studies should investigate the clinical usefulness of the developed technique by implementing it on a large number of VT patients with different disease stages and CIED types.

REFERENCES

1 **Judd RM**, Kim RJ. Imaging time after Gd-DTPA injection is critical in using delayed enhancement to determine infarct size accurately with magnetic resonance imaging. *Circulation* 2002; **106**: e6 [PMID: 12105174 DOI: 10.1161/01.CIR.0000019903.37922.9C]

2 **Judd RM**, Wagner A, Rehwald WG, Albert T, Kim RJ. Technology insight: assessment of myocardial viability by delayed-enhancement magnetic resonance imaging. *Nat Clin Pract Cardiovasc Med* 2005; **2**: 150-158 [PMID: 16265459 DOI: 10.1038/ncpcardio0134]

3 **Kim RJ**, Shah DJ, Judd RM. How we perform delayed enhancement imaging. *J Cardiovasc Magn Reson* 2003; **5**: 505-514 [PMID: 12882082 DOI: 10.1081/JCMR-120026928]

4 **Kim HW**, Rehwald WG, Jenista ER, Wendell DC, Filev P, van Assche L, Jensen CJ, Parker MA, Chen EL, Crowley ALC, Klem I, Judd RM, Kim RJ. Dark-Blood Delayed Enhancement Cardiac Magnetic Resonance of Myocardial Infarction. *JACC Cardiovasc Imaging* 2017 [PMID: 29248655 DOI: 10.1016/j.jcmg.2017.09.021]

5 **Weinsaft JW**, Klem I, Judd RM. MRI for the assessment of myocardial viability. *Magn Reson Imaging Clin N Am* 2007; **15**: 505-525 [PMID: 17976589 DOI: 10.1016/j.mric.2007.08.007]

6 **Simonetti OP**, Kim RJ, Fieno DS, Hillenbrand HB, Wu E, Bundy JM, Finn JP, Judd RM. An improved MR imaging technique for the visualization of myocardial infarction. *Radiology* 2001; **218**: 215-223 [PMID: 11152805 DOI: 10.1148/radiology.218.1.r01ja50215]

7 **Shah DJ**, Judd RM, Kim RJ. Technology insight: MRI of the myocardium. *Nat Clin Pract Cardiovasc Med* 2005; **2**: 597-605; quiz 606 [PMID: 16258572 DOI: 10.1038/ncpcardio0352]

8 **Wagner A**, Mahrholdt H, Kim RJ, Judd RM. Use of cardiac magnetic resonance to assess viability. *Curr Cardiol Rep* 2005; **7**: 59-64 [PMID: 15610650 DOI: 10.1007/s11886-005-0012-8]

9 **Kim RJ**, Albert TS, Wible JH, Elliott MD, Allen JC, Lee JC, Parker M, Napoli A, Judd RM; Gadoversetamide Myocardial Infarction Imaging Investigators. Performance of delayed-enhancement magnetic resonance imaging with gadoversetamide contrast for the detection and assessment of myocardial infarction: an international, multicenter, double-blinded, randomized trial. *Circulation* 2008; **117**: 629-637 [PMID: 18212288 DOI: 10.1161/CIRCULATIONAHA.107.723262]

10 **Wagner A**, Mahrholdt H, Thomson L, Hager S, Meinhardt G, Rehwald W, Parker M, Shah D, Sechtem U, Kim RJ, Judd RM. Effects of time, dose, and inversion time for acute myocardial infarct size measurements based on magnetic resonance imaging-delayed contrast enhancement. *J Am Coll Cardiol* 2006; **47**: 2027-2033 [PMID: 16697321 DOI: 10.1016/j.jacc.2006.01.059]

11 **Bogun FM**, Desjardins B, Good E, Gupta S, Crawford T, Oral H, Ebinger M, Pelosi F, Chugh A, Jongnarangsin K, Morady F. Delayed-enhanced magnetic resonance imaging in nonischemic cardiomyopathy: utility for identifying the ventricular arrhythmia substrate. *J Am Coll Cardiol* 2009; **53**: 1138-1145 [PMID: 19324259 DOI: 10.1016/j.jacc.2008.11.052]

12 **Klem I**, Weinsaft JW, Bahnson TD, Hegland D, Kim HW, Hayes B, Parker MA, Judd RM, Kim RJ. Assessment of myocardial scarring improves risk stratification in patients evaluated for cardiac defibrillator implantation. *J Am Coll Cardiol* 2012; **60**: 408-420 [PMID: 22835669 DOI: 10.1016/j.jacc.2012.02.070]

13 **Tian J**, Ahmad G, Mesubi O, Jeudy J, Dickfeld T. Three-dimensional delayed-enhanced cardiac MRI reconstructions to guide ventricular tachycardia ablations and assess ablation lesions. *Circ Arrhythm Electrophysiol* 2012; **5**: e31-e35 [PMID: 22511662 DOI: 10.1161/CIRCEP.111.968636]

14 **Kalin R**, Stanton MS. Current clinical issues for MRI scanning of pacemaker and defibrillator patients. *Pacing Clin Electrophysiol* 2005; **28**: 326-328 [PMID: 15826268 DOI: 10.1111/j.1540-8159.2005.50024.x]

15 **Russo RJ**. Determining the risks of clinically indicated nonthoracic magnetic resonance imaging at 1.5 T for patients with pacemakers and implantable cardioverter-defibrillators: rationale and design of the MagnaSafe Registry. *Am Heart J* 2013; **165**: 266-272 [PMID: 23453091 DOI: 10.1016/j.ahj.2012.12.004]

16 **Russo RJ**, Costa HS, Silva PD, Anderson JL, Arshad A, Biederman RW, Boyle NG, Frabizzio JV, Birgersdotter-Green U, Higgins SL, Lampert R, Machado CE, Martin ET, Rivard AL, Rubenstein JC, Schaerf RH, Schwartz JD, Shah DJ, Tomassoni GF, Tominaga GT, Tonkin AE, Uretsky S, Wolff SD. Assessing the Risks Associated with MRI in Patients with a Pacemaker or Defibrillator. *N Engl J Med* 2017; **376**: 755-764 [PMID: 28225684 DOI: 10.1056/NEJMoa1603265]

17 **Nazarian S**, Hansford R, Roguin A, Goldsher D, Zviman MM, Lardo AC, Caffo BS, Frick KD, Kraut MA, Kamel IR, Calkins H, Berger RD, Bluemke DA, Halperin HR. A prospective evaluation of a protocol for magnetic resonance imaging of patients with implanted cardiac devices. *Ann Intern Med* 2011; **155**: 415-424 [PMID: 21969340 DOI: 10.7326/0003-4819-155-7-201110040-00004]

18 **Nazarian S**, Roguin A, Zviman MM, Lardo AC, Dickfeld TL, Calkins H, Weiss RG, Berger RD, Bluemke DA, Halperin HR. Clinical utility and safety of a protocol for noncardiac and cardiac magnetic resonance imaging of patients with permanent pacemakers and implantable-cardioverter defibrillators at 1.5 tesla. *Circulation* 2006; **114**: 1277-1284 [PMID: 16966586 DOI: 10.1161/CIRCULATIONAHA.105.607655]

19 **Rashid S**, Rapacchi S, Vaseghi M, Tung R, Shivkumar K, Finn JP, Hu P. Improved late gadolinium enhancement MR imaging for patients with implanted cardiac devices. *Radiology* 2014; **270**: 269-274 [PMID: 24086074 DOI: 10.1148/radiol.13130942]

20 **Rashid S**, Rapacchi S, Shivkumar K, Plotnik A, Finn JP, Hu P. Modified wideband three-dimensional late gadolinium enhancement MRI for patients with implantable cardiac devices. *Magn Reson Med* 2016; **75**: 572-584 [PMID: 25772155 DOI: 10.1002/mrm.25601]

21 **Koch KM**, Hargreaves BA, Pauly KB, Chen W, Gold GE, King KF. Magnetic resonance imaging near metal implants. *J Magn Reson Imaging* 2010; **32**: 773-787 [PMID: 20882607 DOI: 10.1002/jmri.22313]

22 **Koch KM**, Lorbiecki JE, Hinks RS, King KF. A multispectral three-dimensional acquisition technique for imaging near metal implants. *Magn Reson Med* 2009; **61**: 381-390 [PMID: 19165901 DOI: 10.1002/mrm.21856]

23 **Koch KM**, Brau AC, Chen W, Gold GE, Hargreaves BA, Koff M, McKinnon GC, Potter HG, King KF. Imaging near metal with a MAVRIC-SEMAC hybrid. *Magn Reson Med* 2011; **65**: 71-82 [PMID: 20981709 DOI: 10.1002/mrm.22523]
24 **Lu W**, Pauly KB, Gold GE, Pauly JM, Hargreaves BA. SEMAC: Slice Encoding for Metal Artifact Correction in MRI. *Magn Reson Med* 2009; **62**: 66-76 [PMID: 19267347 DOI: 10.1002/mrm.21967]
25 **Kellman P**, Herzka DA, Hansen MS. Adiabatic inversion pulses for myocardial T1 mapping. *Magn Reson Med* 2014; **71**: 1428-1434 [PMID: 23722695 DOI: 10.1002/mrm.24793]
26 **Bernstein MA,** King KF, Zhou ZJ. Handbook of MRI pulse sequences. United States, Boston: Academic Press, 2004
27 **Horwood L**, Attili A, Luba F, Ibrahim EH, Parmar H, Stojanovska J, Gadoth-Goodman S, Fette C, Oral H, Bogun F. Magnetic resonance imaging in patients with cardiac implanted electronic devices: focus on contraindications to magnetic resonance imaging protocols. *Europace* 2017; **19**: 812-817 [PMID: 27256419 DOI: 10.1093/europace/euw122]
28 **den Harder JC**, van Yperen GH, Blume UA, Bos C. Ripple artifact reduction using slice overlap in slice encoding for metal artifact correction. *Magn Reson Med* 2015; **73**: 318-324 [PMID: 24488701 DOI: 10.1002/mrm.25127]

P- Reviewer: Mani V, Sobanski T, Xie Qi **S- Editor**: Cui LJ
L- Editor: A **E- Editor**: Song H

World Journal of Radiology

Submit a Manuscript: http://www.f6publishing.com

World J Radiol 2018 September 28; 10(9): 108-115

DOI: 10.4329/wjr.v10.i9.108

ISSN 1949-8470 (online)

ORIGINAL ARTICLE

Retrospective Study

Korean single-center experience with femoral access closure using the ExoSeal device

Yoonhee Han, Jae Hyun Kwon, Surin Park

Yoonhee Han, Jae Hyun Kwon, Surin Park, Department of Radiology, Dongguk University Ilsan Hospital, Goyang-si 10326, Gyeonggi-do, South Korea

ORCID number: Yoonhee Han (0000-0001-7712-574X); Jae Hyun Kwon (0000-0001-7303-770X); Surin Park (0000-0003-2237-2166).

Author contributions: Han Y performed the clinical procedures, data analysis and manuscript writing; Kwon JH performed the clinical procedures and data analysis; Park S performed the data analysis and manuscript writing.

Institutional review board statement: This study was reviewed and approved by the Dongguk University Ilsan Hospital Institutional Review Board (approval No. DUIH 2017-10-003-001).

Informed consent statement: The study investigators obtained informed consent from all included patients, and the study was conducted in accordance with the principles of the Helsinki Declaration.

Conflict-of-interest statement: All authors declare no conflicts-of-interest related to this article.

Manuscript source: Unsolicited manuscript

Correspondence to: Yoonhee Han, MD, PhD, Associate Professor, Department of Radiology, Dongguk University Ilsan Hospital, 27 Dongguk-ro, Siksa-dong, Ilsandong-gu, Goyang-si 10326, Gyeonggi-do, South Korea. hanyoonhee@naver.com
Telephone: +82-10-52729747
Fax: +82-31-9618281

Received: April 27, 2018
Peer-review started: April 27, 2018
First decision: June 14, 2018
Revised: August 6, 2018
Accepted: August 23, 2018
Article in press: August 24, 2018
Published online: September 28, 2018

Abstract

AIM

To report 17-mo experience of femoral artery puncture site closure during angiographic procedures using ExoSeal vascular closure devices (VCDs).

METHODS

Between November 2015 and April 2017, we performed 179 diagnostic and interventional angiographic procedures *via* a common femoral arterial access. The ExoSeal VCD was used at the puncture site to achieve hemostasis in 125 patients. We evaluated the technical and procedural success rates, the complications, and the factors affecting the hemostasis time of the ExoSeal VCDs.

RESULTS

Technical and procedural successes were achieved in 176 cases (98.0%) and 128 cases (71.5%), respectively. Device failure occurred in 3 (1.7%) cases. In 1 case (0.6%) a small hematoma developed, but there were no major complications. Among the hemostasis-relevant variables, a history of drinking alcohol, low platelet (PLT) count, and high prothrombin time-international normalized ratio (commonly known as PT-INR) values were the statistically significant predictors of the need for longer manual compression (MC). There was no difference in the success rates between the repeat and single ExoSeal procedure groups, and repeated use of

the ExoSeal did not affect hemostasis time.

CONCLUSION

The ExoSeal VCD effectively achieves hemostasis, with few complications. Longer light MC may be needed with alcohol drinkers, low PLT count, and high PT-INR values.

Key words: Vascular closure device; Femoral access; Manual compression; Angiography; Hemostasis

Core tip: This study aimed to report the experience of closure of the femoral artery over a 17-mo period using ExoSeal vascular closure devices (VCDs). Technical and procedural successes were achieved in 176 cases (98.0%) and 128 cases (71.5%), respectively, while device failure occurred in only 3 (1.7%) cases. Repeated use of the ExoSeal did not affect hemostasis time or success rate. Thus, ExoSeal VCD is a simple, safe and effective device for achieving hemostasis with few complications. However, longer light manual compression may be needed with alcohol drinkers, low platelet counts, and high prothrombin time-international normalized ratio values.

Han Y, Kwon JH, Park S. Korean single-center experience with femoral access closure using the ExoSeal device. *World J Radiol* 2018; 10(9): 108-115 Available from: URL: http://www.wjgnet.com/1949-8470/full/v10/i9/108.htm DOI: http://dx.doi.org/10.4329/wjr.v10.i9.108

INTRODUCTION

Femoral arterial puncture using the Seldinger technique is the most common method of gaining vascular access for diagnostic and interventional arterial catheterization procedures. After the procedure, the gold standard method for achieving long-term hemostasis at the femoral arterial puncture site has been manual compression (MC). However, MC has limitations, such as prolonged hemostasis time, patient pain and discomfort, and a requirement for prolonged bed rest. Therefore, various hemostatic devices have been developed to improve the efficacy and safety of percutaneous intravascular treatment[1].

Vascular closure devices (VCDs) can be categorized into two main types, passive and active, according to their mechanisms of action. Passive VCDs include hemostasis pads and compression devices, while active VCDs include suture devices, collagen plug devices, and clips. Schwartz *et al*[2] have reviewed several different types of VCDs. Among these, the AngioSeal-which has been widely applied as an active VCD using collagen plugs such as ExoSeal-reduces hemostasis and ambulation time compared to MC; in addition, it significantly reduced the incidence of major complications.

The ExoSeal VCD (Cordis Corporation, Miami Lakes, FL, United States) is a collagen plug device of the active VCD category. It places a bioabsorbable polyglycolic acid (PGA) plug in the extravascular space at the top of the arterial incision. As far as we know, ExoSeal is the most recently developed VCD that has been approved by the United States Federal Drug Administration. The Ensure's Vascular Closure Device Speeds Hemostasis Trial (ECLIPSE) studies were conducted to compare the safety and effectiveness of MC performed to promote hemostasis and early ambulation of patients experiencing percutaneous arterial, diagnostic or interventional procedures. In the ECLIPSE study, the success rate of the ExoSeal device was 94%. After an average of 2.5 h, ambulation was possible, and there was no significant difference between MC and the device in the incidence rate of complications[3]. The purpose of the present study was to report the experience of closure of the femoral artery using ExoSeal VCDs over a 17-mo period.

MATERIALS AND METHODS

Device description

The ExoSeal VCD is an active VCD, collagen plug device. It consists of a plug applicator and a bioabsorbable PGA plug. The applicator places the plug on the external surface of the arteriotomy site of the femoral artery *via* the previously inserted vascular sheath. When the plug is placed on the arterial incision site, hemostasis is achieved. To ensure that the plug is positioned properly in the extravascular space, the ExoSeal delivery system has two markers that allow the operator to visually identify the location of the plug. These markers allow the operator to determine the position of the plug relative to the vessel wall before dropping the plug. The first indicator of the plug position is leakage of the pulsatile blood flow, and the second is a visual display on the handle.

When the VCD is inserted into and attached to the vascular sheath that has been pre-inserted into the artery, the indicator wire automatically forms a loop in the lumen of the blood vessel. When the VCD/sheath assembly is pulled back slightly at a 45° angle, the nontraumatic loop at the distal end of the indicator wire (Figure 1) contacts the inner surface of the vessel, causing the shape of the loop to change longitudinally. The predetermined displacement of the distal loop of the indicator wire indicates when the plug is placed just above the arterial incision. When the plug is in the correct position, the visual indicator on the handle then changes from white to black, indicating that it is ready for the plug to be dropped (Figure 2). Pulsatile blood leakage is significantly reduced or stopped at this point.

When the button on the handle is pressed, the plug is deployed in the proper position on the arteriotomy site. Then, the VCD and introducer sheath are removed,

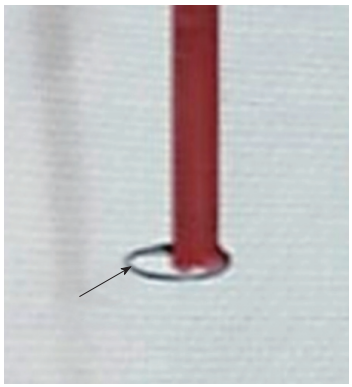

Figure 1 Distal loop of the indicator wire of the ExoSeal vascular closure device (black arrow). A loop is automatically formed in the lumen of the blood vessel when the vascular closure device (VCD) is inserted into and attached to the vascular sheath. When the VCD/sheath assembly is pulled back, this loop contacts the inner surface of the vessel, causing the shape of the loop to change longitudinally.

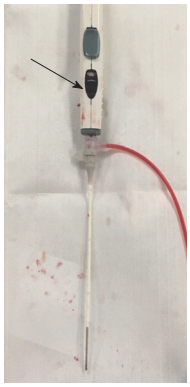

Figure 2 Appearance of the ExoSeal and vascular sheath complex when the polyglycolic acid plug has been normally deployed. The color of the indicator window was black (black arrow), which means the plug is in the correct position, indicating that it is ready for the plug to be dropped.

and the puncture site is lightly hand-pressed for a few minutes. The plug is absorbed considerably over 30 d after implantation and completely absorbed between 60 and 90 d.

Patients and procedures

In our institution, two interventional radiologists with at least 10 years of experience performed a total of 179 diagnostic and interventional angiographic procedures between November 2015 and April 2017. The radiologists used a common femoral arterial access with the ExoSeal VCD at the puncture site, in addition to angiographic control of hemostasis, in 125 patients (91 men, 34 women; mean age: 59.4 years, range: 20-87 years).

A total of 171 interventional angiographic procedures were performed in 117 patients. Among these patients, 24 underwent consecutive interventional procedures, with 23 treated with 76 transarterial chemoembolization (TACE) for hepatocellular carcinoma, ranging from two to six procedures per person. Nine patients received TACE twice, five patients were treated three times, three patients were treated four times, five patients were treated five times, and one patient was treated six times. One of the 24 consecutively treated patients underwent visceral arterial embolization for lower gastrointestinal bleeding twice. The rest of the 93 patients underwent interventional angiographic procedures. Eight patients underwent eight pure diagnostic angiographies. Five patients received interventions with antegrade femoral puncture. Ten patients were on anticoagulation therapy. One patient was taking warfarin, seven patients were taking aspirin, and two patients received 4000 IU heparin peri-interventionally.

Table 1 shows the patient and procedure characteristics. A total of 172 5-Fr ExoSeals were used in 118 patients. Six patients underwent peripheral interventional procedures requiring 6-Fr vascular sheaths, so that six 6-Fr ExoSeals were used. A 7-Fr ExoSeal was used in 1 patient who underwent percutaneous transluminal angioplasty and stenting in the common iliac artery.

After completion of the procedure, the puncture site was closed using the ExoSeal VCD according to the manufacturer's instructions for use, with light MC applied for 3 min. Three minutes later, if any blood leaked after the release of pressure then additional MC was performed for 2 min. If hemostasis was successful after 5 min of MC, compression bandages were not used. Otherwise, the puncture site was pressed by hand until the bleeding stopped completely (at least 10 min), followed by the application of a 2-h compressive bandage. All patients were prescribed 2 h of immobilization.

Definitions and statistical analysis

Technical success of the device was defined as successful placement of the plug in the puncture site without immediate major vascular complications associated with the VCD. Procedural success was defined as successful hemostasis without major vascular complications, and only 3 min of mild MC after successful deployment of the plug.

Complications were classified as either major or minor, as defined in the ECLIPSE trial[2]. Major complications were defined as: (1) needing vascular repair by surgical or nonsurgical techniques; (2) bleeding requiring a blood transfusion; (3) infection requiring antibiotics, extended hospitalization, or both; (4) new-onset ischemia of the ipsilateral lower extremity; (5) need for surgical repair of access-site-related nerve injury; and (6) permanent access-site-related nerve injury. Minor post-procedural complications were defined as: (1) recurrent local bleeding requiring hemostatic interventions, or hematomas $\leqslant$ 6 cm; (2) development of pseudoaneurysms, arteriovenous fistulae, vascular lacerations, or retroperitoneal bleeding; (3) ipsilateral manifestations of vascular insufficiency or embolization, including loss of distal pulse, total arterial occlusion, or deep vein thrombosis; (4) infection; and (5) nerve injury.

We recorded hemostasis-relevant patient history,

Table 1 Patient and procedure characteristics

Characteristic	*n* = 179
Age (yr)	59.4 (20–87)
Men	145 (81)
Hypertension	59 (33)
Diabetes	52 (29.1)
Smoking status	
Current smoker	37 (20.7)
Ex-smoker	53 (29.6)
Nonsmoker	89 (49.7)
Alcohol intake	57 (31.8)
Anticoagulation	10 (5.6)
Aspirin	7 (3.9)
Warfarin	1 (0.6)
Heparin	2 (1.1)
Interventional procedure	171 (95.5)
Consecutive	78 (43.6)
TACE for HCC	76 (42.5)
Visceral embolization of gastrointestinal bleeding	2 (1.1)
Single	93 (51.9)
Diagnostic procedure	8 (4.5)
Antegrade puncture	5 (2.8)
ExoSeal	
5-Fr	172 (96.1)
6-Fr	6 (3.4)
7-Fr	1 (0.5)

Data are presented as *n* (%), unless indicated otherwise. HCC: Hepatocellular carcinoma; TACE: Transarterial chemoembolization.

access size, pre- or intraprocedural anticoagulation[4,5], laboratory findings [activated partial thromboplastin time (aPTT), platelet (PLT) count, and prothrombin time-international normalized ratio (PT-INR)], procedure characteristics, time to hemostasis, and any other complications. We reported the data as mean and standard deviation for continuous variables, and frequency (percentage) for categorical variables.

We analyzed the variables (patient age, sex, history of diabetes, hypertension, smoking or alcohol use, access size, and anticoagulation) using a logistic regression model to determine which variables require more than 3 min of MC to obtain hemostasis after using ExoSeal VCDs. Hemostasis-relevant laboratory tests (aPTT, PLT count, and PT-INR) were performed to determine the interrelation between the need for more than 3-min MC to achieve hemostasis, and the hemostasis-relevant parameters. We evaluated these parameters using the Mann-Whitney U test, also known as the Wilcoxon rank sum test, to evaluate the differences between the two groups based on a single, ordinal variable with no specific distribution. The Student's *t*-test and chi-square test were used to evaluate whether the frequency of ExoSeal use affected the time to hemostasis in patients on who ExoSeal was used several times. Results were considered statistically significant if a *P*-value < 0.05 was reached. All statistical analyses were performed using SPSS statistical software (version 20.0; IBM Corp. Released 2011. IBM SPSS Statistics for Windows, Version 20.0. Armonk, NY, United States).

RESULTS

Device failure occurred in 3 (1.7%) patients. One patient had hypodermal fat so thin that the deployed PGA plug was pushed out of the skin. In 2 patients, plug deployment failed due to product defects (Figure 3). In those 3 patients, hemostasis required MC for 10 to 30 min. The overall technical device success rate was 98.3%. There were no cases of intraluminal plug deployment.

Hemostasis after successful PGA plug deployment and MC < 3 min was achieved in 128 cases. Therefore, as defined above, the procedural success rate was 71.5%. In 3 cases (1.7%), the aforementioned technical failures did not result in procedural success. In 44 cases (24.6%), hemostasis was achieved with MC for an additional 2 min. So, in 172 cases (96.1%) hemostasis was achieved after successful plug deployment in less than 5 min. There were 7 (3.9%) cases that needed MC for > 5 min. The mean compression time for these 7 cases was 10.2 min. In 2 cases hemostasis was unsuccessful, despite prolonged MC. In 1 patient, the blood oozing continued after prolonged MC for 13 min. The other patient's PLT count was 45 ($\times 10^3/\mu L$) and blood oozing continued after plug deployment followed by MC for 10 min. Thus, compressive bandages were applied in these 2 cases and successful hemostasis was achieved after compression bandaging for 2 h.

Among the antegrade femoral punctures performed in 5 patients, one procedural failure occurred. The patient was on warfarin due to heart disease and was admitted due to bleeding from the right deep femoral artery. He underwent embolization of the right deep femoral artery with antegrade puncture of the right superficial femoral artery. Subsequent to embolization, it took 10 min to achieve hemostasis after successful ExoSeal plug deployment. The patient's PLT count ($170 \times 10^9/L$) was in the normal range but his PT-INR value (1.43) was slightly high. There were no major complications.

Of the 179 ExoSeal closure procedures, one (0.6%) minor complication (a 3-cm or smaller hematoma) occurred. The patient with the hematoma, who did not use an anticoagulant, underwent angiography through a 5-Fr vascular sheath. The laboratory results were in the normal ranges.

Table 2 shows the comparison of success rates between the repeated-procedure group and the single-procedure group. There were 78 cases of repeat procedures and 101 cases of single procedures. Successful plug deployment was achieved in 77 patients in the repeated-procedure group and in 99 patients in the single-procedure group, with technical success rates of 98.7% and 98.0%, respectively. Successful hemostasis with MC for 3 min was achieved in 52 cases (66.7%) in the repeated-procedure group and in 76 cases (75.2%) in the single-procedure group. Successful hemostasis with 5 min of MC occurred in 76 cases in the repeated-procedure group and in 96 cases in the single-procedure

Table 2 Success rate comparison between the repeated-procedure group and the single-procedure group *n* (%)

	Technical success	Procedural success	Success within 5 min
Repeated-procedure, *n* = 78	77 (98.7)	52 (66.7)	76 (97.4)
Single-procedure, *n* = 101	99 (98.0)	76 (75.2)	96 (95.0)
Overall, *n* = 179	176 (98.3)	128 (71.5)	172 (96.1)

Table 3 Student's *t*-test for assessing whether the frequency of use of ExoSeal affected the patients' hemostasis time

	ExoSeal	*n*	Mean ± SD	*P*-value
Hemostasis time	Repeat use	78	4.79 ± 4.32	0.606
	Single use	101	4.46 ± 4.38	

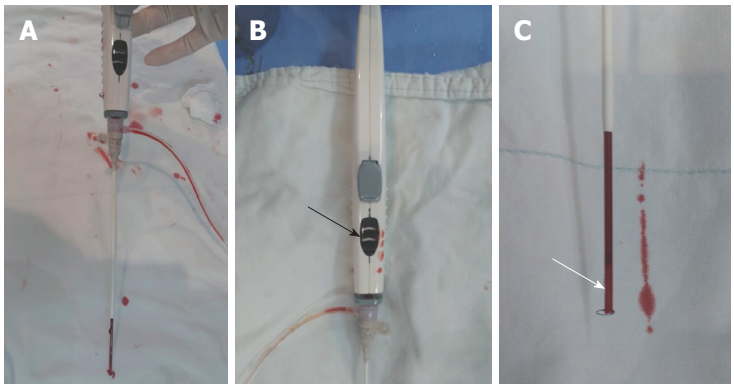

Figure 3 Representations of device appearances when failures occurred. Normally, when the vascular closure devices (VCDs)/sheath assembly is pulled backward, the distal loop changes to a longitudinal shape and the plug is placed just above the arteriotomy. At this point, the indicator changes to black. When this indicator changes to black, pressing of the button deploys the plug. In this case, however, the indicator still did not turn black and the plug could not be dropped, even though the VCDs/sheath came out of the skin. A: Full view of VCDs/sheath in case of device failure; B: The color of the indicator window was white (black arrow); C: The polyglycolic acid plug (white arrow) remained in the delivery shaft of the ExoSeal.

group. The success rates of hemostasis after 5 min of MC were 97.4% in the repeated-procedure group and 95.0% in the single-procedure group. The *P*-values of the Student's *t*-test (Table 3) and chi-square test (Table 4), assessing whether the frequency of ExoSeal use affected hemostasis times for patients with repeated ExoSeal applications, were 0.606 and 0.137, respectively.

Table 5 shows the multiple logistic regression analysis of the continuous variables. History of drinking alcohol (*P* = 0.01) and PT-INR (*P* = 0.001) were statistically significant predictors of a need for > 3 min of MC. The odds ratios for alcohol intake and PT-INR were 3.370 [95% confidence interval (CI): 1.345-8.440] and 0.065 (95%CI: 0.012-0.343), respectively. Table 6 shows the Wilcoxon rank sum test of hemostasis-relevant laboratory findings, yielding statistically significant correlations between the need for > 3 min of MC and PLT count (*P* = 0.032) and PT-INR (*P* = 0.037).

DISCUSSION

This study was conducted to report our experiences with the use of the ExoSeal VCD for femoral artery closure. Until recently, compressive bandages and MC have mainly been used in our intervention unit. Compression bandages have fewer limitations compared to MC, but they do have limitations, such as prolonged hemostasis time, patient pain or discomfort, and prolonged bed rest. Therefore, other VCDs were considered. Several studies have shown that various types of VCDs can achieve generally safe and effective hemostasis[1,6]. In addition, VCDs allow for early ambulation, thereby relieving patient discomfort and improving satisfaction and quality of life[6,7]. Among the VCDs, the ExoSeal is a collagen plug device belonging to the category of active VCDs. The ExoSeal VCD is an extravascular device that acts as a sealant to prevent blood from leaking by placing a bioabsorbable PGA plug directly into the vascular puncture site[8]. Several studies have been conducted on the efficacy of the ExoSeal VCDs in retrograde femoral artery closure as well as antegrade femoral artery closure[3,8-11].

Over a period of 17 mo, two interventional radiologists performed a total of 179 diagnostic and interventional angiographic procedures using ExoSeal VCDs to close 175 retrograde common femoral artery and 5 antegrade superficial femoral artery access sites. The manufacturer recommends a light MC of 2 or 3 min. We positioned the plugs, followed by MC for 3 min. Then, when MC pressure was released, if even scant blood seepage was

Table 4 Chi-square test for assessing whether the frequency of ExoSeal use affected the patients' hemostasis time

Cross table of hemostasis time and ExoSeal repeatability, *P*-value = 0.137					
			ExoSeal repeatability		Total
			Repeat use	Single use	
Hemostasis time	< 3 min	Frequency	52	76	128
		% of hemostasis time	40.6	59.4	100
		% of ExoSeal repeated use	66.7	75.2	71.5
		% of total	29.1	42.5	71.5
	> 3 min	Frequency	26	25	51
		% of hemostasis time	51	49	100
		% of ExoSeal repeated use	33.3	24.8	28.5
		% of total	14.5	14	28.5
Total		Frequency	78	101	179
		% of hemostasis time	43.6	56.4	100
		% of ExoSeal repeated use	100	100	100
		% of total	43.6	56.4	100

Table 5 Multiple logistic regressions of the continuous hemostasis-relevant variables

	B	*P* < 0.05	OR	95%CI for OR	
				Lower limit	Upper limit
Women	0.186	0.707	1.204	0.457	3.176
Age	0.013	0.354	1.013	0.985	1.042
DM, yes	0.666	0.135	1.946	0.813	4.662
HTN, yes	-0.500	0.251	0.606	0.258	1.424
Smoking	0.000	0.241	0.000	0.000	0.000
Ex-smoker	-0.752	0.094	0.471	0.196	1.137
Current smoker	-0.280	0.599	0.756	0.266	2.149
Alcohol use	1.215	0.010	3.370	1.345	8.440
5-Fr	0.000	0.559	0.000	0.000	0.000
6-Fr	-0.992	0.281	0.371	0.061	2.252
7-Fr	-21.226	1.000	0.000	0.000	0.000
Anticoagulation	-0.447	0.599	0.640	0.121	3.386
PT-INR	-2.732	0.001	0.065	0.012	0.343

DM: Diabetes mellitus; HTN: Hypertension; PT-INR: Prothrombin time-international normalized ratio; CI: Confidence inteval; OR: Odd ratio.

Table 6 Wilcoxon rank sum test of hemostasis-relevant laboratory findings

Variable	< 3 min			> 3 min			*P*-value
	n	mean ± SD	Median (min, max)	*n*	mean ± SD	Median (min, max)	
aPTT	100	36.54 ± 8.53	34.6 (22, 77.4)	40	39.53 ± 10.13	36.25 (24.9, 71.7)	0.108
PLT count	128	171.27 ± 93.64	172.5 (27, 706)	51	140.37 ± 86.87	155.5 (28, 347)	0.032[a]
PT-INR	128	1.17 ± 0.18	1.11 (0.91, 1.93)	51	1.26 ± 0.27	1.14 (0.97, 2.34)	0.037[a]

[a]*P* < 0.05. aPTT: Activated partial thromboplastin time; PLT count: Platelet count; PT-INR: Prothrombin time-international normalized ratio; SD: Standard definition.

observed, MC was performed for an additional 2 min. The overall technical success rate was 98.3%, but the procedural success rate was slightly disappointing at 71.5%. However, if we define the procedural success as 5 min instead of 3 min of MC, as recommended by the manufacturer, the procedural success rate will increases to 96.1%. Boschewitz *et al*[9] defined procedural success as successful plug deployment and MC for 5 min or less[12,13]. Their procedural success rate was 97.3%. Also, in the ECLIPSE study[3], that first introduced the ExoSeal in 2009, and in the 7-Fr ECLIPSE study[8], the use of a 7-Fr ExoSeal required only mild MC after plug placement and hemostasis occurred at about 4 min. None of the six major complications defined by the ECLIPSE trial[3] occurred in our study, and there were no minor complications other than a small groin hematoma > 3 cm in size.

Our study was a retrograde study, and we did not make any special exceptions when using the ExoSeal VCD. Therefore, we evaluated the factors affecting hemostasis time in cases of hemostasis obtained with > 3 min of MC in these 179 cases. In this study, the ExoSeal was used many times in the same patient. TACE was performed 76 times in 26 patients with liver cancer, and 1 patient underwent embolization twice because of lower gastrointestinal bleeding. When comparing the success rate of hemostasis between the repeated-procedure group (n = 78) and the single-procedure group (n =

101), the procedural success rates were 67.9% and 74.3%, respectively. This was not different from the overall procedural success rate of 71.5%.

If the definition of procedural success is broadened to 5 min of manual pressure, the success rates of the repeated-procedure group and the single-procedure group become 97.4% and 95.0%, respectively. This was not significantly different from the overall success rate of 96.1%. There was also no difference from the results of Boschewitz *et al*[13] (95.5% procedural success rate), in the report of their experiences using ExoSeal VCDs in 404 repeated closures. The *P*-values of the Student's *t*-test and chi-square test for assessing whether the ExoSeal use frequency affected hemostasis time after multiple ExoSeal uses were 0.606 and 0.137, respectively. This indicated that repeated use of the ExoSeal did not affect the hemostasis times[14].

According to the data from the multiple logistic regressions of the hemostasis-relevant variables (patient age, sex, diabetes, hypertension, smoking, and alcohol history, access size, and anticoagulation), only history of drinking alcohol and PT-INR were statistically significant predictors of the need for > 3 min of MC (Table 5). Anticoagulation or access size did not affect hemostasis time. Also, the PLT count (*P* = 0.032) and PT-INR (*P* = 0.037), among the hemostasis-relevant laboratory findings (aPTT, PLT count, and PT-INR), exhibited statistically significant correlations with the need for > 3 min of MC by the Wilcoxon rank sum test. Therefore, it is predictable that history of drinking alcohol, low PLT counts, and high PT-INR values can lead to a requirement for > 3 min of MC. Schelp *et al*[15] reported the experience of using ExoSeal VCDs in 801 patients who underwent coronary angiography and interventions through the femoral artery. In that article, lengthy procedures, percutaneous coronary interventions, use of GP Ⅱb/Ⅲa inhibitors, and elderly age of patients were the strongest independent predictors of bleeding/vascular complications and device failure.

Our study was limited by the fact that the number of antegrade femoral punctures (*n* = 5) was too small to compare to the number of retrograde femoral punctures (*n* = 174). Among the 5 patients who underwent the antegrade femoral puncture, 1 procedural failure occurred. In the remaining 4 patients, hemostasis was achieved with a 3-min MC. There were no complications among these 5 cases. According to several other articles on the use of ExoSeal in antegrade femoral punctures, ExoSeal VCDs were found to be safe and effective, with high technical success rates and acceptable complication rates in antegrade procedures[9-11,16,17]. Another limitation was that we did not analyze the failure rate according to the operator's learning curve because the ExoSeal was so easy to use.

In summary, the ExoSeal VCD is a very simple, safe and effective hemostasis device for both antegrade and retrograde femoral punctures, and is associated with few complications. In addition, the ExoSeal VCD is an instrument that can effectively obtain hemostasis even when used repeatedly in the same patient. However, longer light MC may be needed in patients with history of drinking alcohol, low PLT counts, and high PT-INR values.

ARTICLE HIGHLIGHTS

Research background

The gold standard method for achieving hemostasis at the femoral arterial puncture site has been manual compression (MC). However, MC has limitations, such as prolonged hemostasis time, patient pain and discomfort, and a requirement for prolonged bed rest. Therefore, various hemostatic devices have been developed to improve the efficacy and safety of percutaneous intravascular treatment and one of those hemostasis devices is ExoSeal.

Research motivation

We have used MC or other compressive devices (such as sand bags or balloon compressive devices) before introducing ExoSeal into our clinical practice. When we first started to use ExoSeal, we began studying the cases in which it was applied.

Research objectives

To report the experience of closure of the femoral artery using ExoSeal vascular closure devices (VCDs) over a 17-mo period.

Research methods

We evaluated the technical and procedural success rates, complications, and factors affecting the hemostasis time of the ExoSeal VCDs.

Research results

Technical and procedural successes were achieved in 176 cases (98.0%) and 128 cases (71.5%), respectively. In one case (0.6%), a small hematoma developed, but there were no major complications. A history of drinking alcohol, low platelet (PLT) count, and high prothrombin time-international normalized ratio (PT-INR) values were the statistically significant predictors of the need for longer MC.

Research conclusions

The ExoSeal VCD is a simple, safe and effective device for hemostasis of femoral punctures. In addition, the ExoSeal VCD is an instrument that effectively achieves hemostasis with few complications, even when used repeatedly in the same patient. However, longer light MC may be needed in patients with a history of drinking alcohol, low PLT count, and high PT-INR values.

Research perspectives

Based on this and other studies, ExoSeal is expected to improve further and other similar VCDs will be developed.

REFERENCES

1 **Eggebrecht H**, Haude M, Woertgen U, Schmermund A, von Birgelen C, Naber C, Baumgart D, Kaiser C, Oldenburg O, Bartel T, Kroeger K, Erbel R. Systematic use of a collagen-based vascular closure device immediately after cardiac catheterization procedures in 1,317 consecutive patients. *Catheter Cardiovasc Interv* 2002; **57**: 486-495 [PMID: 12455083 DOI: 10.1002/ccd.10254]

2 **Schwartz BG**, Burstein S, Economides C, Kloner RA, Shavelle DM, Mayeda GS. Review of vascular closure devices. *J Invasive Cardiol* 2010; **22**: 599-607 [PMID: 21127366]

3 **Wong SC**, Bachinsky W, Cambier P, Stoler R, Aji J, Rogers JH, Hermiller J, Nair R, Hutman H, Wang H; ECLIPSE Trial Investigators. A randomized comparison of a novel bioabsorbable vascular closure device versus manual compression in the achievement of

hemostasis after percutaneous femoral procedures: the ECLIPSE (Ensure's Vascular Closure Device Speeds Hemostasis Trial). *JACC Cardiovasc Interv* 2009; **2**: 785-793 [PMID: 19695549 DOI: 10.1016/j.jcin.2009.06.006]

4 **Kim HY**, Choo SW, Roh HG, Han H, Kim SS, Lee JY, Park YR, Lee SH, Shin SW, Park KB, Do YS, Cho SK, Lee IH, Kim SM, Byun HS, Jeon P. Efficacy of femoral vascular closure devices in patients treated with anticoagulant, abciximab or thrombolytics during percutaneous endovascular procedures. *Korean J Radiol* 2006; **7**: 35-40 [PMID: 16549954 DOI: 10.3348/kjr.2006.7.1.35]

5 **Resnic FS**, Blake GJ, Ohno-Machado L, Selwyn AP, Popma JJ, Rogers C. Vascular closure devices and the risk of vascular complications after percutaneous coronary intervention in patients receiving glycoprotein Ⅱb-Ⅲa inhibitors. *Am J Cardiol* 2001; **88**: 493-496 [PMID: 11524056 DOI: 10.1016/S0002-9149(01)01725-8]

6 **Robertson L**, Andras A, Colgan F, Jackson R. Vascular closure devices for femoral arterial puncture site haemostasis. *Cochrane Database Syst Rev* 2016; **3**: CD009541 [PMID: 26948236 DOI: 10.1002/14651858.CD009541.pub2]

7 **Duffin DC**, Muhlestein JB, Allisson SB, Horne BD, Fowles RE, Sorensen SG, Revenaugh JR, Bair TL, Lappe DL. Femoral arterial puncture management after percutaneous coronary procedures: a comparison of clinical outcomes and patient satisfaction between manual compression and two different vascular closure devices. *J Invasive Cardiol* 2001; **13**: 354-362 [PMID: 11385148]

8 **Wiemer M**, Langer C, Fichtlscherer S, Firschke C, Hofbauer F, Lins M, Haude M, Debèfve C, Stoll HP, Hanefeld C. First-in-man experience with a new 7F vascular closure device (EXOSEAL™): the 7F ECLIPSE study. *J Interv Cardiol* 2012; **25**: 518-525 [PMID: 22762417 DOI: 10.1111/j.1540-8183.2012.00739.x]

9 **Boschewitz JM**, Pieper CC, Andersson M, Nadal J, Schild HH, Meyer C. Efficacy and time-to-hemostasis of antegrade femoral access closure using the ExoSeal vascular closure device: a retrospective single-center study. *Eur J Vasc Endovasc Surg* 2014; **48**: 585-591 [PMID: 25201516 DOI: 10.1016/j.ejvs.2014.08.006]

10 **Schmelter C**, Liebl A, Poullos N, Ruppert V, Vorwerk D. Suitability of Exoseal vascular closure device for antegrade femoral artery puncture site closure. *Cardiovasc Intervent Radiol* 2013; **36**: 659-668 [PMID: 23070109 DOI: 10.1007/s00270-012-0501-2]

11 **Maxien D**, Behrends B, Eberhardt KM, Saam T, Thieme SF, Reiser MF, Treitl M. Evaluation of the 6-F ExoSeal vascular closure device in antegrade femoral artery punctures. *J Endovasc Ther* 2012; **19**: 836-843 [PMID: 23210885 DOI: 10.1583/JEVT-12-3922R.1]

12 **Biancari F**, D'Andrea V, Di Marco C, Savino G, Tiozzo V, Catania A. Meta-analysis of randomized trials on the efficacy of vascular closure devices after diagnostic angiography and angioplasty. *Am Heart J* 2010; **159**: 518-531 [PMID: 20362708 DOI: 10.1016/j.ahj.2009.12.027]

13 **Boschewitz JM**, Andersson M, Naehle CP, Schild HH, Wilhelm K, Meyer C. Retrospective evaluation of safety and effectiveness of the EXOSEAL vascular closure device for single vascular closure and closure after repeat puncture in diagnostic and interventional radiology: single-center experience. *J Vasc Interv Radiol* 2013; **24**: 698-702 [PMID: 23622041 DOI: 10.1016/j.jvir.2013.02.014]

14 **Hieb RA**, Neisen MJ, Hohenwalter EJ, Molnar JA, Rilling WS. Safety and effectiveness of repeat arterial closure using the AngioSeal device in patients with hepatic malignancy. *J Vasc Interv Radiol* 2008; **19**: 1704-1708 [PMID: 18951046 DOI: 10.1016/j.jvir.2008.09.003]

15 **Schelp V**, Freitag-Wolf S, Hinzmann D, Bramlage P, Frey N, Frank D. Large-scale experience with an anchorless vascular closure device in a real-life clinical setting. *Clin Res Cardiol* 2015; **104**: 145-153 [PMID: 25293675 DOI: 10.1007/s00392-014-0766-3]

16 **Hackl G**, Gary T, Belaj K, Hafner F, Rief P, Deutschmann H, Brodmann M. Exoseal for puncture site closure after antegrade procedures in peripheral arterial disease patients. *Diagn Interv Radiol* 2014; **20**: 426-431 [PMID: 25010369 DOI: 10.5152/dir.2014.14002]

17 **Rimon U**, Khaitovich B, Yakubovich D, Bensaid P, Golan G, Silverberg D. The Use of ExoSeal Vascular Closure Device for Direct Antegrade Superficial Femoral Artery Puncture Site Hemostasis. *Cardiovasc Intervent Radiol* 2015; **38**: 560-564 [PMID: 25209597 DOI: 10.1007/s00270-014-0984-0]

P- Reviewer: Gao BL, Paraskevas KII **S- Editor**: Ji FF
L- Editor: A **E- Editor**: Song H

Published by **Baishideng Publishing Group Inc**
7901 Stoneridge Drive, Suite 501, Pleasanton, CA 94588, USA
Telephone: +1-925-223-8242
Fax: +1-925-223-8243
E-mail: bpgoffice@wjgnet.com
Help Desk: http://www.f6publishing.com/helpdesk
http://www.wjgnet.com

ISSN 1949-8470 (online)

World Journal of *Radiology*

World J Radiol 2018 October 28; 10(10): 116-142

Published by Baishideng Publishing Group Inc

World Journal of Radiology

Contents

Monthly Volume 10 Number 10 October 28, 2018

EDITORIAL

ORIGINAL ARTICLE

Observational Study

ABOUT COVER

Editorial Board Member of *World Journal of Radiology*, Xin-Wu Cui, PhD, Professor, Department of Medical Ultrasound, Tongji Hospital of Tongji Medical College, Huazhong University of Science and Technology, Wuhan 430030, Hubei Province, China

AIM AND SCOPE

World Journal of Radiology (*World J Radiol*, *WJR*, online ISSN 1949-8470, DOI: 10.4329) is a peer-reviewed open access academic journal that aims to guide clinical practice and improve diagnostic and therapeutic skills of clinicians.

WJR covers topics concerning diagnostic radiology, radiation oncology, radiologic physics, neuroradiology, nuclear radiology, pediatric radiology, vascular/interventional radiology, medical imaging achieved by various modalities and related methods analysis. The current columns of *WJR* include editorial, frontier, diagnostic advances, therapeutics advances, field of vision, mini-reviews, review, topic highlight, medical ethics, original articles, case report, clinical case conference (clinicopathological conference), and autobiography.

We encourage authors to submit their manuscripts to *WJR*. We will give priority to manuscripts that are supported by major national and international foundations and those that are of great basic and clinical significance.

INDEXING/ABSTRACTING

World Journal of Radiology is now abstracted and indexed in Emerging Sources Citation Index (Web of Science), PubMed, PubMed Central, China National Knowledge Infrastructure (CNKI), and Superstar Journals Database.

EDITORS FOR THIS ISSUE

Responsible Assistant Editor: *Xiang Li*
Responsible Electronic Editor: *Yun-XiaoJian Wu*
Proofing Editor-in-Chief: *Lian-Sheng Ma*
Responsible Science Editor: *Fang-Fang Ji*
Proofing Editorial Office Director: *Jin-Lei Wang*

NAME OF JOURNAL
World Journal of Radiology

ISSN
ISSN 1949-8470 (online)

LAUNCH DATE
January 31, 2009

FREQUENCY
Monthly

EDITORIAL OFFICE
Jin-Lei Wang, Director
World Journal of Radiology
Baishideng Publishing Group Inc
7901 Stoneridge Drive, Suite 501, Pleasanton, CA 94588, USA
Telephone: +1-925-2238242
Fax: +1-925-2238243
E-mail: editorialoffice@wjgnet.com
Help Desk: http://www.f6publishing.com/helpdesk
http://www.wjgnet.com

PUBLISHER
Baishideng Publishing Group Inc
7901 Stoneridge Drive, Suite 501,
Pleasanton, CA 94588, USA
Telephone: +1-925-2238242
Fax: +1-925-2238243
E-mail: bpgoffice@wjgnet.com
Help Desk: http://www.f6publishing.com/helpdesk
http://www.wjgnet.com

PUBLICATION DATE
October 28, 2018

INSTRUCTIONS TO AUTHORS
http://www.wjgnet.com/bpg/gerinfo/204

ONLINE SUBMISSION
http://www.f6publishing.com

World Journal of Radiology

Submit a Manuscript: http://www.f6publishing.com

World J Radiol 2018 October 28; 10(10): 116-123

DOI: 10.4329/wjr.v10.i10.116

ISSN 1949-8470 (online)

EDITORIAL

Could intravoxel incoherent motion diffusion-weighted magnetic resonance imaging be feasible and beneficial to the evaluation of gastrointestinal tumors histopathology and the therapeutic response?

Hou-Dong Zuo, Xiao-Ming Zhang

Hou-Dong Zuo, Xiao-Ming Zhang, Sichuan Key Laboratory of Medical Imaging, Department of Radiology, Affiliated Hospital of North Sichuan Medical College, Nanchong 637000, Sichuan Province, China

ORCID number: Hou-Dong Zuo (0000-0002-1530-3018); Xiao-Ming Zhang (0000-0001-5327-8506).

Author contributions: All authors contributed to writing the paper and had full control over preparation of manuscript; all authors approved the final draft manuscript.

Conflict-of-interest statement: None.

Manuscript source: Invited manuscript

Correspondence to: Xiao-Ming Zhang, MD, PhD, Professor, Sichuan Key Laboratory of Medical Imaging, Department of Radiology, Affiliated Hospital of North Sichuan Medical College, 63# Wenhua Road, Shunqing District, Nanchong 637000, Sichuan Province, China. cjr.zhxm@vip.163.com
Telephone: +86-817-2262218
Fax: +86-817-2222856

Received: June 23, 2018
Peer-review started: June 24, 2018
First decision: July 19, 2018
Revised: August 2, 2018
Accepted: August 2, 2018
Article in press: August 26, 2018
Published online: October 28, 2018

Abstract

Gastrointestinal tumors (GTs) are among the most common tumors of the digestive system and are among the leading causes of cancer death worldwide. Functional magnetic resonance imaging (MRI) is crucial for assessment of histopathological changes and therapeutic responses of GTs before and after chemotherapy and radiotherapy. A new functional MRI technique, intravoxel incoherent motion (IVIM), could reveal more detailed useful information regarding many diseases. Currently, IVIM is widely used for various tumors because the derived parameters (diffusion coefficient, D; pseudo-perfusion diffusion coefficient, D*; and perfusion fraction, f) are thought to be important surrogate imaging biomarkers for gaining insights into tissue physiology. They can simultaneously reflect the microenvironment, microcirculation in the capillary network (perfusion) and diffusion in tumor tissues without contrast agent intravenous administration. The sensitivity and specificity of these parameters used in the evaluation of GTs vary, the results of IVIM in GTs are discrepant and the variability of IVIM measurements in response to chemotherapy and/or radiotherapy in these studies remains a source of controversy. Therefore, there are questions as to whether IVIM diffusion-weighted MRI is feasible and helpful in the evaluation of GTs, and whether it is worthy of expanded use.

Key words: Intravoxel incoherent motion; Metastasis; Gastric cancer; Colorectal cancer

Core tip: In general, the gastrointestinal tumors (GTs) can be diagnosed by routine computed tomography/magnetic resonance imaging (MRI) and biopsy, but the

intravoxel incoherent motion (IVIM), a new emerging MRI technique, plays a important role in the tumor evaluation before and after surgery, and provides more useful information in tumor properties, stage and chemoradiotherapy (CRT) response. What's more, the quantitative parameters derived from IVIM, including D, D* and f, can gain an insight into tumor tissue physiology changes and simultaneously reflect the microenvironment, microcirculation in the capillary network and diffusion in tumor tissues, thus, new imaging biomarkers for monitoring and evaluating the tumor and the CRT response in GTs.

Zuo HD, Zhang XM. Could intravoxel incoherent motion diffusion-weighted magnetic resonance imaging be feasible and beneficial to the evaluation of gastrointestinal tumors histopathology and the therapeutic response? *World J Radiol* 2018; 10(10): 116-123 Available from: URL: http://www.wjgnet.com/1949-8470/full/v10/i10/116.htm DOI: http://dx.doi.org/10.4329/wjr.v10.i10.116

INTRODUCTION

Gastrointestinal tumors (GTs) are common tumors of the digestive system and are among the leading causes of cancer death worldwide[1]. It was estimated that there will be 176960 new cases and 62880 deaths in United States in 2018[2]. The current therapeutic methods for GTs are surgical resection and chemotherapy and/or chemoradiotherapy (CRT)[3]. However, surgery inflicts substantial trauma to both the body and mind. For advanced stage patients, systemic chemotherapy is the better choice. In this situation, imaging monitoring for the chemotherapeutic response and evaluation is essential. Magnetic resonance imaging (MRI) is a promising modality for tumor detection, diagnosis and evaluation, because of its many advantages, including absence of radiation, multiplane and multiple-parameter imaging. Diffusion weighted imaging (DWI) is an important imaging sequence, based on the Brownian motion of water molecules[4]. The apparent diffusion coefficient (ADC) is sensitive to water molecules in the tissues and reflects the microenvironmental changes of tumors[5]. It is used to differentiate malignant from benign tumors and to evaluate tumor responses after chemotherapy[6,7]. However, ADC values of the tumor are not consistent after treatment because treatment may cause cell swelling or fibrosis that decreases ADC values[8]. Based on the ADC reflection of the tissue diffusion and perfusion, Le Bihan *et al*[9] proposed the intravoxel incoherent motion (IVIM) model to depict perfusion and diffusion effects. It is a new dual exponential imaging mode with multiple b values that is applied in oncologic imaging and related studies[10,11]. With multiple b values, IVIM-DWI quantifies microvascular perfusion effects with smaller b-values (0-200 s/mm^2), and quantifies tissue water molecular diffusion with higher b-values (> 200 s/mm^2). Therefore, IVIM-DWI MRI differentiates microvascular perfusion activity from diffusion. Consequently, the following parameters derived from IVIM DW-MRI can be calculated without the contrast: (Slow) diffusion coefficient (D), pseudo-perfusion (fast) diffusion coefficient (D*) and perfusion fractions, (f)[9,12]. The f and D* parameters have the potential to reflect tumor angiogenesis activity noninvasively and are significantly correlated with microvessel density (MVD) scores[13]. D is generally thought to be the pure diffusion coefficient that depicts extracellular and extravascular tissue water molecular motion[14]. Since IVIM-DWI was introduced, this technique showed great potential in tumor evaluation and grading[15,16]. In recent years, IVIM-DWI has also been used to distinguish benign from malignant tumors[17] and to evaluate chemotherapy therapeutic responses in various tumors[10,18]. However, the application of IVIM-DWI in the gastrointestinal tract tumors may be challenged: first, gastrointestinal tract tumors are relatively small and thin, and imaging may be affected by motion artifact; second, the exact nature of the IVIM signal is not well-understood, and there are heterogeneous patterns of signal attenuation on a voxelwise basis in normal tissues and tumors[19,20]; third, the sensitivity and specificity of these parameters used in the evaluation of GTs vary and the results of the IVIM in the GTs are discrepant[15,18]; finally, the variability of IVIM measurements in response to chemotherapy and/or radiotherapy in these studies remains controversial[10]. Nevertheless, the following findings in GTs may dispel our worries to some extent and may provide hope for the use of IVIM for GTs.

GASTRIC TUMORS

Few studies reported the IVIM-DWI was used in the gastric cancers, because gastric cancer can be diagnosed by contrast computed tomography (CT)/MRI[21] and may be confirmed by endoscopy and biopsy[22]. Nevertheless, IVIM has been used to evaluate the biological behavior of gastric cancer, including cell proliferation, differentiation, invasion, metastasis and survival[23-25], as well as to monitor chemotherapeutic responses[10,26]. D* and f values correlated with MVD in tumor tissues[13], suggesting that D* and f might serve as imaging markers for the noninvasive evaluation of MVD of tumor grading and treatment effectiveness.

In fifty-three patients with gastric cancer reported by Ji *et al*[25], the D value positively correlated with human epidermal growth factor receptor-2 (HER2) scores ($r = 0.481$, $P < 0.001$), and the D values of HER2(+) gastric cancers were substantially higher than those of HER2(-) tumors ($P = 0.007$). With the cut-off value of 1.123×10^{-3} mm^2/s, the D value differentiated HER2(+) from HER2(-) gastric cancers with an area under the curve of 0.762 ($P = 0.011$). Therefore, the IVIM-DWI is feasible for preoperative assessment of HER2 status of gastric cancers and could be a potential biomarker in evaluating HER2 status of gastric cancers.

As for chemotherapeutic responses, IVIM-DWI and derived parameters are useful for predicting the

early efficacy of chemotherapy and are more sensitive imaging biomarkers for gastric cancer. In mouse models bearing two kinds of human gastric cancer xenografts, and in human gastric adenocarcinoma AGS cells models (baseline: day 0), when the mouse received 5-fluorouracil (5-FU) (15 mg/kg)/calcium folinate (5 mg/kg) treatment, mean D values in the treated groups (ΔD%: 17.12% ± 8.20%, 24.16% ± 16.87%, 38.54% ± 19.36%) were significantly higher than those of the controls (ΔD%: -0.13% ± 4.23%, 5.89% ± 4.56%, 5.54% ± 4.44%) at days 1, 3, 5 and 7. The f values were significantly lower than those of the control group (-34.13% ± 16.61% *vs* 1.68% ± 3.40%; -50.64% ± 6.82% *vs* 3.01% ± 6.50%; -49.93% ± 6.05% *vs* 0.97% ± 4.38% and -46.22% ± 7.75% *vs* 8.14% ± 6.75%). The D* values were also significantly lower than those of the control group at all-time points (-32.10% ± 12.22% *vs* 1.85% ± 5.54%; -44.14% ± 14.83% *vs* 2.29% ± 10.38%; -59.06% ± 19.10% *vs* 3.86% ± 5.10% and -47.20% ± 20.48% *vs* 7.13% ± 9.88%). Furthermore, the histopathologic findings showed that D positively correlated with tumor necrosis and cellular apoptosis. Values of f and D* correlated positively with MVD and negatively correlated with cellular apoptosis[26]. In MKN-45 human gastric adenocarcinoma xenograft mouse models, after fluorouracil and calcium folinate treatment, D* values in the treated group decreased markedly (ΔD*% = -30%, -34% and -20%, $P < 0.05$) and f values increased dramatically (Δf % = 93%, 113% and 181%, $P < 0.05$) on days 3, 7 and 14. D* and f values correlated well with histopathological changes demonstrating the reduction of cell proliferation and MVD and the increase in tumor apoptosis and necrosis[10]. These findings indicated that IVIM-DWI and derived parameters could be potentially useful for early evaluation of chemotherapy response and may provide additional pivotal information for the evaluation of therapeutic effect in gastric tumors (Figure 1).

COLORECTAL TUMORS

Many studies focusing on the new techniques for the evaluation of the colorectal tumors have been published[27,28]. A newly proposed modified VARiable PROjection (VARPRO) algorithm specifically tailored for fitting the IVIM to DWI showed better performance than did the Levenberg-Marquardt (LM) algorithm in 64% of cases and stronger "segmented" methods in 100% of cases in locally advanced rectal cancer (LARC). Therefore, VARPRO algorithm is a better fit for the IVIM model than is LARC DWI[28].

In colorectal tumors, IVIM and the parameters were used to evaluate tumor histopathology, Kirsten rat sarcoma viral oncogene homologue (KRAS) mutation status, CRT response, pathological response to neoadjuvant chemotherapy (NACT) and relationships with tumor prognostic markers[11,29-32].

IVIM-DWI has been explored in genomic expression experiments to predict the genotype of rectal cancer (KRAS mutant/wild type)[29]. D values were significantly lower and D* values were significantly higher in the KRAS mutant group than in the KRAS wild-type group. According to the ROC curve, D* values displayed moderate diagnostic significance with the area under curve (AUC) values of 0.710. The cut-off value of D* was 26.58 × 10^{-3} mm^2/s. The findings suggest a relatively high tumor cellularity and hypervascularity[13] caused by mutation of the KRAS oncogene[29].

IVIM parameters correlated with histopathology of rectal tumor tissues. D values were more likely to correlate with cell count, Ki-67 index and total nucleic area. The f values showed good correlation with stained vessel area, total vessel area and vessel count. D* values correlated with mean vessel diameter[33]. These findings confirmed that D reflected cell structure and water motion, and D* and f values reflect the vessel microenvironment[11,13].

In rectal non-mucinous carcinoma and mucinous carcinoma, D, D* and f distinguished rectal tumor tissues from normal rectal wall, reflecting tumor tissue cellularity and microenvironment changes. Furthermore, lower f values were observed in poorly differentiated non-mucinous carcinoma and there were significant positive correlations with differentiation degree. This may be related to the fewer glands and glandular architecture in poorly differentiated tumors. D values were higher and D* values were lower in mucinous carcinomas than in non-mucinous carcinomas. Interestingly, correlation analysis showed D and D* had significant correlations with histological type. D was more likely to be related to cellular microstructure than to tumor cellularity[11], and D* actually reflected blood flow and was affected by flow velocity and vascular geometry[34]. IVIM-DWI–derived parameters were also useful for describing rectal tumor aggressiveness and prognosis[31]. D* and f tended to increase with greater tumor differentiation, and D and D* decreased with advanced tumor stages. The f is the partial volume of the whole capillary vascular fraction[9] and the proportion of the arterial blood is greater than the venous component for f at low b values[35]. This phenomenon is reflected in well-differentiated tumors and poorly differentiated tumors: the capillary vascular network is relatively mature in the former, and there is poor structure of luminal vessels leading to low perfusion of the microcirculation in the latter[31]. This could be confirmed by the correlation between the D*, f and MVD in colorectal tumors[13]. Another important finding is that tumor invading the vascular wall had lower D* than did the group with no vascular wall invasion. This suggested that D* may be related to tumor stage. IVIM parameters were associated with some critical clinical indices, such as carcinoembryonic antigen (CEA) and CA199, which are related with prognosis[31].

Another important application of IVIM-DWI is monitoring the therapeutic response. Sun *et al*[36] reported repeatability coefficients for 3.0T MRI in rectal cancer: correlations for D, f, and D* were 11.1%, 55.4%, and

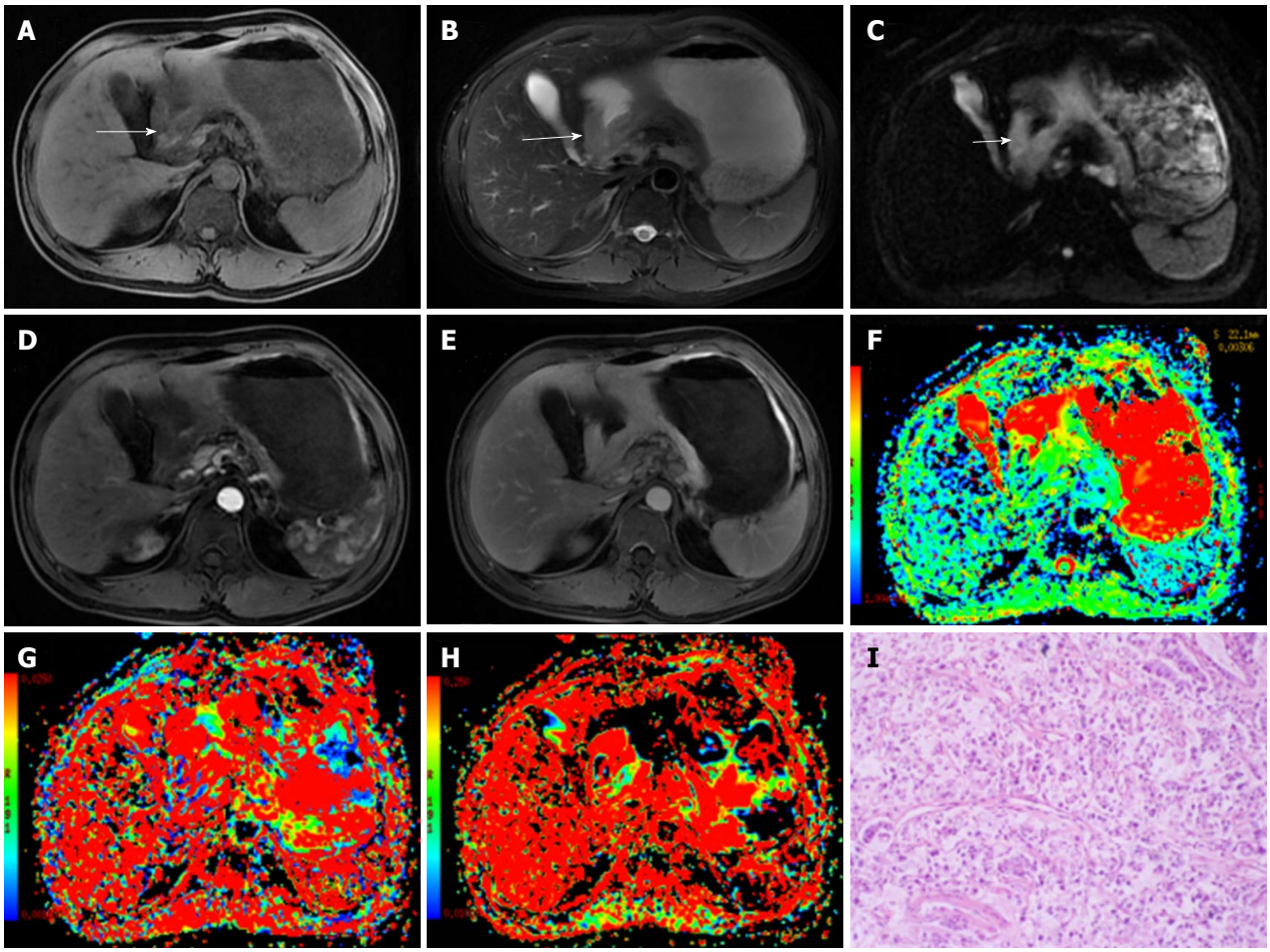

Figure 1 A 48-year-old male diagnosed with malignant gastric carcinoma (signet ring cell cancer). A, B: The lesion has slightly low signal on T1-weighted image (A) and slightly high signal intensity on T2-weighted image (B); C: On DWI, the cancer shows hyperintensity (white arrows); D, E: After contrast agent injection, the lesion shows mild-to-moderate enhancement in arterial and portal venous phases; F-H: The pseudocolor maps of D, D* and f derived from IVIM were displayed, the values of the D, D* and f are 0.92 ± 0.11 × 10^{-3} mm^2/s, 26.75 ± 13.61 × 10^{-3} mm^2/s and 17.24% ± 4.8%, respectively; I: The HE staining of the tissues (100 ×).

40.3%, for intraobserver analysis, respectively, and were 41.6%, 134.0%, and 177.6%, for interobserver analysis, respectively. The test-retest repeatability coefficients for D, f, and D* were 24.5%, 126.3%, and 197.4%, respectively, larger than the intraobserver values. Therefore, D value showed better short-term test-retest reproducibility than did f or D*. The authors concluded that f and D* variance should be understood prudently in longitudinal studies on rectal cancer in which treatment response is monitored[36]. In a report including 25 consecutive patients with advanced rectal carcinoma, D values were highest in the rectum (1.29 × 10^{-3} mm^2/s), then the tumor (0.96 × 10^{-3} mm^2/s) and fat (0.37 × 10^{-3} mm^2/s), and the f values were lower notably in tumor (9.12%) than in fat (16.05%) in patients not receiving neoadjuvant CRT. In patients receiving neoadjuvant CRT, D was higher in tumor (1.10 × 10^{-3} mm^2/s) and the rectum (1.26 × 10^{-3} mm^2/s) than in fat (0.33 × 10^{-3} mm^2/s).

For patients not receiving CRT, the vascular area fraction negatively correlated with D and positively correlated with f. For the rectum, D negatively correlated with cellularity C in patients after CRT[11]. The findings implied that D is related to tumor tissue activity that is frequently strongly vascularized[37] and indicate the heterogeneous tumor tissue microenvironment. Furthermore, the correlation between D and cellularity C reflects the cellular microenvironment in the tumor, adjacent rectal wall and fat that affects water molecule Brownian motion directly[11]. In another report with 31 patients with rectal cancer[18], median D values increased remarkably pre- and post-CRT and were much higher in good responders to CRT. The median D was lower than the median ADC before and after CRT. The relative change was significantly greater in the good responders than in poor responders. Median D values showed higher AUCs than did ADC values for treatment response evaluation. This was because perfusion contributes to ADC in rectal cancer[38] and microcirculation or perfusion effects can be identified by true tissue diffusion with sufficient b value sampling and bi-exponential curve fit analysis with IVIM[9]. Nevertheless, median f and D* values change before and after CRT were not consistent with the degree of tumor response. This may be the limitation of D*, due to its high uncertainty and poor reproducibility[39].

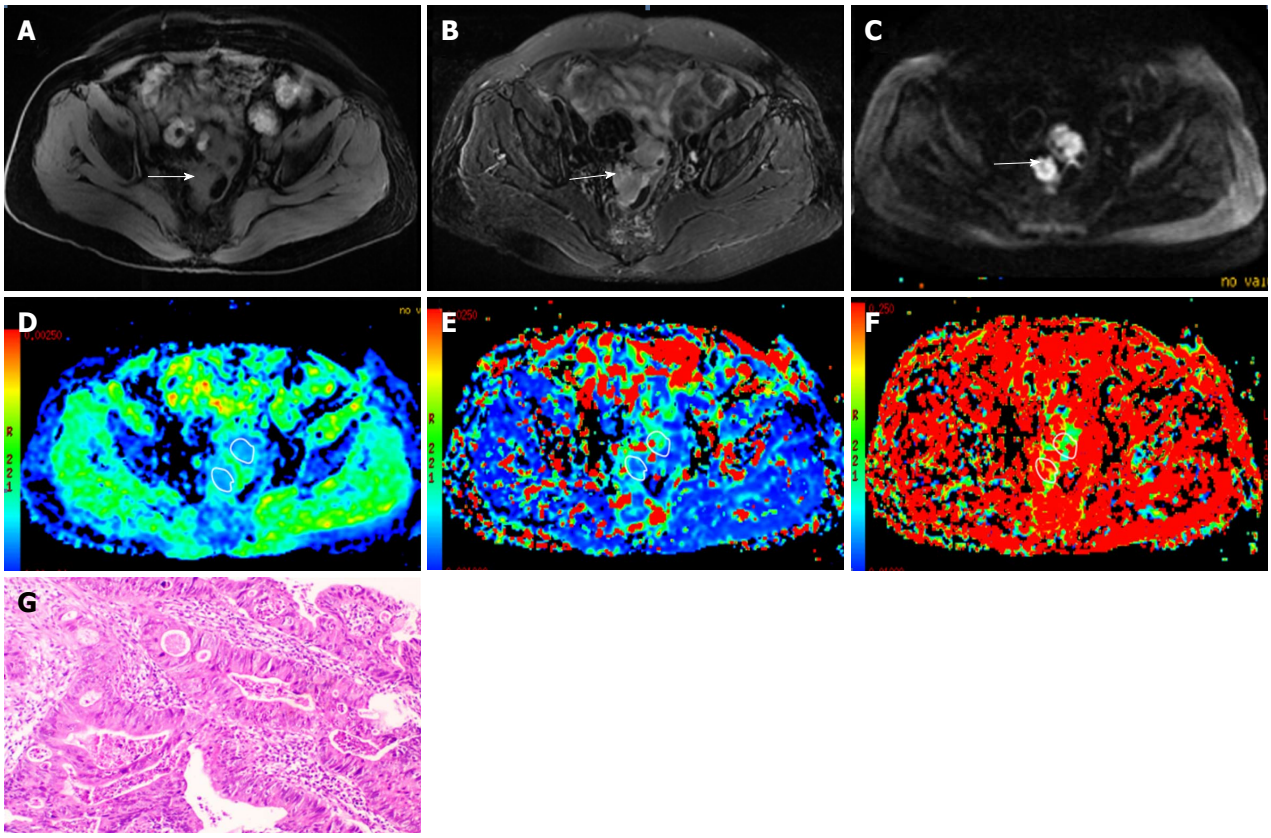

Figure 2 A 67-year-old female diagnosed as rectal cancer (poorly differentiated adenocarcinoma). A, B: The rectal cancer is isointense on T1-weighted image (A) with slightly high signal intensity on T2-weighted image (B); C: On diffusion weighted imaging, the cancer shows hyperintensity (white arrows); D-F: The pseudocolor maps of D, D* and f derived from intravoxel incoherent motion are displayed, the values of the D, D* and f were 1.03 ± 0.12 × 10^{-3}mm^2/s, 50.35 ± 24.96 × 10^{-3}mm^2/s and 20.37% ± 5.9%, respectively; G: HE staining of the tissues (100 ×).

Similar results were reported by Lu *et al*[40] and Xu *et al*[41]. In these two studies, the IVIM-derived D value was a promising tool for predicting and identifying the pCR status prior to therapy. The D percentage changing values after therapy may be helpful and more accurate than traditional DWI for assessing pCR status.

Interestingly, in LARC before and after NACT, high tumor f was found to be useful for predicting better tumor response (tumor regression grade, TRG1-2) and the sensitivity and specificity was 69% and 100%, respectively. More importantly, f combined with tumor volume (fpre/Vpre) offered the best prediction of poor tumor response with a sensitivity of 88% and specificity of 91%, as well as 5-year progression-free survival (PFS) (P < 0.01)[30]. These findings indicated that high f suggests tumor tissues with good vascular structures, and low f indicates poor vascular structures; and high f has been shown to be related to pathologic complete response (pCR)[30] (Figure 2).

METASTATIC LESIONS

The parameters derived from IVIM-DWI are currently used for diagnosis of metastases, intra-tumor changes and therapeutic responses.

In metastasis diagnosis, IVIM-DWI may be useful in differentiating metastatic and non-metastatic lymph nodes in patients with rectal carcinoma. In metastatic lymph nodes, because of the increased water molecular diffusion and microperfusion, reduced cellular density and increased tumor-related blood vessels within the metastatic lymph node, mean D and f values increased significantly, whereas mean D* values were lower than those of normal lymph nodes. The lower D* values may be due to the low blood velocity and MVD of tumor tissues at low b value (< 200 s/mm^2)[34]. Among the parameters, D values and D values combined with the short-axis diameter had the highest AUC, and D* values had the lowest[34,42], suggesting that D is more sensitive and has the highest diagnostic efficacy in distinguishing normal from lymphatic metastasis[15].

In assessment of therapeutic responses of metastatic lesions, parameters derived from IVIM-DWI changes are thought to be surrogate markers of tumor therapeutic responses. IVIM-DWI is usually sensitive to tumor necrosis after chemotherapy, because ADC in CRC metastases change along with specific increases in free molecular diffusion D that correlates with tumor necrosis[43]. In another report, distant metastasis lesions had higher D* and relative perfusion (fD*) values, suggesting that IVIM parameters might reflect different clinical and histopathological features in rectal cancer[33], although there were no significant differences between other IVIM parameters.

In patients with liver metastases from CRC treated with cytotoxic chemotherapy reported by Kim *et al*[44], after the first cycle of chemotherapy, ADC values increased (1191.9 ± 232.2 × 10^{-3} mm^2/s *vs* 1263.5 ± 266.4 × 10^{-3} mm^2/s; $P = 0.012$) and D (1085.9 ± 232.9 × 10^{-3} mm^2/s *vs* 1173.5 ± 248.9 × 10^{-3} mm^2/s; $P = 0.012$), while f values decreased (173.7% ± 39.8% *vs* 133.5% ± 28.3%; $P = 0.017$) in eight responding patients. In 24 responding metastatic lesions and 12 non-responding lesions after neoadjuvant FOLFIRI (5-FU, leucovorin, irinotecan) plus bevacizumab therapy, f values showed statistically significant differences between responder and non-responder lesions, and the f variation sensitivity and specificity were 62% and 93%, respectively[45]. All findings indicated that IVIM-DWI and the parameters were useful for the prediction of therapeutic response after chemotherapy for metastases in CRC.

GASTROINTESTINAL STROMAL TUMORS

IVIM-DWI in gastrointestinal stromal tumors (GISTs) was also investigated to evaluate therapeutic responses to treatment with imatinib. In mice with xenografts bearing GIST-T1 cells, ADC values increased in the treated group. D* values in the treated group decreased significantly (ΔD* = -41%, -49%, and -49%), and f increased significantly (Δf = 79%, 82% and 110%) on days 1, 3 and 7 after treatment. D* and f did not show significant changes in the control group. The parameters from IVIM-DWI showed good correlation with histopathology with a decrease in cell proliferation and MVD and an increase in apoptosis and tumor necrosis in the treated group[46]. Therefore, IVIM-DWI may serve as an effective imaging biomarker to assess GIST response to treatment.

CONCLUSION

It is a great challenge to evaluate and predict histopathological and therapeutic responses after GTs chemotherapy. IVIM, a new sequence derived from DWI, is a potentially useful tool for evaluation of GTs. The derived parameters D, D* and f reflect the microenvironment, microcirculation and blood flow changes in tumor tissues[34], endowing them with the ability to predict tumor pathology and to monitor therapeutic responses. Therefore, the IVIM could offer a potentially accurate evaluation of chemotherapy efficacy, possibly facilitating individualized treatment planning in patients with GTs.

Encouragingly, based on the IVIM technique, more precise and effective parameters emerged for GTs, including α. The parameter α, derived from stretched-exponential model, appears to be more suitable for colorectal tumors in evaluating pCR after CRT because of the superior diagnostic performance of D, D* and f[47] and their better reliability than ADC for assessing pCR after CRT.

In conclusion, with the technical assistance of IVIM, IVIM-DWI will be considerably more useful in evaluating GTs, reflecting histopathological changes and therapeutic responses before and after chemotherapy. Much deeper investigations and applications of IVIM-DWI in GTs are on the horizon.

REFERENCES

1 **Torre LA**, Bray F, Siegel RL, Ferlay J, Lortet-Tieulent J, Jemal A. Global cancer statistics, 2012. *CA Cancer J Clin* 2015; **65**: 87-108 [PMID: 25651787 DOI: 10.3322/caac.21262]

2 **Siegel RL**, Miller KD, Jemal A. Cancer statistics, 2018. *CA Cancer J Clin* 2018; **68**: 7-30 [PMID: 29313949 DOI: 10.3322/caac.21442]

3 **Jang SH**, Jung YJ, Kim MG, Kwon SJ. The Prognostic Significance of Compliance with Postoperative Adjuvant Chemotherapy in Patients with Stage III Gastric Cancer: an Observational Study. *J Gastric Cancer* 2018; **18**: 48-57 [PMID: 29629220 DOI: 10.5230/jgc.2018.18.e4]

4 **Szafer A**, Zhong J, Anderson AW, Gore JC. Diffusion-weighted imaging in tissues: theoretical models. *NMR Biomed* 1995; **8**: 289-296 [PMID: 8739267 DOI: 10.1002/nbm.1940080704]

5 **Shinya S**, Sasaki T, Nakagawa Y, Guiquing Z, Yamamoto F, Yamashita Y. The usefulness of diffusion-weighted imaging (DWI) for the detection of gastric cancer. *Hepatogastroenterology* 2007; **54**: 1378-1381 [PMID: 17708258]

6 **Das A**, Bhalla AS, Sharma R, Kumar A, Thakar A, Vishnubhatla SM, Sharma MC, Sharma SC. Can Diffusion Weighted Imaging Aid in Differentiating Benign from Malignant Sinonasal Masses?: A Useful Adjunct. *Pol J Radiol* 2017; **82**: 345-355 [PMID: 28740564 DOI: 10.12659/PJR.900633]

7 **Hu F**, Tang W, Sun Y, Wan D, Cai S, Zhang Z, Grimm R, Yan X, Fu C, Tong T, Peng W. The value of diffusion kurtosis imaging in assessing pathological complete response to neoadjuvant chemoradiation therapy in rectal cancer: a comparison with conventional diffusion-weighted imaging. *Oncotarget* 2017; **8**: 75597-75606 [PMID: 29088894 DOI: 10.18632/oncotarget.17491]

8 **Thoeny HC**, De Keyzer F, Vandecaveye V, Chen F, Sun X, Bosmans H, Hermans R, Verbeken EK, Boesch C, Marchal G, Landuyt W, Ni Y. Effect of vascular targeting agent in rat tumor model: dynamic contrast-enhanced versus diffusion-weighted MR imaging. *Radiology* 2005; **237**: 492-499 [PMID: 16192323 DOI: 10.1148/radiol.2372041638]

9 **Le Bihan D**, Breton E, Lallemand D, Aubin ML, Vignaud J, Laval-Jeantet M. Separation of diffusion and perfusion in intravoxel incoherent motion MR imaging. *Radiology* 1988; **168**: 497-505 [PMID: 3393671 DOI: 10.1148/radiology.168.2.3393671]

10 **Cheng J**, Wang Y, Zhang CF, Wang H, Wu WZ, Pan F, Hong N, Deng J. Chemotherapy response evaluation in a mouse model of gastric cancer using intravoxel incoherent motion diffusion-weighted MRI and histopathology. *World J Gastroenterol* 2017; **23**: 1990-2001 [PMID: 28373765 DOI: 10.3748/wjg.v23.i11.1990]

11 **Bäuerle T**, Seyler L, Münter M, Jensen A, Brand K, Fritzsche KH, Kopp-Schneider A, Schüssler M, Schlemmer HP, Stieltjes B, Ganten M. Diffusion-weighted imaging in rectal carcinoma patients without and after chemoradiotherapy: a comparative study with histology. *Eur J Radiol* 2013; **82**: 444-452 [PMID: 23219191 DOI: 10.1016/j.ejrad.2012.10.012]

12 **Le Bihan DJ**. Differentiation of benign versus pathologic compression fractures with diffusion-weighted MR imaging: a closer step toward the "holy grail" of tissue characterization? *Radiology* 1998; **207**: 305-307 [PMID: 9577472 DOI: 10.1148/radiology.207.2.9577472]

13 **Lee HJ**, Rha SY, Chung YE, Shim HS, Kim YJ, Hur J, Hong YJ, Choi BW. Tumor perfusion-related parameter of diffusion-weighted magnetic resonance imaging: correlation with histological microvessel density. *Magn Reson Med* 2014; **71**: 1554-1558 [PMID: 23798038 DOI: 10.1002/mrm.24810]

14 **Jain RK**, Duda DG, Willett CG, Sahani DV, Zhu AX, Loeffler JS,

Batchelor TT, Sorensen AG. Biomarkers of response and resistance to antiangiogenic therapy. *Nat Rev Clin Oncol* 2009; **6**: 327-338 [PMID: 19483739 DOI: 10.1038/nrclinonc.2009.63]

15 **Qiu L**, Liu XL, Liu SR, Weng ZP, Chen XQ, Feng YZ, Cai XR, Guo CY. Role of quantitative intravoxel incoherent motion parameters in the preoperative diagnosis of nodal metastasis in patients with rectal carcinoma. *J Magn Reson Imaging* 2016; **44**: 1031-1039 [PMID: 27019309 DOI: 10.1002/jmri.25250]

16 **Zhu SC**, Liu YH, Wei Y, Li LL, Dou SW, Sun TY, Shi DP. Intravoxel incoherent motion diffusion-weighted magnetic resonance imaging for predicting histological grade of hepatocellular carcinoma: Comparison with conventional diffusion-weighted imaging. *World J Gastroenterol* 2018; **24**: 929-940 [PMID: 29491686 DOI: 10.3748/wjg.v24.i8.929]

17 **Iima M**, Kataoka M, Kanao S, Onishi N, Kawai M, Ohashi A, Sakaguchi R, Toi M, Togashi K. Intravoxel Incoherent Motion and Quantitative Non-Gaussian Diffusion MR Imaging: Evaluation of the Diagnostic and Prognostic Value of Several Markers of Malignant and Benign Breast Lesions. *Radiology* 2018; **287**: 432-441 [PMID: 29095673 DOI: 10.1148/radiol.2017162853]

18 **Nougaret S**, Vargas HA, Lakhman Y, Sudre R, Do RK, Bibeau F, Azria D, Assenat E, Molinari N, Pierredon MA, Rouanet P, Guiu B. Intravoxel Incoherent Motion-derived Histogram Metrics for Assessment of Response after Combined Chemotherapy and Radiation Therapy in Rectal Cancer: Initial Experience and Comparison between Single-Section and Volumetric Analyses. *Radiology* 2016; **280**: 446-454 [PMID: 26919562 DOI: 10.1148/radiol.2016150702]

19 **Federau C**. Intravoxel incoherent motion MRI as a means to measure in vivo perfusion: A review of the evidence. *NMR Biomed* 2017; **30** [PMID: 28885745 DOI: 10.1002/nbm.3780]

20 **Koh DM**, Collins DJ, Orton MR. Intravoxel incoherent motion in body diffusion-weighted MRI: reality and challenges. *AJR Am J Roentgenol* 2011; **196**: 1351-1361 [PMID: 21606299 DOI: 10.2214/AJR.10.5515]

21 **Ma L**, Xu X, Zhang M, Zheng S, Zhang B, Zhang W, Wang P. Dynamic contrast-enhanced MRI of gastric cancer: Correlations of the pharmacokinetic parameters with histological type, Lauren classification, and angiogenesis. *Magn Reson Imaging* 2017; **37**: 27-32 [PMID: 27840273 DOI: 10.1016/j.mri.2016.11.004]

22 **Di L**, Wu H, Zhu R, Li Y, Wu X, Xie R, Li H, Wang H, Zhang H, Xiao H, Chen H, Zhen H, Zhao K, Yang X, Xie M, Tuo B. Multi-disciplinary team for early gastric cancer diagnosis improves the detection rate of early gastric cancer. *BMC Gastroenterol* 2017; **17**: 147 [PMID: 29212444 DOI: 10.1186/s12876-017-0711-9]

23 **Hou F**, Shi DB, Chen YQ, Gao P. Human Epidermal Growth Factor Receptor-2 Promotes Invasion and Metastasis in Gastric Cancer by Activating Mitogen-activated Protein Kinase Signaling. *Appl Immunohistochem Mol Morphol* 2018 [PMID: 29734245 DOI: 10.1097/PAI.0000000000000672]

24 **Hwang GY**, Baek DW, Cho HJ, Lee SJ, Chae YS, Kang BW, Lee IH, Kim JG, Seo AN, Bae HI, Park KB, Park JY, Kwon OK, Lee SS, Chung HY. Elevated Neutrophil-to-Lymphocyte Ratio Predicts Survival in Patients with Advanced Gastric Cancer Treated with Trastuzumab Combination Chemotherapy. *Anticancer Res* 2018; **38**: 3151-3156 [PMID: 29715156 DOI: 10.21873/anticanres.12578]

25 **Ji C**, Zhang Q, Guan W, Guo T, Chen L, Liu S, He J, Zhou Z. Role of intravoxel incoherent motion MR imaging in preoperative assessing HER2 status of gastric cancers. *Oncotarget* 2017; **8**: 49293-49302 [PMID: 28514733 DOI: 10.18632/oncotarget.17570]

26 **Song XL**, Kang HK, Jeong GW, Ahn KY, Jeong YY, Kang YJ, Cho HJ, Moon CM. Intravoxel incoherent motion diffusion-weighted imaging for monitoring chemotherapeutic efficacy in gastric cancer. *World J Gastroenterol* 2016; **22**: 5520-5531 [PMID: 27350730 DOI: 10.3748/wjg.v22.i24.5520]

27 **Zhang G**, Wang S, Wen D, Zhang J, Wei X, Ma W, Zhao W, Wang M, Wu G, Zhang J. Comparison of non-Gaussian and Gaussian diffusion models of diffusion weighted imaging of rectal cancer at 3.0 T MRI. *Sci Rep* 2016; **6**: 38782 [PMID: 27934928 DOI: 10.1038/srep38782]

28 **Fusco R**, Sansone M, Petrillo A. A comparison of fitting algorithms for diffusion-weighted MRI data analysis using an intravoxel incoherent motion model. *MAGMA* 2017; **30**: 113-120 [PMID: 27670762 DOI: 10.1007/s10334-016-0591-y]

29 **Xu Y**, Xu Q, Sun H, Liu T, Shi K, Wang W. Could IVIM and ADC help in predicting the KRAS status in patients with rectal cancer? *Eur Radiol* 2018; **28**: 3059-3065 [PMID: 29450716 DOI: 10.1007/s00330-018-5329-y]

30 **Bakke KM**, Hole KH, Dueland S, Grøholt KK, Flatmark K, Ree AH, Seierstad T, Redalen KR. Diffusion-weighted magnetic resonance imaging of rectal cancer: tumour volume and perfusion fraction predict chemoradiotherapy response and survival. *Acta Oncol* 2017; **56**: 813-818 [PMID: 28464745 DOI: 10.1080/0284186X.2017.1287951]

31 **Sun H**, Xu Y, Song A, Shi K, Wang W. Intravoxel Incoherent Motion MRI of Rectal Cancer: Correlation of Diffusion and Perfusion Characteristics With Prognostic Tumor Markers. *AJR Am J Roentgenol* 2018; **210**: W139-W147 [PMID: 29446674 DOI: 10.2214/AJR.17.18342]

32 **Itoh N**, Ohta K, Ohta M, Kawasaki T, Yamashina I. The nucleotide sequence of a gene for a putative ribosomal protein S31 of Drosophila. *Nucleic Acids Res* 1989; **17**: 2121 [PMID: 2928115 DOI: 10.1093/nar/17.5.2121]

33 **Surov A**, Meyer HJ, Höhn AK, Behrmann C, Wienke A, Spielmann RP, Garnov N. Correlations between intravoxel incoherent motion (IVIM) parameters and histological findings in rectal cancer: preliminary results. *Oncotarget* 2017; **8**: 21974-21983 [PMID: 28423540 DOI: 10.18632/oncotarget.15753]

34 **Lu B**, Yang X, Xiao X, Chen Y, Yan X, Yu S. Intravoxel Incoherent Motion Diffusion-Weighted Imaging of Primary Rectal Carcinoma: Correlation with Histopathology. *Med Sci Monit* 2018; **24**: 2429-2436 [PMID: 29679528 DOI: 10.12659/MSM.908574]

35 **Duong TQ**, Kim SG. In vivo MR measurements of regional arterial and venous blood volume fractions in intact rat brain. *Magn Reson Med* 2000; **43**: 393-402 [PMID: 10725882 DOI: 10.1002/(SICI)1522-2594(200003)43:3<393::AID-MRM11>3.0.CO;2-K]

36 **Sun H**, Xu Y, Xu Q, Shi K, Wang W. Rectal cancer: Short-term reproducibility of intravoxel incoherent motion parameters in 3.0T magnetic resonance imaging. *Medicine* (Baltimore) 2017; **96**: e6866 [PMID: 28489784 DOI: 10.1097/MD.0000000000006866]

37 **Baeriswyl V**, Christofori G. The angiogenic switch in carcinogenesis. *Semin Cancer Biol* 2009; **19**: 329-337 [PMID: 19482086 DOI: 10.1016/j.semcancer.2009.05.003]

38 **Woo S**, Lee JM, Yoon JH, Joo I, Han JK, Choi BI. Intravoxel incoherent motion diffusion-weighted MR imaging of hepatocellular carcinoma: correlation with enhancement degree and histologic grade. *Radiology* 2014; **270**: 758-767 [PMID: 24475811 DOI: 10.1148/radiol.13130444]

39 **Kakite S**, Dyvorne H, Besa C, Cooper N, Facciuto M, Donnerhack C, Taouli B. Hepatocellular carcinoma: short-term reproducibility of apparent diffusion coefficient and intravoxel incoherent motion parameters at 3.0T. *J Magn Reson Imaging* 2015; **41**: 149-156 [PMID: 24415565 DOI: 10.1002/jmri.24538]

40 **Lu W**, Jing H, Ju-Mei Z, Shao-Lin N, Fang C, Xiao-Ping Y, Qiang L, Biao Z, Su-Yu Z, Ying H. Intravoxel incoherent motion diffusion-weighted imaging for discriminating the pathological response to neoadjuvant chemoradiotherapy in locally advanced rectal cancer. *Sci Rep* 2017; **7**: 8496 [PMID: 28819296 DOI: 10.1038/s41598-017-09227-9]

41 **Xu Q**, Xu Y, Sun H, Chan Q, Shi K, Song A, Wang W. Quantitative intravoxel incoherent motion parameters derived from whole-tumor volume for assessing pathological complete response to neoadjuvant chemotherapy in locally advanced rectal cancer. *J Magn Reson Imaging* 2018; **48**: 248-258 [PMID: 29281151 DOI: 10.1002/jmri.25931]

42 **Yu XP**, Wen L, Hou J, Bi F, Hu P, Wang H, Wang W. Discrimination between Metastatic and Nonmetastatic Mesorectal Lymph Nodes in Rectal Cancer Using Intravoxel Incoherent Motion Diffusion-weighted Magnetic Resonance Imaging. *Acad Radiol* 2016; **23**: 479-485 [PMID: 26853971 DOI: 10.1016/j.acra.2015.12.013]

43 **Chiaradia M**, Baranes L, Van Nhieu JT, Vignaud A, Laurent A, Decaens T, Charles-Nelson A, Brugières P, Katsahian S, Djabbari M, Deux JF, Sobhani I, Karoui M, Rahmouni A, Luciani A. Intravoxel incoherent motion (IVIM) MR imaging of colorectal liver metastases: are we only looking at tumor necrosis? *J Magn Reson Imaging* 2014; **39**: 317-325 [PMID: 23723012 DOI: 10.1002/jmri.24172]

44 **Kim JH**, Joo I, Kim TY, Han SW, Kim YJ, Lee JM, Han JK. Diffusion-Related MRI Parameters for Assessing Early Treatment Response of Liver Metastases to Cytotoxic Therapy in Colorectal Cancer. *AJR Am J Roentgenol* 2016; **207**: W26-W32 [PMID: 27303858 DOI: 10.2214/AJR.15.15683]

45 **Granata V**, Fusco R, Catalano O, Filice S, Amato DM, Nasti G, Avallone A, Izzo F, Petrillo A. Early Assessment of Colorectal Cancer Patients with Liver Metastases Treated with Antiangiogenic Drugs: The Role of Intravoxel Incoherent Motion in Diffusion-Weighted Imaging. *PLoS One* 2015; **10**: e0142876 [PMID: 26566221 DOI: 10.1371/journal.pone.0142876]

46 **Pan F**, Den J, Zhang C, Wang H, Cheng J, Wu W, Hong N, Wang Y. The Therapeutic Response of Gastrointestinal Stromal Tumors to Imatinib Treatment Assessed by Intravoxel Incoherent Motion Diffusion-Weighted Magnetic Resonance Imaging with Histopathological Correlation. *PLoS One* 2016; **11**: e0167720 [PMID: 27911930 DOI: 10.1371/journal.pone.0167720]

47 **Zhu HB**, Zhang XY, Zhou XH, Li XT, Liu YL, Wang S, Sun YS. Assessment of pathological complete response to preoperative chemoradiotherapy by means of multiple mathematical models of diffusion-weighted MRI in locally advanced rectal cancer: A prospective single-center study. *J Magn Reson Imaging* 2017; **46**: 175-183 [PMID: 27981667 DOI: 10.1002/jmri.25567]

P- Reviewer: Cao D, Ciocalteu A, Hori T, Mastoraki A
S- Editor: Ji FF **L- Editor**: A **E- Editor**: Wu YXJ

World Journal of Radiology

Submit a Manuscript: http://www.f6publishing.com

World J Radiol 2018 October 28; 10(10): 124-134

DOI: 10.4329/wjr.v10.i10.124

ISSN 1949-8470 (online)

ORIGINAL ARTICLE

Observational Study

Reproducibility of thrombus volume quantification in multicenter computed tomography pulmonary angiography studies

Audrey E Kaufman, Alison N Pruzan, Ching Hsu, Sarayu Ramachandran, Adam Jacobi, Indravadan Patel, Lee Schwocho, Michele F Mercuri, Zahi A Fayad, Venkatesh Mani

Audrey E Kaufman, Alison N Pruzan, Sarayu Ramachandran, Adam Jacobi, Indravadan Patel, Lee Schwocho, Michele F Mercuri, Zahi A Fayad, Venkatesh Mani, Department of Radiology, Icahn School of Medicine at Mount Sinai, New York, NY 10029, United States

Audrey E Kaufman, Alison N Pruzan, Sarayu Ramachandran, Zahi A Fayad, Venkatesh Mani, Translational and Molecular Imaging Institute, Icahn School of Medicine at Mount Sinai, Hess Center for Science and Medicine, New York, NY 10029, United States

Ching Hsu, Indravadan Patel, Lee Schwocho, Michele F Mercuri, Daiichi Sankyo Inc., Basking Ridge, NJ 07920, United States

ORCID number: Audrey E Kaufman (0000-0002-9221-9004); Alison N Pruzan (0000-0002-3054-6341); Ching Hsu (0000-0003-0616-2468); Sarayu Ramachandran (0000-0002-9917-5876); Adam Jacobi (0000-0002-9057-9129); Indravadan Patel (0000-0001-6138-0850); Lee Schwocho (0000-0002-3030-799X); Michele F Mercuri (0000-0003-2266-4812); Zahi A Fayad (0000-0002-3439-7347); Venkatesh Mani (0000-0002-0432-2918).

Author contributions: All authors designed the experiment; Kaufman AE, Pruzan AN, Ramachandran S, Mani V performed the experiment; Kaufman AE and Pruzan AN performed the image analysis; Hsu C, Pruzan AN and Mani V performed statistical analysis; Kaufman AE and Mani V wrote the draft of the manuscript; all authors critically reviewed the manuscript.

Institutional review board statement: This study was submitted to the Institutional Review Board (IRB) of the Icahn School of Medicine at Mount Sinai but was deemed that no IRB approval was necessary for conduct of this study [See Determination regarding engagement in human research letter from the program for protection of research subjects (PPHS) office IRB].

Informed consent statement: Waiver of informed consent was obtained from the Institutional Review Board as only deidentified data was used in this study. The images analyzed for this study were anonymized and devoid of any Protected Health Information.

Conflict-of-interest statement: Ching Hsu, Indravadan Patel, Lee Schwocho, Michele F Mercuri are employees of Daiichi Sankyo Inc. All other authors have no conflicts to disclose.

Data sharing statement: Once published and after appropriate safeguard to ensure that the data is devoid of any identifiers, the data used for the analysis for this study will be shared on the Mount Sinai data sharing portal according to Institutional guidelines.

STROBE Statement: The authors have read the STROBE Statement - checklist of items, and the manuscript was prepared and revised according to the STROBE Statement - checklist of items.

Manuscript source: Invited Manuscript

Correspondence to: Venkatesh Mani, PhD, Associate Professor, Department of Radiology, Icahn School of Medicine at Mount Sinai, 1470 Madison Avenue, New York, NY 10029, United States. venkatesh.mani@mountsinai.org
Telephone: +1-212-8248454
Fax: +1-646-5379589

Received: June 1, 2018
Peer-review started: June 1, 2018
First decision: July 23, 2018
Revised: July 27, 2018
Accepted: August 4, 2018
Article in press: August 4, 2018

Published online: October 28, 2018

Abstract

AIM

To evaluate reproducibility of pulmonary embolism (PE) clot volume quantification using computed tomography pulmonary angiogram (CTPA) in a multicenter setting.

METHODS

This study was performed using anonymized data in conformance with HIPAA and IRB Regulations (March 2015-November 2016). Anonymized CTPA data was acquired from 23 scanners from 18 imaging centers using each site's standard PE protocol. Two independent analysts measured PE volumes using a semi-automated region-growing algorithm on an FDA-approved image analysis platform. Total thrombus volume (TTV) was calculated per patient as the primary endpoint. Secondary endpoints were individual thrombus volume (ITV), Qanadli score and modified Qanadli score per patient. Inter- and intra-observer reproducibility were assessed using intra-class correlation coefficient (ICC) and Bland-Altman analysis.

RESULTS

Analyst 1 found 72 emboli in the 23 patients with a mean number of emboli of 3.13 per patient with a range of 0-11 emboli per patient. The clot volumes ranged from 0.0041 - 47.34 cm^3 (mean +/- SD, 5.93 +/- 10.15cm^3). On the second read, analyst 1 found the same number and distribution of emboli with a range of volumes for read 2 from 0.0041 – 45.52 cm^3 (mean +/- SD, 5.42 +/- 9.53cm^3). Analyst 2 found 73 emboli in the 23 patients with a mean number of emboli of 3.17 per patient with a range of 0-11 emboli per patient. The clot volumes ranged from 0.00459-46.29 cm^3 (mean +/- SD, 5.91 +/- 10.06 cm^3). Inter- and intra-observer variability measurements indicated excellent reproducibility of the semi-automated method for quantifying PE volume burden. ICC for all endpoints was greater than 0.95 for inter- and intra-observer analysis. Bland-Altman analysis indicated no significant biases.

CONCLUSION

Semi-automated region growing algorithm for quantifying PE is reproducible using data from multiple scanners and is a suitable method for image analysis in multicenter clinical trials.

Key words: Pulmonary embolism; Arteries; Computed tomography angiography; Computer-assisted image analysis; Thrombolytic therapy

Core tip: Blood clots that occur in deep leg veins can break away and cause the serious complication of clots (then termed emboli) lodged in the lungs. Measuring the volume of the emboli with a semi-automated region growing software program using computed tomography pulmonary angiogram data can be helpful to evaluate treatment efficacy in clinical drug trials. This study demonstrates the technique to be reproducible both between image analysts and when repeated by the same image analyst when the data is obtained in a multicenter setting.

Kaufman AE, Pruzan AN, Hsu C, Ramachandran S, Jacobi A, Patel I, Schwocho L, Mercuri MF, Fayad ZA, Mani V. Reproducibility of thrombus volume quantification in multicenter computed tomography pulmonary angiography studies. *World J Radiol* 2018; 10(10): 124-134 Available from: URL: http://www.wjgnet.com/1949-8470/full/v10/i10/124.htm DOI: http://dx.doi.org/10.4329/wjr.v10.i10.124

INTRODUCTION

Venous thromboembolism (VTE) represents the combined disease states of deep venous thrombosis (DVT) and pulmonary embolism (PE). PE is the most significant sequela of DVT, occurring in more than a third of DVT patients[1]. In the United States, there is a combined average annual incidence of over 275000 new cases of VTE among whites of predominantly European origin and African-Americans[2]. A retrospective study demonstrated an incidence of 117 VTE cases per 100000 in a demographically white population[3]. The same study showed VTE to be predominantly a disease of older age, with males slightly more affected than females, whereas in the younger population the incidence is higher in females during child-bearing age[3].

PE has a high mortality rate[4,5]. The two week and three month post diagnosis all-cause mortality rate was found to be 11.4% and 17.4% respectively[6]. Risk of mortality in PE rests upon multiple factors including clinical findings of shock and hypotension and elevated markers of right ventricular dysfunction and myocardial injury[7,8]. Clot burden alone is not a principal marker in clinical risk stratification, however computed tomography pulmonary angiogram (CTPA), is a commonly used diagnostic tool that has been shown to help with risk stratification of PE[9-11]. Objectively measuring thrombus volume from CTPA data can be particularly useful to evaluate the efficacy of treatments for PE[12]. Indeed, clinical pharmaceutical trials of drugs such as thrombolytics rely upon objective measures including total thrombus volume (TTV), the sum of volumes of all PE present in an individual, to assess drug effectiveness and potency and to help determine the optimal duration of therapy[13]. This study is not performed to assess CTPA measured clot volumes as a clinical prognostic indicator. Rather, the goal of this study is to evaluate the reproducibility of a quantifiable metric; the TTV in PE, especially as new drugs are being developed that

aim to eliminate and reduce clot size. Thrombus volume measured by contrast enhanced CTPA could potentially serve as an imaging biomarker for evaluating burden and/or severity of PE in clinical trials. One such current study is the DS-1040b, a Randomized Study to Assess the Safety, Pharmacokinetics/Dynamics of DS-1040b in Subjects With Acute Submassive Pulmonary Embolism, NCT02923115 (www.clinicaltrials.gov).

Quantifying clot burden with CTPA requires segmentation of emboli from non-thrombotic contrast-enhanced blood within the pulmonary vasculature and computation of clot volume. Semi-automated region growing algorithms can be used for this purpose[12]. The inter and intra-observer reliability of this technique has been tested in data obtained from a single center using one fixed CTPA imaging protocol[12]. Accuracy of this approach has also been established by the relative volume measurement error[12]. However, these types of studies have not been implemented in a multicenter setting. This is a retrospective study performed on sample data obtained from subjects undergoing CT pulmonary angiography for suspected PE. Images were obtained from multiple centers as part of a study qualification visit for a multicenter drug trial evaluating a new thrombolytic agent and were from cases of suspected PE at the site obtained in the week prior to the qualification visit. Therefore, in addition to the stated study goal of evaluating the quantifiable metric of TTV in PE, the broader purpose of this study is to evaluate the hypothesis that repeatable volume quantification can be made using a semi-automated region growing algorithm on *in vivo* PE data obtained in a multicenter setting with inherent variability of CT scanners and acquisition and reconstruction parameters using TTV as a primary endpoint and individual thrombus volume (ITV), Qanadli score and modified Qanadli score as secondary endpoints.

MATERIALS AND METHODS

This study was performed using anonymized data in conformance with HIPAA and IRB Regulations (March 2015-November 2016).

CTPA data was acquired from 23 scanners from 18 different centers using the standard image acquisition for PE at the site. Table 1 describes the image acquisition and reconstruction parameters and contrast agent use protocol at each center. The data was completely anonymized. Patient demographic data was not included in the study as the cases obtained from the multicenter sites were requested as part of our core lab qualification assessment for participation in a clinical pharmaceutical trial, and as such, a deidentified random sample case(s) from each site was requested. From image metadata, limited information on gender and/or age on less than half of the cases were determined. No other demographic information was available to the authors. Of the 23 patients studied, seven were known to be male. Where the male's age was identified the following ages were known: 72, 60, 82, 30 and 73. Two patients were known to be female where their ages were known to be 21 and 77. There were also two patients of unknown gender that were known to be 72 and 81 years old.

Two experienced image analysts performed the *in vivo* study. AEK (a board-certified diagnostic radiologist with six years clinical experience) and ANP (Bachelor of Science with two years vascular imaging experience under the supervision of board certified radiologists (AJ, AEK) assessed each patient for the presence of emboli within the pulmonary arterial tree. The extent of the analysis was from the main pulmonary artery up to and including emboli within segmental arteries bilaterally. See Figure 1 for a schematic of the segmental distribution of the pulmonary arteries. An embolus appeared as a filling defect of soft tissue density within the otherwise contrast enhanced pulmonary arterial tree. An endoluminal filling defect was deemed a single embolus if it was contiguous and demonstrated no intervening contrast material fully separating it from adjacent clot. Embolus volume was the measured parameter and the endpoints were TTV and ITV in each patient and both the Qanadli and modified Qanadli score in all patients. Each separate embolus was analyzed using a semi-automated region growing algorithm implemented in the FDA approved Siemens *syngo*.via image analysis platform. This region growing algorithm was similar to what has been used in previous studies for quantification of PE clot volume[12] and was also based on the methods shown in the following papers[14-16]. Briefly, the region growing algorithm was a pixel-based image segmentation approach involving the initial selection of seed points by the user. This segmentation method examined the nearest neighboring pixels of initial seed points and determined if the pixel neighbors should be added to the region. The process was then iterated on, using data clustering algorithms based on image pixel data intensity and texture.

At the viewing workstation, the image analyst performed segmentation and volumetric quantification of emboli. To acquire these readings, the cursor was placed on the clot and the left mouse button was pressed and held in order to grow into adjacent regions with similar density readings. The analyst then assessed the need to include and/or exclude portions of the segmented mask by visually assessing the anatomic extent of the embolus and the surrounding anatomic structures and then made appropriate corrections and adjustments to the segmented mask. Figure 2 shows an example of *in vivo* region growing. In order to determine the inter observer reproducibility of the data analysis, the two independent observers were blinded to each other's interpretations when computing the clot volumes for each of the datasets using the same semi-automated algorithm and image analysis package[12,14-16]. One reader (AEK) repeated the analysis a second time to establish the intra-reader reproducibility.

A Qanadli score was calculated by assessing the presence and degree of obstruction in the pulmonary

Table 1 Scanner Information and computed tomography pulmonary angiogram acquisition protocol from each scanner

Site	Scan	Manufacturer	Model	Number of slices	Recon thickness (mm)	kVp	Pitch	Contrast agent
Academic Medical Center, Amsterdam, Netherlands	1	Siemens	Definition AS+	128	1	120	0.45	Ultravist 300
	2	Siemens	Force	384	1.5	90	0.55	Ultravist 300
Azienda Ospedaliero Universitaria Ospedali Riuniti Di Ancona, Ancona, Italy	3	Philips	Brilliance 16	16	2	120	0.9	Isovue 350
Fondazione Poliambulanza Istituto Ospedaliero, Brescia, Italy	4	GE	Optima CT660	128	0.625	120	1.375	Ultravist 370
Hôpital de la Cavale Blanche, Brest, France	5	Siemens	Definition AS +	128	1	100	1.2	Iomeron 400
Cliniques Universitaires Saint-Luc, Brussels, Belgium	6	Philips	ICT Brilliance 64	256	1	120	0.797	Iomeron 400
CHU de Clermont-Ferrand, Clermont-Ferrand, France	7	GE	Revolution GSI	64	0.625	120	1.375	Ultravist 370
Hospital Universitario Dr. Josep Trueta, Girona, Spain	8	Philips	Ingenuity CT	64	1	120	0.952	Omnipaque 350
Medical University Graz, Graz, Austria	9	Toshiba	Aquilion64	64	0.5	120	1	Optiray 350
	10	Toshiba	Aquilion64	64	0.5	120	1	Iomeron 400
Universitätsmedizin Greifswald, Greifswald, Germany	11	Siemens	Sensation 16	16	1.5	120	1.2	Iomeron 350
Hopital Michallon - CHUGA, Grenoble, France	12	GE	Optima CT 660	128	0.625	100	0.984375	Iomeron 350
Leiden University Medical Center, Leiden, Netherlands	13	Toshiba	Aquilion ONE	320	1	80	0.8129	Ultravist 370
UZ Gasthuisberg, Leuven, Belgium	14	Siemens	Definition Flash	128	1	100	0.55	Visipaque 320
	15	Siemens	Definition Flash	128	1	100	0.55	Visipaque 320
	16	Siemens	Definition Flash	128	1	100	0.55	Visipaque 320
Cedars Sinai Medical Center, Los Angeles, United States	17	GE	LightSpeed VCT	64	0.625	120	0.984375	Omnipaque 350
Hospital Universitario Ramon y Cajal, Madrid, Spain	18	Toshiba	Aquilion ONE	320	0.5	100	1.375	Iomeron 350
Intercoastal Medical Group, Sarasota, United States	19	Siemens	Definition AS+	128	0.6	120	1.1	Isovue 370
CHU de St. Etienne, St. Etienne, France	20	Siemens	Definition DS	64	1	120	1.2	Xenetix 350
Strasbourg University Hospital, Strasbourg, France	21	GE	Discovery CT750 HD	64	0.625	100	1.375	Iomeron 400
	22	Toshiba	Aquilion One	320	1	100	0.8129	Iomeron 400
Ospedale di Circolo, University of Insubria, Varese, Italy	23	Siemens	Sensation 40	40	0.75	100	1	Iomeron 370

All images were obtained with dose modulation of tube current. Filter and reconstruction kernels varied.

arterial tree bilaterally[17]. More specifically, the Qanadli score was calculated by assessing the CTPA in two ways, first, by evaluating the distribution of emboli in order to arrive at a weighting factor, and second, by determining a level of occlusion score. There are 10 segmental arteries on each side with three segmental arteries feeding the upper lobes, two feeding the right middle lobe and lingula (left) and five feeding the lower lobes. The presence of an embolus in a segmental vessel was given a weighting score of one. Central arteries were given heavier weighting than more distal vessels using the following method: the weighting factor for a vessel with an embolus was based on the number of segmental vessels it feeds. The more distal vessels were then excluded from the score. The scale for the level of obstruction of a given vessel was as follows: 0 represents no embolus detected; 1 represents a partially occlusive embolus; and 2 represent a fully occlusive embolus. When the weighting factor and obstruction factors were multiplied then added together, there was a maximal possible score of 20 per side for a total possible raw score of 40. With this information the Qanadli score was then calculated and reported as a percentage by dividing the raw score by 40, the maximal score[17].

A Modified Qanadli score was also calculated by solely assessing the presence and degree of obstruction in the ten segmental vessels bilaterally[18]. We performed this additional obstruction index to pull out any difference that may be seen by using the

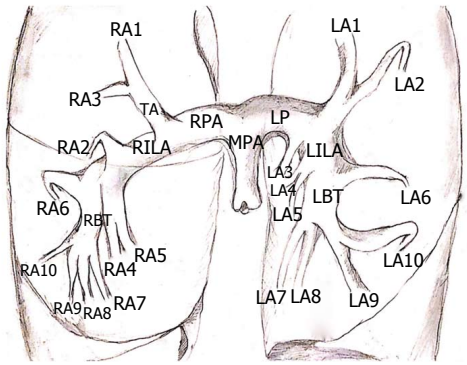

Figure 1 Schematic of segmental distribution of pulmonary arteries. MPA: Main pulmonary artery; RPA: Right pulmonary artery; TA: Truncus anterior; RILA: Right interlobar artery; RBT: Right basal trunk; RA1: Right upper lobe, apical; RA2: Right upper lobe, posterior; RA3: Right upper lobe, anterior; RA4: Right middle lobe, lateral; RA5: Right middle lobe, medial; RA6: Right lower lobe, superior; RA7: Right lower lobe, medial basal; RA8: Right lower lobe, anterior basal; RA9: Right lower lobe, lateral basal; RA10: Right lower lobe, posterior basal; LPA: Left pulmonary artery; LILA: Left interlobar artery; LBT: Left basal trunk; LA1: Left upper lobe, apical; LA2: Left upper lobe, posterior; LA3: Left upper lobe, anterior; LA4: Lingula, superior; LA5: Lingula, inferior; LA6: Left lower lobe, superior; LA7: Left lower lobe, medial basal; LA8: Left lower lobe, anterior basal; LA9: Left lower lobe, lateral basal; LA10: Left lower lobe, posterior basal.

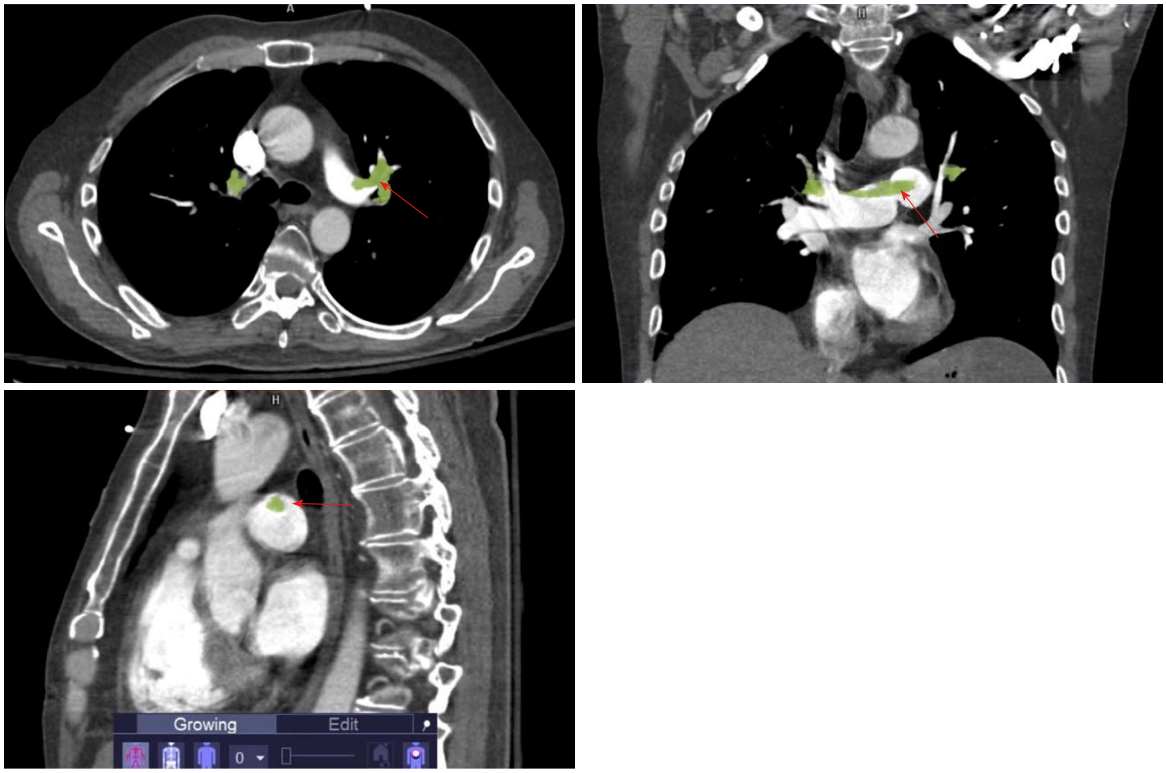

Figure 2 Computed tomography pulmonary angiogram images demonstrating segmentation of a saddle embolus in three orthogonal views (arrows).

Qanadli with its focus on weighted central vessels *vs* simply assessing obstruction in the individual segmental vessels alone as we have done in our modified version. The same Qanadli scale for the level of obstruction was used in our modified version with 0 representing no embolus, 1 representing a partially occlusive embolus, and 2 representing a fully occlusive embolus. As with Qanadli scoring, a maximum raw score of 40 and a final score reported as a percentage relative to 40 was used.

Statistical analysis

All statistical analysis presented here was performed or guided by a biomedical statistician. Intra-class correlation coefficients (ICCs) and Bland-Altman analyses were performed using GraphPad Prism 7 for Mac, GraphPad Software, San Diego California, United States, www.graphpad.com. The ICCs were used to compare the results obtained between the two readers as well as to compare the results obtained from the two analyses of the same reader. The agreement between the measurements by each observer in the two reading sessions and the agreement between the two observers were also assessed using Bland-Altman analyses. According to this method, the mean difference between

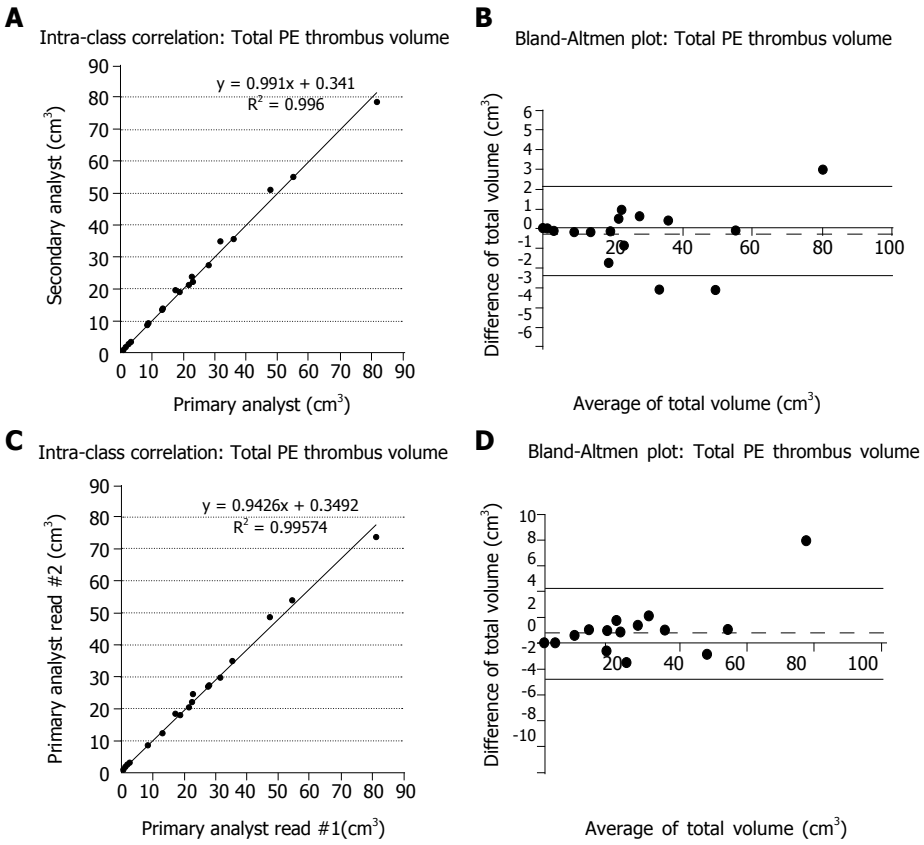

Figure 3 Total thrombus volume inter- and intra-observer reproducibility (A) Intra-class correlation coefficient (ICC) plot and (B) Bland Altman plot comparing the total PE thrombus volume results of the primary and secondary image analyst for the inter-observer reproducibility analysis (C) ICC plot and (D) Bland Altman plot comparing the total pulmonary embolism thrombus volume results of the first and second read of the primary image analyst for the intra-observer reproducibility analysis.

measurements is defined as "bias" and represents the systemic error in measurements. We calculated 95%CI for bias and for the limits of agreement. ICC provides the overall inter- or intra-observer agreement whereas the Bland-Altman method gives the discrepancy in measurements at the individual level. A one sample *t*-test was performed to determine if any bias was observed on the Bland-Altman analysis. For TTV, in addition to evaluating absolute differences by Bland Altman analysis, we also evaluated the % difference between the two readers or two reads.

RESULTS

Analyst 1 found 72 emboli in the 23 patients with a mean number of emboli of 3.13 per patient. With the three negative cases excluded the mean number of emboli per patient was 3.6. Considering all cases there was a range of 0-11 emboli per patient. (0 in 3 patients (pts); 1 in 3 pts; 2 in 7 pts; 3 in 2 pts; 4 in 1 pt; 5 in 3 pts; 6 in 2 pts; 7 in 1 pt; and 11 in 1 pt). The clot volumes ranged from 0.0041–47.34 cm^3 (mean +/- SD, 5.93 +/- 10.15 cm^3). On the second read, analyst 1 found the same number and distribution of emboli. The clot volume range varied on the upper extent as compared to the initial read. The clot volumes for read 2 ranged from 0.0041-45.52 cm^3 (mean +/- SD, 5.42 +/- 9.53 cm^3).

Analyst 2 found 73 emboli in the 23 patients with a mean number of emboli of 3.17 per patient. With the three negative cases excluded the mean number of emboli per patient was 3.65. There was a range of 0-11 emboli per patient. (0 in 3 pts; 1 in 3 pts; 2 in 7 pts; 3 in 2 pts; 4 in 1 pt; 5 in 2 pts; 6 in 3 pts; 7 in 1 pt; and 11 in 1 pt). The clot volumes ranged from 0.00459-46.29 cm^3 (mean +/- SD, 5.91 +/- 10.06cm^3).

The ICC calculated for the TTV measurements per patient for inter-observer analysis was 0.998 and for intra-observer analysis was 0.997, while the associated Bland-Altman analyses for inter-and intra-observer agreement for TTV demonstrated no inter- or intra-observer biases (P = 0.23 for inter-observer results, P = 0.26 for intra-observer results for TTV using a one-sample *t*-test with 0, two tailed). The ICC and Bland-Altman analyses are seen in Figure 3. The ICC calculated for the ITV measurements per patient for inter-observer analysis was 0.996 and for intra-observer analysis was 0.997, while the associated Bland-Altman analyses for inter-and intra-observer agreement for ITV demonstrated no inter- or intra-observer biases. (P = 0.55 for inter-observer results, P = 0.24 for intra-observer results for TTV using a one-sample *t*-test with 0,

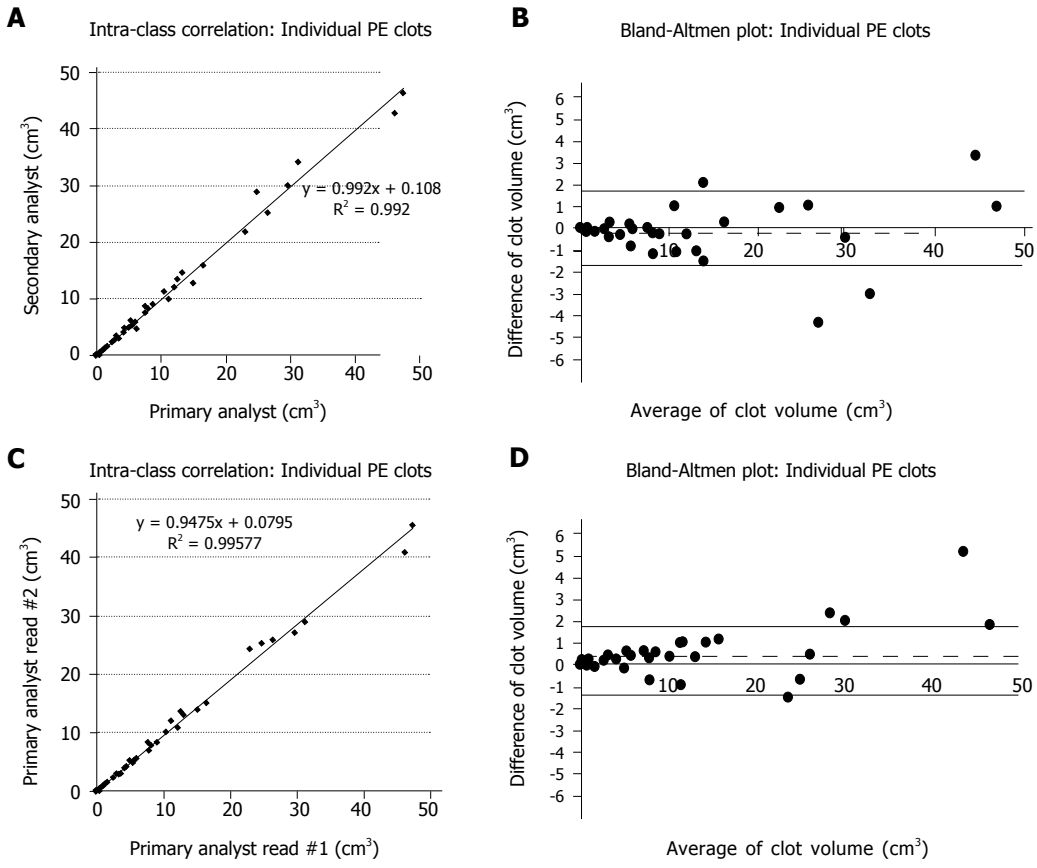

Figure 4 Individual thrombus volume inter- and intra-observer reproducibility (A) Intra-class correlation coefficient (ICC) plot and (B) Bland Altman plot comparing the individual PE thrombus volumes results of the primary and secondary image analyst for the inter-observer reproducibility analysis (C) ICC plot and (D) Bland Altman plot comparing the individual pulmonary embolism thrombus volumes results of the first and second read of the primary image analyst for the intra-observer reproducibility analysis.

two tailed). The ICC and Bland-Altman analyses for the ITV are seen in Figure 4.

A Qanadli score was calculated for each patient. The range of for Analyst 1 was 0%-52.5% for read one and 0%-52.5% for read two. The range for Analyst 2 was 0%-72.5%. The 20 positive cases had a mean Qanadli score with associated standard deviations of 37.25% +/- 16.93 and 39.125% +/- 19.20 for Analysts 1 and 2 respectively. The mean and standard deviation for Analyst 1's second read was 37.25% +/- 16.93. The ICC calculated for the Qanadli score per patient for inter- and intra-observer was 0.944 and 1 respectively. ICC plots and Bland Altman plots for inter- and intra-observer reproducibility for Qanadli assessment are shown in Figure 5.

The Modified Qanadli score was calculated for each patient as a secondary study endpoint. The range for Analyst 1 was 0%-70% for read one and 0%-72.5% for read two. The range of scores for Analyst 2 is 0%-72.5%. The 20 positive cases had a mean and associated standard deviations of 38.125% +/- 20.87 and 36.625% +/- 21.11 for Analysts 1 and 2 respectively. The mean and standard deviation for Analyst 1's second read was 38.5% +/- 21.34. The ICC calculated for the Modified Qanadli score per patient for inter- and intra-observer was 0.996 and 0.999 respectively. ICC plots and Bland Altman plots for inter- and intra-observer reproducibility for the Modified Qanadli assessment are shown in Figure 6.

Finally, we also evaluated the % difference in TTV between the two analysts (P = 0.074, one sample t-test with zero, two tailed) as well as the two reads by Analyst 1 (P = 0.063, one sample t-test with 0, two tailed). These Bland-Altman plots are shown in Figure 7.

DISCUSSION

Emboli to the lungs cause physical obstruction of the pulmonary arteries yielding a pathophysiologic cascade resulting in varying degrees of cardiovascular distress[19]. Although the embolic load and distribution are considered less pertinent than the patient's hemodynamic status in evaluating risk stratification[7] clot burden has been shown to have predictive value of mortality in patients with acute PE[20]. For example, Collomb *et al*[21] have shown that the hemodynamic severity of acute PE can be determined by assessing clot burden through the use of a vascular obstruction index as well as other vascular load measurements such as right ventricular (RV): left ventricular (LV) ratio, minimum LV diameter

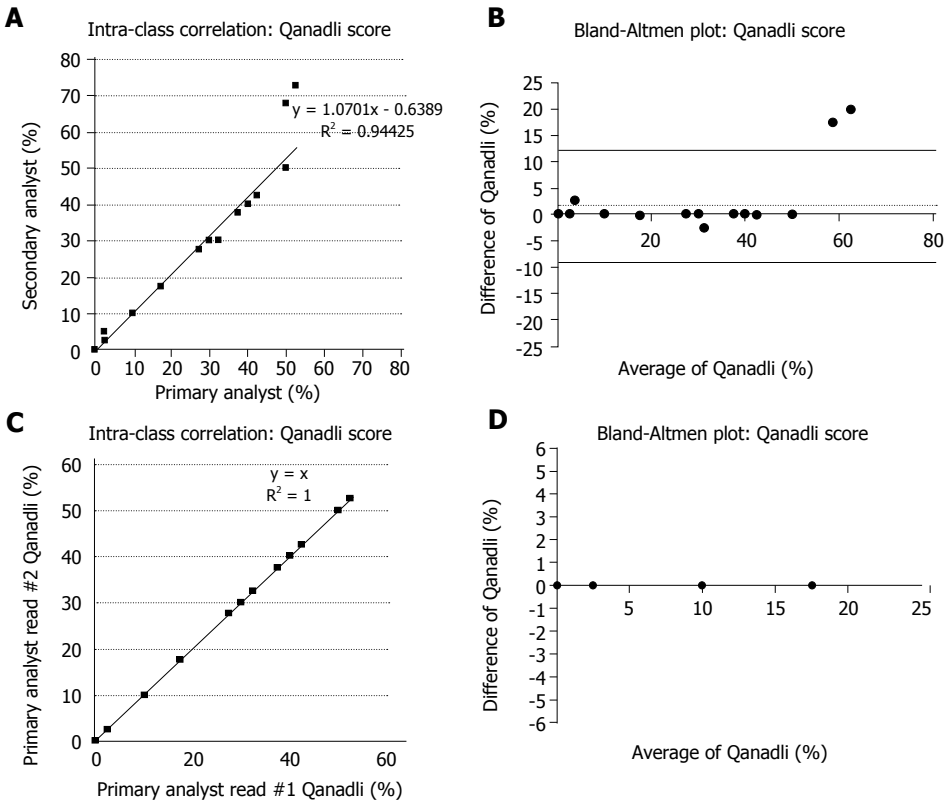

Figure 5 Qanadli score inter- and intra-observer reproducibility (A) Intra-class correlation coefficient (ICC) plot and (B) Bland Altman plot comparing the Qanadli score results of the primary and secondary image analyst for the inter-observer reproducibility analysis (C) ICC plot and (D) Bland Altman plot comparing the results of the first and second read of the primary image analyst for the intra-observer reproducibility analysis of the PE obstruction index (Qanadli score).

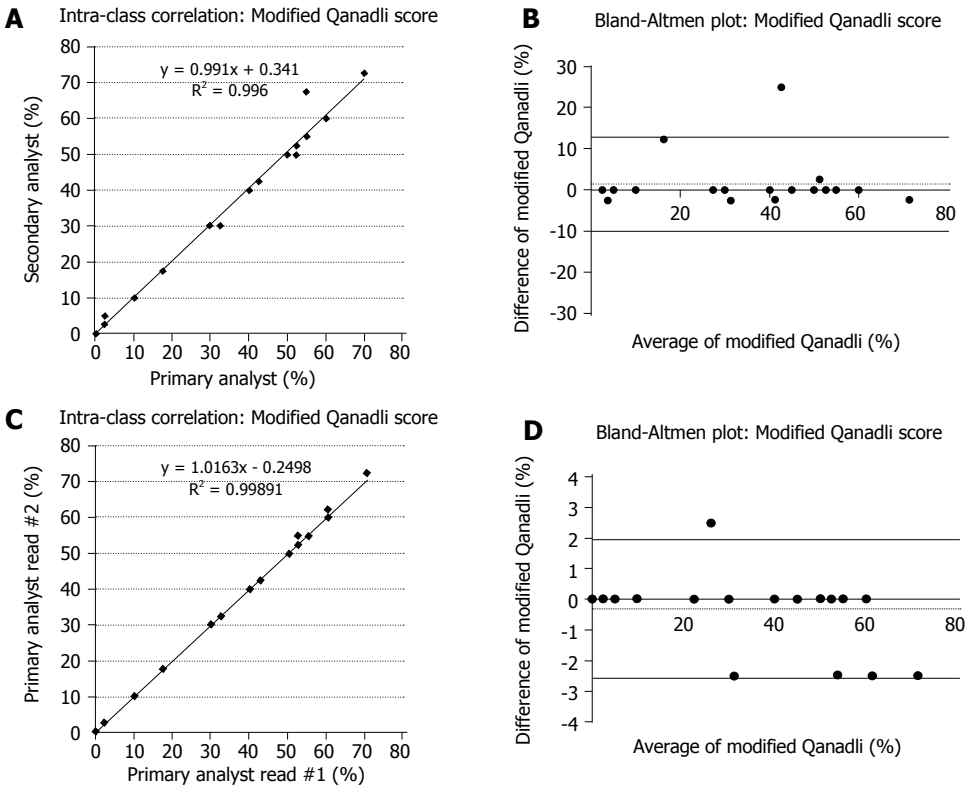

Figure 6 Modified Qanadli score inter- and intra-observer reproducibility (A) Intra-class correlation coefficient (ICC) plot and (B) Bland Altman plot comparing the modified Qanadli results of the primary and secondary image analyst for the inter-observer reproducibility analysis (C) ICC plot and (D) Bland Altman plot comparing the results of the first and second read of the primary image analyst for the intra-observer reproducibility analysis.

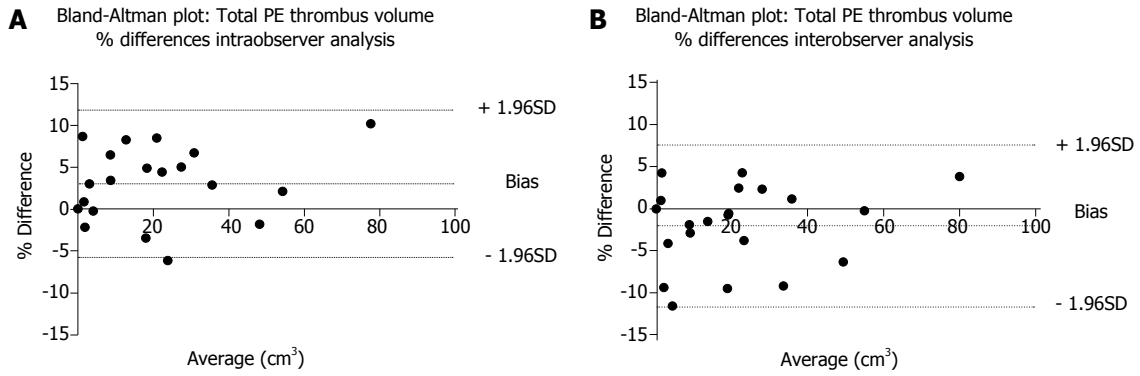

Figure 7 Bland Altman analysis of total thrombus volume normalized to clot size (Mean *vs* Difference/Mean) for (A) intra and (B) inter observer analysis.

and diameter of the central PA[21]. Furthermore, Furlan *et al*[12] have shown that quantification of clot burden can be accurate and reproducible at a single institution. The challenges faced in multicenter studies include the variety of imaging systems and models used and the resultant variability in data acquisition. Additional variables could include differences in the energy level (kVp), pitch, reconstruction methods and contrast agents utilized.

Overall, inter- and intra-observer variability measurements indicated excellent reproducibility of the semi-automated analysis method for quantifying PE thrombus volume/burden. The ICC coefficient for all endpoints TTV (primary), ITV (secondary), Qanadli score (secondary) and modified Qanadli score (secondary) all had ICC values greater than 0.95 for both the inter- and intra-observer analysis. The Bland-Altman analysis also indicated no significant biases in any of the metrics evaluated. Our data showed that even with the variability inherent in multicenter data acquisition and reconstruction, the image analysis methodology employed here is reproducible and therefore suitable for use in a multicenter setting. These findings have implications on future studies of PE by allowing for both the option of multisite data acquisition with evaluation at an imaging core laboratory, as well as inclusion of direct PE volume measurements and assessment of temporal changes in embolic load. For example, in the SEATTLE Ⅱ study, a multicenter investigation to assess the safety and efficacy of ultrasound-facilitated catheter-directed, low dose fibrinolysis therapy in patients with acute submassive PE, the RV/LV diameter ratio was used as a primary efficacy outcome[22]. Subsequent research in SEATTLE Ⅱ and similar studies can add direct clot burden volumetrics in furtherance of the body of knowledge in this area.

Our results compare well with those obtained by Nakada *et al*[23], who evaluated inter- and intra-reader reproducibility studies on manually measured PE volumes and showed no statistical differences in either inter- or intra-reader analyses. The intra-reader analysis in that study was nine months, much greater than in our study.

Implications of our findings on multicenter studies: In a recent study, we have shown that quantification of clot volumes by CT is unaffected by most imaging acquisition and reconsturction parameters (except large differences in pitch used during acquisition)[24]. Results of the current study show that the image analysis of data acquired from a multicenter setting is robust with the size of the clot not affecting the reproducbility of quantification significantly. Absolute quantification differences for TTV and ITV for both inter and inra-observer results were in the range of 2-4 cm^3 (95%CI on Bland Altman plots, Figures 3 and 4). As a percent difference, these were of the order of 5%-10% (95%CI, Figure 7). This indicates that with our methodology we should be able to robustly pick up changes in absolute thrombus volume greater approximately 2 cm^3 or 5% regardless of the starting size of the clots. this data can be used to estimate sample size requirements for clinical trials using clot burden quantification as an endpoint in PE treatment studies.

The study was limited by several factors. First, a small number of subjects were evaluated at a small number of sites. Images of subjects were chosen for this study during a site qualification visit prior to the start of a multicenter clinical trial evaluating a new thrombolytic agent for PE. Cases were also chosen to provide a spread of scanners and variations in imaging protocols across the sites. There could therefore be a selection bias in how these individuals were included as part of this current study. Second, the intra-reader variability analysis may have been affected by recall bias as there was a short interval of two weeks between the reads. This may have been insufficient to eliminate recall bias which could have resulted in the perfect agreement between the scores in the two reads. However, to reduce recall bias, images were presented to the image analyst in a randomized fashion for the two reads. Third, we were unable to assess radiation dose as a variable because the various scanners employ dose modulation and this setting is dependent upon patient size. Fourthly, we do not have access to demographic information of the subjects as the images analyzed were read anonymously and devoid of any Protected Health Information to comply with HIPAA requirements and our IRB approval. Fifthly, the inter reader assessments were only performed by 2 analysts and the intra reader

analysis was performed on two reads by only a single analyst. Analysis by more individuals will improve the robustness of the results. Lastly, Qanadli scoring may also be inherently skewed leading to high ICC because it relies on the weighting of affected proximal vascular branches thereby yielding specific discreet scores. This bias could be emphasized in our patient population that demonstrated large and often proximal PEs.

In conclusion, the data showed that our image analysis methodology is reproducible and therefore suitable for future use in a multicenter setting.

ARTICLE HIGHLIGHTS

Research background

In regard to clinical evaluation of pulmonary embolism (PE), clot burden is not a principal marker for clinical risk stratification, however clot burden is being used to assess for pharmaceutical characteristics in clinical drug trials in multicenter settings. To this point the technique has been studied with data obtained from a single imaging center using one fixed computed tomography pulmonary angiogram (CTPA) imaging protocol.

Research motivation

Data obtained from multicenter sites has not previously been studied. Thus, in order to validate the methods employed in multicenter clinical pharmaceutical trials of drugs such as thrombolytics, this study was commenced to assess for repeatability and consistency of clot volume measurements being obtained using semi-automated region growing techniques. Confirming the reliability of these measures has value in furthering the assessment of drug effectiveness, drug potency and in determination of optimal duration of therapy.

Research objectives

The key objective is to evaluate reproducibility of PE clot volume quantification using a semi-automated region growing algorithm on CTPA data in a multicenter setting.

Research methods

Anonymized CTPA data was acquired from 23 scanners from 18 imaging centers using each site's standard PE protocol. Two independent analysts measured PE volumes using a semi-automated region-growing algorithm on an FDA-approved image analysis platform. Total thrombus volume was calculated per patient as the primary endpoint. Secondary endpoints were individual thrombus volume, Qanadli score and modified Qanadli score per patient. Inter- and intra-observer reproducibility were assessed using intra-class correlation coefficient (ICC) and Bland-Altman analysis. The methods employed in this study were novel in that they previously have not been used in a multicenter setting.

Research results

The results showed excellent reproducibility of inter- and intra-observer variability measurements using the semi-automated region-growing method for quantifying PE volume burden. ICC for all endpoints was greater than 0.95 for inter- and intra-observer analysis. Bland-Altman analysis indicated no significant biases. The results confirm the validity of the methods used in multicenter pharmaceutical trials thereby allowing for advancement in this field.

Research conclusions

Semi-automated region growing algorithm for quantifying PE is reproducible using data from multiple scanners and is a suitable method for image analysis in multicenter clinical trials. The utility of validating this method could affect the advancement of thrombolytic therapy and other interventions that may be used to treat PE.

Research perspectives

Computer-assisted image analysis has a growing role in both diagnostic and investigative imaging. This study solidifies the foundation of semi-automated region growing for volume quantification by proving the repeatability of the technique when used in a multicenter setting.

ACKNOWLEDGEMENTS

This study is supported by Daiichi Sankyo Pharma Development. In addition, we wish to acknowledge the following hospitals, site names, principal investigators, and radiologists. Dr. Saskia Middeldorp and Dr. Ludo Beenen - Academic Medical Center, Amsterdam, Netherlands; Dr. Aldo Salvi, Dr. Cinzia Nitti and Dr. Arianna Lorenzoni - Azienda Ospedaliero Universitaria Ospedali Riuniti Di Ancona, Ancona, Italy; Dr. Claudio Cuccia and Dr. Silvia Magnaldi - Fondazione Poliambulanza Istituto Ospedaliero, Brescia, Italy; Dr. Francis Couturaud and Dr. Michel Nonent - Hôpital de la Cavale Blanche, Brest, France; Dr. Franck Verschuren and Dr. Benoit Ghaye - Cliniques Universitaires Saint-Luc, Brussels, Belgium; Dr. Jeannot Schmidt and Dr. Lucie Cassagnes - CHU de Clermont-Ferrand, Clermont-Ferrand, France; Dr. Fernando Garcia-Bragado and Dr. Pedro Ortuno Muro - Hospital Universitario Dr. Josep Trueta, Girona, Spain; Dr. Marianne Brodmann and Dr. Reinhard Raggam - Medical University Graz, Graz, Austria; Dr. Klaus Empen and Dr. Birger Mensel - Universitätsmedizin Greifswald, Greifswald, Germany; Dr. Helen Bouvaist and Dr. Adrien Jankowski - Hopital Michallon - CHUGA, Grenoble, France; Dr. Menno Huisman and Dr. Lucia Kroft - Leiden University Medical Center, Leiden, Netherlands; Dr. Peter Verhammo, Dr. Johny Verschakelen and Dr. Walter Coudyzer - UZ Gasthuisberg, Leuven, Belgium; Dr. Victor Tapson and Dr. Peter Julien - Cedars Sinai Medical Center, Los Angeles, United States; Dr. David Jimenez and Dr. Agustina Vicente Bartulos - Hospital Universitario Ramon y Cajal, Madrid, Spain; Dr. Maurizio Concha - Intercoastal Medical Group, Sarasota, United States; Dr. Laurent Bertuletti and Dr. Pierre Croisille - CHU de St. Etienne, St. Etienne, France; Dr. Dominique Stephan and Dr. Michael Ohana - Strasbourg University Hospital, Strasbourg, France and Dr. Walter Ageno and Dr. Chiara Floridi - Ospedale di Circolo, University of Insubria, Varese, Italy.

REFERENCES

1 **Wakefield TW**, McLafferty RB, Lohr JM, Caprini JA, Gillespie DL, Passman MA; Executive Committee of the American Venous Forum. Call to action to prevent venous thromboembolism. *J Vasc Surg* 2009; **49**: 1620-1623 [PMID: 19497526 DOI: 10.1016/j.jvs.2009.01.058]

2 **Heit JA**. Venous thromboembolism: disease burden, outcomes and risk factors. *J Thromb Haemost* 2005; **3**: 1611-1617 [PMID: 16102026 DOI: 10.1111/j.1538-7836.2005.01415.x]

3 **Silverstein MD**, Heit JA, Mohr DN, Petterson TM, O'Fallon WM, Melton LJ 3rd. Trends in the incidence of deep vein thrombosis and pulmonary embolism: a 25-year population-based study. *Arch Intern Med* 1998; **158**: 585-593 [PMID: 9521222 DOI: 10.1001/archinte.158.6.585]

4 **Heit JA**, Silverstein MD, Mohr DN, Petterson TM, O'Fallon WM, Melton LJ 3rd. Predictors of survival after deep vein thrombosis and pulmonary embolism: a population-based, cohort study. *Arch Intern Med* 1999; **159**: 445-453 [PMID: 10074952 DOI: 10.1001/archinte.159.5.445]

5 **Laporte S**, Mismetti P, Décousus H, Uresandi F, Otero R,

Lobo JL, Monreal M; RIETE Investigators. Clinical predictors for fatal pulmonary embolism in 15,520 patients with venous thromboembolism: findings from the Registro Informatizado de la Enfermedad TromboEmbolica venosa (RIETE) Registry. *Circulation* 2008; **117**: 1711-1716 [PMID: 18347212 DOI: 10.1161/CIRCULATIONAHA.107.726232]

6 **Goldhaber SZ**, Visani L, De Rosa M. Acute pulmonary embolism: clinical outcomes in the International Cooperative Pulmonary Embolism Registry (ICOPER) *Lancet* 1999; **353**: 1386-1389 [PMID: 10227218 DOI: 10.1016/S0140-6736(98)07534-5]

7 **Tapson VF**. Diagnosis, prognosis and therapeutic management of acute pulmonary embolism. *Hosp Pract* (1995) 2016; **44**: 164-172 [PMID: 27450108 DOI: 10.1080/21548331.2016.1210471]

8 **Torbicki A**, Perrier A, Konstantinides S, Agnelli G, Galiè N, Pruszczyk P, Bengel F, Brady AJ, Ferreira D, Janssens U, Klepetko W, Mayer E, Remy-Jardin M, Bassand JP; ESC Committee for Practice Guidelines (CPG). Guidelines on the diagnosis and management of acute pulmonary embolism: the Task Force for the Diagnosis and Management of Acute Pulmonary Embolism of the European Society of Cardiology (ESC). *Eur Heart J* 2008; **29**: 2276-2315 [PMID: 18757870 DOI: 10.1093/eurheartj/ehn310]

9 **Hariharan P**, Dudzinski DM, Rosovsky R, Haddad F, MacMahon P, Parry B, Chang Y, Kabrhel C. Relation Among Clot Burden, Right-Sided Heart Strain, and Adverse Events After Acute Pulmonary Embolism. *Am J Cardiol* 2016; **118**: 1568-1573 [PMID: 27742425 DOI: 10.1016/j.amjcard.2016.08.025]

10 **Meinel FG**, Nance JW Jr, Schoepf UJ, Hoffmann VS, Thierfelder KM, Costello P, Goldhaber SZ, Bamberg F. Predictive Value of Computed Tomography in Acute Pulmonary Embolism: Systematic Review and Meta-analysis. *Am J Med* 2015; **128**: 747-59.e2 [PMID: 25680885 DOI: 10.1016/j.amjmed.2015.01.023]

11 **Vedovati MC**, Becattini C, Agnelli G, Kamphuisen PW, Masotti L, Pruszczyk P, Casazza F, Salvi A, Grifoni S, Carugati A, Konstantinides S, Schreuder M, Golebiowski M, Duranti M. Multidetector CT scan for acute pulmonary embolism: embolic burden and clinical outcome. *Chest* 2012; **142**: 1417-1424 [PMID: 22628491 DOI: 10.1378/chest.11-2739]

12 **Furlan A**, Patil A, Park B, Chang CC, Roberts MS, Bae KT. Accuracy and reproducibility of blood clot burden quantification with pulmonary CT angiography. *AJR Am J Roentgenol* 2011; **196**: 516-523 [PMID: 21343492 DOI: 10.2214/AJR.10.4603]

13 **Aghayev A**, Furlan A, Patil A, Gumus S, Jeon KN, Park B, Bae KT. The rate of resolution of clot burden measured by pulmonary CT angiography in patients with acute pulmonary embolism. *AJR Am J Roentgenol* 2013; **200**: 791-797 [PMID: 23521450 DOI: 10.2214/AJR.12.8624]

14 **Adams R**, Bischof L. Seeded region growing. *IEEE Trans Pattern Anal Mach Intell* 1994; **16**: 641-647 [DOI: 10.1109/34.295913]

15 **Boser BE**, Guyon IM, Vapnik VN. A training algorithm for optimal margin classifiers. Proc. fifth Annu. Work. Comput. *ACM Press* 1992; 144-152 [DOI: 10.1145/130385.130401]

16 **Malik J**, Belongie S, Leung T, Shi J. Contour and Texture Analysis for Image Segmentation. *Int J Comput Vis* 2001; **43**: 7-27 [DOI: 10.1023/A:1011174803800]

17 **Qanadli SD**, El Hajjam M, Vieillard-Baron A, Joseph T, Mesurolle B, Oliva VL, Barré O, Bruckert F, Dubourg O, Lacombe P. New CT index to quantify arterial obstruction in pulmonary embolism: comparison with angiographic index and echocardiography. *AJR Am J Roentgenol* 2001; **176**: 1415-1420 [PMID: 11373204 DOI: 10.2214/ajr.176.6.1761415]

18 **Obradović D**, Joveš B, Pena Karan S, Stefanović S, Ivanov I, Vukoja M. Correlation between the Wells score and the Quanadli index in patients with pulmonary embolism. *Clin Respir J* 2016; **10**: 784-790 [PMID: 25763885 DOI: 10.1111/crj.12291]

19 **Piazza G**, Goldhaber SZ. Management of submassive pulmonary embolism. *Circulation* 2010; **122**: 1124-1129 [PMID: 20837937 DOI: 10.1161/CIRCULATIONAHA.110.961136]

20 **El-Menyar A**, Nabir S, Ahmed N, Asim M, Jabbour G, Al-Thani H. Diagnostic implications of computed tomography pulmonary angiography in patients with pulmonary embolism. *Ann Thorac Med* 2016; **11**: 269-276 [PMID: 27803753 DOI: 10.4103/1817-1737.191868]

21 **Collomb D**, Paramelle PJ, Calaque O, Bosson JL, Vanzetto G, Barnoud D, Pison C, Coulomb M, Ferretti G. Severity assessment of acute pulmonary embolism: evaluation using helical CT. *Eur Radiol* 2003; **13**: 1508-1514 [PMID: 12835961 DOI: 10.1007/s00330-002-1804-5]

22 **Piazza G**, Hohlfelder B, Jaff MR, Ouriel K, Engelhardt TC, Sterling KM, Jones NJ, Gurley JC, Bhatheja R, Kennedy RJ, Goswami N, Natarajan K, Rundback J, Sadiq IR, Liu SK, Bhalla N, Raja ML, Weinstock BS, Cynamon J, Elmasri FF, Garcia MJ, Kumar M, Ayerdi J, Soukas P, Kuo W, Liu PY, Goldhaber SZ; SEATTLE II Investigators. A Prospective, Single-Arm, Multicenter Trial of Ultrasound-Facilitated, Catheter-Directed, Low-Dose Fibrinolysis for Acute Massive and Submassive Pulmonary Embolism: The SEATTLE II Study. *JACC Cardiovasc Interv* 2015; **8**: 1382-1392 [PMID: 26315743 DOI: 10.1016/j.jcin.2015.04.020]

23 **Nakada K**, Okada T, Osada H, Honda N. Relation between pulmonary embolus volume quantified by multidetector computed tomography and clinical status and outcome for patients with acute pulmonary embolism. *Jpn J Radiol* 2010; **28**: 34-42 [PMID: 20112091 DOI: 10.1007/s11604-009-0380-x]

24 **Kaufman AE**, Pruzan AN, Hsu C, Ramachandran S, Jacobi A, Fayad ZA, Mani V. Effect of varying computed tomography acquisition and reconstruction parameters on semi-automated clot volume quantification. *World J Radiol* 2018; **10**: 24-29 [PMID: 29599936 DOI: 10.4329/wjr.v10.i3.24]

P- Reviewer: Bazeed MF, Bazeed J, Gao BL, Kwok WE, Valek V
S- Editor: Cui LJ **L- Editor**: A **E- Editor**: Wu YXJ

World Journal of Radiology

Submit a Manuscript: http://www.f6publishing.com

World J Radiol 2018 October 28; 10(10): 135-142

DOI: 10.4329/wjr.v10.i10.135

ISSN 1949-8470 (online)

ORIGINAL ARTICLE

Observational Study

Low-radiation and high image quality coronary computed tomography angiography in "real-world" unselected patients

Caryl Elizabeth Richards, Stephen Dorman, Patricia John, Anthony Davies, Sharon Evans, Tishi Ninan, David Martin, Sriranj Kannoly, Gail Roberts-Davies, Mark Ramsey, Daniel Rhys Obaid

Caryl Elizabeth Richards, Daniel Rhys Obaid, Swansea University Medical School, Swansea University, Grove Building, Singleton Park, Sketty, Swansea SA2 8PP, United Kingdom

Stephen Dorman, Mark Ramsey, Daniel Rhys Obaid, Department of Cardiology, Morriston Hospital, Heol Maes Eglwys, Morriston, Cwmrhydyceirw, Swansea SA6 6NL, United Kingdom

Patricia John, Anthony Davies, Sharon Evans, Tishi Ninan, Department of Radiology, Morriston Hospital, Heol Maes Eglwys, Morriston, Cwmrhydyceirw, Swansea SA6 6NL, United Kingdom

David Martin, Gail Roberts-Davies, Department of Radiology, Singleton Hospital, Sketty Ln, Sketty, Swansea SA2 8QA, United Kingdom

Sriranj Kannoly, Department of Cardiology, Singleton Hospital, Sketty Ln, Sketty, Swansea SA2 8QA, United Kingdom

ORCID number: Caryl Elizabeth Richards (0000-0002-1044-1825); Stephen Dorman (0000-0003-3264-521X); Patricia John (0000-0002-7250-9995); Anthony Davies (0000-0002-4445-6427); Sharon Evans (0000-0001-9206-1051); Tishi Ninan (0000-0001-6547-6921); David Martin (0000-0002-1185-0196); Sriranj Kannoly (0000-0002-6840-3899); Gail Roberts-Davies (0000-0002-7880-4450); Mark Ramsey (0000-0003-3912-6658); Daniel Rhys Obaid (0000-0002-3891-1403).

Author contributions: Obaid DR designed the study; all authors performed the research; Richards CE analyzed the data and wrote the paper; Obaid DR revised the manuscript for final submission.

Institutional review board statement: As the study involved no deviation from standard treatment protocols and no randomization it was not considered "research requires ethical approval" by the NHS Research authority tool.

Informed consent statement: As this study does not involve patient randomization or any deviation from standard treatment protocols and as it was deemed "non - research" by the NHS Health Research Authority tool no informed consent forms were used

Conflict-of-interest statement: None of the authors have any conflicts of interest or financial disclosure related to this study.

Data sharing statement: No additional data are available.

STROBE Statement: The authors have read the STROBE Statement-checklist of items, and the manuscript was prepared and revised according to the STROBE Statement-checklist of items.

Manuscript source: Invited manuscript

Correspondence to: Daniel Rhys Obaid, PhD, Associate Professor, Department of Cardiology, Morriston Hospital, Heol Maes Eglwys, Morriston, Cwmrhydyceirw, Swansea SA6 6NL, United Kingdom. daniel.obaid@wales.nhs.uk
Telephone: +44-1792-704123
Fax: +44-1792-704149

Received: April 30, 2018
Peer-review started: April 30, 2018
First decision: June 6, 2018
Revised: August 14, 2018
Accepted: October 8, 2018
Article in press: October 8, 2018
Published online: October 28, 2018

Abstract

AIM

To determine the radiation dose and image quality in coronary computed tomography angiography (CCTA) using state-of-the-art dose reduction methods in unselected "real world" patients.

METHODS

In this single-centre study, consecutive patients in sinus rhythm underwent CCTA for suspected coronary artery disease (CAD) using a 320-row detector CT scanner. All patients underwent the standard CT acquisition protocol at our institute (Morriston Hospital) a combination of dose saving advances including prospective electrocardiogram-gating, automated tube current modulation, tube voltage reduction, heart rate reduction, and the most recent novel adaptive iterative dose reconstruction 3D (AIDR3D) algorithm. The cohort comprised real-world patients for routine CCTA who were not selected on age, body mass index, or heart rate. Subjective image quality was graded on a 4-point scale (4 = excellent, 1 = non-diagnostic).

RESULTS

A total of 543 patients were included in the study with a mean body weight of 81 ± 18 kg and a pre-scan mean heart rate of 70 ± 11 beats per minute (bpm). When indicated, patients received rate-limiting medication with an oral beta-blocker followed by additional intravenous beta-blocker to achieve a heart rate below 65 bpm. The median effective radiation dose was 0.88 mSv (IQR, 0.6-1.4 mSv) derived from a Dose Length Product of 61.45 mGy.cm (IQR, 42.86-100.00 mGy.cm). This also includes what we believe to be the lowest ever-reported radiation dose for a routine clinical CCTA (0.18 mSv). The mean image quality (± SD) was 3.65 ± 0.61, with a subjective image quality score of 3 ("good") or above for 93% of patient CCTAs.

CONCLUSION

Combining a low-dose scan protocol and AIDR3D with a 320-detector row CT scanner can provide high quality images at exceptionally low radiation dose in unselected patients being investigated for CAD.

Key words: Effective radiation dose; Tube voltage; Tube current; Iterative reconstruction; Coronary computed tomography angiography; Image quality; Prospectively electrocardiogram gating

Core tip: Coronary computed tomography angiography (CCTA) is now widely used in the diagnosis of coronary artery disease since it is a rapid, minimally invasive test with high diagnostic accuracy. To meet the demands for increasing spatial and temporal resolution of CT images, a number of dose saving algorithms have been implemented to CCTA to minimise radiation exposure to "as low as reasonably achievable" without compromising diagnostic image quality. This study demonstrates that advances in CT scanner hardware and reconstruction software allow ultra-low dose of radiation with high image quality in routine clinical examination of real-world patients.

Richards CE, Dorman S, John P, Davies A, Evans S, Ninan T, Martin D, Kannoly S, Roberts-Davies G, Ramsey M, Obaid DR. Low-radiation and high image quality coronary computed tomography angiography in "real-world" unselected patients. *World J Radiol* 2018; 10(10): 135-142 Available from: URL: http://www.wjgnet.com/1949-8470/full/v10/i10/135.htm DOI: http://dx.doi.org/10.4329/wjr.v10.i10.135

INTRODUCTION

Coronary computed tomography angiography (CCTA) is increasingly being used in the diagnosis of coronary artery disease (CAD) since it is rapid and minimally invasive[1,2]. However, the high radiation doses[3] previously required for optimising the image signal-to-noise ratio in CCTA were a major healthcare concern due to an associated increase in lifetime risk of radiation-induced malignancy[4]. CCTA has thus been a driving force behind a number of dose reduction strategies to pursue radiation exposure to "as low as reasonably achievable" (ALARA) without compromising image quality[5].

Sub-millisievert CCTA was initially proven feasible in 2009 using dual-source CT with prospectively electrocardiogram (ECG)-triggered high-pitch spiral acquisition[6], and doses as low as 0.06 mSv have been reported using this technique with a combination of iterative reconstruction (IR) and reduced tube voltage[7]. However, these were conducted on highly selected populations with low body weight and heart rate. We prospectively analyzed the radiation exposure and image quality in consecutive unselected patients undergoing CCTA for suspected coronary disease with a 320-detector row CT scanner and IR, and active reduction of tube voltage, exposure window, and volume coverage.

MATERIALS AND METHODS

Patient cohort

This is a prospective single-centre study of 549 consecutive patients (age >18 years) who were referred to our institute between June 2012 and August 2016 to undergo CCTA for suspected CAD. Patients were excluded if they were undergoing cardiac CT for other indications (*e.g.*, assessment for trans-catheter aortic valve replacement or atrial fibrillation ablation). Patients were not pre-selected according to age, heart rate or body mass index (BMI).

CT scanner parameters

All examinations were performed on a 320-slice CT scanner with 320 mm × 0.5 mm detector rows giving

z-axis coverage of 160 mm (Aquilion One, Toshiba Medical Systems, Japan). After acquisition of scout images, prospective ECG-gated CCTA was performed using half-segment reconstruction and a 350 ms rotation time. Scanning field of view was selected based on scout images using volume sizes of 100-160 mm and radiographer led to be the smallest possible that included the area of clinical interest (20 mm below carina to base of heart). Iodinated contrast media-75 mL of Iohexol (Omnipaque 300 if BMI < 30 kg/m$^{2)}$, (Omnipaque 350 if BMI > 30 kg/m^2)-was injected in a biphasic protocol at 5 mL/s triggered by bolus tracking.

The Sure Cardio Prospective Package was used to reduce the exposure window depending on heart rate. For patients with a heart rate below 65 bpm, images were acquired with an acquisition window of 70%-80% of the interval between two consecutive QRS complexes. If patients had a heart rate below 60 bpm the acquisition window could be reduced further at the radiographer's discretion. Tube current and voltage were also minimised according to each patient's BMI and density, using the Sure Exposure 3D (SUREexposure, Toshiba Medical Systems, Japan) with an automatic exposure control system.

Unless contraindicated, patients received rate-limiting medication as required with an oral beta-blocker (atenolol 25 mg) followed by additional intravenous beta-blocker (metoprolol 5-25 mg) aiming for a heart rate below 65 bpm. All patients also received sublingual glyceryl trinitrate (300 μg).

The effective radiation dose for each patient was derived by multiplying the dose-length product (DLP), recorded from the CT scanner, by the conversion factor 0.014 mSv mGy^{-1} cm^{-1}, according to guidelines from the International Commission on Radiological Protection[8]. The effective radiation dose can then be compared to the lowest mean effective doses recorded in literature. In patients with repeated coronary CT angiography scans, the cumulative DLP and the cumulative effective dose were included in the analysis.

Image reconstruction and analysis

Images were reconstructed with a section thickness of 0.5 mm and an increment of 0.25 mm using the Adaptive Iterative Dose Reconstruction 3D (AIDR3D) algorithm. CCTA images were analyzed on a dedicated post-processing workstation by two trained observers. Subjective image quality was assessed by the two trained observers and scored on a four-point scale (4 = excellent, 1 = non-diagnostic). If any patients went on to undergo invasive coronary angiography then the accuracy of CCTA in determining the presence of significant coronary disease (stenosis > 50%) compared with the gold standard of invasive angiography was recorded.

RESULTS

CT data from a total of 543 consecutive patients who underwent CCTA for suspected CAD were assessed. A total of six patients were excluded from the evaluation due to failure to perform CCTA; four patients due to an inability to obtain intravenous access and two patients from incomplete dose data.

Table 1 summarises the characteristics of the 543 patients included in the final analysis. The mean age was 56 ± 11 years; and 33% were male. The mean body weight was 81 ± 18 kg and mean heart rate was 70 ± 11 bpm. Additional Ⅳ metoprolol was required in 47% of the scans. The presence of CAD was confirmed by CCTA in 57 (10%) of patients.

Radiation dose

The median DLP for all 543 patients was 61.45 mGy.cm (IQR, 42.86-100.00 mGy.cm) corresponding to a median effective dose of 0.88 mSv (IQR, 0.6-1.4 mSv). A total of 23 scans were repeated and whose cumulative radiation doses were thus included in the final median dose value. The frequency of the per-patient radiation dose, plotted in Figure 1, indicates a high positive skew with a Pearson coefficient of 3.26 from the normal distribution. This further demonstrates that the majority of patients received a very low dose of radiation and those that received a high dose were few in number.

A total of 328 (56%) patients received an effective dose < 1 mSv, 409 patients (75%) received an effective dose < 1.5 mSv. Moreover, we believe we have demonstrated the lowest ever-recorded effective dose for a CCTA performed in routine clinical practice of 0.18 mSv with a subjective image quality score of 4 (Figure 2).

Image quality

The mean image quality (± SD) for all 543 scans was 3.65 ± 0.61 with a corresponding score breakdown; excellent 392 (72%), good 118 (22%), poor but usable 30 (5%), and poor 3 (1%). We compared the patient characteristics of the excellent and good scans (image quality score 3 + 4) with those that were poor and unusable (image quality score 1 + 2). There was no difference in mean age or sex between the groups. However, compared with excellent and good scans, poor and unusable scans were more likely to occur in patients with heart rates > 65 bpm (31% *vs* 9%, P < 0.0001) and require a higher effective dose (1.98 ± 1.69 *vs* 1.24 ± 1.41, P = 0.0041) (Table 2).

Twenty-one of the patients underwent invasive coronary angiography in addition to CCTA yielding 84 coronary arteries for comparison (21 left main stem, 21 left anterior descending, 21 left circumflex and 21 right coronary artery). CCTA correctly identified a significant (> 50%) stenosis in 16/17 coronary arteries and correctly excluded significant stenosis in 62/67 coronary arteries. This gave CCTA a sensitivity of 94%, specificity 93%, negative predictive value 98% and positive predictive value 76% to identify a significantly (> 50%) stenosis coronary artery in comparison with the gold standard of

Table 1 Patient characteristics

Parameter		*n* (%)
Number of patients		543
Age (yr)		56 ± 11
Gender		Male/Female (33%/67%)
Mean weight (kg)		81 ± 18[1]
Mean heart rate (bpm)		70.3 ± 11.4
Oral Beta-blocker		204 (38)
Ⅳ Beta-blocker		255 (47)
Heart rate during scan (bpm)	< 60 bpm	349 (64)
	60-65 bpm	112 (21)
	65-75 bpm	55 (10)
	> 75 bpm	18 (3)
	Not recorded	11 (2)

[1]Weight data only available for 32% of the patients.

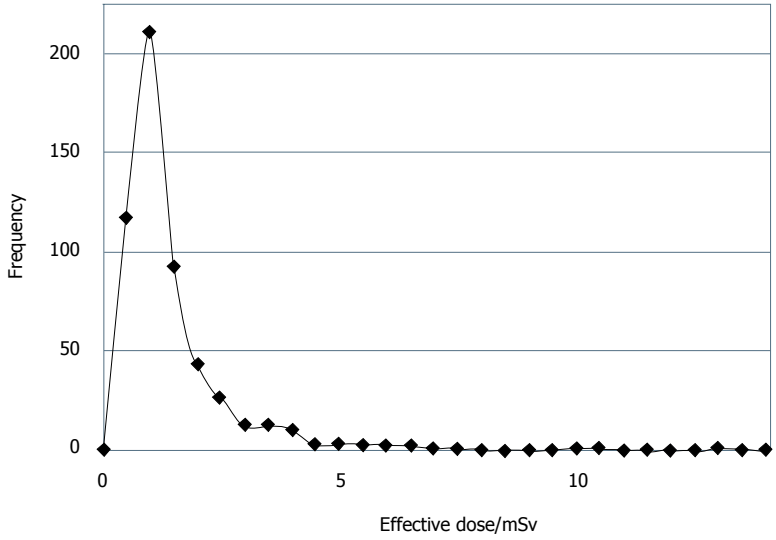

Figure 1 Distribution of effective doses for patients undergoing coronary computed tomography angiography.

invasive angiography. Examples of correct and incorrect CCTA classifications are provided in Figure 3.

DISCUSSION

We analyzed the CCTA data of 543 unselected consecutive patients with suspected CAD. The median effective radiation dose was 0.88 mSv (IQR, 0.6-1.4 mSv) with diagnostic image quality in 99% of patients, verifying that sub-millisievert radiation doses are possible in unselected, real-world patients undergoing CCTA.

A number of integrated strategies were used to achieve this consistently low dose, including; prospective ECG-gated acquisition, lowest possible tube current and voltage, IR (AIDR3D image reconstruction algorithm) and meticulous attention to patient preparation, both pre scan (heart rate control) and during the scan (reduction in volume of coverage to minimal size possible whilst allowing complete acquisition in a single volume.

Prospective ECG-gated tube current modulation is reported to be one of the most effective methods at reducing the radiation dose. Unlike traditional retrospective-gating, where data are acquired over the whole heart phase, in prospective gating the X-ray tube is switched on only at predefined time-points of the cardiac cycle. In their systematic review, Menke *et al*[9] confirmed a pooled effective dose of 3.5 mSv with prospective gating, a factor of 3.5 lower than the pooled effective dose of 12.3 mSv with retrospective gating.

Radiation dose increases with the square of the tube voltage at a constant tube current, reducing the tube voltage further lowers radiation exposure[10]. Tube current and voltage were minimised to each patient's BMI and density, using the Sure Exposure 3D (SUREExposure, Toshiba Medical Systems, Japan) with an automatic exposure control system which reduces tube current and voltage on the basis of scout images and the reconstruction kernel[11].

However, dose reduction by lowering tube voltage and current causes a substantial increase in noise, especially in obese patients[12]. To overcome these limitations and allow further dose reduction, new IR algorithms represent another milestone in CCTA[13]. IR algorithms

Table 2 Characteristics of patients with image quality scores of 1 + 2 *vs* 3 + 4

	Image quality score 1 + 2	Image quality Score 3 + 4	*P* value
Female patient	12/30 (63%)	216/391 (67%)	$P = 0.1068$
Mean age ± SD (years)	57.5 ± 10.5	55.5 ± 10.6	$P = 0.2979$
No. of patients with heart rate ≤ 65 bpm	22 (69%)	457 (91%)	$P < 0.0001$
No. of patients with heart rate > 65 bpm	10 (31%)	43 (9%)	$P < 0.0001$
Effective dose ± SD (mSv)	1.98 ± 1.69	1.24 ± 1.41	$P = 0.0041$

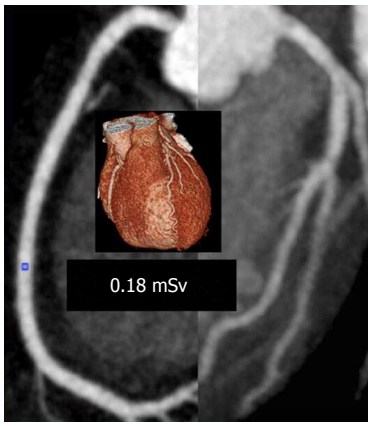

Figure 2 Coronary computed tomography angiography examination with image quality score 4 performed in a 52 years old female patient with heart rate of 56 bpm with a dose of 0.18 mSv.

adaptively apply noise correction at a reduced X-ray exposure without compromising spatial resolution[14]. AIDR and more recently 3D AIDR (AIDR3D) decreases image noise thus allowing for reductions in tube current while preserving overall image quality[15]. BMI-adapted tube voltage and current work synergistically with AIDR3D to reduce image noise while achieving a 75% radiation dose reduction relative to a scan reconstructed with filtered back-projection[16].

Patient irradiation is further limited by decreasing the craniocaudal field of view to the minimum required following analysis of the scout view[17]. The wide area detector row CT scanner can be used with less than the maximum 16 cm (320-detector) craniocaudal coverage. For example, imaging over a 14 cm (280 detectors) craniocaudal field of view will decrease patient dose by 12.5% and is proven sufficient for most patients[18].

The radiation dose with the 320-detector CT scanner is significantly lower if data acquisition occurs as a single volume[19]. To facilitate this we were judicious in our use of beta-blockers to slow the resting heart rate. Lowering the heart rate with beta-blockers has previously shown to be a safe practice[20], reducing radiation exposure and improving image quality[21]. We achieved comparable X-ray doses in our real world population to Chen *et al*[19] using a 320-detector CT scanner despite a slower gantry rotation speed (350 ms *vs* 275 ms due to the aggressive measures to control heart rate, with 65% of patients receiving betablockers [either oral only (15%), iv only (27%) or both (23%)] and 85% of patients achieving a heart rate < 65 bpm. Moreover, we have demonstrated what we believe is the lowest ever-recorded effective dose of 0.18 mSv with a subjective image quality score of 4 ("excellent") from a study of real-world unselected patients. This ultra-low radiation dose for CCTA is comparable to the radiation range reported for a chest X-ray in two views[22]. Advances in radiation dose reduction without compromising image quality justify the use of CCTA as a non-invasive alternative to coronary catheterization in investigating appropriate populations for CAD[23].

The prospective ECG-gated single volume acquisition with AIDR-3D protocol we use at our institution is not the only potential strategy for very low dose CCTA. Another contemporary strategy is Prospective ECG-triggered high-pitch spiral acquisition which also allows the entire heart to be scanned within one single cardiac cycle thus significantly lowering the radiation dose[24-26]. This coupled with IR techniques have shown ultra-low mean effective radiation doses ranging from 0.06 mSv to 0.3 mSv with clinically acceptable diagnostic images[7,27]. While demonstrating the feasibility of ultra-low dose CCTA, these studies were limited to carefully selected patents with a low and regular heart rate (< 60 bpm) and a body weight of less than 100 kg. Other IR algorithms are also in use including Model-based IR (MBIR, GE Healthcare, Waukesha, Wisconsin) which has also shown promising results for noise reduction in very-low-dose CCTA[22]. iDose4 and iterative model reconstruction are alternative IR algorithms released by Philips Healthcare (Philips Healthcare, Best, the Netherlands) that have also maintained image quality at 80% lower radiation exposure[13].

Our study has some limitations. Whilst we included all consecutive patients undergoing CCTA for the evaluation of suspected CAD we did not include cardiac CT performed for other indications such as evaluation of coronary bypass grafts, evaluation of left atrium anatomy prior to atrial fibrillation ablation, pre-operative assessment for trans-catheter aortic valve replacement or assessment of cardiac function so the same low doses may not be achieved in these patient groups. In addition, patients in atrial fibrillation were not included and whilst the patients were not selected on the basis

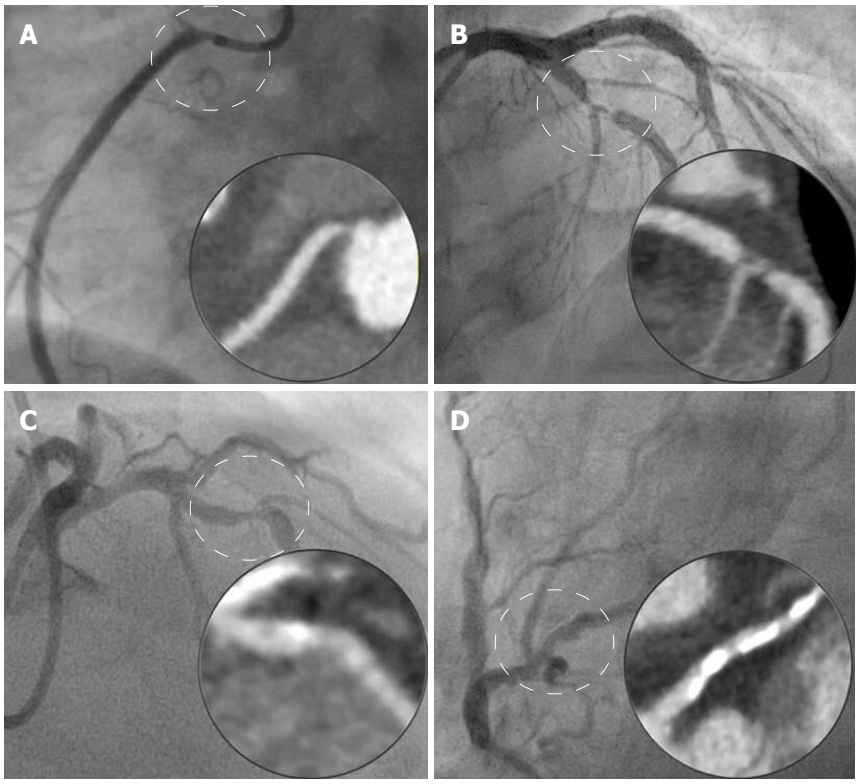

Figure 3 Examples of correlation of coronary computed tomography angiography with invasive angiography. A: Correct identification of ostial stenosis in right coronary; B: Correct identification of significant stenosis in left anterior descending coronary; C: Coronary computed tomography angiography (CCTA) incorrectly classifies lesion as not significant (subsequently proven to be haemodynamically significant with fractional flow reserve); D: CCTA incorrectly identifies a significant lesion in circumflex coronary due to artefact from extensive calcification.

of body weight, body mass index was not recorded and actual weight measurements were only available for 32% of the patients meaning the effect of patient weight on dose could not be investigated in this study. In view of this, the results may not be generalizable to patients who are overweight or in atrial fibrillation.

The image quality score used is a subjective assessment and was performed by the authors. Whilst the results of patients who underwent invasive coronary angiography are included, the proportion is relatively small and a more robust assessment of image adequacy would have been obtained if all patients had undergone the gold standard of invasive angiography.

Finally, the conversion factor to determine effective radiation dose equivalents has been a point of controversy[28]. Previous ICRP conversion factors for the chest have varied from 0.012-0.026 mSv mGy^{-1} cm^{-1} potentially yielding even lower radiation estimates[29].

CONCLUSION

We report a series of over 500 CCTAs performed at our health board with excellent image quality and median effective dose of 0.88 mSv. This includes the lowest ever-reported radiation dose for a routine clinical CCTA (0.18 mSv). We have demonstrated that provided patients are in sinus rhythm and with the judicious use of beta blockers to achieve heart rates < 65 bpm a combination of low-dose CCTA scan protocol and AID-R3D with a 320-detector row CT scanner can provide high quality images at exceptionally low radiation dose in patients being investigated for CAD.

ARTICLE HIGHLIGHTS

Research background

Traditionally, coronary angiography has been the gold standard in diagnosing coronary artery disease (CAD). Coronary computed tomography angiography (CCTA), however, is increasingly being used as a rapid and less invasive alternative in diagnosing patients at risk of CAD. A 3D image of the heart and coronary circulation can be rendered with a CT scanner using only an intravenous injection of iodine-rich contrast, thus circumventing the need for insertion of a catheter via an artery of vein. However, imaging coronary arteries presents increased challenges, since it requires both a high temporal resolution to reduce motion artifacts caused by cardiac motion and a high spatial resolution to differentiate small coronary structures. While images obtained with CCTA scanners are now comparable to coronary angiography these CT requirements have previously resulted in higher radiation doses thus increasing the lifetime risk of radiation-induced malignancy. Advances in CCTA scanner hardware and image reconstruction techniques have led to reports of exceptionally low radiation doses, down to 0.06 mSv, while maintaining diagnostic image quality of the coronary arteries. For example, in prospective electrocardiogram-gated acquisition the X-ray tube is switched on only for a reduced percentage of the cardiac cycle rather than the whole cycle. Automatic exposure control uses the lowest possible CT tube current and voltage adjusted to the patient's body habitus. This works in synergy with novel image IR algorithms that adaptively apply noise correction to offset an increase in image noise caused by a reduced tube voltage. Using pharmacological methods to reduce heart rate, with oral or intravenous beta-blockers, has proven to reduce cardiac motion during the acquisition leading to improved images. An initial

scout view of the thorax can also be used to minimize the volume covered per-patient in a single complete acquisition to further reduce the radiation. However, these previous studies were conducted on small cohorts that were pre-selected for low body weight and heart rate, and were limited by a low prevalence of CAD. The feasibility and effect of these low-dose scan modes on both image quality and radiation exposure in a large patient population with various heart rates is currently unknown. In this study, we determined the radiation dose and subjective image quality using a combination of state-of-the-art CCTA acquisition protocols at our institution in consecutive unselected patients undergoing CCTA for suspected coronary disease.

Research motivation

Ultra-low radiation doses of less than one mSv have been reported in other feasibility studies. While these advances in cardiac CT may effectively lower radiation dose, these studies are limited to small cohorts of pre-selected patients with very low and regular heart rates and low body habitus and are thus not representative of the typical population undergoing screening for CAD. This study aims to determine the feasibility of these low-dose CCTA acquisition protocols adopted at our institution in an unselected cohort from a series of consecutive patients who underwent CCTA for suspected CAD. We hope that the outcome may demonstrate that CCTA is a viable, non-invasive alternative to coronary catheterization for screening low-risk populations with suspected CAD.

Research objectives

The primary end points of the study were effective radiation dose and image quality in patients not selected in term of heart rate and body habitus undergoing routine CCTA. Our objective was to demonstrate that low radiation doses were feasible for the majority of real-world patients undergoing routine screening for CAD with CCTA without losing diagnostic image quality.

Research methods

The radiation dose and subjective image quality were analysed over a total of 543 consecutive patients in sinus rhythm who underwent CCTA at our institute for suspected CAD between June 2012 and August 2016. Subjective image quality was assessed by the two trained observers and scored on a four-point scale (4 = excellent, 1 = non-diagnostic). Images were acquired with a 320-row detector CT scanner (Aquilion One, Toshiba Medical Systems, Japan) and a number of integrated packages that have been developed to reduce the radiation dose to as low as reasonably achievable. Prospective electrocardiogram (ECG)-gated acquisition was implemented using the SURE Cardio Prospective Package over an acquisition window of 70%–80% of the interval between two consecutive QRS complexes in ppatients with a heart rate below 65 bpm. The Sure Exposure 3D package (SUREexposure, Toshiba Medical Systems, Japan) automatically adjusted to the lowest possible tube current and voltage in accordance with each patient's attenuation profile while noise reduction during each acquisition was implemented with the three-dimensional adaptive iterative dose reduction (AIDR-3D) image reconstruction algorithm. If necessary, patients were prepared prior to the scan with rate-limiting oral beta-blockers followed by additional intravenous beta-blocker to achieve a heart rate below 65 bpm unless contraindicated. During the scan, the volume of coverage was reduced to minimal size whilst allowing complete acquisition in a single volume. Contrary to previous studies in which the patients were prospectively selected, the patients were not selected based on age, heart rate, and body mass index. We believe that this is a better representation of real world patients who would be undergoing routine CCTA for diagnosis of CAD.

Research results

The median effective radiation dose was 0.88 mSv, which includes what we believe to be the lowest ever-reported radiation dose for a routine clinical CCTA (0.18 mSv). The mean image quality (± SD) was 3.65 ± 0.61, with a subjective image quality score of 3 ("good") or above for 93% of patient CCTAs. CAD was confirmed by CCTA in 57 (10%) of patients.

Research conclusions

The median effective radiation dose was 0.88 mSv (IQR, 0.6-1.4 mSv) with a mean subjective image quality score (± SD) of 3.65 ± 0.61 averaged over 500 real-world unselected patients undergoing routine clinical CCTA. This ultra-low radiation dose for CCTA is comparable to the radiation range reported for a chest X-ray in two views. The data also includes what we believe to be the lowest ever-reported radiation dose for a routine clinical CCTA 0.18 mSv with a subjective image quality score of 4 ("excellent"). This demonstrates that low radiation dose CCTA can be used as a routine clinical screening tool for CAD without loss of diagnostic image quality. To date, radiation dose reduction advances in CCTA technology have only been reported in feasibility studies on small cohorts of highly selected patients with low body habitus and heart rate. This study demonstrates that low radiation CCTA with good image quality is possible for most patients undergoing routine screening for CAD with CCTA using a combination of commercially available, state-of-the-art cardiac CT technology advances. CCTA is rapid and non-invasive compared with coronary angiography and has reduced patient recovery time. The reduced risk in radiation-induced malignancy implies that CCTA is a feasible alternative to coronary angiography as a primary screening tool for patients with low risk CAD.

Research perspectives

This study did not include patients with atrial fibrillation or other cardiac CT indications such as evaluation of coronary bypass grafts, evaluation of left atrium anatomy prior to atrial fibrillation ablation, pre-operative assessment for trans-catheter aortic valve replacement or assessment of cardiac function. Feasibility studies with alternative dose-saving strategies have also recorded ultra-low mean effective radiation doses ranging from 0.06 mSv to 0.3 mSv with clinically acceptable diagnostic images. These include techniques such as prospective ECG-triggered high-pitch spiral acquisition but again were limited to carefully selected patients. Extending these techniques to unselected patients could highlight the need for alternative protocols for undertaking routine CCTA for assessment of different patient groups or to incorporate existing technology at other institutions.

REFERENCES

1 **Salavati A**, Radmanesh F, Heidari K, Dwamena BA, Kelly AM, Cronin P. Dual-source computed tomography angiography for diagnosis and assessment of coronary artery disease: systematic review and meta-analysis. *J Cardiovasc Comput Tomogr* 2012; **6**: 78-90 [PMID: 22226727 DOI: 10.1016/j.jcct.2011.10.018]

2 **Haberl R**, Tittus J, Böhme E, Czernik A, Richartz BM, Buck J, Steinbigler P. Multislice spiral computed tomographic angiography of coronary arteries in patients with suspected coronary artery disease: an effective filter before catheter angiography? *Am Heart J* 2005; **149**: 1112-1119 [PMID: 15976796 DOI: 10.1016/j.ahj.2005.02.048]

3 **Hausleiter J**, Meyer T, Hermann F, Hadamitzky M, Krebs M, Gerber TC, McCollough C, Martinoff S, Kastrati A, Schömig A, Achenbach S. Estimated radiation dose associated with cardiac CT angiography. *JAMA* 2009; **301**: 500-507 [PMID: 19190314 DOI: 10.1001/jama.2009.54]

4 **Einstein AJ**, Henzlova MJ, Rajagopalan S. Estimating risk of cancer associated with radiation exposure from 64-slice computed tomography coronary angiography. *JAMA* 2007; **298**: 317-323 [PMID: 17635892 DOI: 10.1001/jama.298.3.317]

5 **Halliburton SS**, Abbara S, Chen MY, Gentry R, Mahesh M, Raff GL, Shaw LJ, Hausleiter J; Society of Cardiovascular Computed Tomography. SCCT guidelines on radiation dose and dose-optimization strategies in cardiovascular CT. *J Cardiovasc Comput Tomogr* 2011; **5**: 198-224 [PMID: 21723512 DOI: 10.1016/j.jcct.2011.06.001]

6 **Lell M**, Marwan M, Schepis T, Pflederer T, Anders K, Flohr T, Allmendinger T, Kalender W, Ertel D, Thierfelder C, Kuettner A, Ropers D, Daniel WG, Achenbach S. Prospectively ECG-triggered high-pitch spiral acquisition for coronary CT angiography using dual source CT: technique and initial experience. *Eur Radiol* 2009; **19**: 2576-2583 [PMID: 19760421 DOI: 10.1007/s00330-009-1558-4]

7 **Schuhbaeck A**, Achenbach S, Layritz C, Eisentopf J, Hecker F, Pflederer T, Gauss S, Rixe J, Kalender W, Daniel WG, Lell M, Ropers D. Image quality of ultra-low radiation exposure coronary CT angiography with an effective dose < 0.1 mSv using high-

pitch spiral acquisition and raw data-based iterative reconstruction. *Eur Radiol* 2013; **23**: 597-606 [PMID: 22983283 DOI: 10.1007/s00330-012-2656-2]
8 **Kalender WA**, Schmidt B, Zankl M, Schmidt M. A PC program for estimating organ dose and effective dose values in computed tomography. *Eur Radiol* 1999; **9**: 555-562 [PMID: 10087133 DOI: 10.1007/s003300050709]
9 **Menke J**, Unterberg-Buchwald C, Staab W, Sohns JM, Seif Amir Hosseini A, Schwarz A. Head-to-head comparison of prospectively triggered vs retrospectively gated coronary computed tomography angiography: Meta-analysis of diagnostic accuracy, image quality, and radiation dose. *Am Heart J* 2013; **165**: 154-163.e3 [PMID: 23351817 DOI: 10.1016/j.ahj.2012.10.026]
10 **Sabarudin A**, Sun Z. Coronary CT angiography: Dose reduction strategies. *World J Cardiol* 2013; **5**: 465-472 [PMID: 24392191 DOI: 10.4330/wjc.v5.i12.465]
11 **Sasdelli Neto R**, Nomura CH, Macedo AC, Bianco DP, Kay FU, Szarf G, Teles GB, Shoji H, Santana Netto PV, Passos RB, Chate RC, Ishikawa WY, Lima JP, Rocha MA, Marcos VN, Failla BB, Funari MB. Coronary computed tomography angiography with 320-row detector and using the AIDR-3D: initial experience. *Einstein* (Sao Paulo) 2013; **11**: 400-404 [PMID: 24136773 DOI: 10.1590/S1679-45082013000300025]
12 **Xu L**, Zhang Z. Coronary CT angiography with low radiation dose. *Int J Cardiovasc Imaging* 2010; **26** Suppl 1: 17-25 [PMID: 20058080 DOI: 10.1007/s10554-009-9576-5]
13 **Naoum C**, Blanke P, Leipsic J. Iterative reconstruction in cardiac CT. *J Cardiovasc Comput Tomogr* 2015; **9**: 255-263 [PMID: 26088375 DOI: 10.1016/j.jcct.2015.04.004]
14 **Padole A**, Ali Khawaja RD, Kalra MK, Singh S. CT radiation dose and iterative reconstruction techniques. *AJR Am J Roentgenol* 2015; **204**: W384-W392 [PMID: 25794087 DOI: 10.2214/AJR.14.13241]
15 **Shen H**, Dai G, Luo M, Duan C, Cai W, Liang D, Wang X, Zhu D, Li W, Qiu J. Image Quality and Radiation Dose of CT Coronary Angiography with Automatic Tube Current Modulation and Strong Adaptive Iterative Dose Reduction Three-Dimensional (AIDR3D). *PLoS One* 2015; **10**: e0142185 [PMID: 26599111 DOI: 10.1371/journal.pone.0142185]
16 **Williams MC**, Weir NW, Mirsadraee S, Millar F, Baird A, Minns F, Uren NG, McKillop G, Bull RK, van Beek EJ, Reid JH, Newby DE. Iterative reconstruction and individualized automatic tube current selection reduce radiation dose while maintaining image quality in 320-multidetector computed tomography coronary angiography. *Clin Radiol* 2013; **68**: e570-e577 [PMID: 23838086 DOI: 10.1016/j.crad.2013.05.098]
17 **Maurer MH**, Hamm B, Huppertz A, Lembcke A. Ultra-low-dose dual-source CT coronary angiography with high pitch: diagnostic yield of a volumetric planning scan and effects on dose reduction and imaging strategy. *Br J Radiol* 2015; **88**: 20140602 [PMID: 25710210 DOI: 10.1259/bjr.20140602]
18 **Rybicki FJ**, Otero HJ, Steigner ML, Vorobiof G, Nallamshetty L, Mitsouras D, Ersoy H, Mather RT, Judy PF, Cai T, Coyner K, Schultz K, Whitmore AG, Di Carli MF. Initial evaluation of coronary images from 320-detector row computed tomography. *Int J Cardiovasc Imaging* 2008; **24**: 535-546 [PMID: 18368512 DOI: 10.1007/s10554-008-9308-2]
19 **Chen MY**, Shanbhag SM, Arai AE. Submillisievert median radiation dose for coronary angiography with a second-generation 320-detector row CT scanner in 107 consecutive patients. *Radiology* 2013; **267**: 76-85 [PMID: 23340461 DOI: 10.1148/radiol.13122621]
20 **Roberts WT**, Wright AR, Timmis JB, Timmis AD. Safety and efficacy of a rate control protocol for cardiac CT. *Br J Radiol* 2009; **82**: 267-271 [PMID: 19098083 DOI: 10.1259/bjr/24574758]
21 **Dewey M**, Vavere AL, Arbab-Zadeh A, Miller JM, Sara L, Cox C, Gottlieb I, Yoshioka K, Paul N, Hoe J, de Roos A, Lardo AC, Lima JA, Clouse ME. Patient characteristics as predictors of image quality and diagnostic accuracy of MDCT compared with conventional coronary angiography for detecting coronary artery stenoses: CORE-64 Multicenter International Trial. *AJR Am J Roentgenol* 2010; **194**: 93-102 [PMID: 20028910 DOI: 10.2214/AJR.09.2833]
22 **Stehli J**, Fuchs TA, Bull S, Clerc OF, Possner M, Buechel RR, Gaemperli O, Kaufmann PA. Accuracy of coronary CT angiography using a submillisievert fraction of radiation exposure: comparison with invasive coronary angiography. *J Am Coll Cardiol* 2014; **64**: 772-780 [PMID: 25145520 DOI: 10.1016/j.jacc.2014.04.079]
23 **Moscariello A**, Takx RA, Schoepf UJ, Renker M, Zwerner PL, O'Brien TX, Allmendinger T, Vogt S, Schmidt B, Savino G, Fink C, Bonomo L, Henzler T. Coronary CT angiography: image quality, diagnostic accuracy, and potential for radiation dose reduction using a novel iterative image reconstruction technique-comparison with traditional filtered back projection. *Eur Radiol* 2011; **21**: 2130-2138 [PMID: 21611758 DOI: 10.1007/s00330-011-2164-9]
24 **Alkadhi H**, Stolzmann P, Desbiolles L, Baumueller S, Goetti R, Plass A, Scheffel H, Feuchtner G, Falk V, Marincek B, Leschka S. Low-dose, 128-slice, dual-source CT coronary angiography: accuracy and radiation dose of the high-pitch and the step-and-shoot mode. *Heart* 2010; **96**: 933-938 [PMID: 20538669 DOI: 10.1136/hrt.2009.189100]
25 **Litmanovich DE**, Tack DM, Shahrzad M, Bankier AA. Dose reduction in cardiothoracic CT: review of currently available methods. *Radiographics* 2014; **34**: 1469-1489 [PMID: 25310412 DOI: 10.1148/rg.346140084]
26 **Achenbach S**, Marwan M, Ropers D, Schepis T, Pflederer T, Anders K, Kuettner A, Daniel WG, Uder M, Lell MM. Coronary computed tomography angiography with a consistent dose below 1 mSv using prospectively electrocardiogram-triggered high-pitch spiral acquisition. *Eur Heart J* 2010; **31**: 340-346 [PMID: 19897497 DOI: 10.1093/eurheartj/ehp470]
27 **Hell MM**, Bittner D, Schuhbaeck A, Muschiol G, Brand M, Lell M, Uder M, Achenbach S, Marwan M. Prospectively ECG-triggered high-pitch coronary angiography with third-generation dual-source CT at 70 kVp tube voltage: feasibility, image quality, radiation dose, and effect of iterative reconstruction. *J Cardiovasc Comput Tomogr* 2014; **8**: 418-425 [PMID: 25439789 DOI: 10.1016/j.jcct.2014.09.003]
28 **Christner JA**, Kofler JM, McCollough CH. Estimating effective dose for CT using dose-length product compared with using organ doses: consequences of adopting International Commission on Radiological Protection publication 103 or dual-energy scanning. *AJR Am J Roentgenol* 2010; **194**: 881-889 [PMID: 20308486 DOI: 10.2214/AJR.09.3462]
29 **Gosling O**, Loader R, Venables P, Roobottom C, Rowles N, Bellenger N, Morgan-Hughes G. A comparison of radiation doses between state-of-the-art multislice CT coronary angiography with iterative reconstruction, multislice CT coronary angiography with standard filtered back-projection and invasive diagnostic coronary angiography. *Heart* 2010; **96**: 922-926 [PMID: 20538667 DOI: 10.1136/hrt.2010.195909]

P- Reviewer: Bazeed MF, Pastromas S, Stavroulopoulos A
S- Editor: Wang JL **L- Editor**: A **E- Editor**: Tan WW

Published by **Baishideng Publishing Group Inc**
7901 Stoneridge Drive, Suite 501, Pleasanton, CA 94588, USA
Telephone: +1-925-223-8242
Fax: +1-925-223-8243
E-mail: bpgoffice@wjgnet.com
Help Desk: http://www.f6publishing.com/helpdesk
http://www.wjgnet.com

ISSN 1949-8470 (online)

World Journal of *Radiology*

World J Radiol 2018 November 28; 10(11): 143-183

Published by Baishideng Publishing Group Inc

WJR World Journal of Radiology

Contents

Monthly Volume 10 Number 11 November 28, 2018

MINIREVIEWS

ORIGINAL ARTICLE

Retrospective Cohort Study

Retrospective Study

Contents

World Journal of Radiology

Volume 10 Number 11 November 28, 2018

ABOUT COVER

Editorial Board Member of *World Journal of Radiology*, Gang-Hua Tang, MD, PhD, Professor, Senior Scientist, Department of Nuclear Medicine, The First Affiliated Hospital, Sun Yat-Sen University, Guangzhou 510080, Guangdong Province, China

AIMS AND SCOPE

World Journal of Radiology (*World J Radiol*, *WJR*, online ISSN 1949-8470, DOI: 10.4329) is a peer-reviewed open access academic journal that aims to guide clinical practice and improve diagnostic and therapeutic skills of clinicians.

WJR covers topics concerning diagnostic radiology, radiation oncology, radiologic physics, neuroradiology, nuclear radiology, pediatric radiology, vascular/interventional radiology, medical imaging achieved by various modalities and related methods analysis. The current columns of *WJR* include editorial, frontier, diagnostic advances, therapeutics advances, field of vision, mini-reviews, review, topic highlight, medical ethics, original articles, case report, clinical case conference (clinicopathological conference), and autobiography.

We encourage authors to submit their manuscripts to *WJR*. We will give priority to manuscripts that are supported by major national and international foundations and those that are of great basic and clinical significance.

INDEXING/ABSTRACTING

World Journal of Radiology is now abstracted and indexed in Emerging Sources Citation Index (Web of Science), PubMed, PubMed Central, China National Knowledge Infrastructure (CNKI), and Superstar Journals Database.

NAME OF JOURNAL
World Journal of Radiology

ISSN
ISSN 1949-8470 (online)

LAUNCH DATE
January 31, 2009

FREQUENCY
Monthly

EDITORS-IN-CHIEF
Neeraj Lalwani, MBBS, MD, Associate Professor

EDITORIAL BOARD MEMBERS
https://www.wjgnet.com/1949-8470/editorialboard.htm

EDITORIAL OFFICE
Jin-Lei Wang, Director

PUBLICATION DATE
November 28, 2018

INSTRUCTIONS TO AUTHORS
https://www.wjgnet.com/bpg/gerinfo/204

GUIDELINES FOR ETHICS DOCUMENTS
https://www.wjgnet.com/bpg/GerInfo/287

GUIDELINES FOR NON-NATIVE SPEAKERS OF ENGLISH
https://www.wjgnet.com/bpg/gerinfo/240

PUBLICATION MISCONDUCT
https://www.wjgnet.com/bpg/gerinfo/208

ARTICLE PROCESSING CHARGE
https://www.wjgnet.com/bpg/gerinfo/242

STEPS FOR SUBMITTING MANUSCRIPTS
https://www.wjgnet.com/bpg/GerInfo/239

ONLINE SUBMISSION
https://www.f6publishing.com

World Journal of Radiology

Submit a Manuscript: https://www.f6publishing.com

World J Radiol 2018 November 28; 10(11): 143-149

DOI: 10.4329/wjr.v10.i11.143

ISSN 1949-8470 (online)

MINIREVIEWS

Review of the role of abdominal imaging in irritable bowel syndrome

Richard G Kavanagh, John O'Grady, Brian W Carey, Owen J O'Connor, Michael M Maher

ORCID number: Richard G Kavanagh (0000-0002-7483-0926); John O'Grady (0000-0002-6704-9277); Brian W Carey (0000-0002-6584-8032); Owen J O'Connor (0000-0002-0276-1335); Michael M Maher (0000-0001-7423-7439).

Author contributions: Kavanagh RG and Maher MM involved with study design, manuscript drafting and revising; O'Grady J and Carey BW involved with manuscript drafting and revising; O'Connor OJ involved with study design, data acquisition, manuscript drafting and revising; all authors given final approval to manuscript publication, and agreed to be accountable for all aspects of the work in ensuring that questions related to the accuracy or integrity of any part of the work are appropriately investigated and resolved.

Conflict-of-interest statement: The authors declare that there is no conflict of interest regarding the publication of this paper.

Manuscript source: Unsolicited

Richard G Kavanagh, Brian W Carey, Owen J O'Connor, Michael M Maher, Department of Radiology, Cork University Hospital, Cork T12 DC4A, Ireland

John O'Grady, Department of Gastroenterology, Cork University Hospital, Cork T12 DC4A, Ireland

John O'Grady, Owen J O'Connor, Michael M Maher, APC Microbiome Ireland, University College Cork, Cork T12 DC4A, Ireland

Abstract

The role of radiologic imaging in the investigation of irritable bowel syndrome (IBS) remains a subject of debate and there is some evidence, from recent studies of utilization of imaging in IBS, which focused on associated costs and radiation exposure, that imaging is being used relatively widely in these patients. This review aims to assess current best evidence to accurately define the role of radiologic imaging in IBS patients. Primary and secondary literature searches were performed. Evidence suggests that the lack of "red flag" or alarm features in IBS patients should reassure the clinician that the diagnosis of IBS is correct and United States and United Kingdom guidelines recommend no radiologic imaging for IBS patients if alarm features are not present. In patients presenting with IBS symptoms and alarm features, radiologic testing may be used to exclude an alternative diagnosis and the imaging modality should be chosen based on the most likely alternative diagnosis.

Key words: Abdominal imaging; Rome criteria; Irritable bowel syndrome

Core tip: Radiologic imaging in irritable bowel syndrome (IBS) remains contentious and the evidence guiding its use is limited. Recent studies indicate that imaging is being widely used in these patients. This review assesses current best evidence for the role of imaging in IBS. Primary and secondary literature searches were performed. The cornerstone of diagnosis remains the Rome criteria. Lack of "red flag" features in IBS patients should strengthen diagnosis of IBS and obviate the need for radiologic imaging. If red flag features are present, appropriate imaging may be used to exclude a suspected alternative diagnosis.

Kavanagh RG, O'Grady J, Carey BW, O'Connor OJ, Maher MM. Review of the role of abdominal imaging in irritable bowel syndrome. *World J Radiol* 2018; 10(11): 143-149
URL: https://www.wjgnet.com/1949-8470/full/v10/i11/143.htm

manuscript

Correspondence to: Brian W Carey, BM BCh, Assistant Lecturer, Department of Radiology, Cork University Hospital, Wilton, Cork T12 DC4A, Ireland.
brian_carey@ucc.ie
Telephone: +353-21-49020288

Received: July 14, 2018
Peer-review started: July 17, 2018
First decision: August 2, 2018
Revised: August 30, 2018
Accepted: October 9, 2018
Article in press: October 9, 2018
Published online: November 28, 2018

DOI: https://dx.doi.org/10.4329/wjr.v10.i11.143

INTRODUCTION

Irritable bowel syndrome (IBS) is a chronic functional gastrointestinal disorder (FGID) that is broadly characterized by recurrent abdominal pain and alterations in stool consistency or form[1]. Multinational expert groups in FGIDs have devised the Rome criteria, most recently Rome IV criteria, as a symptom-based diagnostic standard to diagnose IBS. Despite this, as IBS is associated with loss of work days and productivity and negatively impacts quality of life, it often remains a diagnosis of exclusion after invasive investigations are performed to rule out other specific pathology. Interestingly, a comparison of an exclusion approach to diagnosis of IBS, using investigations such as sigmoidoscopy, and a positive diagnostic approach using the Rome criteria, showed little differences in terms of patients' health-related quality of life in one Danish study of over 300 patients[2]. The positive diagnostic approach based on Rome criteria, was however, cheaper when compared to the exclusion approach. This study supports current guideline recommendations and suggests an unnecessary reliance on alternative diagnostic investigations.

Epidemiology

The worldwide prevalence of IBS is estimated to be 7%-10% with wide geographic variability[3]. In the United States the prevalence of IBS is estimated to be approximately 10% to 15%[4] and one large European prospective, population-based cohort study estimated prevalence of 15.4%[5]. IBS is less common in people older than 50 compared with those younger than 50 (OR 0.75)[6] and is more common in women compared with men (OR 1.67)[7]. IBS may be associated with a number of other disorders including fibromyalgia, depression, chronic fatigue syndrome, non-cardiac chest pain and anxiety[4]. There is conflicting evidence regarding IBS prevalence and socioeconomic status[6,8,9] and this relationship remains unproven.

Pathophysiology

That the diagnosis and management of IBS relies on clinical symptoms highlights that the pathophysiology remains incompletely understood. Initial research in the early 20th century utilizing direct visualization of the gastric mucosa in patients with gastrocutaneous fistulae provided the first scientific evidence that the gut is physiologically responsive to stressful emotional and environmental stimuli. Later studies showed that patients with IBS-type symptoms had an enhanced gastrointestinal motor response to various stimuli such as fatty meals, peptide hormones and psychological stressors and increased motility was sometimes associated with pain[10]. Recent advances in knowledge have, however, facilitated an increased understanding of the underlying disease processes, but it remains likely that there are multiple etiological factors involved. Those currently implicated in IBS symptom presentation include altered gastrointestinal motility, visceral hypersensitivity, post-infectious gastroenteritis, intestinal inflammation, altered gut microbiota, food sensitivity and interactions of the brain-gut axis[11]. IBS linked to brain-gut interactions is suggested by the association of IBS with anxiety, depression and other psychiatric conditions[1]. Furthermore, it is recognized that psychological stress exacerbates and exaggerates the symptoms of IBS and associated psychological and psychiatric co-morbidity negatively influence the patient experience of the condition[12]. Persistent post infectious gastroenteritis IBS-type symptoms are common in up to 20% of cases[1], and this is linked to an intestinal inflammatory etiology indicating an alternate pathogenesis to brain-gut interactions[13]. Further etiological factors for IBS development include alterations in gut microbiota and associated predisposing influences on both the microbiome and IBS symptoms including host genetics, stress, diet, antibiotic use and early life experiences[14]. Gut microbiota and their metabolites have notable influences on recognised IBS associations including the brain-gut axis, visceral hypersensitivity, gastrointestinal motility, intestinal barrier function and immune regulation[14]. Though causation is not established, the expanding science of the human gut microbiome and microbe-host interactions suggest gut microbial alterations play a key role in IBS pathophysiology[14]. These various pathophysiological factors may co-exist in the same patient, adding to the heterogeneity and complexity of understanding IBS and may, in part, explain the varying response to current symptom based treatments[15].

Diagnosis

The Rome criteria are criteria that were devised by expert consensus for the diagnosis of FGIDs; these criteria define multiple different FGID including IBS. The most recent iteration of these criteria is the Rome IV, released in 2016. The diagnostic criteria for IBS by the Rome IV criteria are as follows[16]: Recurrent abdominal pain, on average, at least one day per week in the last 3 mo associated with two or more of the following: Pain related to defecation; Associated with a change in frequency of stool; Associated with a change in form (appearance) of stool. The criteria should be fulfilled for the last 3 mo with symptom onset at least 6 mo before diagnosis.

By the Rome IV criteria, the IBS subtype is classified based on the predominant symptom of constipation or diarrhea as follows[16]: IBS with predominant constipation (IBS-C); IBS with predominant diarrhea (IBS-D); IBS with mixed bowel habits (IBS-M); IBS unclassified (IBS-U).

This classification is based upon the percentage of different stool types as defined by the Bristol stool scale. IBS-C is diagnosed if > 25% are stool type 1 and 2 and < 25% are stool type 6 and 7; IBS-D is diagnosed if < 25% are stool type 1 and 2 and > 25% are stool type 6 and 7; and IBS-M is diagnosed if > 25% are stool type 1 and 2 and > 25% are stool type 6 and 7. IBS-U is diagnosed if the patient meets diagnostic criteria for IBS but stool type cannot be accurately categorized into one of the other subtypes.

Assessment for alarm features should be performed in all patients that meet the diagnostic criteria for IBS[17]. The aim of identifying alarm features is to allow consideration of further investigations in patients with signs/symptoms of other possible underlying conditions such as colorectal/ovarian cancer and inflammatory bowel disease. Alarm features include the following[16,18,19]: New onset, or overt, rectal bleeding or melena; Nocturnal pain or diarrhea; Iron-deficiency anemia; Unexplained weight loss; Family history of colon cancer, ovarian cancer, celiac disease, IBD; Fever; Age of onset > 50 years; Severe or progressively worsening symptoms; Abdominal/pelvic/rectal mass or lymphadenopathy; Recent change in bowel habits.

Although the prevalence of alarm features is high in IBS patients[18] the sensitivity of alarm features in predicting organic disease in patients with typical symptoms of IBS is low. This may be due to the fact that besides celiac disease, which a large systematic review demonstrated is four times as prevalent in patients with IBS compared with the general population[20], the prevalence of underlying organic disease is the same in patients with IBS as in the general population[3]. However, certain alarm features such as weight loss and anemia do offer high specificity for organic disease and the American College of Gastroenterology (ACG) state that the absence of alarm features should reassure the clinician that the diagnosis of IBS is correct[3].

IBS burden of disease

IBS is a disease that is associated with significantly reduced health-related quality of life and impaired work productivity[3]. IBS patients utilize 50% more healthcare resources than matched controls without IBS and overall direct and indirect annual healthcare costs in these patients are estimated at $20 billion[3]. This increased cost can be attributed not only to increased medication use but also increased diagnostic testing and lost wages. In 1995, Talley *et al*[21] estimated the excess yearly direct healthcare cost of IBS in the United States to be $8 billion and extrapolating from that study, excess cost of approximately $800 million was estimated for radiology services in these patients. This highlights the importance of accurately defining the role of radiologic imaging in the investigation of patients presenting with IBS-type symptoms in order to rationalize the use of this expensive and, in certain jurisdictions, limited resource.

As well as increased costs, another concern regarding the over-utilization of radiologic diagnostic testing is the radiation exposure imparted as a result of plain radiography, nuclear medicine and CT imaging. Although there is evidence of significant costs associated with radiologic imaging in these patients there is a paucity of studies assessing radiation exposure in this patient group. Englund *et al*[22] demonstrated that over a 10-year period in Sweden, 149 IBS patients had a radiation exposure similar to that of a subgroup of patients with ulcerative colitis. A direct comparison of radiation exposure in IBS patients with that of the general population was not performed in this study so it is difficult to draw conclusions from these results. This result does, however, again demonstrate that radiologic imaging is still being used frequently in the investigation of patients with IBS.

ROLE OF RADIOLOGIC IMAGING IN IBS

The exact role of abdominal radiologic imaging in IBS remains poorly defined and

some studies suggest that imaging is being used relatively widely in this patient population[21,22]. There is a marked paucity of modern scientific studies regarding the appropriate use of imaging in this patient group[23].

In terms of international guidelines, the ACG state the following in their position statement on IBS[3] based on an evidence-based systematic review[24]: "Routine diagnostic testing with complete blood count, serum chemistries, thyroid function studies, stool for ova and parasites, and abdominal imaging is not recommended in patients with typical IBS symptoms and no alarm features because of a low likelihood of uncovering organic disease".

The ACG do recommend serological testing for celiac disease and colonoscopy in patients with alarm features and those over the age of 50 to assess for colorectal cancer. When colonoscopy is performed in patients with IBS-D, the ACG recommend random biopsies are taken to assess for microscopic colitis.

The United Kingdom National Institute for Health and Care Excellence (NICE) guidelines address the use of radiologic testing explicitly in their recommendations as follows[17]: "The following tests are not necessary to confirm diagnosis in people who meet the IBS diagnostic criteria: Ultrasound; Rigid/flexible sigmoidoscopy; Colonoscopy; barium enema; Thyroid function test; Faecal ova and parasite test; Faecal occult blood; Hydrogen breath test".

In an evidence-based review of the role of abdominal radiologic imaging in IBS by O'Connor *et al*[23] in 2012, the authors assessed that the best available evidence that included seven systematic reviews/guidelines and five primary research articles focusing on the use of barium enema and/or ultrasound. The authors concluded that radiologic imaging is not required in patients fulfilling the clinical diagnostic criteria for IBS if alarm symptoms are not present. The authors also concluded that further investigation should be considered in patients with alarm features and the appropriate modality should be chosen on a case-by-case basis and guided by the most likely alternative diagnosis and the American College of Radiology (ACR) Appropriateness Criteria. The lack of robust evidence and prospective studies regarding the role of abdominal radiologic imaging is noted in this review.

Since this review, several studies have used MRI to investigate IBS patients. These studies aimed to demonstrate differences in bowel response to food ingestion in IBS patients relative to healthy volunteers[25,26] and differences between the various IBS subtypes[27]. These studies suggest various sites of pathology to explain IBS symptoms but it is difficult to draw any firm conclusions from these studies due to small numbers and heterogeneous, and sometimes conflicting, results. No definitive role has been established for the routine use of MRI in the investigation of IBS and no studies have been performed to assess the performance of MRI relative to symptom-based diagnostic criteria.

In the setting of IBS patients that also demonstrate alarm features, further investigations should be guided by the most likely alternative diagnosis; this will often involve endoscopic assessment of the bowel but radiologic testing has a role in some circumstances. For example if a patient presents with signs/symptoms suggestive of colorectal cancer NICE guidelines recommend direct visualization with colonoscopy/sigmoidoscopy or CT colonography in patients unfit for colonoscopy. In the setting of a suspected ovarian neoplasm a pelvic ultrasound is the first investigation recommended by the ACR. In a patient with signs/symptoms suggestive of inflammatory bowel disease radiologic imaging studies (*e.g.*, CT or MR enterography) may be used to supplement findings on laboratory and endoscopic studies in order to establish a diagnosis[28].

CONCLUSION

There remains a paucity of robust evidence regarding the appropriate use of abdominal radiologic imaging in the setting of IBS and no modern prospective studies exist. Symptom-based diagnostic criteria have a high sensitivity and specificity for diagnosing IBS. Alarm symptoms are common in IBS patients but demonstrate low sensitivity for alternative organic pathology if diagnostic criteria for IBS are satisfied. Weight loss and anemia have a high specificity for underlying organic disease and in patients meeting diagnostic criteria without alarm features, clinicians should be reassured that the diagnosis of IBS is correct.

Based on the current best evidence, the diagnosis of IBS should be based on clinical findings using expert consensus diagnostic criteria (Rome IV criteria) supplemented by laboratory testing with no role for abdominal radiologic imaging in most patients. In patients presenting with IBS symptoms and alarm features, radiologic testing may be used to investigate for an underlying organic disease and the imaging modality

should be chosen based on the most likely alternative diagnosis (see Table 1 for practice guideline recommendations).

Table 1 Practice guideline recommendations

Patients fulfilling the Rome IV diagnostic criteria for IBS and who do not display "red flag" symptoms such as blood in stool, weight loss, recurrent fevers, anemia, and chronic severe diarrhea and who have no family history of colorectal cancer, inflammatory bowel disease, or celiac sprue do not require radiologic imaging
Radiologic imaging is required in patients with "red flag" symptoms who fulfill the Rome IV diagnostic criteria for IBS
Consideration of the probable alternative diagnosis and adherence to the relevant American College of Radiology Appropriateness Criteria should direct the optimal radiologic imaging of the patient with IBS

IBS: Irritable bowel syndrome.

REFERENCES

1 **Ford AC**, Lacy BE, Talley NJ. Irritable Bowel Syndrome. *N Engl J Med* 2017; **376**: 2566-2578 [PMID: 28657875 DOI: 10.1056/NEJMra1607547]
2 **Begtrup LM**, Engsbro AL, Kjeldsen J, Larsen PV, Schaffalitzky de Muckadell O, Bytzer P, Jarbøl DE. A positive diagnostic strategy is noninferior to a strategy of exclusion for patients with irritable bowel syndrome. *Clin Gastroenterol Hepatol* 2013; **11**: 956-62.e1 [PMID: 23357491 DOI: 10.1016/j.cgh.2012.12.038]
3 **American College of Gastroenterology Task Force on Irritable Bowel Syndrome**, Brandt LJ, Chey WD, Foxx-Orenstein AE, Schiller LR, Schoenfeld PS, Spiegel BM, Talley NJ, Quigley EM. An evidence-based position statement on the management of irritable bowel syndrome. *Am J Gastroenterol* 2009; **104** Suppl 1: S1-35 [PMID: 19521341 DOI: 10.1038/ajg.2008.122]
4 **Wald A**. Clinical manifestations and diagnosis of irritable bowel syndrome in adults. 2014; Available from: https://www.uptodate.com/contents/clinical-manifestations-and-diagnosis-of-irritable-bowel-syndrome-in-adults
5 **Krogsgaard LR**, Engsbro AL, Jones MP, Bytzer P. The epidemiology of irritable bowel syndrome: Symptom development over a 3-year period in Denmark. A prospective, population-based cohort study. *Neurogastroenterol Motil* 2017; 29 [PMID: 27865035 DOI: 10.1111/nmo.12986]
6 **Lovell RM**, Ford AC. Global prevalence of and risk factors for irritable bowel syndrome: a meta-analysis. *Clin Gastroenterol Hepatol* 2012; **10**: 712-721.e4 [PMID: 22426087 DOI: 10.1016/j.cgh.2012.02.029]
7 **Lovell RM**, Ford AC. Effect of gender on prevalence of irritable bowel syndrome in the community: systematic review and meta-analysis. *Am J Gastroenterol* 2012; **107**: 991-1000 [PMID: 22613905 DOI: 10.1038/ajg.2012.131]
8 **Zhu JZ**, Yan TL, Yu CH, Wan XY, Wang YM, Li YM. Is national socioeconomic status related to prevalence of irritable bowel syndrome? *J Gastroenterol Hepatol* 2014; **29**: 1595-1602 [PMID: 24888296 DOI: 10.1111/jgh.12609]
9 **Rey E**, Talley NJ. Irritable bowel syndrome: novel views on the epidemiology and potential risk factors. *Dig Liver Dis* 2009; **41**: 772-780 [PMID: 19665952 DOI: 10.1016/j.dld.2009.07.005]
10 **Drossman DA**. Functional Gastrointestinal Disorders: History, Pathophysiology, Clinical Features and Rome IV. *Gastroenterology* 2016; **pii**: S0016-5085(16)00223-7 [PMID: 27144617 DOI: 10.1053/j.gastro.2016.02.032]
11 **Occhipinti K**, Smith JW. Irritable bowel syndrome: a review and update. *Clin Colon Rectal Surg* 2012; **25**: 46-52 [PMID: 23449495 DOI: 10.1055/s-0032-1301759]
12 **Vanner S**, Greenwood-Van Meerveld B, Mawe G, Shea-Donohue T, Verdu EF, Wood J, Grundy D. Fundamentals of Neurogastroenterology: Basic Science. *Gastroenterology* 2016; **pii**: S0016-5085(16)00184-0 [PMID: 27144618 DOI: 10.1053/j.gastro.2016.02.018]
13 **Keely S**, Walker MM, Marks E, Talley NJ. Immune dysregulation in the functional gastrointestinal disorders. *Eur J Clin Invest* 2015; **45**: 1350-1359 [PMID: 26444549 DOI: 10.1111/eci.12548]
14 **Bhattarai Y**, Muniz Pedrogo DA, Kashyap PC. Irritable bowel syndrome: a gut microbiota-related disorder? *Am J Physiol Gastrointest Liver Physiol* 2017; **312**: G52-G62 [PMID: 27881403 DOI: 10.1152/ajpgi.00338.2016]
15 **Tanaka Y**, Kanazawa M, Fukudo S, Drossman DA. Biopsychosocial model of irritable bowel syndrome. *J Neurogastroenterol Motil* 2011; **17**: 131-139 [PMID: 21602989 DOI: 10.5056/jnm.2011.17.2.131]
16 **Mearin F**, Lacy BE, Chang L, Chey WD, Lembo AJ, Simren M, Spiller R. Bowel Disorders. *Gastroenterology* 2016; **pii**: S0016-5085(16)00222-5 [PMID: 27144627 DOI: 10.1053/j.gastro.2016.02.031]
17 National Institute for Clinical Excellence. Irritable bowel syndrome in adults: diagnosis and management. NICE guidelines [CG61] 2008. Available from: https://www.nice.org.uk/guidance/cg61/chapter/1-recommendations
18 **Black TP**, Manolakis CS, Di Palma JA. "Red flag" evaluation yield in irritable bowel syndrome. *J Gastrointestin Liver Dis* 2012; **21**: 153-156 [PMID: 22720303]
19 **Chey WD**, Kurlander J, Eswaran S. Irritable bowel syndrome: a clinical review. *JAMA* 2015; **313**: 949-958 [PMID: 25734736 DOI: 10.1001/jama.2015.0954]
20 **Ford AC**, Chey WD, Talley NJ, Malhotra A, Spiegel BM, Moayyedi P. Yield of diagnostic tests for celiac disease in individuals with symptoms suggestive of irritable bowel syndrome: systematic review and meta-analysis. *Arch Intern Med* 2009; **169**: 651-658 [PMID: 19364994 DOI: 10.1001/archinternmed.2009.22]
21 **Talley NJ**, Gabriel SE, Harmsen WS, Zinsmeister AR, Evans RW. Medical costs in community subjects with irritable bowel syndrome. *Gastroenterology* 1995; **109**: 1736-1741 [PMID: 7498636 DOI: 10.1016/0016-5085(95)90738-6]
22 **Englund H**, Lidén K K, Lind T, Sundström T, Karling P. Radiation exposure in patients with inflammatory bowel disease and irritable bowel syndrome in the years 2001-2011. *Scand J*

Gastroenterol 2017; **52**: 300-305 [PMID: 27832710 DOI: 10.1080/00365521.2016.1252945]
23 **O'Connor OJ**, McSweeney SE, McWilliams S, O'Neill S, Shanahan F, Quigley EM, Maher MM. Role of radiologic imaging in irritable bowel syndrome: evidence-based review. *Radiology* 2012; **262**: 485-494 [PMID: 22156992 DOI: 10.1148/radiol.11110423]
24 **Rosenblatt WH**, Cioffi AM, Sinatra R, Saberski LR, Silverman DG. Metoclopramide: an analgesic adjunct to patient-controlled analgesia. *Anesth Analg* 1991; **73**: 553-555 [PMID: 1952134]
25 **Undseth R**, Berstad A, Kløw NE, Arnljot K, Moi KS, Valeur J. Abnormal accumulation of intestinal fluid following ingestion of an unabsorbable carbohydrate in patients with irritable bowel syndrome: an MRI study. *Neurogastroenterol Motil* 2014; **26**: 1686-1693 [PMID: 25271767 DOI: 10.1111/nmo.12449]
26 **Pritchard SE**, Marciani L, Garsed KC, Hoad CL, Thongborisute W, Roberts E, Gowland PA, Spiller RC. Fasting and postprandial volumes of the undisturbed colon: normal values and changes in diarrhea-predominant irritable bowel syndrome measured using serial MRI. *Neurogastroenterol Motil* 2014; **26**: 124-130 [PMID: 24131490 DOI: 10.1111/nmo.12243]
27 **Lam C**, Chaddock G, Marciani Laurea L, Costigan C, Cox E, Hoad C, Pritchard S, Gowland P, Spiller R. Distinct Abnormalities of Small Bowel and Regional Colonic Volumes in Subtypes of Irritable Bowel Syndrome Revealed by MRI. *Am J Gastroenterol* 2017; **112**: 346-355 [PMID: 27958282 DOI: 10.1038/ajg.2016.538]
28 **Peppercorn MA**, Kane SV. Clinical manifestations, diagnosis and prognosis of Crohn disease in adults. 2014; Available from: https://www.uptodate.com/contents/zh-Hans/clinical-manifestations-diagnosis-and-prognosis-of-crohn-disease-in-adults

P- Reviewer: Mahajan A, Plataniotis G, Valek V
S- Editor: Ji FF **L- Editor:** A **E- Editor:** Huang Y

Published By Baishideng Publishing Group Inc
7901 Stoneridge Drive, Suite 501, Pleasanton, CA 94588, USA
Telephone: +1-925-2238242
Fax: +1-925-2238243
E-mail: bpgoffice@wjgnet.com
Help Desk: https://www.f6publishing.com/helpdesk
https://www.wjgnet.com

World Journal of Radiology

Submit a Manuscript: https://www.f6publishing.com

World J Radiol 2018 November 28; 10(11): 150-161

DOI: 10.4329/wjr.v10.i11.150

ISSN 1949-8470 (online)

ORIGINAL ARTICLE

Retrospective Cohort Study

Significance of an additional unenhanced scan in computed tomography angiography of patients with suspected acute aortic syndrome

Nikolaos Panagiotopoulos, Felix Drüschler, Martin Simon, Florian M Vogt, Sebastian Wolfrum, Steffen Desch, Doreen Richardt, Jörg Barkhausen, Peter Hunold

ORCID number: Nikolaos Panagiotopoulos (0000-0002-3029-9360); Felix Drüschler (0000-0001-9616-8665); Martin Simon (0000-0003-4187-4663); Florian M Vogt (0000-0002-3720-4010); Sebastian Wolfrum (0000-0001-6941-0030); Steffen Desch (0000-0002-9416-8044); Doreen Richardt (0000-0003-1398-8671); Jörg Barkhausen (0000-0001-8937-1198); Peter Hunold (0000-0003-4416-5934).

Author contributions: Hunold P, Vogt FM, Drüschler F designed research; Vogt FM, Drüschler F, Simon M, Hunold P acquired data; Panagiotopoulos N, Vogt FM, Drüschler F, Hunold P analyzed data; Panagiotopoulos N, Hunold P wrote the paper; Barkhausen J, Drüschler F, Simon M, Vogt FM, Wolfrum S, Desch S, Richardt D, Barkhausen J revised and approved final manuscript version

Institutional review board statement: The institutional review board of the University of Lübeck approved this study. This retrospective cohort study and all procedures performed involving human participants were in accordance with the ethical standards of the institutional review board and with the 1964 Helsinki declaration and its later amendments or comparable ethical standards.

Nikolaos Panagiotopoulos, Jörg Barkhausen, Peter Hunold, Clinic for Radiology and Nuclear Medicine, University Hospital Schleswig-Holstein, Campus Lübeck, Lübeck 23538, Germany

Felix Drüschler, Department of Nephrology, University Hospital, Heidelberg 69120, Germany

Martin Simon, Radiologische Allianz, Hamburg 20259, Germany

Florian M Vogt, Radiologie München, München 80331, Germany

Sebastian Wolfrum, Interdisciplinary Emergency Department, University Hospital Schleswig-Holstein, Campus Lübeck, Lübeck 23538, Germany

Steffen Desch, Department of Cardiology, Leipzig University, Heart Centre Leipzig, Leipzig 04289, Germany

Doreen Richardt, Department of Cardiac and Thoracic Vascular Surgery, University Hospital Schleswig-Holstein, Campus Lübeck, Lübeck 23538, Germany

Abstract

AIM

To assess potential benefits of an additional unenhanced acquisition in computed tomography angiography (CTA) in patients with suspected acute aortic syndrome (AAS).

METHODS

A total of 103 aortic CTA (non-electrocardiography-gated, 128 slices) performed due to suspected AAS were retrospectively evaluated for acute aortic dissection (AAD), intramural hematoma (IMH), or penetrating aortic ulcer (PAU). Spiral CTA protocol consisted of an unenhanced acquisition and an arterial phase. If AAS was detected, a venous phase (delay, 90 s) was added. Images were evaluated for the presence and extent of AAD, IMH, PAU, and related complications. The diagnostic benefit of the unenhanced acquisition was evaluated concerning detection of IMH.

RESULTS

Fifty-six (30% women; mean age, 67 years; median, 68 years) of the screened individuals had AAD or IMH. A triphasic CT scan was conducted in 76.8% (n = 43). 56% of the detected AAD were classified as Stanford type A, 44% as Stanford

Conflict-of-interest statement: None of the authors states a conflict of interest concerning firms and products reported in this study.

Data sharing statement: No additional data are available.

Manuscript source: Invited manuscript

Correspondence to: Peter Hunold, MD, Assistant Professor, Vice Chairman, Clinic for Radiology and Nuclear Medicine, University Hospital Schleswig-Holstein, Campus Lübeck, Ratzeburger Allee 160, Lübeck 23538, Germany. peterhunold@icloud.com
Telephone: +49-451-50017010
Fax: +49-451-50017004

Received: April 30, 2018
Peer-review started: April 30, 2018
First decision: June 14, 2018
Revised: August 30, 2018
Accepted: October 9, 2018
Article in press: October 9, 2018
Published online: November 28, 2018

type B. 53.8% of the detected IMH were classified as Stanford type A, 46.2% as Stanford type B. There was no significant difference in the involvement of the ascending aorta between AAD and IMH (P = 1.0) or in the average age between AAD and IMH (P = 0.548), between Stanford type A and Stanford type B in general (P = 0.650) and between Stanford type A and Stanford type B within the entities of AAD and IMH (AAD: P = 0.785; IMH: P = 0.146). Only the unenhanced acquisitions showed a significant density difference between the adjacent lumen and the IMH (P = 0.035). Subadventitial hematoma involving the pulmonary trunk was present in 5 patients (16%) with Stanford A AAD. The difference between the median radiation exposure of a triphasic (2737 mGy*cm) compared to a biphasic CT scan (2135 mGy*cm) was not significant (P = 0.135).

CONCLUSION
IMH is a common and difficult to detect entity of AAS. An additional unenhanced acquisition within an aortic CTA protocol facilitates the detection of IMH.

Key words: Aortic dissection; Acute aortic syndrome; Intramural hematoma; Pulmonary trunk subadventitial hematoma; Computed tomography angiography

Core tip: A computed tomography protocol in patients with suspected acute aortic syndrome should routinely include an unenhanced acquisition due to the added value in the detection of intramural hematoma.

Panagiotopoulos N, Drüschler F, Simon M, Vogt FM, Wolfrum S, Desch S, Richardt D, Barkhausen J, Hunold P. Significance of an additional unenhanced scan in computed tomography angiography of patients with suspected acute aortic syndrome. *World J Radiol* 2018; 10(11): 150-161
URL: https://www.wjgnet.com/1949-8470/full/v10/i11/150.htm
DOI: https://dx.doi.org/10.4329/wjr.v10.i11.150

INTRODUCTION

Acute aortic syndrome (AAS) is a life threatening condition that subsumes acute aortic dissection (AAD), intramural hematoma (IMH), and penetrating aortic ulcer (PAU)[1]. In-hospital mortality can be as high as 68% within the first 2 d after admission[2]. Recent advances in medical imaging and treatment have further emphasized the importance of rapid and accurate assessment of suspected AAS. In this emergency setting, computed tomography angiography (CTA) is today's benchmark modality[3]. Although detection of an IMH might profoundly influence therapeutic decision-making compared to classic AAD, it is often missed in CT scans of patients with AAS. Thus changes to the routinely performed biphasic CTA protocol with an arterial and a venous acquisition seem necessary. The aim of this study was therefore to assess the potential benefit of a CTA protocol that includes an additional unenhanced acquisition added to contrast-enhanced scans in the diagnostic pathway of patients with AAS. The focus was on the impact on the detectability of IMH in particular. Moreover, we aimed at working out the morphological characteristics of the different entities of AAS (*i.e.*, AAD, IMH, and PAU) as well as the prevalence of related complications (*e.g.*, aortic root subadventitial hematoma and branch vessel involvement).

MATERIALS AND METHODS

Study population

This retrospective cohort study was performed after approval by the institutional review board. CTA examinations of patients with clinically suspected AAS, who had been referred by the emergency department for aortic CTA, were screened. In the surveyed period of 33 mo, 103 aortic CTA scans had been conducted for the indication

of AAS in our radiological department.

Scan protocol

Scans were acquired at a 128-slice CT scanner (Somatom Definition AS+, Siemens Healthcare, Erlangen, Germany). No electrocardiography (ECG)-gating was used. Iodinated contrast agent (IMERON 300, Bracco Imaging, Milan, Italy) was applied by a contrast media injector (ohio tandem, Ulrich medical, Ulm, Germany) injecting 100 mL at a flow of 5 mL/s over an antecubital vein *via* a 18G cannula. We used a potentially triphasic CT protocol consisting of first an unenhanced spiral acquisition of the entire aorta. Secondly, an arterial CTA of the entire aorta was performed. Bolus timing was done using "care bolus" technique with the region of interest (ROI) within the ascending aorta with a threshold of 120 Hounsfield units (HU). If AAS was detected in the arterial phase, a venous phase scan was performed with a delay of 90 s after injection start. The scanning volume of all acquisitions reached from the aortic arch down to the groin.

Image analysis

CT images were digitally reviewed in a Picture archiving and communication system (PACS; IMPAX EE, Agfa HealthCare GmbH, Bonn). To visually delineate and locate AAD, IMH, PAU, and related complications predefined morphological criteria were applied. AAD was identified by findings like an intimal flap and a double lumen in the contrast-enhanced scans[4,5]. If present, the extent of dissection was determined and the Stanford classification system[6] was used according to involvement of the ascending aorta. Moreover, the true lumen of an AAD was distinguished from the false lumen by characteristic features as outer wall calcifications, differences in the caliber of the lumina, the beak sign or the cobweb sign. An essential part of the assessment of the false lumen was to identify a possible partial or total thrombosis by measuring the radiodensity of both lumina in predefined slices in the following regions of the aorta: (1) ascending aorta at the level of the main pulmonary artery; (2) aortic arch; (3) descending aorta at the level of the main pulmonary artery; (4) abdominal aorta at the level of the superior mesenteric artery origin; and (5) abdominal aorta above the bifurcation.

In AAD, radiodensity of both lumina in all acquired phases was measured by placing and adjusting a ROI into the true and false lumen respectively. The radiodensity was recorded as the mean value for each region and phase in HU. In a second step, the discrepancy in density between the true and false lumen was calculated for each region and phase, separately.

Likewise, morphological criteria were applied to identify an IMH. These lesions feature a crescentic, high-attenuating (60-70 HU) region of thickening of the aortic wall on non-contrast CT. The lesions apparently exhibit no enhancement in relation to the aortic lumen on contrast-enhanced scans. An intimal flap is not present. Analogously to AAD, the Stanford classification system was used to classify IMH. Its radiodensity was measured and the discrepancy in density between the wall hematoma and the aortic lumen was calculated and processed for each region and phase separately. The extent or amount of complications related to AAD or IMH like dissections and occlusions of branch vessels, ischemia of abdominal organs, aneurysmal dilatation, aortic rupture, and aortic root subadventitial hematoma were studied in this work as well. The ten evaluated branch vessels were: (1) brachiocephalic trunk; (2) left common carotid artery; (3) left subclavian artery; (4) celiac trunk; (5) superior mesenteric artery; (6) inferior mesenteric artery; (7) renal arteries, left and right; and (8) common iliac arteries, left and right.

For every scan the radiation exposure was measured by the CT dose-length product (DLP; in mGy*cm) which was found in the corresponding DICOM-Header. Gender and age of the study patients was stored and processed.

Statistical analysis

All data were first collected on standardized and anonymized data collection sheets and later transferred into an Excel-file (Microsoft Corporation, Redmond, United States) and SPSS (IBM, Armonk, United States) for statistical analysis. Prior to the comparison of continuous variables in different groups, chi-square test was used to confirm or rule out normal distribution. Since all of the tested groups revealed non-Gaussian distribution, the non-parametric Mann-Whitney *U* test was used to evaluate differences. $P < 0.05$ was considered to indicate statistical significance.

RESULTS

Study cohort

One-hundred-three patients had been diagnosed with aortic dissection or IMH. After the exclusion of those individuals who had chronic aortic dissection (n = 9) or a history of aortic surgery (n = 38) the resulting study cohort consisted of 56 individuals with first diagnosis of AAS (19 women; mean age 66.6 years, range 35-88 years, Figure 1 and Table 1). Among all patients diagnosed with AAS, 76.8% of patients were diagnosed with AAD compared to 23.2% with IMH. PAU was not found in our cohort. There was no significant percentage-difference of Stanford classification between AAD and IMH (P = 1). Age between AAD and IMH patients (P = 0.548) as well as between Stanford A and B (P = 0.650) patients did not differ significantly (Table 1).

Radiation dose

Radiation exposure as well as the share the unenhanced acquisition adds to the examination is depicted in Table 2. There was a higher mean radiation exposure of triphasic (2737.2 mGy*cm) compared to biphasic CT scans (2134.6 mGy*cm).

Characterization of dissection and IMH

Extent and boundaries: Two data sets were excluded as the distal boundary of the AAD/IMH was not within the scan volume. In 31.5%, AAD and IMH were limited to the thoracic aorta. In contrast to IMH, which never involved the iliac arteries, AAD extended into the iliac arteries in 36.6% (Figure 2). Anatomic features such as kinking of the aorta, aortic bifurcation or aneurysm detained a distal progression of AAD and IMH in 41.5% and 53.8%, respectively (P = 0.528, Figure 3).

True and false lumen: In Stanford A AAD, in 95.8% the false lumen was located in the dextrolateral quadrant of the ascending aorta. Stanford A IMH was most frequently found in the sinistrolateral quadrant (57.1%). In the aortic arch, the false lumen and IMH mainly involved the anterior, caudal and posterior quadrant, less frequently they involved the ostia of the supraaortic branches. In Stanford A AAD, the false lumen of the descending thoracic and suprarenal abdominal aorta was predominantly present in the sinistrolateral and dorsal quadrant. In Stanford B AAD, there was only a slight predominance for the dorsal and dextrolateral quadrant. At the level of the renal arteries the false lumen was more often found on the right than the left side (right: Stanford A: 73.9%; Stanford B: 52.6%; left: A: 30.4%; B: 42.1%). In the infrarenal portion of the aorta, there was no significant difference in the position of the false lumen between Stanford A and B (dextroposterior). In the descending thoracic and abdominal aorta, IMH showed no predominance of location.

Involvement of branch vessels: Six data sets were excluded as an assessment of all ten predefined branch vessels was not possible. Branch vessel involvement was only 38.5% in IMH compared to 75.7% in AAD (P = 0.012). In 46% at least two branch vessels and in 20% at least four branch vessels were involved. In 34% there was no branch vessel and in one case (2%) seven branch vessels affected. In AAD there were a total of 225 branch vessels involved (A: 137; B: 88). 131 vessels originated from the true lumen [A: 69 (50.4%); B: 62 (70.5%)], 34 vessels from the false lumen [A: 27 (19.7%); B: 7 (8.0%)], and 60 vessels were supplied by both lumina [A: 41 (29.9%); B: 19 (21.6%)]. Branches that were supplied by the false lumen were patent in 23 cases [A: 19 (70.4%); B: 4 (57.1%)], partly thrombosed in 7 cases [A: 6 (22.2%); B: 1 (14.3%)] and occluded in 4 cases [A: 2 (7.4%); B: 2 (28.6%)]. Branches that were supplied by both the true and the false lumen were patent in 45 cases [A: 30 (73.2%); B: 15 (78.9%)], partly thrombosed in 6 cases [A: 5 (12.2%); B: 1 (5.3%)] and occluded in 9 cases [A: 6 (14.6%); B: 3 (15.8%)]. The brachiocephalic trunk was the vessel most often involved (57.2%). In Stanford A dissections involvement of the coeliac trunk and the superior mesenteric artery was more commonly seen than in Stanford B dissections (A: 38.5%, B: 26.7%; A: 41.7%, B: 13.3%; respectively). By tendency, renal artery involvement was more often present at the left side (A: 63.7%, B: 35.7%) compared to the right side (A: 36.4%, B: 28.6%), (P = 0.424).

Density measurements

In the arterial phase the radiodensity of the patent false lumen of the thoracic aorta was comparable to that of the true lumen, while in the abdominal aorta the radiodensity in the patent false lumen was lower (on average more than 100 HU difference) than in the true lumen (Figure 4 and Figure 5). In the unenhanced and venous acquisitions 241 the radiodensity of the patent false lumen was comparable to that of the true lumen. A false lumen thrombosis resulted in higher radiodensity in the false lumen for the unenhanced acquisitions and lower densities in the arterial and venous phases. IMH had a lower radiodensity compared to the vessel lumen within the arterial and venous phases. In the unenhanced acquisition the radiodensity of the

Table 1 Stanford classification, age and gender distribution

	AAD			IMH		
n (%)	43 (76.8)			13 (23.2)		
mean age (yr)	66 ± 12			69 ± 10		
	Stanford A	Stanford B	A *vs* B	Stanford A	Stanford B	A *vs* B
	55.8%	44.2%		53.8%	46.2%	
mean age (yr)	66 ± 11	67 ± 13	$P = 0.785$	65 ± 10	75 ± 13	$P = 0.146$
Female	41.7%	10.5%	$P = 0.039$	28.6%	50%	

There is no significant difference in the age distribution between Stanford A and B within the entities of acute aortic dissection (AAD) and intramural hematoma. Though, in AAD there is a significant difference in the gender distribution between Stanford A and B dissections. Females showed a significantly higher percentage of type A than type B AAD. AAD: Acute aortic dissection; IMH: Intramural hematoma.

IMH was higher than the adjacent lumen in any of the regions of the aorta in which it occurred (Figure 6). Differences in radiodensity between true lumen and IMH as well as true lumen and thrombosed false lumen, respectively, were only significant in the unenhanced acquisition ($P = 0.035$).

Complications and secondary findings

Table 3 summarizes complications and secondary findings. Subadventitial hematoma involving the pulmonary trunk was present exclusively in patients with Stanford A lesions. It was found in 5 patients, *i.e*. in 16.1% of Stanford A lesions. In these patients pericardial effusion was present in 80%. In two cases there was pulmonary hemorrhage present. The subadventitial hematoma was hypodense in contrast enhanced scans compared to the lumen of the vessel (average HU differences arterial: 436 HU, venous 109 HU) while in non-contrast scans it was hyperdense (average HU difference -13 HU).

Pericardial effusion was significantly more frequent in Stanford A lesions ($P = 0.011$). There was no significant difference in the occurrence of pleural effusion/hemothorax between Stanford A and B ($P = 0.357$). Abdominal aortic aneurysm was more frequent in Stanford B dissections (66.7%). Bleeding or rupture occurred in four Stanford B cases. Although less frequent in IMH, branch vessel involvement was the most frequent complication with 66% in total. Ischemia of abdominal organs was found in 18.2% with kidneys being the most often affected (12.5%).

DISCUSSION

When contemplating the assumption that a multiphasic CTA protocol adding a non-enhanced acquisition significantly improves the detectability of AAD and IMH there is the dimension of fast and accurate visualization and that of radiation protection that has to be evaluated. In this respect, this study shows that the radiodensity of the true lumen and the false lumen of AAD do not differ significantly in contrast-enhanced scans. On the contrary, unenhanced acquisitions featured a high-attenuating region of thickening of the aortic wall with a significant density difference between the IMH and the adjacent lumen in the range of 5 HU up to 21 HU for all examined regions of the aorta. A differentiation between IMH and a thrombosed false lumen was possible due to the significantly higher contrast between IMH and adjacent lumen compared to thrombotic material and adjacent lumen ($P = 0.035$). While the mere figures might seem rather small, the reason for the resulting critical improvement in the visualisation of the potentially life-threatening entity IMH can be found in the way windowing is possible if no contrast agent is used. By lowering the window level and narrowing the window width, the interpreting physician is able to zero in on those aspects that are of diagnostic value. While the arterial phase is essential for the delineation of pathognomonic findings like an intimal flap and a double lumen[7] and the venous acquisitions facilitate the assessment of the patency of the false lumen as well as a possible ischemia of the abdominal organs, adding an unenhanced acquisition of the thoracic aorta should be used whenever an AAS is suspected. In this study we were able to identify 13 IMH and 5 aortic root subadventitial hematomas and to distinguish both these entities from a false lumen thrombosis. This would not have been possible without the data of the unenhanced scan. The diagnosis of an IMH might profoundly influence the therapeutic decision-

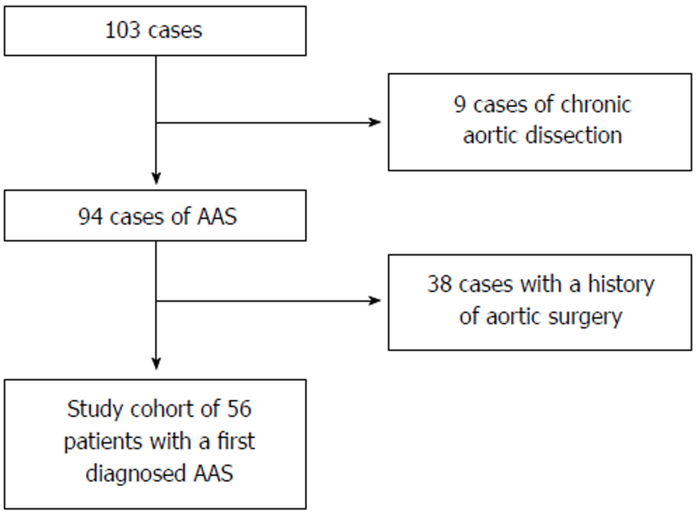

Figure 1 Selection process of the study cohort. After the exclusion of chronic dissections and patients with a history of aortic surgery, 56 cases made up the study cohort of individuals with a newly diagnosed acute aortic syndrome. AAS: Acute aortic syndrome.

making compared to classic aortic dissection. First of all, IMH has a higher rate of rupture as compared to AAD[8]. Research groups around the world have argued about the right treatment of IMH. According to Tsai *et al*[9], similar to Stanford type A and B aortic dissection, surgery is advocated in patients with Stanford type A IMH and initial medical therapy in patients with type B IMH. On the contrary, a study conducted by Song *et al*[10] showed acceptable outcomes of a policy of urgent surgery for unstable Stanford type A IMH patients and initial medical treatment for stable patients with surgery for complications. In 2014 the European Society of Cardiology issued a guideline[11]. In accordance with this guideline, "emergency surgery of IMH is indicated in complicated cases with pericardial effusion (in this study present in type A: 71.4%, B: 0%), periaortic hematoma (in this study present in: type A: 42.9%, B: 0.0%), or large aneurysms [in this study present in (AAA): type A: 0.0%, B: 50.0%]. Surgery within 24 h after diagnosis is required in most of Stanford type A IMH. In elderly patients or those with significant comorbidities, initial medical treatment may be a reasonable option. Medical treatment is the initial approach to Stanford type B IMH. Endovascular therapy or surgery has the same indications as type B aortic dissection. While there might still be debate about the treatment that is clinically indicated if an IMH is detected, the importance of a rapid and accurate detection and assessment of potentially life-threatening complications is out of doubt. Nonetheless the ALARA principle ("as low as reasonably achievable") dictates a limitation of the patients' radiation exposure. Our data indicate that adding an unenhanced acquisition to a biphasic CT scan does, as expected, increase the radiation exposure, but to a moderate degree of only 22% to the total radiation dose. Therefore the risk of overlooking an IMH or aortic root subadventitial hematomata seems to be grossly disproportionate to the benefit of a reduction in radiation exposure. In our opinion the added radiation dose of a triphasic protocol is reasonable and can easily be justified. The data of this study substantiate the common perception that an IMH is a more circumscript thoracic pathology that rarely affects the abdominal aorta. This finding allowed us to further adjust our CTA protocol and operating procedures in a way that reduces the patients' radiation exposure while maintaining most of the benefits the unenhanced acquisition offers. In cases in which there is no clinical suspicion of an abdominal involvement we now limit the unenhanced scan to the thoracic aorta, lowering the radiation exposure.

The 56 cases diagnosed with AAS would translate into an incidence of about 8.9/100000 a year if the population of Lübeck[12] is regarded as the hinterland of our department of radiology and nuclear medicine. This figure is considerably higher than the 2.9/100000/year incidence found in literature[2].

Studies based on the International Registry of Acute Aortic Dissections have found about 6.3% of AAS to be IMH[13]. In our cohort the prevalence was as high as 23.2%. This discrepancy partly originates from the study design and the selection process of the study cohort which excluded about 46% of patients with AAS because of a chronic aortic dissection or a history of aortic surgery. As many IMH evolve into an AAD

Table 2 Radiation exposure as measured by the computed tomography dose-length product

	DLP [mGy*cm]		
	Mean	Min	Max
Triphasic CT scan (unenhanced, arterial and venous)	2737.2	1583.0	4476.9
Biphasic CT scan (arterial and venous)	2134.6	766.2	3494.7
Unenhanced acquisition (percentage of a triphasic CT scan)	602.6 (22.0%)		

Adding an unenhanced acquisition to a biphasic computed tomography (CT) scan does, as expected, increase radiation exposure, however to a moderate degree. On average the unenhanced acquisition contributes only about 22% to the total radiation dose of a triphasic CT scan. DLP: Dose-length product.

there might be a selection bias due to the small study cohort as well. However, one might also suggest that IMH has often been overseen if the utilized CTA protocol misses a focus on detection of even small IMH. Therefore, adding an unenhanced scan to the CTA is suggested.

Limitations

Although the screened cohort of 868 individuals was sizable, the resulting study cohort on which our data is based (n = 56) is not. The small size of this retrospective cohort study limits the generalizability of the results. A further limitation of this work can be found in the definition of branch vessel involvement. A branch vessel involvement was defined as an intimal flap or a hematoma that extended into the branch or alternatively the sole perfusion by false lumen. This definition leaves out any type of dynamic obstruction. Nonetheless, we believe that this study offers some motivational thoughts and descriptions of clinical relevance.

Table 3 Complications and secondary findings *n* (%)

	Total	AAD		IMH	
		Stanford A	Stanford B	Stanford A	Stanford B
Subadventitial hematoma of pulmonary trunk	5 (9.1)	2 (8.3)	0	3 (42.9)	0
Pericardial effusion	20 (35.7)	11 (45.8)	4 (21.1)	5 (71.4)	0
Pleural effusion	14 (25.0)	4 (16.7)	6 (31.6)	2 (28.6)	2 (33.3)
Abdominal aortic aneurysm (AAA)	17 (32.1)	2 (8.7)	12 (66.7)	0	3 (50.0)
Bleeding/rupture	4 (7.1)	0	3 (15.8)	0	1 (16.7)
Branch vessel involvement	33 (66.0)	17 (81.0)	12 (70.6)	3 (50.0)	1 (16.7)
Ischemia	10 (18.2)	5 (20.8)	4 (22.2)	1 (14.3)	0
Kidney	7 (12.5)	4 (16.7)	3 (15.8)	0	0
Liver	2 (3.6)	1 (4.2)	1 (5.3)	0	0
Spleen	3 (5.5)	0	2 (11.1)	1 (14.3)	0
Intestine	1 (1.8)	0	1 (5.3)	0	0

Branch vessel involvement was the most frequent complication. Subadventitial hematoma involving the pulmonary trunk was present exclusively in patients with Stanford A lesions. Pericardial effusion was significantly more frequent in Stanford A lesions. AAD: Acute aortic dissection; IMH: Intramural hematoma.

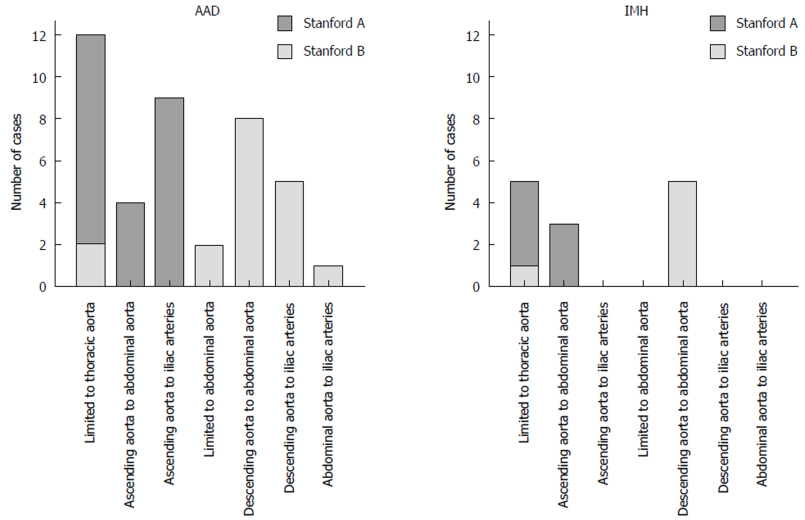

Figure 2 Extent of dissection and intramural hematoma. Nearly one third of acute aortic syndrome was limited to the thoracic aorta. There was no case in which the intramural hematoma extended into the iliac arteries. AAD: Acute aortic dissection; IMH: Intramural hematoma.

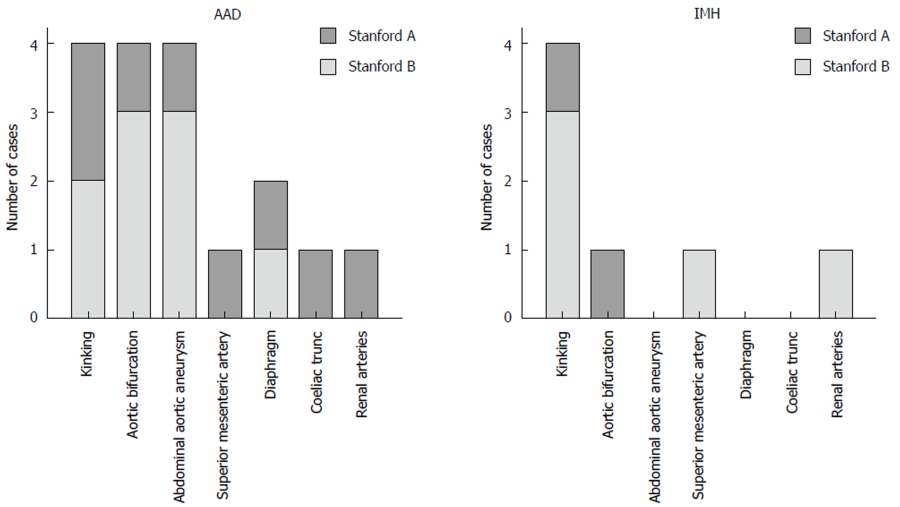

Figure 3 Boundaries of acute aortic dissection and intramural hematoma. Anatomic features detain a distal progression of acute aortic dissection and intramural hematoma. AAD: Acute aortic dissection; IMH: Intramural hematoma.

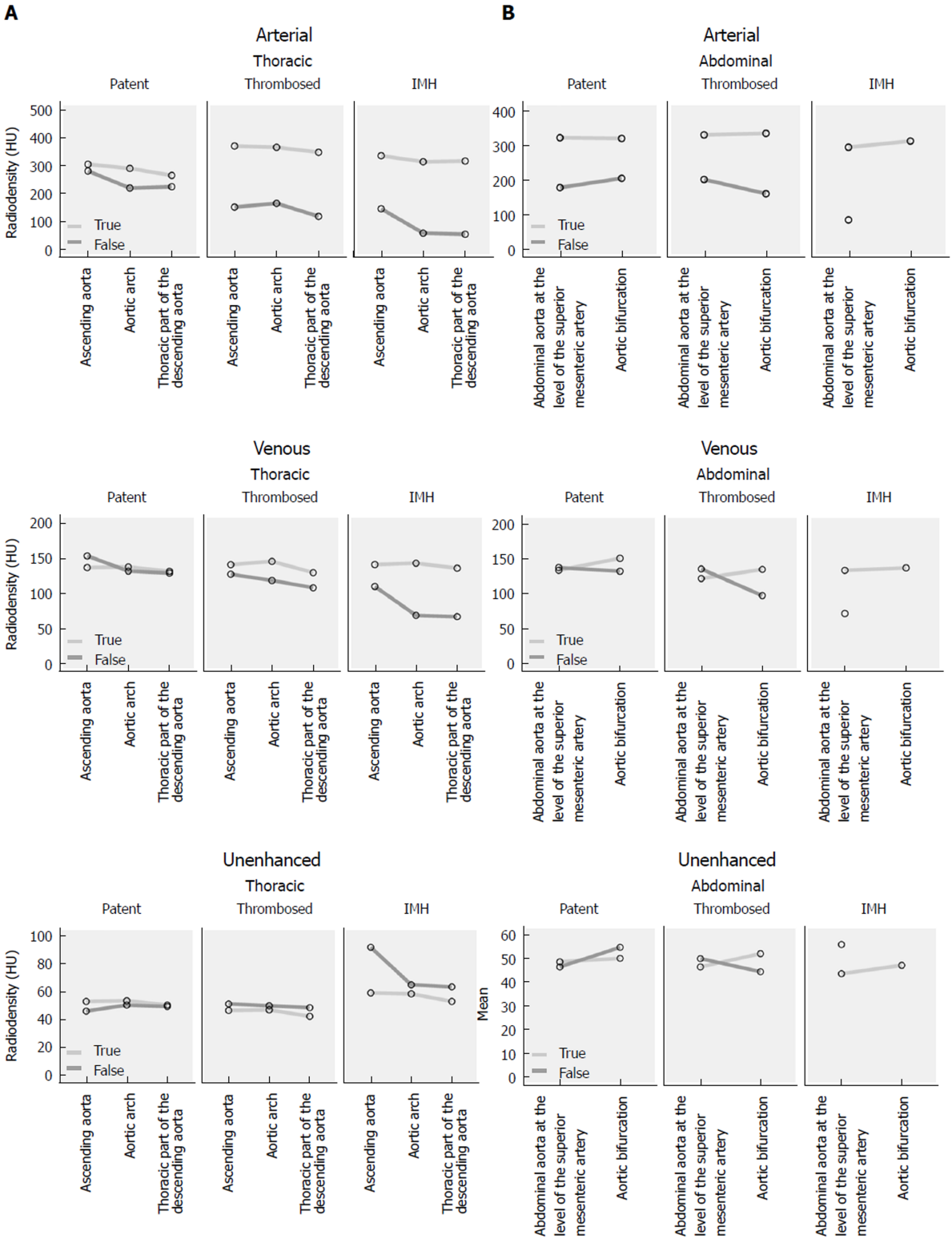

Figure 4 Density measurements, absolute values. Absolute values of the density measurements in true and false lumen/intramural hematoma in arterial, venous and unenhanced phase of (A) thoracic and (B) abdominal aorta. IMH: Intramural hematoma.

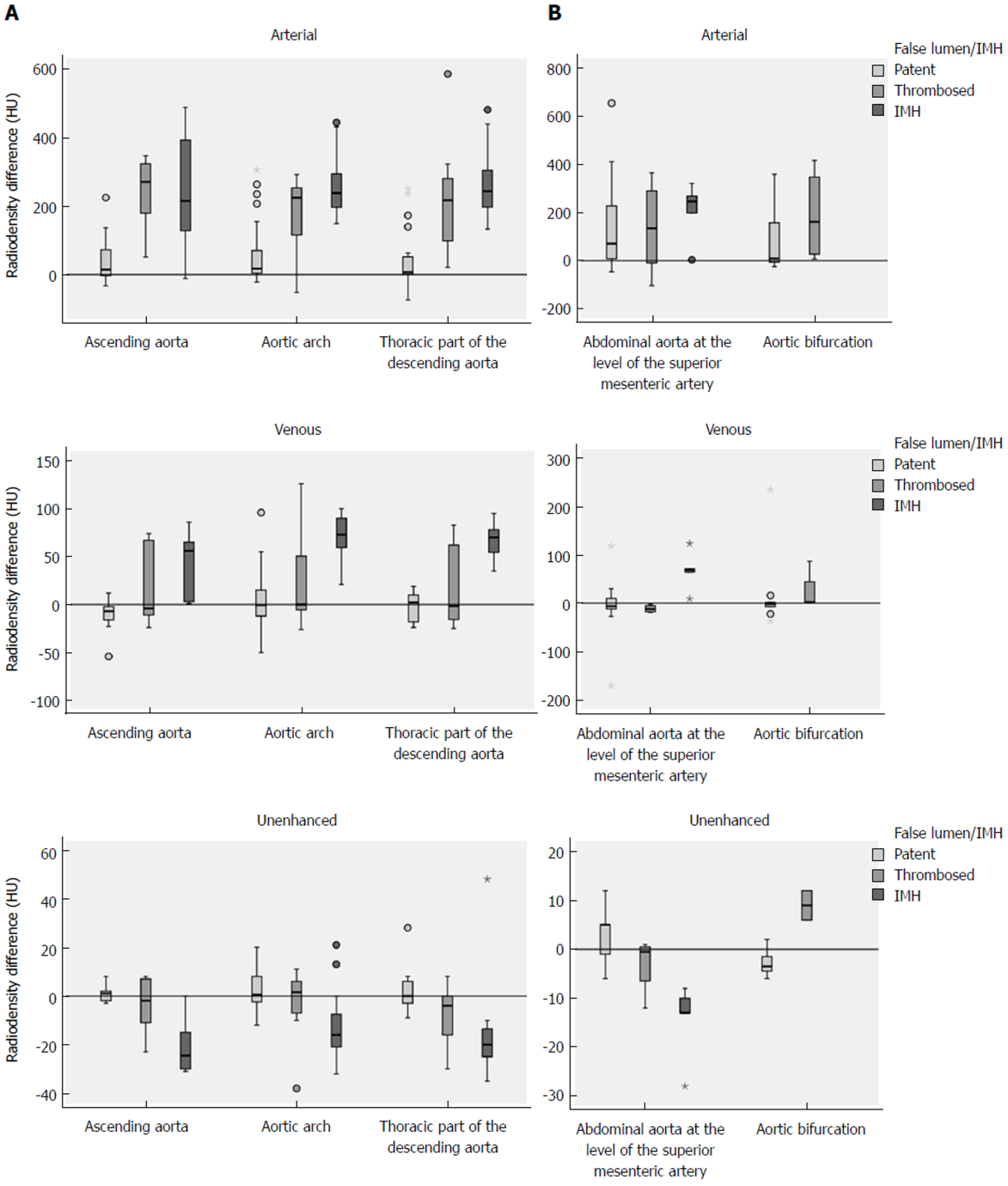

Figure 5 Density measurements, differences. Density differences between true and false lumen/intramural hematoma (IMH) in arterial, venous and unenhanced phase of (A) thoracic and (B) abdominal aorta. Differences in radiodensity between true lumen and IMH as well as true lumen and thrombosed false lumen, respectively, were only significant in the unenhanced acquisition (P = 0.035). IMH: Intramural hematoma.

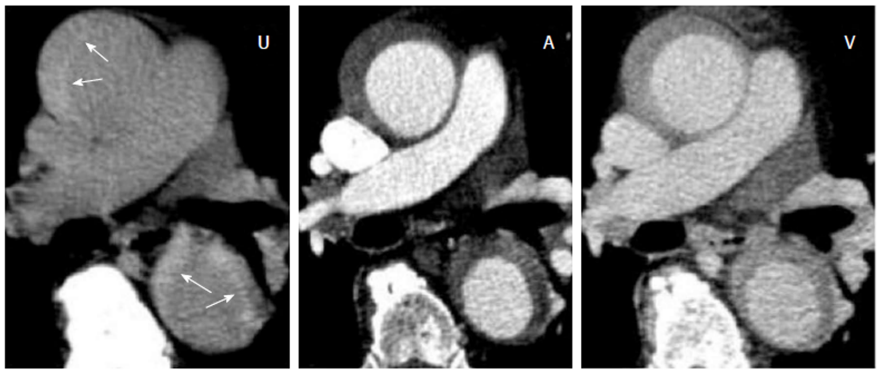

Figure 6 Acute intramural hematoma. Triphasic computed tomography angiography with an acute intramural hematoma (IMH) type Stanford A in the ascending and descending aorta. The unenhanced scan (U) shows a hyperdense wall thickening compared to the lumen (arrows). In the arterial (A) and venous (V) phase of the enhanced scans, the IMH con not be differentiated from a thrombotic layer.

ARTICLE HIGHLIGHTS

Research background

The life-threatening condition of an intramural hematoma (IMH) is often missed on routinely performed contrast enhanced computed tomography (CT) angiographies (CTA) in patients with suspected acute aortic syndrome (AAS).

Research motivation

To optimize the CT protocol for AAS.

Research objectives

To assess the potential benefit of a CTA protocol that includes an additional unenhanced acquisition added to contrast-enhanced scans in the diagnostic pathway of patients with AAS.

Research methods

Aortic CTA of patients with suspected AAS were retrospectively evaluated for acute aortic dissection, IMH, or penetrating aortic ulcer. The spiral CTA protocol consisted of an unenhanced acquisition and an arterial phase. If AAS was detected, a venous phase (delay, 90 s) was added. Images were evaluated for the presence and extent of aortic pathologies, and related complications.

Research results

23% of patients with AAS had an IMH. There was no significant difference in the involvement of the ascending aorta or the average age between dissection and IMH. Only the unenhanced acquisitions showed a significant density difference between the adjacent lumen and the IMH. Subadventitial hematoma involving the pulmonary trunk was present in five patients.

Research conclusions

IMH is a common and difficult to detect entity of AAS. An additional unenhanced acquisition within an aortic CTA protocol facilitates the detection of IMH.

Research perspectives

The results underline the importance of a triphasic CTA as standard diagnostic procedure in patients with suspected AAS.

REFERENCES

1 **Hallinan JT**, Anil G. Multi-detector computed tomography in the diagnosis and management of acute aortic syndromes. *World J Radiol* 2014; **6**: 355-365 [PMID: 24976936 DOI: 10.4329/wjr.v6.i6.355]
2 **Mészáros I**, Mórocz J, Szlávi J, Schmidt J, Tornóci L, Nagy L, Szép L. Epidemiology and clinicopathology of aortic dissection. *Chest* 2000; **117**: 1271-1278 [PMID: 10807810 DOI: 10.1378/chest.117.5.1271]
3 **Achenbach S**, Barkhausen J, Beer M, Beerbaum P, Dill T, Eichhorn J, Fratz S, Gutberlet M, Hoffmann M, Huber A. [Consensus recommendations of the German Radiology Society (DRG), the German Cardiac Society (DGK) and the German Society for Pediatric Cardiology (DGPK) on the use of cardiac imaging with computed tomography and magnetic resonance imaging]. *Rofo* 2012; **184**: 345-368 [PMID: 22426867 DOI: 10.1055/s-0031-1299400]
4 **Chao CP**, Walker TG, Kalva SP. Natural history and CT appearances of aortic intramural hematoma. *Radiographics* 2009; **29**: 791-804 [PMID: 19448116 DOI: 10.1148/rg.293085122]
5 **McMahon MA**, Squirrell CA. Multidetector CT of Aortic Dissection: A Pictorial Review.

Radiographics 2010; **30**: 445-460 [PMID: 20228328 DOI: 10.1148/rg.302095104]
6 **Daily PO**, Trueblood HW, Stinson EB, Wuerflein RD, Shumway NE. Management of acute aortic dissections. *Ann Thorac Surg* 1970; **10**: 237-247 [PMID: 5458238 DOI: 10.1016/S0003-4975(10)65594-4]
7 **Castañer E**, Andreu M, Gallardo X, Mata JM, Cabezuelo MA, Pallardó Y. CT in nontraumatic acute thoracic aortic disease: typical and atypical features and complications. *Radiographics* 2003; **23** Spec No: S93-110 [PMID: 14557505 DOI: 10.1148/rg.23si035507]
8 **Coady MA**, Rizzo JA, Elefteriades JA. Pathologic variants of thoracic aortic dissections. Penetrating atherosclerotic ulcers and intramural hematomas. *Cardiol Clin* 1999; **17**: 637-657 [PMID: 10589337 DOI: 10.1016/S0733-8651(05)70106-5]
9 **Tsai TT**, Nienaber CA, Eagle KA. Acute aortic syndromes. *Circulation* 2005; **112**: 3802-3813 [PMID: 16344407 DOI: 10.1161/CIRCULATIONAHA.105.534198]
10 **Song JK**, Yim JH, Ahn JM, Kim DH, Kang JW, Lee TY, Song JM, Choo SJ, Kang DH, Chung CH. Outcomes of patients with acute type a aortic intramural hematoma. *Circulation* 2009; **120**: 2046-2052 [PMID: 19901188 DOI: 10.1161/CIRCULATIONAHA.109.879783]
11 **Erbel R**, Aboyans V, Boileau C, Bossone E, Bartolomeo RD, Eggebrecht H, Evangelista A, Falk V, Frank H, Gaemperli O. 2014 ESC Guidelines on the diagnosis and treatment of aortic diseases: Document covering acute and chronic aortic diseases of the thoracic and abdominal aorta of the adult. The Task Force for the Diagnosis and Treatment of Aortic Diseases of the European Society of Cardiology (ESC). *Eur Heart J* 2014; **35**: 2873-2926 [PMID: 25173340 DOI: 10.1093/eurheartj/ehu281]
12 Statistikamt Nord. Bevölkerung der Gemeinden in Schleswig-Holstein. Available from: http://www.statistik-nord.de/daten/bevoelkerung-und gebiet/bevoelkerungsstand-und entwicklung/dokumentenansicht/163/produkte-1
13 **Harris KM**, Braverman AC, Eagle KA, Woznicki EM, Pyeritz RE, Myrmel T, Peterson MD, Voehringer M, Fattori R, Januzzi JL. Acute aortic intramural hematoma: an analysis from the International Registry of Acute Aortic Dissection. *Circulation* 2012; **126**: S91-S96 [PMID: 22965999 DOI: 10.1161/CIRCULATIONAHA.111.084541]

P- Reviewer: Abdelghany M, Benson RA, Okutucu S
S- Editor: Wang JL **L- Editor:** A **E- Editor:** Huang Y

Published By Baishideng Publishing Group Inc
7901 Stoneridge Drive, Suite 501, Pleasanton, CA 94588, USA
Telephone: +1-925-2238242
Fax: +1-925-2238243
E-mail: bpgoffice@wjgnet.com
Help Desk: https://www.f6publishing.com/helpdesk
https://www.wjgnet.com

World Journal of Radiology

Submit a Manuscript: https://www.f6publishing.com

World J Radiol 2018 November 28; 10(11): 162-171

DOI: 10.4329/wjr.v10.i11.162

ISSN 1949-8470 (online)

ORIGINAL ARTICLE

Retrospective Study

New scoring system in assessment of Hoffa's fat pad synovitis: A comparative study with established scoring systems

Shigeo Hagiwara, Albert Yang, Shoichiro Takao, Yasuhito Kaneko, Taiki Nozaki, Hiroshi Yoshioka

ORCID number: Shigeo Hagiwara (0000-0002-2734-8408); Albert Yang (0000-0002-2053-8460); Shoichiro Takao (0000-0002-8851-9813); Yasuhito Kaneko (0000-0001-8607-0197); Taiki Nozaki (0000-0002-1922-4085); Hiroshi Yoshioka (0000-0003-2686-1397).

Author contributions: Yoshioka H involved in overseeing the data collection process and data analysis following the data collection; Hagiwara S and Takao S accessed to subject identifiable data and analyzed the data; all the authors have read the manuscript and have approved this submission.

Institutional review board statement: The research protocol of this retrospective study was in compliance with the Helsinki Declaration, was approved by the institutional review board, and was registered with the University of California Irvine Medical Center.

Conflict-of-interest statement: No conflict of interest to be disclosed.

Shigeo Hagiwara, Albert Yang, Shoichiro Takao, Yasuhito Kaneko, Taiki Nozaki, Hiroshi Yoshioka, Department of Radiological Sciences, University of California Irvine Medical Center, Orange, CA 92868, United States

Abstract

AIM

To investigate the reliability of the established and new scoring methods for Hoffa's fat pad synovitis using magnetic resonance imaging (MRI).

METHODS

A total of 139 knees of 115 patients who underwent MRI of the knee with and without gadolinium contrast were enrolled in this study. Proton density (PD)-weighted, PD-weighted fat-suppressed (PD-FS), and postcontrast T1-weighted fat-suppressed (T1CE) images were used for evaluation. Using contrast and non-contrast images, our grading method for synovitis was performed to measure synovial thickness and signal intensity changes of the fat pad [Synovial membrane (SM) score], which was compared with the established methods, including MRI Osteoarthritis Knee Score (MOAKS), parapatellar synovitis score, Whole-Organ Magnetic Resonance Imaging Score (WORMS), and suprapatellar effusion diameter. Intraclass correlation coefficients (ICC) for intra and interobserver reproducibility and Spearman correlation coefficients (r) were calculated for the parapatellar synovitis score and each scoring method.

RESULTS

All of the scores presented substantial to almost perfect intrareliability. Among three readers, effusion diameter had substantial to almost perfect interreliability (ICC = 0.68-0.81) and WORMS had substantial interreliability (ICC = 0.61-0.70). For two out of three readers, there was substantial interreliability for the thickness score in T1CE (ICC = 0.55-0.69), SM scores in T1CE (ICC = 0.56-0.78) and PD-FS (ICC = 0.51-0.79), and parapatellar synovitis score in T1CE (ICC = 0.53-0.72). The parapatellar synovitis score was significantly correlated with the thickness score in T1CE (r = 0.70) and the SM score in T1CE (r = 0.81) and PD-FS (r = 0.65).

CONCLUSION

The newly proposed quantitative thickness score on T1CE and the semi-quantitative SM score on T1CE and PD-FS can be useful for Hoffa's fat pad synovitis.

Manuscript source: Unsolicited manuscript

Correspondence to: Hiroshi Yoshioka, MD, PhD, Chief Doctor, Professor, Executive Vice Chair, Department of Radiological Sciences, University of California Irvine Medical Center, 101 The City Drive South, Orange, CA 92868, United States.
hiroshi@uci.edu
Telephone: +1-877-8243627

Received: August 4, 2018
Peer-review started: August 5, 2018
First decision: August 24, 2018
Revised: September 22, 2018
Accepted: October 6, 2018
Article in press: October 6, 2018
Published online: November 28, 2018

Key words: Magnetic resonance imaging; Hoffa's fat pad synovitis; Semiquantitative score; Quantitative score; Scoring system

Core tip: We proposed a new grading method for Hoffa's fat pad synovitis and compared it with the other established methods. Our method showed substantial to almost perfect reproducibility and significant correlations with the established methods for both non-contrast and contrast images. Our newly proposed scoring system method can be useful for Hoffa's fat pad synovitis.

Hagiwara S, Yang A, Takao S, Kaneko Y, Nozaki T, Yoshioka H. New scoring system in assessment of Hoffa's fat pad synovitis: A comparative study with established scoring systems. *World J Radiol* 2018; 10(11): 162-171
URL: https://www.wjgnet.com/1949-8470/full/v10/i11/162.htm
DOI: https://dx.doi.org/10.4329/wjr.v10.i11.162

INTRODUCTION

Osteoarthritis (OA) of the knee is one of the most common chronic disorders that result in pain, deformity, and loss of function. OA has long been considered a wear and tear disease that leads to loss of cartilage because of mechanical stress. Recent experimental data have shown that OA is a complex disease with inflammatory mediators, which are released by cartilage, bone, and synovial fat pad[1-3].

The Hoffa's fat pad is located in the knee between the patellar tendon, femoral condyle, and tibial plateau. It is adjacent to the synovial layers and the cartilage surface of the femur[4]. Similar to subcutaneous tissue, the Hoffa's fat pad contains a framework of fibrous cords interspersed among adipose tissue[5] and is thought to distribute the synovial fluid and absorb forces through the knee joint[6]. Several studies have revealed that the fat pad produces growth factors and proinflammatory cytokines, which may contribute to the pathologic development of OA[7-9].

Several semiquantitative methods using magnetic resonance imaging (MRI) for the assessment of knee OA have been developed and used in various observational studies and clinical trials; by dividing the knee into subregions for assessment, these methods enable visualization of structures, such as the synovium, joint effusion, and cartilage[10,11]. Although each method have been reported to be clinically useful, the reliability was not perfect[12-14], and the scoring for Hoffa's fat pad synovitis based on non-enhanced sequences has not been sufficient, compared with that for the other subregions of the knee[10,11]. Although enhanced sequences allow for better characterization of synovial inflammation and for differentiation between the synovium and effusion, few scoring methods have been reported to be specific to Hoffa's fat pad synovitis[15,16]. Also, a routine knee MRI is usually obtained without contrast administration.

The aim of this study was to evaluate reliability of the established and new scoring methods, including non-enhanced MRI, for Hoffa's fat pad synovitis.

MATERIALS AND METHODS

Study design and subjects

The subjects enrolled in this study were all patients who underwent knee MRI with and without Gadolinium (Gd) contrast at our institute from January 2012 to July 2015. During this period, MRI of the knee with and without Gd contrast was performed on 205 knees (102 on the right, 103 on the left) of 168 patients. The exclusion criteria of this study were as follows: (1) under 18 years old; (2) postoperation with an implant around the knee; (3) inflammatory arthritis, such as rheumatoid arthritis and infection; (4) acute trauma with hemarthrosis; (5) intraarticular tumor; (6) difficult evaluation due to severe deformity from OA or amputation; and (7) difficult evaluation due to severe artifact. After exclusion of 66 knees of 53 patients, a total of 139 knees (69 on the right, 70 on the left) of 115 patients available for analyses. The subjects had an average age of 54 years.

The research protocol of this retrospective study was in compliance with the Helsinki Declaration, was approved by the institutional review board, and was registered with the University of California Irvine Medical Center.

MRI protocol

Each MRI examination in this study was performed according to a standardized institutional protocol using the 1.5T (Avanto, Siemens Healthcare, Erlangen, Germany) or the 3T MRI system (Achieva or dStream Achieva, Philips Healthcare, Best, Netherland and TtioTim, Siemens Healthcare); 42 knees underwent MRI with 1.5T and 97 knees with 3T. A non-enhanced proton density (PD)-weighted fast spin-echo sequence was performed in the sagittal plane, followed by non-enhanced PD-weighted fat-suppressed (PD-FS) fast spin-echo sequence in the sagittal and axial planes. After injection of 10 mL of Gd contrast (Multihance, Bracco) into a peripheral vein, T1-weighted fat-suppressed fast spin-echo sequence (T1CE) was performed in the sagittal and axial planes. The imaging parameters of all sequences are summarized in Table 1.

MRI assessment

The MRI evaluation of synovitis and joint effusion was performed independently by a board-certified orthopedic surgeon (A), who had 10 years of experience, and two radiology residents (B, C), who had 2 years of experience each. All readers were blinded to the clinical information but not to the MR sequences, because the imaging characteristics were readily apparent to the observer. To evaluate intraobserver reliability, a second trial was performed by Hagiwara S four weeks later.

Synovial evaluation

Thickness score: For the new quantitative scoring system, the thickness of the inflamed synovium was determined as the area of enhancement along the posterior Hoffa's fat pad on sagittal T1CE, as low-signal regions on non-enhanced sagittal PD, and as high-signal regions on non-enhanced sagittal PD-FS. Three sagittal slices, including the medial and lateral aspects of the Hoffa's fat pad and the central patellofemoral groove, were chosen. In each slice, three points (*i.e.*, proximal, middle, and distal) along the posterior surface of Hoffa's fat pad were selected. The average thickness of the synovium from the nine points in each sequence (Figure 1) was graded on a three-point scale: grade 1 ≤ 0.8 mm; grade 2 = 0.8 mm to 1.6 mm; and grade 3 ≥ 1.6 mm.

Synovial membrane score (SM score): The contrast effects and signal intensity changes along the posterior surface of the Hoffa's fat pad on a single sagittal slice through the central patellofemoral groove were used to semiquantitatively grade the synovitis. The score was based on the contrast effects and signal intensity changes[17] on sagittal T1CE; low-signal areas on sagittal PD; and high-signal areas on sagittal PD-FS. The score was graded on a four-point scale as grade 0 for lack of enhancement or signal change; grade 1 for the presence of a linear contrast effect or signal change on the posterior fat pad synovium; grade 2 for the presence of a nodular contrast effect or signal change on the posterior fat pad and/or mild exudation of the fat pad on T1CE; and grade 3 for gross a nodular contrast effect or signal change on the posterior fat pad and/or severe exudation of the fat pad on T1CE, as seen on the sagittal plane at the center of the patella (Figure 2).

MRI Osteoarthritis Knee Score (MOAKS) for fat pad: Hoffa's synovitis was scored with the MOAKS system[11] by grading the size of the diffuse hyperintense signal in the Hoffa's fat pad on T1CE and PD-FS on a four-point scale, as follows: 0 = normal; 1 = mild, 2 = moderate, 3 = severe.

Parapatellar synovitis score: Synovial inflammation in the entire knee was scored, as previously reported[18]. These parapatellar sites included three in the suprapatellar recesses (*i.e.*, lateral, medial, and just above the trochlear groove), as well as the medial and lateral femoral gutters. Thickening of the inflamed synovium was determined in each site and was scored on a four-point scale, according to the thickness, as grade 0 for lack of enhancement of the synovial tissue; grade 1 for < 2-mm thickening of the synovial tissue; grade 2 for 2-4-mm thickening of the synovial tissue; and grade 3 for > 4-mm thickening or nodular pattern of the synovial tissue (Figure 3).

Effusion evaluation

Effusion diameter: Joint effusion was assessed based on the greatest diameter of the fluid accumulation, perpendicular to the long axis of the leg on non-enhanced PD-FS, as follows; grade 0, < 5 mm; grade 1, between 5 mm and 10 mm; grade 2, between 10

Table 1 Magnetic resonance imaging parameters for the sequences

Imaging parameter	Tesla	Sequence				
		Sag PD	Sag PD-FS	Sag T1CE	Ax PD-FS	Ax T1CE
Repetition time (ms)	1.5T	2000	3000	438	3400	714
	3T	2054-3940	3000-4150	530-782	3000-5300	530-782
Echo time (ms)	1.5T	46	46	12	43	13
	3T	22-30	30-43	12-20	13-45	12-20
Matrix resolution (mm)	1.5T	0.7 × 0.7	0.7 × 0.7	0.7 × 0.7	0.6 × 0.6	0.6 × 0.6
	3T	0.3 × 3.3	0.3 × 0.3	0.3 × 0.3	0.3 × 0.3	0.3 × 0.3
Field of view (mm)	1.5T	150	150	150	150	150
	3T	150	150	150	150	150
Slice thickness (mm)	1.5T	3.5	3.5	3.5	5	5
	3T	2.5	2.5	2.5	3	3

Sag PD: Sagittal proton density-weighted sequence; Sag PD-FS: Sagittal proton density-weighted fat-suppressed sequence; Sag T1CE: Sagittal contrast-enhanced T1-weighted fat-suppressed sequence; Ax PD-FS: Axial proton density-weighted fat-suppressed sequence; Ax T1CE: Axial contrast-enhanced T1-weighted fat-suppressed sequence; T1CE: T1-weighted fat-suppressed fast spin-echo sequence; PD: Proton density-weighted fast spin-echo sequence; PD-FS: Proton density-weighted fat-suppressed fast spin-echo sequence.

mm and 20 mm; and grade 3, > 20 mm[19].

Whole-Organ Magnetic Resonance Imaging Score (WORMS) for synovial effusion: Synovial effusion was evaluated to describe the synovitis according to the WORMS system[10]. Joint effusion was graded collectively from 0 to 3 in terms of the percentage of the estimated maximal distention of the synovial cavity, as follows: grade 0, normal; grade 1, < 33%; grade 2, 33% to 66%; and grade 3, > 66%.

Statistical analysis

Statistical analysis was performed by the biostatistics service of our institute using MedCalc software (Ver.16, MedCalc Software, Ostend, Belgium). The inter and intraobserver reliabilities of each score were assessed using intraclass correlation coefficient (ICC) analysis. An ICC of 0.2-0.4 was considered as fair, 0.4-0.6 as moderate, 0.6-0.8 as substantial, and 0.8-1 as almost perfect[20]. Spearman's rank correlation (*r*) was computed to analyze the correlation between each scoring system and the MOAKS score, which was the most popular MRI semiquantitative scoring system for OA[14]. Because an adequate correlation between the parapatellar synovitis score and arthroscopic and microscopic scoring has been reported[21,22], the correlations of the parapatellar synovitis score with each scoring system were computed on 1.5T and 3T, respectively. Correlation was considered negligible for a *r* value < 0.2, low for a *r* value of 0.2-0.4, moderate for a *r* value of 0.4-0.7, strong for a *r* value of 0.7-0.9, and very strong for a *r* value > 0.9[23].

RESULTS

Reproducibility of the scoring systems

The ICCs for inter and intraobserver reliabilities of each score are shown in Table 2. All of the scores had substantial to almost perfect intrareliability. Among the three readers, interreliability was substantial to almost perfect for effusion diameter (ICC = 0.68-0.81) and substantial for WORMS (ICC = 0.61-0.70). For two out of three readers, there was substantial interreliability for the thickness score in T1CE (ICC = 0.55-0.69), SM scores in T1CE (ICC = 0.56-0.78) and PD-FS (ICC = 0.51-0.79), and parapatellar synovitis score in T1CE (ICC = 0.53-0.72).

Correlation with the standard

The Spearman's rank correlation results for the MOAKS are shown in Table 3. On the average, the MOAKS had moderate to strong correlations with each scoring system (*r* = 0.44-0.71). The correlations of each scoring system with the parapatellar synovitis score are shown in Table 4. The parapatellar synovitis score had nearly strong correlations with the thickness score in T1CE (*r* = 0.70), SM score in T1CE (*r* = 0.81), and SM score in PD-FS (*r* = 0.65). There were no significant differences between the

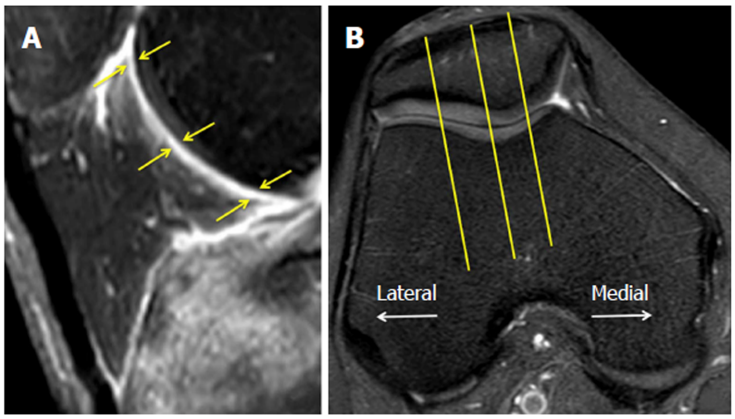

Figure 1 Thickness score. A: The thickness of Hoffa's synovitis is measured at three points at the proximal, middle, and distal synovium along the posterior aspect of the Hoffa's fat pad (yellow arrow); B: Sagittal slices are selected at the medial, lateral, and central patellofemoral groove.

1.5T and 3T sequences.

Figure 4 demonstrates a case with similar scores for Hoffa's synovitis among the PD-FS, PD, and T1CE, whereas Figure 5 demonstrates a case with different PD-FS, PD, and T1CE scores.

DISCUSSION

This study compared the established scoring methods, including the MOAKS score for fat pad, parapatellar synovitis score, WORMS scoring for synovial effusion, and effusion diameter, and the new scoring methods, including the thickness score and SM score for Hoffa's fat pad synovitis. The thickness score and the SM score demonstrated almost equal reproducibility with that of the other scoring systems and were superior to the MOAKS. The associations of the thickness score and the SM score with the MOAKS score were equal with that of the other scoring systems. Furthermore, the parapatellar synovitis score had strong associations with the thickness score in T1CE and the SM scores in T1CE and PD-FS.

Although the MOAKS score is based on the size and degree of hyperintensity on T2/ intermediate-weighted imaging or on the PD-FS within the Hoffa's fat pad[11], it does not clearly define the size and the slice delineation. This may have contributed to the relatively low interreliability for the MOAKS sore in this study. On the other hand, in the WORMS study, interobserver reliability was substantial despite the subjective analysis of the synovial cavity[10]. By evaluating both synovial tissue and fluid, even without clearly distinguishing between the two entities[10], the WORMS system can reliably evaluate the severity of the synovitis. In this study, there was substantial to almost perfect inter and intrareliability for the effusion diameter scoring, likely because measurement of the anterior to posterior dimensions of the joint fluid was straightforward and experience on orthopedic surgery or radiology was not always necessary.

The reliability of the thickness score in T1CE was better than in PD and PD-FS. An advantage of contrast-enhanced MRI is the ability to distinguish synovial inflammation from synovial fluid and fat tissues[20,24]. Guermazi *et al*[25] reported excellent reproducibility using a contrast-enhanced whole-knee synovitis scoring system. In non-contrast sequences, the border of the intensity change of synovitis is difficult to accurately recognize; this can be one of the reasons for the relatively low inter and intrareliability for the non-contrast analyses of the thickness score. The additional problems of the thickness score in T1CE were fragmentation and contrast exudation of the fat pad, which might have significantly increased the variability in measurement and, in severe cases, overestimated synovitis. The SM score is based on a well-known scoring method for synovitis of the wrist[17,26]. In this method, the high-intensity change seems easy to recognize in both T1CE and PD-FS.

Because the MOAKS enables visualization of the signal intensity change within the Hoffa's fat pad in asymptomatic patients[27], it was thought to be a sensitive but non-specific finding for synovitis[24]. This was a possible reason for the relatively low correlations between the MOAKS and the other scoring methods. Although the parapatellar synovitis score evaluates a region of interest that is different from the

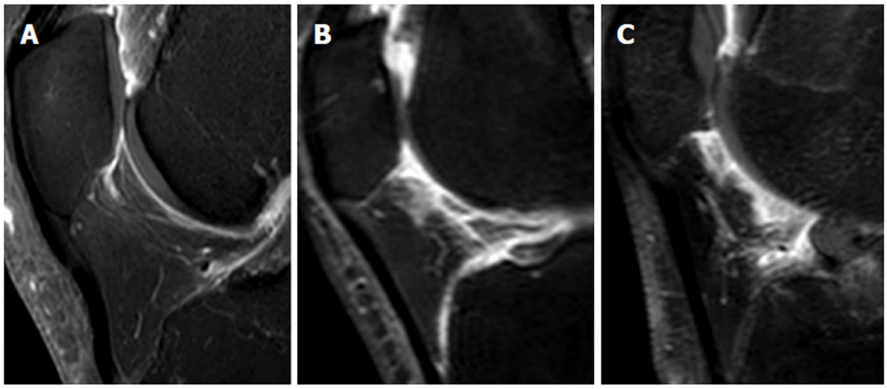

Figure 2 Grading of the Synovial membrane score. A: Grade1 is defined as linear thickening of the posterior Hoffa's fat pad's synovium; B: Grade 2 is defined as mild exudation and signal change in the posterior Hoffa's fat pad; C: Grade 3 is defined as gross nodular thickening of the posterior Hoffa's fat pad's synovium.

Hoffa's fat pad, it can be the standard of this study, considering its correlation with the arthroscopic and microscopic scoring of the knee and its previously reported correlation with the WORMS score of the fat pad[21,22]. The thickness score in T1CE and the SM scores in T1CE and PD-FS had strong associations with the parapatellar synovitis score. This suggested that evaluation of synovitis using the SM score on PD-FS had a similar reliability with that of a contrast-enhanced study. Although most contrast studies for synovitis were based on synovial thickness[15,22], this semiquantitative method can simply evaluate both the intensity change on the posterior fat pad and exudation to the fat pad. Due to concerns of increased cost and risk from contrast injection[11], the SM score in PD-FS may provide a viable alternative to contrast-enhanced examinations for the evaluation of Hoffa's fat pad synovitis.

Several limitations of this study should be acknowledged. First, we did not compare the scores with arthroscopic and microscopic examinations as the standard, because the current study was retrospective and most subjects were not in preoperative status. Second, the parapatellar synovitis score was not a specific scoring method for Hoffa's fat pad. Despite this, ample correlation of the parapatellar synovitis score with the arthroscopic and microscopic scoring had been demonstrated[19,20]. Third, there was variability in experience among the readers who interpreted the knee MRIs. Although two junior radiology residents were included, there was no significant difference in the scoring results among the readers. This suggested that our methods would be available for many physicians who may not be familiar with knee MRI interpretation. Finally, the use of both 1.5T and 3T MRI systems in this study may have produced variability in the tissue contrast on the PD or PD-FS images and in the degree of contrast enhancement on T1CE images, thereby, affecting the scoring for Hoffa's synovitis.

In conclusion, the newly proposed quantitative thickness score on T1CE and the semiquantitative SM scores on T1CE and PD-FS can be useful for Hoffa's fat pad synovitis. Semiquantiative scoring on PD-FS sequences may be a reliable surrogate to contrast-enhanced assessment of Hoffa's fat pad synovitis.

Table 2 Inter and intraobserver reliability

		Intra-observer	Inter-observer		
		A1-A2	A1-B	A1-C	B-C
Thickness	T1CE	0.74 (0.65-0.81)	0.69 (0.60-0.77)	0.67 (0.56-0.75)	0.55 (0.42-0.65)
	PD	0.68 (0.58-0.76)	0.45 (0.31-0.57)	0.49 (0.35-0.61)	0.54 (0.41-0.65)
	PD-FS	0.71 (0.61-0.78)	0.59 (0.48-0.69)	0.49 (0.35-0.60)	0.63 (0.52-0.72)
SM score	T1CE	0.88 (0.83-0.91)	0.67 (0.56-0.75)	0.78 (0.70-0.83)	0.56 (0.43-0.66)
	PD	0.88 (0.83-0.91)	0.49 (0.35-0.60)	0.72 (0.63-0.79)	0.50 (0.36-0.61)
	PD-FS	0.89 (0.85-0.92)	0.51 (0.38-0.63)	0.79 (0.71-0.84)	0.62 (0.50-0.71)
MOAKS	T1CE	0.76 (0.68-0.82)	0.64 (0.53-0.73)	0.54 (0.41-0.65)	0.49 (0.35-0.60)
Synovitis-score	T1CE	0.93 (0.91-0.95)	0.65 (0.54-0.74)	0.72 (0.62-0.79)	0.53 (0.40-0.64)
WORMS (effusion synovitis)	PD-FS	0.77 (0.70-0.83)	0.70 (0.61-0.78)	0.61 (0.50-0.71)	0.68 (0.58-0.76)
Effusion-diameter	PD-FS	0.89 (0.85-0.92)	0.77 (0.69-0.83)	0.81 (0.75-0.86)	0.68 (0.58-0.76)

Data are presented as ICC (95%CI). T1CE: T1-weighted fat-suppressed fast spin-echo sequence; PD: Proton density-weighted fast spin-echo sequence; PD-FS: Proton density-weighted fat-suppressed fast spin-echo sequence.

Table 3 Correlation with the MOAKS score

		1.5T	3T	Total
Thickness	T1CE	0.45	0.49	0.47
	PD	0.32	0.49	0.44
	PD-FS	0.42	0.41	0.41
SM score	T1CE	0.55	0.68	0.64
	PD	0.61	0.64	0.63
	PD-FS	0.64	0.74	0.71
Synovitis-score	T1CE	0.68	0.51	0.56
WORMS (effusion synovitis)	PD-FS	0.48	0.55	0.53
Effusion-diameter	PD-FS	0.58	0.48	0.51

All *P* values are less than 0.01. T1CE: T1-weighted fat-suppressed fast spin-echo sequence; PD: Proton density-weighted fast spin-echo sequence; PD-FS: Proton density-weighted fat-suppressed fast spin-echo sequence.

Table 4 Correlation with the parapatellar synovitis score

		1.5T	3T	Total
Thickness	T1CE	0.63	0.73	0.70
	PD	0.52	0.45	0.47
	PD-FS	0.44	0.51	0.49
SM score	T1CE	0.85	0.79	0.81
	PD	0.42	0.76	0.66
	PD-FS	0.79	0.59	0.65
MOAKS	T1CE	0.66	0.56	0.59
	PD-FS	0.65	0.52	0.56
WORMS (effusion synovitis)	PD-FS	0.64	0.81	0.76
Effusion-diameter	PD-FS	0.52	0.62	0.59

All *P* values are less than 0.01. T1CE: T1-weighted fat-suppressed fast spin-echo sequence; PD: Proton density-weighted fast spin-echo sequence; PD-FS: Proton density-weighted fat-suppressed fast spin-echo sequence.

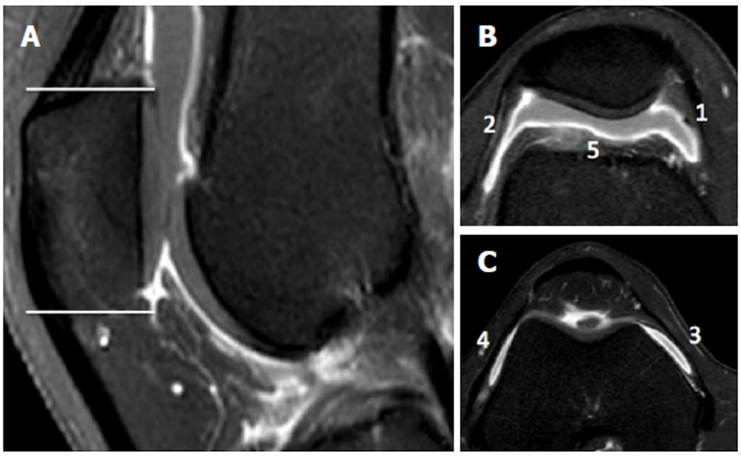

Figure 3 Parapatellar synovitis score. A: Two slices are chosen for the parapatellar synovitis score, and each corresponds with the first and last axial slice, respectively, in which the patella was still visible; B, C: The five sites of interest include three points in the suprapatellar recess, one point in the lateral gutter, and one point in the medial femoral gutter. Thickening of the inflamed synovium is determined in each site and is graded on a four-point scale, according to the thickness.

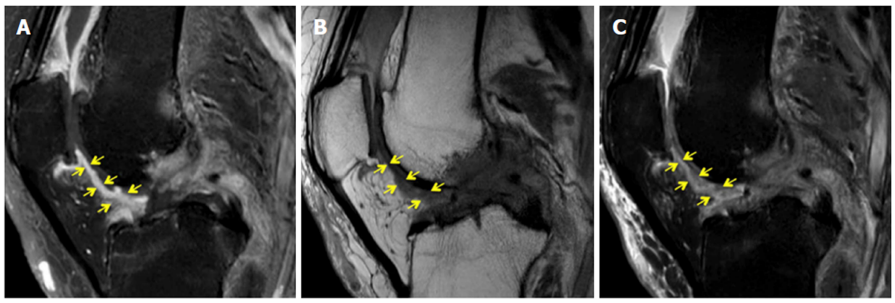

Figure 4 A 69-year-old woman with osteoarthritis and a parapatellar score of 9. A: The thickness score is grade 3, the Synovial membrane (SM) score is grade 3, and the MOAKS score is grade 3 on T1-weighted fat-suppressed fast spin-echo sequence; B: The thickness score is grade 2, the SM score is grade 3, and the MOAKS score is grade 3 on proton density-weighted fast spin-echo sequence; C: The thickness score is grade 3, the SM score is grade 3, and the MOAKS score is grade 3 on proton density-weighted fat-suppressed fast spin-echo sequence.

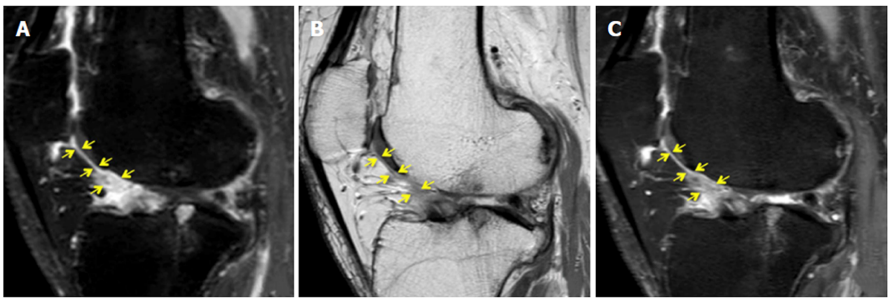

Figure 5 A 71-year-old woman with osteoarthritis and a parapatellar score of 8. A: The thickness score is grade 2, the Synovial membrane (SM) score is grade 3, and the MOAKS score is grade 3 on T1-weighted fat-suppressed fast spin-echo sequence; B: The thickness score is grade 1, the SM score is grade 1, and the MOAKS score is grade 3 on proton density-weighted fast spin-echo sequence; C: The thickness score is grade 2, the SM score is grade 3, and the MOAKS score is grade 3 on proton density-weighted fat-suppressed fast spin-echo sequence.

ARTICLE HIGHLIGHTS

Research background

Osteoarthritis (OA) of the knee is one of the most common chronic disorders resulting in pain, deformity, and loss of function. Several semiquantitative methods using magnetic resonance imaging (MRI) for assessment of knee OA have been developed and used in various observational studies and clinical trials.

Research motivation
Although all assessment methods had been reported to be clinical useful, their reliability was not perfect, and the scoring for Hoffa's fat pad synovitis based on non-enhanced sequence has not been sufficient, compared with that for the other subregions of the knee.

Research objectives
The aim of this study was to evaluate the reliability of the established and new scoring methods, including non-enhanced MRI, for Hoffa's fat pad synovitis.

Research methods
This study enrolled 139 knees of 115 patients who underwent MRI of the knee with and without Gadolinium contrast. Proton density (PD)-weighted, proton density-weighted fat-suppressed (PD-FS), and postcontrast T1-weighted fat-suppressed (T1CE) images were used for evaluation. Our grading method for synovitis was performed using non-contrast and contrast images to measure synovial thickness and signal intensity changes of the fat pad (SM score). Intraclass correlation coefficients (ICC) for intra and interobserver reproducibility and the Spearman correlation coefficients (r) with the parapatellar synovitis score were calculated for each scoring method.

Research results
The thickness score in T1CE and the SM scores in T1CE and PD-FS showed substantial to almost perfect reproducibility. The parapatellar synovitis score statistically significant correlation with the thickness score in T1CE (r = 0.68) and thee SM scores in T1CE (r = 0.71) and PD-FS (r = 0.66).

Research conclusions
The newly proposed quantitative thickness score on T1CE and the semiquantitative SM scores on T1CE and PD-FS can be useful for Hoffa's fat pad synovitis.

Research perspectives
Our findings indicated that the established scoring systems for Hoffa's fat pad synovitis could be further improved. Future research may propose more reliable methods for Hoffa's fat pad synovitis.

ACKNOWLEDGMENTS

We would like to thank Maryam Soltanolkotabi, for helping us make the grading system, and all the staff of the Department of Radiological Sciences at the University of California Irvine, for helping in collecting the data and obtaining the MRI.

REFERENCES

1 **Kapoor M**, Martel-Pelletier J, Lajeunesse D, Pelletier JP, Fahmi H. Role of proinflammatory cytokines in the pathophysiology of osteoarthritis. *Nat Rev Rheumatol* 2011; **7**: 33-42 [PMID: 21119608 DOI: 10.1038/nrrheum.2010.196]
2 **Loeser RF**, Goldring SR, Scanzello CR, Goldring MB. Osteoarthritis: a disease of the joint as an organ. *Arthritis Rheum* 2012; **64**: 1697-1707 [PMID: 22392533 DOI: 10.1002/art.34453]
3 **Goldring MB**, Otero M. Inflammation in osteoarthritis. *Curr Opin Rheumatol* 2011; **23**: 471-478 [PMID: 21788902 DOI: 10.1097/BOR.0b013e328349c2b1]
4 **Hoffa A**. Influence of adipose tissue with regard to the pathology of the knee joint. *JAMA* 1904; **43**: 795-796
5 **Vahlensieck M**, Linneborn G, Schild H, Schmidt HM. Hoffa's recess: incidence, morphology and differential diagnosis of the globular-shaped cleft in the infrapatellar fat pad of the knee on MRI and cadaver dissections. *Eur Radiol* 2002; **12**: 90-93 [PMID: 11868081 DOI: 10.1007/s003300100982]
6 **Saddik D**, McNally EG, Richardson M. MRI of Hoffa's fat pad. *Skeletal Radiol* 2004; **33**: 433-444 [PMID: 15221217 DOI: 10.1007/s00256-003-0724-z]
7 **Ushiyama T**, Chano T, Inoue K, Matsusue Y. Cytokine production in the infrapatellar fat pad: another source of cytokines in knee synovial fluids. *Ann Rheum Dis* 2003; **62**: 108-112 [PMID: 12525378 DOI: 10.1136/ard.62.2.108]
8 **Distel E**, Cadoudal T, Durant S, Poignard A, Chevalier X, Benelli C. The infrapatellar fat pad in knee osteoarthritis: an important source of interleukin-6 and its soluble receptor. *Arthritis Rheum* 2009; **60**: 3374-3377 [PMID: 19877065 DOI: 10.1002/art.24881]
9 **Klein-Wieringa IR**, Kloppenburg M, Bastiaansen-Jenniskens YM, Yusuf E, Kwekkeboom JC, El-Bannoudi H, Nelissen RG, Zuurmond A, Stojanovic-Susulic V, Van Osch GJ. The infrapatellar fat pad of patients with osteoarthritis has an inflammatory phenotype. *Ann Rheum Dis* 2011; **70**: 851-857 [PMID: 21242232 DOI: 10.1136/ard.2010.140046]
10 **Peterfy CG**, Guermazi A, Zaim S, Tirman PF, Miaux Y, White D, Kothari M, Lu Y, Fye K, Zhao S. Whole-Organ Magnetic Resonance Imaging Score (WORMS) of the knee in osteoarthritis. *Osteoarthritis Cartilage* 2004; **12**: 177-190 [PMID: 14972335 DOI: 10.1016/j.joca.2003.11.003]
11 **Hunter DJ**, Guermazi A, Lo GH, Grainger AJ, Conaghan PG, Boudreau RM, Roemer FW. Evolution of semi-quantitative whole joint assessment of knee OA: MOAKS (MRI Osteoarthritis Knee Score). *Osteoarthritis Cartilage* 2011; **19**: 990-1002 [PMID: 21645627 DOI: 10.1016/j.joca.2011.05.004]
12 **Lynch JA**, Roemer FW, Nevitt MC, Felson DT, Niu J, Eaton CB, Guermazi A. Comparison of

BLOKS and WORMS scoring systems part I. Cross sectional comparison of methods to assess cartilage morphology, meniscal damage and bone marrow lesions on knee MRI: data from the osteoarthritis initiative. *Osteoarthritis Cartilage* 2010; **18**: 1393-1401 [PMID: 20816979 DOI: 10.1016/j.joca.2010.08.017]

13 **Felson DT**, Lynch J, Guermazi A, Roemer FW, Niu J, McAlindon T, Nevitt MC. Comparison of BLOKS and WORMS scoring systems part II. Longitudinal assessment of knee MRIs for osteoarthritis and suggested approach based on their performance: data from the Osteoarthritis Initiative. *Osteoarthritis Cartilage* 2010; **18**: 1402-1407 [PMID: 20851202 DOI: 10.1016/j.joca.2010.06.016]

14 **Roemer FW**, Hunter DJ, Crema MD, Kwoh CK, Ochoa-Albiztegui E, Guermazi A. An illustrative overview of semi-quantitative MRI scoring of knee osteoarthritis: lessons learned from longitudinal observational studies. *Osteoarthritis Cartilage* 2016; **24**: 274-289 [PMID: 26318656 DOI: 10.1016/j.joca.2015.08.011]

15 **Roemer FW**, Guermazi A, Zhang Y, Yang M, Hunter DJ, Crema MD, Bohndorf K. Hoffa's Fat Pad: Evaluation on Unenhanced MR Images as a Measure of Patellofemoral Synovitis in Osteoarthritis. *AJR Am J Roentgenol* 2009; **192**: 1696-1700 [PMID: 19457837 DOI: 10.2214/AJR.08.2038]

16 **Ballegaard C**, Riis RG, Bliddal H, Christensen R, Henriksen M, Bartels EM, Lohmander LS, Hunter DJ, Bouert R, Boesen M. Knee pain and inflammation in the infrapatellar fat pad estimated by conventional and dynamic contrast-enhanced magnetic resonance imaging in obese patients with osteoarthritis: a cross-sectional study. *Osteoarthritis Cartilage* 2014; **22**: 933-940 [PMID: 24821663 DOI: 10.1016/j.joca.2014.04.018]

17 **Ostergaard M**, Hansen M, Stoltenberg M, Gideon P, Klarlund M, Jensen KE, Lorenzen I. Magnetic resonance imaging-determined synovial membrane volume as a marker of disease activity and a predictor of progressive joint destruction in the wrists of patients with rheumatoid arthritis. *Arthritis Rheum* 1999; **42**: 918-929 [PMID: 10323447 DOI: 10.1002/1529-0131(199905)42:53.0.CO;2-2]

18 **Loeuille D**, Chary-Valckenaere I, Champigneulle J, Rat AC, Toussaint F, Pinzano-Watrin A, Goebel JC, Mainard D, Blum A, Pourel J. Macroscopic and microscopic features of synovial membrane inflammation in the osteoarthritic knee: correlating magnetic resonance imaging findings with disease severity. *Arthritis Rheum* 2005; **52**: 3492-3501 [PMID: 16255041 DOI: 10.1002/art.21373]

19 **Meredith DS**, Losina E, Neumann G, Yoshioka H, Lang PK, Katz JN. Empirical evaluation of the inter-relationship of articular elements involved in the pathoanatomy of knee osteoarthritis using magnetic resonance imaging. *BMC Musculoskelet Disord* 2009; **10**: 133 [PMID: 19874594 DOI: 10.1186/1471-2474-10-133]

20 **Landis JR**, Koch GG. The measurement of observer agreement for categorical data. *Biometrics* 1977; **33**: 159-174 [PMID: 843571]

21 **Loeuille D**, Rat AC, Goebel JC, Champigneulle J, Blum A, Netter P, Gillet P, Chary-Valckenaere I. Magnetic resonance imaging in osteoarthritis: which method best reflects synovial membrane inflammation? Correlations with clinical, macroscopic and microscopic features. *Osteoarthritis Cartilage* 2009; **17**: 1186-1192 [PMID: 19332177 DOI: 10.1016/j.joca.2009.03.006]

22 **Loeuille D**, Sauliere N, Champigneulle J, Rat AC, Blum A, Chary-Valckenaere I. Comparing non-enhanced and enhanced sequences in the assessment of effusion and synovitis in knee OA: associations with clinical, macroscopic and microscopic features. *Osteoarthritis Cartilage* 2011; **19**: 1433-1439 [PMID: 21930225 DOI: 10.1016/j.joca.2011.08.010]

23 **Guilford JP**. *Fundamental statistics in psychology and education*New York: McGraw Hill; 1956

24 **Crema MD**, Felson DT, Roemer FW, Niu J, Marra MD, Zhang Y, Lynch JA, El-Khoury GY, Lewis CE, Guermazi A. Peripatellar synovitis: comparison between non-contrast-enhanced and contrast-enhanced MRI and association with pain. The MOST study. *Osteoarthritis Cartilage* 2013; **21**: 413-418 [PMID: 23277189 DOI: 10.1016/j.joca.2012.12.006]

25 **Guermazi A**, Roemer FW, Hayashi D, Crema MD, Niu J, Zhang Y, Marra MD, Katur A, Lynch JA, El-Khoury GY. Assessment of synovitis with contrast-enhanced MRI using a whole-joint semiquantitative scoring system in people with, or at high risk of, knee osteoarthritis: the MOST study. *Ann Rheum Dis* 2011; **70**: 805-811 [PMID: 21187293 DOI: 10.1136/ard.2010.139618]

26 **Stomp W**, Krabben A, van der Heijde D, Huizinga TW, Bloem JL, Østergaard M, van der Helm-van Mil AH, Reijnierse M. Aiming for a simpler early arthritis MRI protocol: can Gd contrast administration be eliminated? *Eur Radiol* 2015; **25**: 1520-1527 [PMID: 25636414 DOI: 10.1007/s00330-014-3522-1]

27 **De Smet AA**, Davis KW, Dahab KS, Blankenbaker DG, del Rio AM, Bernhardt DT. Is there an association between superolateral Hoffa fat pad edema on MRI and clinical evidence of fat pad impingement? *AJR Am J Roentgenol* 2012; **199**: 1099-1104 [PMID: 23096185 DOI: 10.2214/AJR.12.8798]

P- Reviewer: Gheita TA, Jennane R
S- Editor: Wang JL **L- Editor:** A **E- Editor:** Huang Y

Published By Baishideng Publishing Group Inc
7901 Stoneridge Drive, Suite 501, Pleasanton, CA 94588, USA
Telephone: +1-925-2238242
Fax: +1-925-2238243
E-mail: bpgoffice@wjgnet.com
Help Desk: https://www.f6publishing.com/helpdesk
https://www.wjgnet.com

World Journal of Radiology

Submit a Manuscript: https://www.f6publishing.com

World J Radiol 2018 November 28; 10(11): 172-183

DOI: 10.4329/wjr.v10.i11.172

ISSN 1949-8470 (online)

ORIGINAL ARTICLE

Retrospective Study

High-resolution computed tomography findings in humoral primary immunodeficiencies and correlation with pulmonary function tests

Lorenzo Cereser, Marco De Carli, Paola d'Angelo, Elisa Zanelli, Chiara Zuiani, Rossano Girometti

ORCID number: Lorenzo Cereser (0000-0003-4480-8872); Marco De Carli (0000-0003-4845-205X); Paola d'Angelo (0000-0003-2218-5571); Elisa Zanelli (0000-0002-7271-0613); Chiara Zuiani (0000-0001-5132-3115); Rossano Girometti (0000-0002-0904-5147).

Author contributions: All authors helped performing the research; Cereser L drafted the concept of the research, designed the study, read the HRCT examinations and wrote the manuscript; De Carli M contributed to designing the study and writing the manuscript; d'Angelo P and Zanelli E collected the data and contributed to analysing the data and writing the manuscript; Zuiani C drafted the concept of the research and contributed to designing the study; Girometti R designed the study, analysed the data and contributed to writing the manuscript.

Institutional review board statement: Our referring Ethical Committee approved this study.

Conflict-of-interest statement: All authors declare no conflicts of interest related to this article.

Lorenzo Cereser, Paola d'Angelo, Elisa Zanelli, Chiara Zuiani, Rossano Girometti, Institute of Radiology, Department of Medicine, University of Udine, Azienda Sanitaria Universitaria Integrata di Udine, Udine 33100, Italy

Marco De Carli, Second Unit of Internal Medicine, Azienda Sanitaria Universitaria Integrata di Udine, Udine 33100, Italy

Paola d'Angelo, Department of Imaging, Bambino Gesù Chlidren's Hospital, IRCCS, Rome 00165, Italy

Abstract

AIM

To compare high-resolution computed tomography (HRCT) findings between humoral primary immunodeficiencies (hPIDs) subtypes; to correlate these findings to pulmonary function tests (PFTs).

METHODS

We retrospectively identified 52 consecutive adult patients with hPIDs who underwent 64-row HRCT and PFTs at the time of diagnosis. On a per-patient basis, an experienced radiologist recorded airway abnormalities (bronchiectasis, airway wall thickening, mucus plugging, tree-in-bud, and air-trapping) and parenchymal-interstitial abnormalities (consolidations, ground-glass opacities, linear and/or irregular opacities, nodules, and bullae/cysts) found on HRCT. The chi-square test was performed to compare the prevalence of each abnormality among patients with different subtypes of hPIDs. Overall logistic regression analysis was performed to assess whether HRCT findings predicted obstructive and/or restrictive PFTs results (absent-to-mild *vs* moderate-to-severe).

RESULTS

Thirty-eight of the 52 patients with hPIDs showed common variable immunodeficiency disorders (CVID), while the remaining 14 had CVID-like conditions (*i.e.*, 11 had isolated IgG subclass deficiencies and 3 had selective IgA deficiencies). The prevalence of most HRCT abnormalities was not significantly different between CVID and CVID-like patients ($P > 0.05$), except for linear and/or irregular opacities (prevalence of 31.6% in the CVID group and 0 in the CVID-like group; $P = 0.0427$). Airway wall thickening was the most frequent HRCT abnormality found in both CVID and CVID-like patients (71% of cases in both groups). The presence of tree-in-bud abnormalities was an independent predictor of moderate-to-severe obstructive defects at PFTs (Odds Ratio, OR, of

Manuscript source: Unsolicited manuscript

Correspondence to: Lorenzo Cereser, MD, Doctor, Institute of Radiology, Department of Medicine, University of Udine, Azienda Sanitaria Universitaria Integrata di Udine, p.le S. Maria della Misericordia 15, Udine 33100, Italy. lcereser@sirm.org
Telephone: +39-432-559266
Fax: +39-432-559867

Received: July 17, 2018
Peer-review started: July 17, 2018
First decision: August 8, 2018
Revised: September 22, 2018
Accepted: October 7, 2018
Article in press: October 7, 2018
Published online: November 28, 2018

18.75, $P < 0.05$), while the presence of linear and/or irregular opacities was an independent predictor of restrictive defects at PFTs (OR = 13.00; $P < 0.05$).

CONCLUSION
CVID and CVID-like patients showed similar HRCT findings. Tree-in-bud and linear and/or irregular opacities predicted higher risks of, respectively, obstructive and restrictive defects at PFTs.

Key words: Bronchiectasis; Multidetector computed tomography; Common variable immunodeficiency; Immunologic deficiency syndromes; Respiratory function tests

Core tip: Humoral primary immunodeficiencies (hPIDs) are a group of conditions characterized by impaired antibody production and presenting with recurrent respiratory infections, autoimmune diseases, and malignancy. Chest high-resolution computed tomography (HRCT) is the imaging technique of choice for detecting, characterizing, and quantifying lung complications in these patients. The aims of this study were to compare HRCT findings in 52 patients with hPIDs subtypes (common variable immunodeficiency disorders - CVID *vs* CVID-like), and evaluate whether these findings may predict pulmonary function tests results. CVID *vs* CVID-like patients showed comparable HRCT findings. The presence of tree-in-bud and linear and/or irregular opacities were independent predictors of, respectively, significant obstructive and restrictive defects.

Cereser L, De Carli M, d'Angelo P, Zanelli E, Zuiani C, Girometti R. High-resolution computed tomography findings in humoral primary immunodeficiencies and correlation with pulmonary function tests. *World J Radiol* 2018; 10(11): 172-183
URL: https://www.wjgnet.com/1949-8470/full/v10/i11/172.htm
DOI: https://dx.doi.org/10.4329/wjr.v10.i11.172

INTRODUCTION

Humoral primary immunodeficiencies (hPIDs), also known as primary predominantly antibody deficiencies, constitute the most common subgroup of primary immunodeficiency disorders (about 50% of diagnoses)[1]. hPIDs encompass a spectrum of conditions characterized by impaired antibody production, manifesting with recurrent respiratory tract infections, increased susceptibility to autoimmune diseases, and malignancy[1,2]. Common variable immunodeficiency disorders (CVID) are the most clinically significant group of hPIDs (with a prevalence of about 1:25000-1:50000 subjects). These disorders show distinct clinical and laboratory phenotypes associated with low levels of IgG and IgA and/or IgM[3,4]. CVID onset is during adult life in 70% of the cases, generally occurring between 20 and 40 years of age[5,6]. Other hPIDs are often referred as "CVID-like" conditions: these conditions are in most cases asymptomatic and include selective IgA deficiency (the most frequent hPID, with a prevalence of 1/600 in white people) and isolated IgG subclass deficiency[2,7,8].

Overall, thoracic complications develop in 60% of patients with hPIDs, representing the leading cause of morbidity and mortality. Chest high-resolution computed tomography (HRCT) is the imaging technique of choice for detecting, characterizing, and quantifying lung complications, as well as for evaluating the response to therapy[1,9,10]. It is generally accepted that the initial evaluation of newly diagnosed patients should include HRCT and pulmonary function tests (PFTs). Early identification of respiratory complications provides a baseline assessment of lung involvement, allows prompt treatment to reduce the number of pulmonary infections, and impacts on quality of life and mortality, the latter being influenced by both structural and functional pulmonary impairment[5,11,12].

Several studies have reported HRCT findings in hPIDs; these findings include non-infective airway disorders (*i.e.*, bronchiectasis, airway wall thickening, and air trapping), pulmonary infections, diffuse lung parenchymal diseases [*e.g.*, Granulomatous and Lymphocytic Interstitial Lung Disease (GLILD), and organising pneumonia], and thoracic neoplasms (*e.g.*, lymphoma)[10,13-16]. However, most papers

refer only to CVID patients, and report that HRCT abnormalities are present in more than 90% of those patients[9,17]. While some Authors reported that the severity of HRCT abnormalities was not significantly different between CVID and CVID-like paediatric patients[18,19], to the best of our knowledge no studies have addressed this issue in adult patients. Demonstrating a difference between CVID and CVID-like patients may influence the time intervals between HRCT examinations during follow-up in these 2 subgroups of hPIDs. In addition to this, previous studies assessing a correlation between HRCT findings and PFTs results demonstrated contradictory results[9,17,18,20].

The purpose of this study was twofold: (1) to compare HRCT pulmonary findings in adult patients among different subgroups of hPIDs (*i.e.*, CVID and CVID-like); and (2) to assess whether HRCT findings predict PFTs results.

MATERIALS AND METHODS

Study population and PFTs

Our referring Ethical Committee approved this study. The need for informed consent was waived due to the retrospective design of the study. By performing a computerized search, we identified 56 adult patients who received a definite diagnosis of hPIDs, in accordance with the European Society for Immunodeficiencies criteria[21], in our tertiary referral centre and between 2012 and 2016. Diagnosis was performed after a history of previously undefined respiratory disease ranging from 1 to 5 years in duration. All patients underwent HRCT and PFTs within one month from diagnosis as a part of the diagnostic workflow performed at our institute. Accordingly, hereinafter we are going to refer to the HRCT performed at the time of diagnosis as baseline HRCT. Four patients were excluded from the study due to infectious respiratory disease at the time of HRCT (clinically unstable disease) or unavailability of the PFTs results. Therefore, the final population included 52 patients and had the following distribution of disease subtypes: 38 CVID, 11 isolated IgG subclass deficiency, and 3 selective IgA deficiency cases.

Lung function was evaluated according to the criteria of the European Respiratory Society/American Thoracic Society task force[22]. The following parameters were measured with a spirometer (Vmax 29c; Sensor Medics, Yorba Linda, CA, United States): Forced expiratory volume in one second (FEV1), forced vital capacity (FVC), vital capacity (VC), peak expiratory flow (PEF), and total lung capacity (TLC). Obstructive ventilatory defects were diagnosed when the reduced FEV1/VC ratio was below the 5th percentile of the predicted value; restrictive ventilatory disorders were diagnosed when a reduction in TLC below the 5th percentile of the predicted value was detected in the presence of a normal FEV1/VC ratio. The severity of ventilatory defects was assessed using a six-point scale (absent, mild, moderate, moderately severe, severe, and very severe)[23]. For the purposes of analysis, patients with obstructive or restrictive defects were classified in two groups: (1) patients with absent-to-mild defects (*i.e.*, ≥ 70% of predicted values); and (2) patients with moderate-to-severe defects (*i.e.*, < 70% of predicted values).

HRCT examinations

HRCT examinations were performed with a 64-row MDCT scanner (Discovery HD 750, GE Healthcare, Milwaukee, WI, United States), with the patient in the supine position. The whole thorax was scanned volumetrically at suspended full inspiration using the following acquisition parameters: tube potential, 120 kV; tube current modulation range, 150-400 mA (based on a Noise Index set at 18.4); rotation time, 0.8 s; detector configuration, 64 mm × 0.625 mm; reconstructed section thickness and reconstructed interval, 1.25 mm; field of view according to patient size. In 32/52 patients an additional end-expiratory volumetric scan with the same parameters was also acquired.

Images were reconstructed using a high-spatial-frequency algorithm, and displayed with lung parenchyma (level, -500 HU; width, 1500 HU) and mediastinum windowing (level, 50 HU; width, 350 HU).

Image analysis

A radiologist with 8 years of experience in pulmonary imaging, blinded to patient history and lung function, reviewed the HRCT examinations on a picture archiving and communication system workstation (Suitestensa Ebit srl, Esaote Group Company, Genoa, Italy). Post-processing techniques, including Multiplanar Reconstruction (MPR), Maximum Intensity Projection (MIP) and Minimum Intensity Projection (MinIP), were available to complement the analysis of thin source images.

For each patient, the reader recorded two classes of abnormalities: airway abnormalities (*i.e.*, airway wall thickening, tree-in-bud, bronchiectasis, mucus plugging, and air trapping), and parenchymal-interstitial abnormalities (*i.e.*, linear and/or irregular opacities, nodules, consolidations, ground-glass opacities, and bullae/cysts). Radiological features were evaluated according to the Fleischner Society glossary[24]. In particular, "linear and/or irregular opacities" describe any linear opacity of irregular thickness that does not respect the lung architecture[9] and has been reported as being a key feature of lung disease in CVID patients.

Any individual abnormality was scored using a double three-point scale (with a total score ranging from 2 to 6), for coding two aspects simultaneously: (1) extension, with 1 = involvement of a single pulmonary lobe, 2 = two-to-three lobes involved, 3 = more than three lobes involved; and (2) conspicuity in the most involved lobe, with 1 = mild, 2 = moderate, and 3 = severe. As to include in the analysis only findings that are reasonably related to hPIDs, the minimum required total score for an abnormality was 3.

Statistical analysis

We calculated the per-patient prevalence of each of the aforementioned HRCT abnormalities in the overall population and in different subgroups of hPIDs patients, *i.e.*, the CVID group *vs* CVID-like group (the latter including both isolated IgG subclass deficiencies and selective IgA deficiencies). Main clinical features (age, duration of symptoms before definite diagnosis, and ventilatory defects) and prevalence of HRCT abnormalities were compared between the two groups using, respectively, the *u*-Mann-Whitney and χ^2 tests. A logistic regression analysis (stepwise approach) was performed to assess whether the HRCT findings could predict a significant obstructive or restrictive defect at PFTs on the overall study population. As variables we used each of the aforementioned airway abnormalities and parenchymal-interstitial abnormalities. Obstructive and restrictive defects were defined as relevant only if they were of moderate-to-severe nature, and not if they were absent-to-mild. Air trapping was excluded from the model since HRCT additional expiratory scan was not available for all patients. Analysis was performed with a commercially available software (MedCalc version 12.5.0.0, MariaKerke, Belgium). The α level was set to 0.05.

RESULTS

Study population and PFTs results

Of the 52 hPIDs patients 37 were females and 15 were males, with a mean age of 53.9 ± 12.7 years. Thirty-eight of the 52 patients (73%) were included in the CVID group, and 14/52 patients (27%) were in the CVID-like group. No significant differences between the two groups were found in terms of age (mean 54.9 ± 12.9 years in the CVID group *vs* 51 ± 11.9 years in the CVID-like group) and average duration of symptoms before definite diagnosis of hPIDs (2 years, range 1-3, in the CVID group *vs* 4 years, range 1-5, in the CVID-like group, $P > 0.05$). None of the patients underwent HRCT before hPIDs diagnosis. Standard CTs were available for 15 of the 52 patients (one examination each) and had been performed 2-4 years before the HRCT at the time of hPIDs diagnosis.

The results of the PFTs show that almost half of the patients (25/52, 48.1%) had ventilatory defects (Table 1). Three patients in the CVID group had concomitant moderate-to-severe obstructive defects and restrictive defects. None of the patients in the CVID-like group showed restrictive defects. No statistically significant differences were found between the two subgroups of hPIDs in terms of prevalence of obstructive (CVID: 44.7% *vs* CVID-like: 42.9%, $P = 0.8474$) and restrictive defects (CVID: 13.1% *vs* CVID-like: 0%, $P = 0.2052$).

Distribution of HRCT abnormalities in the study groups

We recorded a high prevalence of HRCT findings, with one or more abnormalities detected in 47/52 hPIDs patients (90.4%). The prevalence of specific airway abnormalities was not significantly different between the CVID and CVID-like groups ($P > 0.05$, Table 2). Airway wall thickening was the most commonly found abnormality and showed a comparable prevalence in both groups (71.0% in the CVID group and 71.4% in the CVID-like group, Figure 1).

Regarding HRCT parenchymal-interstitial abnormalities, linear and/or irregular opacities were present in 31.6% of the patients in the CVID group and in none of those in the CVID-like group, with borderline significance ($P = 0.0427$, Table 2). Nodules were the most frequent finding in both groups, with a prevalence of 50.0% (Figure 2).

Table 1 Pulmonary function tests results *n* (%)

	Obstructive defect				Restrictive defect			
	Absent	Mild	Significant[1]	Any	Absent	Mild	Significant[1]	Any
CVID (n = 38)	21 (55.3)	10 (26.3)	7 (18.4)	17 (44.7)	33 (86.9)	1 (2.6)	4 (10.5)	5 (13.1)
CVID-like (n = 14)	8 (57.1)	2 (14.3)	4 (28.6)	6 (42.9)	14 (100)	0 (0)	0 (0)	0 (0)
All patients (n = 52)	29 (55.8)	12 (23.1)	11 (21.2)	23 (44.2)	47 (90.4)	1 (1.9)	4 (7.7)	5 (9.6)

Data are presented as number of patients with percentages in parentheses.
[1]Moderate-to-severe defect. CVID: Common variable immunodeficiency disorder; CVID-like: Including isolated IgG subclass deficiency and selective IgA deficiency.

Correlation between HRCT abnormalities and PFTs

The distributions of HRCT-detected airway and parenchymal-interstitial abnormalities according to severity of ventilatory defects assessed at PFTs are reported in Tables 3 and 4.

Regarding HRCT-detected airway abnormalities, both mucus plugging (P = 0.0112, Figure 3) and tree-in-bud (P = 0.0014, Figure 4) were found to be significantly associated with a relevant obstructive defect assessed at PFTs. However, on multivariate analysis, tree-in-bud was the only independent predictor (P = 0.0027) of relevant obstructive defect, with an odds ratio (OR) of 18.75 (95%CI: 2.76-127.52).

Additionally, regarding HRCT-detected parenchymal-interstitial abnormalities, the presence of linear and/or irregular opacities (Figure 5) was the only predictor of relevant restrictive defect both at univariate (P = 0.0029) and multivariate analysis (P = 0.0344; OR, 13.00; 95%CI: 1.21-139.97).

DISCUSSION

Pulmonary abnormalities in hPIDs adult patients were common in our series: Only 9.6% of our patients had negative HRCTs at the time of diagnosis, a finding in agreement with the literature (range 4%-17%)[9,17,25]. The prevalence of most of airways and parenchymal-interstitial findings was not significantly different between the CVID and the CVID-like groups. Similarly, PFTs results were comparable between the two subtypes of hPIDs, showing a larger prevalence of obstructive defects (45% in the CVID group and 43% in the CVID-like group) over restrictive defects (13% in the CVID group and 0 in the CVID-like group). These findings are in agreement with the previously reported prevalences in CVID patients (9%-53% for obstructive defects and 5%-34% for restrictive defects)[9,17,26,27]. Conversely, to the best of our knowledge, this is the first study reporting prevalences in adult CVID-like patients. Overall, our findings support the hypothesis that neither imaging nor PFTs can reliably differentiate between the two groups of CVID and CVID-like patients. One might argue that the relevance of this result is impaired by the relatively small population included in the present study. However, our series reflects the rarity of both conditions, and is one of the largest published reports on HRCT as far as we know.

Of note, linear and/or irregular opacities were more frequently found in CVID patients (32%) than in CVID-like patients (0), although statistical significance was borderline (P = 0.0427). Gregersen *et al*[9] highlighted the importance of this abnormality in CVID adult patients, both because of its frequency (about 52% of cases) and its close association with impaired gas diffusion. In line with the relevant literature[11,28], we found that only one HRCT abnormality, linear and/or irregular opacities, was a predictor of significant restrictive defects. This result emphasizes the importance of prompt identification of this abnormality at baseline evaluation. Overall, our results support the assumption that CVID-like patients are clinically and immunologically comparable to CVID patients[18,29], although the latter show more frequently radiological abnormalities associated to interstitial disease (*i.e.*, linear and/or irregular opacities).

It is likely that the prevalence of different HRCT findings might reflect the effects of the specific disease on the lungs in CVID and CVID-like patients. The most frequent findings in our cohort were bronchiectasis (69.2%) and airway wall thickening (71.2%, Figure 2), and are in line with those previously reported in adult patients (range 40%-70% for bronchiectasis and 68%-75% for airway wall thickening)[9,10,17,25,26]. Such a high prevalence can be explained by the cumulative effect of respiratory tract infections[17,30,31]. Other common findings in our study were nodules (found in 50% of

Figure 1 Airway wall thickening. A 65-year-old male patient with common variable immunodeficiency disorder. High-resolution computed tomography shows diffuse airway wall thickening in the right middle and lower lobes (straight arrows); centrilobular and tree-in-bud nodules in the right lung are also detected (curved arrow).

patients *vs* 29%-55% reported in literature)[9,17,25] and mucus plugging (in 44.2% of patients). We did not differentiate among various types of nodules, since their characteristics reflect a wide spectrum of conditions (including infectious diseases, previous infections or lymphoproliferative and/or granulomatous conditions) that cannot be histologically confirmed in most patients[14,25]. We believe that the high prevalence of nodules should be considered as an epiphenomenon of other coexisting pulmonary abnormalities rather than a definite hallmark of CVID or CVID-like hPIDs. However, the finding of mucus plugging mirrors more specifically the inflammation of large airways[9], with a reported prevalence in hPIDs ranging between 25% and 35%[9,17]. Last, air trapping was frequent (50%) in the subgroup of patients for whom an expiratory scan was available. Although incomplete, the prevalence we describe is in the range of those previously reported in CVID patients (45%-63%)[9,17,25].

Concerning the less frequent HRCT findings, we detected tree-in-bud abnormalities in 19% of the patients, similarly to what reported by Tanaka *et al*[25] (20%) in a study assessing a CVID population. This sign reflects a spectrum of both endobronchiolar and peribronchiolar disorders[24]. The main causes of tree-in-bud findings in the general population are reported to be acute or chronic infections mainly from nontuberculous mycobacteria and bacteria (*e.g.*, *Staphylococcus aureus* and *Pseudomonas aeruginosa*)[32,33]. Previous studies demonstrated the presence of potentially pathogenic bacteria (and viruses) in the lungs of patients with clinically stable hPIDs[34]. In our series, most of the tree-in-bud cases were of infectious origin, albeit asymptomatic, at the time of HRCT. The majority of these patients (80%) showed coexisting bronchiectasis, a major predisposing factor for infections[32]. Follicular bronchiolitis (FB) is another cause of tree-in-bud sign detected at HRCT[35,36]. FB is a reactive pulmonary lymphoid disorder reported in CVID patients, is presumably related to recurrent pneumonia, and is characterized by the development of lymphoid follicles and germinal centres with peribronchial/peribronchiolar distribution[37]. In our population, 2 of the 10 cases with tree-in-bud abnormalities were CVID patients who developed GLILD, a condition in which FB is a typical finding[38,39]. In addition, consolidation was found in 27% of our study population (*vs* 17%-64% reported in the literature) and ground-glass opacities in 25% of the patients (*vs* 12%-34% in the literature)[9,10,17,25]. Although the nature of most of these abnormalities remained undetermined, it is likely that they represent the effects of subclinical or previous infections, thus not requiring specific radiological work-up in the absence of clinical suspicion of lymphoma or cancer.

In patients with CVID, HRCT was proven to detect silent progression earlier than PFTs, because of its capability to assess even subtle structural abnormalities[34,40]. Not surprisingly, alterations detected by PFTs are less frequent than those detected by HRCT[40], an observation confirmed in our study that also includes CVID-like patients (prevalence was 48.1% by PFTs *vs* 90.4% by HRCT). This observation raises some questions on how to follow up the patient after baseline evaluation. Current recommendations suggest PFTs intervals of 6-12 mo, and HRCT intervals ranging from 1 to 5 years[11,17]. By multivariate analysis, we found that detection of tree-in-bud abnormalities predicts obstructive defects (OR 18.75), and detection of linear and/or irregular opacities predicts restrictive defects (OR 13.00). By contrast, none of the other, more frequent findings were independent predictors of obstructive or restrictive defects. This observation supports previous data on CVID showing a moderate correlation between PFTs and HRCT results, as well as the idea that these

Table 2 Prevalence of high-resolution computed tomography-detected abnormalities in the two humoral primary immunodeficiencies subtypes (CVID and CVID-like), and comparison between the two groups *n* (%)

Abnormality	All patients *n* = 52	CVID *n* = 38	CVID-like *n* = 14	*P*-value (CVID *vs* CVID-like)
Airway abnormalities				
Bronchiectasis	36 (69.2)	27 (71)	9 (64.3)	0.8964
Airway wall thickening	37 (71.2)	27 (71)	10 (71.4)	0.7501
Tree-in-bud	10 (19.2)	6 (15.8)	4 (28.6)	0.8464
Mucus plugging	23 (44.2)	16 (42.1)	7 (50)	0.8888
Air trapping[1]	16 (50)	12 (52.2)	4 (44.4)	0.8557
Parenchymal-interstitial abnormalities				
Consolidation	14 (26.9)	11 (28.9)	3 (21.4)	0.8495
Ground-glass opacity	13 (25)	12 (31.6)	1 (7.1)	0.1487
Nodules	26 (50)	19 (50)	7 (50)	1
Linear and/or irregular opacities	12 (23.1)	12 (31.6)	0 (0)[a]	0.0427
Bullae/cysts	5 (9.6)	5 (13.2)	0 (0)	0.3695

[a]P <0.05.
[1]Values are calculated on the 32 patients (23 CVID + 9 CVID-like) for whom additional expiratory scan was acquired. Chi-square test: CVID *vs* CVID-like patients; CVID: Common variable immunodeficiency disorders; CVID-like: Including isolated IgG subclass deficiency and selective IgA deficiency.

two examinations assess different aspects of the disease[40]. Of note, Maarschalk-Ellerbroek *et al*[17] found a poor correlation between detection of tree-in-bud abnormalities and PFTs. However, these authors evaluated tree-in-bud abnormalities in a combined score with mucus plugging, which impairs a direct comparison with our findings. Our results suggest that morphological assessment with HCRT might be postponed as much as possible to maximize cost-effectiveness and reduce radiation exposure. A possible exception to this might be the case of patients showing tree-in-bud or linear and/or irregular opacities: scheduling HRCTs at shorter intervals for these patients might provide a reliable morphological counterpart of pulmonary function. Our hypothesis is extrapolated from the observation of baseline examinations in our population; therefore, further studies with a more specific purpose and a prospective design should be performed to confirm this statement.

We acknowledge that our study has some limitations. First, an HRCT supplementary expiratory scan was not available in 38% of the patients because of the retrospective nature of the study. Hence, we were not able to include air trapping as a variable in the logistic regression analysis to predict PFTs results. Previous studies found a significant correlation between air trapping and airway obstruction both in children and in adult patients with CVID[9,20]. While we acknowledge that we should have included air trapping to study both CVID and CVID-like groups, we believe that most of the relevant HRCT findings support our conclusions. Second, we did not consider the extent and/or distribution of individual HRCT findings in the prediction analysis of PFTs results. The use of dedicated HRCT scoring systems, which were originally developed for CVID patients and/or for paediatric populations only, could help studying this issue also in adult patients with CVID and CVID-like conditions[9,17,18,20]. Third, we were not able to assess the radiologic evolution of the disease over time because of the lack of previous HRCTs, which could have been used for a comparison with the baseline HRCT. However, our study actually reflects the clinical reality, in which a delay between the onset of respiratory infections-related symptoms and the definite diagnosis of hPIDs is common (median of 8 years in adults aged over 30 years old, according to The United Kingdom Primary Immunodeficiency Registry)[41]. In this scenario, the first HRCT is frequently performed only at the time of diagnosis.

In conclusion, we found no significant difference in the prevalence of most of HRCT findings or PFTs abnormalities between CVID and CVID-like conditions. Our results support the hypothesis that these two conditions are comparable hPIDs subtypes and candidate to similar management. The detection of tree-in-bud abnormalities was found to be an independent predictor of obstructive defects assessed at PFTs, while the detection of linear and/or irregular opacities was an independent predictor of restrictive defects assessed at PFTs. Our observations suggest that patients showing these findings might benefit from more frequent HRCTs during follow-up as to evaluate the morphological abnormalities associated with their function impairment.

Table 3 Distribution of high-resolution computed tomography-detected airway abnormalities according to the severity of obstructive defect at pulmonary function tests in the overall study population, and results of logistic regression analysis for prediction of moderate-to-severe obstructive defects at PFTs *n* (%)

Abnormality	Absent	Mild	Moderate	Severe	Univariate analysis	Multivariate analysis
	n = 29	*n* = 12	*n* = 9	*n* = 2	*P*-value	*P*-value (odds ratio)
Bronchiectasis	19 (66.5)	9 (75)	7 (77.8)	1 (50)	NS	NS
Airway wall thickening	20 (69)	9 (75)	6 (66.7)	2 (100)	NS	NS
Tree-in-bud	2 (6.9)	2 (16.7)	5 (55.6)	1 (50)	0.0014	0.0027 (18.75)
Mucus plugging	8 (27.6)	8 (66.7)	5 (55.6)	2 (100)	0.0112	NS

NS: Non-significant.

Table 4 Distribution of high-resolution computed tomography-detected parenchymal-interstitial abnormalities according to the severity of the restrictive defects at pulmonary function tests in the overall study population, and results of logistic regression analysis for prediction of moderate-to-severe restrictive defects at PFTs *n* (%)

Abnormality	Absent	Mild	Moderate	Severe	Univariate analysis	Multivariate analysis
	n = 47	*n* = 1	*n* = 4	*n* = 0	*P*-value	*P*-value (odds ratio)
Consolidation	11 (23.4)	1 (100)	2 (50)	0 (0)	NS	NS
Ground-glass opacity	10 (21.3)	1 (100)	2 (50)	0 (0)	NS	NS
Nodules	23 (48.9)	1 (100)	2 (50)	0 (0)	NS	NS
Linear and/or irregular opacities	8 (17)	1 (100)	3 (75)	0 (0)	0.0029	0.0344
Bullae/cysts	5 (10.6)	0 (0)	0 (0)	0 (0)	NS	NS

NS: Non-significant.

Figure 2 Nodules. A 64-year-old female patient with common variable immunodeficiency disorder. High-resolution computed tomography shows multiple, small nodules with peribronchial and perifissural location in the upper and lower lobes of both lungs (arrows). A diagnosis of granulomatous and lymphocytic interstitial lung disease was subsequently made.

Figure 3 Mucus plugging. A 65-year-old male patient with common variable immunodeficiency disorder. Para-coronal 2-mm minimum intensity projection high-resolution computed tomography image shows mild bronchiectasis with extensive mucus plugging in the left lower lobe (arrow).

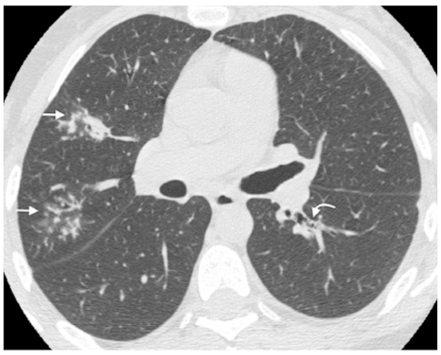

Figure 4 Tree-in-bud. A 40-year-old female patient with isolated IgG2 subclass deficiency. High-resolution computed tomography shows centrilobular and tree-in-bud nodules in the right upper lobe (straight arrows); small mucus plugging in the left lower lobe is also detected (curved arrow).

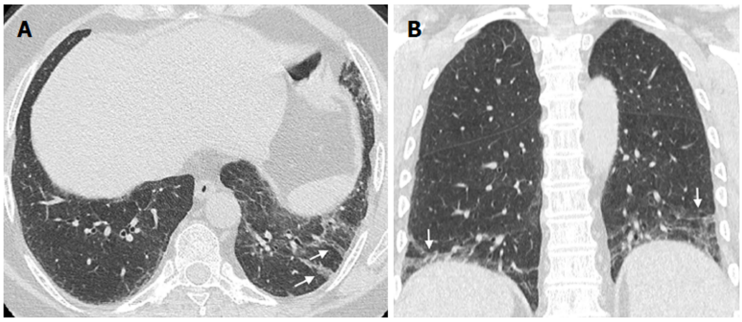

Figure 5 Linear and/or irregular opacities. A 66-year-old female patient with common variable immunodeficiency disorder. A: High-resolution computed tomography shows patchy areas of ground-glass opacity, along with reticulation and linear and/or irregular opacities (arrows) in both lower lobes; B: Coronal reformatted image shows the peripheral and basal-predominant distribution of the findings (arrows).

ARTICLE HIGHLIGHTS

Research background

Common variable immunodeficiency disorders (CVID) are the most clinically significant group of humoral primary immunodeficiency diseases (hPIDs), manifesting with recurrent respiratory tract infections and increased susceptibility to autoimmune diseases and malignancy. Other hPIDs are often termed "CVID-like" conditions, and include selective IgA deficiency and isolated IgG subclass deficiency. The initial evaluation of patients newly diagnosed with hPIDs should include high-resolution computed tomography (HRCT) and pulmonary function tests (PFTs).

Research motivation
To the best of our knowledge no previous studies assessed whether HRCT findings differ in terms of prevalence among the two subtypes of hPIDs in adult patients. Demonstrating a difference between CVID and CVID-like patients may influence the time intervals between HRCT examinations during follow-up in these 2 subgroups of hPIDs. Moreover, previous studies assessing a possible correlation between HRCT findings and PFTs results demonstrated contradictory results.

Research objectives
The purpose of this study was twofold: (1) to compare HRCT pulmonary findings in adult patients with different subgroups of hPIDs (*i.e.*, CVID *vs* CVID-like); and (2) to assess whether HRCT findings predict PFTs results.

Research methods
We included 52 adult patients (38 CVID and 14 CVID-like) who received a definite diagnosis of hPIDs and underwent HRCT and PFTs within one month from the time of diagnosis. One pulmonary radiologist, blinded to patient history and lung function: (1) reviewed the HRCT examinations; (2) recorded two classes of abnormalities, namely airway abnormalities and/or parenchymal-interstitial abnormalities; and (3) scored all abnormalities according to their extension and conspicuity. We calculated the per-patient prevalence of each HRCT abnormality in the overall population and in both subgroups of hPIDs patients, (CVID and CVID-like groups). We performed a logistic regression analysis to assess whether HRCT findings were predictive of a relevant obstructive or restrictive defect at PFTs on the overall study population.

Research results
Of the 52 hPIDs patients, 37 were females and 15 were males, with a mean age of 53.9 ± 12.7 years. We found a high prevalence of HRCT findings (90.4% patients had one or more abnormalities). The prevalence of each of the airway abnormalities considered was not significantly different between the CVID and CVID-like group. Regarding HRCT-detected parenchymal-interstitial abnormalities, the only relevant result was the finding of linear and/or irregular opacities, showing a prevalence of 31.6% in the CVID group and 0 in the CVID-like group, with borderline significance. The presence of tree-in-bud abnormalities was an independent predictor of obstructive defects at PFTs (Odds Ratio, OR, of 18.75, $P < 0.05$), while the presence of linear and/or irregular opacities was an independent predictor of restrictive defects at PFTs (OR = 13.00; $P < 0.05$).

Research conclusions
No previous research compared the prevalence of HRCT findings in different subtypes of hPIDs adult patients. After dividing hPIDs patients in CVID *vs* CVID-like groups, we observed no significant difference in the prevalence of most of airways and parenchymal-interstitial findings between the two groups. This observation supports the hypothesis that these two groups represent comparable hPIDs subtypes, and are candidate to similar management. Tree-in-bud and linear and/or irregular opacities were found to be independent predictors of, respectively, obstructive and restrictive defects on PFTs.

Research perspectives
Our results suggest that morphological assessment with HRCT might be delayed as much as possible to maximize cost-effectiveness and reduce radiation exposure. A possible exception to this might be the case of patients showing tree-in-bud or linear and/or irregular opacities: Scheduling HRCTs at shorter intervals for these patients might provide a reliable morphological counterpart of pulmonary function. Further prospective studies with a proper design are needed to confirm this hypothesis in the follow-up period.

ACKNOWLEDGMENTS

The authors thank Viviana Moroso of MV Medical Writing (Lulea, Sweden) for copyediting the manuscript, a service that was funded by Department of Medicine, University of Udine (Udine, Italy) in accordance with Good Publication Practice (GPP3) guidelines (http://www.ismpp.org/gpp3).

REFERENCES

1 **Bonilla FA**, Khan DA, Ballas ZK, Chinen J, Frank MM, Hsu JT, Keller M, Kobrynski LJ, Komarow HD, Mazer B. Practice parameter for the diagnosis and management of primary immunodeficiency. *J Allergy Clin Immunol* 2015; **136**: 1186-1205.e1-78 [PMID: 26371839 DOI: 10.1016/j.jaci.2015.04.049]
2 **Notarangelo LD**. Primary immunodeficiencies. *J Allergy Clin Immunol* 2010; **125**: S182-S194 [PMID: 20042228 DOI: 10.1016/j.jaci.2009.07.053]
3 Primary immunodeficiency diseases. Report of an IUIS Scientific Committee. International Union of Immunological Societies. *Clin Exp Immunol* 1999; **118** Suppl 1: 1-28 [PMID: 10540200 DOI: 10.1046/j.1365-2249.1999.00109.x]
4 **Picard C**, Bobby Gaspar H, Al-Herz W, Bousfiha A, Casanova JL, Chatila T, Crow YJ,

Cunningham-Rundles C, Etzioni A, Franco JL. International Union of Immunological Societies: 2017 Primary Immunodeficiency Diseases Committee Report on Inborn Errors of Immunity. *J Clin Immunol* 2018; **38**: 96-128 [PMID: 29226302 DOI: 10.1007/s10875-017-0464-9]
5 **Resnick ES**, Moshier EL, Godbold JH, Cunningham-Rundles C. Morbidity and mortality in common variable immune deficiency over 4 decades. *Blood* 2012; **119**: 1650-1657 [PMID: 22180439 DOI: 10.1182/blood-2011-09-377945]
6 **Tam JS**, Routes JM. Common variable immunodeficiency. *Am J Rhinol Allergy* 2013; **27**: 260-265 [PMID: 23883805 DOI: 10.2500/ajra.2013.27.3899]
7 **Janzi M**, Kull I, Sjöberg R, Wan J, Melén E, Bayat N, Ostblom E, Pan-Hammarström Q, Nilsson P, Hammarström L. Selective IgA deficiency in early life: association to infections and allergic diseases during childhood. *Clin Immunol* 2009; **133**: 78-85 [PMID: 19541543 DOI: 10.1016/j.clim.2009.05.014]
8 **Palmer DS**, O'Toole J, Montreuil T, Scalia V, Yi QL, Goldman M, Towns D. Screening of Canadian Blood Services donors for severe immunoglobulin A deficiency. *Transfusion* 2010; **50**: 1524-1531 [PMID: 20158683 DOI: 10.1111/j.1537-2995.2010.02588.x]
9 **Gregersen S**, Aaløkken TM, Mynarek G, Kongerud J, Aukrust P, Frøland SS, Johansen B. High resolution computed tomography and pulmonary function in common variable immunodeficiency. *Respir Med* 2009; **103**: 873-880 [PMID: 19181508 DOI: 10.1016/j.rmed.2008.12.015]
10 **Bondioni MP**, Duse M, Plebani A, Soresina A, Notarangelo LD, Berlucchi M, Grazioli L. Pulmonary and sinusal changes in 45 patients with primary immunodeficiencies: computed tomography evaluation. *J Comput Assist Tomogr* 2007; **31**: 620-628 [PMID: 17882044 DOI: 10.1097/RCT.0b013e31802e3c11]
11 **Verma N**, Grimbacher B, Hurst JR. Lung disease in primary antibody deficiency. *Lancet Respir Med* 2015; **3**: 651-660 [PMID: 26188881 DOI: 10.1016/S2213-2600(15)00202-7]
12 **Hurst JR**, Workman S, Garcha DS, Seneviratne SL, Haddock JA, Grimbacher B. Activity, severity and impact of respiratory disease in primary antibody deficiency syndromes. *J Clin Immunol* 2014; **34**: 68-75 [PMID: 24136152 DOI: 10.1007/s10875-013-9942-x]
13 **Bierry G**, Boileau J, Barnig C, Gasser B, Korganow AS, Buy X, Jeung MY, Roy C, Gangi A. Thoracic manifestations of primary humoral immunodeficiency: a comprehensive review. *Radiographics* 2009; **29**: 1909-1920 [PMID: 19926753 DOI: 10.1148/rg.297095717]
14 **Hampson FA**, Chandra A, Screaton NJ, Condliffe A, Kumararatne DS, Exley AR, Babar JL. Respiratory disease in common variable immunodeficiency and other primary immunodeficiency disorders. *Clin Radiol* 2012; **67**: 587-595 [PMID: 22226567 DOI: 10.1016/j.crad.2011.10.028]
15 **Cereser L**, Girometti R, d'Angelo P, De Carli M, De Pellegrin A, Zuiani C. Humoral primary immunodeficiency diseases: clinical overview and chest high-resolution computed tomography (HRCT) features in the adult population. *Clin Radiol* 2017; **72**: 534-542 [PMID: 28433201 DOI: 10.1016/j.crad.2017.03.018]
16 **Bang TJ**, Richards JC, Olson AL, Groshong SD, Gelfand EW, Lynch DA. Pulmonary Manifestations of Common Variable Immunodeficiency. *J Thorac Imaging* 2018; **33**: 377-383 [PMID: 30067570 DOI: 10.1097/RTI.0000000000000350]
17 **Maarschalk-Ellerbroek LJ**, de Jong PA, van Montfrans JM, Lammers JW, Bloem AC, Hoepelman AI, Ellerbroek PM. CT screening for pulmonary pathology in common variable immunodeficiency disorders and the correlation with clinical and immunological parameters. *J Clin Immunol* 2014; **34**: 642-654 [PMID: 24952009 DOI: 10.1007/s10875-014-0068-6]
18 **van de Ven AA**, van Montfrans JM, Terheggen-Lagro SW, Beek FJ, Hoytema van Konijnenburg DP, Kessels OA, de Jong PA. A CT scan score for the assessment of lung disease in children with common variable immunodeficiency disorders. *Chest* 2010; **138**: 371-379 [PMID: 20299624 DOI: 10.1378/chest.09-2398]
19 **van de Ven AA**, de Jong PA, Hoytema van Konijnenburg DP, Kessels OA, Boes M, Sanders EA, Terheggen-Lagro SW, van Montfrans JM. Airway and interstitial lung disease are distinct entities in paediatric common variable immunodeficiency. *Clin Exp Immunol* 2011; **165**: 235-242 [PMID: 21635229 DOI: 10.1111/j.1365-2249.2011.04425.x]
20 **van Zeggeren L**, van de Ven AA, Terheggen-Lagro SW, Mets OM, Beek FJ, van Montfrans JM, de Jong PA. High-resolution computed tomography and pulmonary function in children with common variable immunodeficiency. *Eur Respir J* 2011; **38**: 1437-1443 [PMID: 21659412 DOI: 10.1183/09031936.00173410]
21 European Society for Immunodeficiencies Registry Working Party. Working definitions for clinical diagnosis of PID. Available from: http://esid.org/Working-Parties/Registry/Diagnosis-criteria
22 **Miller MR**, Hankinson J, Brusasco V, Burgos F, Casaburi R, Coates A, Crapo R, Enright P, van der Grinten CP, Gustafsson P. Standardisation of spirometry. *Eur Respir J* 2005; **26**: 319-338 [PMID: 16055882 DOI: 10.1183/09031936.05.00034805]
23 **Pellegrino R**, Viegi G, Brusasco V, Crapo RO, Burgos F, Casaburi R, Coates A, van der Grinten CP, Gustafsson P, Hankinson J. Interpretative strategies for lung function tests. *Eur Respir J* 2005; **26**: 948-968 [PMID: 16264058 DOI: 10.1183/09031936.05.00035205]
24 **Hansell DM**, Bankier AA, MacMahon H, McLoud TC, Müller NL, Remy J. Fleischner Society: glossary of terms for thoracic imaging. *Radiology* 2008; **246**: 697-722 [PMID: 18195376 DOI: 10.1148/radiol.2462070712]
25 **Tanaka N**, Kim JS, Bates CA, Brown KK, Cool CD, Newell JD, Lynch DA. Lung diseases in patients with common variable immunodeficiency: chest radiographic, and computed tomographic findings. *J Comput Assist Tomogr* 2006; **30**: 828-838 [PMID: 16954938 DOI: 10.1097/01.rct.0000228163.08968.26]
26 **Thickett KM**, Kumararatne DS, Banerjee AK, Dudley R, Stableforth DE. Common variable immune deficiency: respiratory manifestations, pulmonary function and high-resolution CT scan findings. *QJM* 2002; **95**: 655-662 [PMID: 12324637 DOI: 10.1093/qjmed/95.10.655]
27 **Martínez García MA**, de Rojas MD, Nauffal Manzur MD, Muñoz Pamplona MP, Compte Torrero L, Macián V, Perpiñá Tordera M. Respiratory disorders in common variable immunodeficiency. *Respir Med* 2001; **95**: 191-195 [PMID: 11266236 DOI: 10.1053/rmed.2000.1020]
28 **Aghamohammadi A**, Allahverdi A, Abolhassani H, Moazzami K, Alizadeh H, Gharagozlou M,

Kalantari N, Sajedi V, Shafiei A, Parvaneh N. Comparison of pulmonary diseases in common variable immunodeficiency and X-linked agammaglobulinaemia. *Respirology* 2010; **15**: 289-295 [PMID: 20051045 DOI: 10.1111/j.1440-1843.2009.01679.x]

29 **van de Ven AA**, van de Corput L, van Tilburg CM, Tesselaar K, van Gent R, Sanders EA, Boes M, Bloem AC, van Montfrans JM. Lymphocyte characteristics in children with common variable immunodeficiency. *Clin Immunol* 2010; **135**: 63-71 [PMID: 20006554 DOI: 10.1016/j.clim.2009.11.010]

30 **Sweinberg SK**, Wodell RA, Grodofsky MP, Greene JM, Conley ME. Retrospective analysis of the incidence of pulmonary disease in hypogammaglobulinemia. *J Allergy Clin Immunol* 1991; **88**: 96-104 [PMID: 2071789 DOI: 10.1016/0091-6749(91)90306-9]

31 **Berger M**, Geng B, Cameron DW, Murphy LM, Schulman ES. Primary immune deficiency diseases as unrecognized causes of chronic respiratory disease. *Respir Med* 2017; **132**: 181-188 [PMID: 29229095 DOI: 10.1016/j.rmed.2017.10.016]

32 **Miller WT Jr**, Panosian JS. Causes and imaging patterns of tree-in-bud opacities. *Chest* 2013; **144**: 1883-1892 [PMID: 23948769 DOI: 10.1378/chest.13-1270]

33 **Rossi SE**, Franquet T, Volpacchio M, Giménez A, Aguilar G. Tree-in-bud pattern at thin-section CT of the lungs: radiologic-pathologic overview. *Radiographics* 2005; **25**: 789-801 [PMID: 15888626 DOI: 10.1148/rg.253045115]

34 **Kainulainen L**, Nikoskelainen J, Vuorinen T, Tevola K, Liippo K, Ruuskanen O. Viruses and bacteria in bronchial samples from patients with primary hypogammaglobulinemia. *Am J Respir Crit Care Med* 1999; **159**: 1199-1204 [PMID: 10194166 DOI: 10.1164/ajrccm.159.4.9807067]

35 **Gosset N**, Bankier AA, Eisenberg RL. Tree-in-bud pattern. *AJR Am J Roentgenol* 2009; **193**: W472-W477 [PMID: 19933620 DOI: 10.2214/AJR.09.3401]

36 **Tashtoush B**, Okafor NC, Ramirez JF, Smolley L. Follicular Bronchiolitis: A Literature Review. *J Clin Diagn Res* 2015; **9**: OE01-OE05 [PMID: 26500941 DOI: 10.7860/JCDR/2015/13873.6496]

37 **Camarasa Escrig A**, Amat Humaran B, Sapia S, León Ramírez JM. Follicular bronchiolitis associated with common variable immunodeficiency. *Arch Bronconeumol* 2013; **49**: 166-168 [PMID: 22963957 DOI: 10.1016/j.arbres.2012.06.007]

38 **Bates CA**, Ellison MC, Lynch DA, Cool CD, Brown KK, Routes JM. Granulomatous-lymphocytic lung disease shortens survival in common variable immunodeficiency. *J Allergy Clin Immunol* 2004; **114**: 415-421 [PMID: 15316526 DOI: 10.1016/j.jaci.2004.05.057]

39 **Tashtoush B**, Memarpour R, Ramirez J, Bejarano P, Mehta J. Granulomatous-lymphocytic interstitial lung disease as the first manifestation of common variable immunodeficiency. *Clin Respir J* 2018; **12**: 337-343 [PMID: 27243233 DOI: 10.1111/crj.12511]

40 **Touw CM**, van de Ven AA, de Jong PA, Terheggen-Lagro S, Beek E, Sanders EA, van Montfrans JM. Detection of pulmonary complications in common variable immunodeficiency. *Pediatr Allergy Immunol* 2010; **21**: 793-805 [PMID: 19912551 DOI: 10.1111/j.1399-3038.2009.00963.x]

41 **Edgar JD**, Buckland M, Guzman D, Conlon NP, Knerr V, Bangs C, Reiser V, Panahloo Z, Workman S, Slatter M. The United Kingdom Primary Immune Deficiency (UKPID) Registry: report of the first 4 years' activity 2008-2012. *Clin Exp Immunol* 2014; **175**: 68-78 [PMID: 23841717 DOI: 10.1111/cei.12172]

P- Reviewer: Bazeed MF, Chow J, Gao BL, Lacalzada-Almeida J, Tang GH

S- Editor: Ji FF **L- Editor:** A **E- Editor:** Huang Y

Published By Baishideng Publishing Group Inc
7901 Stoneridge Drive, Suite 501, Pleasanton, CA 94588, USA
Telephone: +1-925-2238242
Fax: +1-925-2238243
E-mail: bpgoffice@wjgnet.com
Help Desk: https://www.f6publishing.com/helpdesk
https://www.wjgnet.com

ISSN 1949-8470 (online)

World Journal of *Radiology*

World J Radiol 2018 December 28; 10(12): 184-189

Published by Baishideng Publishing Group Inc

WJR

World Journal of Radiology

Contents

Monthly Volume 10 Number 12 December 28, 2018

ORIGINAL ARTICLE

Retrospective Cohort Study

Contents

World Journal of Radiology

Volume 10 Number 12 December 28, 2018

ABOUT COVER

Editorial Board Member of *World Journal of Radiology*, Edward Araujo Júnior, PhD, Associate Professor, Department of Obstetrics, Paulista School of Medicine - Federal University of Sao Paulo, São Paulo 05089-030, SP, Brazil

AIMS AND SCOPE

World Journal of Radiology (*World J Radiol*, *WJR*, online ISSN 1949-8470, DOI: 10.4329) is a peer-reviewed open access academic journal that aims to guide clinical practice and improve diagnostic and therapeutic skills of clinicians.

WJR covers topics concerning diagnostic radiology, radiation oncology, radiologic physics, neuroradiology, nuclear radiology, pediatric radiology, vascular/interventional radiology, medical imaging achieved by various modalities and related methods analysis. The current columns of *WJR* include editorial, frontier, diagnostic advances, therapeutics advances, field of vision, mini-reviews, review, topic highlight, medical ethics, original articles, case report, clinical case conference (clinicopathological conference), and autobiography.

We encourage authors to submit their manuscripts to *WJR*. We will give priority to manuscripts that are supported by major national and international foundations and those that are of great basic and clinical significance.

INDEXING/ABSTRACTING

World Journal of Radiology is now abstracted and indexed in Emerging Sources Citation Index (Web of Science), PubMed, PubMed Central, China National Knowledge Infrastructure (CNKI), and Superstar Journals Database.

RESPONSIBLE EDITORS FOR THIS ISSUE

Responsible Electronic Editor: *Ying-Na Bian* **Proofing Editorial Office Director:** *Jin-Lei Wang*

NAME OF JOURNAL
World Journal of Radiology

ISSN
ISSN 1949-8470 (online)

LAUNCH DATE
January 31, 2009

FREQUENCY
Monthly

EDITORS-IN-CHIEF
Neeraj Lalwani

EDITORIAL BOARD MEMBERS
https://www.wjgnet.com/1949-8470/editorialboard.htm

EDITORIAL OFFICE
Jin-Lei Wang, Director

PUBLICATION DATE
December 28, 2018

INSTRUCTIONS TO AUTHORS
https://www.wjgnet.com/bpg/gerinfo/204

GUIDELINES FOR ETHICS DOCUMENTS
https://www.wjgnet.com/bpg/GerInfo/287

GUIDELINES FOR NON-NATIVE SPEAKERS OF ENGLISH
https://www.wjgnet.com/bpg/gerinfo/240

PUBLICATION MISCONDUCT
https://www.wjgnet.com/bpg/gerinfo/208

ARTICLE PROCESSING CHARGE
https://www.wjgnet.com/bpg/gerinfo/242

STEPS FOR SUBMITTING MANUSCRIPTS
https://www.wjgnet.com/bpg/GerInfo/239

ONLINE SUBMISSION
https://www.f6publishing.com

World Journal of Radiology

Submit a Manuscript: https://www.f6publishing.com

World J Radiol 2018 December 28; 10(12): 184-189

DOI: 10.4329/wjr.v10.i12.184

ISSN 1949-8470 (online)

ORIGINAL ARTICLE

Retrospective Cohort Study

Management of computed tomography scan detected hemothorax in blunt chest trauma: What computed tomography scan measurements say?

Mahdi Malekpour, Kenneth Widom, James Dove, Joseph Blansfield, Mohsen Shabahang, Denise Torres, Jeffrey L Wild

ORCID number: Mahdi Malekpour (0000-0002-7337-3479); Kenneth Widom (0000-0003-1806-8524); James Dove (0000-0002-5673-5394); Joseph Blansfield (0000-0002-1652-3274); Mohsen Shabahang (0000-0002-7227-3636); Denise Torres (0000-0003-0004-3257); Jeffrey L Wild (0000-0002-1999-4311).

Author contributions: Malekpour M, Shabahang M and Wild JL designed of the Study; Malekpour M, Dove J and Blansfield J collected data; Widom K and Torres D analyzed the data; Malekpour M, Widom K, Dove J, Blansfield J, Shabahang M, Torres D and Wild JL prepared the draft and finalized the manuscript.

Institutional review board statement: Approved by Geisinger Institutional Review Board under the IRB # 2014-0533.

Informed consent statement: Due to anonymity of this research, patients were not required to provide a separate consent form as being approved by IRB of Geiringer Medical Center.

Conflict-of-interest statement: Authors included in this study have no conflict-of-interest and nothing to disclose.

Data sharing statement: No patient identification data is included in this article.

Mahdi Malekpour, Kenneth Widom, James Dove, Joseph Blansfield, Mohsen Shabahang, Denise Torres, Jeffrey L Wild, Department of Surgery, Section of Trauma and Acute Care Surgery, Geisinger Medical Center, Danville, PA 17822, United States

Corresponding author to: Jeffrey L Wild, MD, Doctor, Staff Physician, Surgeon, Department of Surgery, Section of Trauma and Acute Care Surgery, Geisinger Medical Center, 100 North Academy Avenue, MC 21-69, Danville, PA 17822, United States. jlwild@geisinger.edu
Telephone: +1-570-2716361
Fax: +1-570-2717165

Abstract

AIM

To investigate the hemothorax size for which tube thoracostomy is necessary.

METHODS

Over a 5-year period, we included all patients who were admitted with blunt chest trauma to our level 1 trauma center. Focus was placed on identifying the hemothorax size requiring tube thoracostomy.

RESULTS

A total number of 274 hemothoraces were studied. All patients with hemothoraces measuring above 3 cm received a chest tube. The 50% predicted probability of tube thoracostomy was 2 cm. Pneumothorax was associated with odds of receiving tube thoracostomy for hemothoraces below 2 cm (Odds Ratio: 4.967, 95%CI: 2.225-11.097, $P < 0.0001$).

CONCLUSION

All patients with a hemothorax size greater than 3% underwent tube thoracostomy. Prospective studies are warranted to elucidate the clinical outcome of patients with smaller hemothoraces.

Key words: Chest trauma; Blunt; Hemothorax; Chest tube; Occult; Computed tomography scan

Manuscript source: Invited manuscript

Received: June 5, 2018
Peer-review started: June 5, 2018
First decision: July 27, 2018
Revised: September 17, 2018
Accepted: November 24, 2018
Article in press: November 24, 2018
Published online: December 28, 2018

Core tip: There is no clear recommendation for tube thoracostomy in hemothorax management based on computed tomography scan measurements. In this study, we found that any hemothoraces above the cut-off size of 3 cm should be drained using tube thoracostomy. Smaller hemothoraces may warrant drainage based on other findings such as presence of pneumothorax.

Malekpour M, Widom K, Dove J, Blansfield J, Shabahang M, Torres D, Wild JL. Management of computed tomography scan detected hemothorax in blunt chest trauma: What computed tomography scan measurements say?*World J Radiol* 2018; 10(12): 184-189
URL: https://www.wjgnet.com/1949-8470/full/v10/i12/184.htm
DOI: https://dx.doi.org/10.4329/wjr.v10.i12.184

INTRODUCTION

Blunt chest trauma is commonly encountered in the emergency department as an individual presentation or part of the clinical scenario of a trauma patient[1]. According to the 2012 National Trauma Data Bank (NTDB) Research Data Set, 738396 patients with available Abbreviated Injury Scale were admitted nationwide. Patients with chest trauma constituted 87387 (11.8%) of the registered patients among which, 73809 (84.5% of chest trauma patients) had blunt chest trauma and 12200 (16.5% of blunt chest trauma patients) had hemothorax (Committee on Trauma, American College of Surgeons. NTDB 2012. Chicago, IL).

Although hemothorax is managed by tube thoracostomy in hemodynamically unstable and critical patients after initial chest/pelvic x-ray and focused assessment with sonography in trauma (FAST), virtually all stable blunt trauma patients undergo chest computed tomography (CT) scan as part of their trauma workup[2]. This is partially due to higher sensitivity of chest CT imaging in detecting pneumothorax, hemothorax and pulmonary contusions along with suboptimal imaging preparation and positioning for supine chest radiography in the acute setting[3]. Tube thoracostomy is an invasive procedure which can lead to immediate procedural injuries, infections, and pain, which can contribute to respiratory failure in patients with chest wall injury. Patients with hemothoraces managed without chest tube can lead to infections and trapped lung. Therefore, it is clinically important to know which patients should receive a chest tube.

At the advent of helical CT scanning, chest CT scan was reserved for cases where chest radiography had uncertain and equivocal results. Hence, up to 30% of blunt trauma patients had their hemothoraces identified on chest CT images, which were not readily identifiable on plain chest X-rays, a.k.a. occult hemothorax[4-6]. Thanks to fairly universal application of chest CT in assessment of blunt chest trauma patients, "occult hemothorax" is not practically occult anymore. In fact, the previously published research papers on occult hemothorax have included hemothoraces that are undoubtedly within the identification range of chest radiography[6,7]. In addition, these studies have included extrapolations from plain radiography studies as their cutoff value, primarily due to the absence of existing studies focusing on chest CT measurements[6-9].

In this study, we investigated the association between the measured size of hemothoraces on chest CT images and the likelihood of tube thoracostomy in an attempt to identify a CT scan-based cutoff value of chest tube placement in blunt chest trauma patients.

MATERIALS AND METHODS

Following the approval of the Institutional Review Board of Geisinger Medical Center, we retrospectively studied all patients with the diagnosis of hemothorax and blunt chest trauma that were admitted to our level I trauma center from the beginning of September 2009 to the end of August 2014. Excluded patients were those who were admitted after 24 h from the traumatic accident, patients who were admitted with a chest tube in place, those with chest tube placement before CT scan imaging, patients with chronic hemothorax and those with known pleural diseases. The decision to place a chest tube was based on the clinical judgement of the trauma surgeon for each

individual case.

We extracted demographic and clinical data including age, sex, Injury Severity Score (ISS), mechanism of injury, Glasgow Coma Score (GCS), pneumothorax, number of rib fractures, pulmonary contusion and aortic injury. These variables were used in multivariate analysis. Hemothorax was measured as the size (centimeters) of the deepest lamellar fluid stripe in the dependent pleural gutter on axial CT scan images (Figure 1).

Continuous variables were expressed as means ± SD. Non-parametric continuous data were expressed as median with inter-quartile range. Categorical data were expressed as frequencies (%). Logistic regression was used to analyze the predicted probability for tube thoracostomy. Logistic regression with stepwise selection was used to identify variables that increased the chance of tube thoracostomy. SAS 9.4 (SAS Institute, Cary NC) was used for statistical analyses and $P < 0.05$ was considered significant.

RESULTS

Over the 5-year study period, 271 patients were admitted with the diagnosis of hemothorax and blunt chest trauma. Forty-three patients were excluded and the analysis was performed on the remaining 228 patients. A total number 274 hemothoraces were included from 150 males and 78 females. Table 1 summarized the demographic data and the clinical findings of our patients. The mechanism of injury was predominantly fall (41%) and motor vehicle crash (38%). Patients had a mean ISS of 20 ± 11. Most patients (86%) had a mild GCS (13-15). The median number of rib fractures was 5 (3, 8) and pneumothorax was identified in 128 (56%) patients.

The median size of hemothorax was 1.4 cm (0.9, 2.4). As shown in Figure 2, using logistic regression, we plotted the chest tube insertion versus the measured size in the predicted probability graph. All patients with hemothoraces measuring above 3 cm underwent tube thoracostomy. We found that the probability of receiving a chest tube was more than 50% when the hemothorax measured more than 2.05 cm.

Logistic regression with stepwise selection was used to identify variables associated with odds of receiving a chest tube for hemothoraces < 2 cm. As table 2 summarizes, ISS and associated pneumothorax were associated with significantly higher odds of tube thoracostomy ($P = 0.004$ and $P < 0.0001$, respectively). In the 2-3 cm hemothorax range, between 14 patients who underwent tube thoracostomy, pneumothorax was not identified in two (14%). In the same hemothorax range, 15 patients did not receive a chest tube with pneumothorax absent in six (40%). In the remaining 9 patients (60%), pneumothoraces were radiographically identified as compromising less than 5% of the volume of the ipsilateral hemothorax.

DISCUSSION

We have reported the first study investigating the likelihood of tube thoracostomy based on the measurement of hemothoraces in chest CT scans of blunt chest trauma patients. We found that tube thoracostomy was performed in all patients with hemothoraces measuring more than 3 cm. We also found that the chance of tube thoracostomy was above 50% in patients with hemothoraces measuring above 2 cm; with pneumothorax significantly influencing the decision making. Although a few studies have investigated management of occult hemothorax and included the size in their analyses[6,7,10], they are primarily limited in founding their criteria on extrapolations of chest radiography measurements[8,9], which would highlight why our study was necessary.

The first study directly investigating chest tube placement in management of occult hemothorax was published in 2005 by Bilello *et al*[6] As the investigators stated, measurements and the 1.5 cm cutoff was set by extrapolation of pleural fluid measurements in chest radiography. Nearly half of the hemothoraces in this study were classified as moderate/large, which by definition, should have been identified in chest radiography and not be included in the study. The following year, another study was published by Stafford *et al*[10] on the incidence and management of occult hemothorax. In this study, the mean measurement of hemothorax in patients receiving chest tubes was close to 2 cm. More recently, the prospective study by Mahmood *et al*[7] in 2011 also reported 18% of the patients (the comparison group) to have measurements above 1.5 cm.

This discrepancy might be stemming from difficulty of extrapolation of chest radiography measurements into chest CT scan measurements. Some of the earlier

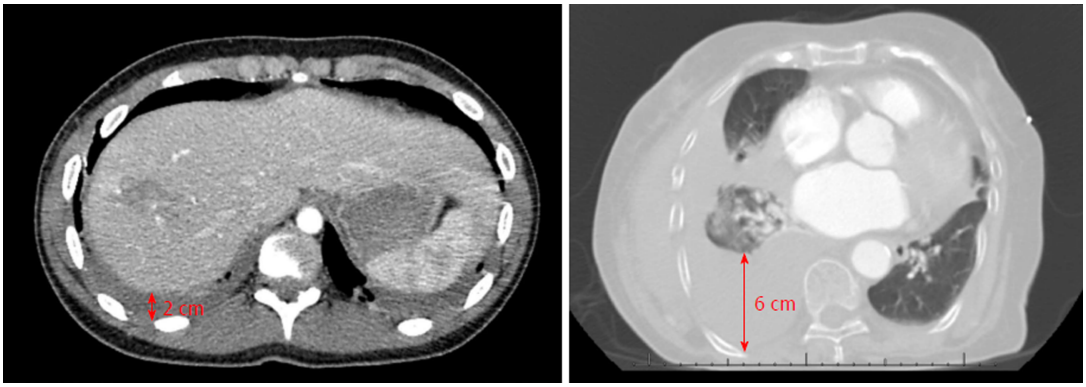

Figure 1 Representative computed tomography scan images of patients with hemothorax. Left: Abdominal window computed tomography (CT) scan showing a 2 cm right-side hemothorax in one patient; Right: Lung window CT scan showing a 6 cm right-side hemothorax in another patient.

chest X-ray measurements were based on lateral decubitus measurements rather than decubitus images[11]. In addition, chest X-ray fluid measurements propose a range of volumes rather than an exact number[8]. The need to have CT scan-based recommendations is also stemming from clinicians' inclination towards chest CT scan rather than relying on chest X-ray images. This inclination is scientifically supported by a very recent study showing that up to 71% of patients with blunt chest injury have some or all injuries identified only on chest CT scans[12]. This shows why there was a need for a study based on CT scan measurements alone.

Based on aforementioned literature, the term "occult hemothorax" might not be a clinically applicable name as almost all patients with blunt chest trauma would undergo chest CT scan, which is capable of picking smallest effusions. Hence, the term "small hemothorax" would better delineate the clinical picture as "overt hemothorax" (*i.e.*, large hemothoraces that are identified readily with FAST or chest X-ray) is the only practically true clinical entity that would undergo tube thoracostomy before chest CT imaging.

Our studied population is rather comparable to previously studied patients. In the Bilello *et al*[6] study, 78 patients with an average ISS close to 25 were included. Less than 40% of patients required tube thoracostomy[6]. The study of Stafford *et al*[10] included 88 patients with an average ISS of 20. Chest tubes were required in 48% of patients[10]. Lastly, the prospective study by Mahmood *et al*[7] included 81 patients with an average ISS of 18. Tube thoracostomy was required in only 17% of patients, which is probably reflecting the better job of a prospective study to include patients with smaller hemothoraces. Our study is thus far the largest study that includes 274 hemothoraces from 228 patients.

This study was limited by the operator-based measurements of hemothoraces. Availability or design of a computerized program to measure hemothorax would potentially eliminate this bias. Another limitation was stemming from the radiographic appearance of hemothorax, which does not always form a complete crescentic shape in trauma. Therefore, it is not always easy to define the deepest lamellar fluid stripe. A program that can measure the volume of the hemothorax rather than one single measurement of the thickness would overcome this limitation. Volumetric measurements have been used in other areas of medicine and would be a reachable goal in hemothorax studies[13,14]. Finally, our study was limited by the absence of tube thoracostomy criteria in small hemothoraces. Although the study was performed in a level I trauma center with well-trained trauma surgeons, the final decision of tube thoracostomy was made by the clinical judgement of the trauma surgeon. By expanding the study period over 5 years and including all patients, we tried to partially overcome this limitation. A prospective study including multiple centers with defined criteria for tube thoracostomy would overcome several of the limitations and would be a promising next-step to our current study.

In conclusion, based on chest CT scan measurements, patients with hemothoraces measuring above 3 cm required tube thoracostomy. Hemothoraces greater than 2 cm had more than 50% chance of receiving a chest tube. Further prospective studies are required to validate the cutoff and to investigate associations with outcomes.

Table 1 Demographic data

Variable	*n* (%)
Age (yr), (mean ± SD)	60.8 ± 19.5
Gender	
Female	78 (34)
Male	150 (66)
Mechanism of injury	
Fall	93 (41)
MCC	25 (11)
MVC	86 (38)
Other	21 (9)
Pedestrian struck	3 (1)
ISS (mean ± SD)	20 ± 11
GCS	
Severe	25 (11)
Moderate	6 (3)
Mild	197 (86)
Associated pneumothorax	128 (56)
Number of rib fractures, median (IQR)	5 (3, 8)
Pulmonary contusion	112 (49)
Aortic injuries	7 (3)
Size (cm) , median (IQR)	1.4 (0.9, 2.4)

MCC: Motor cycle crash; MVC: Motor vehicle crash; ISS: Injury severity score; GCS: Glasgow coma scale; SD: Standard deviation; IQR: Interquartile range.

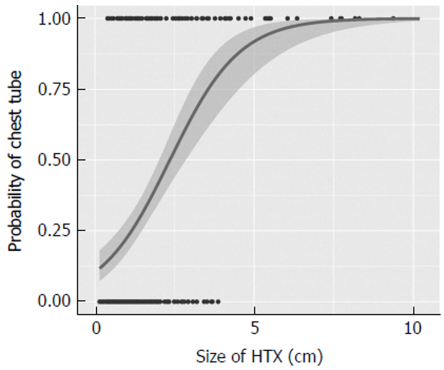

Figure 2 Predicted probability for tube thoracostomy. The x-axis is the size of hemothorax and the y-axis is the probability of chest tube placement, which is either zero (no chest tubes) or one (chest tube placed). Each black dot represents a patient with a corresponding hemothorax size.

ARTICLE HIGHLIGHTS

Research background

No definite recommendation exists on the size of hemothoraces that require drainage using tube thoracostomy.

Research motivation

Hemothoraces are prevalent findings in trauma patients, yet, no standard-of-care exists that identifies need for chest tube placement based on the size of the hemothorax.

Research objectives

Identifying the cut-off size for a hemothorax based on computed tomography findings that would warrant placement of a chest tube.

Research methods

Retrospective study of a trauma center database

Research results

Patients with hemothorax size over 3 cm received chest tube. In patients with smaller hemothoraces, presence of other findings such as pneumothorax warrants placement of chest tube.

Research conclusions

Tube thoracostomy should be performed in any trauma patient with a hemothorax size of greater than 3 cm.

Research perspectives

Findings are immediately applicable to the practice of trauma surgery at our center. It would also be beneficial for other subspecialties including emergency medicine, radiology and pulmonary medicine.

REFERENCES

1 **Karmy-Jones R**, Jurkovich GJ. Blunt chest trauma. *Curr Probl Surg* 2004; **41**: 211-380 [PMID: 15097979 DOI: 10.1016/j.cpsurg.2003.12.004]
2 **Barrios C Jr**, Pham J, Malinoski D, Dolich M, Lekawa M, Cinat M. Ability of a chest X-ray and an abdominal computed tomography scan to identify traumatic thoracic injury. *Am J Surg* 2010; **200**: 741-4; discussion 744-5 [PMID: 21146014 DOI: 10.1016/j.amjsurg.2010.08.004]
3 **Trupka A**, Waydhas C, Hallfeldt KK, Nast-Kolb D, Pfeifer KJ, Schweiberer L. Value of thoracic computed tomography in the first assessment of severely injured patients with blunt chest trauma: results of a prospective study. *J Trauma* 1997; **43**: 405-11; discussion 411-2 [PMID: 9314300 DOI: 10.1097/00005373-199709000-00003]
4 **Karaaslan T**, Meuli R, Androux R, Duvoisin B, Hessler C, Schnyder P. Traumatic chest lesions in patients with severe head trauma: a comparative study with computed tomography and conventional chest roentgenograms. *J Trauma* 1995; **39**: 1081-1086 [PMID: 7500398 DOI: 10.1097/00005373-199512000-00012]
5 **Omert L**, Yeaney WW, Protetch J. Efficacy of thoracic computerized tomography in blunt chest trauma. *Am Surg* 2001; **67**: 660-664 [PMID: 11450784]
6 **Bilello JF**, Davis JW, Lemaster DM. Occult traumatic hemothorax: when can sleeping dogs lie? *Am J Surg* 2005; **190**: 841-844 [PMID: 16307931 DOI: 10.1016/j.amjsurg.2005.05.053]
7 **Mahmood I**, Abdelrahman H, Al-Hassani A, Nabir S, Sebastian M, Maull K. Clinical management of occult hemothorax: a prospective study of 81 patients. *Am J Surg* 2011; **201**: 766-769 [PMID: 21741510 DOI: 10.1016/j.amjsurg.2010.04.017]
8 **Eibenberger KL**, Dock WI, Ammann ME, Dorffner R, Hörmann MF, Grabenwöger F. Quantification of pleural effusions: sonography versus radiography. *Radiology* 1994; **191**: 681-684 [PMID: 8184046 DOI: 10.1148/radiology.191.3.8184046]
9 **Ruskin JA**, Gurney JW, Thorsen MK, Goodman LR. Detection of pleural effusions on supine chest radiographs. *AJR Am J Roentgenol* 1987; **148**: 681-683 [PMID: 3493648 DOI: 10.2214/ajr.148.4.681]
10 **Stafford RE**, Linn J, Washington L. Incidence and management of occult hemothoraces. *Am J Surg* 2006; **192**: 722-726 [PMID: 17161082 DOI: 10.1016/j.amjsurg.2006.08.033]
11 **Moskowitz H**, Platt RT, Schachar R, Mellins H. Roentgen visualization of minute pleural effusion. An experimental study to determine the minimum amount of pleural fluid visible on a radiograph. *Radiology* 1973; **109**: 33-35 [PMID: 4783125 DOI: 10.1148/109.1.33]
12 **Langdorf MI**, Medak AJ, Hendey GW, Nishijima DK, Mower WR, Raja AS, Baumann BM, Anglin DR, Anderson CL, Lotfipour S. Prevalence and Clinical Import of Thoracic Injury Identified by Chest Computed Tomography but Not Chest Radiography in Blunt Trauma: Multicenter Prospective Cohort Study. *Ann Emerg Med* 2015; **66**: 589-600 [PMID: 26169926 DOI: 10.1016/j.annemergmed.2015.06.003]
13 **De Vis JB**, Zwanenburg JJ, van der Kleij LA, Spijkerman JM, Biessels GJ, Hendrikse J, Petersen ET. Cerebrospinal fluid volumetric MRI mapping as a simple measurement for evaluating brain atrophy. *Eur Radiol* 2016; **26**: 1254-1262 [PMID: 26318506 DOI: 10.1007/s00330-015-3932-8]
14 **Yan J**, Schwartz LH, Zhao B. Semiautomatic segmentation of liver metastases on volumetric CT images. *Med Phys* 2015; **42**: 6283-6293 [PMID: 26520721 DOI: 10.1118/1.4932365]

P- Reviewer: Akbulut S, Sergi CM, Kai K
S- Editor: Wang JL **L- Editor:** A **E- Editor:** Bian YN

Published By Baishideng Publishing Group Inc
7901 Stoneridge Drive, Suite 501, Pleasanton, CA 94588, USA
Telephone: +1-925-2238242
Fax: +1-925-2238243
E-mail: bpgoffice@wjgnet.com
Help Desk: https://www.f6publishing.com/helpdesk
https://www.wjgnet.com